The Nature and Evolution of I. Extragalactic Radio Sources, and II. Young Stellar Clusters

by

André B. Fletcher

B.Sc. Physics (Hons), University of Sydney, 1988

Submitted to the Department of Physics
in partial fulfillment of the requirements for the degree of

Doctor of Philosophy in Physics

at the

MASSACHUSETTS INSTITUTE OF TECHNOLOGY

January 1998

Author .....
Department of Physics
January 30, 1998

Certified by .....
Bernard F. Burke
Professor of Astrophysics
Thesis Supervisor

Accepted by .....
George F. Koster
Chairman, Graduate Committee

The Nature and Evolution of
I. Extragalactic Radio Sources, and
II. Young Stellar Clusters

by

André B. Fletcher

Submitted to the Department of Physics
on January 30, 1998, in partial fulfillment of the
requirements for the degree of
Doctor of Philosophy in Physics

Abstract

This thesis is an investigation into the nature and evolution of two distinct classes of astrophysical object, believed to be initially powered by gravitational accretion: extragalactic radio sources, and stars in young stellar clusters. Using the VLA interferometer, the MIT group has observed ~10,000 radio sources in the past 15 years. One goal of this thesis is to extend the MIT gravitational lens search into the Southern Hemisphere via VLA imaging of 1750 Parkes-MIT-NRAO survey sources. I document the observations, reduction and results from 17 years of MIT radio & optical surveys. I have organized the data into an archive. I present new MIT-VLA lens candidates, a large sample of Compact Steep Spectrum close doubles, and observations of both an unusual radio ring galaxy and a binary quasar. From my extraction of the angular size distribution for 4741 MIT-VLA sources, I find that the mean jet advance speed is non-relativistic, given reasonable assumptions about jet ages. I conclude Part I by proposing a unified model for extragalactic radio sources, based in part on my derivation of general mathematical solutions for the evolution of the mass distributions of accreting astrophysical objects.

In Part II, I predict the evolution of the mass and luminosity functions of stars in young clusters. A simple physical model is constructed based on available stellar and protostellar evolutionary tracks; from this, numerical predictions of various statistical distribution functions are made for protostars, pre-main sequence stars and main sequence stars, separately. Application of the results to the Rho Ophiuchus cluster yields an age of 10^6 yr, uncertain by a factor < 2. This agrees with previous crude estimates, and lends support to the underlying model assumptions and stellar theory. If the best fit luminosity function for Rho Ophiuchus is extrapolated to low mass, large numbers of resident brown dwarfs should appear. Though this is not a prediction of my model, it suggests that an optimal brown dwarf search strategy should target their presumed birthplaces.

Thesis Supervisor: Bernard F. Burke
Title: Professor of Astrophysics

To my parents

Acknowledgments

This thesis is the result of 9 gruelling years of hard work at MIT, with many ups and downs along the way, not to mention the burning of many gallons of midnight oil. I could not have done it without the moral and financial support of a large set of people, whom I hereby attempt to acknowledge as best I can.

Firstly, I am indebted to my thesis supervisor Professor Bernard Burke for his many years of financial support of my thesis research, and also for his practical and scientific advice. I have been deeply interested in the mysterious events occuring in the centers of galaxies ever since I researched a secondary school project on "Quasars, Pulsars, Neutron Stars and Black Holes" when I was 13 years old; and since the age of 8, I was struck by the mystery of the expansion of the universe implied by the observational law discovered by Edwin Hubble earlier this century. Working on the huge MIT-VLA Survey of 10,000 extragalactic radio sources, and searching for new examples of gravitational lensing, has allowed me to greatly expand my knowledge on both active galactic nuclei and cosmology. Under Bernie's tutelage, I not only was able to reach the frontier of knowledge in the field of observational cosmology, but I also learnt to work on large-scale surveys, and to carry out independent research in a mature field of astrophysics. Along the way, I have enjoyed every one of Bernie's dinners for students and visiting researchers; and also each of his "rules-of-thumb", and his personal anecdotes of the many interesting events in his life. One famous example of a Burke rule-of-thumb is: "If you are not missing a plane at least 10% of the time, then you are spending too much time in airports". I have certainly missed some flights due to the pressure of preparing for many conferences and optical observing runs, and I don't ever remember spending much time in airports, except for the important international flights; everything worked out well in the end, so it seems that his rule has worked for me, and that I am not wasting time in airports. I enjoyed taking on the role of "human ballast" twice on Bernie's yacht. How many professors sail their own yacht ? Being around Bernie has not only afforded me an excellent opportunity to grow as a scientist, but it also has been an educational, social and cultural experience to be remembered for life.

I also owe many thanks to my other research supervisor, Professor Steven Stahler, who spent innumerable hours, over a period of 5 years, supervising my complex theoretical calculations on the statistics of young stellar clusters. Through his constant and detailed supervision, I was, in the space of 2 years, able to rapidly mature into a scientist able to tackle a complex theoretical problem. Under his wing, I produced 2 substantial papers in the Astrophysical Journal, and also reached the point where I could bring current stellar evolution theory in direct confrontation with the observations of a young cluster of stars. Although there was no planning ahead of time, the intense theoretical training under Steve has allowed me to better explore the theoretical issues related to the much more complex accreting objects at the centers of active galaxies. In this way, I was able to work on two separate topics on my thesis, under the common unifying theme of investigating the consequences of accretion in both stars and extragalactic radio sources.

Much of my research with Steve unfortunately could not enjoy National Science Foundation funding, and I am therefore indebted to both Bernie and the MIT Physics Department, for providing me with the necessary financial support as a Research Assistant and Teaching Assistant for most of my 9.5 years at MIT. I must also thank Steve for having the patience to supervise me long-distance from his new position at UC Berkeley; at times, I was too distracted by the massive data reduction for the MIT-VLA survey to make much progress on the star formation research, and this was extremely frustrating to both Steve and myself. Thanks, Steve, for keeping me to the program.

I owe much to various MIT professors and staff, and CfA scientists, for their advice, administrative support, and also for organising the many excellent colloquia that bring world-class researchers to talk at MIT and Harvard. Thanks go to Paul Joss and Wolfgang Ketterle for their participation and support on my thesis committee; John Tonry for collaborating with me on sharing MDM optical telescope time, and also for advising me on how to use an optical telescope efficiently; Paul Schechter for his courses and "Russian Roulette" seminars, where I learnt much of the astrophysics for my thesis; and also for giving me a definite kick in the pants to finish my degree ! Ed Bertschinger for an excellent course on cosmology

and also for the setting of the highest standards both in the academic courses and in the critical consideration of open research questions; Paul Joss for his comprehensive course on stellar structure and evolution; Jackie Hewitt for her constant interest in my progress on the MIT-VLA survey; Joseph Lehár, Peter Garnavich, Emilio Falco, and Chris Kochanek (CfA) for their collaboration on recent papers resulting from the MIT-VLA survey; George Koster, Peter Dourmashkin, and Anthony French for their guidance of my teaching efforts; Peggy Berkovitz for her constant helpful advice and lending of a sympathetic ear when it seemed like I would never finish my degree; Wendy Hunter, Vicky Taylor, Anne Conklin, Chris Naylor, and Felicia Brady for their cheery manner and extremely efficient administration of supporting duties.

I also thank many scientists from other institutions who took the time to advise and collaborate with me on my thesis research: Alan Wright, Ron Ekers & Dave Jauncey (ATNF); Jim Condon, William Cotton, Barry Clark & Rick Perley (NRAO); Heinz Andernach (Univ. of Guanajuato, Mexico); Adelina Temirova & Oleg Verkhodanov (SAO Russia); Tom Muxlow & Peter Thomasson (NRAL, UK); Malcolm Bremer (IAP, France); Richard McMahon & Isobel Hook (Univ. Cambridge, UK); Charles Lada (CfA); Mary Barsony (UC Riverside).

I thank the following scientists in Australia, who supported me in my undergraduate research, providing me with the solid scientific base which enabled me to come to MIT to follow my dreams: Richard Hunstead, Lawrence Cram & Don Melrose (Univ. Sydney); Russell Cannon, Raylee Stathakis & Max Pettini (Anglo-Australian Observatory); Michael Bessell, Don Mathewson & Vince Ford (Mount Stromlo and Siding Spring Observatories).

It was Dick Hunstead who first introduced me to the field of observational cosmology, and who assigned to me a very interesting project on a damped Lyman alpha absorber towards a high redshift quasar. The discovery of emission from the intervening absorbing galaxy was unexpected, and led to my first refereed paper as a co-author. Dick was the first person to show me the path to observing and interpreting the light from distant powerful objects in our universe, and Bernie Burke was later to allow me to continue on this path by providing me with a substantial dose of hard experience in the field.

A special thanks to Barbara Dunn (Univ. Sydney) for her letters of moral support, and friendly advice on traversing the vagaries of life.

I thank my fellow students for their help, support, and frank discussions on research and life as an MIT student: Sam Conner and Joseph Lehár for leading the MIT-VLA survey effort; Mark Griffith for allowing me to learn about single-dish observing while working on the PMN survey; Lori Herold-Jacobson and Asantha Cooray for their hard work and day-to-day collaboration with me on the results on the MIT-VLA survey sources; Deborah Haarsma, Froney Crawford, John Cartwright, John Blakeslee and Eric Gaidos for assisting with data reduction and telescope observations; Ian Avruch and Brett Bochner for frank discussions on anything under the sun, and commiserating with me while we were all three under great stress in the final year of our massive thesis projects; and to the other students in the MIT radio groups for their honest opinions: Cathy Trotter Wilson, Grace Chen, John Ellithorpe, Christopher Moore, Charles Katz, Michael Schwartz, Carlos Cabrera and Aaron Cohen.

To friends and roommates: Renaud Metz, Stephanie Mailles, David O'Connor, Fang Liu, Brian Sadie, and Sonja Voskuil for being great friends; Amin Salaam for late-night discussions on philosophy, science and life, and being a great roommate at Ashdown House.

To my 'distant' relatives in Australia, who put me up whenever I was in Sydney for conferences or MIT survey work: Michael, Susan, Alex, Tom, Lucinda & Jessica Morris.

To my friends in Australia: Fiona and Sally Skyring, Allan Kreuiter, Peter Edmonds, Trevor Jolly, Constantina Contis, Andrew Woodroffe, Jillian Johnson, Dennis Lam, Ray Younis, Andrew & Sue Tridgell, Pal Fekete, Michael Newberry, Yolande Freke, Anne Lundberg, and Jonathan Ayscouth.

I must especially thank Dean Page for driving my paraphernalia from house to house in Sydney, in the final hectic months before I left for the United States !

To my friends from King George Vth school in Hong Kong, I thank those of you who took the trouble to contact me to see how I was doing: Kish & Kairos Shen, Ian & Robert Quinn, Katsumi Maki, Victor Lam, Winston Leung, Johenn Lee, Jason Leigh, Steven Stringer, Sophie Weston, and Rajeev Ravindran.

To my teachers of the King George Vth School, especially those who taught me my basic science: Sirdar Khan, Mr. Coombes, Mr. Robinson, Mrs. Davies and Angela Smith. Thanks to Caroline Periton for taking an interest in my progress at MIT.

Lastly, but most importantly, words cannot express the deepest gratitude I have to my parents for putting up with long silences from their son, and for never failing to call and inquire about my health, sanity, and financial situation. They love me very much, and I am extremely fortunate to have had their support and advice for the duration of 9.5 long years that I spent toiling away at MIT. Due to lack of both teaching and research funds, I am also indebted to them for the necessary last-minute infusion from their personal life savings, without which I would have been prevented from having a chance to graduate from MIT, after the unusually large amount of work that I had put into 2 complex scientific projects.

Thank you all. MIT has been a wonderful though exhausting trial-by-fire; now I can get on with the rest of my life !

Contents

1 Introduction **25**

1.1 Outline of Dissertation 27

1.2 The Evolving Universe 31

1.3 Extragalactic Radio Sources 50

1.4 Young Stellar Clusters 60

1.5 Summary 66

2 Observations **67**

2.1 The MIT Sky Surveys 72

2.1.1 The MIT-Green Bank Surveys 72

2.1.2 The Parkes-MIT-NRAO Surveys 81

2.2 The MIT-VLA Snapshot Program 100

2.2.1 The MG-VLA C-Band Surveys 102

2.2.2 The MG-VLA X-Band Surveys 111

2.2.3 The PMN-VLA X-Band Surveys 112

2.2.4 The MG-VLA and PMN-VLA Follow-Up Surveys 113

2.3 Optical Observations of MIT-VLA Radio Sources 113

2.3.1 Gravitational Lens Candidates 116

2.3.2 Close Radio Doubles 118

2.4 Summary 119

3 Data Reduction **123**

3.1 Aperture Synthesis Imaging 125

3.2 The MIT-VLA Pipeline 131

3.3 Analysis of MIT-VLA Snapshots 134

3.4 Optical Identifications of MIT-VLA Radio Sources 147

3.5 Optical Data Reduction 150

3.5.1 Optical Imaging 150

3.5.2 Optical Spectroscopy 159

3.6 Summary 160

4 Results **161**

4.1 Cumulative Results 162

4.2 The MIT-VLA Close Radio Doubles 171

4.3 The New MIT-VLA Gravitational Lens Candidates 177

4.4 The Unusual Radio Galaxy MGJ 0248+0641 177

4.5 The New Binary QSO MGJ 2214+3550 178

4.6 The MIT-VLA Angular Size Distribution 179

4.7 Summary 182

5 The Nature and Evolution of Extragalactic Radio Sources **185**

5.1 Active Galactic Nuclei 188

5.1.1 AGN Classification 189

5.1.2 AGN Unification 204

5.1.3 AGN Physics 211

5.2 Intrinsic Properties of Radio-Loud AGN 219

5.3 Energetics and Timescales 226

5.4 Observational Data and Limitations 229
5.5 Proposal of a Formal Model for Radio-Loud AGN 230
5.6 The Evolution of Accreting Astrophysical Populations 238
5.7 Proposal of a Simple Radio Jet Model 266
5.8 Estimation of the Mean Jet Advance Speed in the MIT-VLA EGRS Sample 270
5.9 Summary 274

6 The Nature and Evolution of Young Stellar Clusters 277

7 Conclusions 281
7.1 Extragalactic Radio Sources 281
7.2 Young Stellar Clusters 283
7.3 Future Directions 284

A MIT-VLA Close Radio Doubles 307

B MIT-VLA Gravitational Lens Candidates 317

C Thesis Publications 431
C.1 Publication List 431
C.2 Publications for Part I 435
C.3 Publications for Part II 511

List of Figures

1-1 NRAO Very Large Array Snapshot of a prototypical double lobed radio galaxy, Cygnus A. The central radio source lies in the giant elliptical galaxy M87, residing in the Virgo cluster of galaxies. There are two long jets leading from the central source to each of the radio lobes; these lobes contain the residual shocked material after its passage through the peak intensity hotspots. The high degree of symmetry, and the preservation of the jet stability across many kiloparsecs, are typical of extended structures in EGRS. Inset is a schematic diagram to aid in interpretation. This figure has been reproduced from Kraus (1986). 55

1-2 A possible explanation for what happens close to the central engine of an AGN that produces extended radio structure (jets). The energy is tapped off the rapid rotation of a massive rotating black hole. This process is unknown, but probably involves the allowed extraction of energy from within the ergosphere region of the hole. Two jets of highly magnetized plasma are produced, which traverse the central nucleus in opposite directions along the black hole spin axis. As the temperature drops further away from the hole, the type and motion of the orbiting gas clouds changes from fast and highly excited or ionized, to lower velocities and excitations further away. Accretion of nuclear stars, gas and dust onto the hole can be regulated by a cool outer torus and a hot inner accretion disk. This figure has been reproduced from Megan Urry & Padovani (1995). 57

1-3 The Rho Ophiuchus dark cloud: this is an overlay of the IRAS mid-infrared 12 μm emission peaks onto a red filter photograph from the Palomar Sky Survey. The contour represents a level of carbon monoxide molecular emission. This is a negative photograph, so the cloud is indeed optically dark, with embedded infrared-bright sources which locate the positions of Young Stellar Objects (YSOs). At higher IR sensitivity, at least a few hundred peaks are found. This figure has been reproduced from Wilking, Lada & Young (1989). . . . 62

1-4 The general theoretically assumed scenario for the birth and formation of a star. The mimimal set of important physical effects that need to be understood by any self-consistent physical theory of star formation, and early stellar evolution, should include the following: the role of magnetic fields and turbulence; gravitational collapse accompanied by radiative cooling; accretion probably through an equatorial disk which is a matter and angular momentum repository; the role of magnetic fields; and the mechanism by which the initial angular momentum is dispersed, and how this relates to the bipolar outflows that are observed along the polar axes. This figure has been reproduced from Shu, Adams & Lizano (1987). 63

2-1 A plot of the sky areas observed in each of the MIT-Green Bank 4.8 GHz Sky Surveys MG I, II, III and IV. The Galactic latitudes $b = -10°, 0°, +10°$ are marked by the dashed lines. This figure has been reproduced from Griffith et al. 1991. 73

2-2 The radio continuum sky at 4850 MHz. An Aitoff (equal-area) projection plot of all PMN and 87GB sources with flux densities greater than 80 mJy. The 87GB sources are plotted for the declination range $+10° < \delta < +75°$. This figure was originally produced by M. Griffith in 1995. 83

3-1 Extragalactic Radio Source Morphology Classification Scheme (reproduced from Lawrence et al. 1984). 141

4-1 The MIT-VLA Largest Angular Size (LAS) Distribution for 4741 extragalactic radio sources as imaged at the VLA at 4.8 and 8.4 GHz. The angular resolution is only as good as 0.25″. The contribution from ∼ 1000 flat spectrum sources mainly shows up as compact and unresolved sources near the resolution limit. On removing this spectrally biased subsample, the LAS distribution is not thereby affected on scales larger than ∼ 10″. 181

5-1 Radio and optical imaging of the LINER galaxy NGC 4261 (3C 270). Left: a composite image of the radio jets and a ground-based optical image. Right: a deconvolved HST image of the galaxy core, showing a dusty torus oriented in the plane perpendicular to the radio jets. This figure has been reproduced from Antonucci (1993). 209

5-2 A possible unification scheme for the various types of powerful AGN: The radio-loud objects are different aspects of the same central structure, and are represented by the different viewing arrows drawn in the top half of the figure. The radio-quiet objects share the same structure, but without the presence of the jet. Their viewing arrows are shown in the bottom half of the figure. This diagram has been reproduced from Woltjer's article from Blandford, Netzer & Woltjer (1990). 210

5-3 A possible flowchart diagram for the ultimate fate of the normal products of stellar and galactic evolution in the centers of galaxies, originally proposed by Martin Rees in 1978. Triggered by an unknown mechanism, gas and stars accumulate towards the center of the galactic nuclear potential well, interacting with each other in the process. The final results seem to inevitably be the formation of one or more compact objects, which eventually merge into, or fall into, the most massive collapsed object in the center of the galaxy; a massive black hole. It is this object which may be the key that unlocks the 'central engine' behind many types of powerful activity observed in AGN. This figure has been reproduced from Begelman, Blandford & Rees (1984). 212

5-4 A list of the various physical structures known or believed to exist in radio-loud AGN. Their sizes and the relevant physics are indicated. The figure above the list is reproduced from Megan Urry & Padovani (1995). 213

5-5 Simple Jet Model Geometry for Extended Radio-loud AGN. This figure has been reproduced from Fletcher et al. (1997). 268

5-6 Simple Jet Models for Extended Radio-loud AGN. This figure has been reproduced from Fletcher et al. (1997). 269

List of Tables

2.1 The MIT 4.8 GHz Sky Surveys 72
2.2 The MIT VLA 4.8 and 8.4 GHz Snapshot Surveys. 102
2.3 The MIT-VLA 4.8 and 8.4 GHz Snapshot Surveys (1981–1995). 103
2.4 1993–1996 MIT Optical Runs 117
2.5 MGVX and PMNVX lens candidates: optical observations 118

Chapter 1

Introduction

Gravitation is a universal force that dominates the nature and evolution of many astrophysical systems, not the least of which is the Universe in which we live. The birth of many of the known systems contained within our observable cosmological horizon rely on gravitational **accretion** to initiate energetic processes that generate the radiant photon energy seen by us from our past light cone.

Two examples of accreting systems are studied in this thesis: in Part I, a large MIT survey of extragalactic radio sources is compiled, and the nature of these powerful galaxies is discussed. These objects are a subset of the rare class of **Active Galactic Nuclei (AGN)**, most of which are currently believed to contain a 'central engine' in the nucleus of the host galaxy. This engine is probably powered by the most efficient known physical process available to systems of astrophysical scales: the conversion of gravitational potential energy to radiant energy via the infall of millions of solar masses of stars, dust and gas onto a compact object in the dynamical center of the nucleus. The observed radio emitting structures in the MIT survey are simply the physical consequent effects of the evolution of magnetized plasma ejected from the central engine.

In Part II of this thesis, the nature and evolution of young stellar clusters is given serious

theoretical consideration. All stars are believed to start their lives as accreting **protostars** in dense, cold cores embedded within **giant molecular clouds (GMCs)**. Protostars evolve to become fusion powered **pre-main-sequence (PMS) stars**, with a significant portion of their power output still generated by gravitational contraction, and possibly accretion too. These in turn mature into **main-sequence (MS) stars**, which derive almost all of their luminosity from stable thermonuclear fusion in their cores. The main sequence stars are the ones that are most obvious to the casual observer of the sky; the preceding stellar phases are best detected by infrared and radio telescopes aimed at known star forming nurseries.

Both extragalactic radio sources and young stars are brought to shine by the initiation of gravitational collapse, and both continue to derive their energy from the unrelenting attractive nature of the gravitational force throughout their subsequent evolution. They share a similar behaviour with another type of (sometimes sporadically) accreting object, this time an evolved and dying star: those seen in certain **X-ray binary (XRB) systems**. All three are powered ultimately by gravity, without which none of them would have been seen by us, even if somehow they came into existence in some other way.

It is the purpose of this dissertation to:

1. Make a systematic observational study of the radio-loud AGN compiled in the 17 year MIT survey effort, and gain a deeper insight into their detailed morphological structures, as they might be explained by physical evolutionary effects. A milestone that is aimed for is the formal specification of a descriptive model for extragalactic radio sources, and original contributions will be presented towards just two parts of this complex (and incomplete) model; the accretion history of the central massive object, and the statistical demonstration that the mean population evolution of the radio jet morphology on kiloparsec scales *does not* proceed relativistically, given reasonable assumptions concerning the energetics and lifetime of the central engine. This would be in contrast to the many cases of apparent superluminal jet speeds seen in much

smaller parsec-scale AGN jets which are pointed by chance close to our line of sight.

2. Propose a detailed mathematical model by which the evolution of both the **mass function (MF)** and the **luminosity function (LF)** may be explicitly calculated for accreting systems, as well as for their non-accreting descendants, given an underlying accretion law and observed final mass spectrum. A simplified version of this model will be applied specifically to the case of evolving stars embedded within the quiescent cores of star forming regions, with extra theoretical input from the latest available predictions for the time evolution of young stars of a wide range of masses. The ultimate goal of Part II of this thesis is to attempt direct comparison of young stellar evolution theory with the observations of the bolometric **luminosity function (LF)** of a well-studied embedded stellar cluster.

It is noted that the scientific approach in Parts I and II is based on an attempt to confront theory with observation in a comprehensive manner. Given that one cannot sample *all* the astrophysical objects that actually exist in any part of our Universe, the next best thing that could be done is to attempt a systematic comparison of physically-based evolutionary models (preferably containing some predictive power) with well-defined, statistical samples. It is only in this way that one can learn to improve on the model assumptions and calculations, and thus further our understanding of the vast panoply of individual astrophysical populations, accreting or otherwise.

1.1 Outline of Dissertation

I hereby describe the structure of my thesis research as presented in this document.

In the rest of this chapter, I will sketch a broad outline of evolutionary processes thought to occur within our Universe, with special attention paid to the role played by gravitation, and also to the specific types of galaxies and stars associated with the accreting systems to

be studied. Each chapter will end with a Summary, this also being intended to draw the reader to the most significant issues, results and conclusions discussed for that chapter.

In Chapter 2, I document in comprehensive detail the 17 years of MIT radio and optical observations of extragalactic radio sources. References to the work of previous students of the MIT radio astronomy group are given whenever appropriate. Included are details of my own involvement in the MIT surveys, which has specifically been focussed on exploring new territory in that part of the Southern Hemisphere sky that is accessible to the National Radio Astronomy Observatory (NRAO) Very Large Array (VLA) Interferometer.

In Chapter 3, I document the data reduction techniques employed in the reduction of the 15 year MIT-VLA Snapshot survey of sources, selected in unbiased fashion, from the essentially complete MIT single-dish sky surveys at 4.8 GHz. I also give details of the reduction of optical CCD imaging and spectroscopic data on various selected samples of MIT-VLA sources observed in the 1990s; the main targets being **close double** radio sources discovered in the 1990s VLA snapshots, and also new **gravitational lens** candidates found within these same data sets. I mention a few of the details of the older VLA pipeline reduction methods, but this information may best be found in the the published MIT group papers and past dissertations.

It should be made clear that it was not the original purpose of the MIT-VLA Snapshot survey to make the systematic study of EGRS that I have proposed at the outset of this dissertation. However, after 15 years of reasonably systematic accumulation of images of EGRS, the clear opportunity arises for someone to initiate an in-depth study of the detailed structures found in the large statistical sample that has been established. The original purpose was to discover new examples of multiply imaged gravitational lenses, with the long-term goal of constraining cosmological parameters via time-delay measurements, and also through an analysis of the lensing frequencies. In this thesis, I simply present the most up-to-date list of MIT-VLA gravitational lens candidates, and leave this compilation for

future investigators to mine.

In Chapter 4, I summarize the scientific results that have emerged from the thesis research efforts of past students in the MIT group. I present a current status report on the reduction of the MIT-VLA Snapshot survey, which contains observations of $\sim$ 10,000 sources, about 60% of which are reduced and available for analysis in this thesis. I present a compilation of Close Double (CD) Radio Sources in Appendix A, and summarize the results that have been obtained by two other students who have collaborated with me in the collection and partial reduction of this sample. I then present a list of all the new MIT-VLA Gravitational Lens Candidates (GCs), that I am aware of at the present time. I supply plots of these gravitational lens candidates in Appendix B, I give a brief discussion of two rare types of radio source that have been recently found in the MIT-VLA database, and for which publications have been reproduced in Appendix C. These sources consist individually of a radio galaxy with a highly polarized kiloparsec-scale ring of unknown origin, and a compact optical binary quasar, one of whose components appears as a core-jet radio source in the MIT-VLA survey. I present my own work on the largest angular size (LAS) distribution for about 47% of the MIT-VLA sample, and I conclude Chapter 4 by describing the overall picture that emerges from my consideration of all of the results from the MIT surveys. This will provide a suitable starting point for a much wider discussion on EGRS that follows in Chapter 5.

In Chapter 5, I start by supplying the reader with details of general results that have been published and discussed concerning other systematic samples of AGN and EGRS. The observational data and theoretical viewpoints on AGN in general, and radio-loud AGN in particular, as they appear to the majority of the active research commmunity, are presented in very broad outline. Based on the consideration of these external information sources, as well as on my personal familiarity with the thousands of radio galaxies imaged in the MIT-VLA Snapshot survey, I propose a unified model for EGRS. Since there still remains

much to be done by the AGN community before a fully predictive model can be built for the majority of powerful EGRS, I can only at best present a descriptive model that has limited physical content. However, it is my belief that I have two original contributions to make, each of which is a part of the proposed synthesis; the accretion history of the central engine, for which I supply a detailed mathematical model in Section 5.6, and a statistical estimate of the mean morphological advance speed for the jets in the MIT-VLA sample, which appears in Section 5.8. Each of these two inputs is but a small part of the proposed unified model. It is clear that much remains to be done in the modelling of the various observed properties of the EGRS population, as they appear in detailed systematic surveys such as the MIT-VLA Snapshot Survey.

The statement of the mathematical model, just mentioned, rests on a plausible differential equation for the accretion evolution of astrophysical populations. The derivation is given in some detail. The intention is for these general model solutions to be tailored for application to actual accreting populations, such as the two studied in this thesis. As far as I am aware, this is an original contribution to this general problem, and I am the first to consider its application to accreting populations.

In Chapter 6, I present a brief synopsis of the method of attack on the problem of predicting the bolometric luminosity function of a population of young stars embedded in the cloud core of a star forming region. The relevant papers and conference abstracts are presented in Appendix C, and I summarize the results and conclusions contained therein.

In Chapter 7, I discuss the results and conclusions that I have obtained in each of the two Parts of this thesis. I attempt to identify areas of weakness in my conclusions, and where improvements and further work would be fruitful in deciding any debatable issues. Also, I give my own wish list of scientific programs that could be continued as extensions and additions to the areas of research touched upon in this thesis. There are plenty of ideas here; I estimate that at least 30 person-years worth of effort could go into continuing the

large-scale investigation that I have initiated within this dissertation.

Appendix A contains a table listing all the known MIT-VLA Close Radio Doubles that have been discovered in most of the 1990s VLA snapshots.

Appendix B contains a table listing the newest (1990s) crop of MIT-VLA lens candidates. Radio snapshot image plots of each one of these are provided.

Appendix C contains a list of all publications relevant to this thesis, for each of which I played a substantial or leading role in creating. Pre-publication copies of the articles themselves follow.

1.2 The Evolving Universe

Evolution is the major hypothesis by which we try to understand the many different types of astrophysical systems seen in our observable Universe. While it is comforting and sometimes very revealing to be able to understand and predict the details of the astrophysics of individual systems, this would be a rather empty exercise if no serious consideration is also given to the study of the global properties of different classes of objects, and how one such class would be able to reasonably evolve into another. Indeed, both lines of inquiry are complementary and indispensable to the advancement of our physical knowledge. Given this declaration, I now provide a highly condensed account of the current state of our knowledge on the evolution of our Universe, and the gravitationally bound structures contained within.

The origin of our Universe will remain unknown as long as a correct and consistent theory of **quantum gravity** is out of reach. This limits our theoretical probings of the Big Bang to after the first 10^{-43} of a second, the **Planck time**, which is set by the light-travel time across the maximal mass particle that can can be contained within its own quantum Compton wavelength *without* being too compactified as to collapse into a black hole singularity. This special **Planck mass** (m_{PL}) is set purely by the fundamental constants of Nature that lie at the basis of quantum mechanics (QM) and the General Theory of Relativity (GTR); in

this case, the relevant quantity is $m_{PL} = (hc/2\pi G)^{\frac{1}{2}} = 22\mu$g, or the equivalent of 1.3×10^{19} proton masses. At the Planck time, our horizon was only 1.6×10^{-35} m across, and the corresponding Planck density was a colossal 1.2×10^{96} kg m^{-3}.

Before this time, it is thought that the structure of the so-called 'spacetime foam' would have been of highly chaotic local topology, with Planck mass black holes forming and decaying according to the dynamics of an unknown physical law of ultimate symmetry. This law is known by various names: the 'Theory of Everything', 'supergravity', or 'superstring' theory. Needless to say, these theories will almost certainly continue to remain highly speculative, being unconstrained by experimental observation. Indeed, it is probable that time as we know it ceases to exist 'before' the Planck time, as the concept of a continuous and differentiable manifold for the fabric of spacetime may be manifestly invalid.

After the Planck time, the need for a quantum gravity theory is removed for most of the Universe, as gravity separates out from the three other fundamental forces, which are collectively known as the strong-electroweak force. *Grand Unified Theory (GUT)* can then serve as an adequate description of Nature below the 10^{19} GeV energy scale.

From this moment on, it is expected that the entire evolution of the Universe and its contents may *in principle* be described by the application of the GUT, and its lower-energy approximations, on the background 3+1 space-time metric specified by Einstein's field equations of the classical GTR.

However, it has also become clear, from numerous observations of physical processes in Nature, that there is another very important and general descriptive model of evolutionary events which must be heeded; the time symmetric GUT theories do not bring in the extra fact that as the phase space point of any isolated system (such as the Universe) evolves, it must inexorably move towards larger, more probable, regions of the available phase space. This is simply a probabilistic expectation firmly based on the application of the mathematical 'Law of Large Numbers'. Since the available phase space volumes for any macroscopic system

are so enormous, there is clearly more than ample opportunity for finding more probable states as time goes by. Even if one starts in the most probable macrostate, there is still a chance for energy fluctuations to cause interesting evolution away from this maximum likelihood state (though admittedly with exponentially decreasing probability the further the phase space point ventures away). Of course, this does assume that there is a fixed and reachable maximal state; if there is not, then there will always be a ceaseless evolution towards more likely macrostates. These mathematically rigorous results are encoded in the laws of statistical thermodynamics; the main guiding principle behind evolution in general will turn out to be the well-known 'Second Law of Thermodynamics', which states that, as time passes, an isolated system will almost certainly never increase its 'state of order'. By this is meant that the system will, with overwhelming odds, never remain for long in relatively tiny regions of phase space. In fact, just the reverse happens; in finding larger regions of phase space, the number of parameters required to describe the resulting macrostate are so large that the 'information' content is virtually nil (from the viewpoint of intelligent low-entropy systems such as ourselves). With a decrease of the available information, an increase in disorder is implied, and thus the observable system macrostates must gradually increase their **entropy** with time. Such entropy increases are usually accompanied by a democratic diffusion of available energy into the immediate surrounding future light cone, by which act the system will try to find *lower* energy macrostates, as a corollary to the secular trend to maximize its entropy.

The principle of entropy maximization and energy minimization will turn out to be very fruitful when applied towards the general understanding of evolutionary processes in the Universe. It is noted that these expectations are independent of the underlying physical laws, i.e. independent of the details of the dynamic flow through the universal phase space.

Returning to the account of evolution in the Universe: as a consequence of the apparent creation of our Universe in a highly symmetric state of relatively *low* entropy, the immediate

behaviour must then be driven by a rapid succession of decays towards less and less symmetric states. This first happens in the *spontaneous symmetry breaking* of the supergravity force: gravity diverges from the other three fundamental forces towards weaker interaction strength, starting from the Planck time; then, the strong nuclear force diverges from the electroweak force towards greater strength at $t \sim 10^{-35}$ s; $E \sim 10^{15}$ GeV. Finally, the weak nuclear force splits off at $t = 10^{-10}$ s; $E = 10^{2}$ GeV. In the process of these breakings, various physical events are thought to have transpired; with the breaking of the strong-electroweak symmetry, there was probably a phase transition in which the 'false vacuum state' decayed into the present day 'true vacuum'. This liberated an enormous amount of negative energy arising from the special properties of the negative pressure associated with the false vacuum. Of course, in reaching a more probable state, entropy and disorder were both generated, and the repulsive gravitational effect of the negative false vacuum energy was able to inflate the Universe by ~100 doublings, or more. This process of **inflation**, first proposed by A. Guth [63], has been successful in explaining the abundant store of multi-wavelength observations of the **homogeneity** and **isotropy** seen among radiators in distant parts of our Universe (e.g. in the isotropic distributions of the **cosmic microwave background radiation (CMBR)** and also in the majority of EGRS). Inflation is the only theory so far that can explain why the sky distribution of radio sources is isotropic, despite the fact that distant radio sources on opposite sides of the Universe are out of causal contact with each other (this is the **'horizon problem'**).

Most of the history of the rest of the 1st second of the Hot Big Bang model is governed by a series of decays of various elementary particles; as the temperature drops below twice the rest mass of any given particle P, i.e. $kT < 2m_Pc^2$, the equilibrium previously maintained by the matched annihilation and pair creation rates for P is destroyed. Particle antiparticle pairs of P then make a final annihilation, and there may be a very tiny residuum left for the creation of all the matter that we see today. There do exist unverified GUT theories

that can explain the level of matter-antimatter symmetry required to account for the photon-baryon ratio; the imbalance of 1 part in 10^9 can be explained as being due to a corresponding asymmetry between particles and antiparticles within the actual GUT physics. A hint of this may be recalled from the known CP violations experimentally detected in certain elementary particles a few decades ago.

In order, the most significant transitions were the following; the strong force had separated off from the electroweak by the end of the inflation epoch at $t \sim 10^{-33}$s; $E \sim 10^{14}$ GeV. After inflation, quarks and leptons could no longer interconvert via the exchange of X vector bosons of the GUT superforce. In turn, the electromagnetic and weak forces went their separate ways at $t \sim 10^{-10}$s; $E \sim 100$ GeV, thus starting the *Quark Era.* At $t \sim 10^{-6}$s; $E \sim 1$ GeV, quarks and antiquarks became cool enough to be confined by the strong nuclear force into stable hadrons, and this introduces our familiar neutrons and protons into the fireball. By this point the previous quark-antiquark asymmetry had become fossilized into the residual matter-antimatter asymmetry that we see today, with the entropy held invariant at the level of 10^9 photons per baryon. At $t \sim 10^{-4}$s; $E \sim 100$ MeV, the *Lepton Era* began with the freezing out of the muons and pions. We now have a mixture of leptons, hadrons, and field bosons at about $T = 10^{12}K$. At $t \sim 10^{-2}$s; $E \sim 10$ MeV, electrons and positrons are captured into neutrons and protons, thus setting the n:p ratio to about 15 neutrons for every 100 protons; the precise number would later be very important in determining the yield of light elements generated in Big Bang nucleosynthesis.

By $t \sim 10$s; $E \sim 0.1$ MeV, neutrinos had just decoupled, and electrons and positrons underwent their last annihilations. The photon dominated *Radiation Era* began, and Big Bang nucleosynthesis (BBN) commenced at $\sim 10^9$ K, lasting about a few hours. Fusion of the hydrogen plasma produced some of the primordial light elements that we can measure in our surroundings today: $D^2, He^3, He^4, Li^7, Be^{11}$. By the end of BBN, helium-4 was left at the level of $\sim 25\%$ by mass. From carefully measuring the deuterium abundance, it has

been shown that the amount of baryonic matter in our Universe should be close to the level $\Omega_0.h_0^2 \sim 0.05$. This would imply that there is certainly appreciable non-luminous baryonic matter, a type of **dark matter**, in our Universe; there would need to be roughly about 10 times more non-luminous baryons that luminous ones (these might be, for example, black holes; faint, dying or dead stars; rogue planets and asteroids). Observationally, there are numerous dynamical estimates, from spectroscopic and gravitational lensing measurements (of galaxies, clusters, and larger scale structures and cosmic flows) that indicate that this non-luminous baryonic dark matter *could* exist in galaxy haloes and clusters. However, the dynamical estimates exceed the BBN expectations by not 1, but almost 2 orders of magnitude! This may be a strong sign that our Universe has a good chance of being precisely flat ($\Omega_0 = 1$ exactly), and even if this is not true, there should be yet 2 to 10 times more *non-baryonic* dark matter than baryonic dark matter. These may be light neutrinos, or massive GUT particles left over from the GUT era; however, the form of this dark matter remains as yet unknown.

Since nothing much more is known about dark matter, this leaves open the distinct possibility that it may play a significant role in the evolution of the familiar luminous structures that we see. This is a difficult problem, but it should always be borne in mind.

At $t \sim 10^4$ yr, $T \sim 10^4$ K, the expansion of the Universe ceased to be dominated by radiation, and the Matter Epoch started. In a (flat) Einstein-de Sitter (EdS) Big Bang model, this meant that the scale factor $R(t)$ went from a time variation of $R(t) \sim t^{1/2}$ to $R(t) \sim t^{2/3}$. At $t \sim 3 \times 10^5$ yr, $T \sim 3 \times 10^4$ K, the Universe became transparent as protons and electrons were finally cool enough to combine. This event is usually known as *recombination*; however, this is a misnomer, as the resulting hydrogen had never existed before. The emitted photons form the CMBR that we see today.

After recombination, we enter a *Dark Era*, before the first stars and galaxies could form. An important concept for the study of the evolution of stars and galaxies is afforded by the

consideration of the **Jeans Mass**. This is the minimum mass M an object must have before it can gravitationally collapse in spite of the sum total of forces capable of supporting it. Depending on the particular system, thermal, turbulent or magnetic pressures are all capable of holding up an incipient collapse. Stability will be maintained only if the gravitational potential energy per unit mass is *less* than the sum total of corresponding energies from the supporting pressure forces. If there is some mechanism by which the mass loses enough of its support, then the Jeans criterion will be met and gravitational collapse will ensue. Usually, an *increase in entropy*, via some form of heat production or radiation, is generated in this process, and the total energy of the system decreases. For example, in the case of a collapsing protostellar cloud, the resident atoms and molecules will get heated, and radiate copiously in the infrared. By the **Virial Theorem**, this loss of total energy must be accompanied by a decrease in gravitational potential energy, and a shrinking of the volume. An interesting point to bear in mind is that systems collapsing under the influence of the attractive gravitational force possess a *negative heat capacity*; when they lose gravitational potential energy, they must also increase their kinetic energy by half that amount; the difference is radiated away. This means that they will *heat up* during the radiative cooling, a counterintuitive result. Familiar examples of this are the well known phenomena of re-entering satellites, and contracting stars, which both heat up when they lose energy.

The Jeans mass after recombination is calculated to be about the right scale for globular clusters: $10^6 M_\odot$ (solar masses). By the Jeans criterion, any mass greater than this can collapse during the Dark Era; however, there must be an upper limit set by the efficiency with which huge masses of hydrogen can radiate away their potential energy. A simple calculation shows that masses greater than about $10^{12} M_\odot$ will not be able to cool by radiation fast enough to assist a collapse. Through estimates like these, we can understand the wide range of masses displayed by the globular clusters, dwarf galaxies and normal ellipticals, spirals, and irregulars in our Universe today.

The *Stelliferous Era* probably began with the first generation of stars forming by about $t = 10^6$ yr. It is almost certain that the globular clusters we see today contain the products of stars as old as these.

The much harder problem is understanding when and how *galaxies* were formed. From the observed data on the absorption line spectra of high redshift quasars, it is known that there exist a very large number of **Lyman alpha** ($Ly\alpha$) alpha hydrogen clouds in the distant Universe, stretching all the way to the highest redshift quasars currently known ($z \sim 5$). Some of these are most naturally interpreted as being galactic disks with detectable heavy elements ($Z > 2$) amounting to an appreciable fraction of the solar chemical abundance. The non-detection of heavy absorption by photons capable of ionizing hydrogen atoms, up to the Lyman continuum energy levels, demonstrates that the high-redshift intergalactic medium (IGM) was very likely to have been in an ionized state for redshifts up to 5. The source of the ionizing radiation cannot be the CMBR, which is too cold at these low redshifts, and thus the possibility arises that even by redshift 5, substantial galactic (and stellar) evolution must have occurred. For a flat EdS universe with $\Omega_0 = 1, H_0 = 70$ km s^{-1} Mpc^{-1}, and zero cosmological constant ($\Lambda_0 = 0$), this leaves just 6.8% of the age of the Universe (9.3 billion years), available for the necessary evolution. This is about 600 million years. While it is easy to see that massive stars could have evolved through several generations in this time, it is very much harder to explain how whole galaxies, like our own, could have been assembled. Our Milky Way rotates once every 200 million years, so the assembly of a galaxy like ours would have to be done within just a few dynamical timescales, if it is to appear as a chemically enriched massive structure in the absorption line spectrum of an astronomer sitting in her own galaxy at redshift 5 today. This problem has been known for several decades, but only recently with the new data on the highest redshift objects can we see that the problem is getting worse and worse, as more and more galactic-scale structures are found at receding distances. The detection of *low* levels of fluctuations in the CMBR by

the COBE satellite, at a level of only $\Delta T/T <\sim 10^{-5}$, sets strong constraints on theoretical models of galaxy formation. It has become clear that the dark matter must be taken into account, but it does not help in the cooling process, as it does not interact with baryons except through the gravitational force. Rather, the dark matter assists gravitational collapse through forming its own relatively large and deep potential wells; the galaxies fall into the densest of these. So far, there is no consensus reached as to the correct model for the origin and evolution of dark matter fluctuations.

In this thesis, it will be assumed that sufficient galactic formation has taken place by redshift 5 to allow galactic interactions and mergers to initiate catastrophic collapses within the large numbers of galactic nuclei. This would be necessary for the building of any model for high redshift AGN (such as the quasars). The latest observational results (Shaver et al. 1996) [125] supply strong statistical evidence that the comoving space density of quasars peaked at redshifts in the range $2 < z < 3$, with relatively very few remaining by the time one gets to redshift 5. Thus, quasars must have just started to grow in large numbers not much before redshift 5. The peak space density of quasars then defines the *Quasar Epoch*, and it is known from the available data that much of the luminous activity of quasars is over by redshift 1 (much smaller numbers of quasars become active at lower redshift).

Continuing onwards into the Stelliferous Era: it is expected that galaxy spheroids are in place by about 3 billion years, and disks by 5 billion years (ballpark estimates). There has been much debate about how one could use the statistics of the properties of distant galaxies for constraining evolutionary models. Again, there is no final conclusive understanding of the details of galaxy evolution, but it may be surmised that the following account would not be far from the truth: galaxy formation is mainly governed by at least three determining factors – the initial angular momentum in the collapsing cloud, the efficiency and speed of gas consumption by star formation, and the position of the cloud relative to other galaxies nearby. Those galaxies that have high angular momentum are more likely to grow into

spirals, provided that they do not suffer tidal interactions or intrusive encounters with nearby galaxies. It seems that this 'placidity' criterion would also be responsible for the slow rate of star formation in spirals as compared to ellipticals, and thus the correspondingly lower rate of gas consumption. Spirals today still have much gas and dust available to form new stars in the future; irregular galaxies even more so. In this picture, ellipticals must have suffered relatively strong or violent encounters with their companions; this creates a common scenario in which the shocking of the resident interstellar medium (ISM), during the merging or interaction of two galaxies, would cause the early collapse of gas clouds into stars. The resulting furious *starburst* activity would consume almost all of the available gas within a much shorter time period than that for spirals and irregulars. This rapid gas consumption would be consistent with their negligible rate of star formation seen in local ellipticals today. As supporting evidence for this scenario, it is noted that ellipticals are almost always found in galaxy groups or clusters, i.e. in *high density environments* that are conducive to early galactic interactions when the Universe was significantly smaller than it is today. The most obvious cases showing the importance of the environment in the evolution of ellipticals are the cannibalistic events occuring in the centers of dense galaxy clusters; giant 'cD' galaxies dominate the cluster by sitting at the bottom of its potential well, feasting on hapless smaller galaxies that are unfortunate to pass too close to the 'devourer'. An example of this type is the M87 galaxy in the Virgo cluster; M87 is also known as Virgo A, one of the brightest EGRS in our neighborhood of the Universe. It may be speculated that a 'likely' requirement for the generation of a powerful active nucleus, such as the one in Virgo A, would be some form of violent galactic activity some time in the immediate past. As a corollary to the interaction hypothesis, any initial spin angular momenta in the interacting galaxies will tend to lose their individual directions, through the large increase in entropy; the formation of ellipticals seems to erase the detailed properties of the participating galaxies. In simulations, tidal tails and bridges are generated in the interactions between 2 spirals; these ejecta would

be efficient angular momentum removers, and the end result is an elliptical with relatively little angular momentum. The removal of spiral angular momentum is important, as it has been shown that most ellipticals are *not* primarily supported by rotation. Instead, they generally have stellar orbits that are distributed anisotropically, creating a triaxial shape for the galaxy.

Much of the above is speculative, and there are no doubt many other plausible scenarios not excluded by the vast store of available data on galaxies and AGN. However, it is the purpose of the present discussion simply to lay down the important questions, ideas and issues for the building of a model for an AGN of EGRS type (in Chapter 5).

By 10^{10} yr, the solar system had been in place for about 5 billion years, and life had evolved on this planet. The Sun has by now reached its middle age, and it is destined to end its life in another 5 billion years, via an expansion into the *red giant* stage (the Earth will be engulfed by its atmosphere), the generation of a *planetary nebula* from the outer envelope of this giant, and finally a collapse into a *white dwarf* star (supported by quantum degeneracy pressure from its electrons).

By the **Russell-Vogt** theorem, the evolution of *isolated* stars is governed solely by the evolution of the mass and chemical composition. The mass is the major determining effect, the chemical composition being a secondary perturbation. Just as for gas clouds, the general driving force in stellar evolution is the minimization of total and gravitational energy, and the maximization of entropy via the release of radiation or heat. For stars residing on the stable main sequence, the negative heat capacity of these condensed bound systems allows them to increase their core temperatures sufficiently enough to enjoy the release of thermonuclear fusion power. However, stars with mass less than about $0.085M_{\odot}$ will fail to burn hydrogen. Also, stars with masses greater than about $100M_{\odot}$ cannot remain stable, as the electrons in their outer layers would be blown away through the intense radiation pressure emanating from their cores. For any mass M, there is a maximum *Eddington luminosity*

L_{Edd} that should not be exceeded if that mass is to remain dynamically stable against radiation pressure. (This maximum mass and luminosity scaling turns out to be important in the interpretation of the energy source powering the central engines of AGN). Indeed, observationally we see stars within just these expected limits, and also a few examples have been uncovered of faint 'failed' stars that are below the brown dwarf maximum mass.

Stellar evolution *off* the main sequence is much more interesting than on the main sequence. Here, a broad understanding can be gained simply by the application of simple physical arguments. Firstly, pre-main-sequence (PMS) evolution proceeds in two stages: *protostars* are formed at the centers of supercritical Jeans mass molecular clouds; they then metamorphose into *PMS stars* that evolve towards the main sequence along so-called *'Hayashi' tracks.* The trigger for star formation for a cloud would be anything that tends to lower its Jeans mass. Equation 1.1 gives the numerical value of this mass, as a function of the temperature and the number density of hydrogen atoms.

$$M_{Jeans}/M_{\odot} = 1.1(T/10K)^{3/2}.(n/10^{6}cm^{-3})^{-1/2}. \tag{1.1}$$

Thus, for typical molecular cloud hydrogen atom densities of $10^{6}cm^{-3}$, and temperatures of $\sim$ 10 Kelvin, a solar mass cloud would be cool and dense enough to collapse. The time scale of collapse governed by the ratio of the final mass to the accretion rate: $M/(dM/dt)$. This is the *accretion timescale*, and it is also governed by the same parameters that determine the Jeans mass. The PMS stage begins when either deuterium or hydrogen fusion is initiated in the central core of the protostar. This happens at about 10^{6} K for deuterium, and 10^{7} K for hydrogen. The PMS stage evolves on a *Kelvin-Helmholtz* timescale, which is just the contraction time required for the loss of sufficient potential energy to allow the star to settle on the main sequence, and engage in steady-state hydrogen fusion. The PMS phase is often also supplemented by residual accretion through an equatorial **accretion disk** (there is much observational evidence from infrared data for the existence of such structures). An

accretion disk is the natural result of angular momentum conservation during the contraction of the protostellar cloud, and it is also believed to be a necessary precursor for the formation of planetary systems around stars.

Once near and on the main sequence, the rate of mass inflow and outflow is observed to decrease to essentially negligible levels.

Stars above about 2 $M_\odot$ have a radiative, rather then convective, energy transport in their interiors. Stars more massive than about 8 $M_\odot$ radiate, contract and evolve so rapidly that they join the main sequence while still in the accreting protostellar stage.

The *main sequence lifetime* is simply determined by the amount of available fuel, which is proportional to the mass of the star, and the rate of loss of this energy set by its luminosity. The theoretical *Schönberg-Chandrasekhar* limit derives an estimate for the amount of hydrogen that can be burnt in the stellar core of a main sequence star; this is $\sim$ 12% of the mass of the star. With this fraction to be fused, a star like our Sun would take 10 billion years to consume its core hydrogen. More massive stars evolve faster, as a general rule, due to their elevated luminosity, and the most massive O and B stars can go through their life cycle on a timescale of just a few *million* years. Conversely, *low mass stars* take much *longer* to evolve to the post-main sequence stage, and, just as for our own Sun, none of them have done so in the $\sim$ 10 billion years that our Universe has been in existence.

It should be noted that the effects of mass transfer in binaries, which form perhaps half of all stellar systems, can dramatically alter the stellar evolution described here for *isolated* main sequence stars. However, the current account would be greatly complicated by a discussion of the possible modifications, and thus these scenarios are only mentioned in passing.

Post-main sequence evolution is also governed by the stellar mass, but in a much more dramatic way. The evolution is relatively fast and violent, when compared to the many millions of years of sedate fusion on the main sequence. When stars exhaust their central fuel source and move on to the transient burning of smaller and smaller quantities of higher

elements (e.g. He, C, N, O, Si, Fe), they increase their entropy and lose energy via the contraction of their inert cores; fusion generally takes place in thin shells surrounding the 'dead' core material. The central contraction can often be accompanied by temporary outward expansion or pulsation of the heated envelope. Once iron is produced, the nuclear binding energy per nucleon can no longer increase, and no further support can be gained through fusion. The fully inert center of the star will henceforth collapse catastrophically.

At this stage, stars below the **Chandrasekhar limit** can collapse into a white dwarf, supported by their electron degeneracy pressure. Equation 1.2 shows that this limit is about $1.4M_{\odot}$, and the mass scale is demonstrably set by the fundamental constants of nature.

$$M_{Ch} = (3.1/\mu_e^2)\alpha_G^{-2} m_{PL} = 5.8 M_{\odot}/\mu_e^2. \tag{1.2}$$

Here, the parameter $\mu_e \sim 2$ is the effective number of nucleons per electron. The fundamental quantity m_{PL} is the Planck mass. The fundamental dimensionless ratio $\alpha_G = 2\pi G m_p^2/hc$ is the *gravitational fine structure constant*, which measures the strength of the gravitational force relative to the effective 'spreading' force arising from the Heisenberg uncertainty principle. It turns out that this combination of fundamental constants sets the scale for all stellar masses, since the allowed mass range, of about 3 orders of magnitude for a stable star, is relatively small when other effects are taken into consideration.

For stars in the mass range $1.4 < M/M_{\odot} < 3$, collapse cannot be stabilized by electron degeneracy, and neutron degeneracy pressure will take over, but in a configuration that is much higher in its **compactness** M/R. Compact, as opposed to *dense*, objects suffer general relativistic effects, as their potential wells are so deep that the Newtonian weak-field approximation to the GTR breaks down. The resulting star appears observationally as a neutron star, but only if it is signalled to us by pulsed radiation from its highly magnetized poles, or else by an accompanying accretion flow from a binary companion in an XRB. Without telltale clues such as these, the neutron star is too small and faint to be detected

in isolation.

For stars in the remaining mass range $3 < M/M_{\odot} <\sim 100$, collapse cannot be supported even by neutron degeneracy. The precise limit is not known for sure, as it depends on the equation of state (pressure-density relation) for nuclear matter at the phenomenally high densities within neutron stars. However, it is clear that there will be some maximum mass above which not even an *infinite* pressure will save a star from collapse into a space of volume measure zero. Such an object has the *maximum* possible compactness and entropy for its mass. It is known as a *black hole singularity*, and to date it remains a theoretical prediction emerging from the GTR. In the case of a non-rotating black hole, the externally apparent (horizon) radius, towards which it seems to collapse, s called the *Schwarzschild radius.* This is a length scale set purely by the constants of GTR:

$$R_S = 2GM/c^2 = 2.95km(M/M_{\odot}). \tag{1.3}$$

The black hole has special and unusual physical properties that are worth mentoining in passing. It has been proven, from general considerations, that the *only* static (vacuum-embedded) solution of a neutral mass M in an asymptotically flat spacetime, assuming GTR, is the Schwarzschild solution, which is perfectly spherically symmetric. Any perfectly spherically symmetric mass distribution (or gravitational monopole) cannot radiate energy via gravitational waves. The charged counterpart is called a Reissner-Nordstrom singularity, though such a structure is not expected to remain charged in any real astrophysical context where highly conducting plasma is present. The *only* stationary solution for a (charged or uncharged) mass M is a rotating **Kerr-Newman singularity**. This perfectly axisymetric solution is not static, as the spacetime around the hole is forced into corotation within a toroidal region called the **ergosphere**, via the **Lense-Thirring effect** in GTR. However, at least the vacuum-embedded spacetime solution can remain time-invariant despite the rotation of the central singularity. The internal structure of the Kerr-Newman solution

is very interesting and unusual, consisting of two event horizons, and a circular ring as singularity. It is theoretically possible, in this solution, to travel to connected universes if one can possibly avoid the ring singularity.

In the classical GTR, the unique Kerr-Newman black hole solution can be described by three macroscopic parameters: the mass M, the angular momentum J, and the charge Q. This would imply, contrary to the Second Law, an enormous *loss of entropy* during the catastrophic collapse, essentially a gross violation of the mathematical rules of probability. That this is indeed the incorrect interpretation was first shown in the theoretical prediction by Hawking (1975) [65] of a quantum mechanical effect whereby all black holes radiate blackbody photons generated by the tunnelling through of vacuum polarization charged particles from *within* the event horizon. Associated with the calculated temperature of the Hawking radiation is an entropy S, which is proportional to the *area* of the black hole horizon. Thus, in the eventual correct quantum gravity theory, objects destined to become black holes actually *increase* their entropy to the maximum allowed extent. As soon as the hole forms, it starts to radiate; it is the less massive holes that radiate faster, as their horizon curvature and gravity is much higher. The temperature can in fact be directly related to the surface gravity at the event horizon. The black body radiation law then says that the luminosity is the fourth power of this temperature.

For all black holes above about 10^{12} kg, the Hawking radiative lifetime exceeds the Hubble time, and so one need not worry about these quantum effects for any black holes of stellar or AGN origin (the central engines of AGN are believed to be massive black holes (MBH) exceeding $10^6 M_\odot$). Thus, a black hole has 'no hair' (negligible classical entropy), but the smaller its head, the brighter it shines !

Should black holes exist in Nature ? The theoretical solutions mentioned above are unique, but there is a suspicion that their mathematical existence and uniqueness may simply be due to an *artificial* symmetry imposed by the mathematical boundary conditions of

vacuum embedding in perfectly flat spacetime. However, Hawking & Penrose have proven **black hole singularity theorems** (1970) [67] that, starting again from very general assumptions, once sufficient mass has collected in a given region of GTR spacetime, a collapse to a singularity is *inevitable.* The general conditions are that (1) gravitation is universally attractive (i.e. the cosmological constant is non-positive); (2) any geodesic must encounter a non-zero curvature somehere along its path ; (3) causality violating closed timelike curves do not exist; and (4) there is sufficient matter in some region of the Universe, such that a convergence (coming together) of geodesics occurs in that region. This last condition could arise if there is a closed trapped surface for photons, or else if there exists a demonstrable minimum angular size for distant objects of fixed size. Given all these reasonable conditions, it is clear that the Big Bang singularity passes these tests (there is sufficient matter concentrated in the early universe, as evidenced from the optical depth to the recombination surface). The theorems are correct in that they predict that GTR spacetime cannot be topologically equivalent to a smooth surface that is everywhere mathematically regular. In other words, spacetime must be *geodesically incomplete* provided there is enough compactification of mass-energy in at least one location.

It is not known whether there are other singularities on smaller scales than the Big Bang, but there are many candidates residing in accretion systems of the AGN and XRB type.

To close our overview of evolution in the Universe, we now turn to the question of which are the most likely macrostates to occur within our *future* light cone (for a detailed scientific look into the 'crystal ball', see the remarkable review by Adams & Laughlin (1997) [1]). The future evolution is of course governed by entropy maximization, part of which is the evolution of a wide variety of forms of mass-energy through maximum entropy black hole states, that decay via Hawking radiation.

The Stelliferous Era will end at 10^{14} yr, when conventional stellar evolution will cease due to exhaustion of gas and dust, and through the dimming and dying out of brown dwarfs and

end-state compact objects (white dwarfs and neutron stars). Stellar or Massive Black Holes will not appreciably Hawking radiate this early on. Compact objects will tend to aggregate together within galaxies, via dynamical friction; by the Second Law, the sum of black hole areas (i.e. entropies) can only increase with time.

The *Degenerate Era* lasts until 10^{37} yr, and the major events will be the proton decay of all types of remaining stars or other baryonic matter, and the annihilation of any non-baryonic dark matter.

The *Black Hole Era* lasts until about a *googol* number of years (10^{100}), by which time all black holes up to galactic mass scales will have Hawking evaporated. Generally, these produce extremely long wavelength, ultra-cold radiation (the more massive the hole, the lower is its horizon gravity and surface temperature).

Finally, the furthest one can predict today is the time of the *Dark Era*, where horizon size black holes will evaporate, and all matter will suffer higher-order proton decay effects that are theoretically expected from considerations of current GUT theories. This leaves us at about $\sim 10^{200}$ yr.

The above account does not mention that our Universe not only began in a low entropy state with a high symmetry in the fundamental laws, but that it also must have been 'finely tuned' to produce the structures that we see. The solutions of gravitational evolution of an isolated massive system such as our Universe are highly unstable. For example, at the Planck epoch, the Ω_0 parameter must have been tuned to an accuracy of 1 in 10^{60} in order to ensure that our Universe did not immediately collapse suddenly, or dramatically inflate forever ! There are too many other fine tunings in the physical constants to be regarded as simply the result of accident; the failure of some of these numerical coincidences would have prevented the formation of stars and galaxies, and also of carbon-based life, intelligent or not. An example of a physical scale set by the fundamental constants is the Chandrasekhar mass, though luckily for us it seems that this particular mass only determines the approximate

number of baryons of our Sun. The fusion of hydrogen and helium to carbon in stars is much more directly related to our existence, and it turns out that carbon would *not* have been produced if certain energy resonances in 2 specific atomic levels of beryllium and carbon did not exist ! Much thought has been devoted to the metaphysical reasons for why these tunings should exist; they collectively are known as the discussion of the **Weak and Strong Anthropic Principles**, see Davies (1982) [41] for a lucid account. However, one cannot use *probability* arguments for *isolated cases* like our Universe, so any debate over the fixing of a low level of initial entropy level, or on the 'odds' of creating our Universe, etc., ultimately cannot prove scientifically useful. All we can say is that we may have been *astronomically* lucky that the Universe turned out the way that it did.

Much of the synthesis above is drawn from the abundantly available popular and academic literature. I hereby supply the interested reader with a partial list of reference sources that have proved useful.

Hawking & Penrose (1970) [67], Hawking (1975) [65], Landolt-Börnstein (1982) [68], Clayton (1983) [30], Davies (1982, 1989) [41], [40], Shapiro & Teukolsky (1983) [124], Bowers & Deeming (1984a,b) [22], [23], Ostriker (1991) [112], Ünsold & Baschek (1991) [143], Narlikar (1993) [109], Padmanabhan (1993) [113], Hartmann & Impey (1994) [64], Silk (1994a,b) [128], [127], Rees (1995) [117], Rowan-Robinson (1996) [118], Longair (1996) [102], Adams & Laughlin (1997) [1].

1.3 Extragalactic Radio Sources

Extragalactic radio sources were first detected as discrete sources of fluctuating 'radio noise' by Hey, Parsons & Phillips (1946) [73], However, the first optical identifications were only made 3 years later by Bolton, Stanley and Slee (1949) [21]. These are now known as Virgo A (galaxy), Centaurus A (galaxy), and Taurus A (the Crab Nebula supernova remnant). As the radio resolution achievable at that time was relatively poor with the available technology, it was not possible to identify these sources with an optical object. At first it was believed that these so called 'radio stars' were galactic sources, just as the non-thermal radio continuum radiation was believed to be galactic by virtue of synchrotron emission from the ubiquitous and spiralling cosmic ray electrons in our galactic halo. By 1951, many more such discrete sources were found, and it was Gold (1951) [55], who first publicly proposed the *extragalactic* origin for these sources, by reason of their overall sky distribution, which was consistent with isotropy.

Marked improvements in angular radio resolution were achieved by the advent of the radio **interferometer**, working on the principle of **aperture synthesis**: the receiving (unfilled) aperture is broken up into movable detecting surfaces, and the mutual coherence function, i.e. the correlation, of the separate received signals is painstakingly estimated by measuring the fringe visibility as a function of projected baseline towards the radio source. In effect, this was the first use of a radio wavelength Michelson interfometer in what was soon to become a new field of astronomy. The technique was pioneered first in England by M. Ryle, and in Australia by B. Mills and J. Bolton, and the principle of aperture synthesis was very fruitfully applied to make the first radio sky surveys, from England (Cambridge surveys: 1C & 2C) and Australia (MSH survey).

For a basic understanding and a modern account of the practice of aperture synthesis, it is useful to look at: Perley, Schwab & Bridle (1989) [115], and Thompson, Moran & Swenson (1986) [141].

From diffraction theory, the angular resolution is of order $\theta_{FWHM} \sim \lambda/B$, where B is the projected baseline. With the much improved interferometric positions, due to the use of long baselines B, the first confident optical identifications could be made (Baade & Minkowski 1954, [4]). It was found that Cygnus A had a very unusual optical appearance quite unlike a normal galaxy; it seemed to be in a violent state of disruption, perhaps even reminiscent of a merger or collision of two galaxies. The question arose: perhaps the rarity of the radio emission is directly connected with the rarity of the apparently violent interaction ?

Prior to the identification of Cygnus A, it had just been determined that its radio morphology was *double*, a hint of a common pattern to be repeated in future radio observations. The two components of the double radio source were found to lie roughly *equidistant* on either side of the violently disturbed optical galaxy. It was later realized that many of these double radio structures were located many 10s to 100s of kiloparsecs away from the optical emission of the galaxy. Thus, the picture emerged that perhaps a violent interaction between two normal galaxies, sometime in the past, had somehow caused the central nucleus to eject ionized gas or plasma far out into the surrounding IGM.

In 1963, the mysterious, blue, **quasi-stellar objects** (QSOs), were found to possess highly redshifted lines of well known resonance and forbidden atomic transitions. These early discoveries were coincident with some of the brightest radio sources in the 3C Cambridge Survey; for example, **quasar** 3C 273 was discovered by M. Schmidt (1963) [122] to have a redshift of z = 0.158 (this meant that the wavelengths had all been extended by a factor of *sim* 16%). Thus, if the redshifts were due to cosmological expansion, they would have to be extremely distant, and correspondingly enormously luminous; as bright as 1,000 to 10,000 times the output of a normal optical galaxy. The *mystery* about this huge energy output is that, in some sources, it would fluctuate on timescales of hours to years; this sets a incredibly compact upper limit on the size of an object that is apparently capable of greatly outshining an *entire galaxy* full of stars. This started a great debate about whether the redshift was

really cosmological; could it be a Doppler effect, or perhaps just a gravitational redshift from more local sources, such as the neutron stars ?

The gravitational redshift hypothesis from a compact stellar mass was shown later to be inconsistent with measured redshifts reaching unity or above. Other scenarios, such as ejection of compact sources from our own galaxy, were considered by many to be highly contrived. The majority view today is that the redshifts are due to the expansion of our Universe. This means that we cannot escape the serious problem of exactly how to generate such large powers from such confined regions of space.

Another great debate over the cosmological nature of the radio sources in general (not just the quasars), was their distribution in space. If one assumes a population of constant luminosity sources spread *uniformly* throughout *static Euclidean* space, then since the flux falls off as the -2 power of the distance R, and the volume increases as the $+3$ power of R, it is easy to show that the overall number $N(> S)$ *brighter* than a given flux density S (in units of $10^{-26} W m^{-2} Hz^{-1} = 1$ Jansky (Jy), say) would fall off as the (-3/2) power of S. Even if the population contains sources that span a *range* in brightness, the same argument holds for subsets of equally bright sources, and hence for the whole population. The dimming of radiation due to the stretching of expanding space would tend to be greater for the more distant and apparently fainter sources, and hence any deviations from the static Euclidean ideal would be to *flatten* the slope in the counts $N(> S)$ for lower flux densities S.

However, the better executed of the early radio surveys (3C and Parkes - PKS: the earlier 2C survey gave the 'wrong' counts due to confusion of sources by a low resolution beam) showed that the slope was instead *steeper* than static Euclidean, at least for the the higher flux densities, with a power law of -1.8 instead of -1.5. Later, it was found that the more sensitive 4C survey had encountered at 'hump' in the counts at a level of ~ 1 Jy; this was comprised of the initial steepening to 1 Jy, followed by a flattening to fainter levels. The excess in counts was highly significant; about 1 to 2 orders of magnitude over the expected

static Euclidean trend.

This was the start of another big debate over the interpretation of the radio source data, this time between the Big Bang and the **Steady State** models for our expanding Universe. Whereas the Big Bang simply assumes that all the matter in the Universe came into being at one moment, the Steady State view instead spreads this necessary 'energy violation' over an infinite amount of time; instead of assuming the mere spatial uniformity of the Big Bang, the **Perfect Cosmological Principle** was adopted, by F. Hoyle, H. Bondi and T. Gold (1948) [54], [76], which amounted to saying that the Universe was uniform in the large not only in space, but *also in time.* The idea was that one could avoid mysterious beginnings, and possible ends of time, this way. However, a price in the physics had to be paid; mysterious creations of matter had to occur over infinite time, at a calculable rate of about a few atoms per cubic centimeter a year, to maintain the time invariance of the local density of matter within any region.

These questions of interpretation were finally settled by a combination of events; the increasingly good statistics of larger and larger radio surveys of discrete sources, and the discovery of the CMBR. The latter showed that the existence of a much hotter, dense state, in the past, was the only way in which the photons and the present day abundances of the light elements could have been formed at the observed levels. A steady, unchanging Universe was manifestly inconsistent with the CMBR observations. Also, with regard to the radio source counts, the statistics were undeniably inconsistent not only with the Euclidean expectation, but also with *both* the Big Bang and Steady State predictions (see the review by M. Ryle (1968) [119]).

Ryle's conclusion was that the assumption of a invariantly bright population must have broken down for the distant radio sources (some of the radio sources in the surveys were actually optically-loud quasars with measurably high redshifts, so the approximate distances to these, at least, were not only extragalactic, but cosmological to boot). In other words, the

mean properties of the distant radio source population must have evolved over cosmic time, in the sense that they were more active and luminous, perhaps in greater numbers too, in the distant past.

The CMBR was evidence for the evolution of our Universe. The radio sources were evidence for the evolution of distant luminous matter within our Universe. Thus, it seems that there is incontrovertible evidence that physical laws must drive a non-trivial evolution in the mean properties of gravitating objects, at least over cosmological time scales.

With these early stumbling blocks out of the way, the question still remained: what is the power source behind the EGRS ?

Nowadays, we have the benefit of much more efficient instumentation, and other tools such as ultrafast computers with which to test theories by simulation. As an example of the advance in technology and technique, Figure 1-1 shows a Very Large Array aperture synthesis map of the first EGRS discovered; Cygnus A. One can see all the features of a typical 'core double' radio jet; the morphology and emission suggest a central core 'engine' ejecting highly collimated **jets** in two opposite directions. There are probably strong shocks at the final 'hotspots' (peaks in radio emission), and the post-shock material forms a lobe and perhaps in time develops into an enveloping 'cocoon'. The remarkable linearity and stability of the jet direction indicates a *protracted* period of energy release in the central engine; at a projected size of $\sim$ 200,000 light years per jet, and assuming the plasma flow velocity is less than 10% of light speed (this is not unreasonable given the relativistic speed in the core, and the fact that jet momentum must be lost through entrainment of the IGM), a *minimum* duration for the current engine activity should be $\sim 2 \times 10^6$ yr. If the mean population jet advance speed is non-relativistic, at a level of $\sim$ 0.01c, as I propose to demonstrate from the MIT-VLA Snapshot Survey, then this time is extended to $\sim 2 \times 10^7$ yr. From assuming about an equal amount of magnetic field and particle energy in the radio lobes, brought about during the generation of the observed synchrotron radiation, mature,

Fig. 10-21. Radio picture of Cygnus A obtained by Perley, Dreher and Cowan (1984) with the VLA at 5 GHz with data processing and enhancement of detail done at JPL. Overall extent is about 115 arc sec with resolution of 0.4 × 0.4 arc sec. *(Photograph courtesy of National Radio Astronomy Observatory, operated by Associated Universities, Inc., under contract with the National Science Foundation.)*

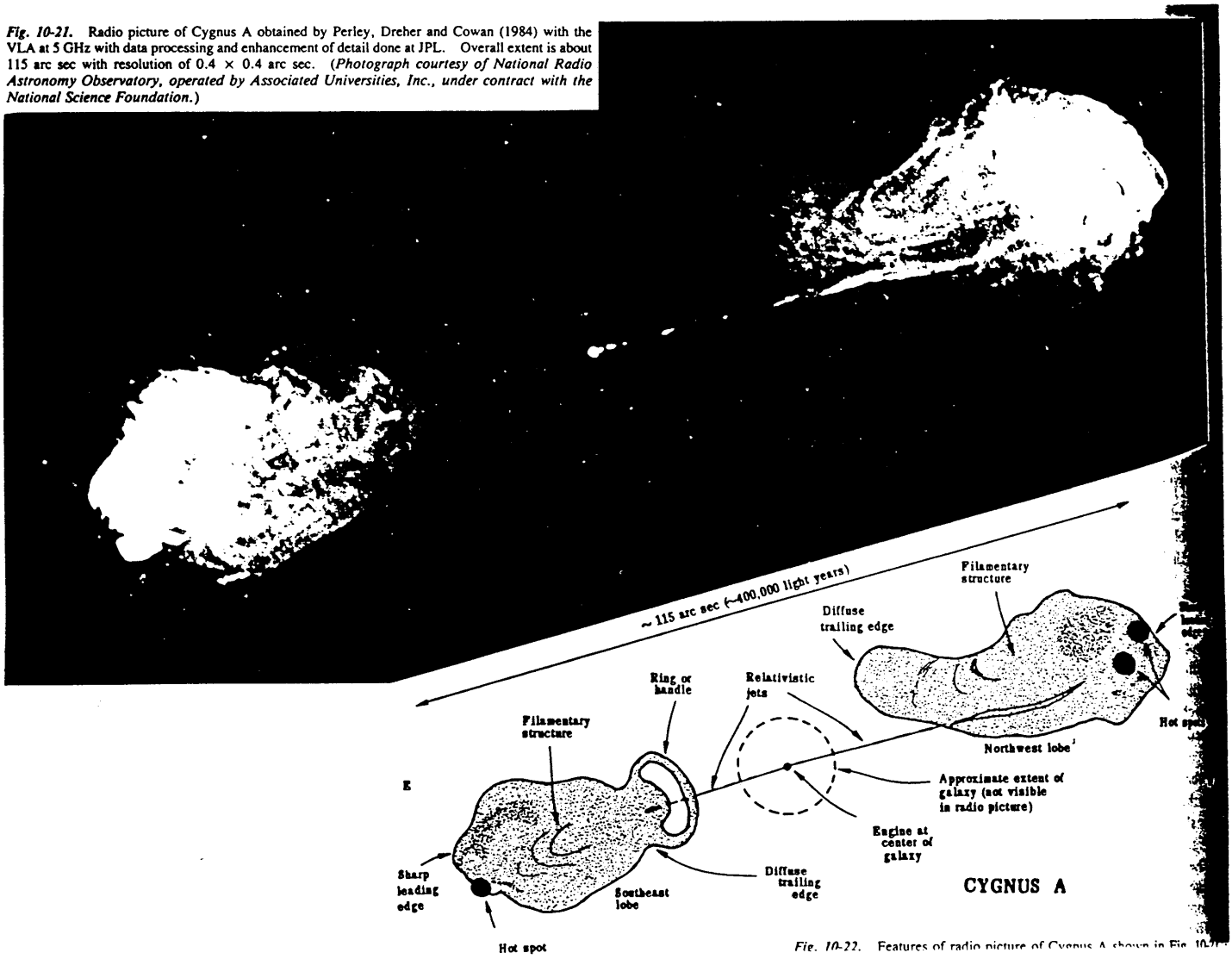

Figure 1-1: NRAO Very Large Array Snapshot of a prototypical double lobed radio galaxy, Cygnus A. The central radio source lies in the giant elliptical galaxy M87, residing in the Virgo cluster of galaxies. There are two long jets leading from the central source to each of the radio lobes; these lobes contain the residual shocked material after its passage through the peak intensity hotspots. The high degree of symmetry, and the preservation of the jet stability across many kiloparsecs, are typical of extended structures in EGRS. Inset is a schematic diagram to aid in interpretation. This figure has been reproduced from Kraus (1986).

powerful, extended radio galaxies such as Cygnus A can be shown to have a **minimum equipartition energy** of $U_{min} \sim 10^{59}$ erg, or more. This enormous figure corresponds to about 10^6 times the *total* energy liberated in a the core collapse of a supernova explosion; it could also be thought of as the *total annihilation* of 55,000 solar masses.

What can possibly cause the generation of this much power, and for so long a time ? Is new physics demanded ? How does the jet remain so stable, despite the fact that it travels to distant regions far outside the M87 host galaxy ? To try to help answer some of these questions, the AGN astronomical community has built up a 'straw-man picture' of the events transpiring within the core of the galactic nucleus; one of these recently published 'pictures' appears in Figure 1-2.

The stability and symmetry of the radio jet axis in extended EGRS strongly suggests that the infall of mass cannot be spherical, i.e. this idealized isotropic symmetry must somehow be broken in jet-producing AGN. The most likely model proposed so far, for reasons of energy and efficiency, would be one involving the extraction of rotational energy from a rapidly spinning Kerr-Newman black hole. This would be energetically allowed by the Penrose process, but a more realistic model would be one akin to the electromagnetic extraction of energy via the torquing up of magnetic field lines threading both the black hole plasma magnetosphere and the accretion disk in the equatorial plane (e.g. Blandford & Znajek 1977 [19]) The accretion disk can be either thin or thick, depending on the fraction of pressure supplied by radiation as opposed to gas pressure; thick disks would tend to occur in AGN accreting at around their maximum allowed rate, their *Eddington luminosity* L_{Edd}. If this happens, a natural collimation mechanism would be predicted for the escaping jet plasma. The accretion disk is itself probably fed from a much larger *torus* of galactic stars and dust. The jet escapes *relativistically* along the black hole spin (symmetry) axis, and it must be so highly collimated that it would be able to survive its long journey of order millions of years, or more. The radio lobe and cocoon act as a 'waste energy baskets' for the collection of

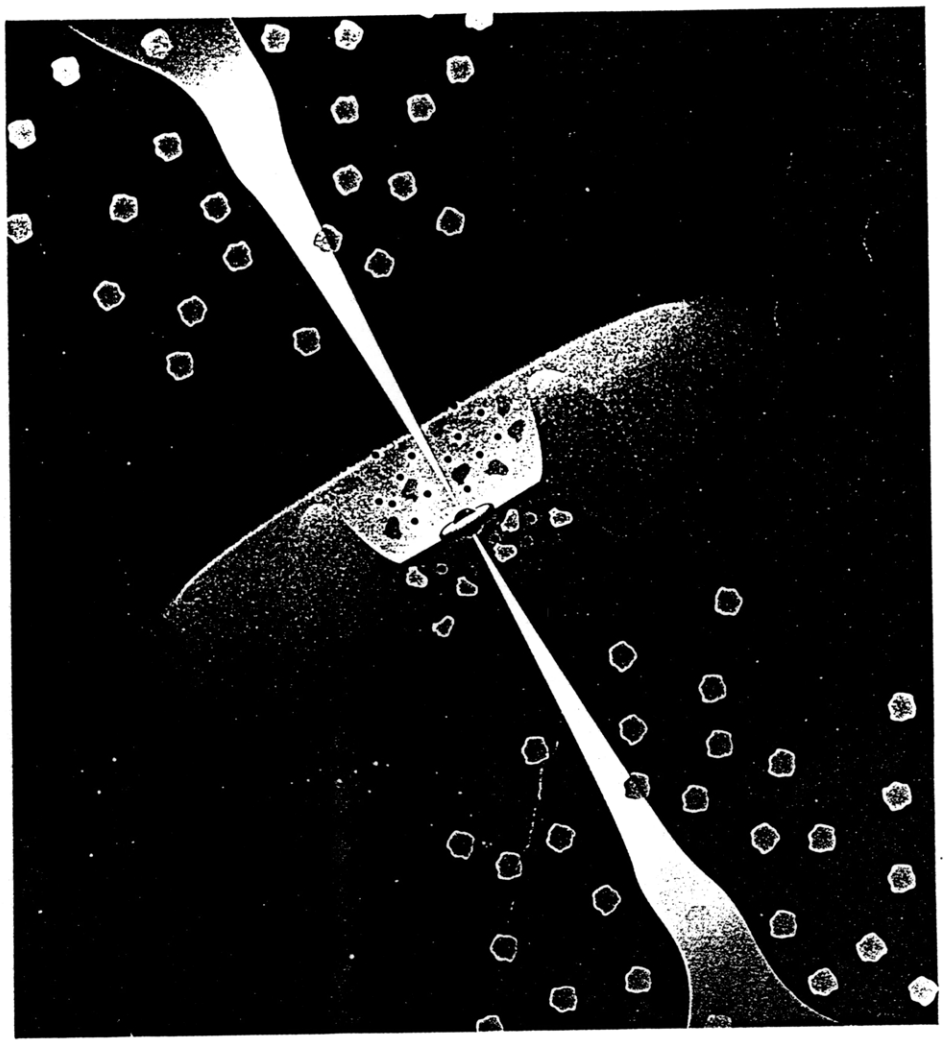

Figure 1-2: A possible explanation for what happens close to the central engine of an AGN that produces extended radio structure (jets). The energy is tapped off the rapid rotation of a massive rotating black hole. This process is unknown, but probably involves the allowed extraction of energy from within the ergosphere region of the hole. Two jets of highly magnetized plasma are produced, which traverse the central nucleus in opposite directions along the black hole spin axis. As the temperature drops further away from the hole, the type and motion of the orbiting gas clouds changes from fast and highly excited or ionized, to lower velocities and excitations further away. Accretion of nuclear stars, gas and dust onto the hole can be regulated by a cool outer torus and a hot inner accretion disk. This figure has been reproduced from Megan Urry & Padovani (1995).

material, which has been sufficiently slowed down by some combination of strong shocking and entrainment of external matter.

This picture seems to be qualitatively consistent with most of the AGN data available, though these ideas are *not* yet at the level of predicting the events for an average EGRS, for this would require 3-dimensional magnetohydrodynamic (MHD) plasma simulation over many orders of magnitude in the physical variables. Near the hole, one also has to be mindful of post-Newtonian GTR effects, such as the 'frame-dragging' of spacetime into corotation with the black hole, as well as the gravitational lensing of the photons around the hole.

In parallel with the highly imaginative physical scenarios that have been proposed for AGN, one must keep in mind that the constraints from the data, while always improving, are still far away from being able to falsify the straw-man pictures. After all, we still do not have *hard evidence* for the existence of bona fide black holes. The proof would require showing that a massive object had a minimum compactness (M/R) greater than that allowed by GTR. For even a billion solar mass black hole, the required maximum Schwarzschild radius is about 3×10^9 km, which is just beyond the orbital radius of Jupiter about our Sun ! Due to resolution and opacity effects, we are well beyond imaging a candidate MBH on these scales; for our Galactic center MBH candidate of $2 \times 10^6 M_\odot$, a resolution as good as 0.1 parsecs would still fall short of the compactness requirement by a factor of fully 5×10^5.

Turning to the acquisition of data on MBH candidates, the best resolutions have been afforded by the various types of modern radio interferometer; the VLA with resolution down to $\sim 0.2''$, the Very Long Baseline Array (VLBA) with baselines of order $\sim$ 10,000 km, and with resolution $\sim$ 1 mas; and the orbiting VLBI satellite Halca/VSOP, with resolution $\sim$ 0.1 mas. At the VLA resolutions for the MIT-VLA Snapshot survey, one can only attempt to investigate the kinematic details of the kiloparsec scale physics; much more model interpretation would be required to guess at the events in the central engine, though one of the aims of this thesis is to reach the milestone of setting forth a theoretical path for the systematic

study of EGRS in the future.

One of the goals of my thesis research is to search for new examples of multiply imaged gravitational lensing, predicted by the GTR, and first discovered for the 'double quasar' Q0957+561 by Walsh, Carswell & Weymann [149] (1979). The subject of **gravitational lensing** of the light from distant AGN by intervening massive galactic and cluster potentials has not been discussed here, but the reader is directed to the excellent textbook by Schneider, Ehlers and Falco (1992) [123] for further information.

Excellent review articles on AGN, aperture synthesis imaging, and EGRS may be found in the following publications and books:

Verschuur & Kellermann (1974) [145], Blandford & Thorne (1979) [18], [66], Miley (1980) [105], Landolt-Börnstein (1982) [68], Bridle & Perley (1984) [25], Rees (1984) [116], Begelman, Blandford & Rees (1984) [9], Blandford (1986) [19], Verschuur & Kellermann (1986) [146], Thompson, Moran & Swenson (1986) [141], Perley, Schwab & Bridle (1988) [115], Bertotti et al. (1990) [15], Blandford, Netzer, Woltjer (1990) [17], Hughes (1991) [77], Blandford & Narayan (1992) [16], Antonucci (1993) [3], McCarthy (1993) [103], Wall (1994) [147], [53], Megan Urry & Padovani (1995) [144], Kormendy & Richstone (1995) [86], Burke, B. & Graham-Smith, F. (1997) [28], Dunlop (1997) [44], [78].

1.4 Young Stellar Clusters

All non-primordial stars are thought to be born inside cool regions of giant molecular clouds. These star forming regions are easily identifiable through their substantial infrared emission, and their association with optical obscuration due to dust, and also with microwave emission from molecular gas (e.g. carbon monoxide emission lines are almost always detected in these clouds). Many of the youngest stars are known to be completely optically obscured, but when some of these are observed in the visible, they are invariably seen to be descending evolutionary tracks in the HR diagram, called **Hayashi tracks**. That is, as a star contracts quasi-statically on its approach to main-sequence maturity as a stable H-burning star, it will tend to decrease its luminosity and radius from the high values it had while still embedded within the collapsing dust and gas. This suggests two things: that the star was initially larger and hotter than its main sequence values, and that it is capable of dispersing its surrounding material (star forming clouds only convert a fraction of their total mass into stars – the process is not efficient under normal quiescent conditions). Indeed, young visible and IR stars (the lower mass 'T Tauri' and higher mass 'Herbig Ae/Be' stars) are often observed to have strong, rapidly variable emission lines of hydrogen, and some are even seen in the ultraviolet and X-rays. In addition, over the past decade, many examples of **bipolar outflows** have been collected in numerous observations of these young stellar regions. It is probably *not* a coincidence that similar 'jet' and 'hotspot' features are seen on a very much larger scale in AGN, and on a similar scale in XRB: the common divisor among these systems is that they are: (1) collapsing and (2) possessed of a large quantity of angular momentum due to their initial conditions. The basic problem of gravitational collapse is to build a theory by which an object will lose its energy, accrete, drive an outflow at some point, and still end up with only a tiny fraction of the initial angular momentum in the residual central object. This is a difficult problem, and it is currently believed that the polar YSO outflows and equatorial accretion disks are somehow involved in engineering these metamorphoses.

Figure 1-3 shows an optical red (negative) image of the very well studied Rho Ophiuchus cluster. The crosses mark the locations of IR sources believed to be young stars (which are hidden from view by large columns of dust).

Figure 1-4 sketches a general picture of our current understanding of what goes on inside the dark clouds.

To turn the clock backwards in the life cycle of a YSO, the Jeans instability criterion predicts that a given stellar mass portion of a molecular cloud will collapse if it loses support from a combination of magnetic, turbulent and thermal energies. The way in which this is achieved is still unknown, but there have been theoretical models published for all three of these effects. Evidently, GMCs of thousands of solar masses must somehow fragment as they cool; provided sufficient breaking up can occur, stars of normal stellar masses can be formed. During the collapse stage, the star will accrete matter and start to radiate its gravitational binding energy away. Conservation of angular momentum favors the higher angular momentum material to fall *away* from the rotation axis of the cloud, forming an equatorial disk. Viscous processes (e.g. due to friction between dust grains, molecules and atoms) will help to radiate some of the binding energy away, but the conservation of angular momentum in a single star system would require that some matter be flung out, if the overall gas velocity and temperature is to decrease with time. Through an unknown set of mechanisms, possibly involving magnetized ionized gas in the disks, the angular momentum of the central core does get removed; and outflows eventually appear (this is reminiscent of models proposed for the evolution of MBHs in AGN). There is evidence that visible young stars arriving at the main sequence tend to have very *little* rotation, though a small fraction of YSOs are indeed fast rotators.

An important observational fact of the distibution of stars in the HR diagram is that those with masses less than about 8 $M_\odot$ are bounded above by a luminosity locus with radius essentially a function of mass only: $R < R(M)$ (Stahler 1983 [131]). This locus

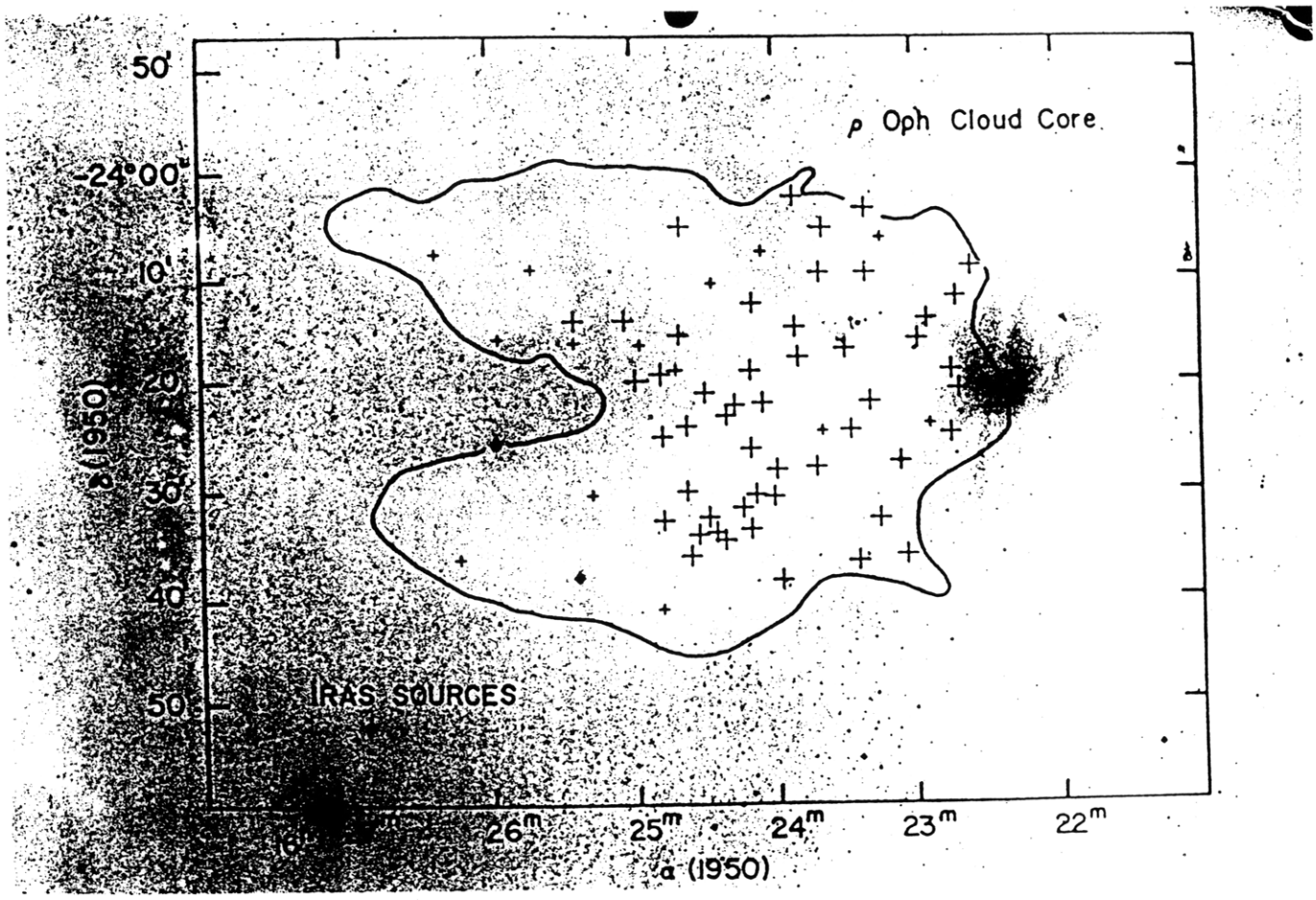

Figure 1-3: The Rho Ophiuchus dark cloud: this is an overlay of the IRAS mid-infrared 12 μm emission peaks onto a red filter photograph from the Palomar Sky Survey. The contour represents a level of carbon monoxide molecular emission. This is a negative photograph, so the cloud is indeed optically dark, with embedded infrared-bright sources which locate the positions of Young Stellar Objects (YSOs). At higher IR sensitivity, at least a few hundred peaks are found. This figure has been reproduced from Wilking, Lada & Young (1989).

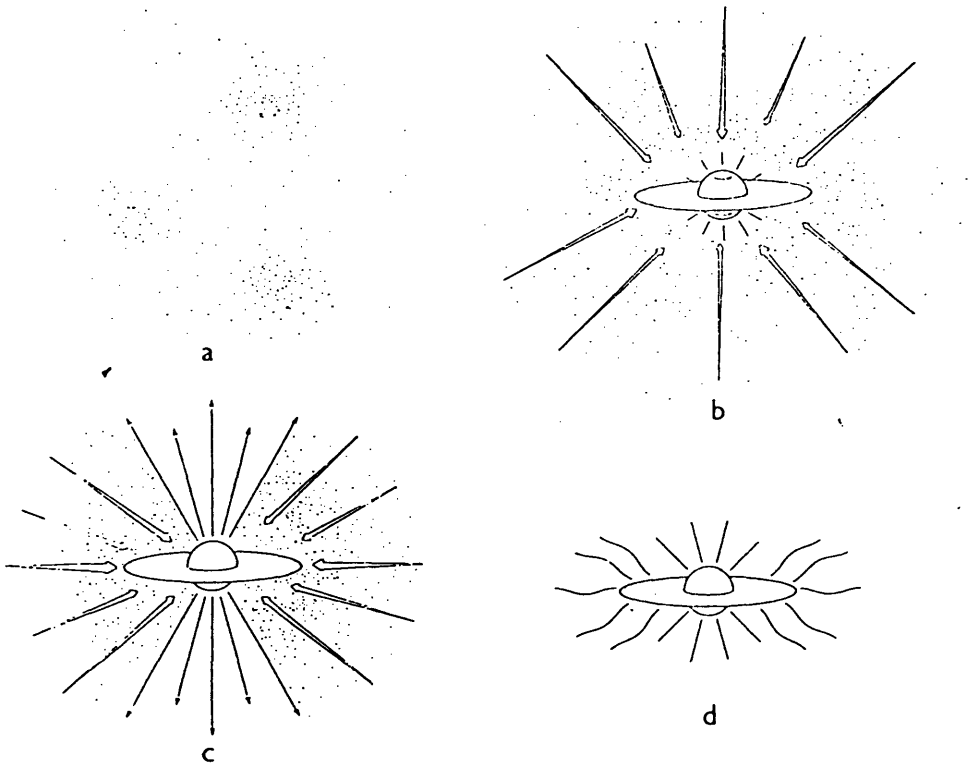

Figure 7 The four stages of star formation. (*a*) Cores form within molecular clouds as magnetic and turbulent support is lost through ambipolar diffusion. (*b*) A protostar with a surrounding nebular disk forms at the center of a cloud core collapsing from inside-out. (*c*) A stellar wind breaks out along the rotational axis of the system, creating a bipolar flow. (*d*) The infall terminates, revealing a newly formed star with a circumstellar disk.

Figure 1-4: The general theoretically assumed scenario for the birth and formation of a star. The mimimal set of important physical effects that need to be understood by any self-consistent physical theory of star formation, and early stellar evolution, should include the following: the role of magnetic fields and turbulence; gravitational collapse accompanied by radiative cooling; accretion probably through an equatorial disk which is a matter and angular momentum repository; the role of magnetic fields; and the mechanism by which the initial angular momentum is dispersed, and how this relates to the bipolar outflows that are observed along the polar axes. This figure has been reproduced from Shu, Adams & Lizano (1987).

is called the **stellar birthline** for low-mass stars, and it can be interpreted essentially as the locus of points where embryonic protostars start to embark on their journey to the main sequence. At about this critical stage, it seems that most YSOs are able to stop accreting (thus forfeiting their membership as protostars), with the major mode of energy output switching to a combination of convective and radiative loss of energy from both fusion reactions and **quasi-static contraction** of the stellar layers. Residual accretion may continue in some objects, but this will not be a major long-term effect at this stage of the life cycle. This phase is known as the PMS stage in this thesis. Stars more massive than the 8 $M_{\odot}$ limit completely bypass this stage.

Once on the main sequence, the stars are observed to follow a statistical mass distribution that is, roughly on the average, invariant over the local solar neighborhood (Miller & Scalo 1979 [106]). It appears that the relative numbers of stars per unit mass, $\Phi(M)$, is approximately a log-normal function (quadratic in the logarithmic quantities), with a high mass power law form $\Phi(M) \sim M^{-2.35}$, first identified by Salpeter (1955) [120]. It has traditionally been assumed that this **initial mass function** could be obtained by simply transforming the *observed* luminosity function $\Phi(L)$ by using a calibrated (or theoretical) **mass luminosity relation** $M = M(L)$.

However, in the context of evolving YSOs embedded in molecular cloud cores, the assumption of 'no evolution' is manifestly violated, as we see that the initial states (the cloud) and the final states (the main sequence stars) are utterly incomparable in all of their measurable physical properties.

Just as for the extragalactic radio sources, it is seen that whether we think about these astrophysical populations theoretically or observationally, we are forced to the conclusion that collapsing systems such as these need to have their evolution explicitly modelled as a basic requirement for any broader physical theory.

It is the focus of this dissertation to predict both the mass and luminosity evolution

of embedded young stellar populations, by use of a simple phenomenological model, The inputs to the mathematical solutions of accreting populations of objects must ultimately be set by *the physics.* It is not intended here to tackle this much harder problem; instead, the plan will be to propagate the mathematical solutions for the evolving mass functions of accreting protostars forwards in time, to the point that the *stellar birthline* is reached. Stahler (1980) [133], [134], [135] has calculated the radius R and luminosity L for spherically accreting protostars, as a function of their mass M Thus, given a mass spectrum predicted from an assumed simple accretion law, and the mass-luminosity relation from the protostar calculations, one can then automatically derive the **protostellar birthline luminosity function.** Using pre-calculated modern evolutionary PMS tracks, one can then simply evolve forward from this point to obtain the luminosity function of the young stellar cluster as a function of time. There are evidently many approximations and assumptions that have to be made, but this type of detailed mathematical calculation has not been done before (one approximation is the assumption of the absence of another stellar companion, and another would be the ignoring of the effect of an accretion disk).

The ultimate aim will be to see if the actual bolometric luminosity function of the Rho Ophiuchus embedded stellar cluster can be *reasonably* modelled by an *a priori* luminosity function of the expected age. It would be very interesting if this mathematical technique, once perfected, could be applied to place confident *ages* on the stars buried in these clouds.

Excellent reviews for further information can be generally found in the papers of, e.g., Steven Stahler, Charles Lada, Fred Adams, and Frank Shu:

Stahler (1980, 1983, 1985, 1988, 1990, 1991, 1994), [130], [133], [134], [135], [131], [132], [136], [137], [114], [138], [139]; Shu, Adams, Lizano (1987) [126].

1.5 Summary

The natural physical evolution of bound gravitational systems is to lose their energy and increase their entropy, via the process of accretion. Various luminous examples of this activity are observed: accretion onto young protostars in molecular cloud clusters; and more speculatively with massive black holes in the nuclei of active galaxies.

The number statistics of extragalactic radio sources can supply some very limited information on the cosmological model for our Universe, but it is clear that the observed properties must be dominated mainly by the effects of the secular evolution of the global population. It should be possible to understand this population evolution as the sum total of the evolutions of individual EGRS, but it is expected that this **unified model** will necessarily be highly complex and speculative, requiring much numerical calculation over a wide range of physical regimes. However, even a comprehensive *phenomenological* model would be a significant first step forward.

The number statistics of young stellar clusters have their own problems with the hoped-for predictions. Using established physical predictions of the evolution and structure of protostars and contracting PMS stars, it should be possible to build a mathematical model to predict the evolution of the statistical distributions as a function of time. An important boundary condition on the mathematical solutions is the matching of the late-time solution to the observed final mass spectrum of mature main sequence stars, known as the **initial mass function**.

The proposed phenomenological models are intended to be an initial bootstrap to more physically representative theories.

Chapter 2

Observations

'Why are sky surveys important in astronomy ?'

The answer to this simple question is that sky surveys are the basic source of data required for the systematic scientific analysis of the myriad objects and structures existing within our Universe.

In particular, radio wavelength sky surveys are especially useful for cosmological applications, as powerful extragalactic radio sources can be seen from across the vast distances spanning our observable Universe, back to a time of just ~10% of its current age. Closer to home, the 21 cm H I spectral line emitted by large columns of neutral hydrogen have greatly helped us discern the spiral structure in our own Milky Way, as well as the rotational velocities of other spirals in our local patch of the Universe.

There are two types of survey: those which produce reasonably **complete samples**, and those which do not. The latter are referred to as **incomplete** samples. Surveys can also come

in two flavors: those which record the **continuous** distribution of surface brightness across the sky, and those which concentrate on extracting the fluxes and positions of any **discrete** sources. Finally, surveys can be executed using photons arriving in different parts of the electromagnetic spectrum. The choice of telescope and observing frequency will affect the **resolution** and **sensitivity** of the survey, and ultimately its **completeness** and **reliability**.

The 'complete' survey is a fiction; nobody can guarantee with absolute confidence that a given survey is perfectly representative and reliable. However, the typical astronomer will usually accept 'essentially complete and reliable' surveys for the purposes of statistical studies of the sources of electromagnetic radiation in the sky; the level below which he will reject the survey, on the grounds of statistical misrepresentation of the target population, is not well defined. If a survey is estimated to be greater than 90% complete, and 90% reliable to boot, then most astronomers will not object to the statistical use of such a survey.

An acceptably 'complete' and 'reliable' survey captures an accurate record of the photons which arrive at a single epoch, at the Earth, from our past-directed light cone in the spacetime of our Universe. Powerful extragalactic radio sources can act as beacons useful for probing the depths of our Universe, sampling it at a wide range of locations and times down the light cone surface. At radio wavelengths, they offer the distinct advantage of being unobscured by intergalactic dust, which may be a more serious problem in the optical window.

The practical scientific uses of a complete and reliable survey are many:

- It forms a statistically representative database with which to constrain physical and empirical models of the population of emitters. For example, differential source counts can be compiled, which quantify the surface density of radio sources on the sky as a function of radio continuum flux density cutoff. Such statistics, and others like these, can provide some weak constraints on both source evolution models and cosmologies. Stronger constraints on evolution can be gained if source redshifts for complete samples are collected.

- Uniform radio continuum surveys invariably contain information on new flux density and position calibrators, for use in the calibration of other surveys.

- A series of such surveys can be used to assess the true completeness and reliabilty of each one, as well as the time variability of the observed properties of a population.

- It may provide preliminary data on sources with interesting physical characteristics, e.g. multiply-imaged gravitational lenses.

- Large-area sky surveys are necessary to provide supporting data on the large-scale clustering and dynamics of galaxies in our Universe.

- In observing cosmologically distant sources, one can use their lack of significant proper (i.e. 'sideways') motion to define an astrometric coordinate reference frame for the purposes of time-keeping and navigation. Presumably such directional frames are non-rotating with respect to the unique comoving frame at rest with respect to the mass-energy within the observable Universe.

Radio continuum surveys have only been in progress since the 1950s. As electronic technology has improved over the past 4 decades, the observing frequencies used in all-sky surveys have been continually extended upwards, from low ($\sim$ 100 MHz) to high ($\sim$ 10 GHz) frequencies. Along with a general increase in the collecting area of the primary antenna dish, this yielded a concurrent increase in both sensitivity and resolution. With the advent of radio interferometric telescope arrays (e.g. the National Radio Astronomy Observatory Very Large Array [VLA] in New Mexico) using the principle of Fourier transform aperture synthesis, sensitivity and especially resolution have far surpassed the original pioneering efforts. The recent launch of the *HALCA* radio astronomy satellite of the Japanese-American VSOP mission, for the purposes of **orbiting-very-long-baseline-interferometry (OVLBI)**, is proof of how far the radio astronomical community has progressed since the initial efforts

of Karl Jansky and Grote Reber. With *HALCA*, one can discern details as fine as $\sim$ 100 millionths of an arcsecond, which is the angular detail presented by the length of an adult thumb viewed from a distance of 100,000 miles.

Starting in 1979, the MIT radio astronomy group has been executing surveys in the radio and optical bands, of both types:

1. Complete and reliable all-sky scanning surveys of radio sources.

2. Representative, but incomplete, VLA interferometer surveys targeted at the brighter sources in the MIT all-sky surveys.

3. Representative, but incomplete, optical follow-up imaging and spectroscopic surveys, targeted at pre-defined sub-samples of MIT-VLA radio sources.

The most comparable independent radio continuum sky surveys are those of the National Radio Astronomy Observatory (NRAO) at Green Bank, which were made at roughly the same time as the northern hemisphere MIT-Green Bank (MG) all-sky surveys. In fact, these two parallel efforts utilized the same telescope (the Green Bank 91m diameter altitude-azimuth-mounted paraboloid), the same receiver, at the same frequency: 4.8 GHz.

Within an American-Australian collaboration, the MIT group has also taken part in an all-sky 4.8 GHz continuum survey from the southern hemisphere. This Parkes-MIT-NRAO (PMN) survey was done with substantial help from the National Radio Astronomy Observatories of both the United States and Australia (NRAO & ANRAO, respectively). The Parkes 64m diameter equatorially-mounted paraboloid, in conjunction with the NRAO 7-beam receiver used for the 91m Green Bank NRAO and MG surveys, were used for this southern sky survey.

The result of these efforts was the publication of 8 radio source catalogs in the literature: 4 MG source lists covering part of the northern hemisphere sky, and 4 PMN lists covering all of the southern hemisphere sky, overlapping with the southernmost MG I survey. The

concurrent work by the NRAO astronomers has produced the 87GB catalog. The more recent GB6 catalog is a higher quality version of the 87GB list, based on the same raw data from the Green Bank 91m telescope. In addition, the NRAO has published their own version of the source list as extracted from the PMN raw data, and the agreement between the MIT and the NRAO versions of the PMN survey is very good above a source flux density level of $\sim$ 70 mJy, at 4.8 GHz.

It is certainly not redundant that the same areas of sky have been surveyed by different groups at the same frequency; the comparison of the various independently-derived catalogs has provided us with a good idea of the completeness, reliability, and the level of systematic error inherent in the individual mapping techniques used. For the sources that sit well above the sensitivity limit of each of these surveys, the agreement in position and flux density is remarkably good. It is only as one proceeds down to the fainter sources that discrepancies due to unknown systematic effects start to appear. It is suspected by both the MIT and NRAO groups that these discrepancies, at the level of 7% in the fluxes of overlapping sources, are mainly due to the different source finding algorithms adopted by each group.

In the rest of this chapter, the MIT surveys will be described in detail. A clear discussion of each survey will be provided, as it is very important in statistical studies of radio sources to establish the completeness and reliability of any given population sample. In the case of incomplete or unreliable surveys, the manner and extent of these shortcomings should be clearly addressed. In the following sections, more details on the MIT all-sky surveys will be provided. Then, the MIT-VLA program to find new examples of gravitational lensing will be described. Finally, the optical identification, imaging and spectroscopic work on selected sub-samples of MIT-VLA radio sources will be described, with emphasis placed on the later observations starting from December of 1993.

Survey	Ω	α_{min}	α_{max}	δ_{min}	δ_{max}	$N_{>5\sigma}$	S_{min}
	sr	hr	hr	deg	hr		mJy
MG I	1.87	$0^h.0$	$24^h.0$	-0°.5	+19°.5	5974	53–106
MG II	1.51	$4^h.0$	$21^h.0$	+17°.0	+39°.2	6182	41
MG III	1.11	$16^h.0$	$5^h.0$	+17°.0	+39°.2	4761	40
MG IV	0.504	$15^h.5$	$2^h.5$	+37°.0	+51°.0	3427	41
PMN E	1.90	$0^h.0$	$24^h.0$	-9°.5	+10°.0	11774	40
PMN T	2.01	$0^h.0$	$24^h.0$	-29°.0	-9°.5	13363	42–55
PMN Z	0.667	$0^h.0$	$24^h.0$	-37°.0	-29°.0	2400	72
PMN S	2.50	$0^h.0$	$24^h.0$	-87°.5	-37°.0	23277	20–50

Table 2.1: The MIT 4.8 GHz Sky Surveys

2.1 The MIT Sky Surveys

The MIT-Green Bank (MG) surveys were made in 4 sections distributed over a large part of the northern hemisphere sky, in the period from 979 to 1988. The Parkes-MIT-NRAO (PMN) surveys were made in another 4 sections distributed over all of the southern hemisphere sky, as well as along an equatorial declination band in the northern hemisphere sky. The PMN observations were carried out during the course of two separate months in 1990.

Table 2.1 shows the details relevant to each of these 8 survey sections. To aid the reader, a plot of the coverage for each of the MG Northern sky surveys is reproduced in Figure 2-1. In addition, the coverage of the PMN and 87GB radio sources is shown in Figure 2-2. In the following pages, details of each of the survey sections are presented.

2.1.1 The MIT-Green Bank Surveys

The MIT-Green Bank (MG) surveys used the NRAO 91m-diameter (300 foot) meridian-transit paraboloid radio telescope at Green Bank, West Virginia, USA. The mapping method was simply to slew the telescope antenna beam continuously in the north-south direction

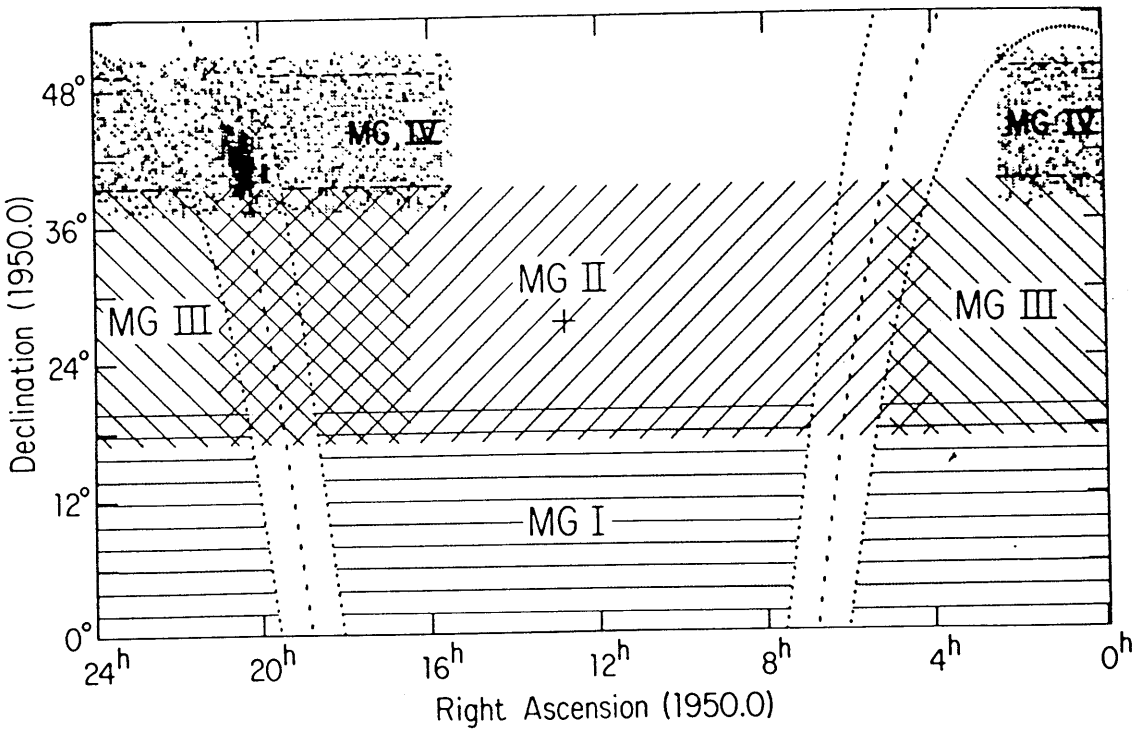

Figure 2-1: A plot of the sky areas observed in each of the MIT-Green Bank 4.8 GHz Sky Surveys MG I, II, III and IV. The Galactic latitudes $b = -10°, 0°, +10°$ are marked by the dashed lines. This figure has been reproduced from Griffith et al. 1991.

along the local sky meridian, at a rate much faster than the Earth's rotation. Unlike in optical astronomical observing, radio astronomers are not excluded from taking data during the day, provided the radiation from the Sun does not significantly enter the main lobe or sidelobes of the antenna beam. The 24-hour observing sessions cover all right ascensions with a series of adjacent scan strips oriented roughly in the north-south direction.

The **First MIT-Green Bank (MG I)** survey used a dual-beam receiver centered at 4775 MHz, with a 580 MHz bandwidth. The nominal full-width-half-power (FWHP) angular width of each of these two beams was $2'.8$, and they were separated by $7'.6$ on the sky. Scanning along the meridian was done at 6 times the sidereal rotation rate, in roughly north-south-oriented strips within the declination range $-3° < \delta < +20°$. Eight separate observing sessions were required to complete the MG I survey, which was in progress from 1979 to 1983. There were 2400 observations made, of known strong radio sources, in order to ascertain the variation of telescope gain with zenith angle (i.e. the 'gain curve': Bennett, Lawrence & Burke 1984 [10]), and thus set the flux density scale. These extensive data were also used to solve for residual telescope pointing errors. The reduction of the survey data made use of the standard CLEAN deconvolution algorithm (Högbom 1974 [74]) to extract reliable source lists of positions and flux densities. Two such lists were published (Bennett et al. 1986 [12]): a 'strong source' catalog of 5974 sources with measured flux densities $S_{4.8} > 5\sigma$, and a less complete and less reliable 'weak source' list of 3836 sources, with flux densities in the SNR range $4\sigma < S_{4.8} < 5\sigma$. The positional errors were estimated using MG I sources that were found to be unresolved at the VLA (Lawrence 1983 [97] ; Lawrence et al. 1984 [94]). From this analysis, the rms errors in the right ascensions were estimated to be $\sigma_\alpha = 28''$, and those in the declinations were $\sigma_\delta = 22''$. All the MIT sky survey catalogs provide an estimate for the error in the quoted flux density of each detected source. In addition to giving the corrected position of the source in both B1950.0 and J2000.0 coordinates, an estimate of the radio spectral index α is obtained ($S_\nu \propto \nu^\alpha$), whenever possible, from positional correlations

with radio sources detected in the lower frequency uniform catalogs; for MG I, the Texas 365 MHz catalog (Douglas et al. 1980 [42]) was used to porvide this spectral information.

The flux error is usually quoted as the quadrature sum of a flux-independent base-level error (attained only for a zero flux source) and an error that is proportional to the flux density. For the 4.8 GHz MG I survey, the base error is $\sigma_0 = 18.4$ mJy, and the mean error for a 100 mJy source is 10 mJy, giving a total flux density error of 20.9 mJy. In the case of the MG I survey, there are additional errors due to the CLEAN deconvolution process, and due to miscalibration for the telescope gain-curve. The latter is strongly dependent on declination, and so the MG I catalog is complete down to varying levels: around the celestial equator ($\delta \sim 0°$) the catalog completeness flux density cutoff can be as high as 106 mJy, whereas closer to the Green Bank zenith this level is allowed to decrease to as low as 53 mJy at $\delta \sim +19°.5$. The latitude of Green Bank is $+38°.43$; evidently, this behaviour of the survey sensitivity is caused by a systematic decrease in the telescope gain by a factor of ~ 2 in going from a zenith angle of 19° to one of 38°.5. The final result is that a 100 mJy MG I source has a quoted signal-to-noise-ratio (SNR) of somewhere between 5 and 10, which corresponds to absolute flux density errors in the range from 10 to 20 mJy.

The **reliability** of a survey is the fraction f_R of sources appearing in the source list that are actually real. Based on Green Bank re-observations of a randomly selected sample of MG I sources, this is estimated to be $f_R = 96 \pm 1.5\%$ for the MG I survey.

The **completeness** of a survey is the fraction of real sources in the sky, with flux densities above the catalog limiting flux density, that appear in the source list. VLA re-observations of the stronger MG I sources leads to a rough estimate of $f_C = 95 \pm 2\%$ for the MG I survey.

Further details for the MG I survey can be found in the published catalog paper (Bennett et al. 1986 [12]). More detailed information can be found in the MIT Ph.D. theses of Charles Lawrence (1983) [97] , and of Charles Bennett (1984) [14].

The **Second MIT-Green Bank (MG II)** survey used a new seven-beam dual-circular-polarization receiver built by George Behrens of the NRAO. All 7 feeds were centered at 4830 MHz, each with a 500 MHz bandwidth. The nominal full-width-half-power (FWHP) angular width of each of these 7 beams was the same as for the MG I survey: 2′.8. The 7 beams were arranged in a perfect hexagonal pattern of 6 beams equidistant from a central beam. The angle between the scanning direction and the nearest symmetry axis of the hexagon was fixed at 19°.1; this geometry allowed simultaneous scanning along equispaced paths on the sky, by all 7 beams. The separation between adjacent sky paths was $\sim$ 1′.4 (about a single FWHP beamwidth). Data were interpreted to arise from the same radio source if independent observations showed signal within a 3′.6 diameter circle. The RA coverage was only partial: $4^h < \alpha < 21^h$. The complementary RA coverage of the same declination strip was carried out in the companion MG III survey made later in the year (July - August 1987). Scanning along the meridian was done at 8 times the sidereal rotation rate. With the great increase in rate of sky coverage compared to MG I, the entire survey was completed in the month of April 1987. To estimate and improve the completeness and reliability of the final MG II list, it was desirable to timeshare between two independent overlapping surveys; a *north* scanning survey from declination $\delta = +19°.0$ to $\delta = +39°15$, and a *south* scanning survey from declination $\delta = +37°.15$ to $\delta = +17°0$. The published MG II catalog (Langston et al. 1990 [91]) lists averaged flux densities and positions for 6182 sources found in both surveys. Essential in the analysis of the completeness and reliabilty of this survey was the comparison of the north and south scanning surveys in their region of overlap. This *comparison region* consists of the declination band $19°.0 < \delta < 37°.15$, with the exclusion of all sources south of galactic latitude $b = +10°$ (i.e. excluding the region confused by a high surface density of Galactic radio sources).

The flux scale was set by daily observations of 3C48, for which the assumed 4.83 GHz flux density from the Baars et al. scale (1977) [5] was 5.42 Jy. Ten other radio sources, drawn from

the Kuhr et al. (1981) [88] list, were also observed daily in order to establish the telescope gain curve. Previous observations by Bennett, Lawrence and Burke (1984) [10] showed that the system gain was weakly dependent on the zenith angle, for the declination range in the MG II survey. This was confirmed by the daily observations of the non-varying Kuhr et al. source calibrators, whose measured fluxes were consistent with the scale set by the primary 3C48 flux calibrator. The final MG II source list contains 6182 sources detected with SNR > 5, with 41 mJy being the lowest flux density recorded. For sources detected in only one of the two independent surveys, the flux density errors are a quadrature sum of a constant 7 mJy rms variation in the system temperature along a scan, and a flux-proportional 12% error estimated from the the rms differences between fluxes measured in the north and south scan surveys. For a 50 mJy source, this amounts to 9.2 mJy (SNR $\sim$ 5.4). However, the flux error is smaller for those 'common sources' detected in both north and south scanning surveys, with a 5 mJy rms system temperature variation and only an 8.2% flux-proportional error; in this case, a 50 mJy source would have a 6.5 mJy flux error (SNR $\sim$ 7.7).

The position errors were similarly gauged by the rms offsets between the positions of 'common sources' found in both north and south scanning surveys. For sources found only in one survey, these are $\sigma_\alpha = 21''$ and $\sigma_\delta = 27''$. For the sources found in both, the errors decrease to $\sigma_\alpha = 15''$ and $\sigma_\delta = 19''$. The 'single survey sources' have about the same total position errors as for those in the MG I survey, but the 'common sources' have significantly better positions.

There is also a **resolution bias**: the source detection algorithm fails for sources which are larger than a few tens of arc-seconds. For example, 3C 223 is a well-known classical double-lobed galaxy with a projected angular size of $5'.9$ from lobe to lobe, which is a full 2.1 FWHP beamwidths. In the MG II survey, it is fully resolved into two apparently separate sources, each with roughly half the full flux density of the actual radio source. Such effects are hard to quantify in the analysis of source counts, but nevertheless one must keep these

issues in mind when interpreting the statistics of even a reasonably complete sample.

By careful analysis of the statistics of the numbers of sources found in each of the north and south surveys in the 'comparison region', it was ascertained that the *completeness* of the MG II survey is $\sim$ 94.8% at the lowest measured flux densities $\sim$ 40 mJy, rising to $\geq$ 99.9% for sources brighter than 90 mJy. A lower limit on the *reliability*, estimated from the ratio of sources seen in one survey to those seen in both, is 97% at 90 mJy.

Finally, the spectral indices were estimated from the positional cross-correlation of MG II source positions with local peaks in the FITS maps resulting from the NRAO-Green Bank 1400 MHz northern sky survey (Condon & Broderick 1985 [34]). Only 1400 MHz peaks both brighter than 50 mJy and within a search radius of 5′ of the MG II position were used in the calculation of the spectral index. It should be noted that spectral indices are notorious for falling prey to corrupting resolution and confusion effects. The NRAO-Green Bank beam at 1400 MHz covers a region of sky that is $\sim$ 18 times larger than the 4.83 GHz beam; the *resolution bias* results simply from the collection of more photons per unit time for those sources that are resolved out by the smaller (2′.8) beam. In addition, the greater solid angle of the larger beam will now and then collect other independent radio sources that happen to fall within its expanded grasp, i.e. the original source at higher resolution becomes subject to *confusion bias* due to the presence of interfering sources. This can be a serious problem when approaching the Galactic plane region. Both these effects lead to higher flux densities at 1400 MHz, and thus to more negative spectral indices ($S_\nu \sim \nu^\alpha$) in the MG II catalog. There is also the expected broadening of the spectral index distribution arising simply from the flux density errors at each of the two frequencies.

Further details on the MG II survey may be found in the published catalog paper (Langston et al. 1990 [91]), and in the MIT Ph.D. thesis of Langston (1987) [90] .

The **Third MIT-Green Bank (MG III)** survey was essentially a continuation of the MG

II survey. The aim of MG III was to complete the RA coverage for the same declination strip scanned in MG II: $+17° < \delta < +39°.15; 16^h.5 < \alpha < 5^h.0$. In doing this, the MIT group ensured that there was substantial overlap in the sky coverage at the neighbouring boundaries of each of these two surveys. This provided a valuable extra check on the completeness and reliability of both the MG II and III surveys.

As the details for MG II and MG III are identical in some respects, only the differences between these two surveys will be focused on here. The lowest flux density recorded for MG III was 40 mJy, above which there are 4761 sources listed in the published catalog (Griffith et al. 1990 [60]). The absolute flux density scale was set using 3C 286, for which the Baars et al. (1977) [5] value is 7.41 Jy. A set of 9 Kuhr et al. (1981) [88] strong sources were observed to calibrate the gain curve, and ensure consistency with the 3C 286 flux scale. A different 'comparison region' to the one in MG II was used, with sources now excluded *north* of galactic latitude $b = -10°$. The flux density and position errors, that were estimated from the correlation between the sources detected in the north and south scanning surveys for MG III, were found to be mostly comparable to those in MG II: for sources found only in a 'single survey', the catalog flux error is a quadrature sum of 7 mJy rms in the scan records, and a flux-proportional error of 11% estimated from the repeatability of measured fluxes in the two independent surveys. For a 50 mJy source, this amounts to an 8.9 mJy error (SNR $\sim$ 5.6). For the more reliable 'common sources' detected in both surveys, these values ameliorate to a level of 5 mJy, 8.1% and 6.4 mJy (SNR $\sim$ 7.8), respectively. The positional errors for 'single survey' sources were $\sigma_\alpha = 34''$ and $\sigma_\delta = 29''$. Those for the 'common sources' were $\sigma_\alpha = 24''$ and $\sigma_\delta = 20''$. It seems that the positional errors are $\sim$ 30% worse in MG III, as compared to MG II. As always, the resolution bias exists, at the same level as in MG II.

Using the survey comparison technique, the MG III *completeness* was estimated to be 93.3% at 40 mJy, rising to $\geq$ 99.9% for sources brighter than 100 mJy. The lower limit on the *reliability* is 96% at 90 mJy. These values are close to those for MG III.

The estimation of spectral indices between 1400 and 4830 MHz was performed in exactly the same manner as for MG II, and the resulting statistical distributions are very similar, with both Galactic and non-Galactic populations exhibiting a heavily skewed distribution with mean $\alpha \sim$ -0.63, and a mode of $\alpha \sim$ -0.95.

Further details on the MG III survey may be found in the published catalog paper (Griffith et al. 1990) [60] .

The **Fourth MIT-Green Bank (MG IV)** survey used the same instrumentation and procedure as for the three earlier MG surveys. However, only six of the seven feeds of the NRAO 4830 Mhz receiver were operational for this survey. In July 1988, two overlapping surveys were made over the declination range $+37°.00 < \delta < +50°.98$ (B1950.0). The *north* survey scanned from +39°.00 to +50°.98, while the *south* survey scanned from +48°.98 to +37°.00. The *comparison region* used lay between +39°.15 and 48°.83, excluding the Galactic Plane strip $-10° < b < +10°$.

Unfortunately, the MG IV survey was abruptly cut short halfway through the program, by the sudden structural failure and collapse of the 30-year-old 300-foot telescope. Thus, the RA coverage is incomplete, and spans the range $15^h.5 < \alpha < 2^h.5$.

The flux density scale was set by observations of 3C 286, and cross-verified with 5 other known strong sources from Kuhr et al. (1981) [88]. 'Single survey sources' had 7 mJy rms scan errors and 15.0% flux-proportional errors. Thus a 50 mJy source has a total flux error of 10.3 mJy (SNR = 4.9). The positional errors for the single survey sources were $\sigma_\alpha = 25''$ and $\sigma_\delta = 29''$. 'Common sources' had 5 mJy rms scan errors and 10.5% flux-proportional errors. Thus a 50 mJy source has a total flux error of 7.25 mJy (SNR = 6.9). The positional errors for the common sources were $\sigma_\alpha = 18''$ and $\sigma_\delta = 20''$. The source detection algorithm was successful for sources smaller than 100″, so the resolution bias is somewhat less severe for MG IV as compared to the earler MG surveys.

The MG IV *completeness* was estimated to be 92.4% at 40mJy, rising to $\geq$ 99.1% for sources above 90 mJy. The MG IV *reliability* was estimated to be $\geq$ 90.5% at 90 mJy.

More elaborate algorithms and stricter criteria were used in the extraction of corresponding 1400 MHz fluxes from the NRAO FITS maps; a search radius criterion was adopted such that if the closest peak was further than 5σ away, the source was deemed confused instead of identified. Faint 1400 MHz sources below 50 mJy were deemed non-detections, as before. However, even with these precautionary measures, the resulting spectral index distributions for Galactic and non-Galactic sources were much the same as for the previous MG surveys.

Further details on the MG IV survey may be found in the published catalog paper (Griffith et al. 1991) [59].

In summary, the four MIT-Green Bank surveys have painted a fairly uniform and consistent picture of a large part of the 4.8 GHz northern hemisphere sky. Based on the detailed analysis of completeness and reliability, it can be stated that each of the MG catalogs forms a reasonably complete and reliable extragalactic radio source sample that would be amenable to further statistical analysis, as well as for the definition of representative or complete sub-samples for targeted follow-up observations.

We now turn to the MIT involvement in mapping the other half of the 4.8 GHz radio Universe.

2.1.2 The Parkes-MIT-NRAO Surveys

The Parkes-MIT-NRAO (PMN) 4850 MHz surveys used the ANRAO 64m-diameter equatorially-mounted paraboloid radio telescope at Parkes, New South Wales, Australia. The two previous major large-area radio continuum surveys of the southern hemisphere sky were undertaken at lower frequencies: at 408 MHz with the Molonglo Cross phased-array 'pencil beam'

telescope (Large et al. 1981 [92]), and at 2700 MHz with the Parkes 64m single-dish telescope (Bolton et al. 1979 [20]). The resulting catalogs have been published as the Molonglo Reference Catalog (MRC), and the PKSCAT90 Catalog (Wright & Otrupcek 1990 [151]).

The main aim of the new PMN surveys was to make a uniform, complete, deep and efficient survey of the entire southern hemisphere sky at 4850 MHz. Before the PMN survey, the only high ($\sim$ GHz) frequency large-area southern sky catalog was the one resulting from the 1960s effort by J. Bolton and collaborators, using the Parkes 64m amongst other radio telescopes. These multiple efforts over the years, often at different frequencies, have been organized by Wright & Otrupcek into the electronically-readable PKSCAT90 catalog. The many individual Parkes surveys are known to be collectively incomplete and non-uniform, and hence restricted in their usefulness for statistical studies, such as source counts or anisotropy searches. A secondary goal of the PMN surveys was to complement and cross-check the NRAO Green Bank 43m 4850 MHz survey of the part of the southern sky accessible from the Northern hemisphere ($-40° < \delta < +5°$; Condon et al. 1991 [35]). This survey used a smaller telescope scanning at relatively large zenith angles, and hence its limiting flux density is not as 'deep' as the PMN surveys.

Thus, the four PMN surveys extend the Northern Hemisphere 4850 MHz surveys to the Southern Hemisphere sky, with approximately the same sensitivity as that of the NRAO 91m telescope surveys at the same frequency. The new Southern surveys partly complement and partly supersede the existing large-area southern sky surveys observed at lower frequencies; the resulting PMN source statistics confirm that the radio source surface density has been increased by significant factors (~ 5) over the older Parkes and Molonglo surveys.

The four sections of the entire PMN survey series were named after the corresponding geographic areas directly 'beneath' each part of the sky: in order, going from the south to the north, they are the *Southern*, *Zenith*, *Tropical* and *Equatorial* surveys.

The combined PMN and 87GB survey source lists generated from the mapping of the

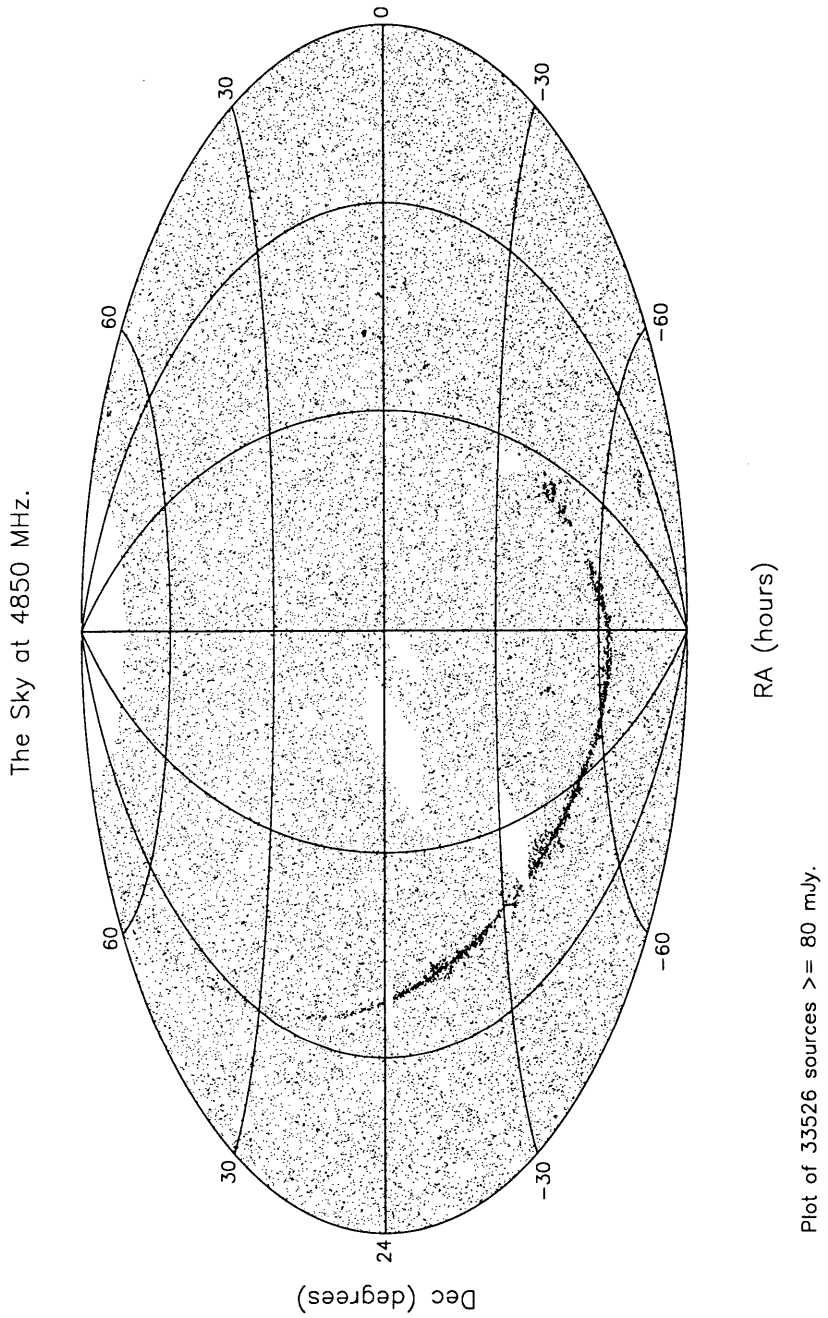

Figure 2-2: The radio continuum sky at 4850 MHz. An Aitoff (equal-area) projection plot of all PMN and 87GB sources with flux densities greater than 80 mJy. The 87GB sources are plotted for the declination range $+10° < \delta < +75°$. This figure was originally produced by M. Griffith in 1995.

4.85 GHz radio continuum sky are plotted in Figure 2-2. Only those sources with $S_{4.85} > 80$ mJy are plotted here, this being well above the completeness and reliability flux density limits for all of the individual sky surveys. The North celestial cap was not surveyed in 87GB (Gregory & Condon 1991 [56]). The dark, curved band across the southern part of the map is the Galactic plane. This is not apparent in the northern 87GB data, since Gregory & Condon excluded most Galactic sources from their catalog. The two broad blanked areas in the PMN Zenith and Equatorial regions were excised due to corrupting solar radiation unavoidably entering the Parkes telescope beam sidelobes. In the far south can be seen the Large Magellanic Cloud at $\alpha = 5^h.5, \delta = -69°$, while the closest powerful radio-loud AGN, Centaurus A, is visible at $\alpha = 13^h.0, \delta = -42°$.

The **Parkes-MIT-NRAO Southern (PMN-S)** survey spanned the declination band $-87°.5 < \delta < -36°.0$. The four PMN surveys were made over two separate sessions in 1990: the 'June' and 'November' sessions. After the conclusion of the companion NRAO 4.85 GHz survey using the Green Bank 43m telescope, the 7-feed dual-circular-polarization receiver was brought over to Parkes for use in the PMN series. This receiver was the same one that survived the collapse of the Green Bank 91m telescope in 1988 (this incident abruptly brought the MIT-Green Bank IV survey to a halt). The receiver suffered only minor damage in the crash, and the opportunity was taken to upgrade the original GaAsFET amplifiers to more sensitive ones of the low-noise HEMT (high electron mobility transistor) type. There were 14 channels, each set at the same 4850 MHz center frequency, with a 600 MHz bandwidth. These channels were fed in dual-circular-polarization pairs from 7 beams, arranged in the same regular hexagonal plus central feed arrangement as was utilized in the Northern sky surveys. The FWHM of each of the circular beams was measured to be $4'.2 \pm 0'.1$, and the 7-beam geometry was rotated to the unique PA that would give rise to equispaced beam tracks while scanning along the local north-south meridian. At this orientation angle, the inter-track spacing was about one FWHM beamwidth ($\sim 4'.2$), and the breadth of the entire

7-beam scan array was $\sim 28'$. In the Southern survey, the scan rate was $\sim 11.1°$ min^{-1}; high scan rates were required to compensate for the long-period '1/f noise' arising from the combined effects of the atmosphere and receiver, as well as to guarantee completion of the survey in a reasonable time. The scanning was done through four independent surveys: 2 sets of 'Regular' scans, one set going north along the meridian, the other south; and 2 sets of 'Nyquist' scans, which are a parallel set of equispaced scans interleaved at positions midway between the Regular scans; the combination of the parallel, interleaved Regular and Nyquist scans ensured the minimum *Nyquist sampling* rate required to adequately sample the sky brightness distribution (see, e.g. Bracewell 1986 [24]). The final result was that there were 4 independent sets of scan data covering the same area of sky. This offered valuable cross-checking and averaging between the separate sets of raw data. Scans missed due to solar, lunar or planetary radiation, impulsive interference and bad weather were assigned to be repeated again in 'mopping up' sessions later in the survey period. In this way, almost all of the sky area below $+10°$ declination was covered in a uniform fashion (however, some sky patches still remained unavoidably affected by the solar sidelobe interference problem by the end of the second session in November 1990).

M. Griffith and A. Wright developed an entirely new and elaborate technique for reducing the large-area PMN multi-beam sky survey data. In order, the following steps were taken to produce the final catalog from the raw survey data:

1. **Telescope pointing calibration**: regular observations of known, accurate positions of ≥ 20 selected PKSCAT90 strong sources were made at many different telescope pointings, in order to correct for differential solar heating and gravitational deformation of the telescope.

2. **Individual Beam Position calibration**: the positions of the beams relative to the central beam were measured using succesive drift scans of each of the beams through a strong point source. Only the position of the central beam and the PA of the hexagon

fiducial symmetry axis were recorded during the programmed scans; the actual sky positions of the other 6 beams could be fixed in th post-observation reduction, by the relative positions measured in this preliminary procedure.

3. **Gain vs. Zenith Angle calibration**: the two strong radio sources PKSB 0521-365 and PKSB 1921-293 were observed at zenith angles spanning the range covered by each of the surveys. This allowed the gain variation to be measured as a function of telescope elevation, for each of the 7 feeds. The typical rms uncertainty introduced in the use of these general gain curves was repeatably 1.6% for the PMN surveys.

4. **Absolute Gain calibration**: observations of the strong source PKSB 0915-118 (Hydra A) were used to set the absolute flux density scale, and noise-calibration signals injected before the start, and after the end, of every scan allowed this flux calibration to be propagated to individual sky scans.

5. **Conversion from Raw Counts to Flux Density**: this was achieved by division of each scan by the averaged counts recorded for the injected noise calibration signal, and then scaling the result with respect to the averaged noise counts as recorded during the calibration scans through the absolute flux calibrator (Hydra A). The assumed absolute flux density for this source is the Baars et al. (1977) [5] value, and the consistency of this scale with the fluxes for 23 strong point sources from the Kuhr et al. (1981) [88] list was verified during the final production of the PMN catalogs.

6. **Removal of Baseline Gain Variation**: a polynomial 'canonical' baseline fit, of the instrumental flux as a function of zenith angle, was removed from each of the beam scans. This variation results from the varying amount of contaminating ground radiation as the dish moves between the zenith and the horizon.

7. **Removal of Data corrupted by Solar Sidelobes**: structures much broader than the telescope beamwidth occuring roughly simultaneously in all of the scan records were

excised if the corresponding positions were calculated to be within 3° of the expected solar sidelobe positions. Data on real extended objects such as the Galactic Plane, LMC, and Centaurus A were also checked for, but not excluded as they fell outside the solar sidelobe contaminated regions.

8. **Removal of Data corrupted by Impulsive Interference**: short-term (narrow) "spike" or "impulsive" interference features were excised if they were found to occur simultaneously in all scans. Again, this filter was turned off when scanning near real extended emission, such as that from the Galactic Plane.

9. **Averaging of Two Polarization Channels**: the signal-to-noise ratio was increased by averaging the right and left circular polarization scans for each feed, on the assumption that none of the actual radio sources were circularly polarized. If one scan was already flagged as 'bad', the other polarization was used without the benefit of averaging.

10. **Median Filtering of Residual Baseline Gain**: a residual baseline gain variation, remaining after the initial canonical baseline was divided out, was removed by use of a broad 57′ median filter (covering 65 scan samples). This caused flux densities to be biased downward, so Monte-Carlo source injection tests (see below) were needed to estimate the required positive bias correction as a function of flux density.

11. **Removal of Outlying Spikes in Data**: a 'spike' filter was applied to the scan data: those points which differed from the average of its neighbours by both (1) $\geq$ 100mJy, and (2) $\geq$ 45%, were blanked.

12. **Correction for Declination Lag**: a 20″ lag in declination was corrected by finding half the difference between the positions of a few bright sources as measured in north-going and south-going scans. This was done for each PMN survey separately.

13. **Gridding of Unconvolved June and November Data:** the (unconvolved) calibrated data points were placed on a $\Delta\alpha = 1'$ by $\Delta\delta = 1'$ grid. This is about one quarter of the beam resolution; each of the individual samples were accumulated on the nearest grid point. This and the following computations were performed on the MIT Cray-1 supercomputer (now retired), and the gridded data were stored in computer files for further processing.

14. **First Pass of Source Finding and Gaussian Profile Fitting:** Three types of least-squares Gaussian fits were tried, and all results were logged. An automatic determination of clearly suitable and clearly unacceptable fits was made on a case-by-case basis. The intermediate case of sources with 'questionable fits' was ignored for this first stage. From this Gaussian profile fitting, the two classes 'good' and 'poor' were subtracted, and blanked, respectively, from the gridded data, in preparation for a second stage of fitting.

15. **Second Pass of Source Finding and Gaussian Profile Fitting:** The same fitting procedures were performed on the modified grid, except that the 'questionable fits' were now recorded as 'good' ones. The 'good' sources from both passes were combined to form a preliminary source list.

16. **Removal of Spurious Weak Signals aroung Strong Sources:** A resolution-angular separation distance criterion was used to automatically search for spurious faint sources around strong sources with $S_{4.8} > 100$ mJy. This was necessary to avoid recording the beam sidelobes that inevitably occur near the bright radio sources. Those sources which are both faint and near a strong source were dropped from the preliminary source list. After this was done, the June and November 1990 preliminary source lists were combined for the final catalogs.

17. **Analysis of Synthetic Radio Universes using Monte-Carlo Source Injection**

Simulations: Monte-Carlo simulated 'synthetic radio universes' were constructed that had known sources injected into real data scans in such a way that the real sources were subtracted out, leaving only the noise and the synthetic sources. With exactly the same procedure applied to these synthetic scans, an accurate estimation of both flux and position biases, introduced by the *entire* pipeline reduction, could be made. The expected biases arise from the use of: (1) the median filter, (2) gridding, and (3) fitting Gaussian profiles in the presence of noise; and there could well be others. However, effects due to the telescope gain, and variation in ground radiation, could not be reproduced exactly in these simulations. These Monte-Carlo analyses also were crucial for making exact estimates of the survey completeness, reliability and limiting flux density cutoff (see below).

18. **Correction for Flux Bias Errors**: The flux densities are affected by small biases, such as from the application of median filtering to each scan, from the data gridding process, and from the fitting of an assumed Gaussian profile to the noisy, gridded, data. More details on some of these well-known effects may be found in Condon et al. 1989. From the Monte-Carlo artificial source injection tests, a bias function B(S), which is defined as the difference between the true and the fitted flux density S, was determined as a fitted linear function in the logarithmic of S:-

$$B(S) = -20.66 + 14.66.\log_{10}(S),$$

where the bias B and flux density S are both in mJy. It was found that this bias function B(S) is essentially the same in both the the Southern and Tropical PMN Surveys. The effect of faint confusing sources on this bias was estimated to be less than 1%.

19. **Estimation of Flux Density Errors**: There are four main contributors to the stan-

dard error on the flux density of each source. Firstly, there is the background confusion from faint sources not appearing in the catalog; this was given an adopted value of EC = 2 mJy for the Parkes telescope, at 4850 MHz (Wright 1992; private communication). Secondly, there are errors EG induced by gain fluctuations, which are estimated to be proportional to the flux density, at a level of $\sim$ 1.6%. Thirdly, there are errors EB introduced by correcting the fitted source flux densities for the biases mentioned above. These were typically about 1 mJy, or 0.6 $\log_{10}$(S), whichever was greater. Lastly, there is the error EF in the source fitting process resulting from the random noise in the gridded data; this had to be determined using the Monte-Carlo tests for each declination band in turn. In the Southern Survey, the flux-fitting error was found to be:

$$EF^2 = (11.8 + 0.085\delta)^2 + (0.050.S)^2$$

The total standard error ES is the quadrature sum of the above four errors:-

$$ES^2 = EC^2 + EG^2 + EB^2 + EF^2$$

With sufficient accuracy, the total standard error ESS for the Southern Survey can be calculated from the following formula:-

$$ESS^2 = (12.3 + 0.085\delta)^2 + (0.052.S)^2(mJy)^2$$

For a source of 50 mJy at $\delta = -60°$, the total standard error in its flux density is then 7.7 mJy, which is 15%. For a 100 mJy source at the same declination, the corresponding values are 8.9 mJy and 8.9%.

In the source lists, those errors exceeding 99 mJy are recorded as "99" because of space

limitations.

20. **Correction for Positional Errors**: Using 265 known, strong, PKSCAT90 sources having accurate (standard error < 2") positions, a cross correlation was made with the PMN preliminary source list. Small, systematic pointing errors were removed from the calculated positions of the PMN counterpart sources.

21. **Estimation of Positional Errors**: The remaining random residual standard errors in the positions were determined from the Monte-Carlo source injection tests: these random errors were found to be well fitted by the quadrature sum of a flux-independent error and a flux-inverse-proportional error. For the Southern Survey, the errors in each of the PMN right ascensions and declinations were:

$$\sigma_{RA}^2 = 6^2 + (1300/S)^2,$$

$$\sigma_{DEC}^2 = 4^2 + (1100/S)^2.$$

where the errors are in arc-seconds and the flux density S is in mJy.

For a 50 mJy source, the standard error in its RA is then 26."7, and it is 22.".4 in DEC. For a 100 mJy source, the corresponding values are 14."3 and 11."7. These errors are small enough that VLA follow-up imaging at X-Band A-array would be well suited for determining much more accurate positions, as well as for mapping both unresolved and almost all extended radio sources.

22. **Estimation of Differential Reliability**: In the establishing of a essentially complete and reliable source catalog, an estimate of both the completeness and reliability, as a function of the catalog flux density, is required. Once this is known, a decision can be made as to where to draw the limiting flux density 'line' for the faintest catalog

sources. In this way, those sources, from the preliminary list, that end up in the catalog are known to be complete and reliable at a well-determined level.

What is **differential reliability** ? The adjective 'differential' indicates that this will be a function of the (final catalog) flux density S. The reliability of the set of all catalos ources above a certain flux density S is called the *integral* reliability. We expect normally that a given catalog will be most reliable at its mid- and upper-range, and pregressively less reliable as the S/N ratio decreases nearer the catalog limit. Crucial to the definition of reliability is the specification of what is meant by a 'reliable' source. According to the adopted definition for the PMN Surveys, such a source is defined as one having a final catalog flux density close enough to its original measured flux density. From the Monte-Carlo tests, the difference between these two flux density values was found to be a small fraction of the fluxes, which indicates the all-round high reliability of the PMN catalog sources. Over a small flux density range, the differential reliability R(S) is defined to the the fraction $N_{RELIABLE}/N_{CATALOG}$ of 'reliable' sources to catalog sources within that flux density bin. Full details of the variation of differential reliability with declination can be found in the published PMN papers. As the catalog flux density limits were set at the 90% differential reliability level, we can rest assured that a firm lower limit to both the integral and differential reliabilities, for all of the PMN catalogs, lies at the 90% level.

23. **Estimation of Differential Completeness**: Reliability refers to the fraction of sources in the catalog which are 'real'. What is **differential completeness** ? This is the fraction of real sources in the sky that are recorded in the catalog. Note that the denominators of these two fractions are defined over *different* populations. Reliability refers to the catalog sources. Completeness refers to the sources actually in the sky. For the PMN surveys, a more restrictive definition was used for differential completeness: this is the fraction $N_{REAL-CATALOG}/N_{ACTUAL}$ of actual sources in the flux density and

solid angle ranges surveyed, that are also in the catalog, and in addition are 'real' in the sense as defined before for the differential reliability. For the PMN catalogs, the differential completeness is greater than 95% for *all* declinations.

Due mainly to the convergence of meridional lines as one approaches the equatorial coordinate singular point at the South Celestial pole (SCP), the sensitivity of the PMN Southern survey increases dramatically as one nears the SCP. For these reasons, the differential reliabilities and completenesses in the PMN Southern Survey improve markedly near the SCP. For the associated reason of non-convergence near the Celestial Equator, these quantities remain essentially constant in the Tropical and Equatorial surveys. The Zenith Survey was scanned using an entirely different techique; this is reflected in its relatively low levels of reliability and completeness near the Parkes zenith declination. Again, full details are provided in the PMN publications.

24. **Assignment of Survey Limiting Flux Density**: The publications of previous radio surveys typically assume a 5σ flux density cutoff limit for the catalog. This was not done for the PMN surveys, since the scan data noise statistics are *not* Gaussian. In addition, this proposed limit is only suitable if the underlying source population has a differential source count slope of $d\log(dN/dS)/d\log S = -2.5$ (Murdoch et al. 1973 [108]). The same analysis applied to the PMN survey, which is expected to have a differential source count slope of -1.6 (from the 4.8 GHz source counts of Bennett et al 1985 [11]), shows that the appropriate limit is 4.4σ. This yields the same reliabilty as the 5σ limit for the slope of -2.5. However, this method does not take into account the complex details of the non-Gaussian PMN noise statistics, and the full reduction procedure with its associated biases and introduction of various sources of noise. As the *reliabilty* of the catalog is being called to question at the faint flux density limits, it was deemed more appropriate to use a 90% differential reliability criterion for the establishing of the PMN catalog flux density cutoff limit. As this is a function of

declination, the PMN limiting flux density S_{lim} is variable. For the PMN Southern Survey, the relevant equation for this flux limit is:-

$$S_{lim} = 79.8 + 0.793\delta mJy; -75° < \delta < -37°,$$

$$S_{lim} = 20mJy; -87.5° < \delta < -75°,$$

At a declination of $-60°$, the PMN Southern Survey catalog flux density limit is then $\sim$ 32 mJy.

It turns out that these two different methods yield comparable values for the catalog flux density limit, to within a difference of 5 mJy, except for the region near the PMN Zenith Survey; this is because the Murdoch et al. method is insensitive to problems with the baseline definition near the ends of the scans in each Survey, whereas the PMN method takes this, and other problems, into account via the Monte-Carlo simulations.

25. **Comparison of Overlapping Sources**: Finally, 400 sources in a comparison region, observed in the two separate June and November observing sessions, were analyzed to reveal their soruce surface density and flux density differences; the results were entirely consistent with the Monte-Carlo determination of the PMN completenesses and reliabilities derived above.

26. **Cross-correlation with Previous Surveys**: The PMN source positions were cross-correlated with 2 previous Southern radio source large-area surveys: the multi-frequency PKSCAT90 catalog (Wright & Otrupcek 1990 [151]) and the Molonglo 408 MHz catalog (Large et al. 1981 [92]). If a PKSCAT90 source appears within 2' of the PMN source, a letter 'P' for that sources is recorded in the PMN catalog. Similarly, a letter 'M' is recorded for a Molonglo radio source within a 2' radius.

The preliminary analysis reported in the *Proc. ASA* 1991 [58] conference article showed

that the PMN source catalog is significantly more sensitive and complete than earlier small-area surveys (such as the Parkes selected regions). Thus the PMN source surface density of ~ 2 deg^{-2} is expected to be truly representative of the actual radio source surface density in the sky at 4850 MHz.

27. **Spectral Index Estimation**: The spectral index α was computed between the PKSCAT90 2700 MHz value and the current PMN 4850 MHz value. This index is defined by the equation for the spectral flux density: $S_\nu \propto \nu^\alpha$.

28. **Production of Final Catalog**: The final PMN catalogs include the following information: the PMN J2000-derived name; the J2000 RA and DEC; the 4850 MHz flux density in mJy (from the fixed-width Gaussian fit); the estimated standard error in the flux density; the spectral index where available; and a list of 7 letter 'indicator codes', which include the 'P' and 'M' flags already mentioned. Also listed is the 'S' flag for the case of possible solar contamination (PMN source within 5° of the Sun), and the 'G' flag for possible Galactic confusion (PMN source within 10° of the Galactic plane). Also, the zenith 'Z' flag indicates that the PMN source is weak ($S_{4.85} < 60$ mJy), and lies within 6° of the Parkes zenith. These sources may have residual problems in the baseline removal, and these PMN source data may be of lower quality.

The PMN surveys are optimized for detecting *point radio sources* at 4850 MHz. Here, 'point' means a source whose angular extent is less than the 4.'2 FWHM of the Parkes telescope beam. Very extended objects will either have been missed in the source detection procedures, or else recorded as a collection of multiple fainter sources; the most obvious examples are e.g. the Galactic plane, Centaurus A, and the Magellanic clouds. Thus, for the purposes of extragalactic source sample definition, source count and anisotropy and clustering analyses, these objects should be excluded from the sky region being analyzed. The flux densities of extended sources in general are *underestimated* by the published fixed-width Gaussian fitted flux density.

Very bright sources ($S_{4.85} >\sim 30$ Jy) are not included in the PMN catalogs, as they invariably saturated the raw data scan records.

An alternative reduction of the PMN data has also been published; this consists of a series of FITS/AIPS image data made by convolving the independently calibrated PMN scan data with a 'restoring beam', into a grid of maps (Condon et al. 1993 [36]). Radio source parameters were extracted using the standard DAO-PHOT package, and an independent PMN catalog was published from these independent results (Gregory et al. 1994 [57]). There are residual problems in the comparison of the flux densities of each of the PMN surveys, as well as with the Northern 87GB survey. These slight mismatches in the flux densities of common (overlapping) sources is no greater than about 7% of the flux, for sources fainter than 70 mJy. Those brighter than this limit show good general agreement in their fluxes. It is not known what is the precise set of causes for these flux density mismatches at low fluxes, and uncorrected systematic errors in the calibration process are thus strongly indicated. However, all the various Northern and Southern sky 4.85 GHz catalogs are mutually consistent at the $\sim 10\%$ flux density level for all detected sources, and complete and reliable as well.

We continue with a description of the differences and peculiarities of the other three PMN surveys.

The **Parkes-MIT-NRAO Zenith (PMN-Z)** survey spanned the declination band $-37°.0 < \delta < -29°.0$. This lies in a declination strip beween the Southern and Tropical Surveys. For the Zenith survey, a meridian scan could not be performed, as the telescope mount is alt-azimuth. Therefore, a special scanning technique was devised, such that the beam was rastered along a predetermined track off in the Western sky. This path was chosen to preserve the equal lateral separation between the beams. In the time available, a fully sampled (Nyquist) survey could not be completed, so the flux limit for the Zenith survey is significantly higher than for the other PMN Survey zones.

The data reduction procedures were essentially the same as those described above for the Southern Survey.

With sufficient accuracy, the total standard error ESZ for the Zenith Survey flux densities can be calculated from the following formula:-

$$ESTZ2 = (11.0)^2 + (0.070.S)^2(mJy)^2$$

For a source of 50 mJy at $\delta = -33°$, the total standard error in its flux density is then 11.5 mJy, which is 23%. For a 100 mJy source at the same declination, the corresponding values are 13.0 mJy and 13%.

For the Zenith Survey, the errors in each of the PMN right ascensions and declinations were:

$$\sigma^2_{RA} = 10^2 + (2050/S)^2,$$

$$\sigma^2_{DEC} = 11^2 + (2250/S)^2.$$

where the errors are in arc-seconds and the flux density S is in mJy.

For a 50 mJy source, the standard error in its RA is then 42."2, and it is 46."3 in DEC. For a 100 mJy source, the corresponding values are 22."8 and 25."0.

As mentioned in the description of the PMN survey procedures above, the differential reliability and completeness is significantly worse for the PMN Zenith strip than for the other PMN zones. The 90% differential reliability flux density limit for the PMN Zenith Survey sources is:

$$S_{lim} = 72mJy; -37.0° < \delta < -29.0°.$$

There are systematic differences in the flux densities between the Zenith and neighbouring

PMN Survey zones, at the level of a few percent.

The **Parkes-MIT-NRAO Tropical (PMN-T)** survey spanned the declination band $-29°.0 < \delta < -9°.5$.

The data reduction procedures were essentially the same as those described above for the Southern Survey.

With sufficient accuracy, the total standard error EST for the Tropical Survey flux densities can be calculated from the following formula:-

$$EST^2 = (10.5)^2 + (0.052.S)^2(mJy)^2$$

For a source of 50 mJy at $\delta = -10°$, the total standard error in its flux density is then 7.7 mJy, which is 15%. For a 100 mJy source at the same declination, the corresponding values are 8.9 mJy and 8.9%.

For the Tropical Survey, the errors in each of the PMN right ascensions and declinations were:

$$\sigma^2_{RA} = 6^2 + (1300/S)^2,$$

$$\sigma^2_{DEC} = 4^2 + (1100/S)^2.$$

where the errors are in arc-seconds and the flux density S is in mJy.

For a 50 mJy source, the standard error in its RA is then 26."7, and it is 22.".4 in DEC. For a 100 mJy source, the corresponding values are 14."3 and 11."7.

The 90% differential reliability flux density limit for the PMN Zenith Survey sources is approximately:

$$S_{lim} = -70.7 - 4.33\delta mJy; -29° < \delta < -26°,$$

$$S_{lim} = 42mJy; -26° < \delta < -9.5°,$$

At a declination of $-26°$, the PMN Tropical Survey catalog flux density limit is then $\sim$ 42 mJy.

The **Parkes-MIT-NRAO Equatorial (PMN-E)** survey spanned the declination band $-9°.5 < \delta < +10°.0$.

The data reduction procedures were essentially the same as those described above for the Southern Survey.

With sufficient accuracy, the total standard error ESE for the Equatorial Survey flux densities can be calculated from the following formula:-

$$ESE^2 = (9.1)^2 + (0.052.S)^2(mJy)^2$$

For a source of 50 mJy at $\delta = 0°$, the total standard error in its flux density is then 9.5 mJy, which is 19%. For a 100 mJy source at the same declination, the corresponding values are 10.5 mJy and 10.5%.

For the Equatorial Survey, the errors in each of the PMN right ascensions and declinations were:

$$\sigma^2_{RA} = 6^2 + (1300/S)^2,$$

$$\sigma^2_{DEC} = 4^2 + (1100/S)^2.$$

where the errors are in arc-seconds and the flux density S is in mJy.

For a 50 mJy source, the standard error in its RA is then 26."7, and it is 22.".4 in DEC. For a 100 mJy source, the corresponding values are 14."3 and 11."7.

The 90% differential reliability flux density limit for the PMN Zenith Survey sources is approximately constant:

$$S_{lim} = 40mJy; -9.5° < \delta < +10.0°,$$

The fullest account of the data reduction procedure and scientific results for the PMN surveys can be found in the MIT Ph.D. thesis of M. Griffith (1993) [62] . Many of the important details can also be found in the publications quoted above.

2.2 The MIT-VLA Snapshot Program

As the results from the MIT large-area surveys became available, the MG and PMN catalog positions were targeted for higher resolution narrow-field 'snapshot' imaging using the NRAO Very Large Array (VLA) interferometer located near Socorro, New Mexico. In the 14 year period from 1981 to 1995, the MIT group has been using the VLA, mostly in its largest (A-array) configuration, to obtain sub-arcsecond-resolution snapshots of the fields in the direction of the brighter MG and PMN radio sources.

The main goal of the MIT-VLA snapshot program is to identify new examples of multiply-imaged 'strong' gravitational lensing of background radio sources. To date, 7 confirmed radio-loud gravitational lenses have been found in the Northern hemisphere MG I, MG II and MG III regions that have been searched using the VLA. These gravitational lenses

are mentioned by name in the next chapter. In this thesis, I will be documenting new *candidate* gravitational lenses in the next chapter. It should be noted ahead of time that these candidates are not yet proven to be *bona fide* gravitational lenses; on the other hand, if a new radio-loud gravitational lens exists in the MIT-VLA snapshot sample, it is very likely that it will be in our list of candidates.

The MIT-VLA follow-up surveys are re-observations of selected sources from previous snapshot programs; as such, they do not expand the membership of the MIT-VLA sample, but they represent an attempt to obtain better, or further, data on the selected sources. With four major series of MIT-VLA observations, there are four prefixes used for naming the "observing days":

- **CDAYn** refers to the 1981–1986 MIT-Green Bank-VLA C-Band (MGVC) A-Array Snapshot Survey series.
- **XDAYn** refers to the 1989–1993 MIT-Green Bank-VLA X-Band (MGVX) A-Array Snapshot Survey series.
- **XSDAYn** refers to the 1991–1995 Parkes-MIT-NRAO-VLA X-Band (PMNVX) A-Array Snapshot Survey series.
- **FDAYn** refers to the 1994–1995 follow-up *re-observations* of sources from the 1990s MGVX and PMNVX Snapshot Survey series; these occured at both C-array and A-array.

Table 2.2 shows the main differences between the three MIT-VLA Snapshot Surveys of the (originally selected samples of) MG and PMN radio sources: listed are the observing epochs, frequencies, sky coverage, and approximate number of MIT radio sources assigned for VLA observations.

Table 2.3 gives the journal of observations for the entire MIT-VLA snapshot program, including the follow-up re-observations (*'FDAYn'*) of selected radio sources. The upper

Survey	Observations	ν(GHz)	δ_{min}	δ_{max}	$N_{\rm VLA}$
MGVC	1981 – 1986	4.87	+0°.0	+20°.0	~ 4100
MGVX	1989 – 1993	8.44	+20°.0	+40°.0	~ 3700
PMNVX	1991 – 1995	8.44	−30°.0	−0°.0	~ 2100

Table 2.2: The MIT VLA 4.8 and 8.4 GHz Snapshot Surveys.

portion of the Table lists the older 1980s C-Band A/B-array observations, while the lower portion lists the more recent 1990s X-Band A-array search efforts.

In the following sections, further details are provided for each of these four MIT-VLA snapshot surveys.

2.2.1 The MG-VLA C-Band Surveys

The first VLA gravitational lens surveys were targeted to find new examples of gravitational lensing within flux-density-limited (but randomly selected and incomplete) bright source samples drawn from the MG I catalog. This search sample is given the name 'MGVC' in this thesis. With the occasional excursion to just outside the MG I sky region, the MIT-VLA sources imaged in the 5-year period 11 May 1981 through 22 April 1986 lay mostly within the declination range $0° < \delta < +20°$. These observations were made in 12 separate VLA observing runs: in this thesis, they will be known by names such as 'CDAY1' and 'CDAY11', where the initial letter represents the radio frequency band used [following standard radio terminology, *C-Band* is $\sim$ 5 GHz (6 cm) and *X-Band* is $\sim$ 8.4 GHz (3.6 cm)].

The selection of the MGVC sources was made from flux-limited, relatively bright, samples of MG I catalog sources. As many of the brightest sources in the flux density range $1000 < S_{4.8}$ mJy have already been observed in bright-source VLA and MERLIN calibration finding surveys, this subset was excluded from the MIT-VLA search program at the outset. Many of the VLA flux and position calibrators fall within this range of flux density. The general

"Day"	Date	Array	$\nu_0/\Delta\nu$ (MHz)	Δt (hr)	N_{obs}	θ_{HPBM} ($''$)	Lens Detected	Note
C1	11May81	B	4885/50	24	362	1.10	MG2019	
C2	11Feb82	A	4885/50	24	359	0.35		
C3A	13Sep82	B	4885/50	13	50	1.10		Shared allocation
C3B	14Oct82	B	4885/50	24	306	1.10		
C4	5Sep83	A	4860/100	24	284	0.35		
C5	8Dec84	A	4860/100	24	499	0.35		
C6	17Dec84	A	4860/100	23	477	0.35	MG0414,MG1131	
C7	6Feb85	A	4860/100	18	334	0.35		
C8	7Feb85	A	4860/100	13	261	0.35		
C9	13Feb85	A	4860/100	11	194	0.35		
C10	7Apr86	A	4860/100	24	462	0.35	MG1654	
C11	21Apr86	A	4860/100	26	508	0.35		
X0	16Jan89	A	8440/100	24	364	0.21	MG1549	
X1	30Apr90	A	8440/100	16	318	0.26		N. arm Power failure
X2	3May90	A	8440/100	18	359	0.26	MG0751	N. arm Power failure
X3	5May90	A	8440/100	20	397	0.26		N. arm Power failure
X4	25Jul91	A	8440/100	24	445	0.21		
X5	26Aug91	A	8440/100	24	486	0.21	JVAS/MG1424	
XS1	2Aug91	A	8440/100	24	495	0.30		
XS2	31Dec92	A	8440/100	16	352	0.30		
X6	3Jan93	A	8440/100	24	489	0.21		
X7	8Jan93	A	8440/100	16	508	0.21		
X8	9Jan93	A	8440/100	16	302	0.21		IFs split by 400 MHz
XS3	7Mar94	A	8440/100	23	709	0.30		Flat Spectrum
XS4	9Mar94	A	8440/100	11	230	0.30		Flat Spectrum
XF1	10Dec94	C	8440/100	10	159	3.00		Exten./Resolv. sources
CF1	10Dec94	C	4860/100	12	376	5.20		Exten./Resolv. sources
XF2	9Jun95	A	8440/100	2	39	0.25		Exten./Missing Flux sources
XF3	11Jun95	A	8440/100	4	77	0.25		Exten./Missing Flux sources
XF4	17Jun95	A	8440/100	13	58	0.25		Close Doubles at CUX bands
XS5	8Jul95	A	8440/100	16	309	0.30		

Table 2.3: The MIT-VLA 4.8 and 8.4 GHz Snapshot Surveys (1981–1995).

algorithm used to produce the final VLA OBSERVE file (which is the electronic file that is used by the VLA computer to schedule the radio source observations) is as follows:-

1. Select a suitable flux density range ($S_{min} \leq S_{4.8} \leq S_{max}$) of MIT catalog sources to observe. The range should be commensurate with the list of MIT catalog sources not yet observed at the VLA.

2. Select a suitable sky area ($\alpha_{min} \leq \alpha \leq \alpha_{max}; \delta_{min} \leq \delta \leq \delta_{max}$) to observe. The area should be commensurate with the list of MIT catalog sources not yet observed at the VLA, and also with the range of Local Sideral Time (LST) at the VLA, that has been assigned for observations.

3. Extract all MIT catalog sources falling in this range.

4. Exclude all MIT catalog sources lying within 10° of the Galactic Plane; i.e. exclude those sources falling within the $-10° \leq b \leq +10°$ galactic latitude band. This will produce a sample that is almost entirely dominated by extragalactic radio sources, as opposed to foreground supernova remnants, planetary nebulae, star forming and HII regions within the disk of our Milky Way. By this point, we still have an (essentially) complete sample of MIT catalog sources.

5. Exclude all MIT catalog sources that have previously been assigned for MIT-VLA Snapshot Survey observations.

6. Sort the MIT catalog sources in RA, and insert a suitable number of VLA position calibration sources. There should be a primary flux calibrator (usually 3C286 or 3C48), and a polarization angle and polarization feed calibrator if such measurements are desired. When using the largest VLA A-Array configuration in poor weather conditions, it is highly desirable to insert a position calibrator at least once every 10 minutes, so that the winding of the atmospheric phase for each antenna and baseline can be

tracked closely enough to ensure reasonable self-calibration (more details will be given of these data reduction procedures in the next chapter). Also, it is recommended that the angular distance between the VLA calibration sources be as close as possible to the final program sources, so that changes in the phase, due to the range of paths through an unstable atmosphere, are minimized. The usual integration time for adequate detection of MIT-VLA sources is in the range 60 to 120 seconds, with 2-3 minutes assigned per position calibrator, and 4-5 minutes for at least two widely separated observations of the flux calibrator.

7. **Randomly exclude** program sources **without reference to their flux densities**, such that the total slew time for the final OBSERVE program source list is minimized to the extent where the total observation time is as close as possible to, but does not exceed, the assigned time. This is done by hand, through an iterative trial-and-error process. Normally, the record of flux densities is not retained after extraction from the MIT catalogs, so it is highly unlikely that the observational selection procedure will bias the distribution of MIT-VLA source properties within each flux density bin; in other words, a sufficiently wide flux density bin, that exists within the range of MIT-VLA source flux densities, should contain a **fair sample** of the actual number of MIT catalog radio sources in that bin, provided only that sufficiently large numbers of MIT-VLA program sources from that bin were successfully observed. This argument is extremely important for considerations of the statistical representativeness of the properties of radio sources imaged in the incomplete MIT-VLA sample. Here, the criterion of 'sufficiently large numbers' can be quantified in terms of simple binomial probabilities, but it is shown later that for all flux density bins above $\sim$ 70 mJy, the fraction of MIT catalog sources in the sky areas imaged exceeds 50%, and that this completeness fraction rises to above 90% of all MIT catalog sources for flux densities exceeding 150 mJy.

8. Make final checks for unintended contingencies, such as antenna shadowing, zenith and horizon limits, antenna cables wrapping round further than the allowed amount, and observing extremely bright radio sources such as the Sun, Moon or a planet. Normally, the NRAO software provided for the construction of the OBSERVE file will warn the user of these undesirable events.

9. Submit the final OBSERVE list to the VLA computer for observations.

The fully-operational VLA has 27 antennae, and thus $27 \times 26/2 = 351$ baselines, each of which measures the time variation of the complex visibility (i.e. a relative amplitude and phase) for the source on the sky-projected baseline. With the symmetric Y shape of the VLA, and the progressively larger inter-antenna spacing as one travels out along each of the arms, the coverage of the source complex visibility plane is typically very good. The large number of antennae yields an over-determined system of equations for the solution of the antenna complex gains as a function of time. Even in a few minutes, the VLA Fourier coverage of the visibility plane allows essentially unambiguous reconstruction of the source total intensity distribution; a good snapshot can be made from these data, and it is possible to observe at least a few hundred sources a day. More details on the data reduction are given in the next chapter.

For the purposes of defining the adopted observing method, the C-Band observations naturally divide into two parts; CDAYS 1–3, and CDAYS 4–11. Charles Lawrence planned and executed CDAY1, 2 and 3B. Charles Bennett planned CDAY 3A. The first 3 CDAYs are distinguished from the others by the use of just a single intermediate frequency (IF) channel tuned to 4885.1 MHz. For the later CDAYs, two IFs were used, and they were set at the standard 4835.1 and 4885.1 MHz frequencies. The VLA IF bandwidth is invariably set to the standard value of 50 MHz for all the MIT-VLA snapshot observations. In addition, CDAYs 1 and 3A/B were made using the smaller B-Array configuration, which provides significantly lower resolution (1″.1 FWHM as opposed to the more typical 0″.35 for the VLA

in A-Array C-Band). For the earlier sessions CDAYs 1–4, only a preliminary MG I list was available, for which a different technique was used to extract positions and fluxes from the raw MIT–Green Bank scan data. The final MG I list was used as the parent sample from CDAY5 onwards. In addition, the alloted time per source was about 3.6 minutes for the earlier observations; this includes overhead in slewing and set-up time. The useful on-source integration time was just under $\sim$ 3 minutes, which yields a theoretical noise limit of $\sim$ 0.25 mJy bm^{-1}, and a maximum dynamic range of 200 for the faintest compact sources in the sample (these have flux density $\sim$ 50 mJy at 4.8 GHz). VLA calibrators were observed about once every 30 minutes, which was found to be sufficiently frequent to track the fluctuations in the antenna complex gain due to the variable atmosphere.

Starting with CDAY5, it was decided that more rapid observations of sources would be feasible, and the time per source was decreased to 2.6 minutes for the rest of the MGVC program. With an on-source integration time of $\sim$ 2 minutes, the theoretical noise is 0.20 mJy and the maximum dynamic range is $\sim$ 250 for the faintest copact sources (with flux density $\sim$ 50 mJy at 4.8 GHz).

From the first MGVC observation on 11 May 1981 to the last one on 22 April 1986, there were $\sim$ 247 hours of VLA C-Band observations, in either A or B array, scheduled in the MIT-VLA OBSERVE files. In all, there were $\sim$ 449 calibration observations, and 4062 target sources imaged: this represents an overhead of $\sim$ 10% in observing calibration sources. Not counted here is an extra time, amounting to just $\sim$ 3% of the time spent in C-Band observations, devoted to observations of targeted sources at other frequencies. The OBSERVE files have not yet been examined to find out what these targeted sources were, but certainly a large fraction of these incidental observations were multi-frequency data on gravitational lens candidates; according to the lensing hypothesis, the ratio of radio fluxes is determined by the nature of the lensing geometry, and hence the flux ratios should remain constant in going from one observing frequency to another.

Not all MGVC program sources consist of MG I catalog sources. For example, in the first session, CDAY1, 79 flat-spectrum sources, for which 600 MHz fluxes were available from Arecibo data, were selected for snapshot observations.

As mentioned above, the source selection was done within predefined flux density and sky coordinate ranges. Since the flux density information was discarded immediately after selection from the parent MIT single-dish catalog, there should be no bias in the source samples within each flux density bin, except for the explicit selection criteria adopted during the original sample definition. Thus, it is expected with very high confidence that the MIT-VLA surveys, even though incomplete in a well-defined quantifiable manner, nevertheless form a statistically representative sample (i.e. a random sample) within each flux density bin, in the range from 50 to 500 mJy at 4.85 GHz. It is estimated that the MG-VLA sample of snapshots is essentially complete for the range 110 to 500 mJy, and the fractional completeness drops off to $\sim$ 50% at 50 mJy. The completeness fraction as a function of flux density, for each of the three MIT-VLA surveys (MGVC, MGVX, PMNVC) is given in the next Chapter.

A detailed discussion of possible selection effects is given in Lawrence's 1983 Ph.D. thesis [97], as well as in Lawrence et al. 1986 [12]. Here, 6 possible cases are listed:

1. **Confusion:** Weak sources falling below the MG catalog flux limit are too sparsely distributed to cause much error in the flux of a stronger source. Sources which are extended on the scale of about the beam separation may be listed as two or more separate sources; in this case, the much higher resolution at the VLA will resolve the detail immediately. Also, independent MG catalog sources that happen to lie close together on the sky, within about 3 to 7 arc-minutes of each other, may be 'confused' as a single source. Again, the radio source surface density is so low that this happens rarely. From the statistical analysis of the MG and 87GB catalogs, it has been found that radio source clustering is only weakly detected on these angular scales, if detected

at all; hence this real physical phenomenon is fortunately limited in its effect on the interpretation of the data.

2. **Resolution:** Large, extended extragalactic radio sources, of angular sizes about the size of the beam separation, will be recorded as separate sources in the MG catalog. However, independent high resolution interferometer maps have shown that such large sources are highly unlikely to occur in practice, at least for the case of extragalactic radio-loud emitters. However, there is a distinct possibility that resolved sources, of a few arc-minutes in angular size, will have their fluxes underestimated. More about this last factor is discussed in the next item.

3. **Variability:** At the upper and lower flux density limits, the time variability of some radio sources will cause them to be improperly included or excluded in the MIT-VLA sample. Due to the fact that there are more fainter sources than brighter ones, the net effect is that the coverage in flux density is shifted somewhat downwards at both the upper and lower cutoffs. This effect is much less away from the predefined flux cutoffs. For steep-spectrum sources, this flux density shift is expected to be small, as the variability of extended emission is negligible. It is the flat-spectrum compact sources that are expected to vary on timescales of weeks to years. In the case of resolved sources with underestimated fluxes, these will be under-represented near the lower cutoff, and over-represented near the upper one. However, as discussed previously, it appears that sources as large as a few arc-minutes are rare exceptions amongst the actual population of extragalactic radio sources, and so the biasing effect is ignorable for these particular sources. The conclusion is that as long as one is prepared to accept poorer sample definition at the selected flux boundaries, the MIT-VLA surveys will together remain a statistically representative sample of extragalactic radio sources.

4. **Flux Errors:** The same effect is mimicked by the presence of errors in the MG catalog

flux densities. Again, if these are random errors, the biasing effect will be small away from the flux cutoffs.

5. **Spectral Index:** There was no selection by spectral index from the parent MG catalog, so this bias was not explicitly incurred. It should be noted that it is probably the case that steep-spectrum, diffuse, extended emission from the older, less-energetic, population of electrons that exist in the 'lobes' and 'bridges' of mature radio sources will not be successfully imaged in the MIT-VLA snapshots. Older sources without active cores or hotspots will fail to be detected in the VLA snapshots, and hence will be conspicuous by their absence from the final VLA maps. However, this is *not* a bias in the definition of the MIT-VLA sample, only one in the classification of the radio source morphology based on the maps. Often, the presence of extended flux will be 'given away' by the rising visibility amplitudes for the shortest baselines. Lori Herold has worked on this problem using the MGVX sample, and she has shown, in her Ph.D. thesis, that these missing sources are almost all recoverably detectable with observations using the VLA in a more compact configuration (she found that the VLA C-Array will recover most of the resolved sources).

6. **Non-representative sky region:** As pains are taken in the MIT-VLA campaign to observe as many radio sources as possible over the selected sky areas, this is not a problem; as far as the author is aware, the scheduled observations were almost all successfully made.

In short, any biases that exist in the MIT-VLA sample are expected to arise: (1) near the flux density limits, and (2) from those in the parent MIT catalogs. As these are essentially complete and reliable, it is not expected that significant bias exists due to the 2nd factor. Thus, the MIT-VLA sample is expected to be unbiased in the intermediate flux density range 50 to 500 mJy, with a caution that this may start to be untrue near these limits.

For the early MGVC observations, the data were hastily calibrated and mapped at the NRAO, in intensive data reduction and analysis sessions. While this was good for the rapid discovery of new gravitational lenses, the resulting calibration and map quality was fairly mediocre, and sometimes quite poor. Only starting with the later CDAY (and XDAY & XSDAY) surveys were the data brought back to MIT for further, and more careful, analysis. This reduction and analysis are described in detail in the next chapter. Over the last two years, the author has taken the pains to organized the raw (i.e. uncalibrated) data into a convenient collection of Data-Certified Media-Recognition-System (MRS) Digital Audio Tapes (otherwise known as DAT tapes) at MIT. These data are also held in the NRAO VLA Archive, and may be requested for analysis, provided that notification is given to principal investigator Professor Bernard Burke (MIT); permission for use is not required, as the NRAO proprietary period is just 18 months. However, it is possible that some of the data have not yet been archived from the old magnetic tapes to the more modern and convenient DAT and EXABYTE tapes yet; in such a case, Bernard Burke at MIT should be contacted for data retrieval.

Finally, much more detail on the observations, reduction and analysis of these data can be found in the following papers, conference proceedings and theses: Lawrence 1983 Ph.D. thesis [97]; Lawrence et al. 1984 [94]; Lawrence et al. 1986 [95]; Hewitt 1986 Ph.D. thesis [72]; Hewitt et al. 1989 [72]; Burke 1990 [27], [104]; Conner 1998 Ph.D. thesis [38].

2.2.2 The MG-VLA X-Band Surveys

Starting in 1989, the MIT group started a new series of VLA A-Array snapshot observations at X-Band, instead of C. This was primarily for two reasons:

- Better resolution at higher frequency: 0″.21 instead of 0″.35. This is especially important, as multiply-imaged gravitational lenses may have fine detail on these and smaller scales, especially if there is extended ring or arc-like emission present in the map.

- Better receiver sensitivity at X-Band, by a factor of $\sim$ 45%.

For the Northern Sky MGVX observations, all except XDAYs 1 through 3 used all 3 arms of the VLA A-array, as per the normal mode of operation. There was a power failure in the North arm for these affected XDAYs. The observations continued until January of 1994.

The observing procedures were very similar to those for the MGVC survey. In all, there were 9 XDAYs, with observations of 3670 MG target sources in flux-limited samples drawn from the MG II and MG III catalogs. The standard 8414.9 MHz and 8464.9 MHz IF frequencies were used, and in dual R and L polarization. The bandwidth was a standard 50 MHz width. The observing times were about 2 minutes per source, with about 90 seconds of on-source integration time. The synthesized beam FWHM resolution was 0."22.

2.2.3 The PMN-VLA X-Band Surveys

In the period 1991-1995, a Southern hemisphere search for new gravitational lens candidates was started, with an entirely similar procedure as for the contemporaneous MGVX observations. The major differences with MGVX were the following:-

- Elongated NS beam for PMNVX.
- Fewer PMNVX sources and thus a brighter sample.
- Flat spectrum selection for PMNVX sources in XSDAYs 3 and 4.
- A competing Alok Patnaik VLA A-array survey of PMN flat-spectrum sources, which were deselected in XSDAYs 1993 and 1994.

In XSDAY5, A. Fletcher attempted a completion of the sample of brighter PMN sources. Also included in XSDAYs 3,4 and 5 were multi-frequency 5 minute integrations on both MG-VLA and PMN-VLA lens candidates.

2.2.4 The MG-VLA and PMN-VLA Follow-Up Surveys

These are the FDAYs: they do not increase the membership of the set of MIT-VLA sources initially imaged in the MIT-VLA program. These provide missing data, or further data.

Conner and herold selected program sources for FDAY1. Fletcher selected program sources for FDAY2,3,4.

FDAY1,2,3: C-Array survey to recover extended and 'missing' A-array radio sources from MGVX. These suffered from severe resolution bias at the VLA A-array. 12 % of the original MGVX sources fell in this category, and almost all were recovered with the VLA in C-array. The MGVX close doubles were reduced by Lori Herold for her 1996 Ph.D. thesis Further details can be found in 1996 Ph.D. thesis of Lori Herold [69].

FDAY4: Fletcher selected program sources. Multiwavelength CXU-band observations of a sample of MGVX and PMNVX close radio doubles. These data are un-reduced.

2.3 Optical Observations of MIT-VLA Radio Sources

Optical identifications of counterparts of radio sources are important in establishing the nature and redshift of the EGRS. Once a redshift is determined from the emission lines in the optical spectrum, the distance to the radio source can then be estimated precisely within an assumed cosmological world model. Thus, optical imaging is the next logical observing step after the accurate VLA A-array coordinates are obtained. Optical imaging will provide photometric magnitudes, and optical colors if more than 1 filter is used. With colors, one can often obtain a crude estimate of the ('photometric') redshift of the optical counterpart. The brightnes of the counterpart will also be important as a selection criterion in further optical spectroscopic work.

With the color photometry, identification of the redshift, and the species and strengths of the emission and absorption lines, one can get a good picture of the nature of the counterpart,

e.g. whether it is an AGN in a host galaxy, or else a foreground star from our own galaxy. With the redshifts, one can also estimate the monochromatic specific intensity of the source at any wavelength, as well as the projected linear size of its associated extended radio structures (jets, hotspots and lobes).

Optical identification of almost 1000 MIT-VLA MG I optical counterparts were attempted using Schmidt wide-field optical plates from the Palomar Observatory Sky Survey (POSS). A full analysis of the results can be found in Lawrence et al. 1986 [95]. The same work is also documented in Lawrence's 1983 Ph.D. thesis [97].

Optical identification of 2004 MIT-MG II and MG III counterparts were attempted using the CD-ROM disks of the Digitized Sky Survey (DSS), which in turn are derived directly from the electronic scanning of original Schmidt plates of the Northern POSS and Southern ESO/SERC Schmidt surveys. The results of this work are documented in Lori Herold-Jacobson's 1996 Ph.D. thesis.

In collaboration with Edwin Turner of Princeton University, some important optical imaging and spectroscopic work was done in the early 1980s by the first group of students active in the MIT-VLA survey (C. Bennett, C. Lawrence, J. Hewitt, G. Langston, S. Conner, J. Lehár, M. Heflin & C. Carilli) using the Kitt Peak National Observatory (KPNO) and Michigan-Dartmouth-MIT (MDM) telescopes. This optical effort was very successful in identifying 6 *bona fide* gravitational lens candidates, including the first discovery of an Einstein Ring (which occurs when the alignment of the lens and background source is near perfect). This fruits of this optical identification work appear in the refereed literature (see Chapter 4). The MIT-VLA: gravitational lenses are MG 2016+112, MG 1131+0456, MG 0414+0534, MG 1654+1346, MG 1549+3047 & MG 0751+2716). Preliminary versions of most of these results, as well as other lens candidates that have been rejected or incompletely investigated, also appear in the Ph.D. theses of: C. Lawrence, J. Hewitt, G. Langston and J. Lehár.

The MIT radio group is collaborating with Hyron Spinrad (UC Berkeley) on obtaining MG radio source identifications and redshifts. These are available through private communication with Hyron Spinrad.

While a Ph.D. graduate student at the University of Cambridge, Isobel Hook included Joseph Lehár's XDAY0 and XDAY2 radio positions in her high redshift ($z > 3$) radio-loud quasar search sample. Optical identifications were readily available through the work of her advisor (Richard McMahon), in which an electronic Automated Plate Machine (APM) database of optical source positions, magnitudes and morphologies was compiled and made freely available over the Internet. The important result from her research was the isolation of a sizeable sample of high redshift quasars, from which she could place useful limits on the shape and evolution of the quasar luminosity function at high redshifts. This is important in constraining the epoch of peak number densities in the evolution of quasars in the early Universe. This important body of research can be found in Isobel Hook's 1994 Ph.D. thesis [75].

Over the past few years, a new optical campaign was started by the second generation of students involved in the MIT-VLA survey: the optical data were taken mostly by A. Fletcher, L. Herold-Jacobson, and S. Conner, with assistance from E. Gaidos, J. Blakeslee, C. Becker, A. Cooray, D. Haarsma, F. Crawford, J. Cartwright and B. Burke. The MDM 1.3m and the CTIO 1.5m telescopes were used. Most of the work was targeted at a new sample of small angular size radio double-lobed galaxies, which henceforth will be referred to as *'close doubles'*, in this thesis. The Northern MGVX close doubles were primarily extracted from the MIT-VLA snapshots by L. Herold, while the Southern PMNVX close doubles were extracted by A. Fletcher.

Some images and spectra of a few close doubles were taken by P. Garnavich (Cfa) using the MMT, CFHT and KPNO telescopes. Images and spectra of gravitational lens candidate ring MG 0248+0641 were taken by both P. Garnavich using the MMT, and also A. Fletcher,

A. Cooray and Christopher Becker (MIT), using the MDM 2.4m telescope. The full results of this work, which also includes KPNO 2.1m infrared imaging data, MERLIN L-band deep radio imaging, and upper limits on Xray emission from ROSAT images, appears in a paper recently accepted for publication: Conner et al. 1998 [37].

The latest optical work was done by our Cfa collaborators Emilio Falco, Christopher Kochanek and Jose Muñoz. They were interested in optical identifications and redshifts for MGVX sources from L. Herold's thesis. Using this and other samples, they were able to estimate the radio luminosity function for a representative sample of MGVX radio sources (Falco et al. 1997 [47]). This is useful, amongst other things, for estimating the probability of multiple-image lensing of EGRS.

In addition, a new binary quasar was discovered in the L. Herold's thesis sample; this research was submitted recently for publication (Muñoz et al. 1997 [107]).

The following sections report on the 10 major optical observing sessions performed by MIT students in the period 1994-1996. A Journal of Observations is presented in Table 2.4. In this thesis, only observations of MGVX and PMNVX close doubles, gravitational lenses, and a control sample of randomly selected sources are reported in detail.

2.3.1 Gravitational Lens Candidates

Most of our effort was concentrated in an investigation of the field of MG 0248+0641, which was identified as the most promising of our gravitational lens candidates; it was discovered in 1994 by Samuel Conner in his remapping of the old MGVC data, and it has a standard Einstein ring morphology expected from lensing by an ellipsoidal galaxy-mass potential. In November 1995, Christopher Becker assisted A. Fletcher and A. Cooray with optical spectroscopic observations of MG 0248+0641, as well as 3 other sources within 1 arcminute of the MG 0248+0641 counterpart. The purpose of obtaining spectra for the nearby sources was to investigate whether there was a galaxy cluster assisting with the proposed gravitational

Table 2.4: 1993–1996 MIT Optical Runs

The 1993-1996 MIT Optical Surveys

Telescope & Diameter	f no	First Date	Last Date	Dark Time?	CCD	Pixel Scale (")	Filt/Spec	Amount of Data	Src	PI	Comments
MDM 1.3m	7.5	??Dec93	??Dec93	No	Wilbur 2048^2	0.635	IRV–	N_{src}= 8	GC-	LH	Poor Flatfields
MDM 1.3m	13.5	03Feb94	06Feb94	Some	Wilbur 2048^2	0.353	IRV–	N_{CCD}= 380	GC-	SC	
MDM 1.3m	7.5	07Feb94	11Feb94	No	Wilbur 2048^2	0.635	IR—	N_{src}= 6	GC-	LH	
MDM 1.3m	7.5	12Sep94	27Sep94	Some	Wilbur 2048^2	0.635	IRV–	N_{CCD}=1051	GC-	AF	
MDM 1.3m	7.5	23Jan95	02Feb95	Some	Wilbur 2048^2	0.635	IRV–	N_{CCD}= 727	GCR	AF	
MDM 1.3m	7.5	08Mar95	22Mar95	Some	Wilbur 2048^2	0.635	IRV–	N_{CCD}= 979	GCR	AF	
MDM 1.3m	7.5	13Oct95	19Oct95	Some	Nellie 2048^2	0.444	IRVBU	N_{CCD}= 639	GCR	AF	
MDM 1.3m	7.5	21Dec95	27Dec95	Dark	Wilbur 2048^2	0.635	IRVBU	N_{CCD}= 805	GCR	AF	
MDM 2.4m	7.5	02Nov95	05Nov95	No	Charlotte 2048^2		MkIII Sp	N_{src}= 6	GC-	AF	Moon&Clouds
CTIO 1.5m	7.5	11Feb96	14Feb96	No	TekQuad 1024^2	0.434	IRVB-	N_{CCD}= 634	GC-	AF	Good South Seeing
MDM 1.3m	7.5	27Feb96	07Mar96	No	Wilbur 2048^2	0.635	IRVB-	N_{CCD}= 703	GCR	AF	

Table 1: Journal of Observations for the 1993-1996 MIT Optical Runs. The principal observation planners were: S. Conner (SC), A. Fletcher (AF) and L. Herold (LH). The sources are coded: G=lens candidate; C=close double; R=random source.

lensing in this source.

In December 1995, Peter Garnavich (Cfa) obtained an MMT spectrum of the counterpart; this showed it to be a typically blue AGN galaxy, with emission lines placing it at a redshift of 0.57. Further details of the investigation into this radio ring source can be found in Chapter 4.

Other lens candidates from the MGVX and PMNVX snapshot surveys were also imaged. These are listed in Table 2.5.

MGVX and PMNVX Lens Candidates with Optical Data

Source	Telescope	Images?	Spectra?
MG 0248+0641	MDM 1.3m	Y	
MG 0248+0641	MDM 2.4m		Y
MG 0248+0641	MMT		Y
PMN 0837-1156	MDM 1.3m	Y	
MG 1011+3155	MDM 1.3m	Y	

Table 2.5: MGVX and PMNVX lens candidates: optical observations

2.3.2 Close Radio Doubles

From the new 1990s MGVX and PMNVX data, we defined 2 samples: $\sim$ 120 close radio doubles, and a Random Source Control Sample consisting of $\sim$ 60 MIT-VLA radio sources. Our adopted empirical definition of a 'close double' was:

- 4.8 GHz Flux Density: $50 < S_{4.8} < 500$ mJy.
- 8.4 GHz Angular Size: $0.''2 < \theta < 2.''0$.
- Roughly Symmetric Double VLA Morphology.

Appendix A lists the close radio doubles and random sources that we chose from our MIT-VLA data. Appendix B lists the MIT-VLA lens candidates that we selected from the 1990s MIT-VLA imaging data.

In November 1995, We had a little time on the MDM 2.4m to obtain mediocre-quality spectra of two close doubles. For these observations, we were hampered by poor weather, and a bright Moon. The guiding was manual and hence tedious and difficult. Nevertheles, we succeeded in obtaining some low S/N MDm 2.4m spectra, with the assistance of C. Becker (MIT), who had a parallel and independent observing program at the same time. C. Becker took care of the calibration and reduction of the final spectra that appear in Chapter 4.

For all the optical observations, standard methods were used to record and reduce the data: the optical reduction software Vista and IRAF were used. More details may be found in the next Chapter (Data Reduction).

2.4 Summary

Surveys are the basic data sources for astronomy and astrophysics. For reliable statistical model fitting, essentially complete and reliable surveys are required to be gathered. For incomplete and unreliable surveys, scientific results may still be extracted provided the shortcomings of the survey selection process are well understood or otherwise quantifiable.

At MIT, single-dish surveys were made to record the 4.8 GHz sky completely and reliably. An extensive follow-up series of VLA snapshot continuum imaging surveys of the brighter single-dish catalog sources was performed in the period 1981-1995. Incomplete selection in the VLA samples arose due to the practical constraints of minimizing the slew time between the final observed set of program sources and VLA calibrators. However, the incompleteness in the final MIT-VLA snapshot program sources is reasonably well understood, and can be precisely quantified relative to the essentially complete and reliable parent MG and PMN single-dish catalog surveys.

The aim of the MIT radio astronomy group surveys was to compile accurate lists of 4.8 GHz radio sources outside the Zone of Avoidance (Milky Way Galactic Plane), and also to obtain a representative sample of high-resolution images of mostly extragalactic radio-loud AGN. The initial priority was to search among the VLA snapshots for new examples of gravitational lensing; but it is clear, from the careful systematic nature of our work, that our database of single-dish catalogs and VLA images can be used for many other purposes: cosmological applications, cross-checking with other radio surveys, definitions of other types of representative samples of EGRS (extragalactic radio source), to name just a few of the more obvious examples.

Systematic optical identifications using Schmidt plate material have been attemped only for 3500 MIT-VLA sources in the MG-I, MG-II, and MG-III regions. Optical identifications have also been attempted for much smaller samples of various specific types of EGRS: about 120 small-angular-size double-lobed radio galaxies, $\sim$ 70 gravitational lens candidates, and a randomly selected sample of $\sim$ 60 radio sources drawn from the newer MIT-VLA X-band snapshots.

The limiting factor in the optical follow-up was the faintness of the optical counterparts. For this reason, optical spectra were taken for only a tiny fraction of the close radio doubles and gravitational lens candidates, mostly in the accessible magnitude range $15 < R < 19$ (any fainter would require many hours at the MDM 2.4m telescope). The optically faint sources and 'empty optical fields' are better done with higher efficiency using larger 4-10m class telescopes, eg. the Multiple-Mirror-Telescope (MMT), the Keck 10m and the planned Magellan 8m telescopes. Redshift identification of complete samples is absolutely essential for deriving useful statistical population functions for the purposes of doing global physical and empirical model fitting; there is a very large body of work to be done in the future, with the accurate MIT-VLA radio source positions.

The results of 15 years of radio and optical observations have been organized into an

archive by the author. A substantial fraction (~50%) of the 10,000 radio VLA snapshots reside as AIPS FITS files on magnetic DAT tape, and hardcopy plots are also readily available for these. For a further ~ 30% of the MIT-VLA sources, hardcopy information on both optical and radio observations have been made readily available in labelled folders place in filing cabinets at MIT. The derived VLA radio source parameters will soon be uniformly organized for 60% of the MIT-VLA sources at MIT, by the author.

Chapter 3

Data Reduction

In this chapter, I will describe the processes used to reduce both the radio and optical data currently existing in the **MIT-VLA Archive.** This comprises the efforts of ~70 person-years of work done by at least two generations of MIT Ph.D. students. For the record, it is important to document at least some of the major evolutionary changes that have occurred in the reduction of the VLA interferometer radio data. Due to the sparsity of such documentation for a large part of the older (1980s) MGVC snapshot survey, the record contained herein will be only a best personal guess as to the true details of these reduction procedures. This second-hand information was relayed to the author through incidental conversations with a more senior graduate student (S. Conner), in the period 1990 through 1994. Details may be found in the current draft of his Ph.D. thesis (1998, in progress [38]). Some of the details may also be found directly from the source: see Lawrence et al. 1984 [94], 1986 [95].

The data reduction was performed primarily with the standard radio and optical software packages: AIPS, Vista and IRAF. Customized software was written using the AIPS POPS scripting language, by C. Lawrence and G. Langston, for the reduction of the 1980s MGVC VLA data. This older software was extensively rewritten, expanded and greatly enhanced

by Samuel Conner for his Ph.D. thesis re-reduction of the old MGVC sample. A series of AIPS pipeline reduction procedures (the **MIT-VLA Pipeline**) was created, developed and tested by S. Conner, for the purposes of high quality efficient reduction of the VLA data that had accumulated in the MIT-VLA Archive. Lori Herold and the author used Conner's later versions of this AIPS pipeline code to reduce their own MGVX and PMNVX datasets. In the process of creating the MIT-VLA Pipeline, S. Conner found it highly desirable to insert new tasks into the then-installed 15 April 1992 AIPS distribution software (these were internally known as 'experimental' modifications). The advantage of this was an increase in efficiency and also better systematization of the information processing through intermediary data reduction stages. However, the disadvantage was that these experimental tasks could not be easily transported in later updated releases of the AIPS software distribution, so the benefits of having these faster, improved and debugged AIPS distributions could not be had.

The author has been in charge of the construction and making of backup DAT tape copies of the MIT-VLA Archive for the past 2 years. There are over 100 DAT and Exayte tapes of radio and optical data. Almost all of the post-1989 data is included in this database, a large fraction of which consists of raw data and also data in intermediate stages of reduction. For the 1980s MGVC survey, only the raw VLA data (and no raw optical data) are available. The processed MGVC radio and optical data were, unfortunately, either deleted after inspection for lens candidates, or else stored on now aging 9-track magnetic tapes at MIT; these data were also written in many different incompatible formats, mostly by a now-defunct proprietary Apollo operating system. It is not worth the effort and time to try to retrieve these old (and probably corrupted) data; a better strategy would be to take advantage of the new sophisticated MIT-VLA pipeline routines, and much faster UNIX operating system computers, to re-reduce the old MGVC radio data.

The major part of the extensive optical data on survey sub-samples remains unreduced or inaccessible. Optical data on the highest priority sources, i.e. the promising gravitational lens

candidates, have been reduced and analyzed more thoroughly, but there are still unreduced 1990s data even for these sources. Further details of the status of the data reduction, and the reduction procedures themeselves, may be found in the following sections.

3.1 Aperture Synthesis Imaging

The major aims and procedures of aperture synthesis imaging were summarized in Chapter 1. The goal is to reconstruct a sky surface brightness distribution that is a faithful as possible to the true one, given the finitely sampled Fourier transform (visibility) data collected by the aperture synthesis array.

The VLA synthesis array is a 27-antenna interferometer located outside of Socorro, New Mexico, USA. It is in the shape of the letter 'Y', with equal angles between its 3 arms, and 9 antenna per arm. To avoid redundancy in the coverage of Fourier spatial frequencies, these antennae are spaced apart from each other according to a geometric series. There are 4 configurations: A, B, C and D, in order of decreasing size (this again is in a geometric series, but with a different factor). The maximum baseline is $\sim$ 36 km in the largest A configuration. As the ultimate resolution of any interferometer is governed by the ratio of the observing wavelength λ and maximum baseline length B:

$$\theta_{FHWM} \sim \frac{\lambda}{B}, \tag{3.1}$$

the highest resolution will be obtained in the largest (A-array) configuration. At X-Band (8.4 GHz) in the VLA A-array, the typical resolution for Northern declination sources is $\sim$ 0.″2. The VLA A-array is the one that is primarily used in the collection of the MIT radio data, as we expect that cosmologically distant sources, lensed by typical galaxies, will have an angular separation of the order of 2″. The highest affordable resolution is necessary to be able to confidently resolve out the various multiply-imaged components of bona fide

gravitational lenses. It also turns out, though this was not clear in the planning stages of the MIT-VLA program, that extragalactic radio sources (EGRS) at these frequencies have a median angular size that is not far different from that seen in the gravitational lenses. Thus, high angular resolution is also necessary for the study of the details of EGRS morphology, and ultimately the physics thereof.

With $N = 27$ antennae and $N(N-1)/2 = 351$ simultaneuos baselines that give a very good instantaneous coverage over the visibility plane, the sensitivity of the VLA is also quite remarkable. In a typical MIT-VLA 'snapshot' of an EGRS, the on-source integration time is typically $\sim$ 90 seconds; this affords us a theoretical rms map noise level of about 0.2 mJy/bm, and thus a dynamic range, for a typical 80 mJy compact source, of up to 400. With an overhead of $\sim$ 40 seconds in slewing, pointing and settling of the array, and a further 10% overhead in observing calibration sources, it is possible to observe up to 600 sources a day. At this rate, it is theoretically expected that each MIT-VLA observing 'day' will contain about 1 bona fide lens, on the average. Thus the potential reward from just 24 hours of VLA data is quite large. In this respect, the VLA is a unique interferometer array, with strengths in resoution, sensitivity as well as effciency and reliability in operation.

The general VLA reduction procedure is straightforward; first, establish a preliminary calibration using the VLA calibrators assigned for that session. This must include a calibration for flux and position, and also for polarization, if that information is desired. Secondly, make an initial Fourier transform of the calibrated visibility data, producing what is called the **dirty image**. This contains the full effects of the convolution with the VLA synthesized beam, whose time development is precisely known from the accurate positions of each of the VLA antennae. A **deconvolution algorithm** is employed to remove this instrumental beam, leaving a **cleaned image**. Using this as an input model to the next stage of an iterative deconvolution-calibration cycle, new improved values of the complex gains of each of the antennae are calculated. This technique is known as **self-calibration**, as now

the snapshot source itself is used to improve its own calibration, rather than an external VLA calibration source. Provided sufficiently good constraints and parameters are supplied to the initial stages of this self-calibration cycle, the process will eventualy converge to an acceptable unique solution for both the calibrations and the final resulting snapshot image. Most of this cycle is automated in the Conner AIPS Pipeline routines, and in fact there is a second automated self-calibration/mapping pass after an important user-interactive step (more details on this will be given in the next section). Finally, each of the resulting snapshot images needs to be analyzed according to a pre-planned and uniform scheme.

Using the notation introduced in Chapter 1, the aim in all calibration procedures is to find the "best" time-dependent values of the antenna-based complex gains $G_i(t), G_j(t)$, and also the baseline-dependent complex gain $G_{ij}(t)$, such that the true visibility $V_{ij}(t)$ can be recovered from the observed visibility $\tilde{V}_{ij}(t)$. If the time-variable additive complex errors in observed visibilities are denoted $\varepsilon_{ij}(t)$, then the relation that applies is the following:-

$$\tilde{V}_{ij}(t) = G_{ij}(t).G_i(t).G_j(t).V_{ij}(t) + \varepsilon_{ij}(t). \tag{3.2}$$

The antenna-based errors usually arise from expected causes, such as the rapid variation of the path length through the atmosphere to particular antennae (these are 'atmospheric phase errors'), the variation of path length in the transmission path from the antenna to the VLA correlator (these are 'instrumental amplitude and phase errors'), loss of antenna pointing or otherwise interruption of the data stream, and impulsive radio frequency interference. In the last two cases, the data from the affected antennae must be discarded.

Normally, the baseline-dependent errors can be ignored. They could arise from errors in the operation of the VLA correlator for particular baselines. It is also possible that there are errors in the assumed positions of the VLA antennae, which lead to errors in the assumed baseline vectors. This often happens after the array has moved to a new configuration. Fortunately, the baseline-dependent errors can be quickly solved for, by use of the

self-calibration technique on bright compact VLA calibration sources. Once the appropriate baseline-dependent errors have been incorporated on-line, subsequent observers need no longer assume that the $G_{ij}(t)$ cannot be ignored.

With the mathematical goal clear in mind, I now give a brief summary of the standard VLA calibration procedure. More details can be found in the AIPS Cookbook (1990, NRAO [110]).

Standard AIPS Calibration Procedure

1. **FILLM**: Read in the raw VLA visibility data.

2. Observing **Log**: Obtain and inspect the log for the times where the smooth recording of data may have been disrupted. The data for these times, and for the affected baselines and antennae, may need to be edited out in next data editing (*'flagging'*) stage.

3. **TVFLG**: Inspect both the amplitude time-variation versus baseline, and rms amplitude variation versus baseline, on the TV screen. Edit out outliers in the data. Include a precautionary 'quacking' procedure if necessary: since the VLA takes a little time to settle down in its pointing, the initial integration records for a source may need to be discarded. Most important is to first edit bad data for all the calibration sources. The program sources can be edited later, or else the outlying visibilities for all sources could be excised using a S/N criterion.

4. **SETJY**: Set the flux density scale the assigned VLA 'flux calibrator' (usually 3C286 or 3C48). Do this for each IF frequency, using the standard values from the Baars et al. (1977) [5] flux density scale. This scale was set assuming a given flux density for the Galactic supernova remnant Cassiopeia A.

5. **GETJY**: Set the flux densities for the other (position and polarization) calibrators, by simply scaling according to the averaged visibility amplitudes. In this step, it is important to specify the correct visibiity amplitudes for the averaging and scaling process; resolution effects are important for most VLA calibrators; at long baselines, the source may start to lose visibility amplitude due to the presence of small-angular-scale slightly-resolved structures, which are nevertheless slightly larger than the VLA synthesized beam resolution. At short baselines, the presence of extended diffuse emission, e.g. from radio lobes, bridges and haloes, may appear as rapidly rising visibility amplitudes at the very shortest baselines. In either case, the absence of unresolved point structure for the affected baselines means that we cannot use these particular data for the setting of a single flux density level. The VLA calibrators usually have a non-zero range of baseline lengths for which the source will appear neither slightly resolved nor with extended emission. It is only for these known baselines that the flux density level can be reasonably set, and it is these values (which can be obtained from the VLA Calibrator Book [111]) which are used as inputs into the GETJY task.

6. **CALIB**: Solve for the complex gains G_i for each of the VLA calibration sources, assuming point models for these sources, with flux densities given by GETJY values. These sources are assumed to be at the the phase centers of their respective fields, and so the position calibration is tied to the coordinate reference frame of the pre-assigned VLA calibrator positions. Typically, these positions are known very accurately, to much better than 1 arc-second, but the systematic plus random errors in the final VLA positions can be as large as 0.″2.

   The system of equations defined by the VLA data stream is an over-determined system: there are plenty more data constraints than model constraints, so the least-squares or some other similar minimization algorithm can be most profitably used to solved for the 'best' values of the antenna-based complex gains. As part of the calibration process

CALIB, the so-called *closure errors* are calculated, which comprise the percentage amplitude deviations of the individual gain amplitudes, and the round-the-loop closure phases. For the assumed point source VLA calibrators, the gain amplitudes should be uniform, and the closure phases should all be zero (the sum of the phase errors around any closed loop should cancel in equal and opposite pairs, thus giving a total error of zero). Typically, one aims for gain amplitude errors of no more than 10% for all antennae, and closure phase errors of no more than 10 degrees for any baseline. The reported closure errors are good diagnostics for which combinations of (time, baselines and antennae) to consider for further data flagging.

7. **Iterate** from step (2) until all significant gain amplitude and gain phase closure errors are removed to beneath the levels of 10% and 10 degrees, respectively. Once a good calibration is in place, all of the *residual* complex gains should be as close to unity as possible, i.e. the corrected visibilities should be equal to the true visibilities, at least in a statistically quantifiable sense.

8. **CLCAL**: Once the complex gains G_i are established for the VLA calibration sources, this calibration of flux density and position is propagated to the entire observing run, i.e. the time-series $G_i(t)$ is established for each antenna i. This is usually done by simple 2-point interpolation.

9. **PCAL**: If polarization information is desired, the VLA polarization calibrators need to be used to solve for (1) the intrinsic polarization properties of the VLA antennae themselves, and (2) any systematic phase offsets between the two systems of orthogonal polarization. For the first task, the ideal VLA polarization calibrator should possess essentially zero linear polarization; thus, any observed polarization in this calibrator would be entirely due to the leakage of polarization between the two orthogonal (Right and Left) channels. This can normally arise from small imperfections in the (electrically

polarized) feeds. For the second task, a second VLA calibrator is required, preferably one with significant and constant linear polarization at the observing frequency. Any systematic phase offset between R and L will cause an apparent rotation of the observed linear polarization vector position angle. From the observed difference between the observed and expected position angles, one can insert a simple phase offset in one of the R or L data to de-rotate the vector back to its expected position.

Having established an initial calibration for the entire data set from a given VLA observing day, we can now proceed to the improvement of the work in this initial phase, via the use of custom-bulit semi-automated AIPS procedures. This is the subject of the following section.

3.2 The MIT-VLA Pipeline

The MG C-Band data were reduced in an era when the self-calibration procedure was not in common use. Typically, only one cycle of CLEAN deconvolution was performed, and the map noise is dominated by poor deconvolution.

The initial data reduction of the early 1980s MGVC data did not have the benefit of a well-desgined Pipeline procedure. In fact, the currently-used deconvolution task MX was not available, and the technique of improving the maps via self-calibration was not implemented in public AIPS releases. Thus, the first maps enjoyed only a single iteration of CLEAN, using a less rigorous deconvolution procedure than MX. The resulting maps were of poor quality, in some cases suffering quite severely from the effects of supra-thermal noise arising from poor deconvolution. These early maps were just good enough for a student to be able to recognize the gravitational lenses. In the mid-1980s, Glen Langston wrote an automatic mapping program, called **MAPIT**, which included cycles of MX deconvolution and self-calibration for individual program sources. The maps made from this program were of much

better quality. Finally, in the early 1990s, Samuel Conner was able to contruct an entire pipeline series of tasks for the current version of the MIT-VLA Pipeline.

We now provide a descriptive account of the individual Conner tasks in the current MIT-VLA Pipeline.

1. **PRELIM**: This makes preliminary maps of all sources, using an automated mapping procedure. As inputs into the batch job run file, crude visibility information is provided to PRELIM; this allows appropriate constraints to be put on the location of assumed real source emission, in the form of restrictive CLEAN boxes placed in the field of view. For example, for sources that were slightly resolved or unresolved could profitably be CLEANed within small boxes of only a few arc-seconds in extent. Those that were clearly extended on the short baselines would be better mapped using much larger CLEAN boxes, of order 10 arc-seconds or so in size. The specification of automatic CLEAN boxes is thus not entirely automatic, as the user must generate and inspect the visibility amplitude vs. baseline plots for every source. However, once this task is done, the mapping is automatic, lasting anywhere from 10 to 40 minutes per source. The CLEAN component models for the extended sources were more complex due to the nature of the emission. The results are written as standard AIPS FITS files, and details of the mapping and self-calibration cycles, such as noise statistics and numbers of CLEAN components used, are written to disk as text log files.

2. **SETBOX**: The PRELIM maps are then inpsected by hand, using the procedure SETBOX. User-defined CLEAN boxes are set down on all regions of suspected real emission, and an option is allowed to map and self-calibrate the data for the current source, for the purposes of advance viewing of the map that would result. Once the user is satisfied with the placement and size of the CLEAN boxes, their coordinates are stored for later use by the final stage of mapping (MAINMAP). SETBOX is the main bottleneck in the entire MIT-VLA Pipeline process; only Herold and Conner have been through

this and the rest of the Pipeline. About 2500 final MAINMAP maps are presented in the Ph.D. thesis of Herold (1996) [69].

3. **MAINMAP**: With the user-defined CLEAN boxes to restrict the areas of the image that are searched for true sources, essentially the same mapping and self-calibration procedures as for PRELIM are let loose on the original calibrated data **check this.** There are options to generate polarization maps (Stokes Q, U and V), a wide-field map, uniform and natural-weighted maps, and a super-resolved map. The results are written as standard AIPS FITS files, and the mapping and self-calibration details are again written to disk as text log files.

4. **ANALYZE**: This routine automatically gets the next map, allows the user to select a field for study, and extracts the radio source parameters of the components appearing above the noise; peak intensities, integrated component fluxes, and peak positions. The user must record separately the radio morphology of the source, and also a note should be made as to its suitability as a gravitational lens candidate. If there are other sub-samples being compiled, such as the close radio double sample, then these must be noted on a case-by-case basis.

5. **AUTOPLOT**: This routine generates the final plots as Postscript figures, with the final synthesized beam shape, size and position angle indicated in the corner. Also, an angular scale is drawn on the plot itself.

The MG X-Band data from XDAY0, XDAY2 were automatically CLEANed and self calibrated by J. Lehár using his routines MGVXMAP. The quality of these maps is comparable to those from Langston's MAPIT procedure. However, this is not the best one can do, as the extended and diffuse structures are poorly imaged, and there are sidelobe emissions still visible in a large fraction of the maps.

The PMN X-Band data were similarly automatically CLEANed and self calibrated by A. Fletcher (XSDAY1, 2, 3, 4) using S. Conner's custom procedure PRELIM. The difference between Lehár's and Conner's procedures is the use of extra information in the running of PRELIM, i.e. the extent of the resolution of the radio source as judged from the visibility amplitude vs. baseline length plots. As expected, the map quality here is visibly better than in Lehár's maps using MGVXMAP. However, residual sidelobes are still faintly visible in some maps, and the thermal noise limit is approached but not reached.

The best maps were made by L. Herold and S. Conner, for their MG-VLA sources. See their Ph.D. theses (1996, 1998). To date, complete passage through the MIT-VLA pipeline has only been fully documented by Herold in her Ph.D. thesis.

3.3 Analysis of MIT-VLA Snapshots

Once the maps are made, the next problem is their analysis; the results appear eventually in an electronic file that can be used for future scientific analysis. The various radio source parameters that might appear in such a file are listed here:

1. **MIT Catalog Source Name**: This is the name from the MIT single-dish 4.8 GHz catalog. It is derived either from the B1950.0 or J2000.0 coordinates. In the case of a VLA calibrator, the closest MIT radio source name is reported here, provided it is within 4 arc-minutes of the the accurate position from the VLA Calibrator Manual (1997 version).

2. **MIT 4.8 GHz Catalog Flux Density**: This is the total flux density (mJy) from the MIT single-dish 4.8 GHz catalog. The beamsize was $\sim$ 4 arc-minutes. In the case of a VLA calibrator, the value is taken from the latest VLA Calibrator Manual if the MIT catalog value is not available.

3. **MIT 4.8 GHz Catalog Flux Density Error**: This is the estimated error (mJy) in the total flux density from the MIT single-dish catalog. In the case of a VLA calibrator, a nominal error of 20% is used if the MIT catalog value is not available.

4. **MIT 4.8 GHz Catalog Spectral Index**: This is the estimated integrated radio spectral index ($F_\nu \sim \nu^\alpha$), derived from the MIT catalog single-dish flux density and from the corresponding flux density at a lower frequency. In the case of a VLA calibrator, an estimate is made using the average from the other flux density values as reported in the latest version of the VLA Calibrator Manual. Due to resolution and variability effects, these indices are only meant to be approximate guesses as to the true (solid-angle) integrated value.

5. **MIT-VLA Day**: This is the internal name for the particular VLA observing run in which the initial snapshot observation of the source was made.

6. **VLA OBSERVE Source ID Number**: This is the internal VLA source identification number, as reported by the AIPS LISTR task. The VLA OBSERVE sequential scan number is not used here, as the same source may have been observed multiple times in the same observing session. No source ID number is given for VLA calibrators.

7. **VLA OBSERVE Source Name**: This is the VLA OBSERVE file name adopted for the radio source. In the case of a VLA calibrator, the name is taken from the latest version of the VLA Calibrator Manual.

8. **VLA OBSERVE Position**: This is the VLA pointing position used for the initial snapshot observation. In the case of a VLA Calibrator, the value from the latest VLA Calibrator Manual is reported.

9. **VLA Calibrator Code**: This is a code that gives an idea of the accuracy of the position as reported in the latest VLA Calibrator Manual.

- **A**: Positional accuracy $< 0.002''$
- **B**: Positional accuracy $0.002''$ to $0.010''$
- **C**: Positional accuracy $0.010''$ to $0.150''$
- **T**: Positional accuracy $> 0.150''$

If a positional accuracy of $< 0.1''$ is required, then only the 'A' and 'B' calibrators should be trusted.

10. **VLA Best Position**: This is the best estimate of the VLA radio source position, for the purposes of optical identification. There is no clear algorithm for determining which particular position should be used from the radio total intensity distribution on the sky, as this requires extra knowledge of the detailed correspondence between the regions of radio and optical emission for the individual source. However, typically the fitted position of the brightest peak in the VLA map is used, unless the source has a typical double (DB), core-double (CD) or almost-collinear triple (TR) morphology. In this case, the 'central position' is reported, which is the average of the positions of the two peaks in the case of the double (DB) morphology.

11. **VLA Best Position Epoch/Equinox Code**: A 'B' here means that the VLA positions reported here are in B1950.0 coordinates. A 'J' means the coordinates are J2000.0.

12. **VLA Observing Frequency**: This is the VLA observing Frequency in GHz. In the case of 2 IF frequencies, the mean is reported here.

13. **VLA Total Flux Density**: The integrated total intensity (flux density) in mJy is reported here. This is usually the sum of the VLA component flux densities, but there may be differences arising from resolution effects. In the case of sources that are clearly extended at the VLA, a lower limit on the VLA flux density is given, which is signalled

by the symbol '>'. In the case that a source is not clearly detected, an upper limit is given, signified by a '<'.

14. **VLA Total Flux Density Error**: This is the estimated error in the VLA flux density (mJy), where this was available from the original data reduction.

15. **VLA Component Position**: This is the best estimate of the peak total intensity position of an individual radio component of the source. The positions of all clearly detected individual radio components are reported on separate lines.

16. **VLA Component Peak Intensity**: This is the estimated peak total intensity in mJy beam^{-1}, for the radio component.

17. **VLA Component Flux Density**: This is the estimated integrated total intensity (flux density), in mJy, for the radio component. To obtain this, the smallest possible rectangular box is usually specified in AIPS.

18. **VLA Component Flux Density Error**: This is the estimated error in the integrated total intensity (flux density), in mJy, for the radio component. To obtain this, the smallest possible rectangular box is usually specified in AIPS.

19. **VLA Radio Morphology**: This is the radio morphology reported by either L. Herold or A. Fletcher, according to the latest version of the MIT classification (see the **Proposed Scheme for Extragalactic Radio Source Morphology Classification** below, for the adopted definitions). Note that, in the interests of uniformity, these codes may differ from the ones reported originally; the original ones may have been derived according to an older (1984) version of the MIT classification scheme, or from an entirely different scheme altogether. As always, it is important to realize the somewhat subjective nature of the adopted classification reported here, and also that the

scheme itself is especially prone to resolution and sensitivity (radio surface brightness) effects.

20. **Optical Identification**: This is the original optical identification as reported by C. Lawrence et al. (1986) [95], L. Herold (1996) [69] or A. Fletcher (1997) (this thesis). The categories adopted were:

    - **O**: object, probably unresolved on Schmidt plate (though a faint galaxy identification remains a possibility).
    - **G**: clearly a galaxy.
    - **F**: object is faint, and morphology cannot be clearly discerned.
    - **E**: empty field; object is below the Schmidt plate limit.
    - **U**: unknown optical morphology; identification remains to be done.

    It should be noted that since these identifications were done by eye, there is some room for error. In addition, the resolution in the Schmidt plates is typically $\sim$ 1."7, so an 'unresolved S' identification reported here may turn out to be a galaxy 'G' at higher resolution.

21. **Filter**: The color of the filter used in making the optical magnitude estimate is given, according to the standard UBVRIJHKLM scheme. In the case of the POSS/SERC Schmidt Plates, this will be from the O (blue) or E (red) plate, and the associated errors are at least 0.5 mag. If there are more accurate estimates available from direct CCD imaging, these are reported instead; in this case, the accuracy would be considerably better: $\sim$ 0.1 mag.

22. **Magnitude**: The optical or IR magnitude corresponding to the chosen filter.

23. **Redshift**: The optical or IR redshift, as identified from emission lines in a spectrum of the optical counterpart.

24. **Comments**: Miscellaneous comments are made here. Codes for standard comments are reported for brevity; a list of these codes may be found in the key attached to the MIT-VLA List.

It should be noted that not all the above parameters were recorded for each source. As there were many students working on the MIT-VLA survey over an extended period of 15 years, the recording and interpretation of the maps, mostly of widely variable quality and fidelity, was extremely difficult. It is the author's intention in the near future to construct a final reasonably uniform electronic **Master Archive File** (MAF) of the MIT-VLA sources.

As regards, the detailed recording of positions, fluxes and intensities, there were at least 5 different methods employed in the construction of the final MAF.

Firstly, there were $\sim$ 1000 sources processed in a uniform manner by Lawrence et al. 1986 [95]. The author was able to scan these data in from the 1986 paper, and also modify the information to make it more readable by future computer programs.

Secondly, there are about $\sim$ 3000 sources with (only) hardcopy plots placed in filing cabinets at MIT. These were generated by the first generation of MIT students in the 1980s. Each source has its own manila folder, and Fletcher was able to laboriously log most of the important information for 600 of these MG sources for the purposes of this Ph.D. thesis.

Thirdly, there were the $\sim$ 800 sources from Lehár's XDAY0 and XDAY2 observing runs. The XDAY0 data were first thoroughly analyzed by Lehár for his 1991 Ph.D. thesis [101], and then both XDAY0 and XDAY2 were re-analyzed by him in 1996, using his own software: the MGVXMAP mapping routine and the MGVXLOG source analysis routine. All of these results were made available to the author in the form of electronic files.

Fourthly, most of the rest of the MGVX data (2450 sources) were analyzed in a uniform manner by Herold for her 1996 Ph.D. thesis. The thesis results for the radio sources were made available as an electronic LaTeXfile to the author.

Fifthly, the PMNVX data (1750 sources) were analyzed by the author using Lehár's MNVXLOG AIPS procedure.

Of particular difficulty in the logging of the source radio parameters, is the somewhat subjective assignment of radio morphology to each source. This was first systematized by C. Lawrence et al. in their 1984 paper. This scheme is both sensitivity and resolution dependent, as would be any other scheme that tries to water down the abundance of detailed information in the maps (in some cases in the presence of considerable noise). The Lawrence scheme was discarded by Lehár for his 1991 Ph.D thesis, and replaced by a simpler and more direct scheme. Lehár's routines enforce the assigning of radio source morphologies according to the Lehár scheme.

The following newer version of Lawrence's scheme was first used by Herold for her 1996 Ph.D. thesis; it includes an extra 3 categories that were found to be of practical necessity: the over-resolved (OR), non-detections (ND) and uncataloged (UN) categories. Apart from the addition of these codes, the rest of the scheme remains essentially unchanged from the 1984 Lawrence proposal. This new Herold scheme was also used by Fletcher for his own PMNVX data, as well as in the logging of the old MGVX hardcopy plots. Figure 3-1 shows the variety of assignments proposed by Lawrence et al. 1984 in their paper. A detailed description of the latest Herold/Fletcher scheme follows:-

Proposed Scheme for Extragalactic Radio Source Morphology Classification

- **Point (PT)**: These are unresolved by the VLA synthesized beam. At a redshift of 0.1 in a standard Big-Bang Friedman-Lemaitre-Robertson-Walker (FLRW) homogeneous, isotropic cosmology, with $H_0 = 70$ km s^{-1} Mpc^{-1}, $\Omega_0 = 1$ and $\Lambda_0 = 0$, this corresponds to a projected linear size that must be less than **1 kpc**, while the corresponding limit at z = 1 is **10 kpc**. These sources are the most common type of morphology for EGRS, and they are thought to correspond to the active cores of radio galaxies and quasars. Depending on the map noise level in the surrounding sky, any associated extended

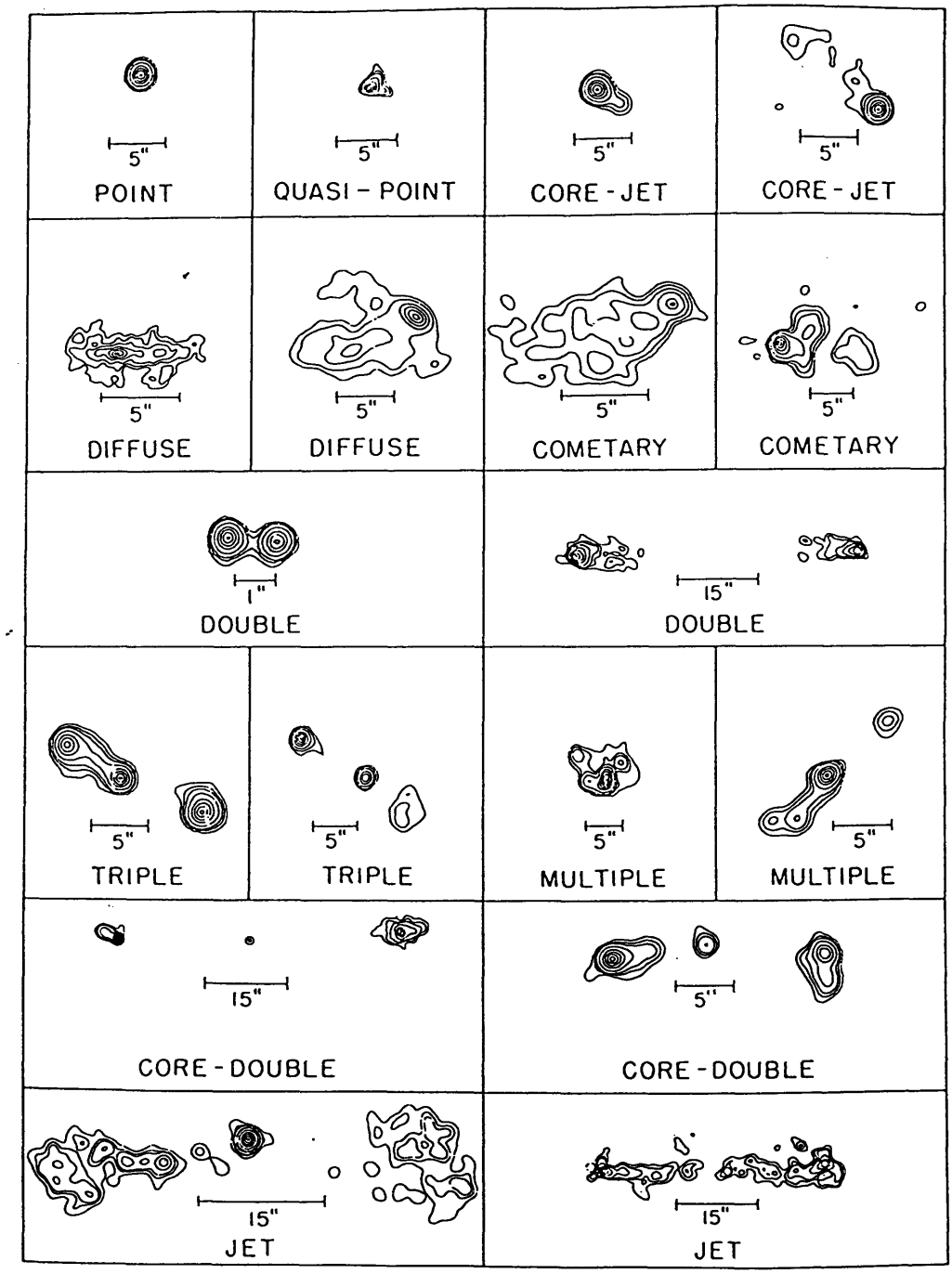

FIG. 2.—Examples of the source structure classification scheme

Figure 3-1: Extragalactic Radio Source Morphology Classification Scheme (reproduced from Lawrence et al. 1984).

flux may have been missed in the map, so the fractional percentage of EGRS in Point sources is an upper limit thereof.

- **Quasi-Point (QP)**: These are primarily point sources, but there is evidence of some extended emission adjacent to the 'point'. This extension is only slight, and is thus not as fully developed as the clear jet-like linear extensions seen in the other categories. At lower resolution, many of these Quasi-Points would be classified as Points.

- **Core-Jet (CJ)**: These consist of a compact peak (the core) and a nearby one-sided jet or lobe of emission (the jet).

- **Core-Double (CD)**: These consist of 3 major components; the two lobes of a typical double source, with a clear detection of a central core source in between. Often, the central core source is coincident with the optical host galaxy. If the three components are not almost collinear, then the Triple category is more appropriate. Typically, the outer two components of a true Core Double are seen as extended lobes of radio emission, though the presence of extended emission may depend on the map dynamic range and the size and brightness of the hotspot peaks in the lobes.

- **Double (DB)**: These consist of just two major components; the two lobes of emission of a typical radio galaxy, with *no* clear detection of a central source in between. In the original scheme proposed by Lawrence et al. (1984) [94], a clear distinction was drawn between the Double category and two others: the Core-Jet and the Cometary. Specifically, if the 6% contour enclosed both components and the dominant peak is compact, the source is categorized as Core-Jet. If both components are enclosed and the dominant peak is resolved, the category is Cometary.

  It should be noted that the Cometary category may in some cases not be indicative of the true overall morphology of the radio source; Cometary sources are likely to

represent just a single lobe of a wide Double source. In this case, the other lobe has, by chance, fallen outside the region mapped at the VLA.

It is also possible that some of the wide Doubles (angular size $>\sim 60''$) may actually be two unrelated radio sources. In this case, the absence of an optical host galaxy in between the radio positions, and the presence of one or more optical galaxies coincident with the radio lobes would be telling evidence against the Double nature of the radio source; a more appropriate morphology would come from the separate classification of the two radio components.

Many of the over-resolved (OR) sources mapped by Herold in the VLA C-Array snapshot program turned out to be Wide Doubles.

- **Triple (TR)**: These consist of three major components that are *not* arranged in a collinear fashion as for the Core Doubles.

- **Multiple (MU)**: These consist of four or more major components. If there are 4 unresolved peaks, the radio source automatically becomes a prime gravitational lens candidate, of the quadruply-imaged type. Two of these confirmed 'quad' lenses have been found in the MIT-VLA Archive to date: MG 0414+0456 and JVAS/MG 1424+2255.

- **Jet (JT)**: These consist of two-sided relatively symmetric emission arranged in a roughly linear (jet) geometry. There may or may not be a central peak, but there would be *no* other evidence of compact emission (as may occur in the Core Double or Double categories).

- **Cometary (CM)**: These consist of a *resolved* peak of emission, with an associated area of extended emission. As noted above for the Double category, this is the appropriate category for sources which have 2 components that are both enclosed by the 6% contour; however, this level of precision in the analysis of the contour levels was only adopted by

Lawrence et al. (1984 [94], 1986 [95]). A less stringent classification was performed by Herold and Fletcher; if the lowest radio contour enclosed both components (whatever the level of the contour), and the peak was resolved, this was sufficient reason for classification as a Cometary source.

S. Conner was the first student to dispute the validity of this category, for the reasons given above. This has some support from the relatively low optical identification rate for Cometary sources: anywhere from 18% (Herold 1996 [69]) to 23% (Lawrence et al. 1984 [94]).

- **Diffuse (DF)**: These consist of resolved, often amorphous emission. There may or may not be a well-defined peak. If there is a peak inside a 'blob' of extended emission, this is often called a 'core-halo' source (though this term is not used in this classification scheme).

  Some of the Diffuse sources may, like the Cometary sources, represent the single lobe of a larger source, whose other components were either too far away, too faint, or otherwise over-resolved, to be detected in the A-array map. The Diffuse sources are best followed up with lower resolution VLA observations; Herold (1996) was able to recover almost all of the MGVX Diffuse sources through snapshot imaging using the VLA C-array.

- **Over-resolved (OR)**: This is a *new category* that was not specified in the original 1984 scheme. It was first systematically used by Herold for her Ph.D. thesis (1996) [69]. These consist of sources which cannot be detected ni the VLA A-array map, but which nevertheless show clear evidence for extended emission on the shortest projected baselines in the visibility amplitude vs. baseline length plot. Almost all of a subset of these sources were recovered by Herold using VLA C-array follow-up observations. Many of these were found by her to be wide-angle double-lobed radio galaxies; such

weak radio emission from an aging population of electrons may be expected from large radio galaxies that have inactive cores and lobes that are no longer energized by jets and internal shocks.

- **Non-detections (ND)**: This is a *new category* that was not specified in the original 1984 scheme. It was first systematically used by Herold for Herold's Ph.D. thesis (1996) [69]. These consist of sources which cannot be found in either the VLA map nor in the visibility amplitude plots.

  These Non-Detections may represent truly large radio galaxies whose structures consist of only extended radio emission regions each with size greater than $\sim 7''$. It is also possible that the original MG or PMN sources are actually spurious, resulting from corrupted data in the single-dish survey scans, or otherwise from an error in the original reduction of these scan data. In her Ph.D. thesis, Herold noted that some of these Non-Detections occured in groups of adjacent sources in the sky, which may be an indication of errors in the parent MIT catalog lists. The recognition of such errors is important for providing upper limits on the reliabilities of the parent MIT radio catalogs, but such an analysis will have to await a more complete and uniform reduction of the entire MIT-VLA Archive data.

  Several of these sources were re-observed by Herold using the VLA C-array, but the author has no further information on the outcome for sources in this category.

- **Unclassified (UN)**: This is a *new category* that was not specified in the original 1984 scheme. It was first systematically used by Herold for her Ph.D. thesis (1996). These consist of sources which were not classified; the reasons for this are varied. Some MIT-VLA days remain unreduced as of December 1997 (e.g. XDAY1 and XSDAY5). Some sources assigned for observations were lost due to bad weather affecting the phase information irrecoverably. Many MGVC sources from the 1980s mapping do not have

an available contour plot stored in the filing cabinets at MIT, and so no information was available for these.

Other sources may contain too little compact emission to survive the multiple attempts at automatic self-calibration by PRELIM or MAINMAP, and so no final maps were made for these sources; though, in principle, given more time, these sources could be remapped by hand (a laborious task). Since this is only meant to be a preliminary list, and as the main objective here is to place the entirety of work completed to date into a uniform format electronic file, these sources will be left for work to be done in the future.

In view of the complicated nature of the above proposed classification scheme, the author adopted a relatively straightforward algorithm for manoeuvering through the multiple definitions, as follows:

Firstly, if there is no plot or map available for classification, the source is left UNCLASSIFIED (UN). If there is no clear detection of emission either in the visibility plot, or in the map, the source is a NON-DETECTION (ND). If the source is not visible in the map, but there is clear emission over the shortest VLA baselines, then it is OVER-RESOLVED (OR). At this point, all remaining sources must have a clear detection in the VLA map.

Next, the number N of clearly detected map peaks is counted. Firstly, we consider the case that $N \leq 1$. If there is 2-sided relatively symmetrical linear emission, with or without a central peak, the source is a Jet (JT). However, if the source is amorphous, with or without a clear peak, it is diffuse (DF).

If it is clear that N=1, and the peak is unresolved with no clear extension, the source is a POINT (PT). If instead there is a slight extension, but not to the extent of being a single jet or lobe, the source is a QUASI-POINT (QP). If the extension is a single jet or nearby lobe, the source is a CORE-JET (CJ).

If the source peak is resolved, with associated extended emission, the source is Cometary (CM).

In the case of N=2 clear peaks, where these are together enclosed by the lowest positive radio contours, and they are *not* comparable in flux density, then the source is either a CORE-JET (CJ) if the peak is also unresolved, or else COMETARY (CM) if it is not. If the two peaks are clearly separated, then the source is a DOUBLE (DB).

In the case N=3, if the arrangement is approximately collinear, then the source is a CORE-DOUBLE (CD), otherwise it is a TRIPLE (TR).

In the case $N \geq 4$, the source is a MULTIPLE (MU).

By this point, all types of radio source should have been classified in one of the above categories of the New Proposed Scheme (1997).

The MAF will be made available by anonymous ftp, or otherwise through Professor Bernard Burke at MIT; a blank DAT tape would be required to hold the data in the electronic files.

3.4 Optical Identifications of MIT-VLA Radio Sources

The first step, after the extraction of the radio source parameters from the final maps, would be to ascertain the presence or otherwise of an optical counterpart to the radio source. In the 1980s and early 1990s, this was best done by direct inspection of the Northern POSS and Southern ESO/SERC Schmidt plates or the photographic print copies thereof. Lawrence et al. were able to do this for $\sim$ 1000 sources from the MGVC survey (see the 1984 and 1986 papers). Lehár did this for $\sim$ 350 sources from XDAY0, using the Minnesota Plate Measuring Machine (see Lehár's 1991 Ph.D. thesis [101]). The same type of procedure was a very laborious process to undertake at MIT, where a makeshift measuring engine with a microscope had to be used to calculate accurate offsets from known bright stars. Due to the crudity of this apparatus at MIT, this was only done for a handful of individual sources of

interest, mostly gravitational lens candidates.

Starting in 1993, this work could be much more efficiently and accurately done using the Digitized Sky Survey (DSS) series of CDROMs. [1] This rather expensive collection of disks was made available on loan from the MIT Center for Space research library. These are a set of compact discs that store hundreds of megabytes of optical sky survey data in digitized form. Through the use of a supplied program *'getimage'*, one could simply specify the coordinate, epoch and equinox (either B1950.0 or J2000.0), and the *getimage* program would return the optical field centered on the specified point, as a standard FITS file. This made optical counterpart identification trivial. There is no easy way, nor any software provided, to obtain accurate estimates of the optical magnitudes of the counterparts, though this information can be gotten through Internet access to various electronic databases, e.g. the Automated Plate Machine (APM), COSMOS and SUPERCOSMOS catalogs. The catalog magnitudes are obtained by fitting source profiles to the digitized optical sky survey data.

The size of the extracted DSS finder chart field can be specified by the user, and it is convenient to choose one that is 10 arc-minutes on a side, for the purposes of easy identification of bright Hubble Space Telescope Guide Star Catalog (HST GSC) stars. These are used for astrometry in the optical data reduction, and they are also very useful at the telescope for the verification of the telescope pointing and field orientation.

In her Ph.D. thesis (1996) [69], Herold attempted optical identifications for all of her MGVX sources with available VLA radio coordinates (XDAYS 3 through 8; $\sim$ 2500 sources). She extracted 3 arc-minute-square fields around *each* of the VLA radio component peak positions; this cautious procedure is necessary if the fewest assumptions are to be made

[1] The image data on these compact discs are based on photographic data obtained using the Oschin Schmidt Telescope on Palomar Mountain. The Palomar Observatory Sky Survey (POSS) was funded by teh National Geographic Society. The Oschin Schmidt Telescope is operated by the California Institute of Technology and palomar Observatory. The plates were processed into the present compressed digital form with their permission. The *Digitized Sky Survey* was produced at the Space Telescope Science Institute (STScI) under U.S. Government grant NAG W-2166.

regarding the correlations between radio and optical emissions. The resulting DSS FITS files were loaded into AIPS, and finder plots were produced as Postscript files using the AIPS tasks GREYS/CNTR and LWPLA. These Postscript files were visually inspected by her for optical counterparts that had a good positional coincidence with the VLA component peak position. A 'good' coincidence was taken to mean that an optical object was found within one DSS pixel ($\sim$ 1.″7) of the VLA radio peak position. According to the thorough analysis of Lawrence et al. (1984 Ph.D. thesis [97], 1984 [94], 1986 [95]), this offset represents a formal 3σ random error in radio-optical positional correspondence. This may be an underestimate of the true error in the radio and optical coordinates, which should correctly include a contribution from the unknown systematic error made in going between the adopted radio and optical coordinate reference frames. It is believed that the radio-optical offset can be as large as 1.″5 near the plate edges, due to the inevitable physical distortions of the Schmidt plate from the forces that kept it mounted in its holder (Paul Schechter, MIT; private communication). If one chooses to adopt a proxy random statistical error in place of this unmeasured systematic offset between the VLA and Schmidt plate reference frames, a suitable 1 σ value would be $\sim$ 0.″5.

The 1.″7 coincidence radius criterion was relaxed by Herold in cases where the optical object is placed in a 'likely' position *between* the VLA radio counterparts, e.g. in the case of a Double source, where a likely optical identification was accepted if it simply lay near or on the line joining the two peaks in the radio lobes.

The author made systematic identifications only for select subsamples of (1) 70 new MG+PMN gravitational lens candidates, (2) 120 MGVX+PMNVX close doubles, and (3) 60 MGVX and PMNVX randomly selected sources. The results of these identification attempts are presented in the next Chapter.

Further details of the MIT-VLA identification attempts may be found in the published papers on MIT gravitational lenses, the papers by Lawrence et al., and in the Ph.D. theses

of Lawrence, Lehár, and Herold.

3.5 Optical Data Reduction

In the period 1994 through 1996, both optical imaging and spectroscopy were performed on the optical counterparts of MGVX and PMNVX gravitational lens candidates and close radio doubles. The data reduction procedures for imaging and spectroscopy are described separately in the following sections.

3.5.1 Optical Imaging

For the new post-1992 optical data on MGVX and PMNVX counterparts, the reduction of the optical images was done mainly by L. Herold (1996) and A. Cooray (1997) [39]; for full details, see their respective theses. The only student to have reduced any optical data for the 1994-1996 period is Cooray, who reduced 2 weeks of MDM 1.3m data (September 1994 observing run). The reduction of the optical spectra were done by P. Garnavich (Cfa) and C. Becker (MIT). The author's role was to plan and execute the optical imaging observations using the MDM 1.3m and CTIO 1.5m telescopes, and also the optical spectroscopic observations using the MDM 2.4m. The author also supervised the optical data reduction of the MDM 1.3m September data by A. Cooray for his 1997 BS thesis. A summary of the optical data reduction techniques employed by these other students is provided here for completeness.

The standard optical data reduction chain was employed, using publicly available packages, mainly IRAF and Vista, with a few small custom-built FORTRAN routines supplied to us by Eric Gaidos (MIT). The general procedure was straightforward:

1. **Bias Correction**: The CCD images were corrected for pixel bias, which is an additive base level that exists even when no light falls on the pixel. The unilluminated part of the CCD was used to define this 'pedestal' level. This is the *overscan* region, which

for the Wilbur Loral 2048^2 CCD, binned at 2×2 pixels, consists of the columns 1024 to 1035 on the righthand side of the CCD. The IRAF task **CCDPROC** was used to perform the bias correction.

At the CTIO, the CCD consisted of 4 separate areas, each with its own amplifier; for these data, the local task **QUADPROC** was used. This task is essentially the same as CCDPROC, but with appropriate modifications for the use of separate data frames for each of the 4 amplifiers. The task QUADPROC was used to pre-process all of the CTIO 1.5m data during the observing run.

2. **Overscan Trimming**: As part of the standard pre-processing done by **CCDPROC**, the overscan region is removed at the same time that each frame is debiased.

3. **Outlier Removal**: Also part of the standard pre-processing done by **CCDPROC** is the removal of individual pixels which deviate more than a given number of rms noise deviations from immediate neighbors. These pixels are almost all due to cosmic rays. The resulting gaps are then interpolated over using standard functions within the task CCDPROC.

4. **Flat Field Construction**: Two types of flats were generally used at MDM and CTIO; *twilight flats* taken either at late dusk or early dawn, and *sky flats* constructed from the average of multiple target frame images that do not share the same telescope pointings. Dome flats were occasionally taken at MDM, and for each of the CTIO nights; these were found in practice to be not very useful compared to the other two types of flats. In general, the twilight flats provide 'smooth' flat fields, i.e. their pixel-to-pixel response is very good. The averaged sky flats, on the other hand, provide an excellent measure of the large-scale illumination response, provided a sufficient number of suitable component CCD frames are used.

   Separate flats are constructed for each of the filters used in a particular observing

run. The IRAF task **IMCOMBINE** was used to combine multiple CCD images to make the each of the twilight and sky flat field frames. In the construction of the averaged flat field frames, it is important to avoid the introduction of 'bad' frames, e.g. those which have common telescope pointings to within $\sim 20''$, those are affected by contaminating illumination from the Moon, and those with stars or galaxies bright enough to have caused saturation of some pixels. For the September 1994 MDM 1.3m observing run, Cooray found that flat fields had to be constructed using CCD frames from multiple nights, rather than a single night; this was because of the heavy lunar illumination during the 'bright time' of this run.

It was found that an excellent flat field frame could be constructed from the combination of information from each of the two types of flat field; using the task **CCDPROC**, the averaged sky flat is divided by the averaged twilight flat for each of the filters. This gives an *illumination correction* frame for each filter. This frame is then applied by the IRAF task **MKSKYFLAT** to the original smooth twilight flat field for that filter. This yields a final flat field that is 'smooth', and which also has the correct large-scale illumination response garnered from the statistics of multiple target field CCD frames accumulated over the night.

5. **Flat Field Correction** The final (illumination-corrected) flat field of the appropriate filter is divided into each bias-corrected object CCD frame, using **CCDPROC**. At this point of the data reduction, the resulting image will have been corrected for both the additive and multiplicative instrumental responses.

6. **Image Registration**: The next step is to increase the signal-to-noise ratio (SNR) for those target sources for which multiple observations are available in the same filter. This is done by first registering the separate pre-processed target frames onto a common image coordinate reference frame, and then averaging the frames together.

The IRAF task **DAOFIND** was used to automatically locate $\sim$ 50 to 100 stars in each of the images to be combined, according to a user specified threshold level (that is chosen by trial and error). A set of FORTRAN77 routines, provided by E. Gaidos (MIT), was then used to estimate the accurate offset vectors required to shift each of the *'slave'* images to a common image reference frame, defined by a user specified *'master'* image. The FORTRAN77 program that calculates these shifts is called **shifter**. Then, using the output from shifter, the IRAF tasks **GEOMAP** and **GEOTRAN** are used to actually perform the required shifts on the slave CCD images (now within IRAF).

7. **Image Combination**: After checking on the results of the previous image registration step, using the IRAF TV display to inspect the master and slave images, the IRAF task **IMCOMBINE** was then used to average these registered images together. The appropriate scaling according to the integration time was used by IMCOMBINE, and the option to reject cosmic rays is still retained here.

8. **Astrometry**: The astrometry was performed using the *Vista* package. To set the absolute optical coordinate reference frame, the known positions of the Hubble Space Telescope Guide Star Catalog (HST GSC) stars were used. These are publicly available over the Internet through the Astrophysical Data System (ADS) site. The routine *'markstar'* within Vista was used to specify the absolute J2000.0 coordinates of typically 5 to 10 bright stars in the 10 arc-minute square field of the CCD frame. The astrometric plate solution was calculated automatically by markstar, and absolute coordinates on the HST GSC optical reference frame could thereafter be obtained for any desired pixel on the CCD image.

9. **Estimation of Astrometric Errors**: The estimated accuracy of the astrometry is documented in Cooray's 1997 BS thesis. These errors are dominated by the unknown systematic errors between the VLA radio coordinate reference frame and the optical

reference frame as defined by the HST Guide Star Catalog, which can be as high as $\sim$ 1.5″ on the rare occasion that a GSC star falls near the edge of the Schmidt plate; the *unmeasured* systematic error can be conservatively taken to have a 1σ rms variation of $\sim$ 0.6″. On the other hand, the random internal errors from the Vista markstar astrometric plate solutions are typically in the range from 0.1″ to 0.3″. Thus, the total astrometric (random + systematic) error is conservatively estimated to be 0.7″ at the 1σ rms level. It should be noted that there was no attempt to correct for the systematic offsets between the radio and optical reference frames, which is the major reason why a conservative estimate of the astrometric error is assumed here. A more thorough astrometric analysis would require a detailed investigation into the correspondence between accurately known positions for sources that emit both in the radio and optical wavelengths, e.g. radio-loud quasars. However, this task is quite time-consuming, so we rely on the more readily available second-hand information from discussion with knowledgeable optical astronomers; the 1.5″ worst-case Schmidt plate distortion error quoted above came from discussions with Paul Schechter (MIT), who was able to ascertain this number through comparing independently derived optical positions from the APM and GSC catalogs.

There is also the random error in the VLA radio coordinates; from the NRAO VLA Observational Status Summary Report (R. Perley 1995), this is typically in the range 0.1″ to 0.2″, relative the coordinate reference frame defined by the VLA calibrators. Typically, these all have highly accurate positions, and this is increasingly true the greater the percentage of calcode 'A' and 'B' calibrators that appear in a given VLA observing run. For the 1990s VLA MGVX and PMNVX observing sessions, there was a conscious decision to use primarily these more accurately positioned VLA calibrators. For the 1980s MGVC sessions, there were fewer accurate positions available for VLA calibrators. Thus, a conservative estimate of the rms error in the VLA positions is

0.2″.

Adding the: total optical random error, radio random error, and the estimated radio-optical rms offset error, we obtain a conservative estimate of the total radio-optical 1σ rms error of 0.7″.

A more complete discussion of the astrometric errors may be found in both Lawrence et al. 1986 [95], and Cooray 1997 [39].

10. **Extinction Correction**: The *instrumental* magnitude is defined from the ratio of the number of counts N_{object} over a given selection of CCD pixels, divided by the integration time t. Assuming that the CCD response is *linear*, this gives an effective photon flux incident on the chosen set of pixels. One usually corrects for the number of counts N_{sky} simply due to the sky surface brightness:

$$N_{object} = N_{total} - N_{sky} \tag{3.3}$$

Once this is done, the instrumental magnitude can be calculated:

$$m_{instrum} = -2.5 \log_{10}(\frac{N_{counts}}{t}). \tag{3.4}$$

The correction of the instrumental magnitude, for the transmission through the Earth's atmosphere, was made using observations of Landolt stars, which are distributed near the celestial equator. These have known, constant optical fluxes in each of the standard UBVRI filters. Following standard analysis, we assume that the instrumental magnitude and the actual apparent magnitude, of each Landolt star, has the following relation:-

$$m_{apparent} = m_{instrum} - m_{zero} - \alpha sec(z) - \beta_{color} \tag{3.5}$$

Here, the zero-point correction m_{zero} translates from the instrumental magnitude scale to the photometric scale defined by the observed Landolt stars. It is the instrumental magnitude of an object with an apparent magnitude of precisely 0, at the top of the Earth's atmosphere. The extinction coefficient α depends on the atmospheric transparency during the night of observation. It is assumed that this is constant throughout the night, though of course this may not be a good assumption. Due to the sparsity of good Landolt field data for most of the 'bright time' September 1994 run, Cooray was forced to adopt a single fit to the extinction law for the entire 2 week observing period. This was justified by spot checks on the constancy of the extinction law coefficient α from night to night. Since the aim of the observations did not include photometric accuracy better than 0.1 mag, this procedure seems to be justfied. The variable z is the zenith angle, which is the angle to the source as measured along a great circle passing through the zenith point. The secant function gives the standard 1st-order variation of air mass as a function of the zenith angle; the air mass is unity when looking up at the zenith, and increases thereon to effectively infinite air mass when looking at the horizon (obviously there are higher order terms that come into play at large zenith angles, but these can be ignored in any useful integration. During observing sessions, we always tried to stay at as low an air mass as possible. Rarely did we exceed 3 air masses). The implicit assumption in the above equation is that the optical scattering and absorption effects increase linearly as the air mass. Lastly, there is the color term, which monitors fine-scale differences between the standard Kron-Cousins photometric system, as employed by Landolt in the observations of his standard stars, and the local photometric system defined by the combination of the local atmospheric conditions, the local telescope filters used, and the details of the photometric data reduction procedures. As mentioned in the next step, we had no good reason to attempt to track the color term in our observations of close doubles

and gravitational lenses, and so we set this to zero identically in our photometric reduction.

11. **Color Correction**: For the September 1994 MDM 1.3m run, the MDM R and I interference filters used were specially constructed by KPNO to be in close agreement with the standard Kron-Cousins filter bandpasses. However, the filter responses are convolved with the CCD response, and so there is a need for an extra color correction if one desires magnitudes measured according to an exactly defined photometric system. Since the optical magnitudes were only desired to be known to within ~ 0.1 mag accuracy, there was no effort made to correct for the relatively small color term. This corrects for the precise bandpass shape of the combination of the telescope filter and CCD response, and brings the resulting magnitude into a standard photometric magnitude system. This correction is normally necessary because the telescope filter is inevitably different from the Kron-Cousins filters used by Landolt for his standard star aperture photometry.

    Another reason for bypassing the color correction, apart from the lack of a good scientific reason to make such an effort, was that this fine tuning of the optical photometry would require photometric observations of most of our sources; as most of the data were taken in non-photometric conditions, the color correction terms could not even be confidently ascertained.

12. **Photometry**: The photometry for the MDM 1.3m September 1994 data was performed by Cooray for his 1997 BS thesis, using standard IRAF routines. Two methods were tried: *aperture* photometry and *point spread function fitting* photometry. The September 1994 PMNVX counterparts that were observed underwent just aperture photometry, while the MGVX counterparts, from the same observing run, underwent both types of photometry. In this way, the merits, failings, and discrepancies between the two methods could be gauged. In general, it is expected that aperture photometry

will be necessary for sources with non-standard profiles (either non-stellar or non-ellipsoidal), and also for images in which the sky noise is not too high. Point spread fitting will perform better for sources of standard morphology that reside in noisy sky.

For the standard (Landolt) star photometry, aperture photometry was used to estimate the variation of the extinction coefficient from night to night over the September 1994 observing period. Cooray reports in his thesis that there were no significant variations in the extinction from night to night, to within the estimated accuracy of the final photometry; on the basis of his finding, a better estimate of the extinction coefficient was obtained by calibration using all of the good Landolt star photometry for the entire run. The extinction calibration curves and final coefficients appear in Cooray's BS thesis.

It should be noted that the December 1993 and February 1994 MDM 1.3m data for Herold's MGVX counterparts was plagued by severe saturation problems in the Landolt standard stars; this makes any photometric calibration of these data extremely difficult. Fortunately, most of the target sources in these early runs were purposely re-observed in subsequent runs, and so the photometry can be recovered from these later frames. It should still be possible to combine frames between these separate runs, for the purposes of increasing the SNR for the detection of faint counterparts.

The **DAOFIND** package in IRAF was used for automatic detection of optical sources in the target frames. A SNR criterion was supplied to DAOFIND; any collection of adjacent pixels with peak count greater than 5σ, but still remaining unsaturated, was regarded as a useful detection of a bona fide optical source. Once this list of objects is established for a frame, the IRAF task **PHOT** in the **DAOPHOT** package was used to extract an instrumental magnitude. Typically, a 10-pixel radius aperture photometry measurement was employed. The aperture radius was decreased to a 5 pixel radius for the case of dense optical fields, e.g. MG counterparts close to the Ecliptic plane.

More details of the optical photometry may be found in Cooray's 1997 BS thesis.

13. **Estimation of Photometric Errors**: The estimated accuracy of the observed fluxes is $\sim$ 0.1 mag, on a typical image of good quality. This may worsen to a few tenths of a magnitude on an image of poor quality. The CCD determined magnitudes are nevertheless all much more accurate and precise than the ones estimated by Lawrence et al. 1986, where the accuracy was estimated to be 0.5 mag at best.

    More details of the optical photometric errors may be found in Cooray's 1997 BS thesis.

3.5.2 Optical Spectroscopy

We now turn the reduction of the optical spectroscopic data. The 1980s efforts are not known, except for those published spectra of gravitational lenses and candidates that appear in the literature, and also in the MIT Ph.D. theses of Lawrence, Hewitt, Langston, Lehár, and Herold. Here, I summarize the data reduction of the more recent 1990s spectrocopy of a handful of (relatively bright) optical counterparts of MGVX and PMNVX close radio doubles and gravitational lens candidates.

The standard procedures within IRAF were used by Christopher Becker to reduce the MDM 2.4m data. Standard lamps were used to calibrate wavelength, and the standard spectra of a few stars were used to calibrate the flux.

Further details, and examples of the few Close Double spectra that were obtained by P. Garnavich, using the MMT, appear in Herold's 1996 thesis.

The same was done by Peter Garnavich in reducing the spectrum of the Radio Ring Source MG0248+0641. Details appear in the paper by Conner et al. (1998) reproduced in Appendix C.

3.6 Summary

15 years of VLA snapshot imaging of MG and PMN radio sources are summarized. Almost 10,000 targets were imaged at the VLA. About 8000 of these have had maps made by various MIT students in the course of their Ph.D. thesis research.

The mapping algorithms have gone through 3 stages of improvement, from the extremely crude single CLEAN deconvolution in the 1980s, to the full-blown Conner semi-automated mapping using CLEAN boxes set by hand, in the 1990s.

The best and worst maps are of very different quality, and it would take at least a few person-years to bring all of the data up to a uniform level.

There are about 4000 CCD images of the counterparts of various types of radio sources: high luminosity QSOs, close radio doubles and gravitational lens candidates.

The confirmed gravitational lenses are all published.

Only a few of CCD images of the gravitational lens candidates have been reduced. It is estimated that all of the PMN and MG candidates published in IAU 173 have faint optical magnitudes in the range $19 < R < 23$.

About 50 Close Radio Doubles have been reduced by Cooray, with results and interpretation appearing in both his thesis and Herold's.

A lot of effort has gone into the follow-up of MG 0248+0641, an apparent Einstein Ring. Details of observations and reduction can be found in the next Chapter, and in the paper in Appendix C.

Chapter 4

Results

The results of the entire set of observations resulting from the MIT surveys of extragalactic radio sources can be organized into four categories:

- **Global Results** arising from the entire sample of $\sim 10^5$ MIT sources, and also from 10^4 MIT-VLA sources.
- **Large Sample Results** arising from $\sim 10^2$ MIT-VLA sources.
- **Small Sample Results** arising from $\sim 10^1$ MIT-VLA sources.
- **Individual Source Results** arising from single MIT-VLA sources.

Section 4.1 is a cumulative summary of the scientific results obtained to date by MIT students, working on the both the single-dish and VLA interferometer surveys. It is included here as a concise and solid base of work upon which to form a good idea of the statistical properties of EGRS at radio continuum frequency 5 GHz.

The particular contribution of the author, which was the extraction of the largest angular size (LAS) distribution for a large sample of 4741 MIT-VLA sources, appears in the 1997 Canary Islands conference paper in Appendix C. The reference for this paper is:

A.B. Fletcher, B. Burke, S. Conner, J. Lehar, & L. Herold, 1997, *"The Angular Size Distribution of 4741 Radio Sources from the MIT-VLA Snapshot Archive"*, in conference on "Observational Cosmology with the New Radio Surveys", eds. M.N. Bremer, N. Jackson, & I. Perez-Fournon, Instituto de Astrofisica de Canarias, Puerto de la Cruz, Tenerife, Canary Islands, Spain, 11-13 Jan 1997, in press.

The author also had varying degrees of involvement in the projects decribed in following Sections: 4.2, 4.3, 4.4 and 4.5.

Radio and optical results for the new sample of MIT-VLA close double-lobed radio galaxies (here: close double, or CD for short) are discussed in Section 4.2.

Radio and optical results for the new crop of MIT-VLA gravitational lenses (that the author is currently aware of) are discussed in Section 4.3.

Results from multi-frequency observations of the unusual radio galaxy MG 0248+0641 are discussed in Section 4.4.

Results from radio and optical observations of the binary optical QSO MGC 2214+3551 are discussed in Section 4.5.

The distribution of MIT-VLA largest angular sizes (maximum separation between emitting radio components) is presented in Section 4.6.

This chapter is concluded with a summary of what was found.

4.1 Cumulative Results

The following is a summary of the observational and scientific results established from the MIT Survey work so far. The relevant literature and dissertation citations are included, and these serve as entry points into the available literature on the MIT results.

Global Results

Isotropy: Each of the 4 Northern MG and 4 Southern PMN source catalogs are consistent with a remakably **uniform** sky distribution of EGRS (see each of the MIT survey papers written from 1986 to 1996, by Bennett, Langston and Griffith). There is a total of about 71,000 EGRS over 86% of the sky, in the MIT catalogs; each of these has been estimated to be greater than 90% complete. Hence the observed isotropy is a robust statistical result, and it is also consistent with reasonably complete radio continuum surveys at other frequencies and epochs. The Galactic plane must be deselected in this analysis; a suitable cut in practice is to ignore the 20 degree wide Galactic strip centered on the Galactic Plane.

Source Counts: The only published differential source counts dN/dS are from the work of Lawrence (1983) [97], and from Bennett et al. (1985) [11]. It was found that the 5 GHz EGRS surface density seen in the MG I Catalog (Bennett et al. 1986 [12]), and at the VLA (Bennett et al. 1983 [13]), was consistent with the the trend seen in independent radio surveys. This trend is signalled by a marked decrease or **convergence** in the surface density on going to lower flux densities, by a factor of $\sim 10^2$ below the expectation from a non-evolving population embedded in a static Euclidean universe. This 100-fold decrease is suffered in traversing 3 decades of flux density down from the source count peak at $\sim$ 500 mJy.

Clustering: Isotropy refers to possible 'clustering' on 180 degree scales. In contrast, any expected source clustering due to gravitational interactions between distant EGRS would be expected to have been seen on much smaller scales; an R = 100 Mpc cluster at an intermediate distance of D = 1 Gpc would subtend $\sim$ 6 degrees. Angular correlation function searches for such clustering have been made on the MG I catalog (Bennett et al. 1986 [12]), the MG II

catalog (Langston 1987 Ph.D. thesis [90], 1990 MG II paper [91]), and in the PMN Southern and Equatorial catalogs (Griffith 1993 [61]). In all cases, there have only been *marginal* detections of possible weak clustering, at a level of typically 2 to 3 times the expected Poisson number count error. Thus, there is no conclusive evidence for angular clustering of EGRS at these sensitivity levels ~ 30 mJy at 4.8 GHz continuum frequency.

Radio Spectral Indices: Each publication of an MIT survey paper has been accompanied by a cross correlation in frequency with other large-area surveys, such as the low frequency 365 MHz Texas and 408 MHz Molonglo surveys, the Southern hemisphere sky Parkes 2.7 and 8.4 GHz surveys, and the Northern Hemisphere sky NRAO 1.4 GHz maps (available on CD-ROM). With a positionally coincident source found in both surveys, as estimate of the power-law spectral index may be made. The spectral index histograms appear in the published survey papers, and in the theses of Lawrence (1984), Langston (1988) and Griffith (1993). For the MIT sources detected at 4.8 GHz, all of the spectral index distributions are **bimodal**, consisting of a minority of 30% of all sources with spectral indices flatter than 0.5 ($F_\nu \sim \nu^{-\alpha}$), and the majority residing in a broader steep-spectrum distribution centered on a spectral index of ~ 0.75.

Cosmic Dipole Search: A search for a *cosmic dipole* distribution was made by Fronefield Crawford; this effect would possibly arise due to small Doppler and special relativistic aberration effects resulting from our motion with respect to the global rest frame of the distant EGRS. Presumably this frame is coincident with the rest frame of the CMB recombining hydrogen atoms, for which the COBE satellite did indeed confirm a Doppler motion of about ~ 600 km/s from the subtraction of a cosine perturbation in the sky intensity. However, there is no evidence yet that the two frames should coincide, though a clear detection of a relative motion between the CMBR and the EGRS would indeed be a surprising (and hence

important) result.

A preliminary analysis pointing out the inability to extract useful information on a possible cosmic dipole has been reported in a joint Canary Islands conference paper (Crawford et al. 1996), which appears in Appendix C. Due to unknown systematic effects on the setting of the flux density scale, which are different in different surveys and can vary with the time of observation, it is not possible to obtain better than 7% agreement, in the fluxes of coincident sources, between two independent but overlapping sky surveys that used the same 4.8 GHz receiver: the Northern NRAO GB87 survey and the Southern PMN Equatorial Survey. This difference only starts to set in below about 70 mJy, so there is indeed good agreement above this level. This would suggest that the discrepancy arises from the different ways in which the same raw data were reduced; there can be a biasing in the relative flux levels for faint sources depending on how one treats the contribution from noise in the data, and from the noise which may be introduced by the source and flux extraction algorithms. This suggested viewpoint has been relayed to the author by Jim Condon, the principal investigator of the NRAO sky surveys, and it has been recorded here for those who would care to investigate this calibration problem further.

Notwithstanding these disappointments, Crawford did indeed find a curious (but unsupportable) result: from running Monte-Carlo simulations that compared the PMN and GB87 surface density counts with those expected from a motion of the Earth with respect to the EGRS population, he consistently found a best fit velocity much *larger* than the one measured from the CMBR by COBE. This velocity is $\sim 10^4$ km/s, which amounts to about 3% of light speed. If this is assumed to be a real result, it would be an important discovery. The direction of the best fit velocity vector is (11.7 hr, -63 deg), which is within a few degrees of the 'Great Attractor' (GA) region. It may be possible that the suspected mass concentration in the GA is 'pulling' us relative to the distant EGRS frame. However, the mystery arises that it apparently is *not* causing a similar Doppler pull on us relative the CMBR. This would

indicate the possible existence of a unexpectedly fast large-scale flow, on *cosmological* scales, between the EGRS frame and the CMBR. Such a detection would go far beyond the volume sample in the controversial claimed detection of a 689 km/s large-scale bulk flow of the Abell cluster reference frame with respect to the CMBR (e.g. Lauer & Postman 1994 [93]).

If these large velocity flows relative to the CMBR are indeed real, then one possible explanation would be that mass perturbations on scales of 100 to 3000 Mpc (the horizon scale) are *not* consistent with a homogeneous and isotopic distribution of matter. This would be a fundamental breakdown in the assumption of the Cosmological Principle. The cause of such large matter fluctuations might be understood as the inflation of much smaller (sub-horizon) sized perturbations generated by natural means prior to the inflationary epoch.

However, at this point, this is pure speculation, as it is already known that the statistical robustness of the raw MIT survey data fails for fluxes fainter than about 70 mJy. As long as flux calibration to better than 1% cannot be routinely achieved by large scale radio surveys, it will *not* be possible to detect any cosmic bulk flow of $\sim$ 10,000 km/s of the EGRS with respect to the CMBR. At this point, it is not possible to support the claim that the vector is real, due to the known 7% mismatch in the flux densities between the NRAO and MIT surveys, at low flux level.

Large Sample Results

Radio Morphology: The morphologies of the large sample of MIT-VLA EGRS have been extensively classified, analyzed and cataloged by Lawrence et al. (1984), Lehár (1991 Ph.D. thesis), Herold-Jacobson (1996 Ph.D. thesis), and also by the author in course of this dissertation. A standard classification scheme was initially proposed by Lawrence, with a few additional categories attached by Herold-Jacobson for her thesis research. The resulting

scheme has been documented by the author in Chapter 3. The resulting fractional percentages in each category are fairly stable from each section of the MIT-VLA survey to the next, showing that the original source selection criteria are basically the same. This is not surprising, as the only criterion for selection that is related to the source parameters is the flux density, and the range of flux densities over the entire MIT-VLA survey is within just a factor of 10.

The resulting structures are fairly standard in comparison with those discussed in the classic review by Miley (1980) [105]. An EGRS in an active phase of its life will be expected to look like one of the following: a compact 'point' core source; a core with an emerging linear structure; a core with two emerging linear structures; diffuse emission surrounding terminal hot spots placed at the ends of the linear structures; in some cases, the symmetric distortion of the initially linear structures can be seen to come in two types – inversion symmetric and mirror symmetric.

There is one category that is probably not physically meaningful in itself; the cometary class may sometimes arise from our truncated view of a classical double lobe source that happens to extend beyon the image boundaries. In this case, the source should really be a 'double'; but it may also be possible that some sources do indeed have an intrinsic cometary structure, so this category is probably best retained, in the interest of not making any unwarranted assumptions.

It should be noted that the classification of an individual source depends on frequency and resolution. Large diffuse radio emitting lobes, bridges and cocoons will tend *not* to appear in these high resolution VLA maps, as the Fourier response to intensity angular scale fluctuations larger than about 6 arc-seconds (for A-array X-band) is much reduced from the response for more compact sources. A source in this state would be classified as 'over-resolved' in the current scheme. By contrast, high surface brightness features such as hotspots, active jets, and cores, will be detected with ease. Herold-Jacobson describes in

her thesis (1996) how she was able to recover almost all of her 'over-resolved' sources with a much lower resolution snapshot program using the VLA in the smaller C-array configuration.

By far the most populated category is that of an unresolved 'point', at $\sim$ 30%. The 'doubles' follow at $\sim$ 20%. Most of the points are flat spectrum, and most of the doubles are steep-spectrum; the correlation between steep spectral indices and extended structure is very well established in other surveys. The least populated category is the 'multiple', at $\sim$ 1%, and it is in this one where the standard quadruply-imaged gravitational lenses ('quads') might be found.

Optical Morphology:

This was studied in detail by Lawrence et al. (1983 Ph.D. thesis [97], 1984 [94], 1986 [12]), Lehár (1991 Ph.D. thesis [101]) and Herold (1996 Ph.D. thesis [69]). The overall success rate at finding an optical identification on the POSS plates is $\sim$ 40%, but this is most likely a complicated function of the radio flux density and spectral index, in addition to any variations in the local optical magnitude limit on the plate, which has a nominal detection limit of about 20 to 21 magnitudes, depending on whether the blue or red plate is used.

The positional coincidence between the optical counterpart and the radio emission is generally as good as 0.5 arc-seconds rms (see Lawrence et al. 1986 [95]), at least in those cases where a clear choice for the optical core position can be found by inspecting the radio snapshot.

There is a distinct trend for sources of *weaker* radio flux density and *steeper* spectral index to be harder to detect optically (i.e. these sources have relatively lower identification rates). An example of this trend for the close doubles appears in Cooray's thesis (1997 [39]).

Close Doubles: An account of the results on the MIT-VLA Close Doubles is presented in

Section 4.2.

Angular Size Distribution: Based on the work of the author, the distribution of maximum angular separations for 4741 available MIT-VLA sources is presented in Section 4.6. With this extensive dataset, the aim will be to set an upper limit on the mean advance speed of the jets seen in the large sample of MIT-VLA EGRS.

Small Sample Results

Gravitational Lenses:

To date, 7 examples of multiply-imaged gravitational lensing have been discovered in the MIT-VLA Survey region, 1 of which was found during an independent flat-spectrum radio source survey carried out by the Jodrell Bank VLA Astrometric Survey/Cosmic Lens All Sky Survey, a collaboration between the Jodrell Bank and Caltech groups (JVAS/CLASS B1422+231 = MG 1424+2255).

The remaining 6 gravitational lenses and the references to the initial discovery papers are:

MG 2016+112 (Lawrence et al. 1984 [96]); MG 1131+045 (Hewitt et al. 1988 [71]); MG 1654+1346 (Langston et al. 1989 [89]); MG 0414+0534 (Hewitt et al. 1992 [70]); MG 1549+3047 (Lehár et al. 1993 [100], 1996 [99]); MG 0751+2716 (Lehár et al. 1997 [98]).

Of these 7 lenses, 4 are Einstein rings, 2 are quadruples, and 1 is a triple. Rings and quads are common lensing configurations in systematic radio surveys such as the MIT-VLA and CLASS efforts, and can be understood in terms of lensing of the background source through an ellipsoidal potential (Burke et al. 1992 [26], [83]).

The range in lens redshifts is 0.25 to 1.01, with a mean of 0.47 (see Keeton & Kochanek 1996 [84]). The range in source redshifts is 1.74 to 3.62, with a mean of 2.82. Thus it appears that these and other lensing data strongly support the *cosmological* interpretation of the observed redshifts; all the lenses are found to be *closer* to us than their respective sources, with the lenses situated invariably at low to intermediate redshift, and the background sources at very high redshift.

The lenses and sources have about the same mean optical magnitudes, ranging from the brightest at 16th magnitude, to the faintest detectable one at 23rd, the mean being 20th magnitude. By the time an object is a faint as the 23rd magnitude, one needs a long integration on a large telescope in order to secure a good chance of obtaining the redshift.

Finally, there is a modest spread in maximum image separation, ranging from 0.8 to 3.8 arc-seconds, with mean 2.0 arcseconds. At distances of $\sim$ 1 Gpc, a simple point mass model predicts a Einstein radius of 1 arc-second for a mass M $\sim 10^{11} M_{\odot}$. The angular scale goes as the square root of the mass, so the range in mass in the MIT-VLA lenses should be from about $10^{10} M_{\odot}$ to $4 \times 10^{11} M_{\odot}$. These are consistent with the known masses of typical galaxies.

Gravitational Lens Candidates:

Over the 15 year period of the MIT-VLA survey, many lens candidates have been selected from the thousands of MIT-VLA snapshots. These have in general been very liberal selections of sources with one or more of the following features: a double consisting of compact sources, non-collinear triple, quadruple, multiple, arc-like or ring-like morphology. These compilations have usually appeared in the theses of MIT students: (Lawrence 1983 [97], Hewitt 1986 [72], Langston 1987 [90], Lehár 1991 [101], Herold-Jacobson 1996 [69], and Fletcher 1998 (this thesis)).

An account of the results on the latest crop of MIT-VLA lens candidates is presented in

Section 4.3.

Individual Source Results

Discovery of a Radio Ring Galaxy: An account of the observational results and preliminary interpretations, of the unusual and highly polarized elliptical ring in MG 0248+0641, appears in Section 4.4. This work has been published in collaboration with other co-authors (Conner et al. 1998 [37]).

Discovery of a Binary QSO: An account of the observational results and interpretation of the optical binary QSO MG 2214+3551 appears in Section 4.5. This work has been published in collaboration with other co-authors (Muñoz et al. 1998 [107]).

Environmental Effects: It may be reasonably speculated that MG 0248+0641 and MG 2214+3551 may be rare cases where the observed phenomena are the direct results of dynamical interactions between the host galaxy of the EGRS and a nearby companion galaxy. See the discussion in Sections 4.4 and 4.5.

4.2 The MIT-VLA Close Radio Doubles

The new sample of MIT-VLA Close Doubles is presented in a table in Appendix A. The author was responsible for the collection of most of the CCD imaging data, and also for supervising the data reduction presented in Cooray's MIT BS thesis (1997) [39]. The main results come from the reduction of 2 weeks of data from the MDM September 1994 run, and

they appear in the theses of Cooray (1996) and Herold (1996) [69].

Radio Angular Size: the CDs were selected from the MIT-VLA X-Band snapshots by an *angular size* criterion: $\theta < 2''$. For a source at a distance of 1 Gpc, this would correspond to a radio structure no larger than 10 kpc. Probably due to the limit of $\sim 0.25''$ to the VLA resolution, no CDs were found to be smaller than $0.6''$.

Radio Flux Densities: these spanned the entire range represented in the MIT-VLA sample: 70 to 500 mJy.

Radio Spectral Indices: the spectral indices were subsequently found to be mostly steep spectrum, ranging from 0.2 to 1.6 ($F_\nu \sim \nu^{-\alpha}$), with the usual mean of ~ 0.8 for steep spectrum sources. Thus, the MIT-VLA sample of CDs is a subset of the **Compact Steep Spectrum (CSS)** class of radio galaxies.

Radio Flux Ratios: the ratios of the fluxes in the 2 components range from 1 to 3, suggesting that differential Doppler boosting, due to a radio source axis pointed close to the line of sight, is probably not a major factor in determining the observed total flux density, nor the ratio.

Optical Identifications: provided that CCD imaging could reach as faint as 23rd magnitude in R or I, there was great success ($> 85\%$) in locating likely optical counterparts at the accurately known interferometric radio positions for MIT-VLA CDs. Herold has found that most of the optical counterparts (56%) are unresolved (called 'stellar') in the prevailing atmospheric seeing. Visible galaxies are about 32% of the optically imaged sample, while the remaining 12% have no identifications to the limiting magnitudes reached with the MDM 1.3m (this can range from 21st to 23rd magnitude depending on the prevailing observing conditions, and on whether multiple CCD exposures were co-added or not).

Optical Magnitudes: these range from about 17 to 23 in the red R and infrared I filters, with more CDs found at the fainter levels. The MIT-VLA CDs are fairly faint, with a mean magnitude of about R = 19.5, which is not far from the detection limit of the POSS

and ESO sky surveys. The remaining 'empty field' CDs are likely to be further away than the majority, and would require deeper imaging in better seeing conditions, in order to be detected.

Optical Colors: the CDs have a marked tendency to be infrared bright compared to amount of red light emitted; in astronomical jargon, these sources are still labelled 'red', as an indication of the sense of the slope of the optical continuum. The color index (R-I) ranges from -1 (infrared faint) to +5 (infrared bright), with a mean of +0.7.

Optical Color versus Magnitude: shows a clear trend for optically *fainter* sources to be *redder* in color.

Optical Detection Rate versus Radio Spectral Index: shows a clear trend of *decreasing optical brightness* with *increasing radio spectral index.*

Optical Spectra: for a small sample and highly incomplete optical sample of 8 MIT-VLA CDs, the redshifts range from 0.3 to 1.1, which shows that the CD population extends from low to intermediate cosmological distances; to probe further in distance would probably require imaging to 25th or 26th magnitude, but the requisite spectroscopy for redshift identification would be difficult to justify, at these very faint levels.

The spectra themselves show typical AGN emission lines (Balmer Hα, [OII] λ3737, and [OIII] λ4959/5007), and stellar features commonly seen in the spectra of normal galaxies (Ca H and K absorption). The forbidden oxygen lines are probably from the narrow line region (NLR), as they are seen with widths less than 1000 km/s in FWHM. However, in one case (MG 0821+1747) Herold found that the [OIII] lines were remarkably broad ($\Delta V > 3000$ km/s), and that there was evidence for Faraday depolarization in one of the radio lobes, but not the other. This particular source could be interpreted as having an energetic NLR core region , with a high amount of ionized gas collected in the halo of the host galaxy. This may be evidence for a recent or current galactic interaction or merger causing the dumping of large amounts of gas onto the core, and with an attendant release of much gas into the

halo of the AGN host galaxy.

High-resolution morphologies from MERLIN: Herold has found 3 types of morphology for the CDs, using the larger MERLIN array (at 60 mas angular resolution): doubles, core-jets and complex shapes. The complex sources may be interpreted as having their jet axes close to the line of sight, causing a marked exaggeration of any bending in the jet due to projection. Herold has provided a complete analysis of the interpretation of her own sample of CDs observed with the MERLIN array. Her results are incorporated into the account in the next section.

Interpretation of the MIT-VLA Close Double Data:

The first question that springs to mind is: why are these MIT-VLA CDs so small in angular size, when compared to typical extents of 5 to 20 arcseconds seen in other extended sources ? Five possibilities might be considered, for any individual CD:

- **Projection**: the CD radio axis is pointed close to our line of sight.
- **Gravitational Lensing**: the CD is actually a gravitational lens.
- **Distance**: the CD is a normal double at high redshift.
- **Frustration**: the CD is an intrinsically normal double whose jet growth has somehow been stunted by reason of a dense enshrouding enviroment (e.g. a dense IGM).
- **Youth**: the CD is intrinsically youthful, and has been caught in the initial stages of pushing out jets into the IGM.

The Projection hypothesis has been shown by to be untenable for the CSS population as a whole (Fanti et al. 1990 [49]); at least 70% of the CSS sources must be intrinsically small in their linear sizes; for the MIT-VLA CDs, which are evidently members of the CSS class, Doppler boosting from source jets pointed close to our line of sight is certainly *not* suggested by the measured low flux ratios.

The Gravitational Lens hypothesis is probably untenable for the population as a whole, as the empirical experience from the MIT-VLA radio survey is that cosmological galaxy scale lensing is expected at a rate not exceeding about 1 in 500, given the current sensitivity limits in the radio and optical detections (see the theoretical prediction by Turner, Ostriker & Gott 1984 [142]). As the CDs form about 2 to 3% of the MIT-VLA population, the probability of lensing for the majority of CDs is clearly excluded. However, the close double sample is just the type of source set that should be carefully inspected for the rare lensing case that may happen to be contained within.

The Distance hypothesis, by itself, is unlikely, as there is no reason why the CDs should be systematically further away than the general EGRS population, which has been statistically estimated to be at redshifts of order ~ 1 (Condon 1984ab [32], [31]). In fact, the few spectra that have been collected show that the redshifts tend to be in the low to intermediate range (less than about 1), so they are clearly systematically *closer* than the majority of EGRS.

The Frustration hypothesis has been shown by Herold (1996 Ph.D. thesis [69]) to be unlikely. She argued that the jets in the CDs would have enough mechanical power to not be confined even by a dense IGM. Instead, she concluded that the most likely hypothesis for the majority of CDs is that of Youth.

It is not clear to the author that Herold's conclusion is completely warranted; it is quite possible to have a young radio galaxy with intrinsically young *and* weak jets, that are easily frustrated by a dense cocoon of infalling gas liberated by a tidal interaction between the host galaxy and a companion. Thus, the Frustration and Youth hypotheses are not mutually exclusive, and may even be connected in reality precisely for the set of young radio sources.

The Youth hypothesis can be invoked in another way; as an evolutionary link in a chain linking the structures seen at a wide range of available resolutions: VLBI, MERLIN, VLA. It has been proposed in the past that VLBI sources (some of which are also CSS sources) have relativistic jets that eventually must grow (after probably many thousands of years)

to appear on kiloparsec scales in the MERLIN and VLA maps. In this scenario, the MIT-VLA sources would be a set of 'missing links' between the small parsec-scale VLBI sources and the larger 100 kpc-scale classical extended doubles. Thus, the the VLBI sources have just recently been born, and the MIT-VLA CDs are simply the result of jet growth after a relatively short period of time compared to mature EGRS population. This idea has been presented by the author and Cooray in a 1996 AAS poster and press release (Cooray et al. 1996 [39]), which is reproduced in Appendix C.

The fact that the MIT-VLA CDs tend to be infrared bright may be understood as evidence for enshrouding dust, which is usually attended by a proportionate fraction of gas. This prediction could be put to the direct test by deep CCD infrared imaging data.

The optical dimming of the steeper spectrum sources may be interpreted as a redshift dilution effect (otherwise known as the cosmological K-correction). In this scenario, the relatively older CDs will have fewer energetic electrons at high radio frequencies, with spectra curving downwards with frequency. On redshifting the radio photons to the observed frequency of 8.4 GHz, the apparent spectral slope will indeed be as steep as that seen in the MIT-VLA CD sample. As a corollary, the older sources are likely to be less energetic overall than when they were younger, which would be a possible explanation for the reason why they are dimmer optically. It has been known for some time that high redshift radio galaxies have a good correlation between radio and optical brightness (McCarthy 1993 [103]), and the evidence indicates that the cause is due to an energetic interaction between the radio jet and the ambient ISM and IGM of the host galaxy. A similar mechanism may also be operating in the MIT-VLA CDs (at lower redshift), as these young radio sources will essentially have no choice but to push out their jets through the ISM and local IGM. The work done by the jet while entraining the ambient medium into its path would be expected to deplete the energy reserves of the central engine, at least temporarily. This may then be a possible explanation for why the core is radio weak relative to the lobes, and also for why the optical brightness

of the AGN core seems to fade with the age as inferred from the steepening of the spectral index.

Overall, it seems that the most likely hypotheses for the MIT-VLA CDs are 'Youth' and 'Frustration' during the earlier stages of jet production. It would be be interesting to test the Frustration theory by direct IR imaging and spectroscopy of the expected large amounts of gas and dust that are here proposed to be the barriers to jet growth.

4.3 The New MIT-VLA Gravitational Lens Candidates

About 70 new gravitational lens candidates have been found from the 1990s efforts of MIT students. This includes three very promising candidates from Conner's 1998 Ph.D. thesis research (in progress [38]). The candidates known to the author have their names and coordinates, and a subjective estimate of lensing likelihood for the PMN candidates, documented in a table in Appendix B. From the sample of 1750 PMN sources imaged at the VLA by the author, about 30 PMN candidates were culled, and these plots are included after the table. Plots from Herold's and Conner's thesis are also included on the MG candidates.

These lens candidates will be studied in detail by P. Schechter and J. Hewitt (MIT) in the near future.

4.4 The Unusual Radio Galaxy MGJ 0248+0641

This radio galaxy was discovered initially by Conner during his Ph.D. thesis research. It contains an elliptical and highly polarized radio ring in the western half of a classic core-double structure. At first, the elliptical ring was thought to be a prime Einstein ring lens candidate, but imaging down to 25th magnitude using the MDM 2.4m telescope failed to show up a possible lens, despite the fact that a normal galaxy of the mass implied by the ring size should already have been detected at about 18th magnitude. An unlikely set of

alternative hypotheses relying on the chance interposition of a supernova remnant, nova, planetary nebula or H II region was found to be very unlikely, given the lack of optical evidence for Galactic sources of these types in the vicinity of the ring, and also given the fact that the radio spectrum is non-thermal, which would automatically rule out all of the proposed interlopers except for the supernova remnant.

It only became clear, in the final stage of writing the paper, that there is a marginal optical and IR detection of a faint source located close to the western hot spot, just on the edge of the ring. If this optical source can be shown to be at the same redshift as the AGN core (which has been spectroscopically measured to reside at z = 0.57), then the distinct possibility arises that this faint source is a small galactic companion to the host galaxy of the AGN. Though a detailed model for the production of the ring from a strong dynamical interaction between the galaxies has not been given any serious thought, it is suspected that the jet has somehow been disrupted by such an interaction in the recent past. The rarity of this phenomenon is also implied by the fact that this type of radio structure is one of a kind in a sample of about 8000 VLA maps.

Further profitable study would include a detailed investigation of the faint optical companion.

4.5 The New Binary QSO MGJ 2214+3550

This radio source was routinely cataloged in Herold's thesis research. A collaboration was organized between Falco, Kochanek and Munoz (Cfa) and MIT to start a redshift survey of a selected sample of MG radio sources, and MG 2214+3550 was included in the target list. During optical observations, it was noticed that there was an optical double in the direction of the radio position, and the subsequent spectra were found to be almost identical. Unfortunately for the gravitational lensing hypothesis, it later transpired that significant differences between the optical spectra would entail a consideration of non-lensing hypotheses.

In addition, the expected lens was never found in either the radio or optical.

The author's role was to measure the radio surface brightness at the positions of the two optical quasars. In this way, the radio brightness ratio was shown to be very different from the optical ratio, which poses further problems for galactic gravitational lens models.

The data, analysis and conclusions are presented in a paper for which the author had some significant input. This paper is reproduced in Appendix C.

It is finally proposed that MG 2214+3550 is an example of a binary QSO, i.e. two quasars in host galaxies separated by a distance of order the size of a galaxy or galaxy halo. In this configuration, there would be some interaction expected between the two galaxies, and indeed the Southern one has a clear core-jet morphology typical of radio-loud AGN. It is not known why the Northern galaxy has no similar radio emission; evidently, it is either 'turned off' at the current epoch, or else the presence of significant galactic interaction is *not* a sufficient condition for the activation of a galaxy nucleus. It is also possible that the jet will eventually 'turn on' in the future, given the fact that there may not yet have been enough gas and stars supplied to the central regions of the Northern host galaxy.

One important realization that came partly as a result of this work, and which was intially proposed by the Cfa collaborators, is that the sizeable sample of optical QSO doubles that now exists are more likely to be systems similar to MG 2214+3550, *rather than* gravitationally lensed pairs. It would be interesting to see whether their probabilistic arguments, which are based on galaxy merger models, could be applied to the case of *close double* radio galaxies. In general, one would expect that the low rate of multiply-imaged gravitational lensing seen in distant AGN would argue against the lensing hypothesis for the majority of distant galaxies, *independent* of their detailed physical natures.

4.6 The MIT-VLA Angular Size Distribution

The following results in this section have arisen exclusively from the author's own research.

There can be no *direct proofs* of the morphological evolution of an individual source, as the expected dynamical timescale for a jet travelling on kiloparsec scales is at least thousands of years (this limit is set by causality). However, physical arguments would lead one to expect an overall increase in the largest angular size (LAS) of an individual source with time, due to the forward propagation of jet material. Indeed, the motion of the knots in the jet fluid has been seen in some sources, though this velocity refers to the flow velocity v_F, rather than the morphological velocity of advance of the jet head v_H. By momentum conservation, it is expected that the jet advance velocity will set a lower limit on the jet flow velocity: $v_H \leq v_F$.

In Figure 4-1 is shown the distribution of maximum angular separation for 4741 MIT-VLA sources, that had been organized by the author in March 1997. Resolution limits a statistical analysis to angles greater than ~ 0.25", and the field of view chosen during the snapshot reduction limits the analysis to angles smaller than $\sim 120''$. In principle, it would be possible to extend the field of view by searching for flux in individual cases, but this would be too time-consuming. It is already clear from the available angular window that most MIT-VLA EGRS are found to be fairly compact. 74% of all sources reside within a $5''$ circle, and 82% lie within $10''$. Most of the sources in the smallest $5''$ bin are found to be point sources, the majority of which are flat-spectrum. Removing the flat spectrum sources does not significantly affect the statistics in the larger angular scale bins.

These firm statistical results are the first to come from a detailed analysis of the angular sizes of a large sample of thousands of radio sources. The histogram presented here appears in the Canary Islands paper in Appendix C; in that paper, a simple jet model is proposed, and more discussion of the the modelling of radio sources is presented in Chapter 5.

It is intended to place tentative upper limits on the mean jet advance velocity v_H in the MIT-VLA EGRS population, via a theoretical estimate of the mean age of the jets; this work is also detailed in Chapter 5.

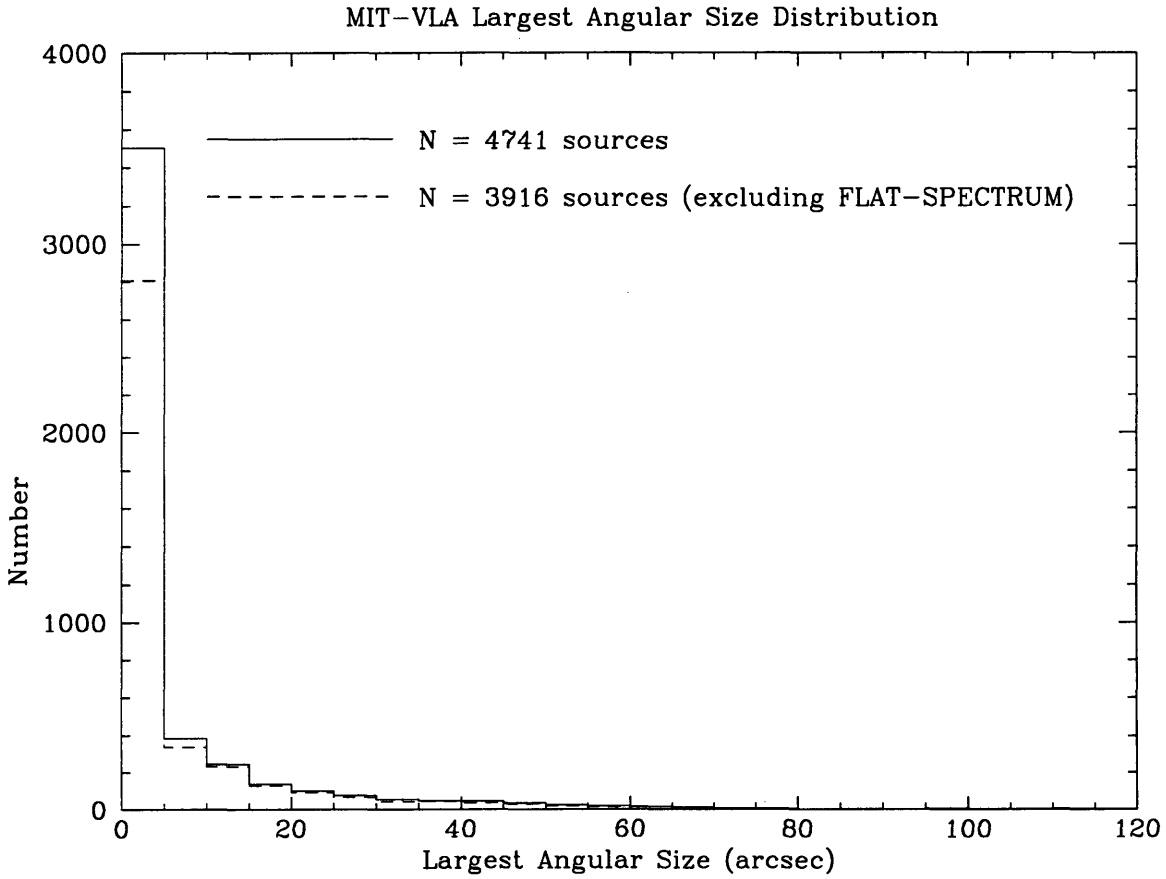

Figure 4-1: The MIT-VLA Largest Angular Size (LAS) Distribution for 4741 extragalactic radio sources as imaged at the VLA at 4.8 and 8.4 GHz. The angular resolution is only as good as 0.25″. The contribution from $\sim$ 1000 flat spectrum sources mainly shows up as compact and unresolved sources near the resolution limit. On removing this spectrally biased subsample, the LAS distribution is not thereby affected on scales larger than $\sim$ 10″.

4.7 Summary

The MIT single-dish surveys have shown that the EGRS population is consistent with an isotropic distribution of evolving radio sources. At the sensitivity limit of $\sim$ 30 mJy at 4.8 GHz, the MIT sources are sufficiently sparsely populated that they do not show conclusive evidence for clustering on large scales. An attempt to statistically measure the velocity of the Earth with respect to the EGRS population was rendered ineffective by the discovery of flux calibration mismatches between independent radio survey catalogs. However, if the data are left untreated, a very interesting velocity of 10,000 km/s towards the Great Attractor appears to fit the sky distribution of source counts best.

The morphologies and spectral indices are consistent with a unified model in which the 'young' flat-spectrum radio core evolves by the ejection of large quantities of magnetized plasma, turning eventually into source with physical extensions of the plasma on scales far exceeding 1 kpc. In the process of growth, the electrons adiabatically lose energy, creating a steep spectrum for most of the extended structures observed. As an exception to the strong correlation between angular size and spectral index, the class of CSS sources has been shown to contain the new crop of MIT-VLA close doubles, which are invariably faint and red, with typical AGN spectral lines indicating low to intermediate redshifts for the brighter CDs. It is most likely that the CDs are sources intermediate in age between those seen on VLBI scales, and those classical doubles seen on 100 kpc scales in other surveys. The hypothesis that CDs are small due to 'frustration' by a large quantity of gas, supplied possibly by a galactic interaction, can be put to the direct test via IR CCD imaging.

The existence of a stable morphological classification scheme suggests that the underlying physical processes govering the *individual* source evolutions are similar across the board for the *global* population. Thus, there is a hope that a *Unified Model* for EGRS might be able to reproduce the relatively small number of configurations seen.

In rare cases, one does find a source that does not fit the general pattern for morphology.

This has been a strong criterion for identifying new examples of gravitational lensing, but it appears that the MIT-VLA survey is coming to a ceiling in detection of obvious lenses; of the 70 new candidates culled over the past 5 years, the best (Einstein ring) candidate has turned out to probably be the result of a recent violent instability in the jet, and another promising binary quasar was found to be consistent with a galactic merger hypothesis.

If these 'red herring cases' are indeed as rare as the phenomenon of graviational lensing, an immediate statistical result would be that the timescale of radio emission caused by dynamical interactions would be much shorter than the mean lifetime of the EGRS population as a whole; at a frequency of 1 in 1000, the active radio lifetime would then be about 10^6 years, assuming a mean age of 10^9 yr for AGN in general. This seems to be a reasonable duration for a 'fast' galactic encounter. For the prospects of a Unified Theory, it seems that while dynamical interactions are essential to the formation of powerful AGN, the formation process itself is probably well modelled as a Poisson rate $C(t)$ of AGN core creation events as a function of time, with the level of activity in the Universe determined mainly by the probability of strong galactic encounters, which in turn should be a calculable function of the cosmic epoch, given a theory for structure formation on galactic and cluster scales.

Finally, the specfic work of the author was to organize the detailed results for 4741 available MIT-VLA snapshots, and hence show that the largest angular size distribution should place strong constraints on any models that propose a mean relativistic advance speed of the jet into the IGM. This development wil be detailed in Chapter 5.

Chapter 5

The Nature and Evolution of Extragalactic Radio Sources

In this chapter, the observed physical properties of AGN will be reviewed, in preparation for a more detailed discussion of the subset of *radio-loud* AGN. The many different types of intrinsically powerful AGN that are classified by their apparently different observational parameters are believed by most to be be driven essentially by the same mechanism: gravitational infall of large masses of stars and gas into a central relativistically deep well. If this is true, then the different classes of powerful AGN should be able to be *unified* into an overall scheme, that ultimately would be able to explain the different observational class membership criteria as *incidental* to the underlying similarity between the classes.

The main astrophysical contributions that are put forward in this Chapter are in connection with the following two issues, both related to the physics of extragalactic radio sources:

1. The Evolution of the Masses of the Central Accreting Objects.

2. The Evolution of the Lengths of the Radio Jets.

After briefly reviewing the observations that have been made so far of radio-loud AGN,

a formal, descriptive statement of a radio-loud AGN model will be proposed to unify these observations. It is clear that almost all of the component parts of the proposed model have already been published by many different authors. However, a unifying synthesis is not so easily found. Further, there are no publications that deal in detail with the 2 issues mentioned above.

With regard to the first issue above, a general model for the statistical distribution of a population of accreting objects, and of their non-accreting descendants, is constructed starting from basic principles; the system of differential equations, and the resulting solutions, are presented in Section 5.6. Any model builder who needs a mathematical framework for representing the evolution of the masses of populations that evolve through continuous (not sporadic) accretion, would be encouraged to consult the solutions in that Section. The condition that the accretion be continuous, in a single-burst, is simply to avoid the ill-posed mathematical problem of evolution though states in which the mass does *not* change. However, in principle, the accretion solutions proposed here may be modified for repeated use in a sporadic accretion scenario, provided one has a model for when the accretion starts and stops, and how the dynamics of accretion may change from burst to burst.

It is emphasized at this point that the models outlined in this Chapter are *not* predictive. They are simply there to define a mathematical language and formalism for the purpose of later insertion of physically predictive theories.

For the second issue, it is shown that the morphological speed of advance of the jet head in the radio-loud AGN in the MIT-VLA survey is likely *not* to be relativistic in the mean. Here, one must make a reasonable assumption about the mean ages of jets, and the timescale set by the evolution of the central engine will play an important role in constraining the jet age.

While these two contributions are modest steps forward, as far as the author is aware, they are original.

In more general terms, the major problem with the understanding and modelling of AGN has always been the search for a power source vigorous and compact enough to last for millions, perhaps in some cases a billion or so, years. A consideration of the energetics of an accreting black hole, and its evolutionary timescale, are key factors to keep in mind when constructing a unified model for AGN. In the case of radio jet-producing AGN, it seems that the most efficient energy extraction mechanisms utilize an accretion disk that is magnetically tied to the plasma magnetosphere that corotates with a central Kerr-Newman black hole. Further quantitative discussion of the energetics, and timescales of AGN growth and evolution, may be found in Section 5.3.

As for the question of how such a compact object would come into existence in the center of the host galaxy, one very attractive idea posits that fairly rare galaxy interaction or merging events may allow the dumping of a sufficient amount of stars and gas into the center of the proto-EGRS. It is also possible that the bars found in some galaxies may encourage gas to propagate inwards more efficiently, once given an external impulse from an interacting galaxy companion. The merging and interaction hypothesis is promising because many radio galaxies are identified with ellipticals, and some of these are noticeably disturbed or peculiar in morphology, as if having engaged in a recent violent encounter (see the review by Barnes & Hernquist (1992) [7]). Also, these events are probably rare enough to be compatible with the relatively few galaxies in our Universe that are powerful AGN. However, the evidence for the galaxy merging and interaction hypothesis for AGN remains somewhat indirect (though not entirely speculative, as one of the first EGRS identified with an optical galaxy, Centaurus A (NGC 5128), is clearly seen to reside in an elliptical of peculiar morphology, with a massive planar dust lane running directly over a very luminous bulge of spheroidal shape).

The rest of this Chapter is organized as follows: in Section 5.1, the classification, unification and physics of all types of AGN will be reviewed. In Section 5.2, the focus will converge on the properties of radio-loud AGN. In Section 5.3, the energetics and timescales

of AGN growth are considered. In Section 5.4, a few brief cautionary remarks will be made in regard to actual survey samples of radio-loud AGN. In Section 5.5, a descriptive model will be outlined for radio-loud AGN. Many of its component sub-models will also be applicable to other powerful (but radio-quiet) AGN. In Section 5.6, details will be given for a proposed mathematical formalism for the evolution of accreting astrophysical populations. In Section 5.7, an example of a Monte-Carlo algorithm will be given, for the express purpose of modelling the evolution of jets in EGRS. In Section 5.8, an estimate of the mean advance speed of jets in the MIT-VLA sample will be given, using reasonable 90% confidence limits on the various potentially observable parameters. The database used is the distribution of largest angular sizes in the MIT-VLA sample. In Section 5.9, a summary will be given of the scientific contributions of this chapter.

5.1 Active Galactic Nuclei

Active Galactic Nuclei (AGN) is a generic name for many different (and rare) types of galaxy, including quasars (QSOs), radio galaxies (RG), blazars, Seyferts, LINERs and strong infra-red luminous galaxies. These all show energy output not usually associated with normal stellar processes, coming from a compact region within the nucleus.

An object may be classified as an AGN if it meets at least one of the following criteria:

- **Compact nucleus** brighter than the one seen in galaxies of similar Hubble type.
- **Non-thermal continuum** radiation from the nucleus.
- **Non-stellar excitation** processes indicated by the nuclear emission lines.
- **Variable** continuum or emission lines.

Attendant to this basic set of properties come many others, such as the morphology in the radio or optical bands, and the intrinsic luminosity of the active emission. Since AGN

emit over such a wide range of the accessible electromagnetic spectrum, a distinct need for an unambiguous classification system is required. However, since this classification is to a major extent motivated by the observational biases and limitations inherent to the practice of astronomy, it is equally important to counterbalance the trend towards the multiplication of observational categories with a clear analysis of AGN phenomena, in terms of the unifying principles of physics.

5.1.1 AGN Classification

Active galactic nuclei are further classified into subgroups, mainly according to their intrinsic luminosity and spectrum. There have been many different types of AGN proposed for the organization of the abundant observational data collected over the past $\sim$ 4 decades:

Radio-loud Quasar(RLQ): Quasars are the most intrinsically powerful emitters of all AGN, with visual luminosities in the range -31 $\leq M_V \leq$ -24 (10^{38} to 10^{41} Watt). They lie over a wide range in redshift, from z $\sim$ 0.1 to z $\sim$ 5.0. About $\sim$ 10% of bright optically-detected *quasi-stellar objects (QSO)* are also radio-loud. Both types of quasar are unresolved on photographic plates, but deep imaging of low redshift quasars, in good seeing, sometimes reveals a faint fuzz surrounding the central bright nucleus, which is usually bluish in color due to the non-thermal continuum from the AGN core. High redshift quasars are more efficiently found by looking for the *red* color of the redshifted continuum. The host galaxy is usually an elliptical. Like all powerful AGN, the emitted spectrum covers the entire range from radio to gamma-rays, with a broad peak somewhere in the ultra-violet, optical, or infrared (UVOIR) range. There are invariably strong, broad resonance emission lines (FWHM $>\sim$3000 km/s), indicating rapid motion of excited and ionized gas within the **Broad-Line Region (BLR)** deep in the galactic nucleus. There are also narrow forbidden lines (FWHM $<\sim$1000 km/s) from the **Narrow-Line Region (NLR)**. In high redshift quasars, a dense series of absorption lines, arising from intervening galactic disks and other

IGM clouds, form the *Lyman alpha forest.* Regarding the radio morphology, there can be radio emission from both a compact core, and also from an accompanying extended halo. If the core dominates the radio emission, we have a *Compact Radio Quasar (CRQ)*; if the halo is dominant, we have an *Extended Radio Quasar (ERQ).* The radio spectral index is a good indicator of observed structure and behaviour; the *Flat-Spectrum Radio Quasars (FSRQ)* are radio-compact, showing optical variability on timescales of weeks to years, and stable optical linear polarization in the nucleus, whose direction is usually aligned parallel to the extended radio jet structure, if it exists. About 10% of RLQ (1% of all QSOs) are *Optically Violent Variables (OVV)* belonging to the *blazar* class; these are distinguished by their high optical linear polarization ($3\% < P < 20\%$), rapid variability, and wildly fluctuating polarization directions, on timescales of days to weeks. These OVV quasars are FSRQ, with compact radio structure. By contrast, the *Steep-Spectrum Radio Quasars (SSRQ)* are dominated by the extended radio emission, and do not have significant optical linear polarization, nor rapid variability.

RLQs and most other AGNs have a very broad spectrum that approximately emits the same amount of power per decade of frequency (to within a few orders of magnitude). Roughly speaking, the entire AGN spectrum consists of a non-thermal power law continuum that stretches from the radio to the X-rays, with a peak and a thermal 'bump' component at UVOIR wavelengths. The underlying non-thermal continuum becomes optically thick and turns over at a low radio frequency (in the range $\sim 10^7 - 10^{10}$ Hz). It also falls off steeply somewhere in the X-ray or gamma-ray region. The usual interpretation is that the non-thermal continuum is driven out by a region very close to the central compact object, and the overlying thermal bump is due to an accretion disk or torus containing fast-moving hot plasma, gas and dust, in the region surrounding the continuum source.

The local space density of RLQ is very low, at 3 Gpc^{-3} for $P_{1.4GHz} > 10^{25} WHz^{-1}$. Much of the quasar and radio galaxy population is enormously more active, and hence more

numerous, at high redshift $z > 1$. Evidence for this **strong cosmological evolution** in the quasar luminosity function can be readily obtained by applying a V/V_{max} test to a well-defined sample of quasars (with available redshifts). Recently, strong evidence has been published for a *turnover* (peak) in the quasar comoving space density, in the range $2 < z < 3$ (Shaver et al. 1996 [125]). In an $\Omega_0 = 0$ universe, this is the period lasting from 2.5 h^{-1} Gyr to 3.3 h^{-1} Gyr, while in an $\Omega_0 = 1$ universe, the corresponding times are 0.8 h^{-1} Gyr to 1.3 h^{-1} Gyr. All the powerful AGN, of the quasar and radio galaxy type, reach peak densities in a period of enhanced activity at high redshift ($1 < z < 5$), sometimes known as the **Quasar Epoch**. Depending on the radio or optical luminosity, the peak increase in number densities can be as high as factors of 10^2 to 10^3, over the local values.

Examples of RLQs are: 3C 147; 3C 263 ($\beta_{app} = 3$); 3C 273 (FSRQ, $\beta_{app} = 17$); 3C 345 ($\beta_{app} = 22$); 3C 351 (SSRQ); PKS 2135-14 (SSRQ); PKS 2000-330 (z = 3.78).

Optically Violent Variable (OVV): About 1% of QSOs (10% of RLQ) are the radio-loud, optically violent variables, belonging to the generic *blazar* class. Blazars, which include high polarization quasars (HPQs), and the less powerful BL Lacertae objects (BLLs), are distinguished from other AGN by their high optical linear polarization ($P > 3\%$), rapid variability and mostly smooth continua. OVVs indeed fit all these criteria for blazar membership: they have high optical linear polarization ($3\% < P < 20\%$), rapid variability, and (wildly) fluctuating polarization directions, on timescales of days to weeks. They are FSRQ, and hence have compact radio structure. Unlike the BL Lac objects, which have featureless continua, the OVVs do show broad emission lines, though these are weaker than in more typical quasars.

Examples of OVV quasars are: 3C 345 ($\beta_{app} = 22$); 3C 454.3 ($\beta_{app} = 22$).

High Polarization Quasar (HPQ): About 1% of all QSOs have a high optical linear

polarization $P > 3\%$. This group consists of the radio-loud OVVs and the radio-quiet BAL QSOs, and it is a subgroup of the generic blazar class. Thus, in addition to showing high polarization, HPQs also exhibit rapid time variability and relatively smooth continua. By contrast, almost all (99%) quasars show a slow variability of $\Delta t > 1$ yr, low polarization ($P < 1\%$), and have more complex continua, and prominent emission lines.

Radio-quiet Quasar (RQQ): The majority of quasars are dubbed "radio-quiet", but they actually do have weak levels of radio emission in the range $10^{22} < P_{5GHz}/WHz^{-1} < 10^{24}$. A reasonable dividing level to choose for the separation of RLQ from RQQ would be $P_{5GHz} = 10^{24.7}WHz^{-1}$, which is comparable to that separating the Weak and Powerful Radio Galaxies (WRG & PRG; see below). With this definition, the RQQ are about 10 to 30 times more abundant than the RLQ. The 2 keV X-ray emission of the RQQ is, on the average, weaker relative to the optical emission, than in the RLQ. This fact is succintly written as the statement: $\alpha_{OX}(RLQ) > \alpha_{OX}(RQQ)$, where $\alpha_{OX} = dlogF_\nu/dlog\nu$ is the optical to X-ray spectral index between the continuum fluxes at 2500 Å and 2 keV. So it seems that the radio and X-ray emissions are somewhat correlated in the quasar population as a whole. This may possibly be interpreted as arising from synchrotron self-Compton radiation of energetic electrons emitted by the AGN core. Between 1 to 2 percent of the RQQ have very Broad Absorption Lines; these are known as the *Broad Absorption Line Quasars (BAL QSOs)*. It is invariably true that BAL QSOs do *not* show radio emission, though there has been a recent exception found in the FIRST radio survey (Becker et al. 1997 [8]). The reason for an anti-correlation between the broad absorption lines and the radio loudness in quasars is not known. However, the broad absorption features are always found *blueward* of a strong resonance emission line, which indicates a strong outflow of gas from a central power source. Roughly 20% of the BAL QSOs are HPBALQs, with high optical linear polarization ($P > 3\%$).

Except for the HPQs, which consist of the radio-loud OVVs and the radio-quiet BAL QSOs, almost all quasars ($\sim 99\%$) have low optical polarization ($P < 1\%$), with electric field vectors oriented roughly parallel to the axis defined by the extended radio structure. The timescale of optical variability for most quasars is of order years, or more.

Examples of RQQs are: Q 0002-422; PHL 938; PHL 1226; Ton 1187; I Zw 1; Mrk 231; Mrk 1014; Fairall 9 (RQQ/Sy1), UM 232 (BAL QSO).

Radio Galaxy (RG): There have been numerous ways to classify radio galaxies. One of the more physically meaningful partitions is based on the radio power level: as *weak* radio emission with $P_{1.4GHz} < 10^{23.3} WHz^{-1}$ occurs in many 'normal' spiral galaxies, and arises due to relativistic electron production by supernovae, these examples clearly belong to the class of **Weak Radio Galaxies (WRG)**. In contrast, the emission from **Powerful Radio Galaxies (PRG)** comes from energetic phenomena specifically associated with the host galaxy *nucleus*. The dividing luminosity level may be roughly set at $P_{1.4GHz} \sim 10^{25} WHz^{-1}$. The PRG are invariably found in luminous elliptical galaxies that emit strong emission lines. These hosts are often marked by distinguishing peculiarities, such as a massive dust lane, or a strongly disturbed morphology. By contrast, the WRG are found in less luminous galaxies, both spiral and elliptical, and which have weak or no emission lines.

It should be noted that the generic term **extragalactic radio source** (EGRS) includes many of the different classes of AGN listed here, as well as those that are *not* AGN; at some level, all galaxies emit radio continuum radiation, if only from supernova activity in their stellar population. Normal and starburst galaxies actually exist in much greater numbers than the more powerful radio emitters (radio-loud quasars, radio galaxies, radio-loud blazars and radio Seyferts). However, the latter gravity-driven sources are some several orders of magnitude more powerful than the weak stellar-driven sources, and hence it is the powerful radio sources which appear exclusively in flux density-limited surveys of EGRS. A natural

dividing line between the stellar-driven radio sources and the gravity-driven ones may be placed at $P_{1.4GHz} \sim 10^{24} WHz^{-1}$. The stellar-driven sources are incapable of generating the large jets and lobes seen in gravity-driven powerful radio galaxies. In addition, the host galaxies associated with Seyferts, radio galaxies and quasars are usually very optically luminous ($M_B < -20$).

An extragalactic radio source found as an AGN in a spiral will most likely be one of the various types of *Seyfert galaxy.* Unlike in the quasars, the nuclei of the Seyfert spirals, while being relatively bright, do *not* outshine their hosts. The maximum radio luminosity of Seyferts places them mostly in the WRG class: $P_{1.4GHz} \leq 10^{25.5} WHz^{-1}$. Radio sources more powerful than this are found to be associated exclusively with luminous ellipticals.

Radio sources also divide naturally into *Flat Spectrum Radio Sources* and *Steep Spectrum Radio Sources.* Flat spectrum sources are mostly, but not always, compact (linear sizes less than about 10 pc) and potentially variable. Steep spectrum sources are extended, with a morphology that is consistent with a classical core-double shape, and which is too physically large to show much variability, except perhaps in the localized hotspot regions. It is noted that there are many violations of the general rule connecting steep spectral index with extended structure: there is a class of *Compact Steep Spectrum sources*, and extended sources may appear to be flat-spectrum if they are dominated by emission from their cores. Both compact and extended sources show evidence of jets on their respective scales, and the remarkable fact is that most of these linear structures have matching directions in going out from the parsec scale to many hundreds of kiloparsecs in the largest radio galaxies (e.g. NGC 6251).

Strong emission lines are commonly found in the spectra of radio galaxies. The *Broad Line Radio Galaxies (BLRG)* have very broad permitted lines (FWHM $\sim$ 8000 km/s), and narrow forbidden lines (FWHM $\sim$ 500 km/s), and are morphologically classified as N galaxies (meaning they have bright nuclei and faint envelopes). The BLRGs resemble in many aspects

the Seyfert 1 galaxies, especially in the optical spectral lines. It is possible that BLRGs are the radio-loud versions of the (radio-weak) Seyfert 1s. The *Narrow Line Radio Galaxies (NLRG)* have permitted and forbidden lines of similarly narrow width (FWHM $\sim$ 500 km/s), and thus have the same spectral characteristics as those for Seyfert 2 galaxies. It appears that the NLRGs may be radio-loud versions of the Seyfert galaxies of Type 2.

Substantial radio linear polarization ($p > 10\%$) , up to the theoretical maximum for synchrotron radiation ($p \sim 70\%$), is observed in the extended structures of powerful radio sources. This suggests that well-ordered magnetic fields are present. From multi-frequency Faraday depolarization measurements, it is found that *thermal electrons* are present at distances of 100 kpc from the centers of large radio galaxies; on going closer to the radio core, the electrons become hotter, and produce X-ray emission.

The local space density of PRGs is only $\sim$ 10 Gpc^{-3} for $P_{1.4GHz} > 10^{25} WHz^{-1}$; that for WRGs with $P_{1.4GHz} > 10^{23.5} WHz^{-1}$ is $\sim$ 3000 Gpc^{-3}. Unlike the WRGs, PRGs show strong cosmological evolution, with numbers and redshifts comparable to those already mentioned under the entry for RLQs.

Examples of RGs: Cygnus A = 3C 405 (FR2, NLRG); 3C 452 (FR2); Centaurus A (FR1); 3C 31 (FR1); 3C 449 (FR1); 2354+471 (FR1); M84 (FR1); Hercules A = 3C 348 (FR I/II); Fornax A (Wide Double); Virgo A = M87 (Wide Double); 3C 310 (Wide Double); 3C 236 (Giant RG); 3C 129 (NAT); 3C 83.1B = NGC 1265 (NAT); 4C 39.49 (NAT); 3C 465 (WAT); 1919+479 (WAT); 3C 449 (C-shaped); 3C 47 (S-shaped); 3C 315 (S-shaped); 3C 223.1 (NLRG); PKS 2322-12 (NLRG); PKS 1417-19 (BLRG); 3C 390.3 (BLRG: variable $\sim$ 1 yr); 3C 445 (BLRG); 3C 273 (VLBI core-jet); CTD-93 (VLBI double); NGC 1275 (WRG); M 84 (WRG).

More details on the properties of radio galaxies will be presented in Section 5.2.

BL Lacertae Object (BLL): These are another subset of the blazar class. They are not as

powerful as the radio galaxies and quasars, and hence are found in low redshift host galaxies ($0.04 < z < 0.6$), invariably elliptical. The central non-thermal source is optically bright: $-26 < M_V < -21$. They resemble the QSOs in that the optical continuum is power-law. However, their distinguishing spectral characteristic is that they have extremely *weak or no emission lines.* Their peak luminosity is in the infrared, where they exhibit a wide range of luminosities ranging from $10^{37} < L_{IR} < 10^{40}$ Watt. BL Lacs are also relatively strong in X-ray emission, with flat values of α_{OX}. Their radio luminosity is dominated by a flat spectrum nuclear core source, but extended structures on scales of 10s to 100s of kpc have been detected in more sensitive radio maps. In contrast to most QSOs, the BL Lacs satisfy the requirements of the blazar class, and they appear to be related to the 10% of RLQ that are classified as OVV quasars. They are highly variable in the radio, optical ($\Delta m > 1$ mag) and X-rays. The timescale for variation is days, and usually less than a week. Their smooth optical and IR continua are highly polarized ($5\% < P < 40\%$), with position angles that vary on the similar timescales. In BL Lac objects with two-sided extended radio structure, the preferred polarization position angle is observed to lie parallel to the radio linear axis. In some BL Lacs, superluminal motions have detected using VLBI, with apparent projected motions similar to those seen in the flat spectrum compact cores of the more powerful radio galaxies and quasars.

The local space density of BL Lacs is $\sim$ 80 Gpc^{-3} for $P_{1.4GHz} > 10^{23.5} WHz^{-1}$. As for other WRGs, the BL Lacs show weak or no cosmological evolution, but the absence of detectable high redshift BL Lacs leaves open the question of possible strong density evolution at high redshift (i.e. there may be many more BL Lacs of similar luminosities lying beyond our current sensitivity levels, in the Quasar Epoch).

Examples of BL Lacs: Mkn 501 (z = 0.034); Mkn 421 (z = 0.308; variable $\sim$ 2 months); BL Lac = 2200+420 (z = 0.0688; variable days-months; $\beta_{app} = 8$); OJ 287 (z = 0.306; $\beta_{app} = 7$); 2007+77 (z = 0.342; $\beta_{app} = 5$); PKS 0521-365 (z = 0.55); Ap Lib (z = 0.049).

Seyfert Type 1 (Sy 1): Seyfert galaxies of both Types 1 and 2 are found mostly in early type spiral galaxies (Sa, Sab, Sb, Sbc). Seyfert 1 (Sy 1) spirals tend to be face-on rather than edge-on. The opposite is true for Seyferts of Type 2 (Sy 2). About 2% of all bright spirals are Sy 1s, and a further 2% are Sy 2 galaxies. About 10% of the Markarian blue galaxies are found to be Seyferts. Also, about 10% of giant spirals are found to be Seyferts. The dividing line between Seyfert spirals and normal spirals is $M_B \sim -20$, and Seyferts can be as bright as $M_B \sim -23$. Unlike normal spirals, Seyferts have bright bluish nuclei, surrounded by relatively inconspicuous spiral disks and arms. The visual luminosity of the nucleus ranges from 10^{35} W to greater than 10^{38} W. The nuclear to galaxy visual luminosity ratio tends to increase with redshift; for nearby Seyferts, $L_{nuc}/L_{gal} \sim 0.1$, whereas for Seyferts with $z > 0.1$, this ratio can exceed 0.5. Due to Malmquist bias, only the intrinsically brightest Seyferts are found at higher redshifts. Sy 1s are very similar in their properties to RQQs, having optical spectra that are essentially the same as in RQQs, but scaled down enough in luminosity by factors of $\sim 10^2$ to allow the underlying host galaxy to be revealed. It is quite possible to interpret the higher redshift intrinsically bright Sy 1s as transitional cases with properties close to those of the RQQs; a higher redshift Sy 1 could easily be classified as a low redshift RQQ, due to the strong fading of the disk surface brightness as $I_\nu \sim (1+z)^{-4}$ (valid in all Friedmann cosmologies). Conversely, HST images of low redshift RQQs reveal them to reside in both spiral and elliptical host galaxies (Bahcall et al. 1997 [6]). Thus, apart from the luminosity scale, the physical distinction between RQQs and Sy1s is unclear. Nevertheless, a dividing line between RQQs and Sy 1s at $M_V = -23$ can be chosen.

Seyfert galaxies are classified into the two major groups (Sy 1 and Sy 2) according to their spectroscopic emission line properties. In Sy 1s, *broad permitted lines* ($3000 < FWHM < 5000$ km/s), and *narrow permitted and forbidden lines* ($300 < FWHM < 1000$ km/s) are found. The broad permitted lines can have very broad wings, e.g. the hydrogen lines can have a full width at zero intensity in the range $7000 < FWHM < 20000$ km/s).

Seyfert 1s have relatively strong emission in the IR and X-rays. The observation of the $10\mu m$ silicate absorption feature in both Sy 1s and Sy 2s indicate that there is some dust obscuration. Seyferts have weakly polarized continua ($P < 1\%$), whose polarization is wavelength dependent, suggesting dust scattering. The polarization PA is along the direction of elongation of the radio emission, just as for the majority of (low polarization) quasars. Variations on timescales of weeks is seen in the optical and UV continuum and emission lines. It is the low luminosity Seyferts that tend to vary by larger factors. In a very rare case atypical of Seyferts, NGC 6814 was found to vary by a factor of 10 in just a few hundred seconds!

All Seyferts are WRGs, with $10^{20} < P_{5GHz}/WHz^{-1} < 10^{24}$. However, they may be radio-weak versions of BLRGs. Many Seyferts have S-shaped kpc radio structures, suggestive of disrupted jets. These small and stunted jets typically are no large than a few kpc in size, and they tend to run continuously into extended structures no larger than 10 kpc. The absence of the powerful > 10 kpc jets, that are typically seen in the RGs and RLQs, may be due to: (1) lower power for central engine, and (2) frustration of the putative jet in its propagation through the dense ISM found in spiral disks. In detailed mapping of the Seyfert NGC 4388, a 2 kpc 'jet' was found, which was highly depolarized, indicating a substantial entrainment of thermal material from the surrounding ISM. There is more direct evidence for interaction between the jets and the ISM, this being from the correlation between radio luminosity and the width of optical [OIII] emission line. This may be due to the acceleration of line emitting clouds which drift from the ISM into the jet.

The local space density of Sy 1s $\sim$ 40,000 Gpc^{-3} for $M_V < -20$. As for other WRGs, the Sy 1s show only weak evolution at low redshift. The evolution at high redshift is an open question (see the comments made for BL Lacs).

Examples of Sy 1s: Mrk 236 (z = 0.052); Mrk 290 (z = 0.031); Mrk 486 (z = 0.039); I Zw 1 (z = 0.061); NGC 3227 (z = 0.003); NGC 3516 (z = 0.009; variable $\sim$ 2 months); NGC

4151 (z = 0.003; variable $\sim$ 1 month); NGC 5548 (variable $\sim$ 2 years); NGC 6814 (variable: this AGN has the shortest observed variability timescale, of 100 seconds in X-rays, but this is rare for Sy 1s. More typical is the 2 yr variability in this AGN); NGC 7469 (z = 0.017; variable); Fairall 9 (Sy1/RQQ).

Seyfert Type 2 (Sy 2): Seyfert 2s are very similar in most respects to Seyfert 1s, the major difference being that *no broad permitted emission lines* are seen. The narrow permitted and forbidden lines are about equal in width ($300 < FWHM < 1000$ km/s). The narrow lines are similar in width to those seen in Sy 1s. Sy 2s are somehat less optically luminous than Sy 1s, and they tend to occur in edge-on spirals. There is some evidence to suggest that Sy 2s may actually be *obscured Sy 1s* (see below). As for Sy 1s, there is evidence for dust obscuration. In the well-studied Sy 2, NGC 1068, the far IR emission comes from a region of $\sim$ 100 pc size. Most Sy 2s are weaker as X-ray sources than Sy 1s, perhaps due to much higher photoelectric absorption columns. The IR emission from dust, and the possibly greater absorption of X-rays by intervening electons, are consistent with the overall picture of Sy 2s as being intrinsic Sy 1s obscured by hot gas and warm dust.

Like Sy 1s, Sy 2s are all radio-quiet (WRGs), and it is possible that they are a radio-weak version of NLRGs. There is no statistical difference in the radio luminosities and sizes between Sy 1s and Sy 2s. The diameters for the nuclear radio source in Sy 2s range from 0.1 to 3 kpc, with a median of 0.5 kpc. Linear structures not uncommon, and in some Sy 2s, a miniature classical double radio source can be seen on scales $<$ 1 kpc. The radio emission in the extended structure is often co-spatial with the narrow line emitting gas, just as for Sy 1s.

There is evidence to suggest that Sy 2s may actually be inclined and obscured Sy 1s. Faint broad wings are seen in the hydrogen lines in off-nuclear spectra, and also in the polarized light from the nucleus. In the well-studied Seyfert 2, NGC 1068, Miller and Antonucci (1985)

[2] interpreted the broad polarized wings of the hydrogen Balmer emission lines as due to electron scattering of light from a 'hidden Sy 1' BLR continuum source.

Like Sy 1s and most (low polarization) QSOs, most Sy 2s have low optical polarizations ($P < 2\%$). In some cases, higher polarization ($P < 20\%$) is revealed when the stellar component of the light is removed. However, the optical electric field vector in Sy 2s is *perpendicular* to the extended radio structure, unlike in Sy 1s and low polarization quasars.

Since the original scheme was proposed of Seyfert 1 versus Seyfert 2, it was later found that intermediate categories were required: Sy 1.5, Sy 1.8 and Sy 1.9. These can be quantitatively defined from the ratio of narrow emission line flux to total emission line flux. Seyferts of Type 1.0 do not show *any* narrow permitted lines, whereas Seyferts of Type 2.0 show *only* narrow permitted lines. In Sy 1.5, the narrow hydrogen lines are only 10–20% as intense as the broad lines. NLXGs and LINERs (see later) show only faint broad $H\alpha$ wings, and are classified as Sy 1.8 or Sy 1.9.

The local space density of Sy 2s $\sim$ 100,000 Gpc^{-3} for $M_V < -20$. As for other WRGs, the Sy 2s show only weak evolution at low redshift. The evolution at high redshift is an open question (see the comments made for BL Lacs).

Examples of Sy 1.Ns: Mrk 926 (Sy 1.5).
Examples of Sy 2.0s: NGC 1068 (z = 0.004; variable $\sim$ 10 days) Mrk 3 (z = 0.014); Mrk 34 (z = 0.051); Mrk 1157; Mrk 270 (z = 0.009); Mrk 348; Arp 220 (Sy2/IRLG).

Narrow Line X-Ray Galaxy (NLXG): These were first found in X-ray surveys, and later were identified with galaxies showing narrow emission lines. An older (1980s) name for these objects is *Narrow Emission Line Galaxies.* Their X-ray spectra and optical-to-X-ray spectral indices α_{OX} are similar to those in Seyfert 1s, and the more luminous NLXGs have narrow lines similar in width and excitation to the narrow lines in Seyfert 1s and 2s. NLXGs are hard to classify, as they resemble several types of lower power AGN, each in different

ways. The spectral lines of NLXGs are, at first sight, very similar to the narrow lines seen in Sy 2s; however, closer inspection reveals weak, very broad wings in $H\alpha$. This places NLXGs in the intermediate class of Sy 1.8 or Sy 1.9, and strengthens the case that NLXGs are actually obscured Sy 1s. Another difference is that the UV continuum of NLXGs is weaker than in Sy 1s; there is evidence that this is due to a large amount of reddening, and it is possible that the lines may also be attenuated. It has been suggested that this extinction is correlated with the inclination of the host galaxy, being larger in edge-on galaxies. In any case, an anisotropic distribution of extinction strength would naturally arise from a flattened distribution of gas and dust. On the hypothesis that NLXGs reveal their true Sy 1 nature in their weak broad-winged $H\alpha$ lines, the amount of dust that is indicated would cause a visual extinction of $A_V \sim 2$ mag. This would be enough dust to attenuate the UV continuum, but the associated gas column is apparently not sufficient to attenuate the X-ray emission via photoelectric absorption. The dust is probably associated with the ISM of the host galaxy (as opposed to the dust sometimes invoked to cause a lesser amount of ~ 0.6 mag reddening in the central BLR of powerful AGN).

Like the Sy 1s, NLXGs show time variability in X-rays, on timescales as short as a week. It seems that Sy 1s, Sy 1.5s, Sy 1.8s, Sy 1.9s, NLXGs and Sy2s show the following continuous and monotonic sequence of properties: decreasing overall luminosity; decreasing hard X-ray luminosity; decreasing presence of broad permitted emission lines; increasing inclination angle between the galaxy rotation axis and the line of sight; increasing covering factor; increasing soft X-ray photoelectric absorption; increasing dust columns, reddening and extinction; and increasing thermal IR radiation by dust. If these trends are to be interpreted as arising from a single cause, that would be simply that we are witnessing the observational selection effects that would result from viewing a population of similar anisotropic emitters that have been obscured by similar anisotropic distributions of gas and dust within the central nuclear regions.

Low Ionization Emission Line Region (LINER): The LINERs are the *least* luminous, and most common, type of AGN that are known to contain non-stellar power sources. They are found in otherwise normal early type spirals (Sa, Sb), and ellipticals. At least 30% of all spirals show LINER activity. The non-stellar continuum luminosity is usually *small* compared to the stellar continuum, and the LINER emission region is less than 1 kpc in size. The low contrast between the stellar and non-stellar emission makes it very difficult in general to ascertain the true continuum luminosity over much of the electromagnetic spectrum; thus, most of the useful information on the physical properties of LINERs comes from their emission lines. The strongest of these are in *low* ionization stages, e.g. [O I], S II; very high ionization stages are never seen. In contrast to the Seyferts, which appear to be photoionized, some LINERs show possible evidence for a combination of photoionization and *collisional excitation and ionization*, perhaps due to shocks. The emission lines are somewhat narrower ($200 < FWHM < 400km/s$) than the narrow lines seen in Seyfert galaxies. LINERs commonly also show weak, broad ($\sim$ 4000 km/s) emission lines in $H\alpha$. This may be taken to be a hint that LINERs have a shared characteristic with more obviously luminous members of the AGN family. This observation indicates that LINERs possess a weak, low-excitation BLR similar to the one in Sy 1 nuclei. However, other broad lines are not observed in LINERs; this may be interpreted as possible evidence of structural obscuration, or dust extinction.

The debate continues over whether shock-wave excitation is important in LINERs. A sign that this is the case comes from the observation of the [OIII] λ4363 and [OI] λ6300 lines. A strong [OIII] λ4363 line indicates very high kinetic temperatures of $\sim$ 40,000 K, which is inconsistent with the normal $\sim$ 10,000 K temperatures seen in typical photoionization spectra. Shock wave models usually assume that the emitting clouds are moving through the ISM with velocities of order $\sim$ 200 km/s. Unfortunately, at this point, the theoretical speculations are under-constrained by the difficulties inherent to LINER observations.

Examples of LINERs: Mrk 298 (Sb: z = 0.035); Mrk 700 (Irr: z = 0.034); Mrk 1158 (z = 0.015); NGC 4036 (E6: z = 0.005); NGC 4261 = 3C 270 (see 1993 Jaffe et al.–HST image of torus); NGC 4278 (E1: z = 0.002); NGC 7213.

Strong IRAS Galaxy (IRLG): These have enormous IR luminosity, exceeding $10^{12}L_{\odot}$. They were first found in great numbers in the IRAS catalogs of mid- and far-IR sources (λ = 12, 25, 60 & 100 μm). Some of these IRAS galaxies are *Ultra-Luminous Infra-Red Galaxies (ULIRGs)*, with IR luminosities in excess of $10^{14}L_{\odot}$. Much of the IR radiation is believed to be re-radiation from dust heated either by a non-thermal AGN continuum source, or else by a thermal starburst. Like Starbursts and Nuclear Emission Line Regions, IRLGs do *not* show broad emission lines.

The local space density of strong IRAS IRLGs $\sim$ 300 Gpc^{-3} for $L_{IR} > 10^{12}L_{\odot}$. Just as for other the other low power AGN, such as LINERs and Starburst Galaxies, there is *no* evidence for evolution with redshift.

Examples of IRLGs: Arp 220 (IRLG/Sy 2).

Starburst Galaxy (SBG): are those in which star formation takes place at a rate much higher than the average rate over a lifetime. The clues come from the optical colors and spectra, which indicate high numbers of young stars, accompanied by strong IR emission. Starbursts occur in all types of galaxies. It is believed that they are induced by galaxy mergers and interactions. This is reminiscent of the hypothesis that the more powerful AGN activity is due to strong interactions between galaxies; in fact, it is quite possible that these more powerful AGN *also* have brief episodes of high rates of star formation, caused by chance galactic interactions.

Like IRLGs and Nuclear Emission Line Regions, Starburst Galaxies do *not* show broad emission lines.

Examples of SBGs: 3C 231 = M82.

Nuclear Emission Line Region (NELR): These are also known as Nuclear H II Regions (Nuc HII). Galaxy surveys reveal that many normal galaxies contain nuclei which exhibit narrow emission lines, such as the Balmer and [OIII] lines. Almost every bright spiral has a NELR. Late type spirals (Sb, Sc) without bulges have extended emission regions smaller than a kpc. The observed narrow emission lines are characteristic of H II regions ionized by hot stars. Apart from the rare cases where the emission line luminosity is very intense, most NELRs are probably stellar-driven, and hence *not* bona fide AGN. Like IRLGs and Starbursts, NELRs do *not* show broad emission lines.
Examples of NELRs: NGC 625.

The following sources were found to be invaluable for compiling the above review of the physical properties and classification of AGN:
Landolt-Börnstein (1982) [68]; Phinney (1983 Ph.D. thesis) [140]; Begelman, Blandford & Rees (1984) [9]; Blandford, Netzer & Woltjer (1990) [17]; Hughes (1991) [77]; Antonucci (1993) [3]; Megan Urry & Padovani (1995) [144].

5.1.2 AGN Unification

The many different categories of AGN can be reduced, or 'unified', into various sets containing fewer AGN types. One of the most influential observational factors allowing this process of *unification* is the inclination angle of the central AGN axis relative to our line of sight. Where this is the actual determining factor for the observational selection criteria, it is clear that the differences between the categories that are being unified are *incidental*, rather than essential.

The following is a list of the main avenues by which unification of various types of AGN

has been proposed in the past:

1. The **Optically Violent Variable Quasars (OVVs)**, **High Polarization Quasars (HPQs)** and **BL Lacertae Objects (BL Lacs)** can be viewed as belonging to the class of *Blazars*. They all have strong, non-thermal power-law optical continua, are variable on short timescales (days to weeks), and have significant optical linear polarization. Many of the radio-loud class show apparent superluminal beaming of jets from the parsec-scale radio core. With respect to the inclination angle, if 'side-on' radio galaxies are deemed to be Class 2 AGN, and 'peering-into-the-top' quasars are deemed to be Class 1 AGN, then it logically follows that the 'pole-on' blazars should be the Class 0 AGN. The main difference between the quasars and the BL Lacs is that the latter have less powerful continua, and the emission lines are weak or entirely absent. The physical interpretation is that we have an unobstructed view of the parsec-scale central BLR of the AGN. Any radio jets emitted in our direction show superluminal motions resulting from simple Doppler beaming and time delay effects. The continuum is so relatively strong in the BL Lacs that it drowns out both the broad and narrow lines normally seen in the cores of AGN.

2. The **Low Polarization Quasars (QSOs, RLQs, RQQs)**, **Broad Line Radio Galaxies (BLRGs)**, and **Seyfert 1s (Sy 1s)** are systems in which the inclination angle between the AGN axis and our line of sight is *low* say from 10 to 40 degrees, or thereabouts. These would be the 'Class 1' AGN systems (note that in this naming scheme, Sy 1s are Class 1 and Sy 2s are Class 2). Probably included with the Class 1 AGN are the intermediate Seyferts of Type 1.5. The main difference between the Seyfert 1s and the Quasars and BLRGs is that the Sy 1s are less powerful, and also are not able to generate prominent radio jet structures on scales of 10 kpc or more. The physical interpretation is that there is an anisotropic structure shielding the central BLR in the equatorial plane, often referred to as the 'molecular torus'. Provided our

inclination angle is less than about 40 degrees or so, or view of the central BLR is still fairly clear, but we lose the rapid time variability and strong Doppler boosted continuum radiation seen at almost pole-on ('down the throat') inclinations. In particular, our view of the central BLR is important in classifying the resulting optical spectrum as that from an AGN known to contain a region emitting broad emission lines.

3. The **Narrow Line Radio Galaxies (NLRGs)**, **Narrow Line X-ray Galaxies (NLXGs)** and **Seyfert 2s (Sy 2s)** are Type 2 AGN systems, in which the inclination between the AGN axis and our line of sight is *high*, say, greater than 40 degrees. Probably included in Class 2 are the intermediate Seyferts 1.8 and 1.9. The main difference between the NLRGs and the other NLXGs and Seyfert systems is that the NLRGs would be much more radio luminous, and also easily capable of generating jets on scales of 10 kpc or more. The physical interpretation of the Class 2 AGNs is that our view of the central BLR, in the infrared, optical, ultraviolet and X-rays, is 'blocked' to varying degrees depending on the observing wavelength (though the radio emission, if any, could still penetrate the torus). Thus, Class 2 AGN do not show obvious evidence for broad emission lines, except in careful observations of scattered light from regions that themselves have an *unobstructed view* of the BLR.

4. The Class 0 **OVVs & BL Lacs**, the Class 1 **RLQs**, and the Class 2 **RGs** are all radio-loud. This may be because their central engines can more readily drive a powerful radio jet out through the ISM and IGM. One suggestion is that these AGN contain a Kerr black hole that is rotating near its maximal rate; under these conditions, the ionized and magnetized plasma around the hole is swung into corotation, and, through a process still unknown, is eventually ejected from the black hole atmosphere at ultra-relativistic speeds.

5. The Class 0 **HPQs**, the Class 1 **RQQs**, and the Class 2 **Sy 2s & NLXGs** are all

radio quiet. They evidently lack the special physical properties that allow strong radio emission and extended structures to be formed in the radio-loud AGN.

6. The **Low Ionization Emission Line Regions (LINERs)**, the **Infrared Luminous Galaxies (IRLGs)**, the **Starburst Galaxies (SBGs)** and the **Nuclear Emission Line Regions (NELRs)** are collectively the 'Least Luminous' of AGN. Their power is mainly derived from stellar sources. They may be regarded as *currently* having insufficient power to excite a BLR, or drive a radio jet. Whether individual members of these classes once were more powerful, or else will be destined to be more powerful, is unknown. A possible physical interpretation is that these galaxies do not have an active central black hole that is accreting at the minimum rate required to generate the non-thermal power seen in the more luminous AGN. This is different from saying that these galaxies do *not* have black holes, but if such compact objects are found lying dormant in the centers of these more numerous galaxies, then that would indeed be a surprising and important discovery; it would suggest that a large fraction of all galaxies go through a phase of MBH accretion.

For further details on the evidence for unification of the different types of AGN, see the following review articles:
Begelman, Blandford & Rees (1984) [9]; Blandford, Netzer & Woltjer (1990) [17]; Antonucci (1993) [3]; Megan Urry & Padovani (1995) [144].

Many unification schemes depend on the existence of one or both of the following two effects:

- **Anisotropic Non-thermal Emission** from a central continuum source. This may be achieved most naturally by the Doppler beaming and boosting, in the forward direction, of broadband synchrotron radiation from a initially ultra-relativistic jet emerging from the vicinity of the compact central object.

- **Anisotropic Obscuration & Scattering** of the light from the central continuum source. In the case of obscuration, this effect would require the existence of an obstructing body in the plane normal to the rotational axis of the central AGN object. This has been proposed to arise from a dense, hot, molecular torus of gas and dust, with inner radius about 1 pc from the central object, and perhaps with an outer extent as large as 10 to 100 pc. Its purpose is to 'hide' a direct view into the BLR contained within a radius of 1 pc.

  In the case of anisotropic scattering, a dense cloud of dust or hot electrons may be able to provide the required scattering surface. This would still have to be distributed in a non-isotropic fashion, so the existence of a torus of the dimensions indicated above would indeed be consistent with the interpretation of the observed scattering anisotropies.

There is already much evidence for superluminal beaming from VLBI multi-epoch observations of compact, time-variable radio cores (see Zensus 1997 [152]).

Direct imaging of a possible obscuring torus has been obtained for the nearby LINER galaxy NGC 4261, using the HST. Figure 5-1 shows the geometric relation between the torus and the circumscribed radio jets. The torus is estimated to have an overall size of 2×10^{18} m, or about ~ 60 pc. This image presents suggestive evidence that the spin axis of the torus somehow determines the direction of the radio jet axis. In a similarly remarkable image of the radio-quiet galaxy M 51, a torus of similar dimensions found there lies perpendicular to the optical emission line 'ionization cone'.

Figure 5-2 shows one representation of how some of the various AGN classes may be unified together.

Having organized the observational facts into a (temporary) unified scheme, we can now turn to a discussion of the physics of the structures and emissions seen in AGN.

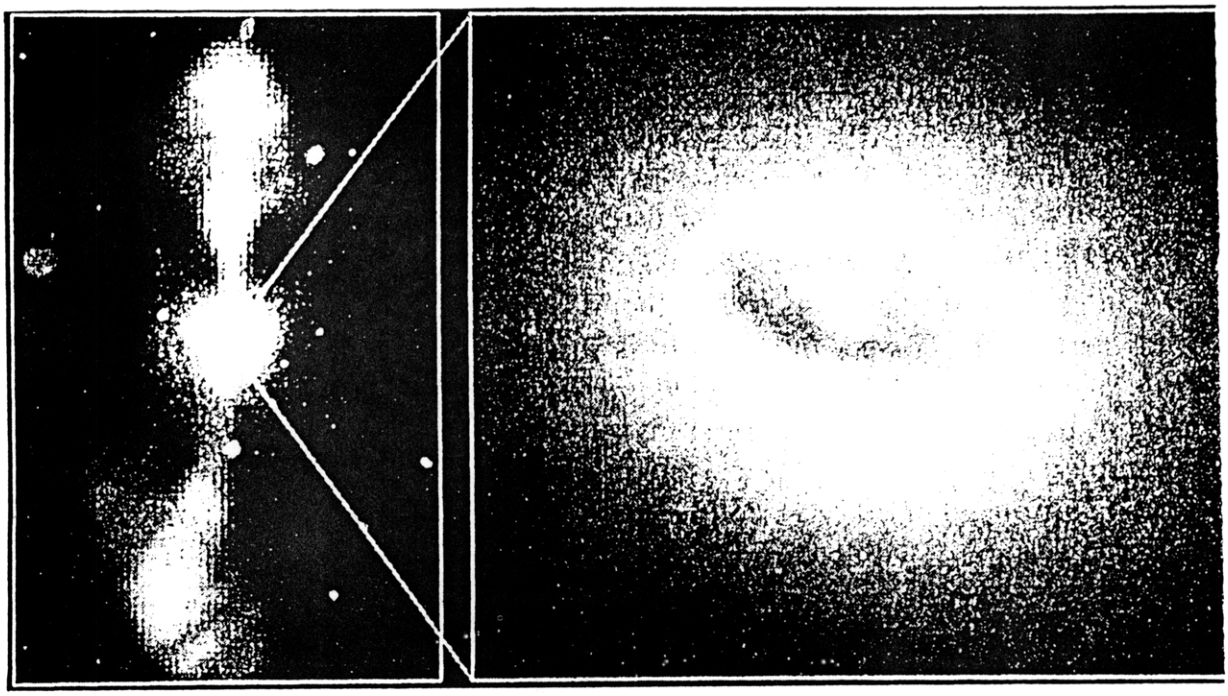

Figure 3 (*a*) Composite image of the radio jets and optical galaxy as observed from the ground (NGC 4261). (*b*) High-resolution optical image of the galaxy core, showing a dusty torus oriented perpendicular to the radio jets. Deconvolved *HST* image from Jaffe et al 1993.

Figure 5-1: Radio and optical imaging of the LINER galaxy NGC 4261 (3C 270). Left: a composite image of the radio jets and a ground-based optical image. Right: a deconvolved HST image of the galaxy core, showing a dusty torus oriented in the plane perpendicular to the radio jets. This figure has been reproduced from Antonucci (1993).

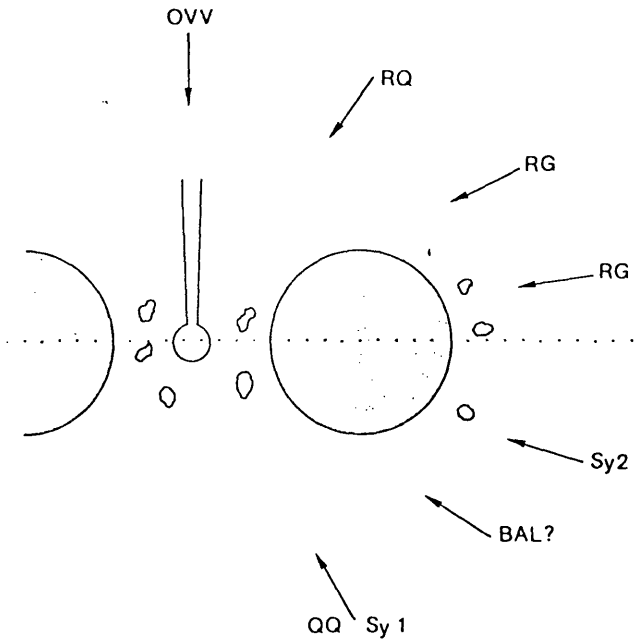

Fig. 13 : A unified model for AGN. An absorbing torus with a radius of a few pc surrounds the radiating nucleus. Inside the torus are the fast moving clouds of the Broad Line Region and outside the slower clouds of the Narrow Line Region. In the upper half of the figure is the case where relativistic jets are generated in the nucleus; in the lower half such jets are absent. Looking (nearly) into the jet the rapid variability of OVV's and BL Lac Objects would be seen; when the broad line clouds would be absent or the Doppler boosting very strong, no broad emission lines would be visible. At a larger angle from the jet axis a radio quasar would result. When the central source is obscured, but some of the broad line clouds still in view, the appearance is that of a radio galaxy with broad lines and at still larger angles a radio galaxy with only narrow lines would remain.

When, as in the lower half of the figure, no jet (or only a very weak one) is present radio quiet quasars and Sy 1 would result if the nucleus is in view and Sy 2 if not. Even though the collimated jet is missing a fast wind from the nucleus could be expected. Perhaps when this wind ablates the torus or a broad line cloud the Broad Absorption Line quasars would result. While this figure shows how much of the phenomenology of AGN may be produced in a simple model, the real situation is likely to be more complex with variability of the nucleus and intrinsic differences in the distribution of the gas clouds also playing a role.

Figure 5-2: A possible unification scheme for the various types of powerful AGN: The radio-loud objects are different aspects of the same central structure, and are represented by the different viewing arrows drawn in the top half of the figure. The radio-quiet objects share the same structure, but without the presence of the jet. Their viewing arrows are shown in the bottom half of the figure. This diagram has been reproduced from Woltjer's article from Blandford, Netzer & Woltjer (1990).

5.1.3 AGN Physics

The problems of understanding the physics of AGN, as implied by the complicated and abundant array of observational data, are many and difficult.
The two basic questions that need to be answered are:

1. How does the Central Engine form ?

2. Once the Central Engine is in place, how does it produce all of the observed phenomena in the various types of AGN ?

Figure 5-3 shows how it is expected that (given enough products of stellar evolution, or gas), a MBH will inevitably accumulate in the center of a galaxy (à la Hawking & Penrose theorem (1970) [67]).

Figure 5-4 shows how complicated the physics can be for the entirety of the structures associated with an active galaxy.

We now proceed to describe a possible series of physical structures and scales that could make up a radio-loud AGN, such as a Radio Galaxy or Radio-Loud Quasar.
Black Hole: From the observations of the dynamics of stars and gas in the centers of local galaxies, the inactive remnants of possible massive black holes are found, with masses in the range $10^6 < M_h < 10^{9.5} M_\odot$ (Kormendy & Richstone 1995). A statistical survey finds that as many as $\sim 20\%$ of nearby E-Sbc galaxies contain (mostly inactive) **Massive Dark Objects (MDOs)** in their nuclear centers. Since quasars were much more numerous, by factors of 10^2 to 10^3 in the Quasar Epoch, we do indeed expect some significant fraction of local galaxies to possess 'dead AGN engines' in their centers. However, it should be cautioned that a *proof* of the existence of MBH remnants in nearby galaxies is still beyond our current technologies.

According to a proposal by Roger Blandford, there are at least *four* major parameters that determine the observational features of the wide variety of AGN:

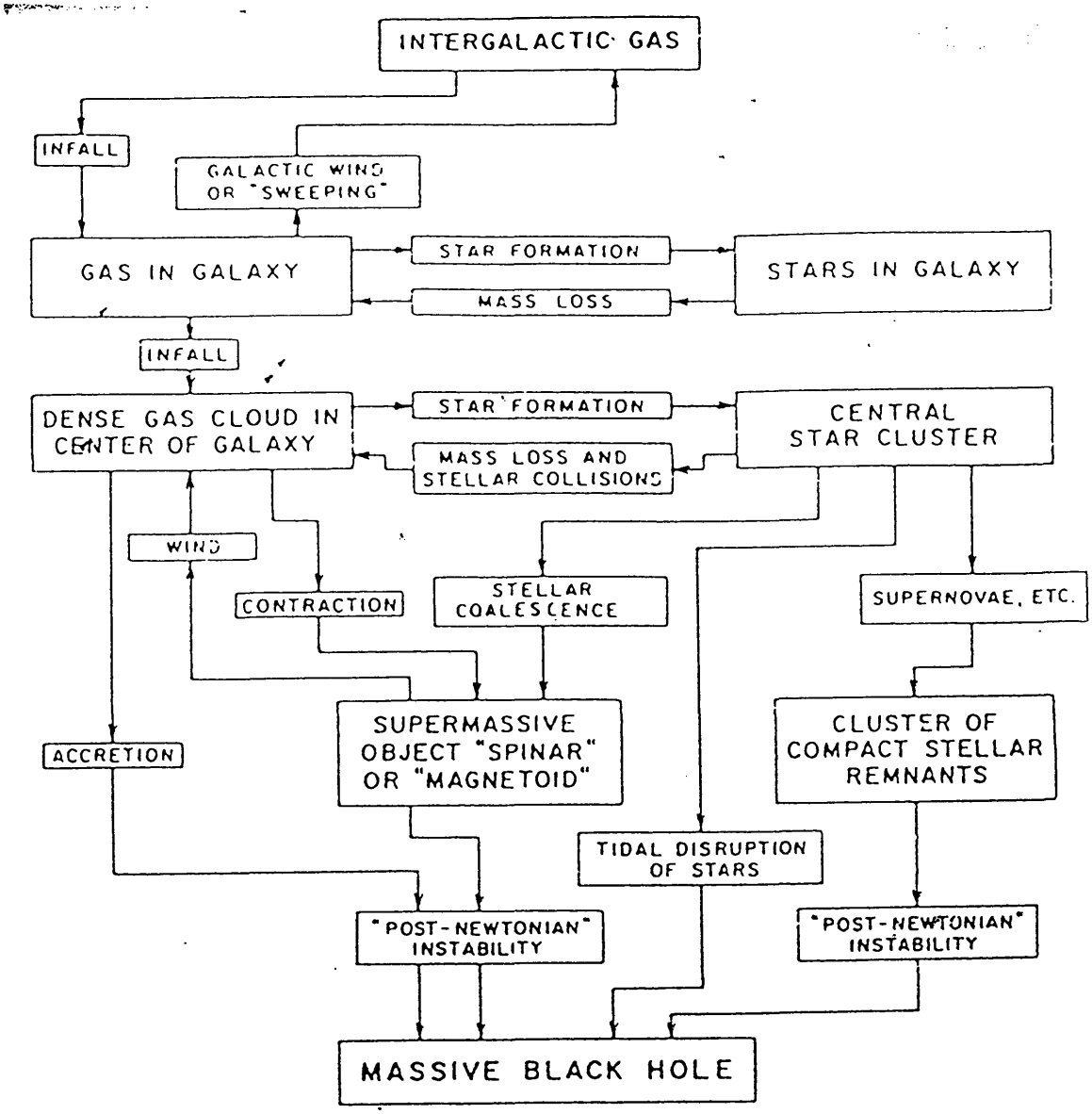

Figure 5-3: A possible flowchart diagram for the ultimate fate of the normal products of stellar and galactic evolution in the centers of galaxies, originally proposed by Martin Rees in 1978. Triggered by an unknown mechanism, gas and stars accumulate towards the center of the galactic nuclear potential well, interacting with each other in the process. The final results seem to inevitably be the formation of one or more compact objects, which eventually merge into, or fall into, the most massive collapsed object in the center of the galaxy; a massive black hole. It is this object which may be the key that unlocks the 'central engine' behind many types of powerful activity observed in AGN. This figure has been reproduced from Begelman, Blandford & Rees (1984).

EGRS: WHAT ARE THEY ?

See 1995 PASP review by C. Megan Urry.

FIG. 1—A schematic diagram of the current paradigm for radio-loud AGN (not to scale). Surrounding the central black hole is a luminous accretion disk. Broad emission lines are produced in clouds orbiting above the disk and perhaps by the disk itself. A thick dusty torus (or warped disk) obscures the broad-line region from transverse lines of sight; some continuum and broad-line emission can be scattered into these lines of sight by hot electrons that pervade the region. A hot corona above the accretion disk may also play a role in producing the hard X-ray continuum. Narrow lines are produced in clouds much farther from the central source. Radio jets, shown here as the diffuse jets characteristic of low-luminosity, or FR I-type, radio sources, emanate from the region near the black hole, initially at relativistic speeds. For a $10^8 M_\odot$ black hole, the black hole radius is $\sim 3\times10^{13}$ cm, the accretion disk emits mostly from ~ 1–30×10^{14} cm, the broad-line clouds are located within ~ 2–20×10^{16} cm of the black hole, and the inner radius of the dusty torus is perhaps $\sim 10^{17}$ cm. The narrow-line region extends approximately from 10^{18}–10^{20} cm, and radio jets have been detected on scales from 10^{21} to several times 10^{25} cm, a factor of ten larger than the largest galaxies.

2. OBSERVED PROPERTIES AND EMPIRICAL CLASSIFICATION OF AGN

- **Massive Kerr Black Hole**; 10^{-5} pc; GTR; MHD
- **Accretion Disk**; $10^{-4} - 10^{-2}$ pc; MHD+gas
- **Torus and Funnel**; $10^{-3} - 10^{-1}$ pc; MHD+gas+dust
- **Relativistic pc-Jet**; $10^{0} - 10^{3}$ pc; MHD; Doppler beaming
- **BLR Clouds**; $10^{0} - 10^{1}$ pc; gas+photons; dynamics
- **Dense Stellar Core**; $10^{1} - 10^{2}$ pc; stars; dynamics
- **NLR Clouds**; $10^{2} - 10^{3}$ pc; gas+photons
- **kpc-Jets, Hotspots, Lobes**; $10^{3} - 10^{6}$ pc; MHD; shocks; instabilities
- **Galactic Environment**: $10^{3} - 10^{4}$ pc; ISM, Star Formation
- **Clustering Environment**: $10^{4} - 10^{6}$ pc; ICM; Tidal Companions; Cooling Flows

Figure 5-4: A list of the various physical structures known or believed to exist in radio-loud AGN. Their sizes and the relevant physics are indicated. The figure above the list is reproduced from Megan Urry & Padovani (1995).

1. **Mass** M of the black hole. This is thought to range from $10^6 M_\odot$ up to no more than $10^{10} M_\odot$. The final black hole mass M_{final} determines the amount of available energy released over the lifetime of the AGN.

2. **Accretion Rate** $\dot{M}$ into the black hole. This determines the efficiency and speed with which enrgy can be extracted from infalling material.

3. **Spin** J of the black hole. The spin is important in some proposed theoretical processes that claim to be able to tap the large store of rotational energy of the black hole, at appreciable efficiencies. It seems that these processes are necessary for the efficient generation of powerful radio jets.

4. **Inclination** i of the rotation axis of the orbiting material to our line of sight. This is the key parameter that determines the incidental appearance of the AGN to us (e.g. radio galaxies look like quasars when viewed with low inclination angles i).

The scale size of the black hole is set by the Schwarzschild radius, which is $2.95 \times 10^{11} M_8$ m $= 1.97 M_8$ A.U. $= 9.57 M_8 \mu$pc $= 984 M_8$ light-seconds.

Accretion Disk: Accretion disks are expected to form in the equatorial plane of the rotating black hole, due to the infall of material with more than some small amount of specific angular momentum. Direct capture of material with low specific angular momentum can only occur for a small fraction of orbits lying within a given 'loss cone', whose opening angle decreases with distance from the hole. The accretion disks are essential components in theories of MBH power generation:

- They allow the gradual loss of gravitational binding energy, that drives at least some of the power output from the AGN.

- They store and transport angular momentum (via some viscous process which is unknown, but which may involve magnetic field lines threading an ionized plasma magnetosphere).

- They can generate heat, radiation, ionized particles, and gamma rays. The latter may be useful for the initiation of pair cascades within a central funnel along the hole's rotation axis.

- They naturally form massive toroidal structures of gas and plasma that may be crucial for the initial collimation of the parsec scale radio jets.

- They ultimately are the main fuel reservoir for the central black hole.

The source of the material can be local gas, dust, clouds, tidally-disrupted stars, and stars disrupted in collisions with others. Accretion disks may be geometrically thin or thick in local areas; far from the hole, the pressure support is from ionized gas, and the disk can be thin. Close to the hole, the radiation pressure can build up to the point where the disk becomes a thick torus. This accretion torus can serve to collimate outflows along the polar direction. Generally, a radiation-supported torus will develop as the accretion rate approaches the Eddington limit L_E.

The size of the accretion disk will be from the innermost stable orbit around the black hole, to as far as many hundreds of Schwarzschild radii away. The innermost stable orbit sets the maximum possible efficiency for the release of binding energy. The minimum stable orbital radius is $6GM/c^2$ for a Schwarzschild black hole, with a maximum efficiency $\varepsilon \sim 0.057$ of the rest mass energy. For a Kerr black hole, the radius and efficiency depends on how close to maximum spin the hole is rotating, and whether the orbit is corotating or not. A maximum efficiency of 42% of the rest mass energy can in principle be extracted via corotating orbits that reach in as far as half the Schwarschild radius: GM/c. Such orbits actually lie within the so-called 'ergosphere' of the Kerr black hole.

It is noted, in passing, that the *Penrose process* of energy extraction from the ergosphere region has a maximum efficiency of 29%. The Blandford & Znajek (1977) [19] electromagnetic extraction process can not only attain this level, but also provide a mechanism for

jet production to boot. Thus, the maximal efficiencies of energy extraction are of order $\sim$ 35% for rotating black holes, and $\sim$ 5% for non-rotating holes. Schwarzschild holes will be expected to be very rare, as the amount of local available angular momentum in the vicinity of a compact black hole region would exceed even the maximal Kerr angular momentum by about 7 orders of magnitude for a 100 million solar mass Kerr hole.

It is expected that hot, radiating accretion disks have sizes from about $10^{12}M_8$ m to $10^{14}M_8$ m, or more. The accretion disks may lead into cooler molecular gas tori further out.

Highly variable Xray emission (e.g. in Seyferts) is believed to originate from within about 100 μpc $\sim 3 \times 10^{12}$ m, which is about a few light hours away from the hole. UV radiation comes from radii 10 times further out, at 1 mpc $\sim 3 \times 10^{13}$ m. At this point, the disk is still probably a thick, radiation-supported torus. However, at 10 mpc $\sim 3 \times 10^{14}$ m, the disk can be cool enough to be supported by ion pressure, and it probably becomes thin. Its hot surface may be able to generate the broad band optical continuum seen in quasars, for example.

Compact Radio Core: At 0.1 pc $\sim 3 \times 10^{15}$ m, we reach the smallest physical scale that can be imaged (by the high frequency VLBI interferometers). The radio core and jet are optically thick, and hence undergo self-Compton scattering of the synchrotron radiation photons. On this scale are seen the emerging superluminal jets, which are evidence for bulk relativistic flow with measured Lorentz factors typically in the range $5 < \gamma < 30$. The mechanism for the driving and collimation of these relativistic bulk flows is unknown. The material could possibly be made up of plasma, electron-positron pairs, or even simply intense Poynting flux. From the optical spectra of Seyferts and other nearby AGN, the maximum size inferred for a possible electron scattering region is about at this scale, $\sim 10^{15}$ m.

Broad Line Region & Molecular Torus: The Broad Line Region (BLR) consists of many hot clouds that are in vigorous motion around the central regions. They lie roughly within the region from 0.1 to 10 pc ($3 \times 10^{15} < R < 3 \times 10^{17}$ m). The observed line widths,

if interpreted as Doppler motions along the line of sight, can be anywhere from 1,000 km/s to as high as 10,000 km/s. No narrow forbidden lines are detected in some AGN spectra, implying high electron densities ($n_e > 10^8 cm^{-3}$). The presence of the semi-forbidden line CIII] λ1909 requires electron densities to not exceed a certain level ($n_e < 10^{10} cm^{-3}$) in at least part of the BLR. As recombination times at these densities is of order a few days, so the BLR should respond on this timescale to changes in the continuum luminosity of the central source.

A thick torus of molecular gas starts at $\sim$ 1pc (3×10^{16} m), and it is implicated in causing the observed obscuration of Sy 1 BLRs in Sy 2s. The molecular torus can stretch over 2 decades of length, from 1 – 100 pc ($3 \times 10^{16} - 3 \times 10^{18}$m). It contains relatively cool clouds, dust and gas. This structure has been imaged clearly by HST in the nearby galaxies NGC 4261 and M 51.

Dense Stellar Cluster: On a scale of $\sim$ 10 pc (3×10^{17} m), the local stars are likely to form a cuspy spatial distribution in the strong gravitational field of the massive black hole.

Narrow Line Region: The Narrow Line Region (NLR) stretches from 100 pc to 1 kpc ($3 \times 10^{18} - 3 \times 10^{19}$ m), and consists of cooler, slower moving clouds than in the BLR. The intensity ratios of forbidden lines imply NLR electron densities in the range $10^3 < n_e < 10^4 cm^{-3}$. A recent observational discovery, from HST imaging of nearby galaxies, is that the NLR region may be concentrated into two 'ionization cones' leading from the central BLR. These cones are found to be aligned with the radio jets, which themselves presumably emerge from along the rotation axis of the central MBH.

Galactic Nuclear Bulge: The host galaxy nucleus is about 1 kpc in size (3×10^{19} m), and it is on this scale that the VLA and other aperture synthesis imaging arrays can start to resolve out the jets on kiloparsec scales. Radio sources smaller than this are either 'weak radio sources', or else powerful but 'compact'. In the starburst nuclei, there is evidence for widespread high rates of star formation throughout the galaxy nucleus; the resulting

emission will generate much radio and IR emission; these may be attributed to the more rapid evolution of high mass stars, accompanied by their supernova explosions and mass-loss winds.

In some galaxies, there is observational evidence for non-axisymmetric mass distributions, in the form of stellar bars and warped molecular and gas disks. Such irregularities may help to drive mass into the central NLR and BLR, and thus fuel the AGN. A trigger is required, and it may be the same as the one thought responsible for the starbursts seen in active galactic nuclei.

Host Galaxy: The host galaxy itself is of order 10 kpc in radius (3×10^{21} m). Powerful radio galaxies are known to invariably occur in elliptical hosts, which are often giant ellipticals in high density environments. Due to the very strong quasar optical continuum, it is not yet possible to find out which types of galaxy host the distant QSOs, but the low redshift examples have been seen in HST images to occur in both spirals and ellipticals. The lower power Seyferts are found in spirals, many of which have peculiar properties. Large quantities of dust and molecular gas, on galactic scales of 1 to 10 kpc, can efficiently re-radiate central continuum light in the IR.

Sometimes, on this scale, evidence is found for orbiting companions in the middle of an interaction or merging process. Such events are expected to be relatively fleeting, so it is more likely to see the results of such an event, rather than to see it in progress. External clouds, satellite galaxies and globular clusters may be able to sink into the nucleus by the gravitational process of dynamical friction.

Kiloparsec-scale Radio Jets: On 100 kpc scales (3×10^{21} m), only a mature and powerful radio jet will be able to reach out into the IGM. These structures are enormous, and contain much of the energy liberated by the MBH accretion processes on a scale that is about 9 orders of magnitude smaller in linear size, and 27 orders of magnitude more compact in volume ! An orbiting companion on this scale may eventually interact strongly with the host galaxy

of an AGN. Tides can be raised in the host galaxy, which may encourage the flow of gas into the central regions. If the AGN is near the center of a cluster, we may see evidence for a cooling flow nearby, with enormous mass flow rates of 1000 $M_{\odot}yr^{-1}$, a potentially excellent fuel source for a powerful AGN.

Environment of AGN Host Galaxy: On 1 Mpc scales (3×10^{22} m), only the very largest kiloparsec scale jets of the Giant Radio Galaxies will be seen. The general environment of an AGN may be important in providing conditions likely to influence the birth of the AGN (high galactic densities would increase the rate of strong interactions and mergers), and also the kinematic development of the extended radio jets as they travel through the IGM.

For further details, see the following references:
Rees (1984) [116]; Begelman, Blandford & Rees (1984) [9]; Phinney (1983 Ph.D. thesis) [140]; Blandford, Netzer & Woltjer (1990) [17].

5.2 Intrinsic Properties of Radio-Loud AGN

All galaxies are radio sources at some level, as they are able to produce at least the synchrotron radiation from supernovae, as well as thermal bremsstrahlung from ionized gas in HII regions. However, we are interested in the properties of radio-loud AGN, which require a *non-stellar* component to be present in the emitted radiation. This usually comes in the form of a very broad-band power-law continuum that can run over the entire accessible electromagnetic spectrum, in some cases. This is *non-thermal* radiation, and it usually emanates from a central core source. To make a comparison between an AGN and a 'normal' galaxy, we note that out own Galaxy has a radio luminosity of around $10^{30}WHz^{-1}$, while the most powerful radio galaxies and quasars can emit as much as $10^{38}WHz^{-1}$ in radio power. The energy contained in the extended structures of powerful radio-loud AGN can be as high as

10^{60} erg, or more. This presents a definite challenge to those who try to model the way in which this enormous power and energy can be generated.

Of the many different types of AGN reviewed in the previous Section, radio-loud AGN include: radio-loud quasars, FR II and FR I Radio Galaxies, OVV Quasars, BL Lac objects, and Broad and Narrow Line Radio Galaxies. The properties of radio-loud AGN have been classified in a wide variety of ways: via their radio luminosity; radio spectral index; radio morphology; and the width of their optical emission lines. Here, we concentrate on some of the more important physical characteristics of radio-loud AGN.

Optical Counterparts: Radio galaxies and BL Lacs are invariably found in luminous ellipticals. Powerful radio galaxies emitting about 10^{34} to 10^{39} W are usually associated with giant ellipticals of absolute visual magnitudes of $\sim$ -21. Radio loud quasars are too optically bright to tell what the type of the host galaxy is, though HST imaging of low redshift QSOs show that they are not restricted to lie in one type of host galaxy. The identifications of optical counterparts are crucial for the estimation of redshifts to AGN, and the optical spectra provide valuable information on the physical conditions. Without the redshifts, one cannot directly obtain estimates of the intrinsic physical properties of their underlying structures. High redshift radio galaxies and quasars are usually *red*, due to the cosmological Doppler shifting of their intrinsically blue continua. Very high redshift radio sources may need to be detected in the infrared, as the blue light from the elliptical hosts rapidly decreases in the near UV.

Spectra: Radio galaxies and quasars all show strong emission lines, both narrow and weak. These lines are superimposed on a power-law continuum, often with a broad or 'big blue bump' in the optical and UV wavelengths. This bump has been modelled as arising from thermal radiation from a central accretion disk or torus. Broad line radio galaxies share similar characteristics with the Seyfert 1s, while Narrow Line radio galaxies can be unified with the Seyfert 2s. It is possible that these two types of radio galaxy are the radio-loud

versions of the Seyferts.

Redshifts: The mean redshift of extragalactic radio sources in the well-defined bright radio surveys is about ~ 0.8 (Condon, 1984ab [32], [31]). Radio galaxies are found at low redshift, but their spatial density in our neighborhood is much lower than their density and luminosity during the 'Quasar Epoch', which shows a peak in the region $2 < z < 3$. The highest known redshift quasars and radio galaxies are now approaching 5, by which time there seems to have been a real decline from the great activity seen in the lower redshift peak in the quasar counts.

Projected Linear Sizes: The radio emitting structures span a very wide range in projected linear size, from the highest routinely achievable VLBI resolution limit of ~ 1 milli-arcsecond (which is ~ 5 parsecs, for a source at a typical cosmological distance of 1 Gpc), up to several Megaparsecs or more for the rare *Giant Radio Galaxies.* At least 2% of bright radio galaxies appear to have projected linear sizes in excess of 1.5 Mpc. The largest known radio galaxy is 3C 236, which at 1.4 GHz has a projected linear size of ~ 6 Mpc.

The Power-Projected Size (P-D) Diagram for the well-studied 3CR sample shows that the more powerful radio galaxies seem to be smaller in projected linear size D. The reason for this is unclear, and several physical and observational selection effects may have come into play. For example, the higher redshift galaxies in a flux limited sample must be intrinsically brighter. If for some reason radio galaxies were relatively stunted in their growth at high redshifts, this would then explain the apparent trend. There are other possibilities, including the beaming scenario; Doppler boosting would cause a bias towards bright, small objects.

Radio Luminosities: The intrinsic luminosities of AGN vary over a wide range. However, the FR I sources invariably have hot spots close to the core, with decreasing surface brightness with distance away from the core. The more powerful FR II sources have terminal hot spots far from the core. There is a clear luminosity cut between the two populations, and this is thought to signal a transition from subsonic to supersonic flow. This flow refers to the

velocity of the jet fluid, not of the advance of the jet head.

The morphologies and spectra come in a limited variety of types. See the review article on 'Radio Galaxies and Quasars' by Kellermann & Owen, in the book by Verschuur & Kellermann (1988) [146], for further details.

Radio Morphologies: The morphologies of PRGs have been especially important in helping us understand the physics of the synchrotron emitting plasma ejected by the central engine. There are two broad angular size classes for radio-loud AGN: compact and extended. As a first significant step after the discovery of double lobed structure in radio galaxies, Fanaroff & Riley (1974) [48] found a clear connection between radio morphology and radio power: if the ratio of the distance between the two most intense hot spots on either side of the nucleus is greater than half of the overall source size, the radio galaxy was invariably more powerful than a certain measurable luminosity level, which at 178 MHz was $P_{FR} \sim 2 \times 10^{26} WHz^{-1}$. Translating this figure to the standard 1.4 GHz value, using a typical steep-spectrum index of $\alpha \sim -0.8$, gives $4 \times 10^{25} WHz^{-1}$. This is about half a decade above the chosen dividing luminosity between WRGs and PRGs. One interpretation of this result is that the hot spots represent a transition from supersonic to subsonic flow; in more powerful sources, this would be expected to occur further away from the central engine. The radio galaxies above the Fanaroff-Riley break are named FR II, or *Edge-brightened Radio Galaxies*, while the weaker ones are FR I, or *Edge-darkened Radio Galaxies.* Classic examples are Cygnus A (FR II), and Centaurus A (FR I). Hercules A shows both inner bright areas, and outer hot spots. It luminosity is near the FR break, and so it appears to be a transitional case.

With improvements in aperture synthesis interferometry, it was found that the ubiquitous double-lobed structures, first seen in the pioneering aperture synthesis of Cygnus A (Dennison & Das Gupta 1953, [80]), were actually fed by *jets.* These are thought to be the channels through which highly energetic and magnetized plasma is pumped outwards from the radio

core. The hotspots are sites where the plasma is shocked through sudden deceleration, and the lobes are repositories of the aging post-shock plasma. Some hotspots are seen to emit non-thermal radiation in the optical regime – as the radiative lifetimes of electrons at the very high optical frequencies are so short, this clue is an indication of the need for *continued* energy input from the central engine through the beam pipeline. It is remarkable to note that, in the majority of cases, the jets retain their stability and alignment over their entire journey from the pc to Mpc scales (as evidenced by closer VLA and VLBI inspection of the giant radio galaxies, for example).

There is an interesting sequence of morphologies that correlate with radio luminosity; the FR IIs are powerful, symmetric and double-sided. The radio axis is linear, adhering to the classic core-double mold. The magnetic field **B** is oriented parallel to the jets (it is assumed that it is perpendicular to the **E** field, and that there is no appreciable Faraday rotation along the line of sight).

FR Is are more complex in structure; they can be asymmetric or symmetric. Symmetrical FR Is have the classic edge-darkened morphology on both sides of the core, and are generally of lower luminosity than the Asymmetrical FR Is. The magnetic field **B** is oriented perpendicular to the jets. Asymmetrical FR Is have two lobes, but just a single visible jet. They are intermediate in luminosity between the FR IIs and the symmetric FR Is. The magnetic field **B** is initially oriented parallel to the jet on kpc scales, but this gradually evolves to being perpendicular to the jet on $\sim$100 kpc scales. It thus seems that the orientation of **B** depends on the flow speed of the jet. Fast flow will tend to shear the **B** field closer to being parallel to the flow.

The Narrow Angle Tails (NATs) and Wide Angle Tails (WATs) show evidence for orbital motion in progress.

There are 3 types of symmetry: most show the linear structure that is consistent with the double beam model. Some show C-type mirror symmetry (e.g. 3C 449), which could be

due to orbital or ballistic motion in a dense IGM. Others show S-shaped inversion symmetry (e.g. 3C 47; 3C 315) that may be due to the precession of the spin axis of the central object, due to the torquing from a companion massive object or disk.

Compact radio sources are revealed in their structure by VLBI mapping. The basic VLBI structures seen are: point; core-jet (e.g. 3C 273), and compact VLBI Doubles (e.g. CTD-93). There are also the famous superluminals.

Radio Spectral Indices: A natural bimodality in the radio spectral indices of powerful extragalactic radio sources appears in high frequency radio continuum surveys; those sources with relatively flat, or inverted, non-thermal spectra are named *Flat Spectrum Radio Sources*, with $\alpha < 0.5$; $F_\nu \sim \nu^{-\alpha}$. Those with steeper radio spectral indices are named *Steep Spectrum Radio Sources.* These categories of powerful extragalactic radio source include both the RLQs and the PRGs.

The majority of flat spectrum radio sources tend to be compact, variable, with a prominent and optically thick radio core. This core is found to be coincident with the nucleus of the host galaxy, and it may, from time to time, eject new components that seem to travel outwards at superluminal speeds. Very Long Baseline Interferometry (VLBI) is required to resolve the details and motions, on length scales of 1–10 pc and timescales of weeks to years, of a radio core component,

The majority of steep spectrum radio sources have extended radio emission (i.e. external to the radio core). This is usually optically thin, except in the recently energized regions, such as in the hotspots.

In the early radio continuum survey investigations of powerful radio sources, it was found that the flat spectrum sources were almost all compact, and the steep spectrum ones were almost all of the same classical 'double-lobe' type. This dichotomy has since been broken by the discovery of the class of *Compact Steep Spectrum* sources, which appear at VLBI resolution to be much smaller versions of the classical doubles found on the kiloparsec scale.

As steep spectral index is no longer a sufficient condition for the presence of kpc-scale extended radio emission, the terminology that is now used is simply: *Core-dominated Radio Source* versus *Lobe-dominated Radio Source.*

There are other types of radio sources classified by radio spectrum: the Ultra Steep Spectrum (USS) Radio Source, and Gigahertz Peaked Spectrum (GPS) Radio Source.

Superluminal Motions: These show apparent proper motion speeds ranging anywhere from 5 to 30 times the speed of light.

Variability: only the radio cores are variable, as the extended structures are very large. The variability can be as short as a day, as in the so-called Intraday Variables, or as long as the several years it takes some parsec scale jets to emerge from the inner BLR (at near light speed).

Linear Polarization: radio linear polarizations can be quite high in radio sources, as this is a natural prediction of the synchrotron radiation mechanism. However, there is the effect of differential Faraday rotation due to different columns of ionized gas along the line of sight to the various parts of the radio source. This tends to reduce the levels from $\sim$ 10–70% down to just a few % or less.

Cosmological Evolution: For the latest reviews on the cosmological evolution of EGRS, see the work of J. Condon, J. Wall, J. Dunlop and J. Peacock. The general picture is that the comving space densities of both powerful radio galaxies and radio-loud quasars was much higher in the redshift range $1 < z < 5$, than it is locally today. Either they were more numerous, or more luminous, or both (one cannot exactly tell how the balance lies between density and luminosity evolution, as this information is not directly measurable from the evolution of the global radio LF).

Condon (1984a [32], 1984b [31], 1988 [146], 1989 [33]); Wall, Shaver et al. (1994 [147], [53], in IAU 175, Ekers et al. 1996, [46], 1996 [125], 1997 [148]); and Dunlop, Peacock et al. (1990 [45], 1997 [44], [78]).

The following sources proved to be very useful for the detailed accounting of AGN radio source properties:
Begelman, Blandford & Rees (1984) [9]; Kellermann & Verschuur (1974, 1988) [85]; Blandford, Netzer & Woltjer (1990) [19]; Hughes (1991) [77].

5.3 Energetics and Timescales

The following are the basic observational facts related to MBH models (Kormendy & Richstone 1995, [86]):

- Rapid timescale for variability of the radio core, implying compactness.
- VLBI imaging of radio core, also implying compactness: the AGN engines are tiny.
- Superluminal jets in AGN cores, implying relativistically deep wells.
- AGN engines remember their jet ejection directions for a very long time, suggesting that they are excellent gyroscopes that are not easily torqued. This implies that the compact engines are very massive.
- The large energy output from a compact region entails very high efficiency not available from normal stellar processes (not even from thousands of supernovae per year that may result from starbursts).

The overall power scaling is expected to be some appreciable fraction of the Eddington luminosity L_E. The associated Eddington accretion rate $\dot{M}_E$ and Eddington/Salpeter timescale t_E are important for the consideration of the evolution of all powerful AGN. (see the article by Blandford, in book by Blandford, Netzer & Woltjer, 1990).

The **Eddington luminosity** L_E sets the maximum level for the release of radiant energy from any gravitating ionized gas of mass M. It is the maximum radiant luminosity whose

(outward) pressure L_{rad} can just be balanced by the (inward) pull of the emitting mass M. The outward radiation pressure will tend to blow apart the outer layers of the mass, due to the interaction between free electrons and photons, whose strength is set by the Thomson cross-section.

$$L_E = \frac{4\pi G c m_p M}{\sigma_T}. \tag{5.1}$$

It is about 32,700 $L_\odot$ for a 1 $M_\odot$ object:

$$L_E/L_\odot = 3.27 \times 10^4 (M/M_\odot). \tag{5.2}$$

Associated with the Eddington luminosity is the **Eddington accretion rate**, which is the mass accretion rate that would need to be supplied in order to sustain a steadily radiating system at the Eddington limit, assuming a *perfect* conversion of matter into energy:

$$\dot{M}_E = \frac{L_E}{c^2} = \frac{4\pi G m_p M}{\sigma_T c}. \tag{5.3}$$

The Eddington accretion rate is about 2.2 $M_\odot yr^{-1}$ for a billion solar mass object, assuming 100% mass to energy conversion:

$$\dot{M}_E/(M_\odot yr^{-1}) = 2.22(M/10^9 M_\odot). \tag{5.4}$$

Salpeter (1964) [121] was able to show that any object whose luminosity is limited by the Eddington criterion will grow in mass on a timescale *independent of the mass.* This timescale is about 4×10^8 yr, and it is set by the fundamental constants of Nature, and the Thomson opacity of an ionized gas. It can be derived by dividing the mass M of the object by the Eddington accretion rate $\dot{M}_E$:

$$t_E = \frac{M}{\dot{M}_E} = \frac{\sigma_T c}{4\pi G m_p} = 4.51 \times 10^8 yr. \tag{5.5}$$

This evolutionary **Eddington/Salpeter timescale** for accretion onto the central AGN mass will be an important theoretical link in the chain of inference to be presented in the argument for non-relativistic jet advance speed in the MIT-VLA EGRS sample. It should be noted that in AGN which have a mean accretion rate of some fraction f of the Eddington limit, the corresponding timescale for the growth of the central engine would be *longer* by that factor f. However, for AGN, f cannot stray too far away from unity, as otherwise the required energy conversion efficiency would drop below the level required to explain the observed luminosities.

The lifetime of the central engine might also be estimated very crudely by dividing the minimum equipartition energy in the extended structures, by their total radio luminosity, as both measures directly originate with the activity in the nucleus. The following is a pure thought experiment, with reasonable guesses made for the input numbers: for a powerful FR II radio galaxy radiating at $10^{27} W Hz^{-1}$, over a bandwidth of 10 GHz, the power output would be $10^{37} W$. If such a galaxy had 10^{53} J of minimum equipartition energy in the jets and lobes, the implied radiative lifetime would be 320 million years. These numbers show that the derived minimum equipartition energy, for a powerful galaxy such as this, is roughly consistent with the Eddington/Salpeter timescale for the engine growth. It seems that the radiative lifetime of the extended structures might be of the same order as the lifetime of the central engine. Certainly, we would expect that the radiative lifetime could be *no longer* than the engine lifetime. But it might also be possible that the radiative lifetime could be much shorter than the engine lifetime. The above thought experiment is suggestive, but inconclusive without further data on the lifetimes of AGN cores, and of the radiating extended structures.

The direct radiative output from nucleus is of order $10^{35}W$, which is typically much less than the beam luminosity required to supply the extended radio jets and lobes (Rees 1984 [116]). It is estimated that there is 10 times more luminosity in the Cygnus A jets than in the core radio emission. Radio galaxies are therefore expected to channel most of the available energy into the directed kinetic energies of the twin jets. Thermal output from powerful radio-loud AGN is less than $10^{-3}L_E$, implying slow accretion through an ion-supported torus onto a massive spinning black hole.

The integrated quasar light places lower limits on the amount of massive remnants in the form of compact objects in centers of galaxies (Choksi & Turner 1992 [29], Small & Blandford 1992 [129]). From arguments such as these, there should be an appreciable fraction of local galaxies that contain Massive Dark Objects (MDOs) in the centers of their nuclei.

However, against the MBH hypothesis for the MDOs in the centers of nearby galaxies: why are AGN MDOs elusive, and MDO nuclei so inactive ? We are still 10^5 orders of magnitude away from detecting a MBH within its Schwarzschild radius. Could MDOs be dead star clusters, from starbursts ? Could MDOs be just concentrations of halo dark matter ?

Perhaps a study relating the mass of the central object in a radio-loud AGN, to the amount of energy, and kinetic and radiative luminosity in the extended structures, would reveal more about the remnants in the centers of local galaxies.

5.4 Observational Data and Limitations

There is abundant observational data on radio-loud AGN. The best studied sample, in terms of completeness in radio and optical identifications, and redshifts, is the $\sim$ 350 source 3rd Cambridge Revised Sample. The reader is referred to the literature publications by Longair, Dunlop, Peacock and Wall for the results of this well studied survey. There are also other well-defined and larger surveys, but none have reached 100% completeness as the 3CR has

done (only in 1996!).

The limititations of dealing with incomplete samples can be severe. Lack of redshift information is frustrating, but, as the author will show, making a reasonable assumption for the mean redshift will not have a significant effect on the measurement of projected linear sizes, as there is a *convergence* in the angular size distance beyond a given redshift in all Friedmann universes.

5.5 Proposal of a Formal Model for Radio-Loud AGN

The following is a sketch of what a unified model for radio-loud AGN might look like. It is based purely on the author's synthesis of ideas readily obtainable from the published literature. At the end of this section, a partial list of researchers is given, whose models have inspired the current synthesis. The numerical details have not been filled in, but these would more appropriately be ascertained when a decision is made as to which "sub-models" would be compatible with the general framework outlined here.

It is noted that some of the following sub-models are specified in more detail later in this Chapter. These are the sub-models that address the particular issues mentioned at the beginning of this Chapter: (1) accreting massive black hole populations, and (2) the speed of advance of the jet head in the extended jets of EGRS. The first detailed sub-model is given in Section 5.6, and the second detailed sub-model is given in Section 5.7.

Galaxy Creation: In the merging/interaction hypothesis for the trigger of AGN activity, the basic ingredients are galaxies, preferably packed in dense environments. Thus, AGN activity requires the existence of galaxies prior to the observed phase of rapid AGN evolution in the redshift range $1 < z < 5$. The highest redshift AGN detected so far is a quasar close to $z = 5$. This is at an epoch 6.8% of the age of the Universe ($t_0 = 6.7\ h^{-1}$ Gyr) for $\Omega_0 = 1$, which is 450 h^{-1} Myr. For $\Omega_0 = 0$, the corresponding values are 16.7%, 10.0 h^{-1} Gyr, and 1670 h^{-1} Myr. Thus, by about 1 billion years after the Big Bang, galaxies are required to be

well on their way to forming, if AGN are to be initiated by their strong mutual interactions.

Galaxy Interaction Rate: On the hypothesis that powerful AGN are initially triggered by the *strong interactions* between galaxies, one needs to know the rate of such strong interactions as a function of the cosmic time t (or redshift z). It is noted that a strong encounter is a necessary requirement, as it is the nuclear region that needs to be disturbed, not the galaxy peripheries. One might expect that such strong encounters are to be preferentially found in relatively high density environments, such as in galaxy groups and clusters. This is observationally borne out by the fact that most powerful radio sources are found in ellipticals, rather than spirals or irregulars, and also by the fact that ellipticals are known to be preferentially found in dense galactic environments (this is known as the galaxy morphology-density relation, originally noticed by Hubble and Zwicky in their observations of high spatial densities of ellipticals in rich galaxy clusters, and also clearly quantified more recently by A. Dressler (1980) [43]).

Before proto-galaxies formed, the interaction rate is clearly nil. As galaxies start to form at very high redshift ($z > 10$, say), the interaction rate between the proto-galactic clouds, somewhat enriched by the first few generations of massive stars, would start to rise, but it is not clear that AGN activity would necessarily start this early. Sometime just beyond the redshift of the most distant known quasar ($z \sim 5$), AGN activity must have started to develop in a well-organized way.

When clusters form, bringing galaxies into closer proximity, the interaction rate would be expected to increase. With the expansion of the Universe, the proper galaxy density decreases, so the general expectation is that the merging rate will have a peak at some early epoch in the past. It may be possible that the so called *Quasar Epoch*, stretching from $1 < z < 5$, with a peak in the region $2 < z < 3$, is mainly determined by the galaxy interaction rate, though this is at the level of an inspired guess.

With the above considerations in mind, and also in the spirit of the mathematical formalism developed in Section 5.6, we may posit that the AGN creation rate $C(t)$ is strictly proportional to the Galaxy Strong Interaction Rate, denoted by $R_{gi}(t)$.

$$C(t) = f_1.R_{gi}(t), \tag{5.6}$$

where the precise value of the proportionality constant f_1 would have to emerge from a theory and computation of galactic interactions in the high redshift universe.

A further complication to this simple formula will be given in the next stage of the model.

Black Hole Creation: If we divide all AGN into subpopulations parameterized by the unique value of the *final remnant mass* M_f of the central *massive black hole (MBH)*, a possible formulation that addresses the wide variation in power output of AGN might be the following:

$$C(M_f; t) = f_1(M_f).R_{gi}(t), \tag{5.7}$$

where, according to the results of Section 5.6, the function $f_1(M_f)$ may be determined from a knowledge of the MBH accretion law, and the observed final mass spectrum $\Phi(M_f)$ of MBH remnants in the centers of a well-defined, large sample of local galaxies (e.g. see the review by Kormendy & Richstone 1995 [86]).

It should be noted that the core collapse times of the centers of galaxies is too long for MBHs to have accumulated via dynamical relaxation of the central dense stellar clusters. This is definitely *not* a route for the turning on of quasars in the high redshift Universe.

Massive Black Hole (MBH) Accretion: The actual accretion law for a Kerr black hole should include at least its only 3 parameters: mass, spin and charge. Charge is not

expected to last very long, due to the presence of ionized plasma. It has been suggested that the rapid spin of the hole is a strong requirement for the generation of radio jet and lobe structures. The simplest possible accretion law is one which gives the accretion rate as a function of mass only, by perhaps selecting some appreciable fraction of the Eddington limited accretion rate. In this case, the accretion law is a simple proportionality between the fractional Eddington-limited accretion rate and the mass of the massive black hole.

Evolution of MBH Accreting Population: Given a final mass spectrum for black hole remnants, and an assumed accretion law, one can find out what the time evolution of the mass distribution in holes was. The necessary formalism appears in Section 5.6, and a concrete example in the case of young stars can be found in the 1994 ApJ papers of the author (Fletcher et al. 1994a,b [51], [52]).

Final MBH Mass Spectrum: Here, we may assume, somewhat arbitrarily, that the final MBH mass spectrum is proportional to the mass function of elliptical host galaxies. This in turn should be related to the observed luminosity function for ellipticals. Once a remnant MBH spectrum is obtained, the branching ratio between sudden cessation of accretion $\mu(M)$ and continued accretion $\dot{M}$ can be calculated.

Efficiency Models: Once a power output scale is set, e.g. by the assumption of an Eddington-limited energy production by a compact MBH and accretion disk, the question of the efficiency comes up. Firstly, how much of the rest-mass energy of the infalling matter can be expected to be turned into useful energy output ? Theoretical estimates of the maximum possible efficiencies show that not more than about 30–40% of the rest mass is available in the case of rotating Kerr black holes.

Secondly, once the bolometric power output has been calculated, one needs to ask how

the energy is distributed among the many possible modes (e.g. heat, radiation, mechanical power). A large fraction of the energy must go into each one of these processes, which are all known to occur in the core.

Compact Core Luminosity: In the case of observations in a particular band, the compact core luminosity is an important quantity to calculate, as often this will determine whether the AGN is visible or not. In the case of radio synchrotron emitting cores, the radiation is known to be optically thick, with a turnover or peak frequency determined by the compactness and the magnetic field strength. The spectral index at low frequencies will be inverted ($\alpha = -2.5$), while at higher frequencies, it will tend to be flattish. Spectral information such as this can only be used in a phenomenological model; predictive models are still a long way off. This spectral modelling would be important for the fitting of multi-frequency differential source count data.

Doppler Beaming Model: The core luminosity can be easily Doppler boosted by the emerging relativistic jet material. Studies show that the LF can be drastically altered by the Doppler beaming effects. See the review by Megan Urry & Padovani (1995) [144] for further details.

Jet Production: It is assumed that a large fraction of the available power from the core region can be used to mechanically drive a relativistic radio jet bulk flow. This is done via the assumption of a suitable efficiency factor, that one can tune to yield AGN with varying levels of radio luminosity and morphology.

Jet Flow Velocity: The jet flow velocity v_f is to be distinguished from the advance velocity

of the jet head v_h (also called the morphological velocity in this thesis). The flow velocity v_f is known to be superluminal in some sources, on the parsec scales. On the kiloparsec scale, it is believed that the flow velocity must have slowed down appreciably, becoming at most mildly relativistic, if not non-relativistic altogether. An independent predictive model is required for the slowing of the jet fluid velocity.

Jet Advance Velocity: This is the speed v_h with which the radio jet morphology propagates itself into the IGM. By momentum transfer, we expect that this speed to have an upper limit set by the jet fluid velocity. It is possible, as the author demonstrates near the end of this Chapter, to set some tentative limits on the jet head advance velocity v_h, from a large statistical sample of images of EGRS. It is found that the jet advance velocity is non-relativisitc, and hence that the slowdown of the jet fluid itself *may* be quite severe by the time the scale of 10s–100s of kiloparsecs is reached.

An important part of the jet model is the prescription for a universal jet head velocity as a function of radius ($v_h(r)$). Integration of this equation will give the maximum length of each jet as a function of the age t of the source: $R(t)$. This physical dimension is necessary for the calculation of the angular sizes of the separations between components.

Morphology Model: With a prescribed power output, and a velocity flow and velocity advance model for the jets, it is important to decide on the rough geometry and size for the radiatively emitting areas. The radio cores could be modelled as flat spectrum unresolved spheres; the pc and kpc jets as optically thin, steep-spectrum thin circular cylinders; the hot spots as optically thick, steep spectrum flat cylinders; and the lobes and bridges as cylindrical or spheroidal, optically thin, ultra-steep spectrum cavities, that grow in size in step with the jet.

It should be noted that the radio structures are so large, in some cases, that there will be

a time delay asymmetry in the lengths of the individual jets. Even if both are intrinsicallly of the same length, the approaching jet will always tend to be brighter and longer than the faint receding one. These effects of time delay and (mild) relativistic Doppler boosting need to be explicitly modelled in order to make interesting comparisons with the abundance of detailed data in the images of EGRS.

Spectral Model: As mentioned in the last item, the spectral index will vary systematically from each radio structure to the next. It is likely that older radio sources will show a spectral index distribution that is significantly *steeper* than the one seen in much younger radio structures such as pc scale jets. A spectral model is important for the calculation of the amount of radio flux density that will be seen in each of the various radio frequencies chosen by the many different radio surveys. There is a technique for estimating the age of synchrotron emitting electrons in the extended structures of radio sources, called 'spectral ageing' (e.g. see Deborah Katz-Stone 1997a,b [81], [82]); however, the latest analyses suggest that care should be exercized when using the spectral index maps to estimate ages, as there are other complicating factors that can interfere with the originally proposed analysis procedure.

Radio Radiation Model: Combining all the results of the calculations for the radio luminosities, the final intrinsic luminosity will be the *sum* of the radio luminosities over all the separate morphological structures of the radio-loud AGN (core, 2 jets, 2 hot spots and 2 lobes). The resulting radio spectrum can also be calculated.

World Model: The radio source axis is embedded in a background cosmology of one's own choosing, such as an Einstein-de Sitter universe, with $h_0 = 70$ km/s/Mpc. The cosmology will affect the apparent flux density S, and angular size θ of the radio source. One could

assume at first that the distribution of radio source axes is isotropic, but it would eventually be necessary to take into account selection effects that arise from non-isotropic beaming of the radio radiation.

EGRS Distribution Function: Once the apparent parameters (S, θ, α, z) have been calculated, a global distribution function $\Phi_\nu(S, \theta, \alpha, z)$ for the powerful radio sources can be compiled for any observing frequency ν. It is the marginal distributions of this basic underlying function that can be compiled in a systematic manner from well-defined large-sample radio surveys.

Observed Distributions: Examples of derivable distributions are: differential source counts; redshift distribution; spectral index distribution; radio morphology breakdown; joint angular size-redshift distribution; joint angular size-flux density distribution.

With the proposed formulation, given in outline above, one can make some very general tests using multiple radio samples: source counts as a function of flux; as a function of both flux and angular size; as a function of redshift, etc. One can also calculate the final mass spectrum of massive black holes at any epoch, given the formalism developed in Section 5.6 This formalism is essentially a generalized version of the accretion model built for young stellar clusters in Part II of this thesis.

The following is a list of researchers, whose literature has inspired the synthesis outlined above:

Ginzburg, Syrovatskii, Pacholczyk, Rees, Blandford, Begelman, Phinney, Norman, Winkler, Smarr, Scheuer, Carlberg, Richstone, Kapahi, Daly, Chyzy, Dunlop, Peacock, Wall, Shaver, Lister, Ubachukwu, Cavaliere, Wilson, ...

5.6 The Evolution of Accreting Astrophysical Populations

A mathematical formalism for the evolution of accreting populations will be developed in this Section.

Definition of the Accretor Mass Function

The evolution of the mass distribution of an accreting astrophysical population may be represented by the following function:

$$\Phi = \Phi(M;t), \tag{5.8}$$

where M is the instantaneous mass of the accreting object, and t is the time elapsed since the oldest object in the population started its accretion. $\Phi(M;t)$ is then the number of accreting objects, per unit mass M, at time t. The convention is adopted that all variables over which the population is distributed (in this case, just the mass M) be written to the *left* of a semicolon in the argument list of the distribution function.

Dynamical Accretion Law

The model presented here has no *physical content.* This must be put in by hand, via a dynamical law for the accretion. In general, one might expect that the accretion law would involve some finite number of parameters, in addition to the instantaneous mass M of the accreting object:

$$\dot{M} = \frac{dM}{dt} = f(M, \alpha_i);\ 1 \leq i \leq N, \tag{5.9}$$

where the parameters α_i represent the dependencies on all parameters other than the mass M. For example, in the Kerr-Newman rotating black hole solution, the *"No-Hair"* Theorem would suggest that the only dynamical parameters associated with the hole, that could possibly affect the accretion rate $\dot{M}$, would be the mass M, spin J and charge Q. For mathematical reasons, it will be assumed that the value for $\dot{M}(t)$ will always be *strictly positive*; see the discussion in the section below on the Single Burst Accretion Requirement.

Sum over Independent Populations

In general, it cannot be expected that *all* objects in a given accreting population will obey the *same* dynamical law of accretion. While the "single accretion law" assumption is what will allow a straightforward solution of the population evolution equations, a more general formulation would have to allow for the existence of many (N) subsets of the population, each having their own accretion law. It is assumed that each of these subsets is a partitioning into *independently accreting* sub-populations, i.e. that the dynamical accretion law for any given subset depend on the parameters for that subset, and on that subset *only*. With this convenient partitioning, one can simply add the N independently evolving distribution functions to obtain the solution for the entire population (should that total solution be desired):

$$\Phi(M;t) = \sum_{i=1}^{N} \Phi_i(M;t). \tag{5.10}$$

As an example of a possible astrophysical scenario of independently accreting populations, we can simply turn to case of independently accreting AGN, which are all essentially isolated by cosmological distances from each other (for the most part – we must treat the rare 'binary quasars' specially). One partition to choose might be the division of AGN into 'powerful' and 'weak' AGN, where the border between the two populations is set by some selected

observational measure, such as the absolute visual magnitude of the AGN.

In the case of subpopulations that are partitioned by a *continuous* parameter p, we would need to know the dynamical accretion law as a function of p:

$$\dot{M} = \frac{dM}{dt} = f(M, p, \alpha_i). \tag{5.11}$$

Given this more detailed accretion law, we may simple rewrite the discrete sum over the original parameter i, in Equation 5.10 above, as an integral over the continuous parameter p:

$$\Phi(M;t) = \int_{-\infty}^{\infty} \Phi(M, p; t) dp. \tag{5.12}$$

As a concrete example, one could partition all AGN into continuous subsets of objects labelled by p, where p is the *final mass* of the AGN remnant:

$$p = M_{final} = lim_{t \to \infty} M(t). \tag{5.13}$$

One expects that more powerful AGN would have larger energy output and lifetime than less powerful AGN; more powerful AGN would be associated with higher values of the final mass M_{final}, and hence with higher values of the continuous subpopulation parameter p. Mathematically, this choice for p is convenient for defining the precise instant t_{max} when an object with mass M(t) will finally stop its accretion.

Definition of the Remnant Mass Function

Once accretion has stopped for a given object, it can be thought to jump instantaneously into the population of *non-accreting Remnants.* This population has its own distribution Φ_r:

$$\Phi_r(M;t) = \int_{-\infty}^{\infty} \Phi_r(M,p;t)dp. \tag{5.14}$$

An important assumption made in the derivation of the mathematical solutions of this model is that the Remnant population remain forever inactive, i.e. Remnants do not engage in accretion or mass loss, so that the only transitions between Φ and Φ_r will be in the direction:

$$\Phi\ (ACCRETORS) \longrightarrow (REMNANTS)\ \Phi_r \tag{5.15}$$

Physically, this encodes the assumption that every Accretor will attain its maximum mass M_{final} in a single burst of accretion (see below). The reason for making this simplifying assumption is that the dynamical accretion law, *by itself*, will not be able to track evolution in the mass $M(t)$ if $\dot{M}(t)$ were allowed to pass to and from the value zero. More discussion of this technical point will be given in the Section below on the *Single Burst Accretion Requirement.*

Another corollary of this assumption is that the Remnant mass spectrum will remain *forever fixed.* This feature of the solutions will turn out to be extremely important for the estimation of the time-evolving mass function for Accretors, given astrophysical observations of the mass function for Remnants.

Restriction to the Two Level Cascade

In the most general case, there will be a series of populations, each evolving from one to the next 'phase'. Accretors will have *proto-accretors* Φ_0 as parents, and the population of Remnants may decay into one of *grand-remnants* Φ_{r2}, which in turn may eventually metamorphose into *grand-grand-remnants* Φ_{r3}. Such a *Multi Level Cascade* process may be symbolized as follows:

$$\cdots \longrightarrow \Phi_0 \longrightarrow \Phi \longrightarrow \Phi_r \longrightarrow \Phi_{r2} \longrightarrow \Phi_{r3} \longrightarrow \cdots \tag{5.16}$$

If we are only interested in the process of accretion, then the solutions presented here will be restricted to the *Two Level Cascade* process:

$$\cdots \longrightarrow \Phi \longrightarrow \Phi_r. \tag{5.17}$$

It is implicitly assumed that the Remnants *do not* decay further into another population. If this happens, then the resulting function $\Phi_r(M;t)$ could only be interpreted as the mass function of the sum total of *all* the Remnant populations Φ_{ri}. This sum total is only meaningful if there are no new injection or extraction processes that interfere with the linear chain assumed in Equation 5.16.

The existence of some form of proto-population Φ_0 is necessary in the case that there are no pre-existing Accretors. However, this 3rd population will not be modelled explicitly here; instead, it will be represented mathematically by an externally imposed *Creation Rate* function $C(M, \dot{M}, p; t)$ for Accretors. This important function will be discussed further below.

The Single Burst Accretion Requirement

The solutions presented here cannot directly track the evolution in any other variable than the mass $M(t)$. This is simply a consequence of the fact that only a *single* dynamical law (for mass accretion) is assumed. Thus, the evolutionary mathematical solutions will potentially become ill-posed if the accretion rate drops to zero; for in that case the mass evolution will be the trivial solution:

$$M(t) = M_0;\ \dot{M}(t) = 0;\ t_1 \leq t \leq t_2. \tag{5.18}$$

The dynamical accretion law will not be able to provide information on when the accretion will start again, i.e. the value of the time t_2 will be indeterminable. Hence, we require that the accretion take place in a single continuous burst, instead of sporadically. To put it another way, one would have to define *another* evolutionary law in some parameter $p_i(t)$, so that evolution can still be tracked for the mass-conserving periods when $\dot{M}(t) = 0$.

In practice, we would expect that the Single Burst Accretion Requirement *fail* for real astrophysical systems. This problem might be circumvented if we use a *time-averaged accretion rate* $< \dot{M} >$:

$$< \dot{M} >= \frac{1}{\delta t} \int_{t-\delta t}^{t+\delta t} \dot{M}(\tau) d\tau, \tag{5.19}$$

with an appropriate averaging time window δt that is *short* compared to the typical evolutionary timescale of the Accretor objects, but *long* compared to the typical duration of the bursts.

In both AGN and XRB, the accretion will be expected to be sporadic – direct evidence of this is readily seen, especially in the XRB systems. The time averaging technique could be profitably used in the AGN systems, with a time window of anywhere from 10^2 yr to 10^4 yr; the MBH will eject plasma on shorter timescales of years, and it may gain appreciable mass in the space of 10^5 yr or so.

However, the time averaging procedure may not work for XRB, as each accretion event may have its own individual physical characteristics that depend on the amount of injected gas or fuel, the local pressure and temperature of the compact object or accretion disk surface, the velocity of impact of new material on the reaction site, and a myriad of other possible contributing factors. Provided, however, that one can supply the dynamical accretion law for *each individual accretion burst*, one can in principle use the mathematical solutions derived here. It may be best, though, to approach this more physically demanding problem for the XRBs via a numerical Monte Carlo approach.

Validity of the Non-Interaction Requirement

Another important condition for the use of the proposed solutions is the requirement that the accretion process for each Accretor be entirely *independent* of those of other Accretors. This is manifestly true of accretion in AGN, which are separated from each other by cosmological distances. It is also true of the population consisting of most XRB systems so far observed in our Galaxy. However, the requirement may break down in the case of *accreting protostars in binary and multiple systems.* This possibility has *not* been addressed in the protostar calculations of Part II of this thesis. Indeed, the issue of accretion in binary accretion systems is a very difficult one, as many more physical factors come into play.

In the case of AGN, it may also be possible that binary MBHs are formed in the nuclei of a few galaxies, perhaps as a result of a merger between two galaxies that each had a seed precursor to a black hole. However, such events are not known to be common, and the formalism adopted here will make the assumption that the accretion can be modelled as a set of statistical processes in independent systems, each according to the prescribed dynamical accretion law. This will be known as the *Non-Interaction Requirement.*

The Non-Interaction Requirement is actually a necessary condition for the assumption of a single dynamical law for the global population of Accretors; such a dynamical law for $\dot{M}(t)$, when applied to each individual Accretor, should be expressible as a function of parameters related *only* to that Accretor. In the case that Accretors have mutual interactions, the possibility opens up that the dynamical law for interacting accretion systems will be significantly altered, and the set of independent variables for the resulting accretion law for such an N-Accretor system would include at least the parameter list from every one of the participating systems.

Given the vailidity of the Non-Interaction Requirement, we can now move safely to the establishment of the evolutionary partial differential equations, via the use of a formal analogy with the dynamical evolution laws for classical mechanical systems.

Translation to Classical Liouville Form

We are now in a good position to start constructing a partial differential equation for the evolution of accreting objects (the 'Accretors') and their non-accreting descendants (the 'Remnants').

One can draw much from the mathematical formalism familiar to us from the study of the dynamical evolution of classical systems. In this time-honored case, the function analogous to our time-evolving mass function Φ is the classical particle distribution function Φ_c, defined over the available position-velocity phase space:

$$\Phi_c = \Phi_c(x_i, v_i; t), \tag{5.20}$$

$$v_i = \frac{dx_i}{dt}, \tag{5.21}$$

$$\frac{d\Phi_c}{dt} = \frac{\partial \Phi_c}{\partial t} + \frac{\partial (v_i \Phi_c)}{\partial x_i} + \frac{\partial (\dot{v_i} \Phi_c)}{\partial v_i} = 0. \tag{5.22}$$

This physical meaning of this equation is that the phase space number density of particles is *conserved.* For classical mechanical systems, the requirement for the conservation of phase space density is that the system be energy conservative, and that there is no injection or removal of particles from the system. As a real example, the above Liouville equation can be used in both low density plasmas (Vlasov equation), and in astrophysical gravitational systems such as galaxies (Jeans equation); in both these cases, the collisions between the particles are ignorable over the timescale of evolution of the distribution function, and this means that the appropriate equation would be the Liouville conservation equation give above.

The Non-Interaction Requirement for our population of Accretors is just the condition one needs in order to be able to write down the evolution of the population mass function as a Liouville phase space density conservation equation. It is manifestly true that the mass evolution of each of the population members is *'collisionless'*, and hence the RHS of

the translated Liouville conservation equation is identically zero. However, we may use the Liouville differential equation as a formal mathematical analogy only so long as we are sure that there is *no injection or extraction* of Accretors or Remnants in the population being modelled.

To effect the translation to the Liouville form, we write down the formal correspondence between the astrophysical and classical variables:

$$t \longleftrightarrow t \tag{5.23}$$

$$M \longleftrightarrow x \tag{5.24}$$

$$\dot{M} \longleftrightarrow v \tag{5.25}$$

$$\frac{d\dot{M}}{dt} \longleftrightarrow a \tag{5.26}$$

$$\Phi(M, \dot{M}, p; t) \longleftrightarrow \Phi_c(x, v, p; t) \tag{5.27}$$

$$\dot{M} = f(M, \dot{M}, p) \longleftrightarrow a = \frac{dv}{dt}, v = \frac{dx}{dt}. \tag{5.28}$$

$$\tag{5.29}$$

With the above translation constructed, the appropriate Liouville conservation equation for the mass evolution of the Accretor population in the phase space $(M, \dot{M})$ will be:

$$\Phi = \Phi(x, v, p; t), \tag{5.30}$$

$$v = f(x, v, p, t), \tag{5.31}$$

$$\frac{d\Phi}{dt} = \frac{\partial\Phi}{\partial t} + \frac{\partial(v\Phi)}{\partial x} + \frac{\partial(a\Phi)}{\partial v} = 0. \tag{5.32}$$

This is not yet the final form of the differential equation for the evolution of the accreting masses, but it is a significant step along the way. We now consider the necessary modifications

that need to be made to this kernel of our model.

Creation and Removal of Accretors

Classical particles cannot be created or detroyed, but real astrophysical systems are by their very nature *transient.* Hence the Liouville conservation of phase space flow is invalid for the purposes of modelling accreting populations. Taking our cue from quantum mechanics, we require the definition of 'creation' and 'destruction' functions that can act as source and sink terms on the RHS of the Liouville equation. Thus, Equation 5.33 acquires two extra terms:

$$\frac{d\Phi}{dt} = \frac{\partial\Phi}{\partial t} + \frac{\partial(v\Phi)}{\partial x} + \frac{\partial(a\Phi)}{\partial v} = C(x,v,p;t) - D(x,v,p;t). \tag{5.33}$$

The non-negative term $C(x,v,p;t)$ is the rate of creation of new Accretors of subpopulation p (we assume that a single parameter p will suffice to partition the actual range of accretion laws and accreting populations). The non-negative term $D(x,v,p;t)$ is the rate of removal of Accretors of type p. To attain a state where the number of Accretors is conserved, these two rates would have to be exactly zero, or else exactly balanced. Needless to say, in real astrophysical populations, this will not be true almost all of the time that accretion is occuring somewhere in the population.

Example: The Zero Mass Seed Approximation

As an example of a Creation function that may be useful for certain astrophysical cases, we may consider the *Zero Mass Seed Approximation* in the case of protostellar collapse. This assumes that the protostellar core starts growing from a negligible mass that is virtually indistinguishable from zero. In this case, the Creation Rate function is best modelled as

a delta function at zero mass, i.e. the accreting objects are all created with virtually zero mass:

$$C(x, v, p; t) = C'(v, p; t)\delta(x). \tag{5.34}$$

In Part II of this thesis, the Zero Mass Seed Approximation was made for the growing protostars. However, in the spirit of generality, this particular form of the Creation function will not be assumed when calculating the general solutions in this Section. The substitution of any arbitrary Creation function can be made directly into the final general solutions.

Example: The Poisson Probability Model for Accretor Removals

As another example, this time of the 'sink' term, we could profitably choose a Poisson probability model for the decay versus survival of the Accretors in population. The results of decays will directly feed into the number of Remnants that are retired from the population Φ to the population Φ_r. It is proposed that the rate of removal of the Accretors is given in terms of an invariant Poisson probability per unit time, $\mu(M)$, that is *only* a function of the mass M of the accretor. Clearly, this is a gross simplification of the physics in actual accreting systems, but it is the most obvious and simple choice to make in the case that there is a well-defined, observed, *final Remnant mass spectrum* $\Phi_{rf}(M)$. If this simple model is approximately true, then we might expect that the *Poisson probability per unit time for the stopping of accretion at mass M be directly proportional to the relative number of Remnants at that mass.* This is a very important realization, and it will be proved in the following pages. Mathematically, we write:

$$\mu(M) \propto \Phi_{rf}(M) = lim_{t\to\infty}\Phi_r(M; t). \tag{5.35}$$

This last proportionality is the key which will unlock the door towards specifying closed form solutions for both $\Phi(M;t)$ and $\Phi_r(M;t)$, based on (1) an assumed accretion law, and (2) the observed final Remnant mass spectrum. A specific application of the proportionality has been proved and utilized for the case of accreting protostars in young stellar clusters, in Part II of this thesis.

Given the Poisson decay rate $\mu(M)$ at mass M, we can write down the Destruction function that would be consistent with this model as:

$$D(x,v,p;t) = \mu(x)\Phi(x,v,p;t). \tag{5.36}$$

We now turn to a simplification of the general accretion law proposed earlier.

The Simple Accretion Model

One of the simplest possible dynamical laws that could be chosen for an accreting population is the one where the accretion is at most a function of the mass M of the Accretor. In the quiescent conditions deep in the cold embedded cores of giant molecular clouds, one might expect that a cluster of young protostars would accrete at an invariant rate set by the fixed temperature and density of the ambient gas. In this special scenario, the accretion rate might be expected to remain essentially constant throughout space and time, within the confines of the embedded cloud core:

$$\dot{M} = \frac{dM}{dt} = \dot{M}_0. \tag{5.37}$$

However, such a stable scenario cannot hold true for the global population of AGN (or XRBs, for that matter), as each AGN system is spacelike separated from each other, at a given epoch. We would like to specify a *simple* dynamical law of accretion that is intermediate in complexity between the trivial model given in Equation 5.37, and the full generality

demanded by the most general case, as it would appear if the analogy with classical mechanical systems were to be formally adopted:

$$\begin{aligned} \dot{M} = \frac{dM}{dt} &= f_1(M, \dot{M}, p, t), \\ \frac{d\dot{M}}{dt} &= f_2(M, \dot{M}, p, t). \end{aligned} \tag{5.38}$$

Here, the accretion rate and its second time derivative must be specified. This is a complication that goes even further beyond our original accretion law given in Equation 5.9.

An appropriately simple accretion law can be obtained by simply postulating that, as for the Poisson probability decay function for Accretors, the accretion rate is a function *only* of the Accretor mass, for each given subpopulation p. In this case, the 1st and 2nd time derivatives of the mass are given by:

$$\begin{aligned} \dot{M} = \frac{dM}{dt} &= f_1(M, p), \\ \frac{d\dot{M}}{dt} &= f_1'(M, p).\dot{M}, \end{aligned} \tag{5.39}$$

where the prime denotes differentiation with respect to the independent variable mass M. It is assumed here that the Accretors and Remnants of each subpopulation p do not leave that group, once they enter it. This will be manifestly true if the value of p is chosen to be the *final Remnant mass* M_{final}, as this is uniquely specified. Given these reasonable requirements, the value of p will remain invariant with time, and hence its time derivative does not appear in the second equation above for the time derivative of the accretion rate $\dot{M}$.

It will also be required to assume that the accretion rate be *non-negative*, i.e. we are only interested in populations of Accretors that either stay constant, or gain in mass, with time. By the Single Burst requirement discussed above, the zero accretion rate is *only* allowed before and after a single period of accretion. During this period of accretion, then, the rate must be *strictly positive.* This is to avoid dealing with an ill-defined mathematical behaviour that arises when the accretion rate becomes zero in the proposed solutions. In terms of the

Simple Accretion Model, we may state the Single Burst Requirement in mathematical terms. This would be the statement that for each and every Accretor $M_i(t,p)$, in each subpopulation p, there exists two times, and only two times, t_{1i} and t_{2i}, which span a maximal time period, and in which the accretion rate is strictly positive:

$$\forall M_i(t,p),\ \exists t_{1i}, t_{2i} :\ \dot{M}(t) > 0;\ t_{1i} \leq t \leq t_{2i}. \tag{5.40}$$

It is noted in passing that it should be possible to make small modifications to the solutions presented here, such that they can be used for systems which exclusively *lose* mass with time (such as some types of massive stars in our Galaxy).

Secular Increase of the Remnant Population

The Remnant Population will always monotonically decrease in number, provided accretion has started, and that it does not decay into yet a third population. The evolutionary differential equation for the Remnants has a source term that is equal to the Destruction term for the Accretors:

$$\frac{\partial \Phi_r}{\partial t} = D(x,v,p;t) = \mu(x)\Phi(x,v,p;t). \tag{5.41}$$

Accretors that Never Accreted

As a potential complication that should be entertained for the general case being solved for, there are possibly some 'Accretors' that never manage to start accreting. In this case, they are assumed to simply decay from the Accretor population according to the same Poisson law as for the other successful Accretors. These special cases will be known as the

Non-Accretors. By the Non-Interaction Requirement, their solutions can be treated as an entirely different and independent subset of the Accretor population; that is the approach that will be adopted here. The terms associated with these Non-Accretors will have the subscript n, e.g. Φ_n instead of Φ. The distribution function for the Non-Accretors is:

$$\Phi_n(M,p;t), \forall j : \dot{M} = 0; M_j = M_j(t=0). \tag{5.42}$$

They will decay into Remnants Φ_{nr}, just like the other Accretors:

$$\frac{\partial \Phi_{nr}}{\partial t} = D_n(x,v,p;t) = \mu(x)\Phi_n(x,v,p;t). \tag{5.43}$$

Boundary Conditions

Due to the assumption of the Simple Accretion Law in Equation 5.39, the tracks in the phase space $(M,\dot{M})$ collapse in the vertical $\dot{M}$ direction, since the accretion rate is now a *unique* function of the mass M of the object. In this case, we may integrate all the distributions over the 'velocity' dimension (to use the classical analogy). In addition, we restrict ourselves to the solution for a single subpopulation parameter p, and henceforth drop all mention of this extra parameter. In the accretion law, it will be implicitly assumed that the solution will be evaluated for the relevant parameter p. It is important that p does not change with time in the evolution of the mass $M(t)$, as this would invalidate the derivation of the solutions. We also henceforth use the translated 'classical' variables, as far as possible.

Given these simplifications, we now postulate the existence of an initial population for each of the three groups: Accretors $\Phi_i(x)$, Non-Accretors $\Phi_{ni}(x)$, and Remnants $\Phi_{ri}(x)$. Thus, we have the following conditions conditions:

$$\Phi(x;0) = \int_{-\infty}^{\infty} \Phi(x,v;0)dv = \Phi_i(x) + \Phi_{ni}(x), \tag{5.44}$$

$$\Phi_r(x;0) = \int_{-\infty}^{\infty} \Phi_r(x,v;0)dv = \Phi_{ri}(x). \tag{5.45}$$

In practice, we will only need the solutions for the trivial case in which all three populations are *empty* at the initial time $t = 0$.

Finally, we note that the integration over the 'velocity' coordinate v produces the expected marginal distributions for the creation rate C, and the destruction rate D:

$$C(x,t) = \int_{-\infty}^{\infty} C'(x,v,t)dv, \tag{5.46}$$

$$D(x,t) = \int_{-\infty}^{\infty} D'(x,v,t)dv. \tag{5.47}$$

The Importance of the Final Remnant Mass Spectrum

Though the following is not a necessary boundary condition, the specification of the *Final Remnant Mass Spectrum* $\Phi_{rf}(M)$ will prove to be crucial for ensuring the concrete application of the abstract, general solutions presented here. In order for this to occur, we need to make an observational determination of the Final Remnant Mass Spectrum, which is mathematically obtained by the asymptotic limit:

$$\lim_{t\to\infty} \Phi_r(M;t) = \Phi_{rf}(M) \approx \Phi_{rf,obs}(M). \tag{5.48}$$

The goal is now clear: solve the evolutionary differential equations for the time-evolving Remnant distribution function $\Phi_r(M;t)$; take the infinite time limit of this solution, and

set it equal to the *observed* statistical distribution that has been carefully estimated for the Remnant population. Then, in the light of this identification, it should be possible to rewrite all the solutions for each of the populations in terms of the observed information from the Final Remnant Mass Spectrum.

To put the idea across more plainly, what will be aimed for is a procedure whereby one can *retrodict* the time evolution of the evolving population mass functions, given the knowledge of the Final Remnant Mass Spectrum, and the Simple Dynamical Law for Accretion.

Vanishing of the Acceleration Term

We note that the adoption of the Simple Accretion Law allows us to drop the third (acceleration) term in the Liouville total derivative of Φ, since the accretion rate (velocity) coordinate is no longer independent of the mass M (position coordinate), being fully and uniqely specified at all times by the Accretion Law (during the single burst). In other words, using the Classical Analogy:

$$\frac{\partial}{\partial v}(a\Phi) = \frac{\partial}{\partial v}(f'(x).v.\Phi) = \frac{\partial}{\partial v}(f'(x).f(x).\Phi(x;t)) = 0, \tag{5.49}$$

where the $'$ denotes differentiation with respect to the mass (position) variable x.

Summary of the Evolutionary Equations

The evolutionary equations for the three populations are now brought together in one place, for future reference.

$$\frac{dx}{dt} = v(x) \geq 0, \tag{5.50}$$

$$\frac{\partial \Phi}{\partial t} + \frac{\partial}{\partial x}(v(x)\Phi) = C(x,t) - \mu(x)\Phi(x;t), \tag{5.51}$$

$$\frac{\partial \Phi_n}{\partial t} = C_n(x,t) - \mu(x)\Phi_n(x;t), \tag{5.52}$$

$$\frac{\partial \Phi_r}{\partial t} = \mu(x)(\Phi(x;t) + \Phi_n(x;t)), \tag{5.53}$$

$$\Phi(x;0) = \Phi_i(x) + \Phi_{ni}(x), \tag{5.54}$$

$$\Phi_r(x;0) = \Phi_{ri}(x). \tag{5.55}$$

Note that we have written the *total* accretion rate ($C_{TOTAL}(x,t)$) as the sum of two independent accretion rates: $C(x,t)$ for the Accretors, and $C_n(x,t)$ for the Non-Accretors.

Propagation Time Function

Three useful functions will emerge from the ensuing analysis. The first is the time it would take for an object to evolve from 0 to x, at speeds given locally by $v(x)$, at each point x:

$$t(x) = \int_0^x \frac{dy}{v(y)}. \tag{5.56}$$

This is a strictly monotonically increasing function of x, provided the accretion rate law yields positive values for v. The propagation time from position x_1 to x_2 is given by the difference in the t-values for the two times:

$$t(x_1, x_2) = t(x_2) - t(x_1). \tag{5.57}$$

Survival Probability Function

The second function is the one that supplies the exponent in the Poisson survival probability for an object that evolves from 0 to x:

$$Prob\,[0 \longrightarrow x] = e^{-g(x)}, \tag{5.58}$$

$$g(x) = \int_0^x \frac{\mu(y)}{v(y)} dy. \tag{5.59}$$

The corresponding survival probability for propagation from x_1 to x_2 is given by an exponent which is the difference between the respective exponents:

$$g(x_1, x_2) = g(x_2) - g(x_1). \tag{5.60}$$

Retarded Position Function

The third function gives a well-defined 'retarded' position x_r, for an object at time $t = 0$, given that it is at position x at time t.

$$x_r(x, t) = t^{-1}[max(0, t(x) - t)]. \tag{5.61}$$

Here, t^{-1} is the inverse function of t. The use of the maximum function in the argument of t^{-1} is necessary in order to obtain a well-defined answer for the case that the elapsed time t is longer than the time it takes to reach position x via evolution from zero mass.

Use of the Laplace Transformation

It is noted that the solution for the Non-Accretors will be a special case of the more general solution for Accretors, i.e. we could simply make the substitution $v(x) = 0$ in the

latter solution in order to retrieve the solution for the Non-Accretors. Hence, we will simply solve the *two* differential equations, for $\Phi(x;t)$ and $\Phi_r(x;t)$, for arbitrary $v(x)$.

The most efficient way to solve this 1st order linear partial differential equation, valid for non-negative t, is by use of the *Laplace Transformation.* We define the Laplace Transform of $\Phi(x;t)$ to be $\Psi(x;s)$:

$$\Psi(x;s) = \int_0^\infty e^{-st}\,\Phi(x;t)\,dt. \tag{5.62}$$

We then define the Laplace Transform of $C(x,t)$ to the $\Gamma(x,s)$:

$$\Gamma(x,s) = \int_0^\infty e^{-st}\,C(x,t)\,dt. \tag{5.63}$$

We also apply the Laplace Transform to the differential equation:

$$v(x)\frac{\partial \Psi}{\partial x} + [v'(x) + s + \mu(x)]\,\Psi(x;s) = \Phi_i(x) + \Gamma(x,s). \tag{5.64}$$

Solution for the Failed Accretors

The solutions for the Non-Accretors are given by the simpler differential equation that results from substituting $v(x) = 0$ in Equation 5.64. Remembering to retain the subscripts n for the Non-Accretor solutions, we obtain the simplified equation:

$$\Psi_n(x;s)|_{v=0} = \frac{\Phi_{ni}(x)}{s+\mu(x)} + \frac{\Gamma_n(x,s)}{s+\mu(x)}, \tag{5.65}$$

which has a solution readily obtainable by Laplace Inversion:

$$\Phi_n(x;t)|_{v=0} = \Phi_{ni}(x)e^{-\mu(x)t} + \int_0^t C_n(x,\tau)e^{-\mu(x)(t-\tau)}\,d\tau. \tag{5.66}$$

The solution for the Remnants *that come from the Non-Accretors* follows by direct integration of (the simplified version of) Equation 5.43:

$$\Phi_{nr}(x;t) = \mu(x) \int_0^t d\tau \, \Phi_n(x;\tau). \tag{5.67}$$

The integration is straightforward, leading to the general solution:

$$\Phi_{nr}(x;t)|_{v=0} = \Phi_{ri}(x) + \Phi_{ni}(x)(1 - e^{-\mu(x)t}) + \int_0^t C_n(x,\tau)(1 - e^{-\mu(x)(t-\tau)})\, d\tau. \tag{5.68}$$

The terms of these solutions are easily interpreted:

1. The exponential term in the Non-Accretor Solution simply represents the surviving part of a pre-existing population of Non-Accretors.

2. The integral term in the Non-Accretor Solution is the surviving part of a newly injected population of Non-Accretors.

3. The constant term in the Remnant Solution is the pre-existing Remnant population, which by assumption does not evolve whatsoever.

4. The exponential expression in the Remnant Solution is the population of Non-Accretors that have made the transit out of their original population.

5. The integral term in the Remnant Solution is the population of new objects that were initiated as Non-Accretors, but have since fallen into the Remnant population.

This completes the solution for the case $v(x) = 0$.

Solution for the Accretors

When the accretion is not held constant at zero, the differential equation for the Accretors takes the full form shown in Equation 5.64:

$$\frac{\partial \Psi}{\partial x} + Q(x,s)\,\Psi(x;s) = \frac{\Phi_i(x) + \Gamma(x,s)}{v(x)}, \tag{5.69}$$

where the function $Q(x,s)$ is defined to be:

$$Q(x,s) = \frac{v'(x) + s + \mu(x)}{v(x)}. \tag{5.70}$$

Equation 5.69 is a 1st-order linear partial differential equation in $\Psi(x;s)$ and its derivative with respect to x. The solution is standard, leading to:

$$\Psi(x;s) = e^{-\int_{x_1}^{x} Q(y,s)dy}.[\Psi(x_1;s) + \int_{x_1}^{x} dz\,(\Phi_i(z) + \Gamma(z,s)).e^{\int_{x_1}^{z} Q(y,s)dy}], \tag{5.71}$$

where the point x_1 can be chosen to fix the value of the solution. To simplify the equations, we demand that $\Phi(x;t) = 0$ in the case that $\Phi_i(x) = 0$ and $C(x,t) = 0$ ($\Psi_i(z) = 0$ and $\Gamma(z,s) = 0$ in the integrand). This condition fixes the constant term to be $\Psi(x_1;s) = 0$.

The rest of the derivation requires the use of delta functions, Heaviside step functions, the propagation time functions, retarded time functions and the survival probability exponent function. The final solution for the Accretor population is:

$$\Phi(x;t) = \Phi_i(x_r)\frac{v(x_r)}{v(x)}e^{-g(x_r,x)}H(t(x) - x) + \frac{1}{v(x)}\int_{x_r}^{x} C(z, t - t(z,x))e^{-g(z,x)}\,dz. \tag{5.72}$$

Solution for the Remnants

The solution for the Remnants *that come from the Accretors* is obtained by the appropriate integration with respect to time t:

$$\Phi_r(x;t) = \frac{\mu(x)}{v(x)} \int_{x_r}^{x} \Phi_i(z)\, e^{-g(z,x)}\, dz + \frac{\mu(x)}{v(x)} \int_{x_r}^{x} dz\, e^{-g(z,x)} \int_0^{t-t(z,x)} d\tau\, C(z,\tau). \tag{5.73}$$

Summary of the General Solutions

We now bring the Accretor and Non-Accretor cases together to form the most general solution to the evolutionary accretion equations.

The full solution for the Accretors (whether they succeed to accrete or not) is:

$$\begin{aligned}
\Phi(x;t) &= \Phi_{ni}(x)\, e^{-\mu(x)t} && (5.74)\\
&+ \int_0^t C_n(x,\tau) e^{-\mu(x)(t-\tau)} d\tau && (5.75)\\
&+ \Phi_i(x_r) \frac{v(x_r)}{v(x)} e^{-g(x_r,x)} H(t(x)-t) && (5.76)\\
&+ \frac{1}{v(x)} \int_{x_r}^{x} C(z, t-t(z,x)) e^{-g(z,x)} dz. && (5.77)
\end{aligned}$$

The full solution for the Remnants (whether they come from Accretors or Non-Accretors) is:

$$\begin{aligned}
\Phi_r(x;t) &= \Phi_{ri}(x) && (5.78)\\
&+ \Phi_{ni}(x)(1 - e^{-\mu(x)t}) && (5.79)\\
&+ \int_0^t C_n(x,\tau)(1 - e^{-\mu(x)(t-\tau)}) d\tau && (5.80)\\
&+ \frac{\mu(x)}{v(x)} \int_{x_r}^{x} \Phi_i(z)\, e^{-g(z,x)}\, dz && (5.81)
\end{aligned}$$

$$+ \frac{\mu(x)}{v(x)} \int_{x_r}^{x} dz\, e^{-g(z,x)} \int_{0}^{t-t(z,x)} C(z,\tau) d\tau. \tag{5.82}$$

Interpretation of the Terms of the General Solution

The terms of the Accretor Solution Φ can be easily interpreted:

1. The exponential term is the surviving part of a pre-existing population of Non Accretors.

2. The τ-integral term is the surviving part of a newly injected population of Non Accretors.

3. The Heaviside term is the result of the propagation of an initial accreting population, from the retarded position x_r, to the current position x at time t.

4. The second integral term is the result of the propagation of a newly injected population of Accretors to position x, from all possible positions between x_r to x, inclusive, in the available time.

The terms of the Remnant Solution Φ_r can be easily interpreted:

1. The constant term is the initial Remnant population, which does not evolve in any way.

2. The exponential expression in the Remnant Solution is the population of Non Accretors that have made the transit out of their original population.

3. The τ-integral term in the Remnant Solution is the population of new objects that were initiated as Non Accretors, but have since fallen into the Remnant population.

4. The Φ_i integral term is the result of the propagation of the decaying part of an initial accreting population, from the retarded position x_r to the current position x at time t.

5. The double integral term is the result of the propagation, to position x, of the decaying part of a newly injected population of Accretors, from all possible positions between x_r to x, inclusive, in the available time.

This completes the General solution for the case $v(x) \geq 0$.

Final Solutions

Provided a *finite* number of Accretors are generated, and that the Poisson decay probability is everywhere *positive*, the infinite time limit will give the null solution for the Accretor population.

$$\Phi_f(x) = \lim_{t\to\infty} \Phi(x;t) = 0. \tag{5.83}$$

Taking the infinite time limit of the 5 equations up to and including Equation 5.82, the result is:

$$\begin{aligned}
\Phi_{rf}(x) &= \lim_{t\to\infty} \Phi_r(x;t) && (5.84)\\
&= \Phi_{ri}(x) + \Phi_{ni}(x) && (5.85)\\
&+ \int_0^\infty C_n(x,\tau)d\tau && (5.86)\\
&+ \frac{\mu(x)}{v(x)} \int_0^x e^{-g(z,x)}[\Phi_i(z) + \int_0^\infty C(z,\tau)d\tau]. && (5.87)
\end{aligned}$$

Number Conservation

It can be easily shown that the number of objects must have increased by the (double) integral (over both position x and time τ) of the creation functions C and C_n:

$$\int_0^\infty [\Phi_{rf}(x) - \Phi_{ri}(x) - \Phi_i(x) - \Phi_{ni}(x)]dx = \int_0^\infty dx \int_0^\infty d\tau [C(x,\tau) + C_n(x,\tau)]. \quad (5.88)$$

Observational Determination of the Branching Ratio

The *branching ratio* is a measure of the relative likelihood of an Accretor, at mass M, to stop accreting and enter the Remnant population, as opposed to continuing with the accretion. The relevant expression that controls this selection process (at position x) is the ratio of the two functions $\mu(x)$ and $v(x)$, and it may be shown that this ratio is:

$$\frac{\mu(x)}{v(x)} = \frac{\Phi_{rf}(x) - \Phi_{ri}(x)}{\int_x^\infty dz[\Phi_{rf}(z) - \Phi_{ri}(z) - \Phi_i(z) - \Phi_{ni}(z) - \int_0^\infty C_{TOTAL}(z,\tau)d\tau]}. \quad (5.89)$$

This very general expression can be simplified by adopting the following four reasonable assumptions:

1. Initial Accretor population Φ_i is zero.
2. Initial Remnant population Φ_r is zero.
3. There are no "Failed Accretors" Φ_n at any time.
4. All Accretors grow from zero mass, i.e. they obey the Zero Mass Seed Approximation. This means the Creation Rate function can be written as $C'(x,t) = C(t)\delta(x)$.

These assumptions may be applied in many practical scenarios (e.g. protostars forming in young stellar clusters). The branching ratio then simplifies to:

$$\frac{\mu(x)}{v(x)} = \frac{\Phi_{rf}(x)}{\int_x^\infty \Phi_{rf}(z)dz} \tag{5.90}$$

We have the simple result, mentioned before as a key finding, that the Poisson decay probability $\mu(x)$ is proportional to the Final Remnant Mass Spectrum. In fact, it is the branching ratio of 'decay versus accretion' that is proportional to $\Phi_{rf}(x)$. Only in the case of the simplest possible *constant accretion* law would the unknown probability function $\mu(x)$ be *precisely proportional* to $\Phi_{rf}(x)$. It is this last, most simplest, case that has been assumed in Part II of this thesis.

For this case, the general solutions up to Equations 5.77 and 5.82 reduce to:

$$\Phi(x;t) = \frac{C(t-t(x))}{N_T v(x)} \int_x^\infty \Phi_{rf}(y)dy, \tag{5.91}$$

$$\Phi_r(x;t) = \frac{\Phi_{rf}(x)}{N_T} \int_0^t C(\tau - t(x))d\tau, \tag{5.92}$$

$$N_T = \int_0^\infty C(\tau)d\tau. \tag{5.93}$$

We see that the Accretor solution is proportional to (1) the retarded Creation Rate, (2) the reciprocal Accretion Rate, and (3) the upper integral of the Final Remnant Mass Spectrum. The Remnant Solution is proportional to (1) the Final Remnant Mass Spectrum, and to (2) the time integral of the retarded Creation Rate. Both distributions are normalized by the factor N_T, which is the *total* number of objects created.

Application to The Mass Spectrum of Accreting Massive Black Holes

If we make some reasonable, educated, guesses as to the Creation function, the Accretion Law, and the Final Mass Spectrum for MBHs, we can then calculate the time evolution of their mass spectrum. If there is a law relating mass to luminosity (e.g. via the assumption of the Eddington limit), then the time evolution of the MBH luminosity function may be estimated as a corollary.

The MBH assumptions may look something like the following:

(1) The Creation Rate of MBHs is a peaked function of the time, starting at $(t = 0, C = 0)$. We may arbitrarily choose a power-exponential law as a first approximation. The power law will have a positive index q, and the exponential function of time will have a decay constant t_0. These parameters may be estimated by fitting to the observational data.

$$C(M,t) = C_0(t/t_0)^q e^{-(t/t_0)}\delta(M). \tag{5.94}$$

(2) The Accretion Rate is held at a constant fraction f_E of the Eddington limit. If the Eddington-limited value of the accretion rate is known to be $\dot{M}_0$, at mass M_0, then the assumed scaling will result in the following Simple Accretion Law:

$$\dot{M}(M) = f_E \dot{M}_0 \frac{M}{M_0} \tag{5.95}$$

(3) The Final Mass Spectrum of MBHs is proportional to the *Fractional Mass Schechter Function* for elliptical galaxies. This is the same as the Schechter function, but with the mass of the black hole remnant made proportional to the mass of the host galaxy, which in turn is assumed to have a constant mass-to-light ratio (invariant over all elliptical galaxies). If we assume a proportionality constant f_M, given by a $\sim 10^8 M_\odot$ massive black hole for a typical massive elliptical of $\sim 10^{12} M_\odot$, then the Fractional Mass Schechter Function will be:

$$\Phi_{rf,obs}(M) = \frac{C_1}{f_M M_*}(M/f_M M_*)^{-\alpha} e^{-(M/f_M M_*)}. \tag{5.96}$$

Here, the mass $M_* \sim 10^9 M_\odot$ is the mass of an $L_* \sim 10^{10} L_\odot$ galaxy, assuming a mass-to-light ratio of 10.

Inserting these into the Accretor Solution for the simple case given in Equations 5.93, and absorbing the constants C_1 and $f_M M_*$ into the definitions of C_0 and M_0, we finally arrive at the simple retrodiction of the time evolution of the masses of massive black holes in the centers of galaxies:

$$\Phi_{MBH}(M;t) = \frac{C_0(t - t(M))/t_0)^q e^{-(t-t(M))/t_0)}}{\dot{M}_0(M/M_0)} \int_{M/M_0}^{\infty} d(M/M_0)(M/M_0)^{-\alpha} e^{-(M/M_0)}. \quad (5.97)$$

The time-evolving **Bolometric Luminosity Function for Massive Black Holes** can be instantly obtained via a change of variable from mass M to bolometric luminosity L. This entails an assumption concerning the mean radiative accretion efficiency η for the MBH population. If the Eddington related luminosity is given by $L_E = \eta \dot{M} c^2 = \eta f_E \dot{M}_0 (M/M_0) c^2$, the MBH Bolometric Luminosity Function will be given by the following transformation:

$$\Phi_{MBH}(L;t) = \frac{\Phi_{MBH}(M;t)}{dL/dM} = \frac{\Phi_{MBH}(M;t)}{\eta f_E (\dot{M}_0/M_0) c^2}. \quad (5.98)$$

5.7 Proposal of a Simple Radio Jet Model

See the Canary Islands paper (Fletcher et al. 1997) for a statement of an algorithm that assumes a simple jet model for extended EGRS. This is simply a detailed sub-model of the general scheme proposed in Section 5.5. We do not carry out the numerical calculation here, as the basic scientific result is limited by the appreciable uncertainties in the unmeasured physical parameters in the MIT-VLA Survey. Instead, we aim to set limiting constraints on the mean jet advance speed in the extended kpc-scale jets in the radio-loud AGN appearing in the MIT-VLA Survey; this can be done using simple arguments based on estimated 90%

confidence limits of both the measured and unmeasured parameters of the MIT-VLA survey sources. These arguments, and the resulting findings, are presented in Section 5.8.

The following pages show the geometrical configuration assumed, and a plot of suggested power law models for the jet advance speed $v(r)$.

The jet angular size follows from Equation 5.99:

$$\theta = \frac{\int_0^t v(\tau) \sin i \, d\tau}{d_A(z; H_0, \Omega_0, \Lambda_0)}. \tag{5.99}$$

Here is a simple algorithm whose aim is to make a reasonable Monte-Carlo estimation of the jet angular size distribution for a large sample of EGRS.

1. Choose a cosmology $(H_0, \Omega_0, \Lambda_0)$.
2. Choose a radio luminosity function evolving with redshift $\Phi(L, z)$.
3. Integrate $\Phi(L, z)$ to obtain the redshift distribution $N(z)$.
4. Choose a jet head propagation velocity model $v = v(r)$.
5. Loop through each source (index j): Pick a random z_j from $N(z)$.
6. Assign a random age t_j from a uniform distribution ($t_j < 10^8$ yr).
7. Assign a random inclination i_j from an isotropic distribution.
8. Assign a random luminosity L_j, from $\Phi(L, z)$, that survives Malmquist bias.
9. Integrate velocity v to estimate jet length $r_{est,j}$ at age t_j.
10. Calculate the actual jet length r_j (if this depends on L_j and z_j) from $r_{est,j}$.
11. Calculate core-lobe separation θ_j fro Eqn 5.99; bin into histogram $N_{model}(\theta)$.
12. Repeat from step 5, looping through j for ~ 10 ksrc.

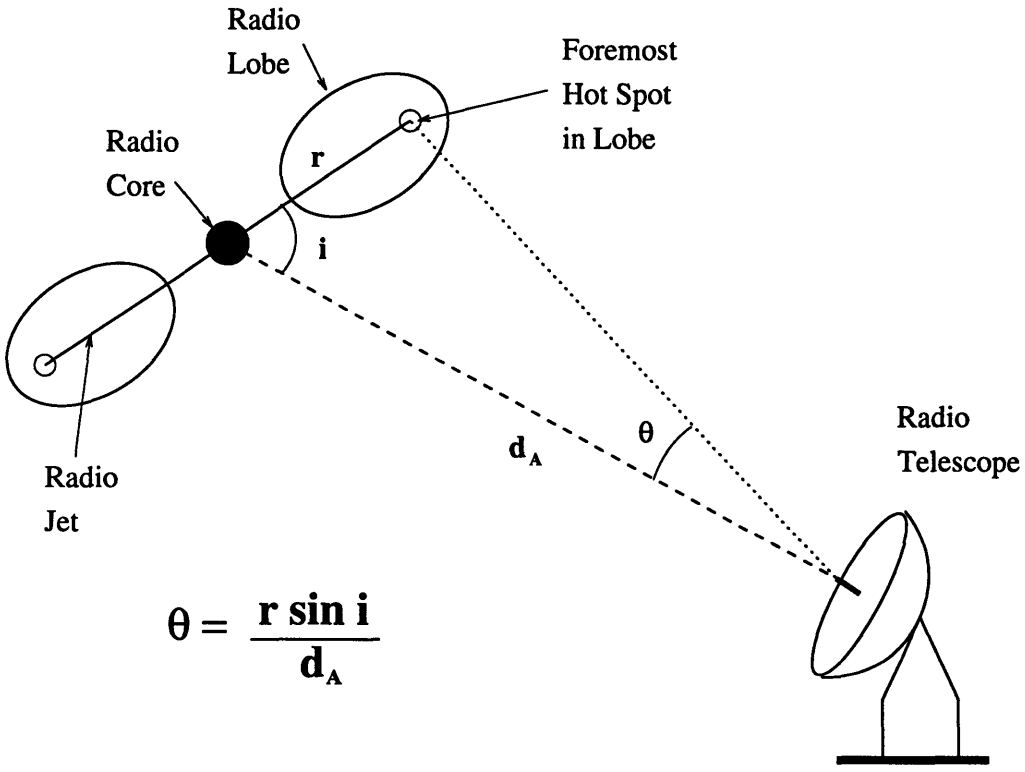

Figure 5-5: Simple Jet Model Geometry for Extended Radio-loud AGN. This figure has been reproduced from Fletcher et al. (1997).

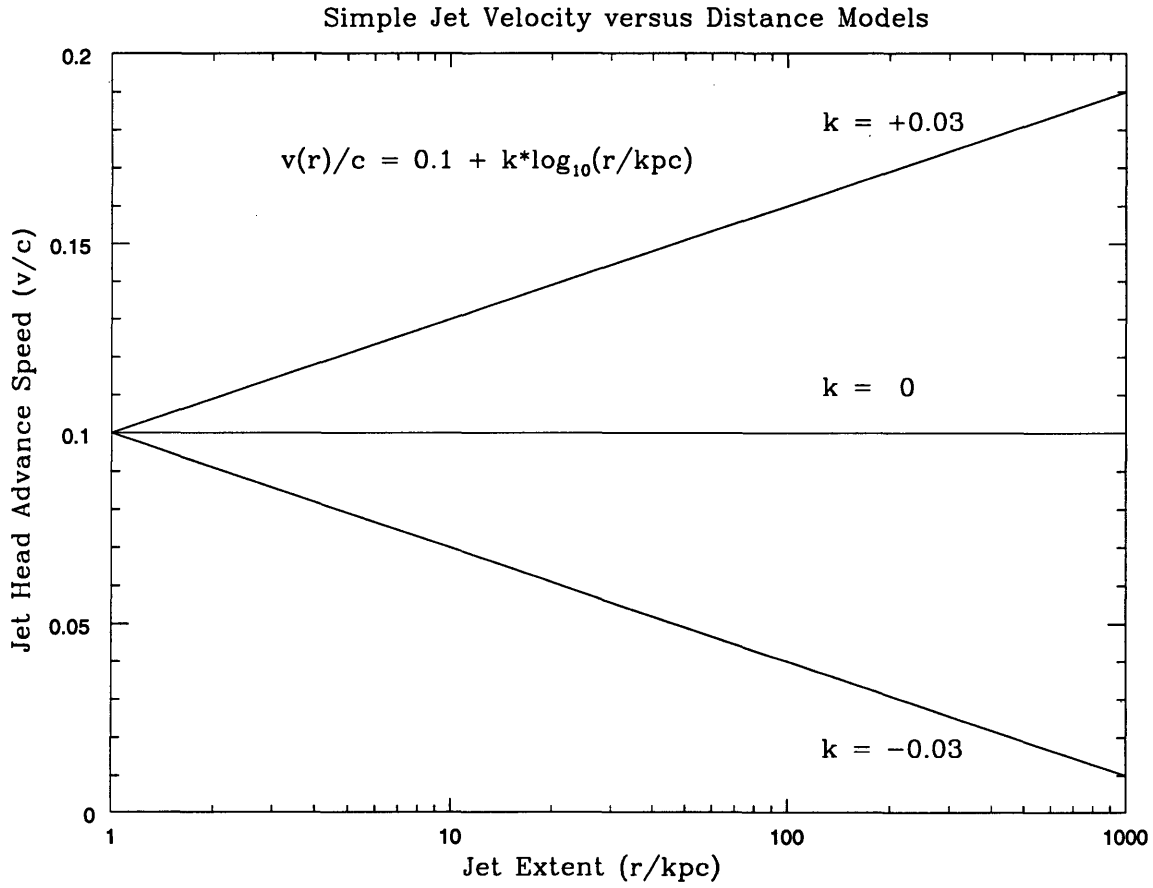

Figure 5-6: Simple Jet Models for Extended Radio-loud AGN. This figure has been reproduced from Fletcher et al. (1997).

13. Find χ^2_ν of N_{model} fitted to N_{data}, in the region of available resolution.

14. Repeat from step 1, until the best fits are found.

The above Monte-Carlo model algorithm could be used to further investigate the potentially complicating effects of flux density and angular size biasing that may occur in the MIT-VLA sample. The simple arguments presented in Section 5.8 assume that biasing effects such as these will not change the mean LAS, nor the 90% LAS limits, of the MIT-VLA sample by more than a factor of 2 (if biasing is indeed found to be important, which is not the expectation for the MIT-VLA sample, then the appropriate limits on the mean jet advance speed would have to be modified).

5.8 Estimation of the Mean Jet Advance Speed in the MIT-VLA EGRS Sample

I now apply the basic geometrical relation from the simple jet model in Section 5.7 to the MIT-VLA EGRS sample. The relevant formula is Equation 5.100:

$$v = \frac{r}{t} = \frac{D\theta_{LAS}}{2.sin(i).t}. \tag{5.100}$$

where r is the estimated jet length, t is the jet age, D is the distance to the source, θ_{LAS} is the largest angular size of the source (assumed to span from one lobe hotspot to the other), and i is the inclination angle between the jet axis and the line of sight.

The main assumptions made in the following analysis are listed as follows:

1. **Unbiased Representation of the EGRS Population**: The MIT-VLA sample of 4741 sources was selected without intentional bias, from the available reduced survey data as of March 1997. The original MIT-VLA sample is incomplete, with almost all

source flux densities in the range 50 to 500 mJy at 4.8 GHz. After selecting according to a pre-decided flux density rang from the parent MIT survey catalogs, the subsequent individual source selection was done without reference to the flux density value. The MIT-VLA survey area outside the 20 degree galactic plane strip was made as maximal as possible. The completeness of the MIT-VLA sample has not recently been quantified in a serious manner, but the current wisdom is that it is essentially complete above 150 mJy, about 70% complete by 100 mJy, and falling to 50% at 50 mJy, though the lower flux limit is very ragged. In view of the fact that the flux densities span no more than an order of magnitude, the MIT-VLA sample is expected to be representative in terms of the flux density, over this narrow range. A more sophisticated analysis would entail the compilation of the LAS-Flux Density distribution.

2. **Friedmann Cosmological Model with Zero Cosmological Constant**: The cosmology will have a relatively minor effect if the standard Friedmann models are chosen. This is because the angular size distance has a maximum at redshifts comparable to the expected redshifts of the majority of EGRS ($z \sim 1$). From Condon's (1984 [32], [31]) work on a sample about 10 times brighter, it is estimated that the mean redshift is 0.8.

3. **Strong Cosmological Evolution similar to other well-studied Quasars and Radio Galaxies**: The EGRS population in the MIT-VLA sample will be assumed to be most luminous and numerous in the 'Quasar Epoch', given the fact that it is about 10 times fainter than Condon's bright sample. This places the population squarely in the redshift range $1 < z < 5$, these limits being quite conservative. Even more conservative limits are assumed in the following calculations: $0.5 < z < 5$. This last choice probably contains almost all powerful radio-loud AGN.

4. **No Bias on Angular Scales between 0.3 and 100 arc-seconds**: The resolution

and field of view limit the analysis to statements about the kiloparsec scale jet motions.

5. **Negligible Doppler Boosting Bias due to Pole-On Sources**: The 'pole-on' sources are well resolved on angular scales greater than about 0.5 arc-seconds. In addition, they occupy small solid angles, and hence the underestimation of their numbers, due to resolution bias at the very smallest angles, should not be severe. A potentially strong biasing effect is that of the Doppler boosting of these sources; however, due to dynamic range limitations, and the intrinsic flat spectrum nature of the beamed radio cores in such sources, it would be very likely that such special cases are few in number; and would be essentially excluded from the analysis, as they would appear as unresolved points. The exclusion of precisely the PMN flat spectrum sources from the MIT-VLA LAS distribution is shown in the histogram in Chapter 4, and it is seen that the basic shape of the LAS distribution is changed only in a minor way, given that there are much larger uncertainties in other parameters.

6. **Isotropic Distribution of Radio Source Axis Inclination Angles**: Given that we can safely ignore the effect of Pole-On sources, the MIT-VLA EGRS inclinations will be assumed to be isotropic.

7. **Assumption of Semi-Angular Size as Jet Length**: It is assumed that the jet length is, on the average, about half the largest angular size of the source. However, this assumption will fail in the cases where the morphology is 'core-jet', for example. Note that the deviations from this geometrical assumption are such as to cause an overestimate of the jet length, and hence the final conclusion would be *strengthened* were a proper accounting to be made of the radio morphology of each individual source (this information is uniformly available in the MIT-VLA sample, but was not used at the time of compilation of the LAS histogram).

8. **Uniform Distribution of Jet Ages with Maximum Age set by the Salpeter**

Timescale for MBH Evolution: The most difficult assumption to justify is the expectation that the ages of the jets have a similar distribution as the ages of the MBH engines, which grow and fade on an Eddington/Salpeter time scale of 4.5×10^8 yr. A uniform distribution is assumed, i.e. it is assumed that there is no observational or intrinsic bias in the age distribution of the observed jets.

The *main theoretical assumption* made here is that the mean age of the jet is about the same as the mean age of the central engine that generates it. The latter is known both theoretically and obsevationally to be of order 4.5×10^8 yr for AGN; the observational constraint comes from the study of the evolution of various samples of optical and radio AGN (the powerful quasars and radio galaxies). If the further assumption is made that the each jet is visible in the radio throughout its lifetime (with about equal probability of being detected irrespective of age), then the 90% confidence limits on the jet age are at 22.5 and 427.5 Myr.

The other assumptions are probably more secure; an isotropic distribution of jet axes can be shown to lie between $i = 18.2$ through $i = 87.1$ degrees. The median pointing angle is 60 degrees. The mean redshift to EGRS is ~ 1; this is not surprising, as most EGRS are detected at cosmological distance – they are active during the Quasar epoch, and do not survive in great numbers for much longer after that. The 90% limits will be conservatively taken to lie from $z = 0.5$ to $z = 5$, with mean 1.0. The Hubble constant will be allowed to vary in the range $50 < H_0 < 100$ km/s/Mpc. Friedmann cosmologies with $\Lambda = 0$ will be assumed, with $0 \leq \Omega_0 \leq 1$. Cosmology will be a weak effect in a zero cosmological constant universe, as the angular size goes through a minimum at a particular redshift of order unity.

The MIT-VLA LAS distribution shows that 90% of all EGRS lie between 0.3 and 30 arc-seconds, with median 3.6 arc-seconds.

The order of magnitude of the mean velocity can be estimated from the following equation:

$$\beta = \frac{v}{c} = 7.91 \times 10^{-5}(D/Gpc)(\theta/'')(sin(i))^{-1}(t/100Myr)^{-1}. \quad (5.101)$$

When one works out the mean case according to Equation 5.101, using the following: $H_0 =$ 75 km/s/Mpc; $\Omega_0 = 0.5$; $z = 1.0$; $\theta_{LAS} = 3.''6$; $i = 60$ degrees; $t = 2.25 \times 10^8$ yr, the value for the mean jet advance speed obtained is $\beta = v/c = 1.9 \times 10^{-4}$. The minimum possible velocity occurs in an $\Omega_0 = 1; h_0 = 1$ cosmology, with redshift $z = 5$, (due to the convergence in the light rays at high redshift), and it is $\beta = 3.3 \times 10^{-6}$. The **maximum possible velocity for the advance of the jet head** occurs in an $\Omega_0 = 0; h_0 = 0.5$ cosmology, with redshift $z = 5$, and it is $\beta = 9.8 \times 10^{-2}$. Thus, we can say with great confidence (greater than 90%) that the mean jet advance speed is no faster than 10% the speed of light, i.e. that it is *non-relativistic.* The mean jet advance speed is well into the non-relativistic regime.

5.9 Summary

A description of a formal model has been outlined for EGRS.

From a statistical analysis of a large sample of MIT-VLA sources, it can be shown that **the 'population mean' jet head advances into the IGM at a speed of at most 10% the speed of light.** This non-relativistic result is expected from a physical consideration of linear momentum transfer during the entrainment of material external to the jet. This result has not yet been shown for a sample as large as the MIT-VLA survey, though the result here is consistent with previous analyses of independent and smaller surveys (such as the 3CR).

More detailed analysis can be made using comprehensive Monte-Carlo modelling of multiple survey catalogs, based on specific models following the general framework outlined in the formal prescription above. A key link in the chain is the developement of a general accretion model, and this approach has already proved useful in the construction of a successful

predictive model for young stellar clusters (see 6).

It is clear that much work remains to be done to extract more science from the abundance of radio survey data pouring in at the present time. In a few years time, the ultra-sensitive FIRST, NVSS VLA surveys, the Dutch WENSS Westerbork survey, and the Australian MOLONLGO WIDE FIELD survey will have collected *several million* radio sources. The path will then be open for statistically constrained science through detailed modelling along the general lines proposed in this thesis.

Chapter 6

The Nature and Evolution of Young Stellar Clusters

This chapter simply summarizes the approach used to calculate the time dependent mass and luminosity functions of stars in young stellar clusters, and also the numerical results and application to the well-studied embedded cluster in the Rho Ophiuchus cloud core.

This work has been published in 2 refereed journal papers, which are reproduced in Appendix C. The references for these 2 papers are:

A.B. Fletcher & S.W. Stahler, 1994, *"The Luminosity Functions of Embedded Stellar Clusters. I. Method of Solution and Analytic Results"*, Astrophys. J. 435: 313–328 (Paper I).

A.B. Fletcher & S.W. Stahler, 1994, *"The Luminosity Functions of Embedded Stellar Clusters. II. Numerical Results"*, Astrophys. J. 435: 329–338 (Paper II).

For brevity, these papers will be known as Paper I and II, respectively.

First, a simple mathematical model for the time evolution of an accreting astrophysical

population was constructed from the solution of an appropriate partial differential equation in the independent variables M and t (mass M, and time t since the initial formation of a collapsed object, respectively). As a result of this simple model, the time evolution of the non-accreting *descendants* of the accreting objects can be obtained as a corollary. Paper I shows that a necessary condition for isolating a particular solution to the general population evolution equations is the providing of (1) an **accretion law** (for embedded young stars, this was assumed to be a constant independent of M and t in Paper I), and (2) an observed **final mass spectrum** $\Phi(M)$.

With the strong observational constraint from the second requirement, the equations supply explicit solutions for the **mass functions** $\Phi(M,t)$ for both the accreting and post-accretion populations.

It is noted that since the publication of this work, the author has generalized the mathematical solutions to the case of arbirtrary (but well-behaved and differentiable) functions for both the *accretion rate* $\dot{M}$ and the *creation rate* $C(t)$. These solutions are explicitly given in Chapter 5, and they would be indispensable for the modelling of accretion in non-uniform physical environments. One example of an application, that is relevant to the other work in this thesis, is the calculation of the time evolving mass functions for populations of *unrelated* accreting objects, e.g. the cosmological population of AGN.

With the mass M essentially 'frozen' after the protostellar stage is completed, a numerical model was then used to construct the time evolution of the **luminosity function** $\Phi(L,t)$ for each of the populations of protostars, pre-main-sequence stars, and main sequence stars. Massive post-main-sequence evolution would disrupt the cluster in short order, so the model proposed in the Papers will not be applicable to regions of massive star formation (such as in the OB stellar associations). Thus, the model is aimed at observational comparison with quiescent star formation in clusters containing low mass stars ($M < 8M_{\odot}$). For the luminosity evolution of the contracting PMS stars, tracks from the work of Iben, Vandenberg

and Nelson were used.

The simple star formation model presented here has four adjustable inputs: the creation rate $C(t)$, the accretion rate $\dot{M}(t)$, the cutoff time t_c beyond which cloud core collapse no longer occurs, and the final mass function $\Phi(M)$, otherwise known as the IMF in the usual context of stellar studies. For the IMF, the standard Miller-Scalo log-normal function was assumed, with various extensions from $0.1M_\odot$ to zero mass, representing 4 different brown dwarf scenarios.

The results of this simple star formation model are surprisingly robust; the modifications expected from reasonable variations of the parameters for young stellar cluster populations are minor. The assumed mass function for brown dwarfs would only be significant at *early* times, when they are still freshly luminous from their protostellar accretion stage, which is relatively very brief for the very low mass brown dwarfs. The accretion rate has the most marked effect on bolometric luminosity functions, again at early epochs comparable to a typical accretion timescale $\sim 10^5 M_\odot$. The creation rate only determines the overall number of stars, and the cutoff time has a transient effect that rapidly disappears in about an accretion time.

From a comprehensive analysis of the grid of models obtained by the variation of parameters, the emergence of the overall robust nature of the model predictions allowed the definition of a representative *Canonical Model* for the time evolution of stars in young stellar clusters. This particular model assumes: an analytic extension of the Miller-Scalo IMF to zero mass, $\dot{M} = 10^{-5} M_\odot/yr$, $C(t) = C_0.H(t).H(t-t_c)$, and $t_c = 10^7$ yr. The time evolution of the Canonical Model is given in Paper II, as are several selected representative examples of variations in the parameters.

In addition to the mass and luminosity functions, the number and luminosity fractions of each of the three populations of protostars, PMS stars and MS stars were calculated. It was shown that the protostar number fraction is never much more than about $\sim 10\%$, and is

more typically 1%, due to the marked brevity of the accretion phase when compared to the later phases. Also, the cluster luminosity is at early times dominated by the light from a few massive protostars, switching over to domination at later times by the few main sequence stars. The majority of the stars are the low mass PMS stars, but these never contribute more than a small fraction of the total light. This can be understood as the logical result of the generally steep dependence of stellar luminosity on mass, with $L \sim M^{3-4}$ being typical of MS stars.

Using the above numerical predictions, it was shown that the age of the Rho Ophiuchus embedded stellar cluster, as judged from a fit to the published bolometric luminosity function of Wilking, Lada & Young (1989) [150], is 1 million years, to within a factor of 2. This is consistent with previous published (cruder) estimates.

A clear result of this project is the explicit demonstration that the *time evolution* of populations of stars in embedded clusters is an important effect to consider during the interpretation of the luminosity statistics. It is also comforting to have shown by direct calculation that the basic stellar structure theory of protostars, PMS and MS stars, when convolved with a reasonable and simple mathematical accretion model as proposed in Paper I, is indirectly verified by the observational test published in Paper II.

Chapter 7

Conclusions

The main conclusions of the thesis research are briefly discussed in the following two sections. The last section is a lengthy research proposal written by the author, for the purposes of defining possible future scientific goals that might extend on the work presented in this dissertation.

7.1 Extragalactic Radio Sources

The MIT VLA survey is one of the largest samples of detailed images that has been systematically analyzed for various interesting phenomena. It has so far produced the largest number of radio-loud gravitational lenses of any targeted search, and a new crop of plausible candidates has been compiled and presented here. However, none of the new candidates are obvious examples of lensing, and the one candidate, MG 0248+0641, that was thought to be the best case of lensing, turned out to be a possible rare discovery of transient galactic interaction. The galaxy merging/interaction hypothesis cannot be shown explicitly from the data alone, but such events have been indicated from many independent lines of inquiry; a smaller and denser Universe in the past would be conducive to an increased interaction

rate. The binary QSO MG 2214+3551 is another (clearer) example of a transient interaction between galaxies. The rarity of these sources should be a strong argument for the transient nature of interactions, but this conclusion needs to be verified with a much larger number of positive cases (i.e. much larger search samples would be required).

The MIT-VLA Close Doubles forms a large statistical set of uniformly gathered data on CSS sources of double morphology. Indications of youth and frustration by a dense and dusty medium cannot be pinned down with greater precision at the current stage, but it seems clear that at least one of these two factors will be applicable to the majority of MIT-VLA close doubles.

From an attempt to build a formal model for EGRS, it is concluded that the complexity of the multiple physical mechanisms involved would demand serious computational input to render the theory predictive, instead of just phenomenological. However, a clear conclusion resulting from the author's investigations into both EGRS and YSO evolution is that it is of central importance to start with a good accretion model. The general mathematical form of the solutions for an accreting population are presented in Chapter 5. As a corollary, one will be able to calculate the mass spectrum of non-accreting 'remnants' as a function of cosmic time.

The limitations of the proposed model are likely to be: poor knowledge of the actual accretion law and final mass distribution in real AGN, and poor knowledge of the merging rates as a function of cosmic epoch. The other problems of predicting the efficiency of energy transfer among the structures of AGN (core to jet to lobe) have been attacked many times in the past, and it should be quite possible to select a reasonable model for this external evolution from a detailed literature search.

It has been shown, at greater than the 90% confidence level, and assuming reasonable ages for the jets in the large MIT-VLA EGRS sample, that the maximum possible mean speed of advance of the jet head is almost certainly less than 10% of light speed, i.e. that the

mean speed is very likely to be non-relativistic. This result may be brought to lower levels of significance if the assumption that the jet ages are about the same as the central engines breaks down. However, it is physically expected that entrainment will slow down the jets by the time they reach 10-100 kpc scales, so the result seems to be in accord with this notion. To put the argument another way, the population of jets would have to be mostly younger than about 1 million years if they are to reach mean distances of order 20 kpc that are indicated by the mean angular size of seen in the MIT-VLA sample. This time is a fraction 3×10^{-9} of the mean evolution time of the EGRS population, and it seems too small to be realistic; how does the population regenerate its energy reserves if there are to be 400 million generations of EGRS producing jets within the observed cosmological evolution timescale ?

7.2 Young Stellar Clusters

A detailed mathematical accretion model has been constructed and used as as base for predicting the evolution of the statistical properties of YSOs. The simplifying assumptions seem not to have seriously compromised the fit of the predictions to the LF of the Rho Ophiuchus cluster. The indicated age of Rho Ophiuchus is 1 million years, to within a factor of 2, from judging the goodness of fit. This is consistent with previous estimates from naive assumptions. The underlying stellar evolution theory, and the *independent* model proposed in this thesis, seem to have meshed well together at the first attempt.

It was shown that the assumption of an accretion law and the specification of an observed final mass spectrum was sufficient to construct a retrodiction of the evolution of the mass function.

The known deficiencies of the simple Canonical Model cannot collectively be causing important perturbations on the model proposed here: these shortcomings might be any of the following: the unknown effect of disk accretion, the unknown numbers of brown dwarfs, the possibility of effects from outflows, rotation and magnetic torques from the accretion disk.

However, one serious problem that has *not* been addressed here is that of stars in binary and multiple systems. Perhaps the techniques developed in post-main-sequence evolution can be profitably used in the context of pre-main-sequence evolution.

One cannot say how many brown dwarfs there are in Rho Ophiuchus cluster. However, a simple analytic extrapolation of the Miller-Scalo log-normal function to zero mass suggests that there are at least $\sim$ 10 times as many brown dwarfs as there are bona fide stars. Hundreds of IR sources have been observed in Rho Ophiuchus, at fainter levels than before. A significant fraction of these *should* be brown dwarfs if there is no physical deselection principle that prevents objects of less than 0.085 solar masses from stopping their accretion process at an early stage in their evolution from essentially negligible mass. IR array cameras on space platforms could be profitably used for the testing of this idea.

7.3 Future Directions

The following pages are a copy of a comprehensive proposal of future research, written by the author.

Proposal of Future Research

The following addresses the shorter-term research that could be done to build on the work described above. Ideas for long-term projects are given in the next section. Interested collaborators should contact me at MIT.

With regard to the evolution of the luminosity functions of young stellar clusters, a prediction that has not yet been attempted is that of the time evolution of the infrared color distribution. All the tools exist to perform this calculation. Another problem is to take into account estimated extinction maps for the observed young stellar clusters, in order to more accurately derive bolometric luminosity functions that would be statistically representative of a larger portion of the cluster volume. Finally, my thesis predictions of the bolometric luminosity functions should be compared to the available data for other clusters known to contain young stellar objects, e.g. those in the Taurus-Auriga and Chameleon molecular clouds.

The remainder of the proposed work will concentrate on the publication of, and extraction of scientific results from, the MIT-VLA Archive. The motivations for such efforts are many: defining new representative samples of various types of radio source in the survey region $-30° < \delta < +40°$; systematically finding new examples of gravitational lensing in order to constrain cosmological Big Bang parameters from time delays and lens count statistics; theoretical interpretation of the broad-band spectra of these radio-loud AGN; probing the cosmological distribution, clustering and evolution of extragalactic radio-loud AGN, to mention some of the major long-term goals.

Once a preliminary version of the MIT-VLA Archive list of radio sources is compiled, I will submit these data for publication in the Astrophysical Journal Supplement, probably in the AAS CD-ROM series. Concurrently, I am organizing a DAT tape collection of $\sim$ 5000 FITS images from the newer MIT-VLA 8.4 GHz surveys. Much work could be done to improve the quality of this preliminary version of the Archive, and especially worthwhile

would be to find resources to uniformly re-reduce the older VLA 4.8 GHz (C-Band) data to a much higher level of quality, using the latest AIPS algorithms written by Conner. The re-reduction of the MIT-VLA C-Band data (4000 sources) is a long-term project that would take at least a few person-years to finish, on a part-time basis.

Already, the MIT-VLA Archive in its current form has proved useful to several other astronomers [Oleg Verkhodanov & Adelina Temirova (SAO), Richard McMahon & Isobel Hook (IoA), Malcolm Bremer (IAP)] requiring accurate positions to define representative samples of various types of radio sources in our survey region. Once I have electronically cataloged the VLA radio data, by the end of 1997, automatic positional cross-correlation becomes feasible with all-sky surveys in other wavelength bands, e.g. using the digitized POSS CD-ROMs, COSMOS, and the APM catalog. In addition to the optical regime, correlation with the infrared IRAS and X-ray ROSAT surveys could be made. This groundwork would pave the way towards understanding the physics of radio-selected AGN via analysis of both their broad-band spectra and morphologies, at the various observed wavelengths.

Having acquired 4000 CCD images over the past 2 years, Herold, Cooray and I will reduce and publish the data on the optical and radio emission from the MIT-VLA close radio doubles and gravitational lens candidates. Many other types of radio source subsamples could be searched for in the Archive, and in its correlations with other bands: new unresolved sources for orbiting VLBI observations, and also for the VLA, MERLIN and AT calibrator lists; USS, CSS and GPS sources; high-redshift radio galaxies and quasars; and radio galaxies with distorted shapes, to mention just a few possibilities. The results from all of the large-area high angular resolution snapshot programs of thousands of radio sources (e.g. MIT-VLA, PMN-ATCA, JVAS/CLASS) are a statistically significant sampling of all the radio-loud AGN in our observable universe. These high-resolution surveys are complementary to the latest ultra-sensitive all-sky radio surveys (e.g. FIRST, NVSS, WENSS, Molonglo Wide Field) that are expected to find at least several million such sources, but at lower resolution.

High angular resolution is essential for discerning the detailed morphology and angular sizes of most extragalactic radio sources; in my thesis, I show that a full 80% of all such radio sources are smaller than 10 arc-seconds in maximum projected angular size – about half of these remain unresolved with the VLA A-Array at 8.4 GHz.

Finally, another long-term project with great scientific payoff is the systematic compilation of redshifts for reasonably complete and representative samples of radio-loud AGN, almost all of which reside at cosmological distance. Initially, the optical identification must be completed for the preliminary list as compiled by Herold and myself in our Ph.D. theses. Meanwhile, I propose working with Lori Herold, Jacqueline Hewitt (MIT), Emilio Falco, Christopher Kochanek (CfA), and Hyron Spinrad (UC Berkeley) on first defining reasonably complete samples of bright MIT-VLA sources. E. Falco, C. Kochanek, H. Spinrad and their collaborators have already begun to obtain redshifts for the northern MG sources (e.g. Muñoz et al. 1997). Much work remains to be done, especially for the southern sky PMN sources (as the identifications within the older Parkes survey catalog [PKSCAT90] are quite incomplete). Since the MIT-VLA radio source surface density is no greater than ~ 0.5 per square degree, this could be most efficiently executed by regularly reserving a few fibers, in the AAT 2-degree-field (2dF) spectroscopic observations, for PMN-VLA sources. Our PMN collaboration with Alan Wright (Wright et al. 1995) would include PMN-ATCA radio source fibers for the more southerly declinations. This effort, though painstaking and difficult, would eventually allow serious study of the cosmological evolution of a few thousand radio sources, *conjointly* in radio luminosity, physical size, morphology and spectral index. The sky coverage would be much wider than previous efforts to study evolution down to much fainter radio flux densities (e.g. Benn et al. 1993; Windhorst et al. 1993). In this way, the MIT-VLA sample would start to fill in the massive increase in source count between the Jy and mJy apparent radio flux densities. The results would include statistically significant estimates of the redshift-dependent radio and optical luminosity functions for sources found at

GHz frequencies. It should eventually be possible to continue the search for 3-dimensional void and filamentary structure on cosmologically large physical scales. This has recently been started by Chris Benn & Jasper Wall for the 5th Cambridge (5C) sample (Benn & Wall 1995); they were careful to obtain redshifts for a reasonably complete sample of radio sources within a small sky patch. Without redshift information, it is impossible to determine anything significant about the 3-dimensional structure from just the 2-dimensional sky distribution – the latter has already been extensively studied for the extragalactic radio source population (e.g. Loan et al. 1996; Kooiman et al. 1995; Shaver 1991; Shaver & Pierre 1989).

In conclusion, the long-term benefits of finishing the work on the MIT-VLA archive are great, and there are several routes to useful publication of more immediate and focused results in the near future.

Ideas for a Research Program

The following array of research projects in the study of extragalactic radio sources would take at least 34.0 person-years to complete. The time for each project is given after the title of each section. Interested collaborators are invited to contact me at MIT.

1. **Observations of New MIT-VLA Gravitational Lens Candidates [2.0 py]**

   The MIT group has the world record for the discovery of gravitationally lensed radio sources. In my thesis, I display a new sample of good lens candidates, which require optical follow-up observations to confirm or deny the lensing hypothesis for each case.

2. **New Southern Hemisphere PMN-VLA Gravitational Lenses [1.0 py]**

   As the observable Universe is known to be isotropic and homogeneous on the largest scales, there should be roughly the same number of gravitational lenses visible in the Southern hemisphere as are already known in the North. The current number of (mostly Northern) multiply-imaged lenses is about 40. Given the incompleteness and bias in most lens search surveys in the North, there should be more than 100 lenses visible down our past light cone surface. The remaining lenses of this set therefore remain undiscovered in the South. In my thesis, there are at least 3 good PMN VLA lens candidates that wait optical imaging and spectroscopy at large telescopes. In collaboration with Alan Wright of the ATNF, their PMN Archive of 8000 snapshots could be similarly inspected for gravitational lenses.

3. **Database of MIT-VLA Radio Sources lensed through Model Gravitational Potentials [2.0 py]**

   One of the main problems in finding radio lenses is recognizing good candidates from thousands of images. There is no objective algorithm for this arduous task. To aid the future lens hunter, I propose to systematically compile and investigate the morphologies

and brightness distributions of actual MIT-VLA radio sources, as lensed through model gravitational potentials of typical galaxies. This investigation could be extended to include galaxy cluster lenses.

4. **Completion & Publication of MIT Archive of 10,000 Radio Source Snapshots: Preliminary [0.5 py]; Completion [3.0 py]**

   I am organizing detailed information on the positions and fluxes of radio galaxy components for 8000 MIT-VLA radio sources in my Ph.D. thesis. I intend to make this preliminary catalog available electronically to the astronomical community, via publication in a journal, such as the ApJS/AAS CD-ROM. It will take a further 3 person-years to process the unreduced VLA data, and also to bring all of the images up to a uniform level of quality.

5. **Reduction & Publication of MIT-VLA CSS Compact Double-Lobed Radio Galaxies [1.0 py]**

   At MIT, we have defined a sample of small double-lobed radio galaxies of the compact steep-spectrum (CSS) class (Cooray 1997 BS thesis; Cooray et al. 1996; Herold-Jacobson 1996). Over the past 3 years, I have obtained 4000 multi-color CCD images, and some spectra, of the optical counterparts of these galaxies, using the Michigan-Dartmouth-MIT Observatory telescopes. These data need to be uniformly reduced and published. The statistics of the spectral properties of these sources may be able to tell us whether they are truly young, or otherwise confined by a dense environment.

6. **Physical Modelling of the Observed Statistical Distributions within Large-Area Surveys of Extragalactic Radio Sources; constraining the Cosmological Evolution and Unification of radio-loud AGN [2.0 py]**

   There is an enormous amount of information on the observed properties of powerful radio sources in the public catalogs, such as those derived from the FIRST and NVSS

all-sky VLA surveys. The statistical distribution of fluxes, spectral indices, angular sizes and redshifts from all well-defined radio and optical surveys can be used to place constraints on the parameters of reasonable physical models (e.g. Pacholczyk 1977; Begelman et al. 1984; Chyzy 1997). An important aspect of this proposal is the consideration of how each individual survey is defined. Such selection effects can be easily programmed into Monte-Carlo simulations. With a large amount of RAM, disk space and computing power, it would be possible to get quick feedback on whether the assumed cosmological and radio source models are fitting the totality of the observed data well, or not. In iterative fashion, I expect to be able to place constraints on the realistic combinations of cosmology and physical source model that are allowed by the large body of data on extragalactic radio sources. This has already been done extensively for the well-defined and completely identified 3CR survey (e.g. Dunlop & Peacock 1990); it is now time to use *all* of the radio surveys, at complementary frequencies, resolutions and sensitivities, to constrain the refinement of existing models. If the cosmological world model is assumed from independent work, one can place definite constraints on the evolution of the luminosity and physical sizes of the radio source population. Candidate models for the cosmological evolution of powerful radio sources are to be constrained by the very stringent requirement that every one of the available catalogs be well fit by the model predictions, in a statistical sense. With the enormous numbers of observations made over the past 3 decades, the possibility of a particular behaviour of the evolution of these sources being missed in the modelling is remote.

7. Definition of New Subsamples from Radio Source Surveys [0.5 py]

Many interesting sub-samples may be defined from large-area radio source surveys, both from single-dish and interferometer data. Spectral indices, morphologies and angular sizes can be used to define samples likely to contain the following subsets of

the radio source population :-

- New examples of Gravitational Lenses.
- Unresolved, Flat-Spectrum Sources suitable for position calibration of interferometers (e.g. VLA, MERLIN, AT).
- High-redshift Quasars and Radio Galaxies.
- Compact Steep-Spectrum sources.
- Gigahertz-Peaked-Spectrum sources.
- Quasars and Radio Galaxies with disturbed morphologies.

8. **Search for new High-Redshift Radio Galaxies and Quasars [1.0 py]**

   Distant quasars and radio galaxies have a strong tendency to have steep radio spectra. High redshift quasars usually have red optical colors. Distant radio galaxies are usually optically faint, and relatively small in their radio linear sizes. Using these established observational properties (McCarthy 1993, Röttgering 1993, Hook 1994), one can greatly reduce the number of spectroscopic targets down to a reasonable level. With the systematic compilation of redshifts for well-defined samples of radio sources selected according to these discriminating criteria, one can infer the evolution of the luminosity functions of these objects at high redshift (e.g. Hook et al. 1996; Hook 1994).

9. **Cross-Identification of Radio Source Surveys with those at other wavelengths [1.0 py]**

   AGN typically emit over the entire electromagnetic spectrum, ranging from radio to gamma-rays. These data provide constraints on the combination of physical processes at work in different regions of the AGN galaxy. In order to understand the complicated physics involved in producing the phenomena associated with AGN, one must first compile and study their broad-band spectra, ideally in both frequency and time. As

a basic first step towards understanding the energetics and timescales for radio-loud AGN evolution, radio source catalogs should be cross-correlated with other well-defined catalogs, in a search for positional coincidences. The correlation between two radio surveys at different frequencies can yield the distribution of radio spectral indices, while one between two different epochs at the same frequency can yield constraints on radio source variability at that frequency. Optically-loud radio sources are especially valuable in fixing the distribution of intrinsic luminosities and physical sizes, via the redshifts of the optical emission lines. In particular, cross-correlation between various large-area surveys such as FIRST, NVSS, MOLONGLO WIDE FIELD, DSS/POSS/ESO, APM, COSMOS, IRAS, EINSTEIN, ROSAT will provide abundant data for physical modelling.

10. **Redshift Identifications of Complete Samples of bright MIT Radio Sources [2.0 py]**

A realistic investigation into radio source evolution depends greatly on optical identification and redshift compilation for complete and well-defined samples. With Jacqueline Hewitt (MIT), I would propose to execute such a campaign for a complete sample of 400 MIT-Greenbank sources, for which the VLA data are already in hand. Redshifts for those with optical counterparts should be obtainable in a few good-weather observing sessions at large telescopes. This would complement other efforts to map bright radio sources in depth (e.g. Falco et al. 1997). Multiple long-term campaigns are absolutely necessary if we are to eventually establish the cosmological evolution of large complete samples of radio sources in the universe. My effort will be a small but necessary contribution to this massive program.

11. **Supernova Ia Cosmology using distant Extragalactic Radio Sources [1.0 py]**

I propose to use a large search sample of intermediate power extragalactic radio sources at redshifts of $0.5 < z < 1.0$, as markers for possible sites of explosions of SNe Type Ia. Such events have been demonstrated to have remarkably small dispersion in the absolute peak brightness, and also in the form of the light decay curve; since these properties can be understood from the "local physics" of the explosions themselves, the "standard" decay curves can be used to put tight constraints on both q_0 and H_0. Of the many various methods of determining the Hubble parameter, SNe Ia yield the smallest dispersion. The limiting factor in the search for SNe Ia is that the outbursts are very faint by the time one probes a distance at which q_0 causes a measurable deviation from the low-redshift Hubble law. To help delve deeper into redshift space, I propose to use optically visible intermediate-luminosity AGN as a search sample for SNe Ia. This restriction on AGN power is necessary due to the dynamic range limitations in relative photometry from the ground. Confirmation of the SN Ia outburst could be obtained from deep spectroscopy. This project would have to be adopted by one of the existing SN Ia collaborations (e.g. Kim et al. 1997; Schmidt et al. 1996). I would simply provide these groups with lists of optically visible radio galaxies and quasars with $z > 0.5$, as derived from known radio source databases (including unpublished data, with the help of Heinz Andernach [ESO]). As a by-product of this program, confirmed discoveries of SNe Ia in extragalactic radio sources will start extending the cosmic distance ladder to the highest redshifts; with large statistical samples of such distant supernovae, we would be finally be able to definitively measure the geometry of the space-time of our Universe.

12. **Spatial Correlation with Abell Clusters, and known Superclusters [1.0 py]**

Powerful radio sources are commonly found near or in the centers of galaxy clusters, such as the relatively nearby Abell clusters, where they are likely to have been triggered by the high rate of dynamical interactions expected for such dense environments. With

the recent discovery of approximate periodicity on the supercluster scale, of $\sim 120/h_0$ Mpc (Einasto et al. 1997), I would like to investigate the placement of extragalactic radio sources in relation to the known superclusters. My aim would be to ascertain what physical conditions, on the supercluster scale, are conducive to forming powerful radio sources in the local universe.

13. **Search for Radio Source Hyperclustering in a Broad Conical Region [2.0 py]**

Previous large-scale-structure studies of complete radio source samples have been all-sky or small-solid-angle in coverage. I propose to obtain redshifts for radio sources over both a broad and deep conical region, e.g. in the north galactic cap of the FIRST survey area. As there are too many sources which need identification and spectra, the principle of random stratified sampling would be carefully implemented, so that a representative, well-defined sample would be able to yield significant statistical results. This should be complemented by independent pencil-beam surveys in the same sky area, for verification purposes. The idea here is to detect *hyperclustering*, i.e. on scales larger than superclusters. This can be practically achieved only by dedicated optical follow-up surveys using distantly visible sources distributed over large areas of sky. In the southern hemisphere, the 2dF multi-fiber spectrograph at the AAT might be profitably used, while the Sloan Digital Sky Survey (SDSS) database would be the information source in Northern hemisphere.

14. **Upper Limits on Gigaparsec Cosmic Bulk Flow extending beyond the Observable Universe [1.0 py]**

If our Universe contains insufficient dark matter for closure, its topology is open, and its extent is infinite within the context of FLRW cosmologies. Within an unlimited volume, there might well exist descendants of truly massive quantum fluctuations of

much larger scale than the ones seen in the current optical and infrared redshift surveys – these are technologically constrained to probe only our local patch of the universe. I propose to use distant powerful radio sources to detect the presence, or otherwise, of cosmic bulk flow on Gigaparsec scales, caused by enormous mass fluctuations that may reside beyond our observable horizon. Such a search presumes that the inflation theory is not correct in predicting a universe that is vanishingly close to being flat at the present time, and thus the detection of such cosmic flows would put severe constraints on the inflation paradigm. External mass fluctuations, of even 1% of the entire mass within the observable universe, would give rise to detectable differential velocity fields, or *"cosmic tides"*, in the bulk flow within our Hubble volume. The absence of such a detection would provide strong upper limits on the power spectrum of physical fluctuations on truly cosmic (Gpc) scales. These data would go beyond the physical size scales accessible to COBE, as the causally-connected volume around the recombination epoch was a factor of $\sim 10^9$ smaller than the volume accessible to current-day observations. In practice, one looks for detectable spherical harmonic signatures in the distribution of radio sources in the sky, both in position and in flux. The sensitivity of such a search is limited mainly by the unknown systematic errors in the flux scale of the radio surveys used to detect such Doppler effects. For even a velocity of 10,000 km/s, which is a few percent of the speed of light, the level of random plus systematic error in the radio source fluxes must be less than a similar percentage if there is to be good chance for detecting such bulk flows (see Loan et al. 1996; Crawford et al. 1997; Baliesas et al. 1997). It should be noted that there has been a controversial bulk flow velocity found by Tod Lauer and Marc Postman, using the relatively distant Abell clusters (Lauer & Postman 1994). Their survey depth is just $z \leq 0.1$, so the proposed radio survey analysis would be probing a volume $\sim 10^3$ times larger than their local Abell cluster survey.

15. **Follow-up Observations of Radio-Loud AGN at Millimeter, Infrared, and X-ray Wavelengths [3.0 py]**

In order to understand the complex physical processes that generate the radiation from AGN, and that cause the extended radio morphologies, it is first necessary to obtain spectral information over as wide a range as possible. This would be even more useful if uniform temporal monitoring was also ensured, but this is in practice extremely difficult even for a single AGN. In particular, the mm, IR and X-ray data should provide useful constraints on AGN at different size scales: mm from the core; IR from throughout the stellar extent of the host, but especially in the nuclear region; and Xrays from the innermost parts of the accretion disk. There have already been preliminary cross-correlations between radio catalogs and the IRAS and ROSAT surveys. There is yet to be a uniform all-sky survey in the sub-cm radio wavelengths.

16. **New Radio Continuum Surveys at Higher Radio Frequencies [3.0 py]**

At Haystack, there is an opportunity to embark on two all-sky sub-cm radio surveys. Regardless of the location of the mm-wave telescope used, some of the major scientific results from such data would be:-

- *Millimeter-wave calibrators*

  We need to locate reliable flux calibrators to define a suitable flux scale, as well as position and polarization calibrators for mm-wave interferometers.

- *Uniform Radio Source Counts in the sub-cm regime*

  Counts at these frequencies provide further constraints on emission mechanisms in AGN, as well as on source evolution models. Once the source counts have been established, their contribution to the CMB measurements can be more accurately subtracted.

- *Radio Spectral Characteristics in the sub-cm regime*

Do all extragalactic radio sources cut off at these high frequencies, or do some rise towards shorter wavelengths ? Such a signature would be proof of the onset of a changeover from synchrotron to a new emission mechanism.

- *Radio Source Variability in the sub-cm regime*
  The relation between spectrum and variability should be explored for these higher frequencies.

Independent surveys, each at a different frequency chosen from the atmospheric absorption windows (e.g. 3 and 7mm – 84.0 and 35.5 GHz), could be interleaved at daily or weekly intervals; this would provide new spectral index information. I propose to scan the declination strip $20° < \delta < 30°$, which includes the North Galactic Cap, and also part of the sky covered by the FIRST and NVSS 1.4 GHz VLA surveys. In addition, the SDSS optical survey will overlap with the proposed area. It should be noted that problems with unrealistically high slew rates, in near-zenith crossings by the altitude-azimuth Haystack dish, are avoided at these declinations. To complete the survey in minimum time, meridian circle scanning in the North-South direction would have to be near maximum rate (10 deg/min or $\sim 40\times$ sidereal). The spatial separation between adjacent scans would best be at double Nyquist rate, so that there would be four entirely independent Nyquist surveys at each frequency; two interleaved surveys going North, and two going South. With a FWHM beamsize of 27″ at 84 GHz, a complete survey would take 400 days at 84.0 GHz, and 170 days at 35.5 GHz: a total of 19 months for a dual frequency survey. This would mean that the survey would be in progress over a $\sim$ 3 year period, on a half-time basis. If this is considered too long a period, then one could simply reduce the width of the proposed declination strip accordingly; the important thing for the survey sample definition and source counts is to ensure that all of the proposed area, no matter how small it is, will be covered in a uniform way.

Known, unresolved, flux calibrators at these high frequencies should be checked regularly on an absolute scale, and suitably stable sources are to be observed on a weekly basis, for the calibration of the telescope gain as a function of zenith angle. A major problem at these frequencies is the systematic variation of gain due to atmospheric fluctations in water and oxygen content. These can be circumvented somewhat *a posteriori*, using a vane calibration technique (e.g. see the 1995 Haystack Observatory note, and Charles Katz's 1997 MIT Ph.D. Thesis for a description of his flux calibration procedure for Haystack 37m data). Another potential problem that may arise is the loss of pointing accuracy at high slew rates. In view of these realities, and with the inevitability of poor weather and corruptive radio interference, it would be wise to ensure completion of all four independent surveys by devoting blocks of time for repeat scans of problem areas, near the end of the program.

The reduction could be done in two ways: direct gridding of the data using a powerful cluster of fast workstations or a supercomputer, with the analysis done entirely by custom-built code; and single-dish mapping and analysis using existing AIPS software. The comparison between these two methods in the PMN survey, at the lower PMN flux densities, has not been favorable (differences exist between the independently derived catalogs, up to a level of 7%). The proposed cross-checking between these mapping methods would then be a precautionary measure. Finally, an estimation of the completeness and reliability should be made for the survey, using a Monte-Carlo artificial source-injection procedure running on a powerful multi-processor. A catalog would then be produced, listing the source names, positions, fluxes, errors, profile fitting results, and accurate sub-cm spectral indices. The interleaving of the scans in the multiple surveys would provide information on the time variability of the radio sources at these high frequencies, as well as an invaluable check on the reliability of the data.

17. **Study of Local Universe AGN using multi-wavelength surveys [2.0 py]**

In terms of radio brightness, the apparently fainter extragalactic radio sources are expected to be closer to us in the Universe, i.e. they are mostly at the low end of a very broad radio luminosity function. As there are many more such sources per unit interval of flux density than at brighter apparent fluxes, there is a huge population of low-power AGN easily visible in our local region of the Universe. Correlation between the new, sensitive radio catalogs (FIRST, NVSS, WENSS and Molonglo Wide Field Surveys), which together will contain about a few million extragalactic radio sources, and other large-area catalogs will help identify the relation between radio waves and emissions in other bands. Especially important will be the mm and IR surveys of low-power AGN powered by starburst nuclear activity, which are an entirely different population from the powerful radio-loud AGN (the latter are commonly pictured to arise through the gravitational infall of gas, dust and stars through a viscous accretion disk into a MBH). It is essential to distinguish between these two populations appearing in the source count distribution; very different physical models would be appropriate for each of these types of extragalactic radio source.

18. **Construction of an Public, Comprehensive Electronic Catalog of the Properties of Extragalactic Radio Sources [5.0 py]**

To construct reasonable models for the cosmological evolution of powerful radio sources, one has first to make a systematic study of their observed properties: fluxes at different frequencies, component flux ratios, angular sizes, radio morphologies, optical and infrared fluxes and morphologies, and redshifts. It would also be interesting to note unusual and peculiar distinguishing characteristics. In 1978, A. Pacholczyk single-handedly compiled, from the available literature, information on a few hundred radio galaxies and quasars in the range $0^h < \alpha < 12^h$. This appeared in a handbook (Pacholczyk 1978), but the full RA coverage was never published. His purpose was to

have a handy reference to use in the construction of realistic radio source models (e.g. Pacholczyk 1970, 1977). I propose to retrace his steps, and bring this compilation up to the current date. This database would have a uniform format for all the entries, and be in the form of a flat ASCII file readable by both computer and human. It would be made available to the community via the Internet. A companion atlas of radio maps could be compiled into a technical report, during the course of this endeavour. It is hoped that other researchers would make use of this compilation in their work, and that some will try to improve the latest radio source models. These would be my own strong motivators for completing such a task.

Predictions from theoretical models can be best tested against the incidence of anomalies and unusual characteristics that will be compiled into the database from the literature; indeed, the literature is already heavily biased in favor of such peculiarities (e.g. giant radio galaxies; sources with more than 2 jets, or with highly polarized rings and shells in their jets and lobes; compact steep-spectrum, ultra-steep-specrum and inverted-spectrum sources). The models can be improved by testing their weak points against the broad-ranging and rarer phenomena seen in radio-loud AGN, but this can only be fruitfully done via an unbiased analysis. This is a long-term project best undertaken by a small team of a few people, who are able to synchronize their recording algorithms at the beginning of the task. Some of the immediate uses of this catalog would be to define known samples of radio sources for the various observing projects listed above. The "Extragalactic Radio Source Bible" would also be invaluable in the construction of observing lists of all types of radio sources; instead of laboriously and incompletely sifting through the literature to establish exactly which radio sources already have the requisite data (e.g. redshift information from a deep optical integration), they would simply cross-check against the latest version of the bible, thus saving an enormous amount of time. This projected capability demands completeness,

uniformity and accuracy in the construction of the reference volume.

References for Research Proposal

Baliesas, A., Lahav, O., Loan, A.J., Wall, J.V. 1997, *MNRAS preprint*, astro-ph/9709205

Benn, C.R., Rowan-Robinson, M., McMahon, R.G., Broadhurst, T.J., Lawrence, A. 1993, *MNRAS* **263**: 98

Benn, C.R., Wall, J.V. 1995, *MNRAS* **272**: 678

Begelman, M., Blandford, R.D., Rees, M.J. 1984, *Theory of Extragalactic Radio Sources*, *RMP* **56(2)**: 255

Chyzy, K.T. 1997, *MNRAS* **289**: 355

Condon, J.J. 1984a, *ApJ* **284**: 44

Condon, J.J. 1984b, *ApJ* **287**: 461

Condon, J.J. 1988, "Radio Source Cosmology", in *Galactic and Extragalactic Radio Astronomy*, eds. K.I. Kellermann & G.L. Verschuur, Springer-Verlag: Germany, 641

Condon, J.J. 1989, *ApJ* **338**: 13

Conner, S.R. 1997, MIT Ph.D. Thesis, *"The MIT-Green Bank-VLA λ6cm Gravitational Lens Search"*, in progress

Daly, R. 1994, *ApJ* **426**: 38

Dunlop, J., Peacock, J. 1990, *MNRAS* **247**: 19

Einasto, M., Tago, E., Jaaniste, J., Einasto, J., Andernach, H. 1997, *A&AS* **123**: 119

Falco, E.E., Kochanek, C.S., Muñoz, J.A. 1997, preprint *astro-ph* 9707032

Fanti, C., Fanti, R., Dallacasa, D., Schilizzi, R.T., Spencer, R.E., Stanghellini, C. 1995, *A&A* **302**: 317

Griffith, M. *et al.* 1991, *Proc. ASA* **9(2)**: 243 (PMN)

Griffith, M.R. 1993, MIT Ph.D. Thesis, *"The Parkes-MIT-NRAO (PMN) Survey of the Southern Sky"*

Griffith, M.R., Wright, A.E. 1993, *AJ* **105(5)**: 1666 (PMN)

Griffith, M.R., Wright, A.E., Burke, B.F., Ekers, R.D. 1994, *ApJS* **90**: 179 (PMN-Tropical)

Griffith, M.R., Wright, A.E., Burke, B.F., Ekers, R.D. 1995, *ApJS* **97**: 347 (PMN-Equatorial)

Haystack Observatory, Westford MA, USA 1995, *An Introduction to Radio-Astronomical Observing at Haystack*

Herold-Jacobson, L.K. 1996, MIT Ph.D. Thesis, *"Identification of Radio Sources from the MG-VLA Survey"*

Hook, I.M., McMahon, R.G., Irwin, M.J., Hazard, C. 1996, *MNRAS* **282**: 1274

Hook, I.M. 1994, University of Cambridge Ph.D. Thesis, *"Quasars at High Redshift"*

Kapahi, V. 1989, *AJ* **97**: 1

Katz, C.A. 1997, MIT Ph.D. Thesis, *"Surveys for Transient Astronomical Radio Emission"*

Kellermann, K.I. 1993, *Nature* **361**: 134

Kim, A.G. & the UC Berkeley Supernova Cosmology Collaboration 1997, *ApJL* **476**: 63

Kooiman, B.L., Burns, J.O., Klypin, A.A. 1995, *ApJ* **448**: 500

Lehár , J.L. 1991, MIT Ph.D. Thesis, *"The Time Delay in the Double Quasar Q0957+561 and a Search for Gravitational Lenses"*

Lauer, T., Postman, M. 1994, *ApJL* **425**: 418

Loan, A.J., Wall, J.V., Lahav, O. 1996, *MNRAS* **286**: 994; astro-ph/9612190

Marcy, G.W., Butler, R.P. 1996, *BAAS* **189**: 34.01

McCarthy, P.J. 1993, *ARA&A* **31**: 639

Neeser, M.J., Eales, S.A., Law-Green, J.D., Leahy, J.P., Rawlings, S. 1995, *ApJ* **451**: 76

Pacholczyk, A. G. 1970, *Radio Astrophysics*, Freeman: San Francisco CA, USA

Pacholczyk, A. G. 1977, *Radio Galaxies*, Pergamon Press: Oxford, UK

Pacholczyk, A. G. 1978, *A Handbook of Radio Sources*, Pachart Publishing House: Tucson AZ, USA

Peacock, J.A. 1985, *MNRAS* **217**: 601

Röttgering, H.J.A. 1993, Leiden University Ph.D. Thesis, *"Ultra-Steep Spectrum Radio Sources: Tracers of Distant Radio Galaxies"*

Schmidt, B.P. & the CfA Supernova Cosmology Collaboration 1996, *BAAS* **189**: 108.05

Shaver, P.A., Pierre, M. 1989, *A&A* **220**: 35

Shaver, P.A. 1991, *AusJPhys* **44**: 759

Shaver, P.A., Wall, J.V., Kellermann, K.I., Jackson, C.A., Hawkins, M.R.S. 1996, *Nature* **384**: 439

Subramanian, K., Swarup, G. 1990, *MNRAS* **246**: 263

Swarup, G. 1975, *MNRAS* **172**: 501

Turner, E.L., Ostriker, J.P., Gott, J.R. III 1984, *ApJ* **284**: 1

Wall, J.V. 1994, *AusJPhys* **47(5)**: 625

Wall J.V. 1995, IAU 175, *Extragalactic Radio Sources*, Kluwer Academic Publishers: Dordrecht, Holland, 547

Wilking, B.A., Lada, C.J., Young, E.T. 1989, *ApJ* **340**: 823.

Windhorst, R.A., Fomalont, E.B., Partridge, R., Lowenthal, J.D. 1993, *ApJ* **405**: 498

Wright, A.E., Tasker, N.J., Savage, A., Vaughan, A.E. 1996, IAU 175, *Extragalactic Radio Sources*, eds. R. Ekers, C. Fanti & L. Padrielli, Kluwer Academic Publishers: Dordrecht, Holland, 507

Appendix A

MIT-VLA Close Radio Doubles

The following pages are a copy of the original coordinate log files for the MIT-VLA Close Doubles, Random Sources, Gravitational Lens Candidates and other 'Interesting' MIT-VLA Sources.

The Close Doubles are signalled by the code 'CD' in the column labelled 'Morph' in the middle of each page. The Random Sources have the word 'RANDOM' written next to this column.

The radio maps, reduced optical photometry, and optical spectra, for a substantial subset of the MIT-Green Bank Close Doubles appears in the 1996 Ph.D. thesis of Lori Herold-Jacobson [69], and the 1997 BS thesis of Asantha Cooray [39].

The MIT-VLA radio and MDM/CTIO optical data reside in a EXABYTE/DAT tape archive at MIT. This archive is currently being organized by the author (1998).

master.feb96.list Thu Jan 29 04:37:48 1998 1

*** MASTER MG/PMN OPTICAL TALLY RESULTS LOG : LAST MODIFIED - 13 MAR 1996 04:00 AM ***

OBJECT NAME	F ?	P R	POSS MAG	CTIOTek/MDMNell/MDMWilb #I	#R	#V	#B	TAL	Radio J2000 Position RA	DEC	Radio	Morph	.Jy	*NMV#	Optic Morph	z	Mag
PMN0003-1727	Y		<20		+1+	+ +4	+1+		00 03 21.955	-17 27 11.93	3"	XS1 Ncoltrp					
PMN0008-1419	Y		<20	+1+3	+1+9	+1+	+1+		00 08 16.867	-19 39 41.99	1.3"	XS2 Cre-Dbl(dffse)?					
MG0020+2350	Y		>20		+1+				00 20 46.658	23 48 34.06		X6 MG RANDOM $21					
MG0026+3509	Y		<20	+1+4	+1+7	+1+	+1+		00 26 41.7255	35 08 42.265		Cls Trp?	.30	* M			
PMN0029-1111	Y		>20	+ +8	+ +13	+1+	+1+		00 29 22.639	-11 11 51.19	1.5"	XS2 CD					
MG0032+1953	Y		<20	+1+	+1+				00 32 38.3266	19 53 53.709		X3 MG RANDOM $6			# nr Gal 4C19.03		
PMN0035-1635	Y		<20	+1+6	+2+5	+2+	+2+		00 35 37.290	-16 35 02.35		XS2 Arc Lens ?					
MG0041+2549				+ +2	+ +4				00 41 18.42	25 50 04.13		X5 CD		*			
MG0046+2035					+ +3				00 46 39.561	20 35 40.06		X3 CD					
MG0052+3815	Y		>20	+1+	+1+	+1+2	+1+		00 52 16.955	38 15 29.58		X8 CD			# QSO 4C37.03		18.5
MG0055+2903				+ +3	+9+				00 55 46.24	29 03 49.84		X5 CD					
PMN0108-1604	Y		>20	+1+	+1+	+ +2	+1+		01 08 20.731	-16 04 54.22		XS2 PMN RANDOM $6					
MG0112+2728	Y		>20		+1+				01 12 13.212	27 28 40.08		X5 MG RANDOM $22					
MG0124+2804	Y		<20	+1+1	+1+1	+ +1	+ +1		01 24 55.879	28 05 11.36		X5 MG RANDOM $23					
MG0130+2338	Y		<20	+1+	+1+	+1+	+1+		01 29 59.8337	23 38 20.241		X3 MG RANDOM $7			# QSO 4C23.06	1.459	19.0
PMN0140-0957	Y		>20	+ +1	+ +5	+ +1	+ +1		01 40 12.840	-09 56 57.50	0.5"	XS1 CD					
MG0151+2934	Y		>20		+1+				01 51 44.680	29 35 56.28		X7 MG RANDOM $24					
PMN0157-1043	Y		<20	******	N O	D A T A	******		01 57 41.555	-10 43 41.04	2.0"	XS1 NColtrp					
MG0200+2156				+ +1	+ +1	+ +1	+ +1		02 00 07.6297	21 57 00.846	0.25"	CD	.16	* M			
PMN0201-1132	Y		<20	+ +1	+ +4	+ +1	+ +1		02 01 57.179	-11 32 32.65	1.6"	XS1 CD					
MG0204+2825	Y		>20	+ +3	+ +7	+1+			02 04 50.95	28 25 06.56		X5 CD					
PMN0205-1801	Y		>20		+ +4				02 05 20.751	-18 01 47.37	1.5"	XS1 Arc ?					
PMN0209-1003	Y		>20		+ +3				02 09 59.125	-10 03 27.60		XS2 PMN RANDOM $1					
MG0210+3249				+ +1	+ +9				02 10 16.80	32 49 33.75		X4 CD		*N			
MG0215+3618	Y		<20		+1+				02 15 18.319	36 17 51.44		X8 MG RANDOM $25					
MG0232+3424				+ +1	+ +9				02 32 28.57	34 24 08.03		X4 CD		*N			
PMN0234-0935	Y		>20	+ +2	+ +6				02 34 15.919	-09 35 15.85		XS2 Asym Dbl					
PMN0237-1932	Y		>20	+ +1	+1+5				02 37 44.727	-19 32 36.98	0.8"	XS1 CD -Ring?					
PMN0240-1034	Y		>20		+1+	+ +3			02 40 15.568	-10 35 20.18		XS2 PMN RANDOM $5		*			
MG0245+2405	Y		<20	+ +1	+1+1	+ +4	+ +1		02 45 16.8533	24 05 35.076		X3 MG RANDOM $8			Fnt POSSID		
MG0246+2622				+ +4	+ +8				02 46 45.07	26 23 25.44		X5 CD					
MG0246+064	Y		R18.6	+ +4					02 48 58.100	06 41 43.14	2.4"	XS34 Sam RngCnt>.22		*			
MG0249+3333					+ +2				02 49 56.771	33 32 36.844		X4 MG RANDOM $15					
MG0256+3246	Y		<20	+1+1	+ +7	+ +1	+ +1		02 56 22.848	32 46 48.03		X7 CD			Fnt POSSID		
PMN0301-1608	Y		>20	2+ +1	2+1+1	2+ +1	2+ +1		03 01 07.856	-16 10 06.29	0.7"	XS3 CD-Corrp?		*N			
MG0304+2551	Y		>20		+2+				03 04 58.622	25 51 47.20		X5 MG RANDOM $26					
MG0307+1220				+ +3	+ +10	+ +1	+ +1		03 07 46.342	12 21 01.599	1.5"	Dbl/Trp?	.06	* M			
MG0312+3848					+ +6				03 12 11.717	38 49 08.96		X8 CD					
PMN0311-1311	Y		>20	+ +5	+ +2				03 11 45.227	-13 11 31.70		'S' Dbl Lobe					
PMN0312-1613	Y		>20	+1+2	+1+	+1+	+1+		03 12 37.323	-16 13 29.64	0.6"	XS2 CD					
PMN0320-1334	Y		>20	2+ +2	2+ +6	2+ +	2+ +		03 20 17.256	-13 34 51.07	0.5"	XS2 CD					
PMN0321-2940	Y		<20	+ +1	+ +5	+ +1	+ +1		03 21 28.812	-29 40 46.17	0.5"	XS1 CD					
PMN0324-2254	Y		>20	2+ +1	2+ +1	2+ +	2+ +		03 24 18.211	-22 56 12.46	0.7"	XS3 CD-Corrp?		*N			
MG0325+2130				+ +2	+ +9				03 25 27.072	21 29 57.803		X6 CD		*			
PMN0325-1801	Y		~20	+ +3	+ +7	+ +1	+ +1		03 25 53.224	-18 01 58.21	0.3"	XS2 CD					
MG0334+3628	Y		>20			+ +2			03 34 28.202	36 28 41.85		X8 MG RANDOM $27		*N			
PMN0335-1142	Y		>20	+ +1	+ +9	+ +1	+ +1		03 35 08.202	-11 42 10.42	0.6"	XS2 CD					
PMN0343-2530	Y		<20	+1+	+1+				03 43 19.528	-25 30 17.32		XS1 NColtrp		*N			
MG0349+3354	Y		<20	+1+	+1+	+1+	+1+		03 49 21.320	33 54 50.37		X7 MG RANDOM $28					
MG0352+2220					+ +3				03 52 33.588	22 20 21.41		X3 CD					
PMN0352-2514	Y		>20	+ +1	+1+1	+ +1	+ +2		03 52 13.565	-25 16 46.54	0.5"	XS3 CD-Corrp?		*N			
MG0353+3826	Y		>20		+4+				***** NEED TO FIND COORDINATES *****								
MG0355+2112	Y		<20	+1+	+1+	+1+	+1+		03 55 30.0022	21 13 21.486		X3 MG RANDOM $9				??Coord Discrep.	
PMN0401-2034	Y		>20	2+ +	2+1+	2+ +	2+ +		04 01 56.489	-20 36 49.11	0.7"	XS3 CD-Corrp?		*N			
PMN0403-2444	Y		>20	+ +1	+1+1	+ +1	+ +1		04 03 45.852	-24 43 47.16	0.6"	XS3 CD-Corrp?		*N			
PMN0405-1307	Y		<20	+1+	+1+	+1+	+1+		04 05 33.989	-13 08 14.30	1.1"	XS1 CD					
MG0413+2648	Y		<20		+ +5				04 13 23.551	26 49 16.250		X6 CD					
MG0414+3419	Y		>20	+1+	+ +6				04 14 37.2586	34 18 51.144		X4 MG RANDOM $16					
MG0416+3108	Y		>20		+5+				04 16 47.37	31 08 12.37		X4 CD					
MG0425+094				******	N O	D A T A	******	B04	25 30.70	09 26 05.5	1.5"	Trp	.10	* M			
MG0432+2013					+ +5				04 32 54.898	20 13 08.18		X3 CD					
PMN0432-0923	Y		>20?	2+ +	2+ +5	2+ +	2+ +	AST04	32 31.200	-09 23 11.00	2.5"	XS3 CD					
PMN0433-0721	Y		>20	+ +1	+1+1	+ +1	+ +1		04 34 01.160	-07 20 48.76	0.5"	XS3 CD-Corrp?		*N			

master.feb96.list Thu Jan 29 04:37:48 1998 2

```
PMN0436-2312  Y   >20          + +3                          04 35 57.827 -23 33 28.95        XS4 PMN RANDOM $10
 MG0436+2621  Y A >20    + +4          + +4                  04 36 25.981  26 21 38.84         X5 CD                 *N                  ***NEW CD(Feb96)
 MG0440+2728  Y   <20    +1+     + +4    + +1    + +1        04 40 27.739  27 28 40.62         X5 MG  RANDOM $29
 MG0441+3003  Y   >20          + +2                          04 41 02.773  30 02 23.04         X7 MG  RANDOM $30
PMN0444-1822  Y   >20   2+ +    2+ +6   2+ +2   2+ +        04 44 58.444 -18 23 09.08  1.0" XS2 Ring?-Corrp
PMN0452-0306  Y   <20          + +2    + +3                  04 52 31.143 -03 06 21.61        XS4 PMN RANDOM $8
PMN0456-1144  Y   <20          + +3            + +1          04 56 23.056 -11 44 14.51  2.5" XS2 CD
PMN0505-1558  Y   >20   2+ +    2+ +3   2+ +1   2+ +1        05 05 41.645 -15 56 55.37  0.6" XS2 CD
PMN0508-0943  Y   >20   2+ +    2+ +6   2+ +    2+ +         05 08 13.445 -09 43 03.50  1.1" XS2 CD
 MG0509+1956  Y   >20    +1+     + +6                        05 09 01.323  19 57 19.52         X3 CD
PMN0515-1337  Y   >20     + +5   +1+1     + +1    + +1        05 15 21.513 -13 38 15.87  1.1" XS1 CD                 *N
PMN0521-2047  Y   >20   2+ +    2+1+3   2+ +    2+ +         05 21 38.872 -20 47 39.47  1.3" XS1 CD                 *N
PMN0522-1209  Y   <20     + +1    + +4    + +1    + +1        05 22 19.951 -12 09 10.12  1.0" XS1 CD                 *N
PMN0527-1053  Y   >20   2+ +1   2+ +4   2+ +1   2+ +1        05 27 10.882 -10 53 28.72  0.35"XS2 CD
PMN0531-1417  Y   <20     + +1    + +8    + +4    + +1        05 31 56.406 -14 17 25.77 ?1.6" XS2 Trp?
PMN0533-0426  Y   >20          + +3    + +3                  05 32 54.137 -04 26 43.64        XS4 PMN RANDOM $9
PMN0541-0525  Y   >20     + +1    + +3    + +4    + +1        05 41 55.086 -05 25 13.68        XS4 PMN RANDOM $7
PMN0553-1709  Y   >20   2+ +1   2+ +5   2+ +1   2+ +1        05 53 51.605 -17 10 12.17  0.3" XS2 CD
PMN0607-0623  Y   <20?   1+     +1+1     +1+     +1+ AST06 07 46.500 -06 23 02.00                 Ext.Flat.Spec.
PMN0617-1134  Y   <20   4+1+1   2+1+5   1+1+1    +1+1    06 17 29.105 -11 34 29.07  1.0" XS2 CD
PMN0617-1517  Y   <20    +1+     +1+3    +1+3    +1+     06 17 07.444 -15 18 02.41        XS2 PMN RANDOM $2
PMN0618-1330  Y   >20     + +1    + +8    + +1    + +1    06 18 31.771 -13 30 37.26  3.1" XS1 Ncoltrp
PMN0621-1715  Y   <20     + +1    + +4    + +7    + +1    06 21 01.308 -17 15 55.10  2.4" XS2 CD
 MG0623+3711                  +5                          06 23 33.134  37 11 07.18         X8 CD                 *
PMN0625-1018  Y   >20     + +1    + +9    + +4    + +6    06 25 42.897 -10 17 56.52        XS2 Comp Trp Lens?  *N
PMN0632-2614  Y   <20   2+1+    2+1+4   2+ +1   2+ +1    06 32 06.505 -26 14 13.92        XS1 CD              *N
PMN0636-2241  Y   <20?    + +1    + +8    + +1    + +1AST06 36 43.577 -22 41 39.80  0.7" XS3 Asymm.CD
PMN0641-2409  Y   <20   1+ +1   1+ +8   1+ +7   1+ +1    06 41 51.569 -24 11 36.97        XS4 Faint Ring ?
 MG0649+2751  Y   <20    +2+     + +9                    06 49 53.16   27 51 39.83         X5 CD
 MG0651+2249  Y   >20          + +3                    06 51 16.361  22 49 22.12         X6 MG  RANDOM $31
 MG0718+2009  Y   <20          + +9                    07 18 10.639  20 10 03.11         X3 CD                    V
 MG0750+2908  Y   ~20          + +9    + +3            07 50 39.54   29 07 11.08         X5 CD                 *  V
 MG0751+3410  Y   >20          + +3    + +5            07 51 31.8401 34 09 04.842        X4 MG  RANDOM $17      V
 MG0754+3519          ******   N O   D A T A  ******   07 54 44.74   35 20 03.64         X4 CD                 *
 MG0809+3455          ******   N O   D A T A  ******   08 09 43.31   34 56 10.66         X4 CD                 *
 MG0810+2651  Y   >20          + +8    + +3            08 10 25.96   26 50 51.28         X5 CD                    V
 MG0817+3226  Y   >20          + +5                    08 17 24.5875 32 27 21.537        X4 MG  RANDOM $18
 MG0818+179   Y   <20   ******   N O   D A T A  ****** B08 18 52.65   17 57 56.0   0.5"      Dbl/CJ       .33 * M [ALIAS MG0821+1747]
 MG0819+3227                  + +5    + +2            08 19 03.98   32 27 44.93         X4 CD                 *
 MG0819+2641  Y   <20          + +6                    08 19 16.615  26 42 03.24         X6 MG  RANDOM $32
 MG0819+2614  Y   >20          + +5                    08 19 11.30   26 14 11.85         X5 CD
 MG0820+3640  Y   >20          +1+                     08 20 18.48   36 41 24.11         X4 CD
 MG0829+3627  Y   >20          +1+                     08 29 05.72   36 31 23.24         X4 CD
PMN0837-1156  Y   >20   3+ +14 12+ +9   3+ +6   3+ +1    08 37 02.842 -11 55 10.84        XS2 Ring Lens ?
PMN0837-1939  Y   <20   2+ +1   1+ +4   1+ +    2+ +1    08 44 58.452 -18 45 56.05  2.7" XS4 Dbl
 MG0848+3147  Y   >20          + +4    + +3            08 47 57.92   31 46 15.92         X5 CD                    V    HDR WRNG NAM: MG0818+3147
 MG0851+142   Y   >20   [SEE TWO LINES BELOW THIS ONE] B08 51 53.38   14 17 20.0   2"        Trp          .20 * M [SAME as MG0854+1405]
 MG0853+3255          ******   N O   D A T A  ****** 08 53 21.1075 32 54 59.282        X4 MG  RANDOM $19
 MG0854+1405  Y   >20     + +1    + +6    + +1    + +1    08 54 39.416  14 05 52.47         CD                 * M [SAME as MG0851+142]
PMN0902-0459  Y   >20   2+ +    2+ +5   2+ +4   2+ +1    09 02 36.748 -05 00 05.14  2.4" XS4 Quad Lens ?
 MG0906+2200  Y   >20          + +3                    09 06 12.2009 21 59 55.586        X3 MG  RANDOM $10
 MG0907+3149  Y A >20    + +9    + +4            + +3    09 07 51.546  31 49 05.49         X5 CD                 *N                  ***NEW CD(Feb96)
 MG0908+2253  Y A >20          + +9            + +3    09 08 00.072  22 54 02.48         X5 CD                 *N                  ***NEW CD(Feb96)
 MG0910+2539  Y   <20     + +1    + +4    + +1    + +1    09 10 55.236  25 39 21.46         X6 MG  RANDOM $33
PMN0914-1842  Y   >20   2+ +1   2+ +2   2+ +1   2+ +1    09 14 27.616 -18 42 58.28  0.8" XS2 CD
PMN0915-1630  Y   >20   2+ +1   2+ +4   2+ +1   2+ +1    09 15 14.656 -16 30 47.07  0.5" XS2 CD
PMN0923-0935  Y   ~20     + +5    + +7    + +11   + +5    09 23 42.712 -09 35 23.18  1.2" XS1 Ncoltrp
 MG0925+3612                  + +6                    09 25 47.41   36 11 14.95         X4 CD                 *
 MG0926+2201  Y   >20          + +6    + +3            09 26 01.674  22 01 37.38         X6 CD                 *  V
 MG0930+3503                  + +3                    09 30 50.59   35 03 08.71         X4 CD
PMN0931-1830  Y   >20     + +1    + +7    + +10   + +1    09 31 23.133 -18 30 21.83        XS2 CompTrp?-Corrp
 MG0932+3339  Y   >20          + +3    + +3            09 32 50.8513 33 40 05.069        X4 MG  RANDOM $20      V
 MG0935+3633  Y   >20          + +3                    09 35 42.12   36 33 31.89         X4 CD
 MG0952+3606                  + +6                    09 52 24.07   36 05 10.10  5" XS4X4 FlatSpTrp?
 MG0952+0000  Y   >20     + +1    + +10   + +1    + +1    09 52 46.572  00 00 20.84      0414 Struct ?     .05 * M  *Only MG MERL CD/NO ID(Mar95)
 MG1006+3453  Y   <20     + +1    + +1    + +4    + +2    10 06 01.756  34 54 10.33         X8 CD                    # Gal 3C236       0.099  16
PMN1006-1743  Y   <20   2+ +1   2+ +4   2+ +1   2+ +1    10 06 18.285 -17 43 17.03  0.7" XS2 CD
 MG1008+3331  Y   >20          + +2    + +3    + +3    10 08 22.709  33 32 02.51         X7 CD                    V
```

```
 MG1008+2624                  + +6                          10 08 57.07   26 24 21.15        X5 CD
 MG1011+3155  Y   <20    + +1    + +13    + +1    + +1     10 11 18.925  31 55 05.59  1.0" TrpStpSp=-1.5   .08 *N                          R21
 MG1013+3446              ******   N O   D A T A  ******   10 13 44.10   34 44 48.61        X4 CD                *
 MG1017+040   Y   <20   (SEE THE LINE BELOW THIS ONE ] B10 17 58.32   04 05 58.5       Arc-like Trp      .08 * M [SAME as MG1020+0350]
 MG1020+0350  Y   <20    + +1    + +6     + +1    + +1     10 20 34.042  03 50 51.54           CD               * M [SAME as MG1017+040 ]
 MG1021+2158                  + +3     + +3                10 21 54.572  21 59 30.64        X3 CD                  # Gal 3C241       1.617  23.5
 MG1028+3845  Y   <20    + +1    + +1     + +1    + +1     10 28 44.282  38 44 36.74        X8 CD                  # Gal 4C39.32      0.361  18.4
PMN1029-1508  Y   ~20   2+ +1   2+ +4    2+ +1   2+ +1     10 29 36.646 -15 08 27.10  0.6" XS2 CD
 MG1030+2359  Y   ~20    + +2     + +5     + +1    + +2     10 30 47.21   23 59 37.92        X5 CD
 MG1034+3349  Y   >20              + +4     + +3             10 34 35.6969 33 50 57.920       X4 MG  RANDOM $11      V
PMN1036-1955  Y   >20              + +3     + +7    + +3     10 36 40.286 -19 56 09.12        XS2 PMN RANDOM $3
PMN1041-1537  Y   >20    + +1      + +9     + +1    + +1     10 41 25.603 -15 37 05.48        XS2 Arc?-Corrp
PMN1043-1353  Y   >20   3+ +1   2+ +5    2+ +1   2+ +1     10 43 15.592 -13 53 31.22  0.3" XS2 CD-Corrp
PMN1102-0941  Y   >20   2+ +1   2+ +5    2+ +1   2+ +1     11 02 31.131 -09 41 24.95  2.2" XS2 CD
PMN1105-2204  Y   <20   1+ +1   1+ +3    1+ +7   1+ +1     11 05 16.264 -22 04 35.16  0.2" XS3 CD
 MG1110+2131  Y   >20              + +8                     11 10 18.986  21 30 54.43        X5 CD/RANDOM?                  ??Check RANDOM or CD
PMN1110-1858  Y   >20                       + +3    + +3     11 10 00.408 -18 58 48.72        XS2 PMN RANDOM $4
PMN1117-1123  Y   <20    + +2     + +2     + +6    + +1     11 17 34.073 -11 23 50.67  1.8" XS2 Ncoltrp
PMN1123-0948  Y   <20    + +1     + +4     + +3    + +4     11 23 23.619 -09 49 04.63        XS4 Ncoltrp          *N
 MG1128+2328                  + +3                          11 28 54.59   23 27 06.38        X5 CD                *
 MG1129+3747                  + +3                          11 29 55.494  37 48 04.77        X8 CD                *
 MG1131+3012  Y   >20         + +3     + +2                 11 31 26.830  30 13 34.41        X7 MG  RANDOM $34      V
 MG1133+2105  Y   <20    + +1     + +1     + +5    + +1     11 33 57.022  21 05 39.01        X3 CD                  # Gal E 4C21.32  0.0667 16.5V
 MG1135+2053  Y   >20              + +3     + +3             11 35 07.284  20 53 01.18        X3 CD                *  V
 MG1139+3642  Y   >20              + +3                      11 39 24.777  36 42 02.01        X8 MG  RANDOM $35
 MG1146+052               ******   N O   D A T A  ******   11 48 49.155  04 55 17.95        XS4 SE Ring Lobe ?   *N
 MG1149+2634  Y   >20              + +2                      11 49 08.940  26 34 20.03        X6 MG  RANDOM $36
PMN1209-2032  Y   >20   2+ +1   2+ +7    2+ +4   2+ +1     12 09 10.796 -20 32 51.02  0.3" XS1 CD-Corrp          *N
 MG1212+2032  Y   >20              + +3     + +3             12 12 56.05   20 32 37.09        X5 CD                  V# Gal   4C20.27          18.5
 MG1222+2934  Y   ~20                       + +2             12 22 43.201  29 34 41.52        X7 MG  RANDOM $37
PMN1225-1144  Y   >20   2+ +     2+ +5    2+ +3   2+ +     12 25 24.321 -11 44 32.53  2.1" XS2 CD (CJ?)
PMN1226-2630  Y   <20   1+ +     1+ +3    1+ +3   1+ +     12 26 38.942 -26 30 03.97  0.5" XS1 CD
 MG1237+2024  Y   >20              + +3                      12 37 13.159  24 57 55.55        X5 MG  RANDOM $38
 MG1240+2251                  + +4                          12 40 03.78   22 50 19.31        X5 CD                *
 MG1244+3609  Y   >20    + +2     + +2     + +1    + +3     12 44 49.6836 36 09 25.483 0.5"      CD          .50 * M                          19.6R
PMN1245-1616  Y   >20   1+ +     1+ +2    1+ +     1+ +4    12 45 53.400 -16 14 18.15  0.9" XS1 CD-Corrp
PMN1254-2822  Y   <20   2+ +    11+ +7    2+ +     2+ +     12 54 22.864 -28 22 57.40  0.5" XS3 Quad Lens?
 MG1257+3643  Y   <20              + +7     + +1    + +1     12 57 23.8649 36 44 19.140 0.4"      CD          .18 * M                          18.1R
PMN1308-0950  Y   <20              + +3     + +3    + +4     13 08 39.159 -09 50 32.43  0.6" XS1 CD
PMN1311-2216  Y   ~20              + +2                      13 11 39.341 -22 16 41.22  1.0" XS1 CD
PMN1312-1334  Y   >20              + +5                      13 12 51.475 -13 34 34.37  35"  XS2 CreDbAC114?
 MG1322+2148                  + +6                          13 22 10.51   21 47 15.70        X5 CD                *
 MG1322+2244  Y   >20    + +4     + +6                      13 22 21.701  22 45 06.77       New Ring?             *N
 MG1323+2532                  + +3                          13 23 09.088  25 32 27.621       X6 CD
 MG1327+2210                  + +3                          13 27 00.00   22 09 53.50        X5 CD                *
PMN1342-1225  Y   ~20   1+ +     1+ +3    1+ +     1+ +4    13 42 06.222 -12 25 38.92  0.2" XS2 Sl.Res. CD
PMN1351-1019  Y   <20              + +3                      13 51 31.989 -10 19 34.61  12"  XS2 Ncolmult
 MG1352+2014  Y   >20              + +3                      13 52 30.406  20 14 24.61        X5 MG  RANDOM $39
PMN1401-1510  Y   >20             2+ +7     + +4             14 02 09.244 -15 10 08.15  1.6" XS2 Arc?-Corrp
PMN1402-2822  Y   >20             3+ +2              1+ +    14 02 08.229 -28 21 46.91  0.5" XS1 CD-Corrp
 MG1413+2228  Y   <20    + +3     + +1     + +1    + +1     14 13 12.098  22 28 11.42        X5 MG  RANDOM $40      # nr Gal A1880:[OWG93]  15.4
 MG1415+3859  Y   >20              + +3     + +3             14 15 03.235  38 59 16.43        X8 CD                V
PMN1415-1502  Y   >20   1+ +     1+ +     1+ +    1+ +4    14 15 23.216 -15 02 57.02  0.3" XS2 CD
 MG1424+2102  Y   >20              + +3                      14 24 25.951  21 02 36.53        X5 MG  RANDOM $41
 MG1425+2416  Y   >20              + +3                      14 25 43.937  24 16 01.52        X6 MG  RANDOM $42
 MG1429+2148  Y   >20              + +6     + +3             14 29 25.64   21 48 58.30        X5 CD                *
 MG1438+2934  Y   >20              + +3                      14 38 32.963  29 33 54.51        X7 MG  RANDOM $43
 MG1444+2035  Y   >20              + +3                      14 44 05.801  20 35 18.17        X6 MG  RANDOM $44
PMN1448-1122  Y   <20    + +1     + +6     + +1    + +1     14 48 51.171 -11 22 15.75  1.5" XS2 Ncoltrp
PMN1506-1637  Y   <20    + +1     + +3     + +1    + +1     15 06 52.884 -16 37 54.50  2.7" XS2 Ncolmult
 MG1507+3643  Y   <20              + +6                      15 07 19.5399 36 42 45.411 0.2" DblStpSp=-1.1   .12 *NM                          R19
 MG1507+2433  Y   <20              + +7                      15 07 46.972  24 34 32.639       X6 CD                *
 MG1513+2229  Y   >20              + +1                      15 13 27.594  22 30 23.569       X6 CD                *
 MG1528+3738  Y   >20      ******   N O   D A T A  ******   15 28 27.926  37 38 09.74        X8 CD                  # Gal 4C37.44            18.5
 MG1528+3247  Y   >20              + +4                      15 28 09.124  32 47 37.47        X7 CD
PMN1531-1659  Y   >20    + +4     + +2     + +4    + +3     15 31 22.614 -16 59 55.03  1.1" XS2 Comp Trp
 MG1534+2330  Y   <20    ******   N O   D A T A  ******   15 34 57.223  23 30 11.48        X3 CD                  # Gal Sy2 IC1127 0.0181 13.94
PMN1542-1803  Y   <20   1+ +2    8+ +13    + +4    1+ +4    15 42 04.747 -18 03 40.69        XS2 Quad Lens ?
```

master.feb96.list Thu Jan 29 04:37:48 1998 4

OBJECT NAME	F I	P R	Mag #I	CTIOTek/MDMNell/MDMWilb #R	#V	#B	FIL	TAL	Radio J2000 Position RA	DEC	Radio	Morph	.Jy	*NMV#	Optic	Morph	z	Mag
MG1544+3712	Y		<20		+ +3	+ +1			15 44 45.022	37 13 08.98	0.25"	X8	Dbl/Trp?	.13	*	M	# QSO	4C37.45	0.972	17.7
MG1544+3513	Y		>20		+ +4				15 44 18.803	35 02 28.62		X8	MG RANDOM	$45						
PMN1544-1436	Y		<20	+ +1	+ +3	+ +2	+ +2		15 44 47.509	-14 36 07.29	1.2"	XS2	NcolTrp							
MG1555+2406	Y		>20	******	N O	D A T A	******		15 55 50.637	24 06 25.21		X6	MG RANDOM	$46						
MG1602+2410					+ +4				16 02 12.532	24 10 09.240		X6	CD							
PMN1612-1419	Y		<20	+ +1	+ +5	+ +3	+ +3		16 12 09.254	-14 19 14.28	0.3"	XS2	CD							
PMN1622-1128	Y		>20	+ +7	+ +8	+ +4			16 22 42.486	-11 28 59.33	4.7"	XS2	CD							
MG1624+2139					+ +9				16 24 29.576	21 40 09.016		X6	CD							
MG1635+3721	Y		>20	******	N O	D A T A	******		16 35 02.098	37 21 51.80		X8	MG RANDOM	$47						
PMN1639-2330	Y		>20	+ +2	+ +3				16 39 00.961	-23 29 56.29	1.2"	XS1	CD			*N				
MG1640+2209	Y		>20		+ +3				16 40 44.386	22 10 16.50		X6	MG RANDOM	$48						
MG1647+2705	Y		<20	******	N O	D A T A	******		16 47 33.608	27 05 58.30		X7	MG RANDOM	$49						
MG1653+3501	Y		>20		+ +3				16 53 44.056	35 00 57.25		X8	MG RANDOM	$51						
MG1653+1937	Y		>20	******	N O	D A T A	******		16 53 04.411	19 37 54.01		X6	MG RANDOM	$50						
PMN1701-1903	Y		>20?		+ +2			AST17	01 27.100	-19 03 39.00			Ext Flat Spec							
PMN1701-2149	Y		>20?		+ +1			AST17	01 32.400	-21 49 23.00			Ext Flat Spec							
MG1703+2438	Y		>20		+1+				17 03 07.279	24 37 47.60		X6	MG RANDOM	$53						
MG1710+1930				+ +7	+ +9				17 10 53.090	19 30 37.17			CD	.08	*	M				
MG1732+2037				+ +6	+ +5				17 32 50.450	20 38 15.95			CD	.13	*	M				
MG1746+2342	Y		>20		+ +1				17 46 27.893	20 09 15.19		X3	CD							
MG1751+3457				+ +6	+ +9				17 51 55.3433	34 57 07.764	3"		Dbl?	.12	*	M	HDR WRNG NAM: MG1751+3427			
MG1802+2430				+ +4	+ +8				18 02 28.138	24 31 23.305		X6	CD							
MG1823+2246				******	N O	D A T A	******		18 23 05.8106	22 47 00.303		X3	MG RANDOM	$1						
MG1836+3122				******	N O	D A T A	******		18 36 26.3326	31 22 03.122		X4	MG RANDOM	$12						
MG1842+2401	Y		>20		+ +3				18 42 51.682	24 01 46.18		X3	CD							
MG1846+2036				******	N O	D A T A	******		18 46 04.3478	20 36 10.283		X3	MG RANDOM	$2						
J1854+001				******	N O	D A T A	******		18 54 34.812	00 11 04.34			Comp.Ring	.06	*	M				
MG1911+3234				******	N O	D A T A	******		19 11 21.3091	32 34 47.440		X4	MG RANDOM	$13						
PMN1916-1315	Y		>20?		+ +9			AST19	16 23.700	-13 15 49.00	2.5"	XS3	CD							
PMN1952-1936	Y		>20	******	N O	D A T A	******		19 52 43.866	-19 36 10.80		XS1	CD			*N				
PMN2013-2724	Y		>20?	+1+	+ +3			AST20	13 39.600	-27 24 49.00			Ext Flat Spec							
MG2035+1949	Y		>20		+1+				20 35 41.619	19 50 05.29		X3	CD							
MG2047+2324	Y		<20	+ +9	+ +8	+1+1	+1+1		20 47 48.72	23 24 49.463	0.5"		Trp/Dbl	.25	*	M				
MG2049+2012	Y		<20	+ +8	+ +9	+1+	+1+		20 49 09.323	20 13 38.086		X6	CD							
MG2055+2252	Y		<20		+1+				20 55 54.549	22 53 50.71		X5	MG RANDOM	$54						
MG2059+2245	Y		>20	+ +10	+ +9				20 59 03.58	22 46 14.62		X5	CD							
MG2102+2001	Y		>20	+1+11	+1+6				21 02 43.128	20 02 12.527		X6	CD							
MG2105+2920	Y		>20	+ +9	+ +9	+ +1	+ +1		21 05 46.53	29 21 32.09		X4	CD							
MG2108+2414				+ +11	+ +9				21 08 18.474	24 15 29.453	1.0"		CD	.10	*	M				
PMN2119-2625	Y		>20?	+ +2	+ +7			AST21	19 53.600	-26 25 54.00		XS3	Mul?ExtFltSp		*					
PMN2132-1103	Y		>20?	+ +3	+ +7			AST21	32 32.700	-11 03 51.00		XS3	Mult -CD?		*					
PMN2138-1750	Y		>20?	+ +2	+ +8	+ +1		AST21	38 37.700	-17 50 32.00	1.0"	XS3	CD							
PMN2147-1740	Y		<20	+1+	+1+	+1+	+1+		21 47 03.257	-17 40 11.57	0.9"	XS1	CD							
MG2150+2004	Y		>20	+ +1	+ +3				21 50 55.065	20 04 43.82		X3	CD							
MG2201+2246				******	N O	D A T A	******		22 01 26.2888	22 46 47.444		X3	MG RANDOM	$4						
MG2202+2941				+ +9	+ +11				22 02 51.81	29 42 06.94		X4	CD							
MG2204+2030				******	N O	D A T A	******		22 04 27.9778	20 31 02.547		X3	MG RANDOM	$3						
MG2217+2800				******	N O	D A T A	******		22 17 40.8350	28 00 39.645		X4	MG RANDOM	$14						
PMN2238-1240	Y		>20?	+ +3	+ +7			AST22	38 15.800	-12 40 40.00	2.0"	XS3	CD			*				
MG2241+2430				******	N O	D A T A	******		22 41 32.5229	24 30 41.974		X3	MG RANDOM	$5						
MG2249+2315	Y		~20	+1+10	+1+8	+1+2	+1+2		22 49 04.850	23 16 06.54			CD	.08	*	M				
MG2249+2048				+ +6	+ +6				22 49 18.49	20 48 32.83		X5	CD							
MG2337+2717				******	N O	D A T A	******		23 37 43.72	27 18 15.84		X4	CD							
MG2341+2352				******	N O	D A T A	******		23 41 40.619	23 51 58.19			CD	.09	*	M				
MG2350+2331	Y		>20		+3+				23 50 15.454	23 31 59.30		X5	MG RANDOM	$52						

NOTES

1) 'B' before a coordinate signifies that it is epoch B1950.0 instead of the J2000.0 default.
2) X1 = XDAY 1 from the MG-VLA survey :
3) X2 = XDAY 2 from the MG-VLA survey :
4) X3 = XDAY 3 from the MG-VLA survey :
5) X4 = XDAY 4 from the MG-VLA survey :

```
6)  X5  = XDAY 5 from the MG-VLA survey :
7)  X6  = XDAY 6 from the MG-VLA survey :
8)  X7  = XDAY 7 from the MG-VLA survey :
9)  X8  = XDAY 8 from the MG-VLA survey :
10) XS1 = XDAY 1 SOUTH from the PMN-VLA survey :  2 AUG 91
11) XS2 = XDAY 2 SOUTH from the PMN-VLA survey : 31 DEC 92
12) XS3 = XDAY 3 SOUTH from the PMN-VLA survey :  7 MAR 94
13) XS4 = XDAY 4 SOUTH from the PMN-VLA survey :  9 MAR 94
14) CD  = Close Double (typically < 2")
15) Dbl = Double Lobe Radio Galaxy
16) Trp = Triple component Radio Galaxy
17) *   = High Priority source for optical follow-up
18) N   = Newly mapped radio source
19) M   = MG-VLA radio source observed later with MERLIN
20) V   = Observed at MDM 1.3m in the KPNO_V filter only in January 1995 - may need some R exposures.
21) #   = Low Priority source due to known optical ID - good source for bright time
22) AST = Only single-dish PMN position measured; accurate to about 10-15 arc-seconds rms.

-------------------------------------------------------------------------------------------------------------------------------------------------------
QUESTIONS

1) 2 APR 95: Check the correct coordinate for random source MG0355+2112 using AIPS/IMPOS.
2) 2 APR 95: Check the V exposure entries.
3) 2 APR 95: Check whether the source MG1110+2131 is RANDOM or not - it appears in BOTH the target and random lists.
4)

$ END OF MASTER COORDINATE & FILTER TALLY FILE : 13 MAR 1996  04:00 AM.
-------------------------------------------------------------------------------------------------------------------------------------------------------
```

Appendix B

MIT-VLA Gravitational Lens Candidates

The following pages are a copy of the original coordinate log files for the MIT-VLA Gravitational Lens Candidates from the thesis work of A. Fletcher (AF: the author), Lori Herold-Jacobson (LH), and Samuel Conner (SC). The Search Sample of MIT-VLA maps was $\sim$ 6000 sources.

Plots are given for most of these lens candidates. Figures have been reproduced from the work of the author, the work of L. Herold-Jacobson (1996 Ph.D. thesis [69]) and the work of S. Conner (1998 Ph.D. thesis [38], in progress, private communication via B. Burke).

The MIT-VLA radio and MDM/CTIO optical data reside in a EXABYTE/DAT tape archive at MIT. This archive is currently being organized by the author (1998).

Also are included some electronic mail messages from Joseph Lehár, that document his opinions on the likelihood of gravitational lensing in the Southern PMN-VLA sample of the author.

mitvla.glens.table.100797.lis Thu Jan 29 04:46:24 1998 1

% 7. Table of new MIT-VLA Lens Candidates (1991-1996):-

**** This is from the Ph.D. thesis work of 3 students only **** :-

Conner 1998, Fletcher 1998, Herold 1996.

New MIT-VLA Gravitational Lens Candidates (work done 1991-1996)

Source Catalog Name	RO AP DT II	Parent Catalog	B	RA J Coord	DEC Coord	Flux Dens mJy	Spect Indx	MIT VLA Day	VLA Resol asec	VLA Freq	VLA Flux Dens mJy	VLA Mor	LAS asec	Opt ID	GL Pr	PI: Comments
PMN0003-1727	R	PMN		J 00 03 21.955	-17 26 58.84 F5=							CD	2.8		PB	AF: Ring
PMN0205-1801	R	PMN		J 02 05 20.770	-18 01 38.17 F5=							DF	1.6		PC	AF: Arc
MG0232+3424	R	MG		J 02 32 28.568	+34 24 08.03 F5=			X4				MU		EF		LH:
PMN0237-1932	R	PMN		J 02 37 44.727	-19 32 25.85 F5=							DB	0.9		PC	AF: Close Double + Ring
MG0246+064	RO	MG	I	J 02 48 58.276	+06 41 54.78 F5=							CD	2.0	G	PB	SC: Core-Double + 1.97" Ring + 5,8,11 spots
MG0256+3246	RO	MG		J 02 56 22.848	+32 46 48.03 F5=			X7				MU	3.6	FO		LH:
MG0325+2130	R	MG		J 03 25 27.078	+21 29 57.62 F5=			X6				DF		EF		LH:
PMN0335-1832	R	PMN		J 03 35 04.502	-18 32 24.46 F5=							CJ	0.9		PC	AF: Core + Arced Jet
PMN0347-2900	R	PMN		J 03 47 01.694	-29 00 17.04 F5=							DB	1.2		PB	AF: Close Double + Ring
MG0353+3826A	R	MG		J 03 53 10.792	+38 26 43.09 F5=			X8				MU	12	EF		LH:
MG0356+0255	R	MG	I	B 03 53 22.45	+02 47 50.05 F5=							CD	1.5		PB	SC: Split Lobe w/lens-like geometry 1.5"
MG0421+2348	R	MG		J 04 21 21.833	+23 49 04.42 F5=			X3				DB		EF		LH:
MG0432+2013	R	MG		J 04 32 55.044	+20 13 10.49 F5=			X3				MU		EF		LH:
MG0509+1956	R	MG		J 05 09 01.236	+19 57 18.34 F5=			X3				MU		EF		LH:
PMN0521-2047	R	PMN		J 05 21 38.892	-20 47 30.23 F5=							TR	1.9		PB	AF: Triple/Quad
PMN0608-0738	R	PMN		J 06 08 03.685	-07 38 23.35 F5=		FlatSp					DB	2.9		PB	AF: Flat Spect Close Double
PMN0618-1330	R	PMN		J 06 18 31.884	-13 30 27.78 F5=							MU	3.7		PC	AF: Strange Double Double + Ring
PMN0625-1018	R	PMN		J 06 25 42.894	-10 17 45.30 F5=							MU	1.2		PC	AF: Triple 1.2"
PMN0636-2241	R	PMN		J 06 36 43.577	-22 41 28.63 F5=		FlatSp					DB	0.8		PC	AF: Flat Spect Close Double
MG0744+3753	RO	MG		J 07 44 17.520	+37 53 16.51 F5=			X8				MU	2.2	OB		LH:
MG0810+2651	R	MG		J 08 10 26.044	+26 50 48.90 F5=			X5				DB	2.6	EF		LH:
PMN0811-0520	R	PMN		J 08 11 59.741	-05 20 45.59 F5=		FlatSp					TR	1.0		PC	AF: Flat Spect Strange Core+Arc
PMN0820-129	R	PMN		J 08 20 57.445	-12 58 47.99 F5=		-0.54					DB	0.8		PC	AF: Flat Spectrum Double (VLA Cal)
PMN0837-1156	R	PMN		J 08 37 02.916	-11 55 11.44 F5=							DB	57.3		PB+	AF: Ring = Lensed SW Radio Lobe
PMN0837-1939	R	PMN		J 08 37 09.206	-19 39 45.51 F5=		FlatSp					DB	2.7		PC	AF: Flat Spect Double
PMN0902-0459	R	PMN		J 09 02 36.773	-04 59 52.99 F5=		FlatSp					DB	2.5		PB+	AF: Flat Spect Core + Arc
MG0912+3751	R	MG		J 09 12 02.449	+37 51 38.39 F5=							JT	2.4	EF		LH:
PMN0935-3633	R	PMN		J 09 35 31.835	+36 33 28.72 F5=		FlatSp					DB	0.6		PC	AF: Flat Spect Close Double (Bandw.Sm)
MG1008+3331	R	MG		J 10 08 22.709	+33 32 02.51 F5=							JT	5.0	EF		LH:
MG1011+3155	R	MG		J 10 11 18.855	+31 55 05.22 F5=							TR	1.0	EF		LH:
PMN1017-0220	R	PMN		J 10 17 19.956	-02 19 38.61 F5=		FlatSp					TR	1.5		PC	AF: Flat Spect Triple
MG1030+2359	RO	MG		J 10 30 47.205	+23 59 37.94 F5=							CJ		FO		LH:
PMN1123-0948	R	PMN		J 11 23 23.609	-09 48 53.21 F5=		FlatSp					TR	1.3		PC	AF: Flat Spect Close Triple
MG1128+3729A	R	MG		J 11 28 30.904	+37 28 54.01 F5=							JT	23	EF		LH:
MG1129+3748	R	MG		J 11 29 55.560	+37 48 04.84 F5=							TR		EF		LH:
MG1133+2105	RO	MG		J 11 33 57.021	+21 05 39.14 F5=							CD		G		LH:
MG1148+0455	R	MG	I	B 11 46 11.200	+05 12 06.00 F5=							MU	1.4		PA	SC: Ring or Quad in Radio Lobe
PMN1149-1057	R	PMN		J 11 49 49.799	-10 58 19.67 F5=		FlatSp					MU	3.0		PB+	AF: Flat Spec small 957
PMN1218-0952	R	PMN		J 12 18 12.436	-09 52 22.44 F5=		FlatSp					DB	0.5		PC	AF: Flat Spec Close Double (Unresolv)
PMN1254-2822	R	PMN		J 12 54 22.853	-28 22 45.71 F5=		FlatSp					MU	0.9		PB	AF: Flat Spec Close Triple/Quad
PMN1304-2106	R	PMN		J 13 04 59.100	-21 06 30.69 F5=							MU	2.0		PC	AF: Multiple Peaks; Double Double
PMN1402-1510	R	PMN		J 14 02 09.247	-15 09 58.35 F5=							MU	6.2		PC	AF: Quadruple
PMN1419-1423	R	PMN		J 14 19 55.818	-14 23 11.06 F5=							CD	3.3		PC	AF: Double + Arc
PMN1419-1918	R	PMN		J 14 19 55.142	-19 17 26.43 F5=		FlatSp					DB	4.4		PC	AF: Flat Spect Double
MG1424+2255	RO	MG		J 14 24 38.066	+22 55 59.83 F5=							MU		OB		LH: *** CONFIRMED CLASS LENS B1422+231
MG1446+2251	R	MG		J 14 46 52.902	+22 52 00.81 F5=							DF		EF		LH:
PMN1436-1909	R	PMN		J 14 36 33.900	-19 09 47.39 F5=		FlatSp					DB	0.3		PC	AF: Flat Spect Close Double (Unresolv)

mitvla.glens.table.100797.lis Thu Jan 29 04:46:24 1998 2

PMN1448-1122	R	PMN	J 14 48 51.169	-11 22 04.56	F5=		TR	1.5		PC	AF:	Triple
MG1507+2433	RO	MG	J 15 07 47.199	+24 34 27.99	F5=		TR		OB		LH:	
MG1533+1332	R	MG I	B 15 30 54.000	+13 42 40.00	F5=		CD	1.1		PA	SC:	Ring in Radio Lobe
PMN1542-1803	R	PMN	J 15 42 04.746	-18 03 28.33	F5=		MU	1.5		PB	AF:	Triple or Quad
MG1544+3712	RO	MG	J 15 44 45.030	+37 13 09.02	F5=		TR		OB		LH:	
PMN1544-1436	R	PMN	J 15 44 47.509	-14 35 54.85	F5=		MU	2.3		PC	AF:	Triple
PMN1547-1416	R	PMN	J 15 47 52.720	-14 16 00.65	F5=	FlatSp	DB	0.8		PC	AF:	Flat Spect Close Double
MG1628+3330	R	MG	J 16 28 11.657	+33 30 29.88	F5=		TR		EF		LH:	
PMN1631-2723	R	PMN	J 16 31 01.401	-27 22 57.77	F5=	FlatSp	DB	0.5		PC	AF:	Flat Spect Close Double + Arc
PMN1703-2031	R	PMN	J 17 03 16.929	-20 31 28.78	F5=		CJ	3.1		PC	AF:	Core + Gently Curved Long Arc
PMN1720-1520	R	PMN	J 17 20 44.589	-15 21 20.36	F5=	FlatSp	DB	2.7		PC	AF:	Flat Spect Double
MG1842+2401	RO	MG	J 18 42 51.809	+24 01 48.44	F5=		MU		FO		LH:	
PMN1916-1315	R	PMN	J 19 16 23.035	-13 15 31.91	F5=	FlatSp	DB	0.5		PC	AF:	Flat Spect Close Double
PMN1926-1836	R	PMN	J 19 26 01.310	-18 36 32.25	F5=		DB	22.8		PC	AF:	Arc of 1.7" diam.ring=lensed lobe
PMN1927-1455	R	PMN	J 19 27 39.014	-14 55 24.22	F5=		MU	9.8		PC	AF:	Triple
PMN1933-2634	R	PMN	J 19 33 48.488	-26 33 14.38	F5=		DB	49.1		PC	AF:	Triple+Faint 4th Image in NE Lobe
PMN2059-1440	R	PMN	J 20 59 59.540	-14 40 29.38	F5=		MU	2.9		PC	AF:	Quad + Ring
PMN2102-2114	R	PMN	J 21 02 01.155	-21 13 48.67	F5=		TR	2.2		PC	AF:	Triple
PMN2127-1211	R	PMN	J 21 26 57.186	-12 12 42.03	F5=	FlatSp	DB	1.1		PC	AF:	Flat Spect Close Double
PMN2138-1750	R	PMN	J 21 38 38.302	-17 50 28.84	F5=	FlatSp	DB	1.0		PC	AF:	Flat Spect Close Double
PMN2138-1843	R	PMN	J 21 38 05.307	-18 43 23.16	F5=		DB	14.6		PC	AF:	Triple
PMN2157-1120	R	PMN	J 21 57 10.352	-11 20 27.68	F5=	FlatSp	MU	2.6		PB	AF:	Flat Spect Double Double
PMN2238-1240	R	PMN	J 22 38 16.223	-12 40 25.64	F5=	FlatSp	DB	0.6		PC	AF:	Flat Spect Close Double

Notes:

1. In 2nd column, R means radio-loud (all here are radio-loud).
   O means optically-loud (seen in POSS or ESO plate, so opt.mag > 21).

2. Parent Radio Source Catalogs are:-

MG I	MG	1st	-0.5 < dec < +19.5 deg
MG II	MG	2nd	+17.0 < dec < +39.2 deg ; 4.0h < RA < 21.0h
MG III	MG	3rd	+17.0 < dec < +39.2 deg ; 16.0h < RA < 5.0h
MG IV	MG	4th	+37.0 < dec < +51.0 deg ; 15.5h < RA < 2.5h
PMN E	PMN	Equatorial	- 9.5 < dec < +10.0 deg
PMN T	PMN	Tropical	-29.0 < dec < - 9.5 deg
PMN Z	PMN	Zenith	-37.0 < dec < -29.0 deg
PMN S	PMN	Southern	-87.5 < dec < -37.0 deg

3. B means B1950.0 coordinates.
   J means J2000.0 coordinates.

4. F5= means Radio Flux Density at 5 GHz (actually 4.8 GHz).

5. FlatSp means source was selected as a flat spectrum target at the VLA (nu^-alpha; alpha < 0.5).

6. Radio Morphologies:-
   PT point
   QP quasi-point
   CJ core-jet
   CD core-double
   DB double
   TR triple
   MU multiple
   EX extended
   CM cometary
   DF diffuse
   OR over-resolved
   UN unclassified

7. LAS = largest radio angular size (if compact candidate not measured yet) in arc-seconds
       = maximum size of compact lens candidate

8. Optical classifications:-

   OB object seen

```
    G  object resolved, looks like galaxy
    FO faint object
    EF empty POSS/ESO field
    UN unknown

9. Gravitational Lens Candidate Priority for Optical Follow-up (subjective estimate):-
    PA = very good to excellent
    PB = good
    PC = possible
    PD = unlikely
    PX = subsequently known "not" to be a lens

9. Under the column 'PI', the
     students were: AF= Andre Fletcher
                    LH= Lori Herold-Jacobson
                    SC= Samuel Conner
                    JL= Joseph Lehar
                    JH= Jackie Hewitt
                    GL= Glen Langston
                    CL= Charles Lawrence


-------------------------------------------------------------------------------------------------------------------------------------------------------------------------------
% 8. List of Comments on Individual MIT-VLA Lens Candidates

The following is a list of comments that is "under construction":


-------------------------------------------------------------------------------------------------------------------------------------------------------------------------------
For comments on Lori Herold's MG-VLA candidates, see her Ph.D. thesis, pages 67-73.


-------------------------------------------------------------------------------------------------------------------------------------------------------------------------------
1st EMAIL FROM JOSEPH LEHAR:-
----------------------------

Received: from cfa.harvard.edu by maggie.mit.edu (4.1/2.0)
        id AA11013; Mon, 19 May 97 13:01:03 EDT
From: jlehar@astrometry.harvard.edu (Joseph Lehar)
To: fletcher@maggie.mit.edu
Subject: better discussion on your candidates

Hi Andre,

I finally finished making plots of those candidates you sent me,
and have looked them over.  These are the ones that I considered
to be particularly interesting:


HOT CANDIDATES!
---------------

PM06362241:  compact double with a bright optical counterpart.
             definitely worth an IR or optical obs.

PM0820-129:  compact double with large brightness ratio.
             Bright optical ID.  Definitely worth follow-up.

PM12542822:  compact quad-like structure, with an optical ID.
(*)          definitely worth an IR or optical obs.

PM15471416:  compact double with large brightness ratio.
             moderately bright optical ID. Definitely worth follow-up.

PM19332634:  2 widely separated lobes, but northern one has 4 blobs
(*)          in a familiar quad arrangement.  There is a bright optical
             ID on top of the lobe, and a faint one between the lobes.
```

This is an excellent candidate, but not for IR imaging.

PM21571120: compact double with large ratio, and extra lobey stuff to south.
Does have a faint optical ID. "Double" could just be counterjet,
but merits further study.

PM22381240: compact double with a faint optical counterpart.
Merits an IR image, I think.

INTERESTING:

PM00031727: core-double with a ring-like thing in western lobe.
very low snr on lobe. No optical counterpart to lobe,
but there is another optical object nearby which may be
generally distorting radio source. Interesting.

PM03472900: Very odd source. I'm not sure what it is.
Geometry doesn't look very lens-like but it is peculiar.
Optical counterpart looks like two merging galaxies.
Probably worth another look.

PM06181330: compact double with a lobe-like thing off to the side.
The double has a faint optical counterpart.
Perhaps worth pursuing with IR obs.

PM06251018: funny shaped lobe that might be lensed.
However, it has no optical counterpart to lobe.
Worth a deep IR integration at some time, but not urgent.

PM08110520: why is source so far off center? It is a funny shape,
but could be a lens. I would guess, that it is a radio lobe.
Bright, stellar, optical object on it, but field is crowded.
Probably just a star, but merits a better look.

PM08371939: compact double, but no optical ID. Merits further study.

PM09020459: the horseshoe blob. No optical counterpart.
A weak candidate.

PM12180952: horizontally stretched source, but not BW smeared.
No optical counterpart though.

PM15421803: funny radio source with a complex optical counterpart
Worth optical follow up.

PM15441436: Probably just a bent jet. Worth a further look.

PM17032031: long jet-like structure with a bright blob at one end.
No optical ID there. The jet looks like it could be part
of an arc, but there are no counterimages.
Probably just a jet.

PM17201520: compact double? Perhaps with an optical ID, but the
optical field is extremely crowded. Prob in galactic plane.

PM19161315: compact double, very faint opt ID 5" to south.
probably just 2 hotspots, but merits further investigation.

PM21022114: Could be three images in a quad, or a bent core-double.
I favor the latter, since the more separated image is
brighter (unexpected). No optical ID.

PM21381750: compact double with no optical ID.

PROBABLY RUBBISH:

This is an excellent candidate, but not for IR imaging.

PM21571120: compact double with large ratio, and extra lobey stuff to south.
Does have a faint optical ID. "Double" could just be counterjet,
but merits further study.

PM22381240: compact double with a faint optical counterpart.
Merits an IR image, I think.

INTERESTING:

PM00031727: core-double with a ring-like thing in western lobe.
very low snr on lobe. No optical counterpart to lobe,
but there is another optical object nearby which may be
generally distorting radio source. Interesting.

PM03472900: Very odd source. I'm not sure what it is.
Geometry doesn't look very lens-like but it is peculiar.
Optical counterpart looks like two merging galaxies.
Probably worth another look.

PM06181330: compact double with a lobe-like thing off to the side.
The double has a faint optical counterpart.
Perhaps worth pursuing with IR obs.

PM06251018: funny shaped lobe that might be lensed.
However, it has no optical counterpart to lobe.
Worth a deep IR integration at some time, but not urgent.

PM08110520: why is source so far off center? It is a funny shape,
but could be a lens. I would guess, that it is a radio lobe.
Bright, stellar, optical object on it, but field is crowded.
Probably just a star, but merits a better look.

PM08371939: compact double, but no optical ID. Merits further study.

PM09020459: the horseshoe blob. No optical counterpart.
A weak candidate.

PM12180952: horizontally stretched source, but not BW smeared.
No optical counterpart though.

PM15421803: funny radio source with a complex optical counterpart
Worth optical follow up.

PM15441436: Probably just a bent jet. Worth a further look.

PM17032031: long jet-like structure with a bright blob at one end.
No optical ID there. The jet looks like it could be part
of an arc, but there are no counterimages.
Probably just a jet.

PM17201520: compact double? Perhaps with an optical ID, but the
optical field is extremely crowded. Prob in galactic plane.

PM19161315: compact double, very faint opt ID 5" to south.
probably just 2 hotspots, but merits further investigation.

PM21022114: Could be three images in a quad, or a bent core-double.
I favor the latter, since the more separated image is
brighter (unexpected). No optical ID.

PM21381750: compact double with no optical ID.

PROBABLY RUBBISH:

mitvla.glens.table.100797.lis Thu Jan 29 04:46:24 1998 5

PM02051801: Too faint, shoudn't be a candidate.

PM02371932: Too faint, shoudn't be a candidate.

PM03351832: Looks like an ordinary double to me.

PM05212047: A double, but components aren't compact.

PM06080738: Double, but components are not compact.

PM08371156: vague ring-like structures in very faint lobes.
no optical ID to the lobe. So faint that it shouldn't be
a candidate really.

PM09353633: Clearly a bandwidth-smeared point source.

PM10170220: Too faint to tell, probably just a point source with sidelobes.

PM11230948: Probably just a radio jet.

PM11491057: that question-mark source. Has an ID on brightest comp.
Probably just a core-jet.

PM13042106: hotspots along a jet. Not a candidate.

PM14021510: Too faint to tell. Shouldn't be a candidate.

PM14191423: Probably just an FR I galaxy.

PM14191918: Extended double. Looks like two lobes.

PM14361909: Not very lens-like, but odd.

PM14481122: triple with a funny morphology. Optical ID on brightest.
Probably just a bent jet, and morphology hard to model as lens.

PM16312723: Probably just two hotspots in a lobe.

PM19261836: double with blobby lobes. No optical counterparts.

PM19271455: slightly funny lobes. Not interesting though.

PM20591440: This looks just like a swept-jet radio source to me.

PM21271211: Too faint to tell. Shouldn't be a candidate.

PM21381843: double source with funny shaped lobe. No optical ID.

Joseph

2ND EMAIL FROM JOSEPH LEHAR:-

Received: from cfa.harvard.edu by maggie.mit.edu (4.1/2.0)
id AA03493; Thu, 11 Jul 96 11:35:07 EDT
From: jlehar@astrometry.harvard.edu (Joseph Lehar)
To: fletcher@maggie.mit.edu

Hi Andre,

Well, things are looking more hopeful now.
I wouldn't say that any of your candidates so far are an "A",
but pm0902 and pm1149 are definitely "B"s.
Some comments:

MG0249:
Looking at the map on greyscale (the first time for me!)
I think that this is an excellent candidate. There are lots of
little features there that I think tie in quite well.
I would love to get hold of the UV data to see if anything can be
done to fix up the map. Lots of dreadful stuff happening away
from the source. Are you sure that the calibration and flagging
proceeded normally?
I think this is definitely a case like MG1549, and the deeper maps
should be very interesting.

PM0837:
A nice compact double with a good separation (about 2").
Could just be hotspots at the edges of a double though.
If you have polarization for this one, map it immediately
to see how things go. Definitely a good candidate for follow-up.
Check if it is steep spectrum or not, and look for optical counterparts.
In fact, I'll look up the POSS field for you right now and send you an image.
Don't worry, this is just enthusiasm, not an attempt to be an author.

PM0902:
Very intriguing shape. It actually looks lots like some lens configurations.
Making a model will be easy, and the separation is also reasonable.
I would gues that this is a steep spectrum source, from the look of it.
Looks pretty faint too. Still, very useful if it can be confirmed.
Definitely a candidate for another VLA observation.

PM1149:
Another interesting shape, but less compelling to me.
If you name the 4 blobs from SouthWest to NorthEast as A,B,C,D,
it seems to me that C+D could be images of each other with a
connecting arc. The only problem is that you would then expect
a counter image to them due south of their midpoint.
Maybe something can be fiddled, but it is not as strong as PM0902.

So I think you should definitely prepare a "proposal" to follow up
PM0902 using the VLA, and send it to Barry Clark. He may allow you
to slip it in using discretionary time, or you may be able to beg
some time off from AB705 (Debbie Haarsma's 0957 stuff).
I would look for a longer X-band integration. The peak is only 2.6 mJy,
so you probably shouldn't try to to lots of multifrequency stuff.
Maybe also some C-band time as well. Don't bother with K,U, or L.
Keep the C-band integration to less than 10% of your time, though.
You can get rough spectra from the C-band and good structure from the Xband.
Check with Bernie on all this before you submit, of course.
A-array will be up this winter, so you are well timed.
In the meantime, try to get optical counterparts for all your candidates.

Joseph

% END of file.

---

lensc1.list Thu Jan 29 04:52:27 1998 1

File	Source Name	RA (J2000.0)	DEC	Morph	LAS	Prior	Spec.Ind	Lens Morph	Mbytes	Date Created	UNIX File Name
c1	P0003-1727	00 03 21.955	-17 26 58.84	CD	2.8"	Pr=B		Ring	2151360	Jul 13 05:53	00031727H.ICLN.3.MAFITS
c2	P0205-1801	02 05 20.770	-18 01 38.17	Df	1.6"	Pr=C		Arc	1080000	Jul 13 05:58	02051801H.ICLN.4.MAFITS
c3	P0237-1932	02 37 44.727	-19 32 25.85	DB	0.9"	Pr=C		Close Double + Ring	1091520	Jul 13 05:56	02371932H.ICLN.3.MAFITS
c4a	M0246+064	02 48 58.274	+06 41 54.78	CD	10.4"	Pr=A		Core-Double + 1.92" Ring	1094400	Jul 13 08:45	0246+064H.ICLN.4.V1.MAFITS
c4b	M0246+064	02 48 58.276	+06 41 54.78					8o'clock spot+ 1.97" Ring	1261440	Jul 10 21:02	0246+064H.ICLN.4.V2.MAFITS
c4c	M0246+064	02 48 58.277	+06 41 54.78					8,11,5 spots + 1.97" Ring	1097280	Jul 14 04:20	0248E.FITS
c5	P0335-1832	03 35 04.502	-18 32 24.46	CJ	0.9"	Pr=C		Core + Arced Jet	1719360	Jul 13 05:01	03351832H.ICLN.2.MAFITS
c6	P0347-2900	03 47 01.694	-29 00 17.04	DB	1.2"	Pr=B		Close Double + Ring	1094400	Jul 13 05:56	03472900H.ICLN.4.MAFITS
c7	P0521-2047	05 21 38.892	-20 47 30.23	TR	1.9"	Pr=B		Triple/Quad	1097280	Jul 13 05:57	05212047H.ICLN.5.MAFITS
c8	P0608-0738	06 08 03.685	-07 38 23.35	DB	2.9"	Pr=B	FlatSp	Flat Spect Close Double	1094400	Apr 8 11:50	06080738H.ICLN.4.MAFITS
c9	P0618-1330	06 18 31.884	-13 30 27.78	MU	3.7"	Pr=C		Strange Double Double + Ring	2157120	Jul 13 06:25	06181330H.ICLN.5.MAFITS
c10	P0625-1018	06 25 42.894	-10 17 45.30	MU	11.0"	Pr=C		Triple 1.2"	1728000	Jul 13 05:33	06251018H.ICLN.4.MAFITS
c11	P0636-2241	06 36 43.577	-22 41 28.63	DB	0.8"	Pr=C	FlatSp	Flat Spect Close Double	1080000	Apr 8 11:50	06362241H.ICLN.4.MAFITS
c12	P0811-0520	08 11 59.741	-05 20 45.59	TR	1.0"	Pr=C	FlatSp	Flat Spect Strange Core+Arc	1094400	Jul 13 09:16	08110520H.ICLN.4.MAFITS
c13	V0820-129	08 20 57.445	-12 58 47.99	DB	0.8"	Pr=C	-0.54	Flat Spectrum Double (VLA Cal)	1082880	Jul 13 09:16	0820-129H.ICLN.5.MAFITS
c14	P0837-1156	08 37 02.916	-11 55 11.44	DB	57.3"	Pr=B		Ring + Lensed SW Radio Lobe	1716480	Jul 13 05:33	08371156H.ICLN.1.MAFITS
c15	P0837-1939	08 37 09.206	-19 39 45.51	DB	2.7"	Pr=C	FlatSp	Flat Spect Double	1074240	Jul 10 21:03	08371939H.ICLN.2.MAFITS
c16	P0902-0459	09 02 36.773	-04 59 52.99	DB	2.5"	Pr=B	FlatSp	Flat Spect Core + Arc	1071360	Jul 10 20:59	09020459H.ICLN.1.MAFITS
c17	P0935-3633	09 35 31.835	+36 33 28.72	DB	0.6"	Pr=C	FlatSp	Flat Spect Close Double (Bandw.Sm)	1241280	Jul 13 15:21	09353633H.ICLN.2.MAFITS
c18	P1017-0220	10 17 19.956	-02 19 38.61	TR	1.5"	Pr=C	FlatSp	Flat Spect Triple	1071360	Jul 13 15:22	10170220H.ICLN.1.MAFITS
c19	P1123-0948	11 23 23.609	-09 48 53.21	TR	1.3"	Pr=C	FlatSp	Flat Spect Close Triple	1094400	Jul 15 15:01	11230948H.ICLN.4.MAFITS
c20	P1149-1057	11 49 49.799	-10 58 19.67	MU	3.0"	Pr=B	FlatSp	Flat Spec small 957	1097280	Jul 10 22:33	11491057H.ICLN.5.MAFITS
c21	P1218-0952	12 18 12.436	-09 52 22.44	DB	0.5"	Pr=C	FlatSp	Flat Spec Close Double (Unresolv)	1077120	Jul 13 19:43	12180952H.ICLN.3.MAFITS
c22	P1254-2822	12 54 22.853	-28 22 45.71	MU	0.9"	Pr=B	FlatSp	Flat Spec Close Triple/Quad	1082880	Jul 13 10:20	12542822H.ICLN.5.MAFITS
c23	P1304-2106	13 04 59.100	-21 06 30.69	MU	2.0"	Pr=C		Multiple Peaks; Double Double	1097280	Jul 13 07:32	13042106H.ICLN.5.MAFITS
c24	P1402-1510	14 02 09.247	-15 09 58.35	MU	6.2"	Pr=C		Quadruple	1088640	Jul 13 05:22	14021510H.ICLN.2.MAFITS
c25	P1419-1423	14 19 55.818	-14 23 11.06	CD	3.3"	Pr=C		Double + Arc	1097280	Jul 13 07:32	14191423H.ICLN.5.MAFITS
c26	P1419-1918	14 19 55.142	-19 17 26.43	DB	4.4"	Pr=C	FlatSp	Flat Spect Double	1085760	Jul 11 20:26	14191918H.ICLN.1.MAFITS
c27	P1436-1909	14 36 33.900	-19 09 47.39	DB	0.3"	Pr=C	FlatSp	Flat Spect Close Double (Unresolv)	1080000	Jul 13 10:20	14361909H.ICLN.4.MAFITS
c28	P1448-1122	14 48 51.169	-11 22 04.56	TR	1.5"	Pr=C		Triple	1716480	Jul 13 05:23	14481122H.ICLN.5.MAFITS
c29	P1542-1803	15 42 04.746	-18 03 28.33	MU	1.5"	Pr=B		Triple or Quad	1088640	Jul 13 05:24	15421803H.ICLN.2.MAFITS
c30	P1544-1436	15 44 47.509	-14 35 54.85	MU	2.3"	Pr=C		Triple	1728000	Jul 13 05:25	15441436H.ICLN.4.MAFITS
c31	P1547-1416	15 47 52.720	-14 16 00.65	DB	0.8"	Pr=C	FlatSp	Flat Spect Close Double	1091520	Jul 13 10:20	15471416H.ICLN.3.MAFITS
c32	P1631-2723	16 31 01.401	-27 22 57.77	DB	0.5"	Pr=C	FlatSp	Flat Spect Close Double + Arc	1094400	Jul 13 10:20	16312723H.ICLN.4.MAFITS
c33	P1703-2031	17 03 16.929	-20 31 28.78	CJ	3.1"	Pr=C		Core + Gently Curved Long Arc	1094400	Jul 13 07:35	17032031H.ICLN.4.MAFITS
c34	P1720-1520	17 20 44.589	-15 21 20.36	DB	2.7"	Pr=C	FlatSp	Flat Spect Double	1094400	Jul 13 10:20	17201520H.ICLN.4.MAFITS
c35	P1916-1315	19 16 23.035	-13 15 31.91	DB	0.5"	Pr=C	FlatSp	Flat Spect Close Double	1082880	Jul 13 14:04	19161315H.ICLN.5.MAFITS
c36	P1926-1836	19 26 01.310	-18 36 32.25	DB	22.8"	Pr=C		Arc of 1.7" diam.ring=lensed lobe	1091520	Jul 13 08:04	19261836H.ICLN.3.MAFITS
c37	P1927-1455	19 27 39.014	-14 55 24.22	MU	9.8"	Pr=C		Triple	1091520	Jul 13 08:03	19271455H.ICLN.3.MAFITS
c38	P1933-2634	19 33 48.488	-26 33 14.38	DB	49.1"	Pr=C		Triple+Faint 4th Image in NE Lobe	1091520	Jul 13 08:04	19332634H.ICLN.3.MAFITS
c39	P2059-1440	20 59 59.540	-14 40 29.38	MU	2.9"	Pr=C		Quad + Ring	1088640	Jul 13 08:05	20591440H.ICLN.2.MAFITS
c40	P2102-2114	21 02 01.155	-21 13 48.67	TR	2.2"	Pr=C		Triple	1097280	Jul 13 08:05	21022114H.ICLN.5.MAFITS
c41	P2127-1211	21 26 57.186	-12 12 42.03	DB	1.1"	Pr=C	FlatSp	Flat Spect Close Double	1085760	Jul 13 14:06	21271211H.ICLN.1.MAFITS
c42	P2138-1750	21 38 38.302	-17 50 28.84	DB	1.0"	Pr=C	FlatSp	Flat Spect Close Double	1091520	Jul 13 14:05	21381750H.ICLN.3.MAFITS
c43	P2138-1843	21 38 05.307	-18 43 23.16	DB	14.6"	Pr=C		Triple	1094400	Jul 13 08:06	21381843H.ICLN.4.MAFITS
c44	P2157-1120	21 57 10.352	-11 20 27.68	MU	2.6"	Pr=B	FlatSp	Flat Spect Double Double	1094400	Jul 13 14:05	21571120H.ICLN.4.MAFITS
c45	P2238-1240	22 38 16.223	-12 40 25.64	DB	0.6"	Pr=C	FlatSp	Flat Spect Close Double	1074240	Jul 13 14:06	22381240H.ICLN.2.MAFITS

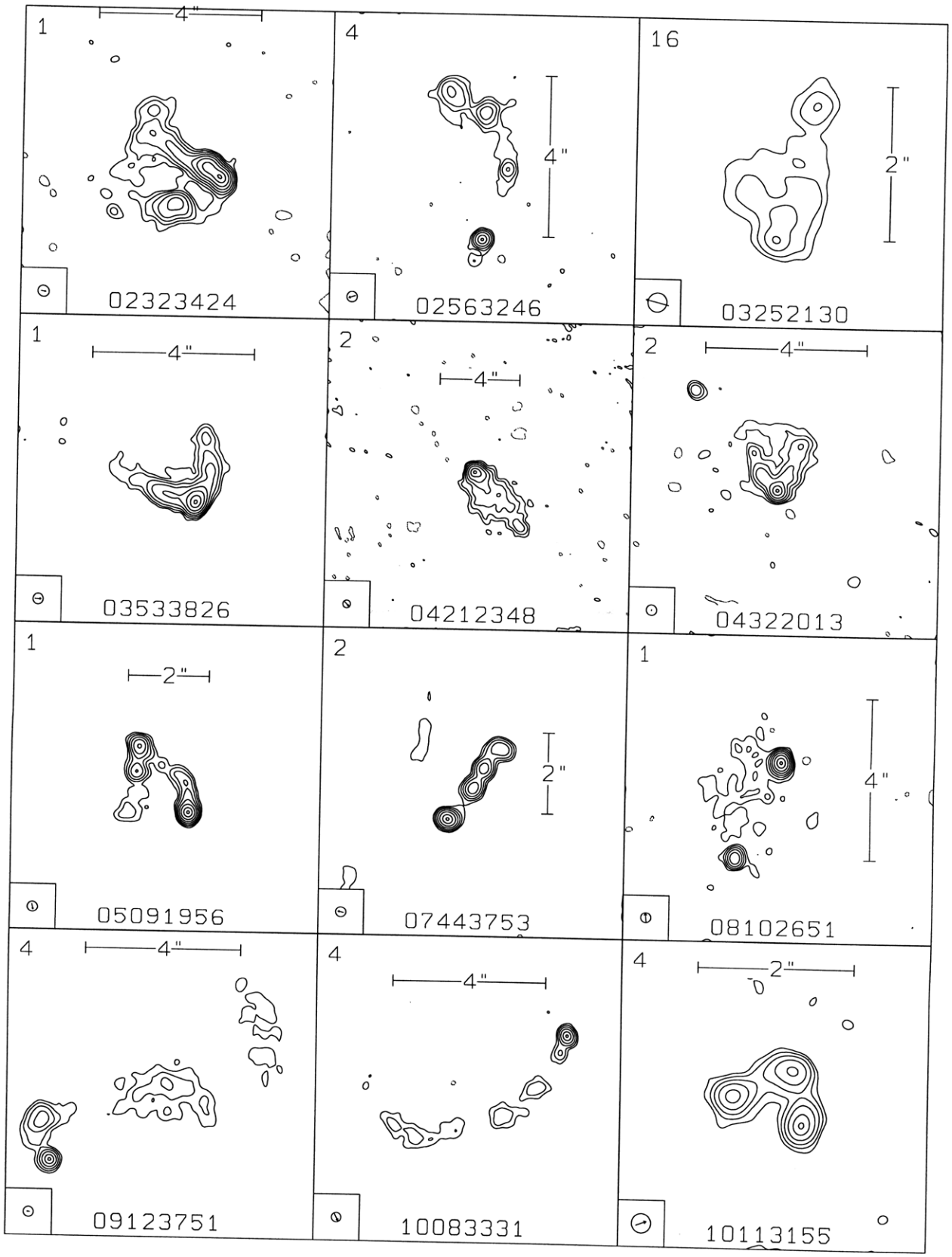
1
4"
02323424
4
4"
02563246
16
2"
03252130
1
4"
03533826
2
4"
04212348
2
4"
04322013
1
2"
05091956
2
2"
07443753
1
4"
08102651
4
4"
09123751
4
4"
10083331
4
2"
10113155

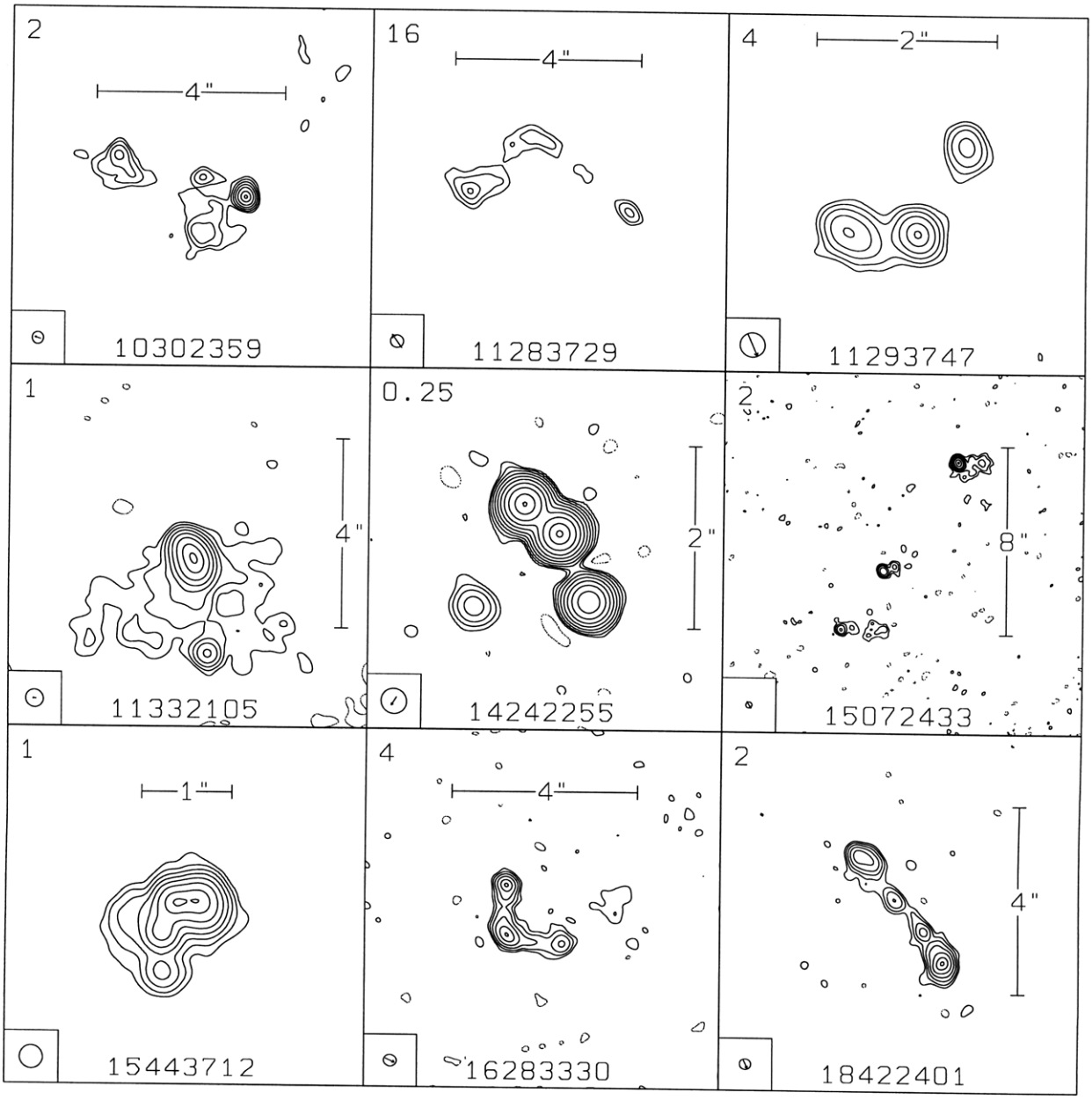
2
4"
10302359
16
4"
11283729
4
2"
11293747
1
4"
11332105
0.25
2"
14242255
2
8"
15072433
1
1"
15443712
4
4"
16283330
2
4"
18422401

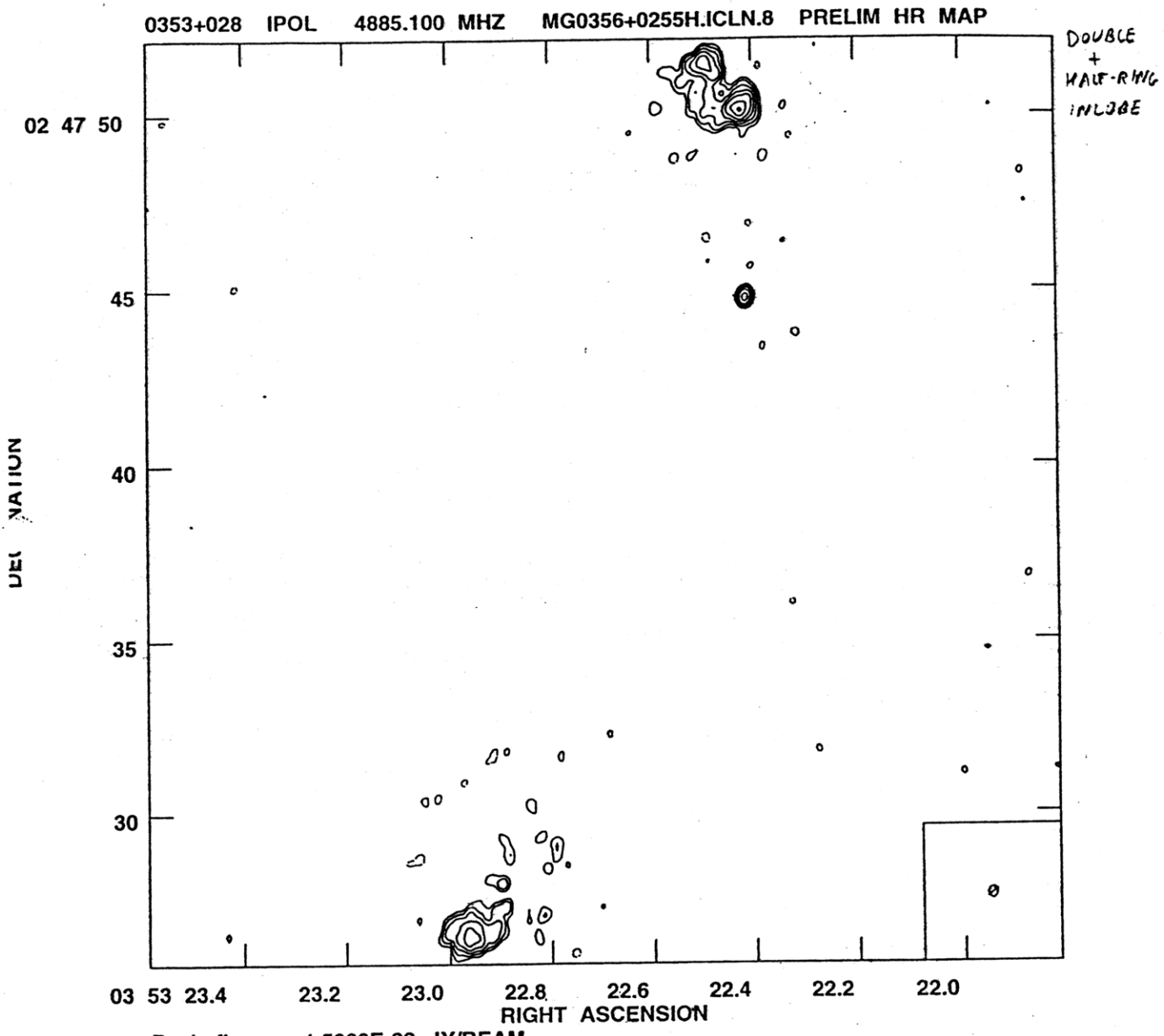

Peak flux = 1.5909E-02 JY/BEAM
Levs = 1.5909E-04 * (-2.00, 2.000, 4.000,
8.000, 16.00, 32.00, 64.00, 95.00)

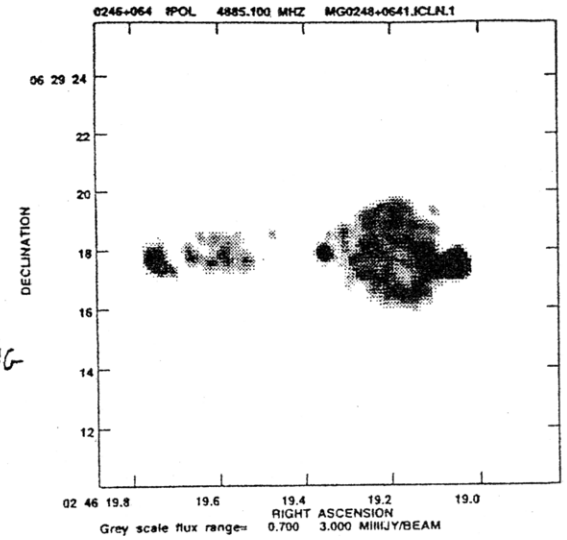

RING

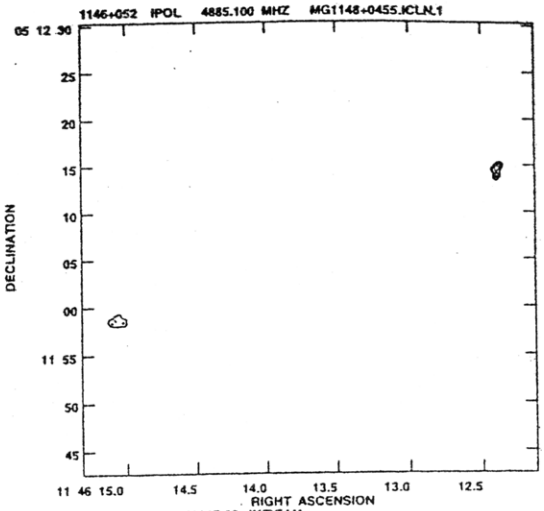

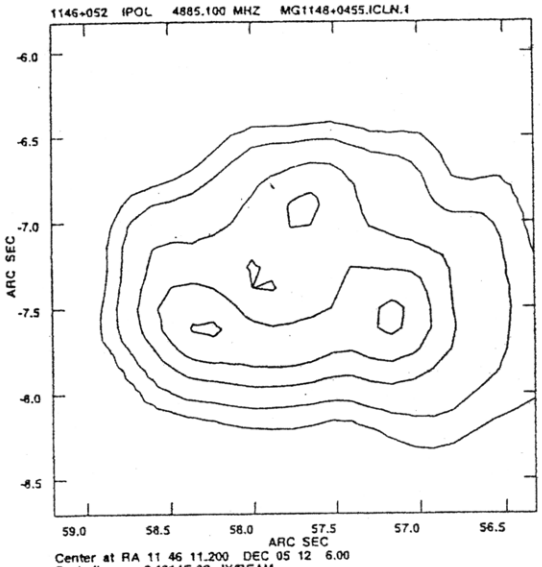

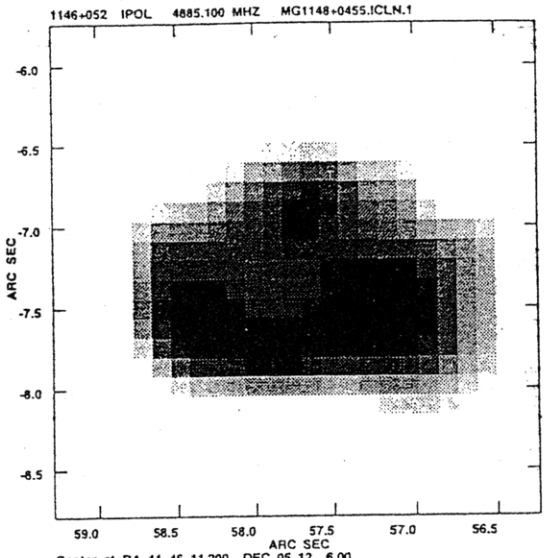

RING SOMEWHAT INNER

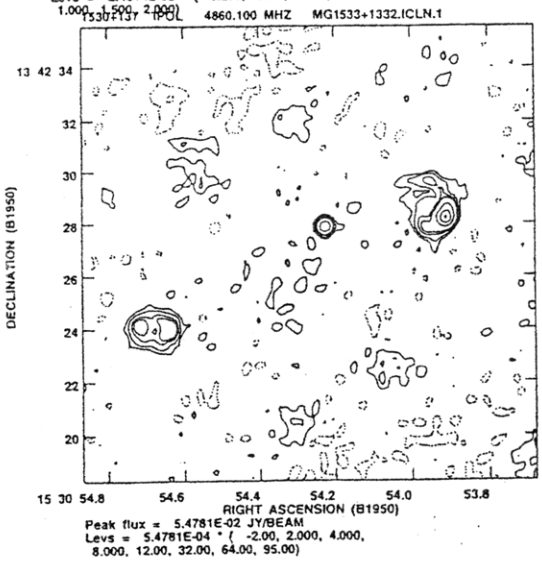

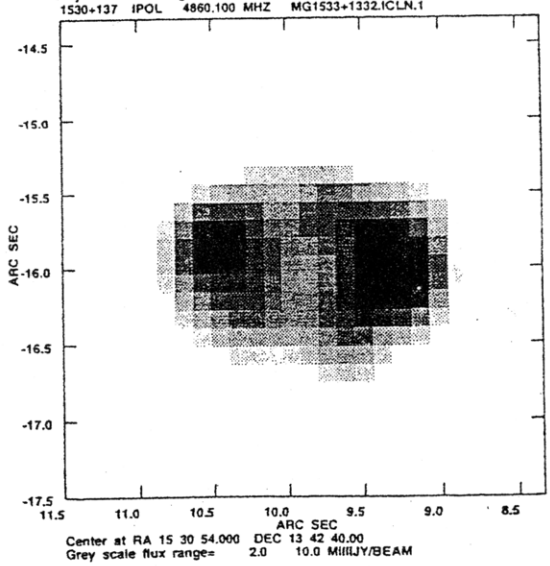

RING IN LOBE

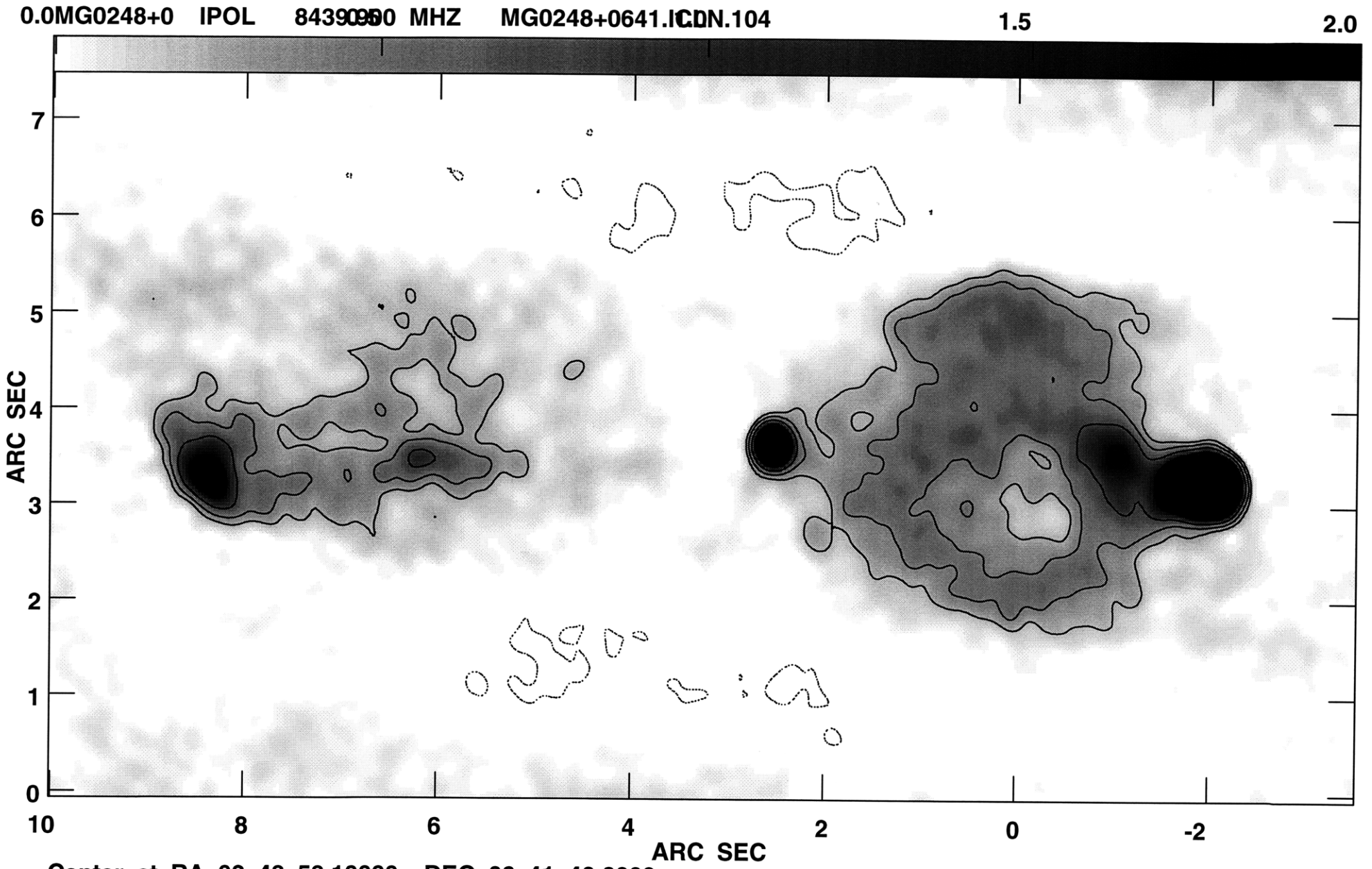

Center at RA 02 48 58.10000 DEC 06 41 40.0000
Grey scale flux range= 0.000 2.000 MilliJY/BEAM
Peak contour flux = 2.1973E-02 JY/BEAM
Levs = 2.1973E-04 * (-1.00, 1.000, 2.000,
4.000, 8.000, 16.00, 32.00, 64.00, 95.00)

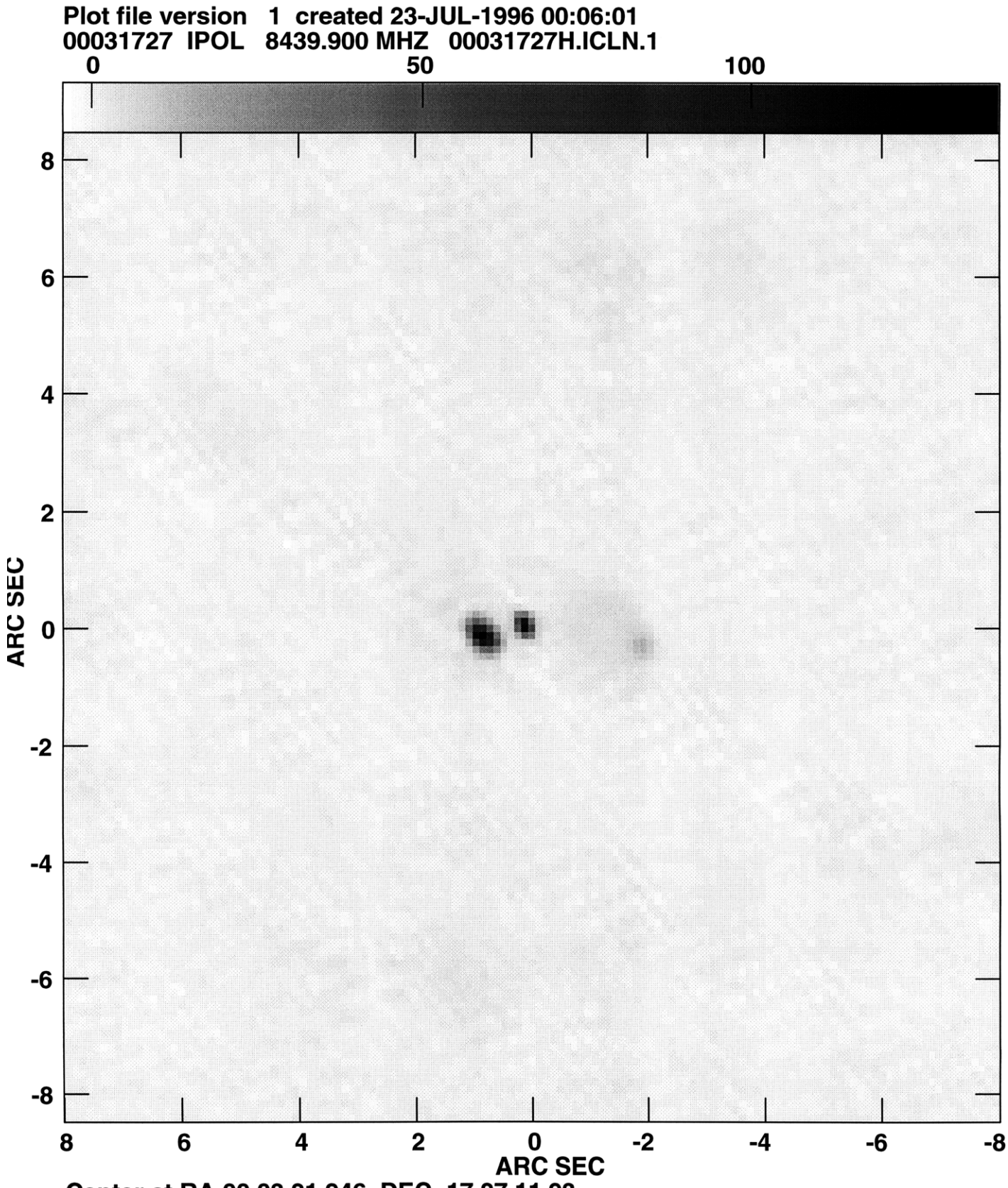
Plot file version 1 created 23-JUL-1996 00:06:01
00031727 IPOL 8439.900 MHZ 00031727H.ICLN.1
0
50
100
8
6
4
2
0
-2
-4
-6
-8
ARC SEC
8
6
4
2
0
-2
-4
-6
-8
ARC SEC
Center at RA 00 03 21.946 DEC -17 27 11.93
Grey scale flux range= -3.6 136.7 MilliJY/BEAM

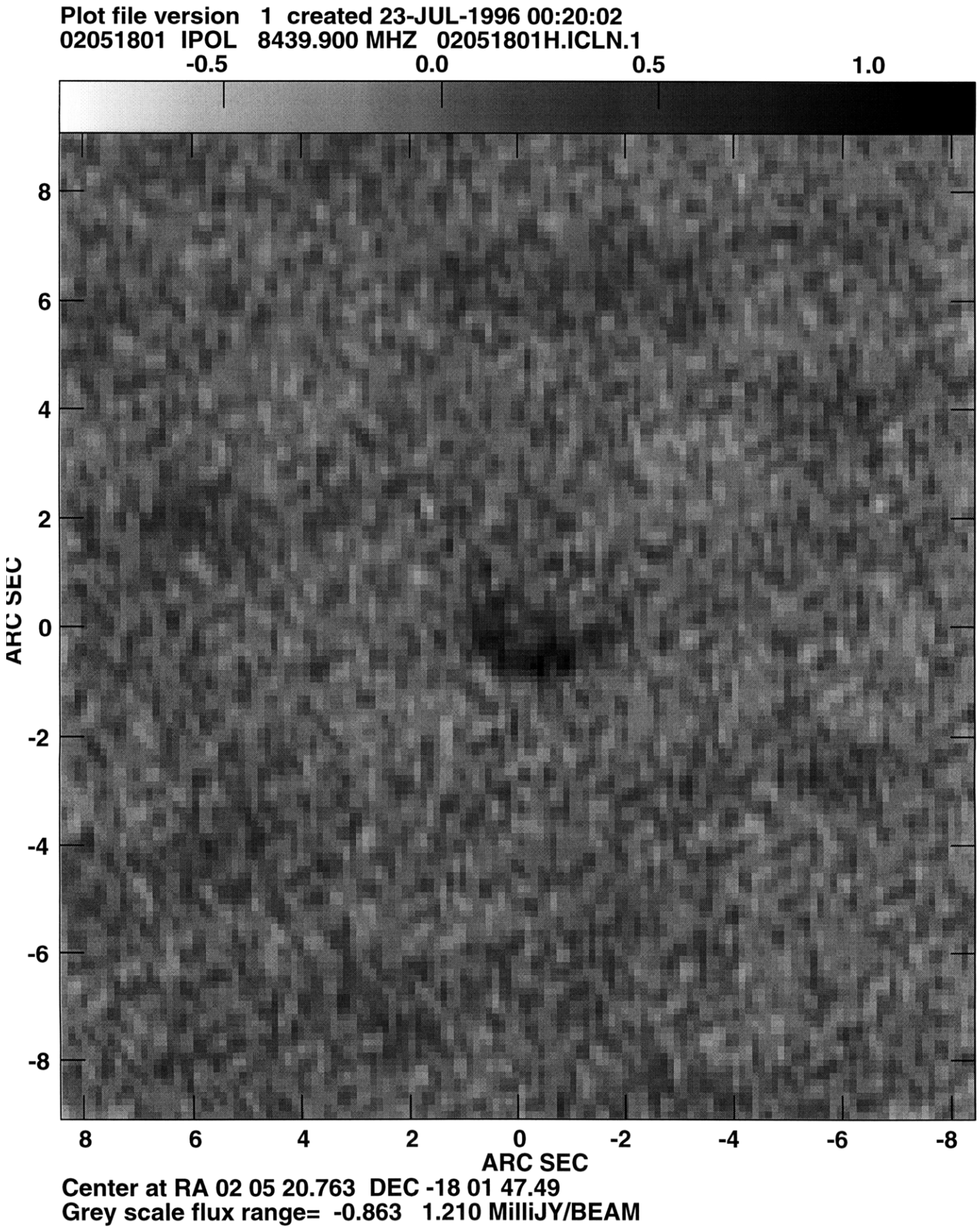
Plot file version 1 created 23-JUL-1996 00:20:02
02051801 IPOL 8439.900 MHZ 02051801H.ICLN.1
-0.5
0.0
0.5
1.0
8
6
4
2
0
-2
-4
-6
-8
ARC SEC
8
6
4
2
0
-2
-4
-6
-8
ARC SEC
Center at RA 02 05 20.763 DEC -18 01 47.49
Grey scale flux range= -0.863 1.210 MilliJY/BEAM

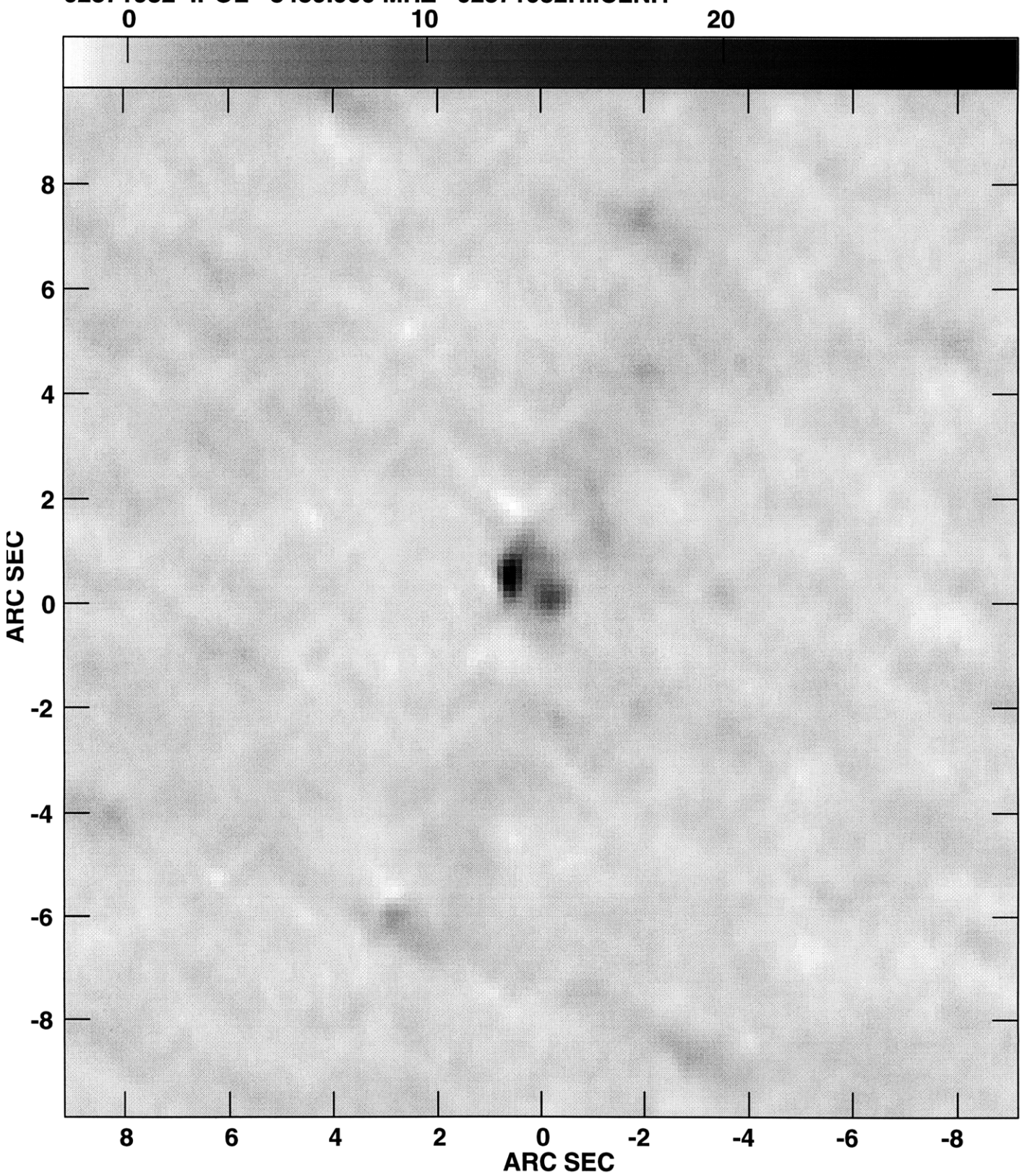
Plot file version 1 created 23-JUL-1996 00:23:26
02371932 IPOL 8439.900 MHZ 02371932H.ICLN.1
0
10
20
8
6
4
2
0
-2
-4
-6
-8
ARC SEC
8
6
4
2
0
-2
-4
-6
-8
ARC SEC
Center at RA 02 37 44.714 DEC -19 32 37.40
Grey scale flux range= -2.0 29.7 MilliJY/BEAM

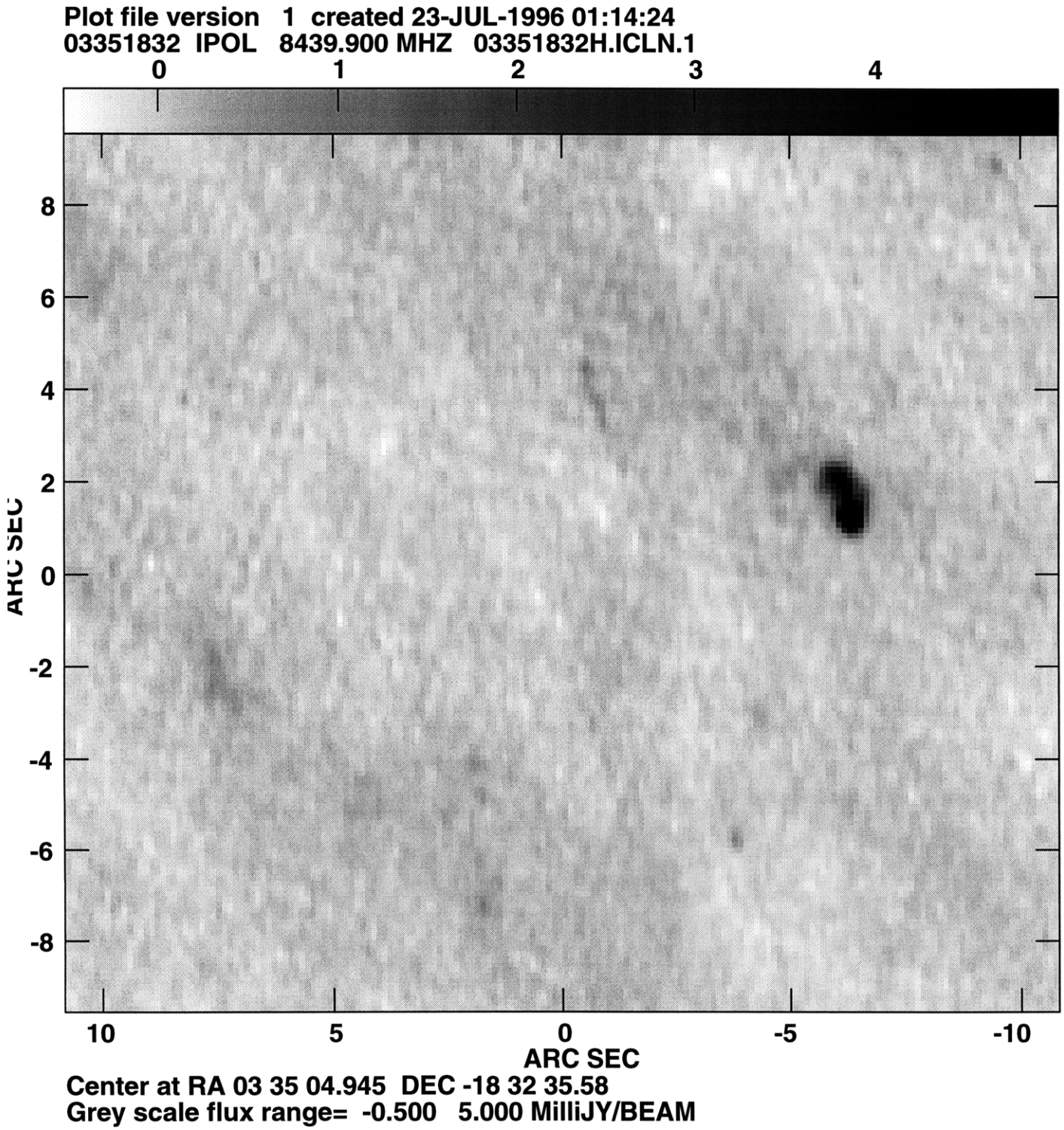
Plot file version 1 created 23-JUL-1996 01:14:24
03351832 IPOL 8439.900 MHZ 03351832H.ICLN.1
0
1
2
3
4
8
6
4
2
0
-2
-4
-6
-8
ARC SEC
10
5
0
-5
-10
ARC SEC
Center at RA 03 35 04.945 DEC -18 32 35.58
Grey scale flux range= -0.500 5.000 MilliJY/BEAM

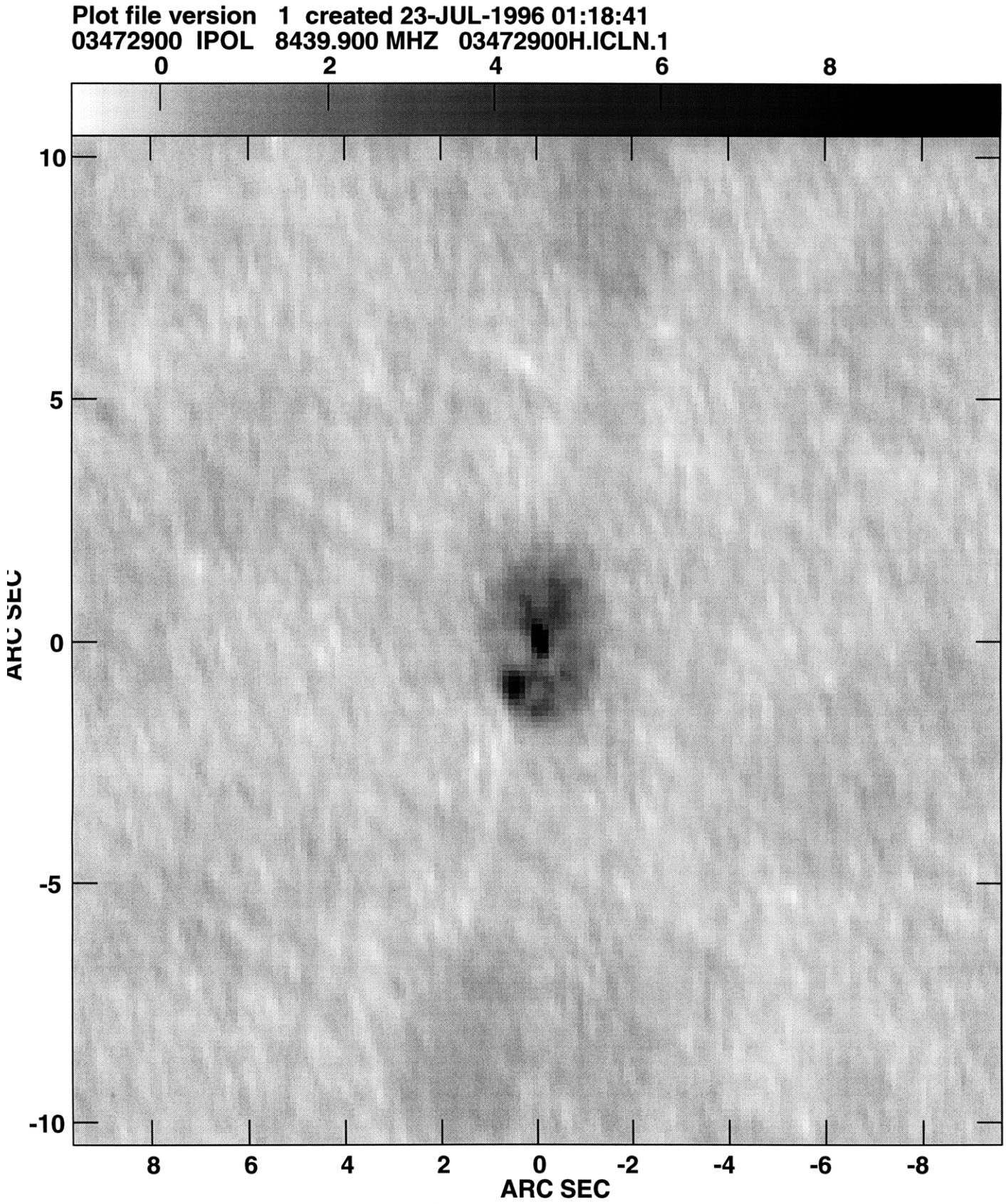
Plot file version 1 created 23-JUL-1996 01:18:41
03472900 IPOL 8439.900 MHZ 03472900H.ICLN.1
0
2
4
6
8
10
5
0
-5
-10
ARC SEC
8
6
4
2
0
-2
-4
-6
-8
ARC SEC
Center at RA 03 47 01.679 DEC -29 00 28.50
Grey scale flux range= -1.0 10.0 MilliJY/BEAM

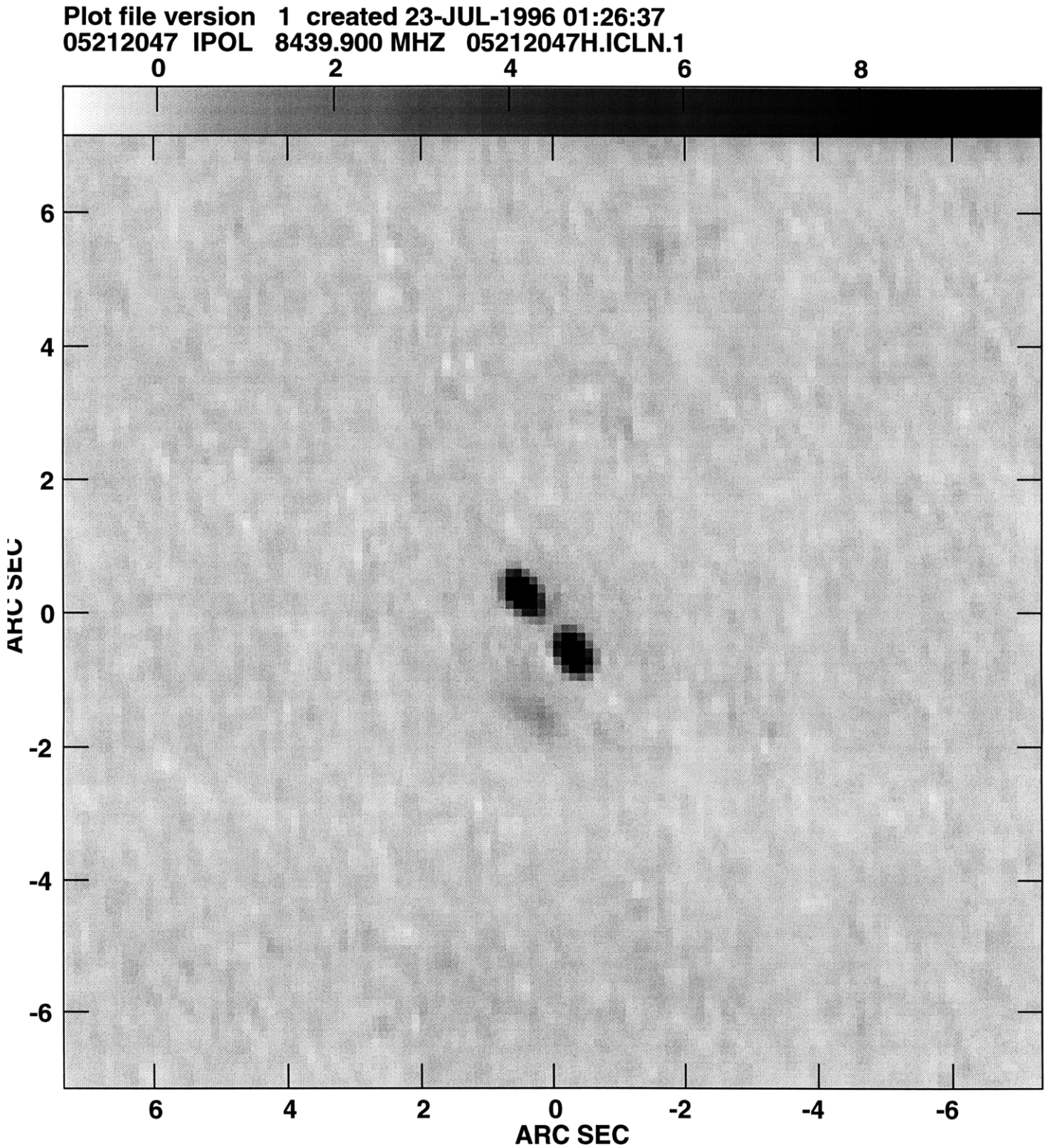
Plot file version 1 created 23-JUL-1996 01:26:37
05212047 IPOL 8439.900 MHZ 05212047H.ICLN.1
0
2
4
6
8
6
4
2
0
-2
-4
-6
ARC SEC
6
4
2
0
-2
-4
-6
ARC SEC
Center at RA 05 21 38.877 DEC -20 47 39.35
Grey scale flux range= -1.0 10.0 MilliJY/BEAM

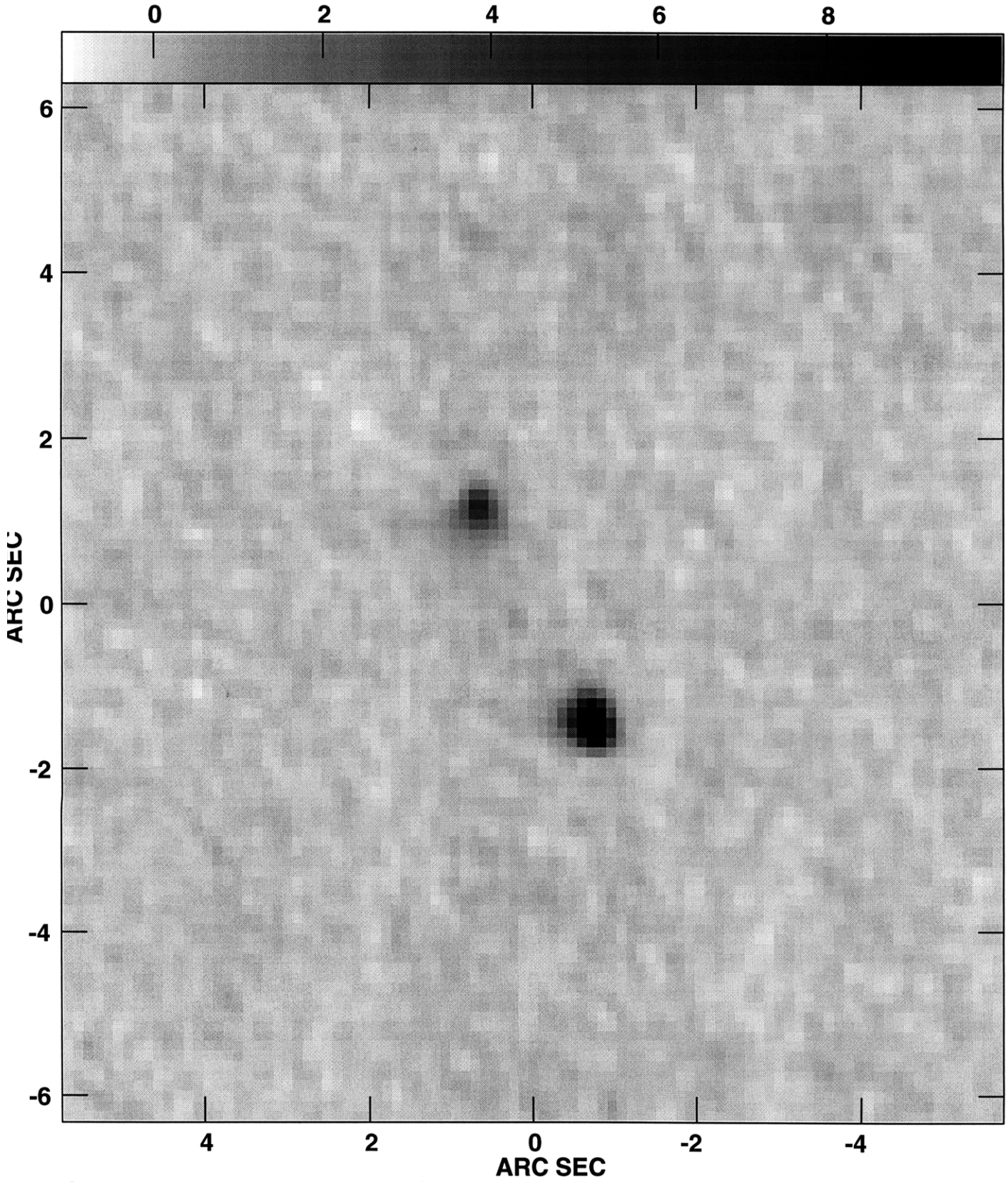
Plot file version 1 created 23-JUL-1996 01:29:48
06080738 IPOL 8439.900 MHZ 06080738H.ICLN.1
0
2
4
6
8
6
4
2
0
-2
-4
-6
ARC SEC
4
2
0
-2
-4
ARC SEC
Center at RA 06 08 03.686 DEC -07 38 30.67
Grey scale flux range= -1.0 10.0 MilliJY/BEAM

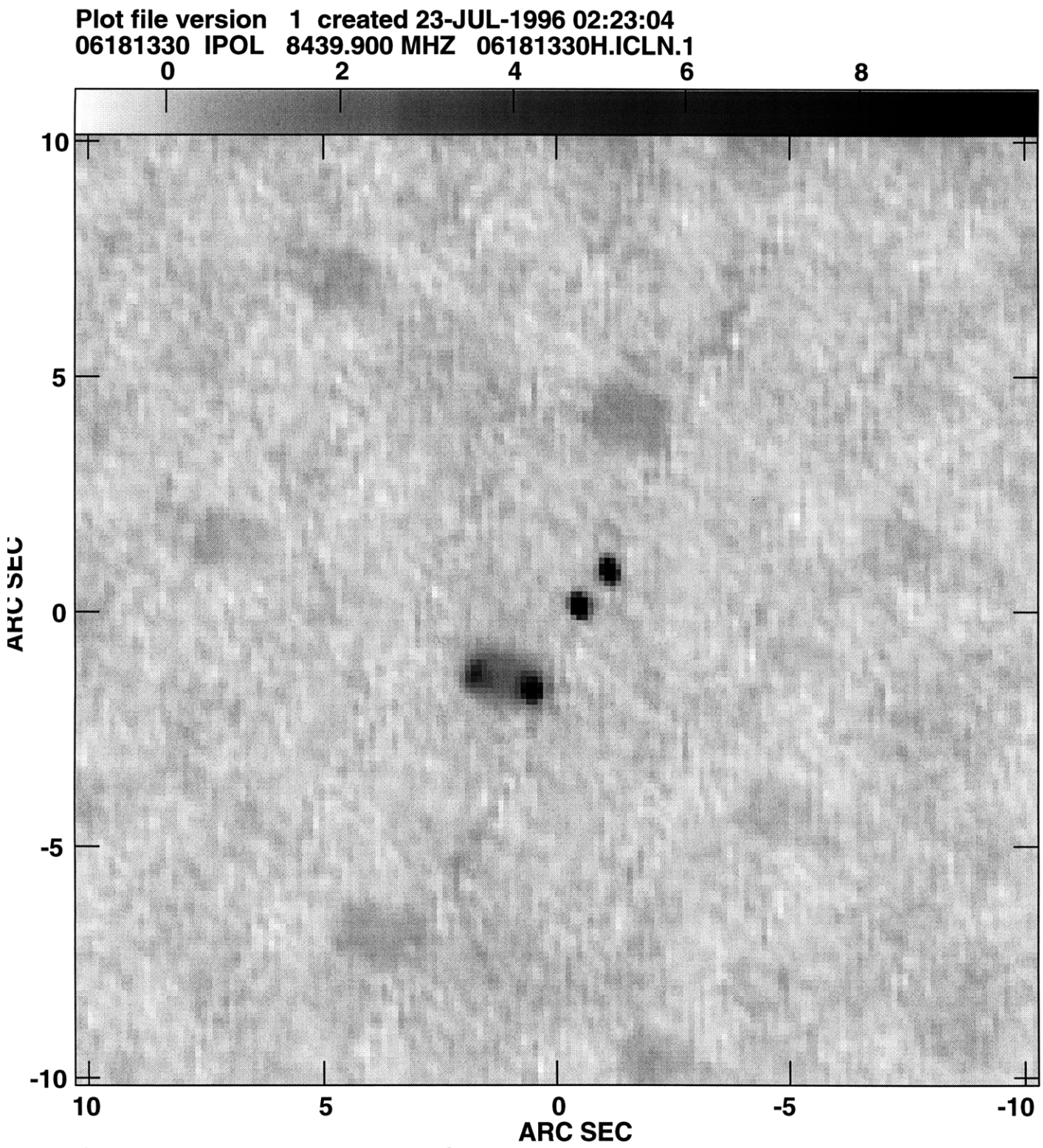
Plot file version 1 created 23-JUL-1996 02:23:04
06181330 IPOL 8439.900 MHZ 06181330H.ICLN.1
0
2
4
6
8
10
5
0
-5
-10
ARC SEC
10
5
0
-5
-10
ARC SEC
Center at RA 06 18 31.803 DEC -13 30 37.38
Grey scale flux range= -1.0 10.0 MilliJY/BEAM

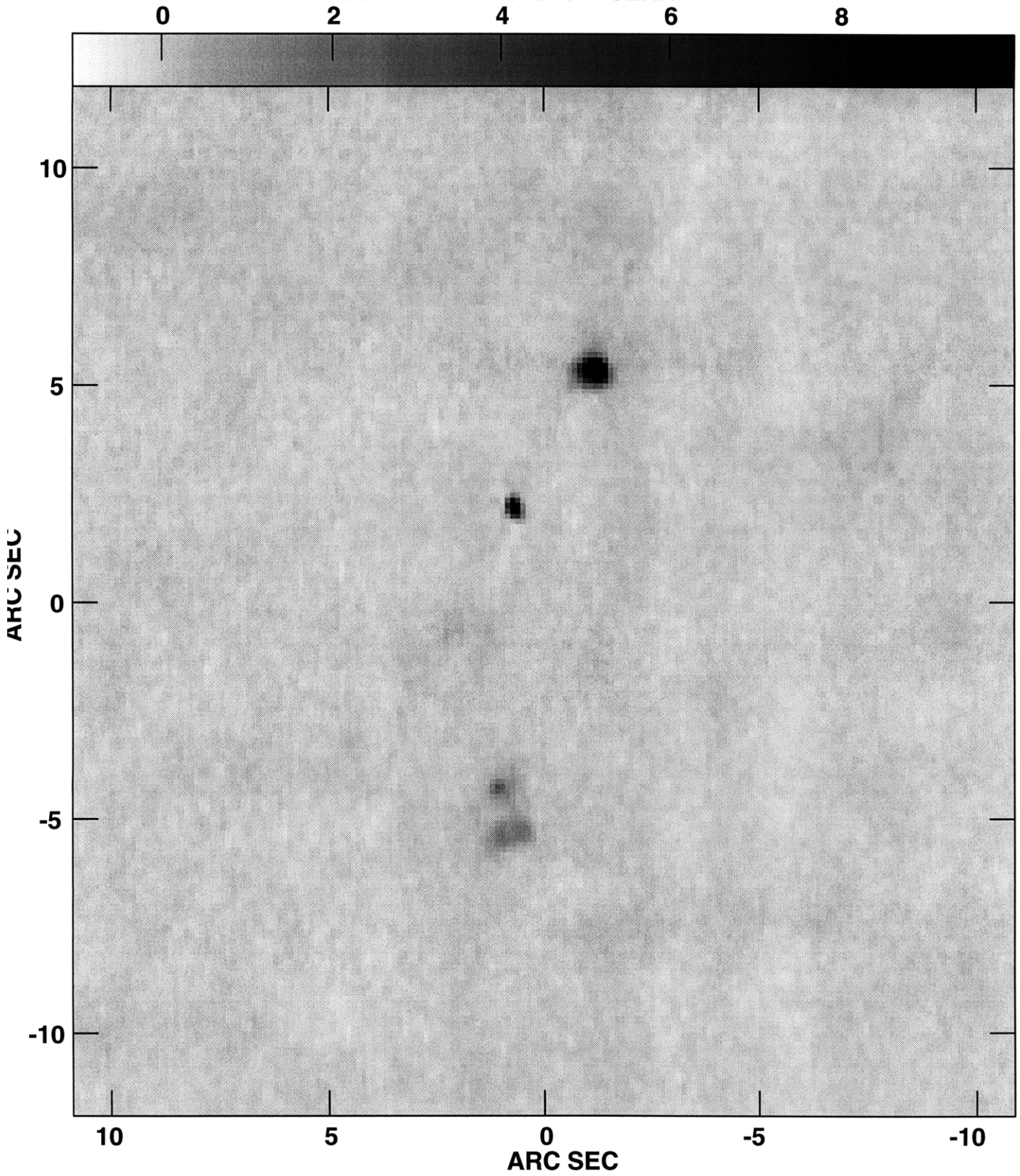
Plot file version 1 created 23-JUL-1996 02:27:18
06251018 IPOL 8439.900 MHZ 06251018H.ICLN.1
0
2
4
6
8
10
5
0
-5
-10
ARC SEC
10
5
0
-5
-10
ARC SEC
Center at RA 06 25 42.837 DEC -10 17 51.54
Grey scale flux range= -1.0 10.0 MilliJY/BEAM

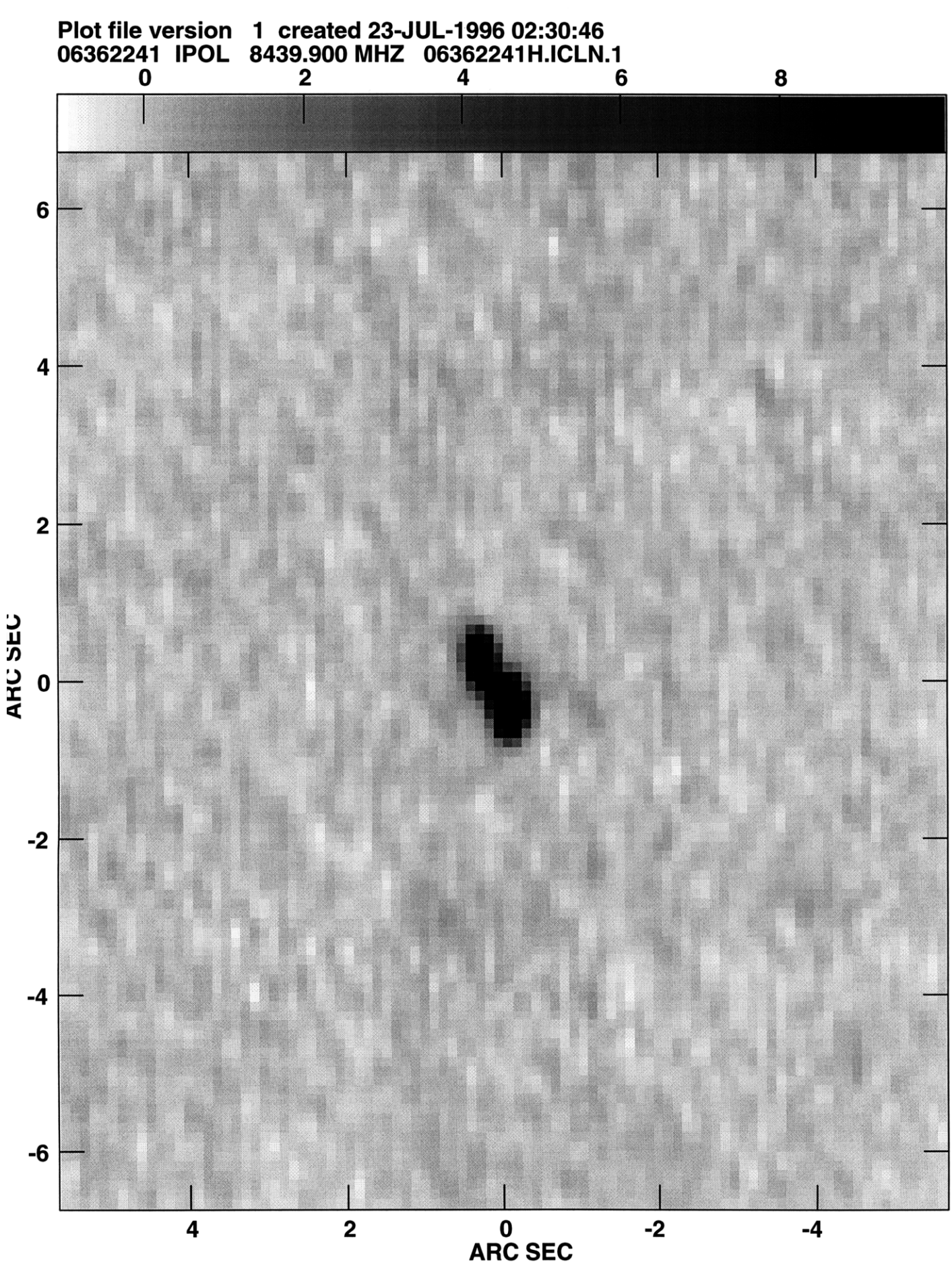
Plot file version 1 created 23-JUL-1996 02:30:46
06362241 IPOL 8439.900 MHZ 06362241H.ICLN.1
0
2
4
6
8
6
4
2
0
-2
-4
-6
ARC SEC
4
2
0
-2
-4
ARC SEC
Center at RA 06 36 43.571 DEC -22 41 39.83
Grey scale flux range= -1.0 10.0 MilliJY/BEAM

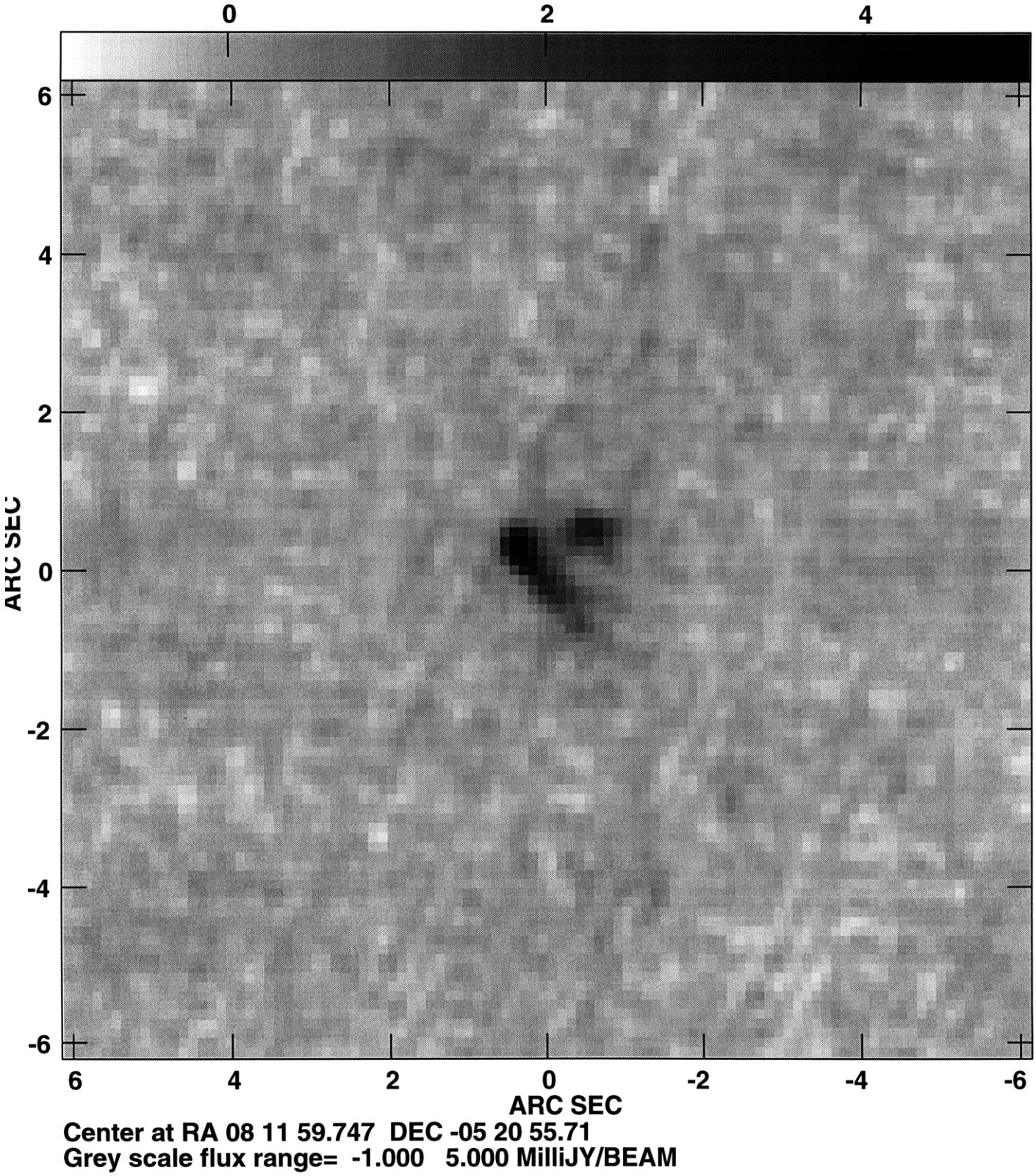
Plot file version 1 created 23-JUL-1996 02:34:00
08110520 IPOL 8439.900 MHZ 08110520H.ICLN.1
0
2
4
6
4
2
0
-2
-4
-6
ARC SEC
6
4
2
0
-2
-4
-6
ARC SEC
Center at RA 08 11 59.747 DEC -05 20 55.71
Grey scale flux range= -1.000 5.000 MilliJY/BEAM

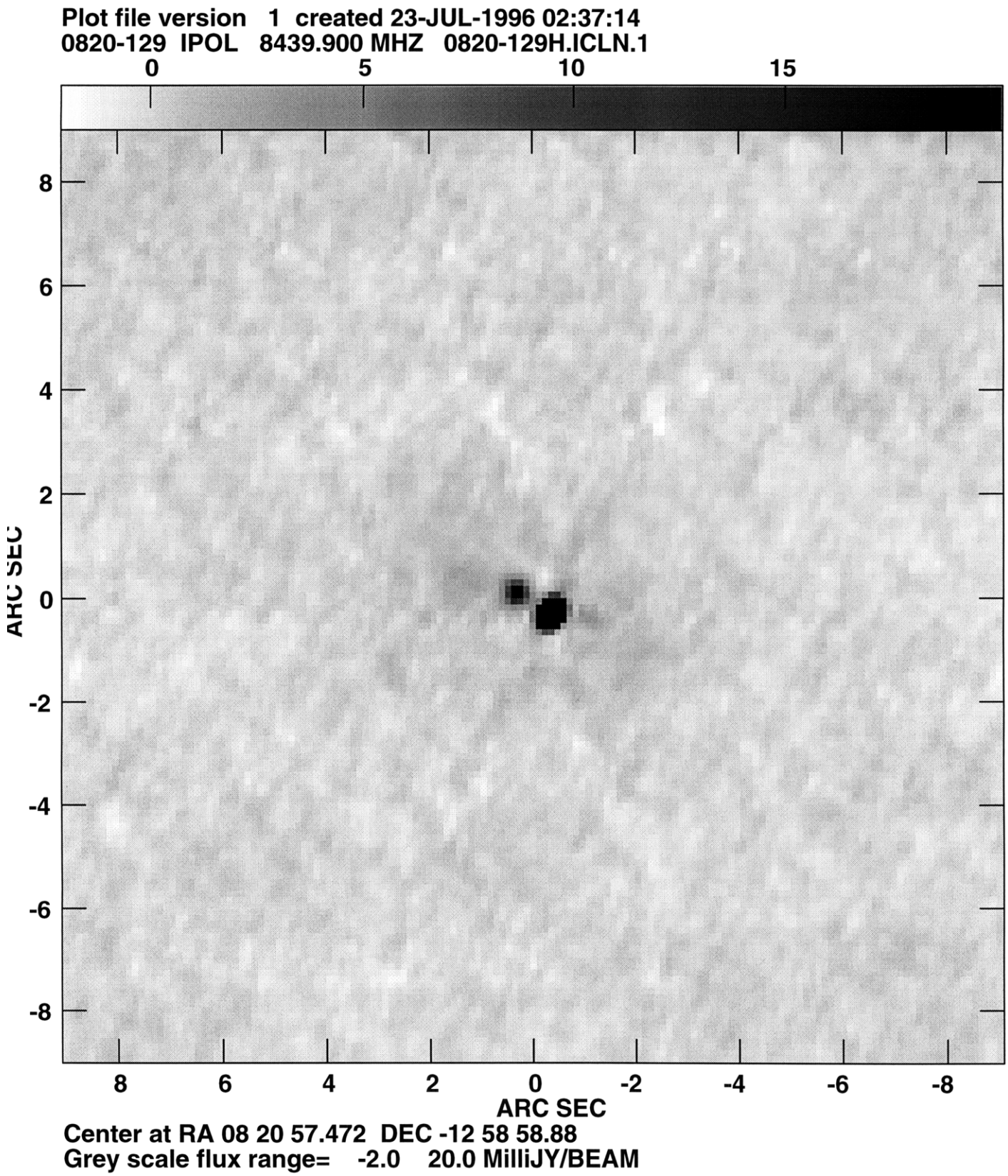
Plot file version 1 created 23-JUL-1996 02:37:14
0820-129 IPOL 8439.900 MHZ 0820-129H.ICLN.1
0
5
10
15
8
6
4
2
0
-2
-4
-6
-8
ARC SEC
8
6
4
2
0
-2
-4
-6
-8
ARC SEC
Center at RA 08 20 57.472 DEC -12 58 58.88
Grey scale flux range= -2.0 20.0 MilliJY/BEAM

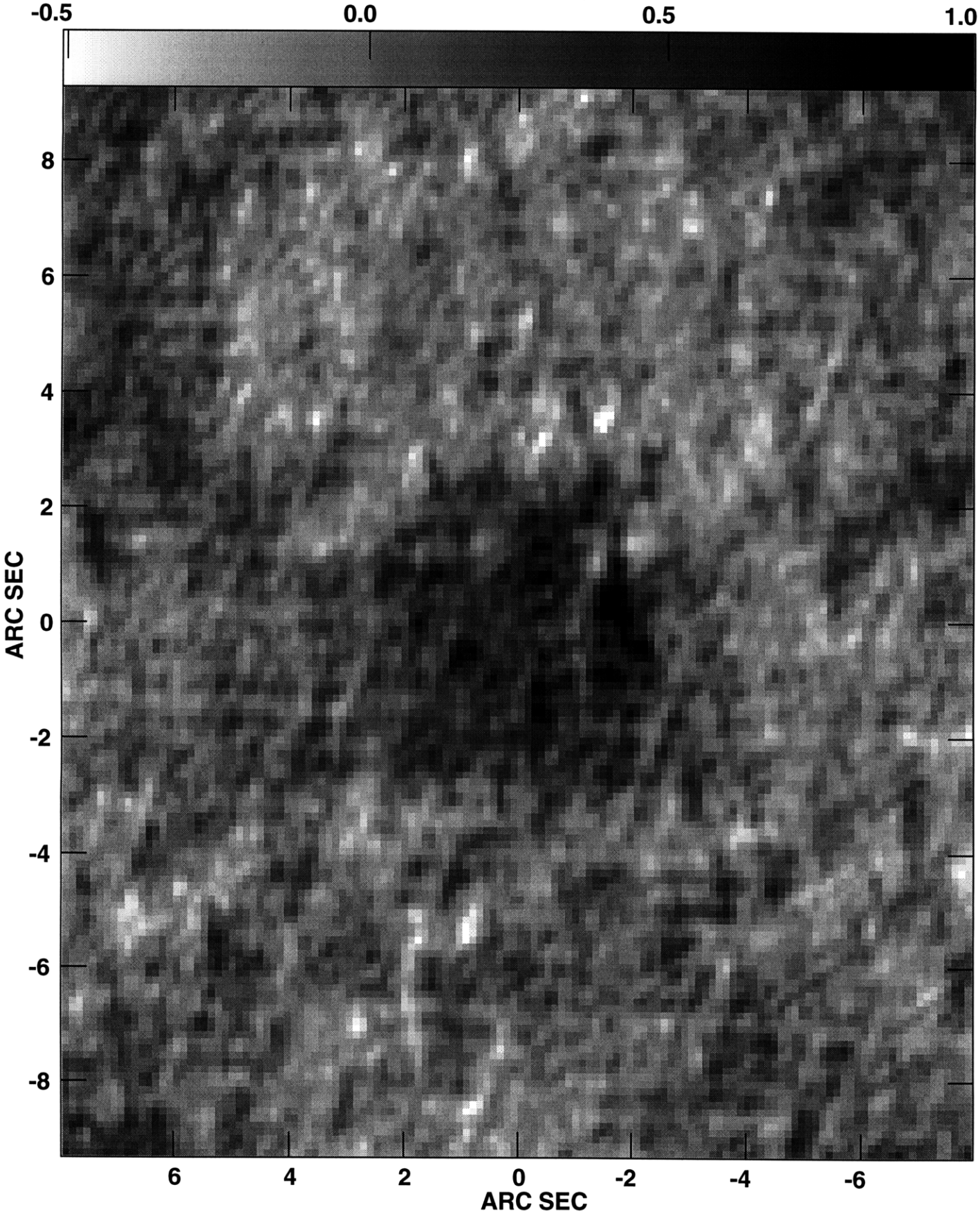
Plot file version 1 created 23-JUL-1996 02:52:18
08371156 IPOL 8439.900 MHZ 08371156H.ICLN.1
-0.5
0.0
0.5
1.0
8
6
4
2
0
-2
-4
-6
-8
ARC SEC
6
4
2
0
-2
-4
-6
ARC SEC
Center at RA 08 37 02.953 DEC -11 55 11.08
Grey scale flux range= -0.500 1.000 MilliJY/BEAM

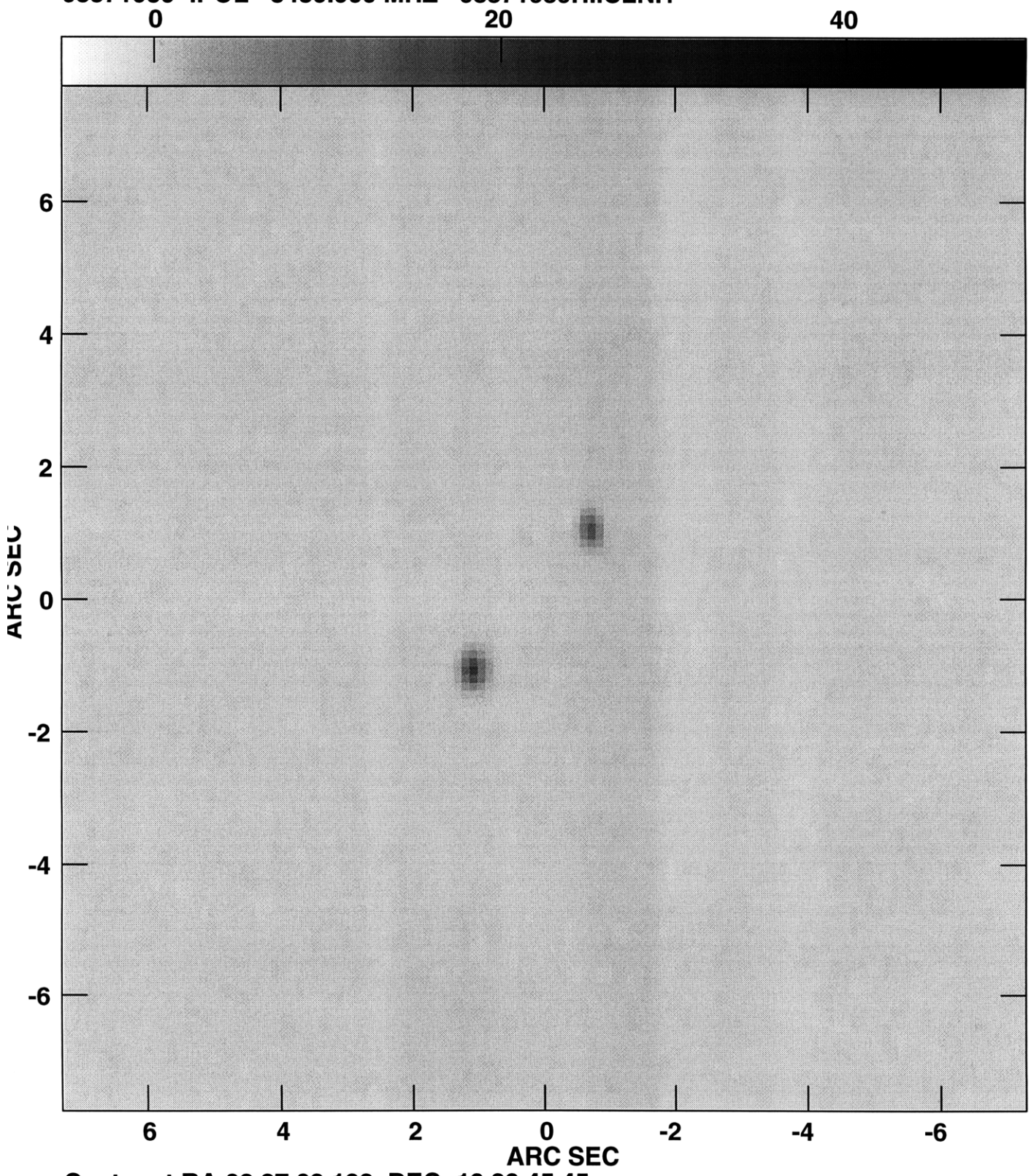
Plot file version 1 created 23-JUL-1996 02:47:11
08371939 IPOL 8439.900 MHZ 08371939H.ICLN.1
0
20
40
6
4
2
0
-2
-4
-6
ARC SEC
6
4
2
0
-2
-4
-6
ARC SEC
Center at RA 08 37 09.193 DEC -19 39 45.45
Grey scale flux range= -5.0 50.0 MilliJY/BEAM

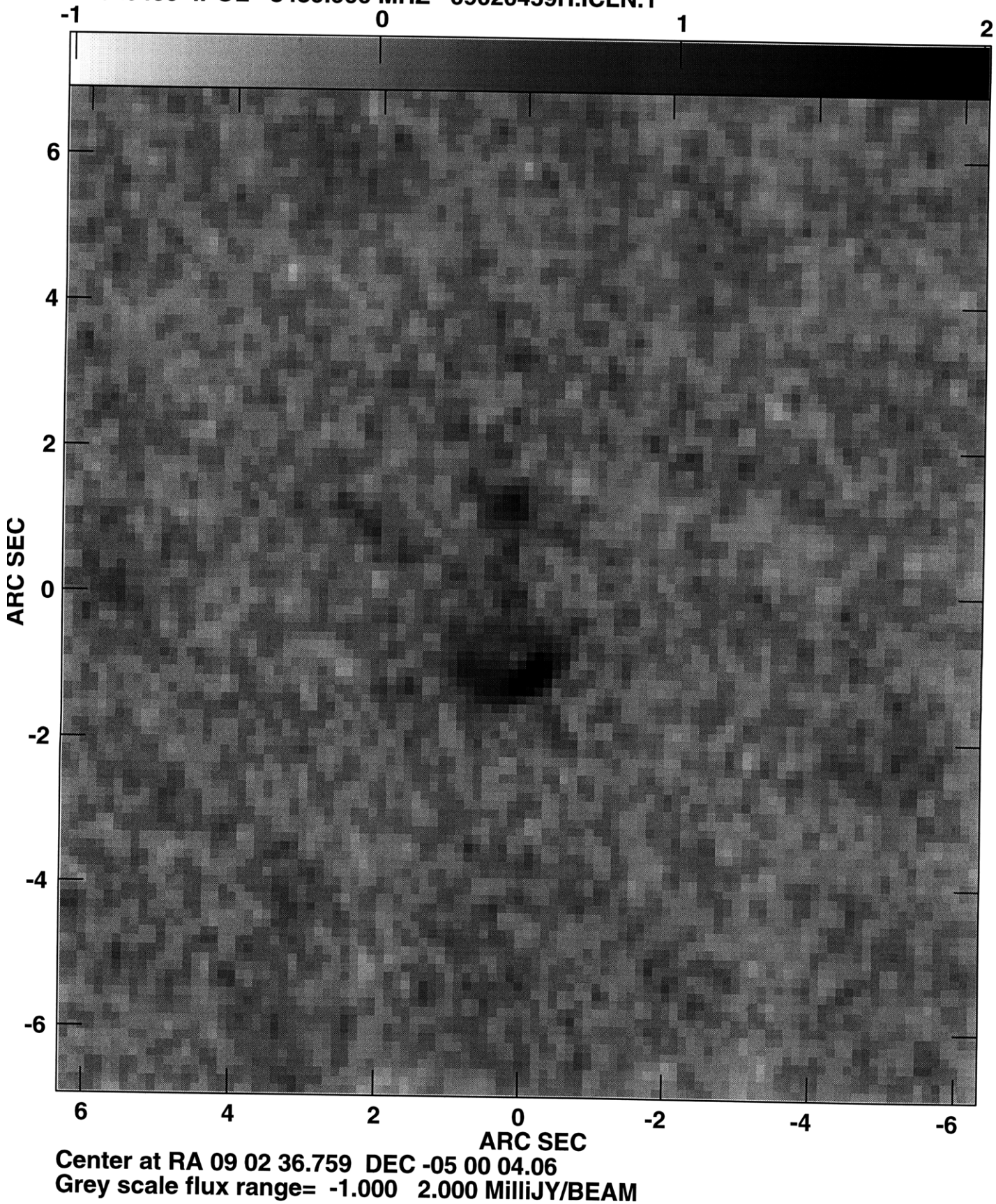
Plot file version 2 created 23-JUL-1996 03:56:08
09020459 IPOL 8439.900 MHZ 09020459H.ICLN.1
-1
0
1
2
6
4
2
0
-2
-4
-6
ARC SEC
6
4
2
0
-2
-4
-6
ARC SEC
Center at RA 09 02 36.759 DEC -05 00 04.06
Grey scale flux range= -1.000 2.000 MilliJY/BEAM

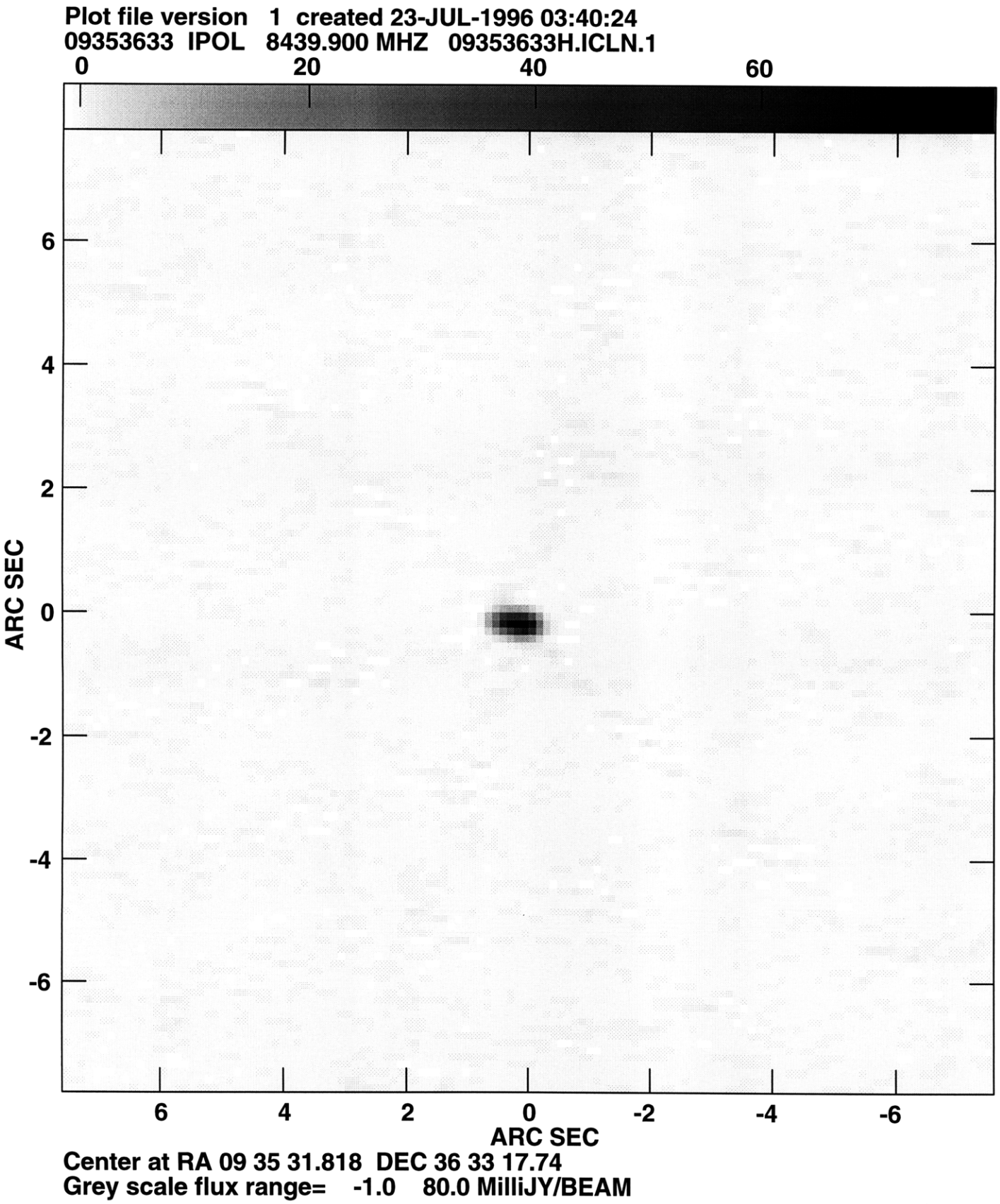
Plot file version 1 created 23-JUL-1996 03:40:24
09353633 IPOL 8439.900 MHZ 09353633H.ICLN.1
0
20
40
60
6
4
2
0
-2
-4
-6
ARC SEC
6
4
2
0
-2
-4
-6
ARC SEC
Center at RA 09 35 31.818 DEC 36 33 17.74
Grey scale flux range= -1.0 80.0 MilliJY/BEAM

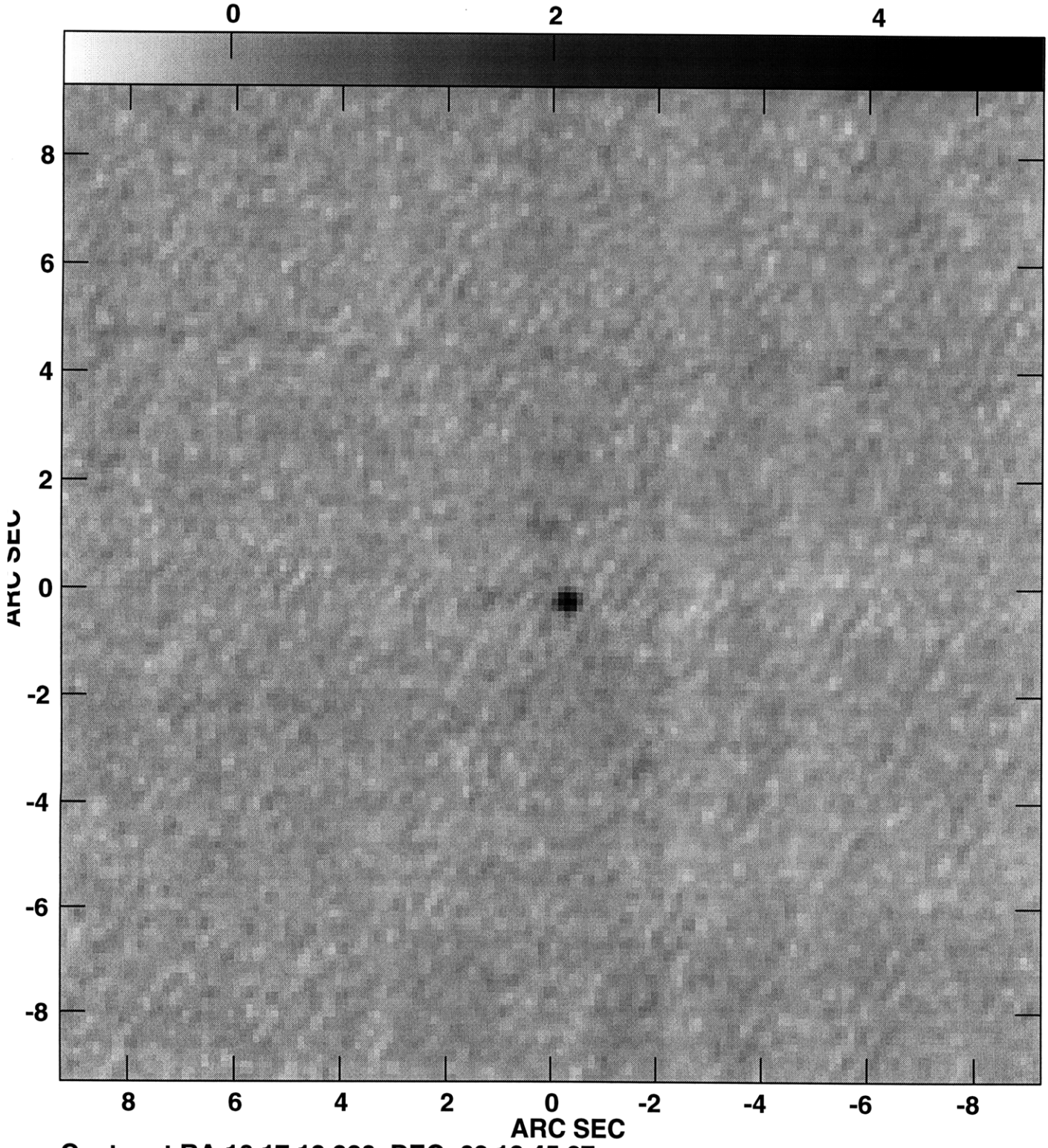
Plot file version 1 created 23-JUL-1996 03:44:51
10170220 IPOL 8439.900 MHZ 10170220H.ICLN.1
0
2
4
8
6
4
2
0
-2
-4
-6
-8
ARC SEC
8
6
4
2
0
-2
-4
-6
-8
ARC SEC
Center at RA 10 17 19.980 DEC -02 19 45.87
Grey scale flux range= -1.000 5.000 MilliJY/BEAM

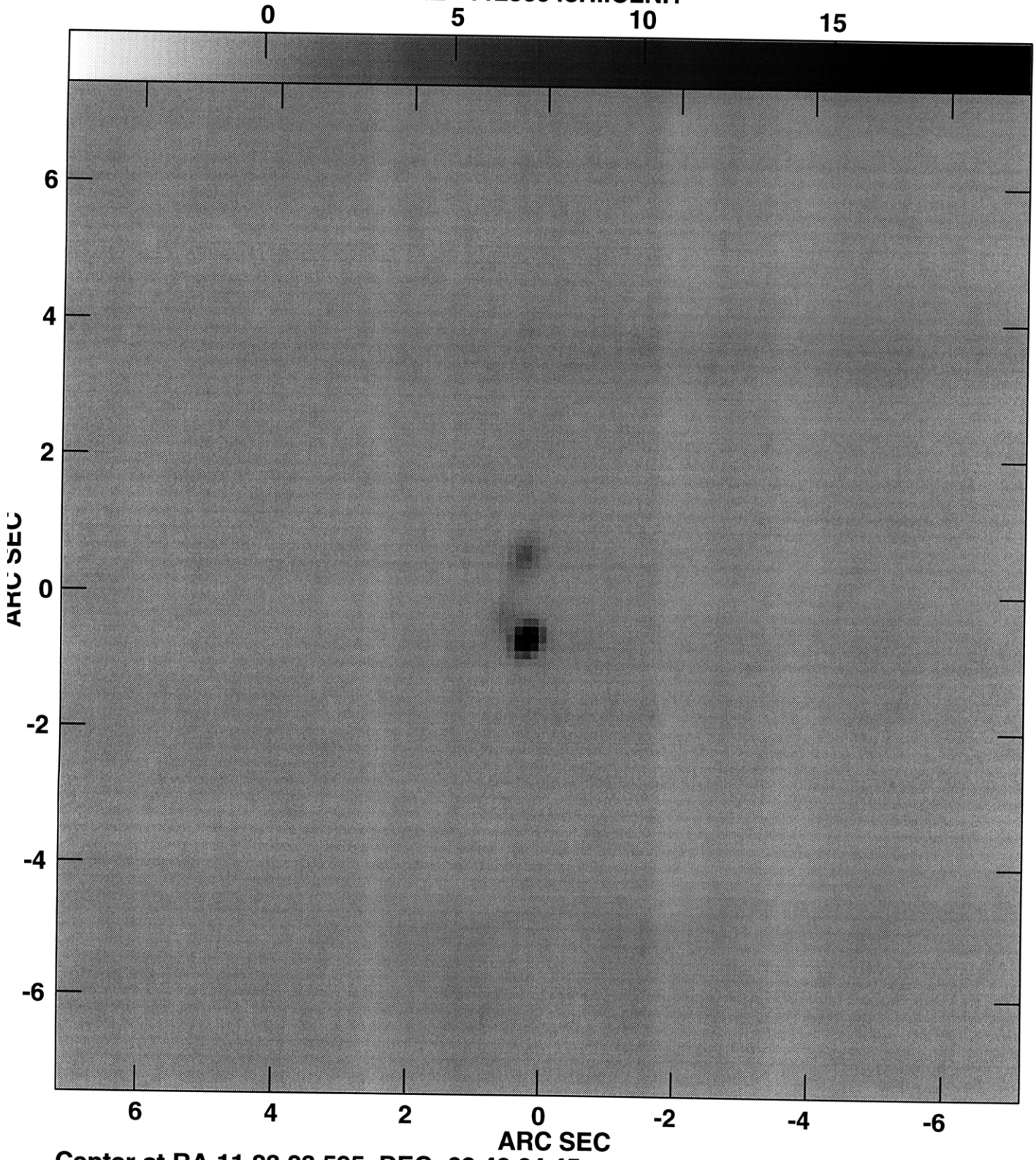
Plot file version 1 created 23-JUL-1996 03:48:18
11230948 IPOL 8439.900 MHZ 11230948H.ICLN.1
0
5
10
15
6
4
2
0
-2
-4
-6
ARC SEC
6
4
2
0
-2
-4
-6
ARC SEC
Center at RA 11 23 23.595 DEC -09 49 04.45
Grey scale flux range= -5.0 20.0 MilliJY/BEAM

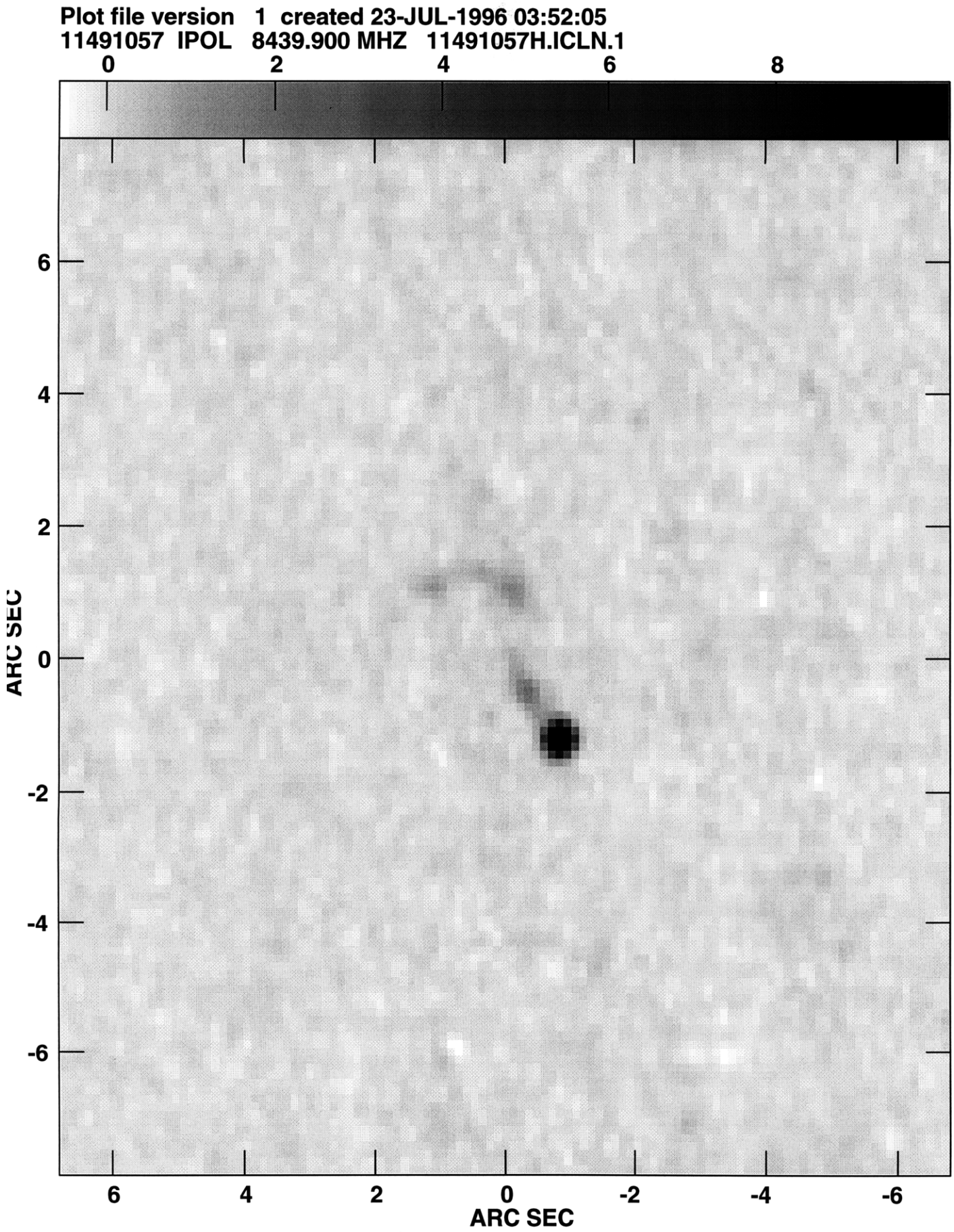
Plot file version 1 created 23-JUL-1996 03:52:05
11491057 IPOL 8439.900 MHZ 11491057H.ICLN.1
0
2
4
6
8
6
4
2
0
-2
-4
-6
ARC SEC
6
4
2
0
-2
-4
-6
ARC SEC
Center at RA 11 49 49.811 DEC -10 58 31.36
Grey scale flux range= -0.5 10.0 MilliJY/BEAM

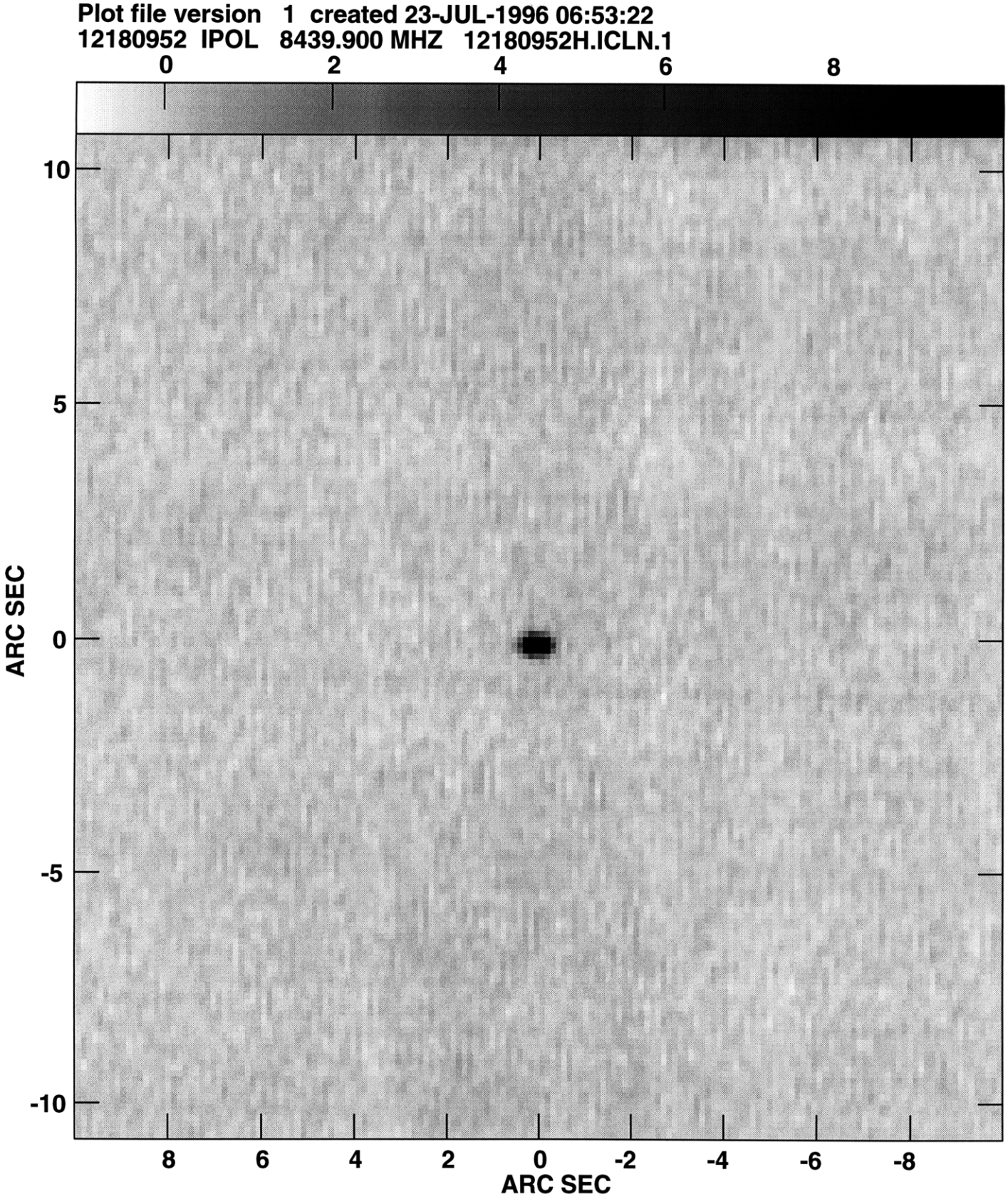
Plot file version 1 created 23-JUL-1996 06:53:22
12180952 IPOL 8439.900 MHZ 12180952H.ICLN.1
0
2
4
6
8
10
5
0
-5
-10
ARC SEC
8
6
4
2
0
-2
-4
-6
-8
ARC SEC
Center at RA 12 18 12.432 DEC -09 52 34.22
Grey scale flux range= -1.0 10.0 MilliJY/BEAM

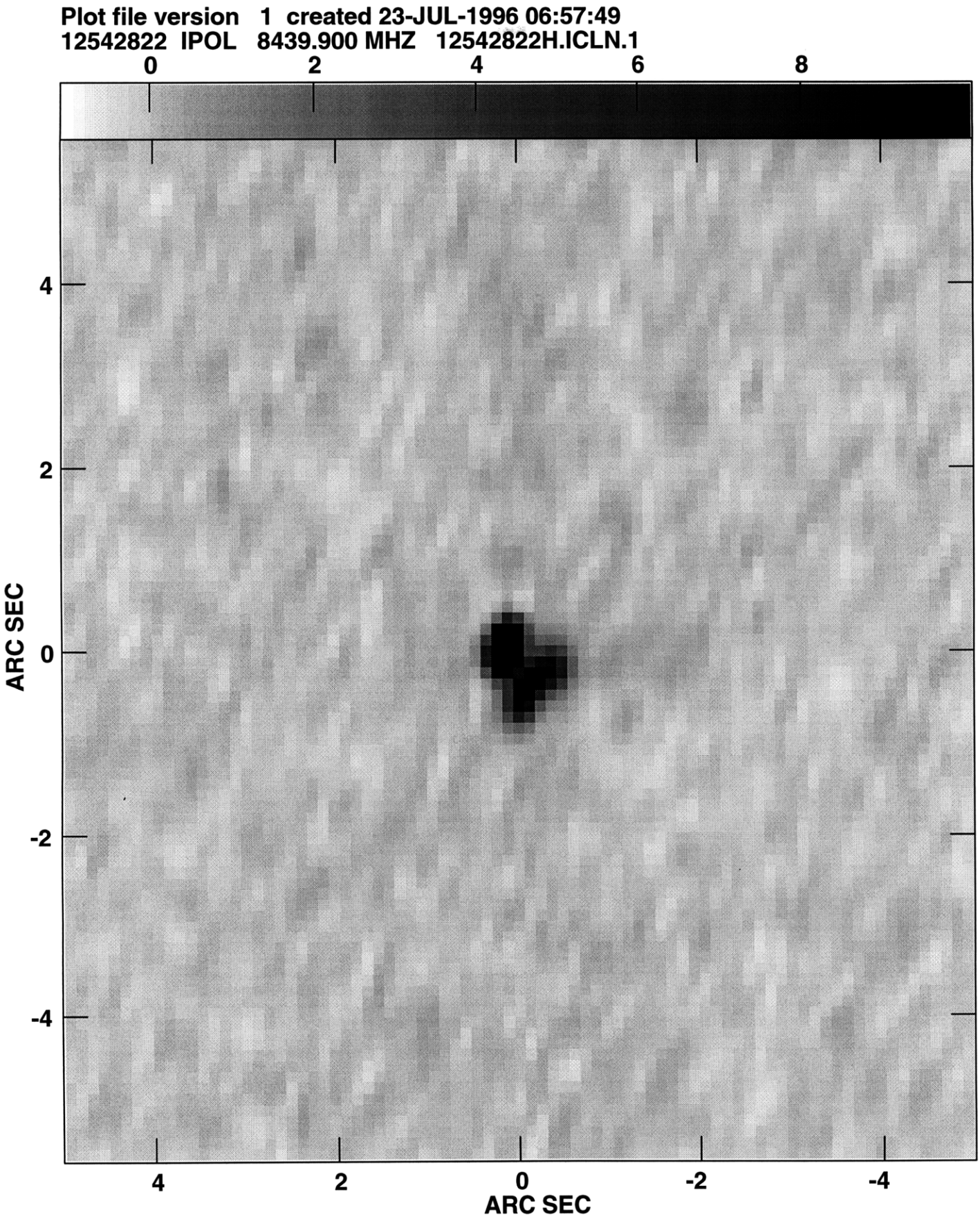
Plot file version 1 created 23-JUL-1996 06:57:49
12542822 IPOL 8439.900 MHZ 12542822H.ICLN.1
0
2
4
6
8
4
2
0
-2
-4
ARC SEC
4
2
0
-2
-4
ARC SEC
Center at RA 12 54 22.855 DEC -28 22 57.42
Grey scale flux range= -1.0 10.0 MilliJY/BEAM

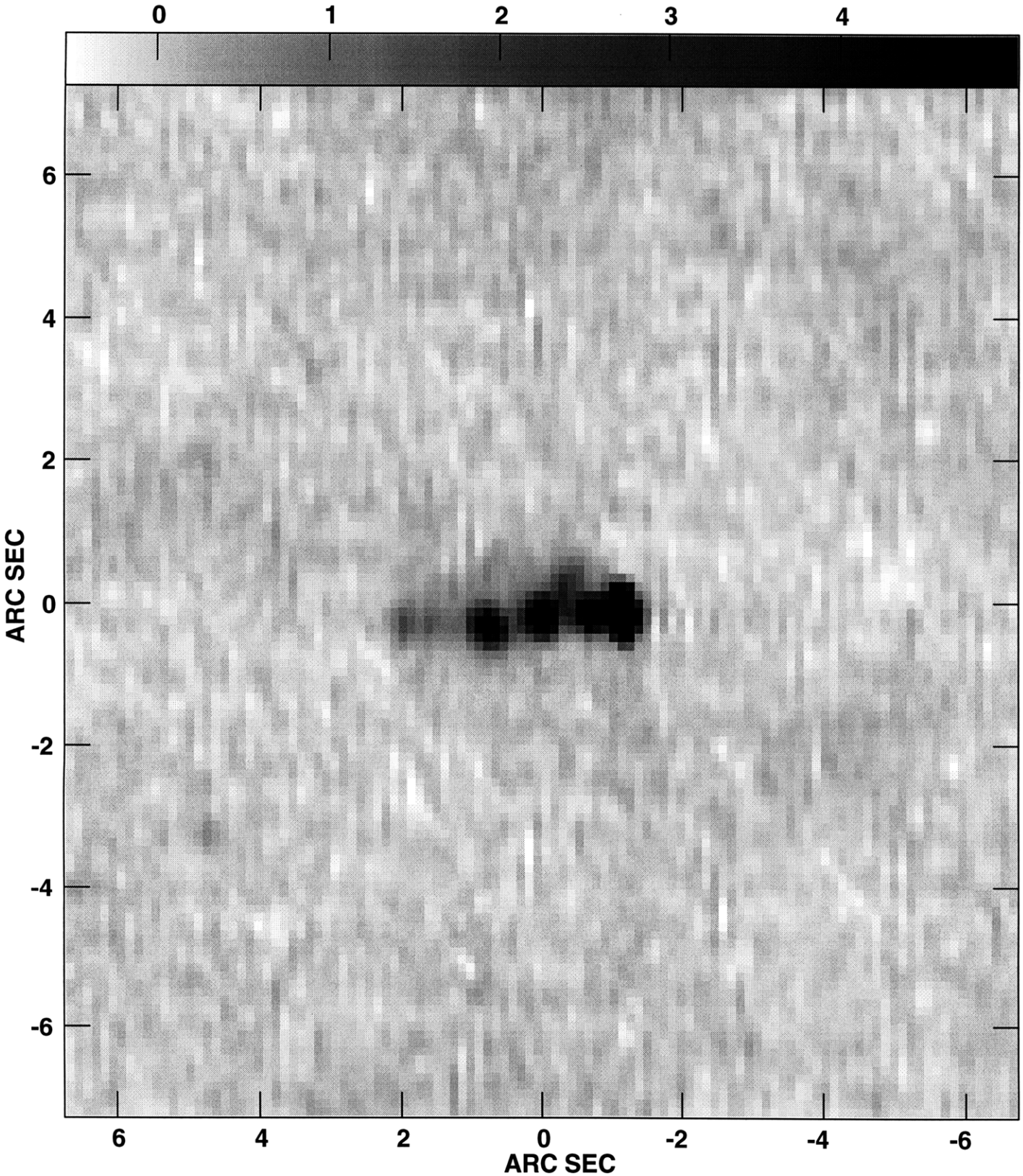
Plot file version 1 created 23-JUL-1996 07:01:48
13042106 IPOL 8439.900 MHZ 13042106H.ICLN.1
0
1
2
3
4
6
4
2
0
-2
-4
-6
ARC SEC
6
4
2
0
-2
-4
-6
ARC SEC
Center at RA 13 04 59.154 DEC -21 06 42.45
Grey scale flux range= -0.500 5.000 MilliJY/BEAM

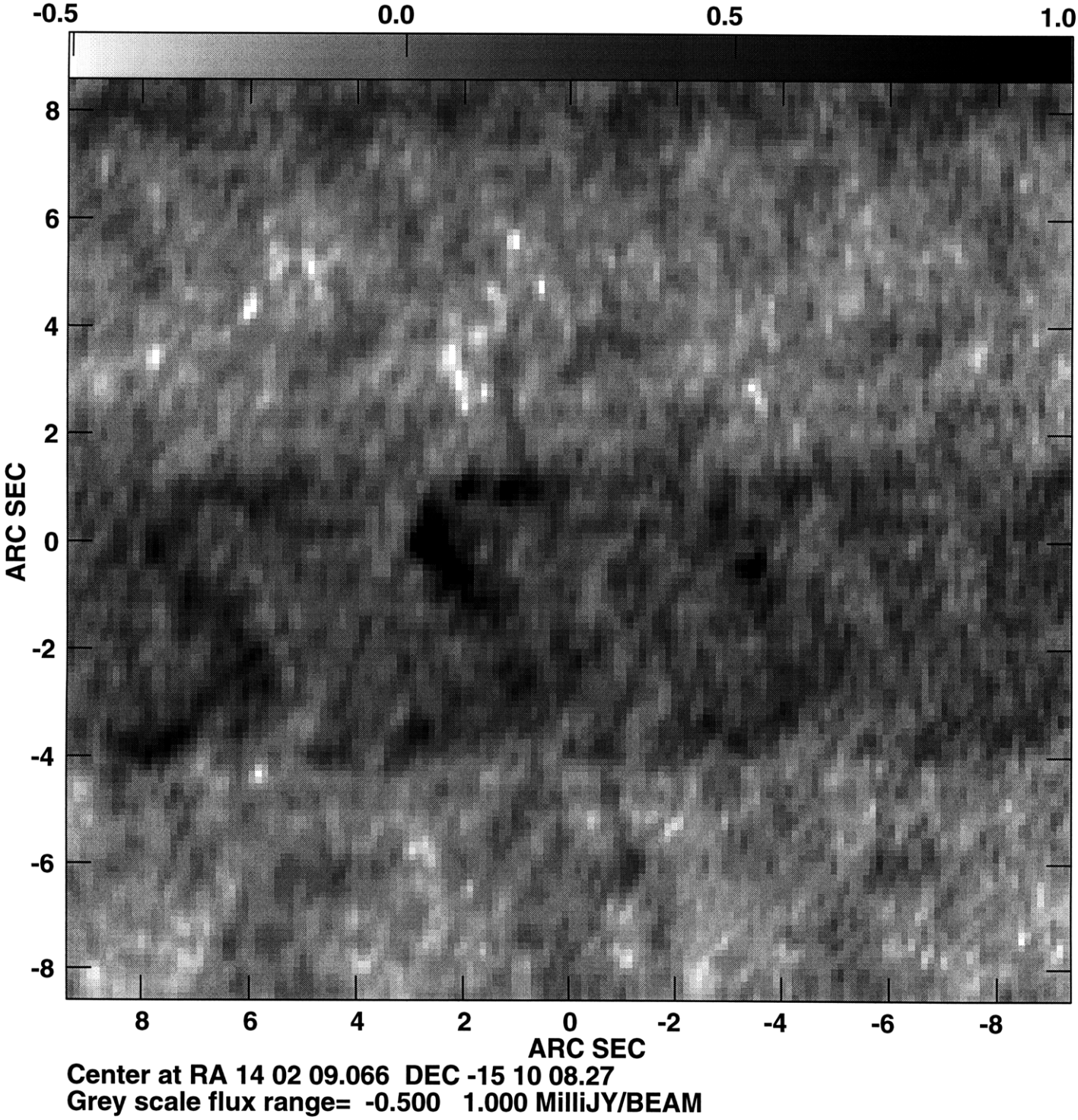
Plot file version 1 created 23-JUL-1996 07:05:18
14021510 IPOL 8439.900 MHZ 14021510H.ICLN.1
-0.5
0.0
0.5
1.0
8
6
4
2
0
-2
-4
-6
-8
ARC SEC
8
6
4
2
0
-2
-4
-6
-8
ARC SEC
Center at RA 14 02 09.066 DEC -15 10 08.27
Grey scale flux range= -0.500 1.000 MilliJY/BEAM

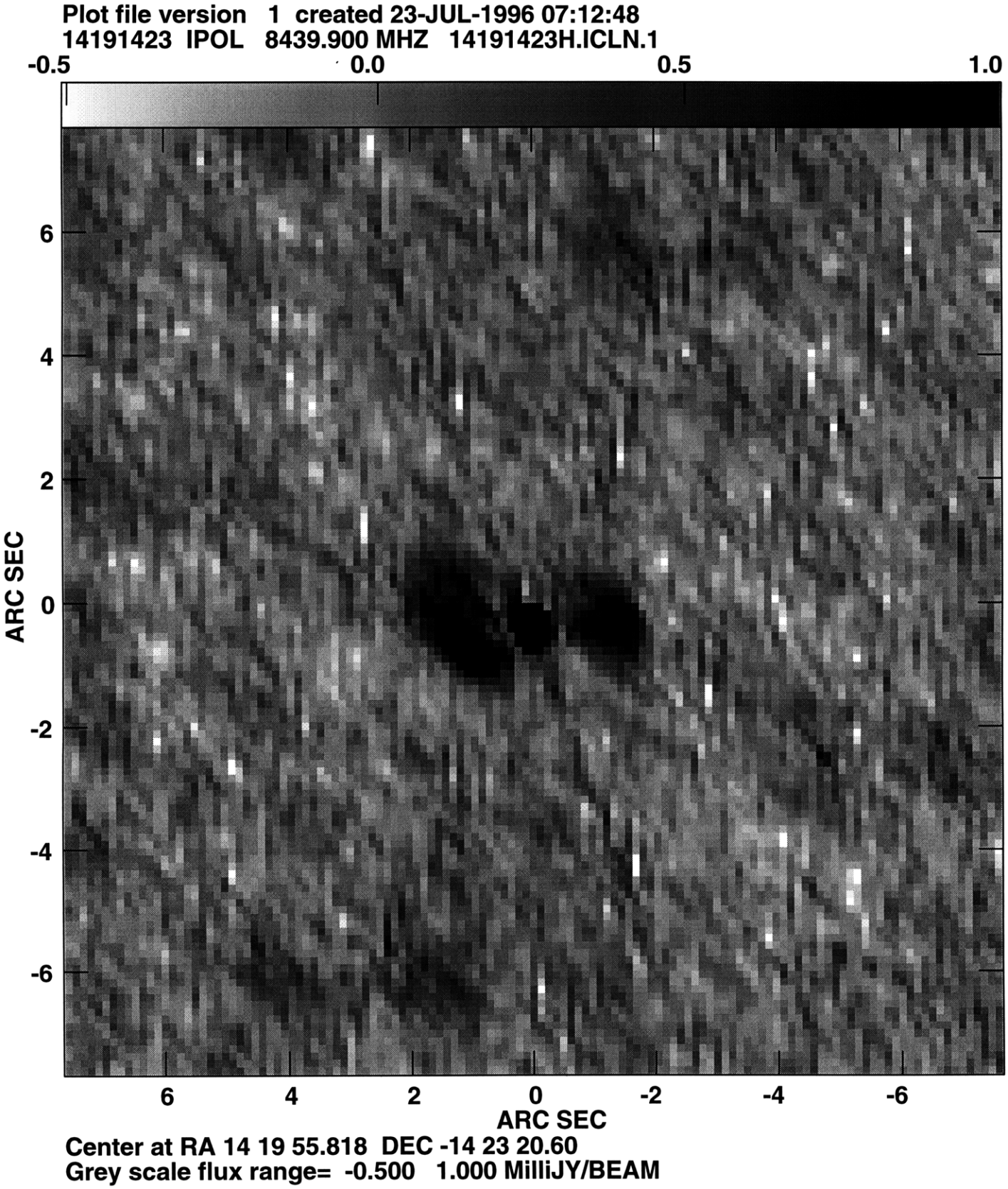
Plot file version 1 created 23-JUL-1996 07:12:48
14191423 IPOL 8439.900 MHZ 14191423H.ICLN.1
-0.5
0.0
0.5
1.0
6
4
2
0
-2
-4
-6
ARC SEC
6
4
2
0
-2
-4
-6
ARC SEC
Center at RA 14 19 55.818 DEC -14 23 20.60
Grey scale flux range= -0.500 1.000 MilliJY/BEAM

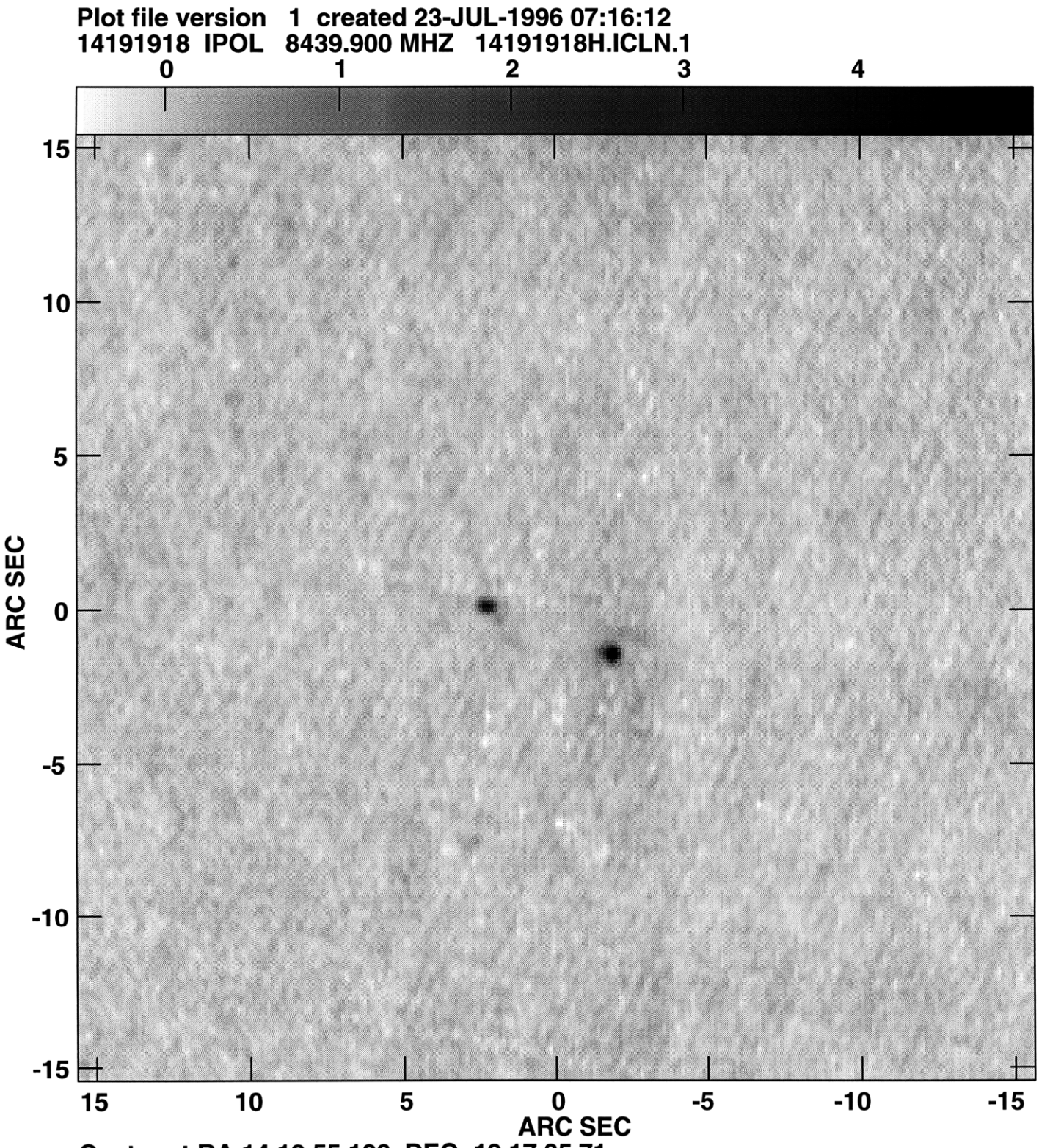
Plot file version 1 created 23-JUL-1996 07:16:12
14191918 IPOL 8439.900 MHZ 14191918H.ICLN.1
0
1
2
3
4
15
10
5
0
-5
-10
-15
ARC SEC
15
10
5
0
-5
-10
-15
ARC SEC
Center at RA 14 19 55.126 DEC -19 17 35.71
Grey scale flux range= -0.500 5.000 MilliJY/BEAM

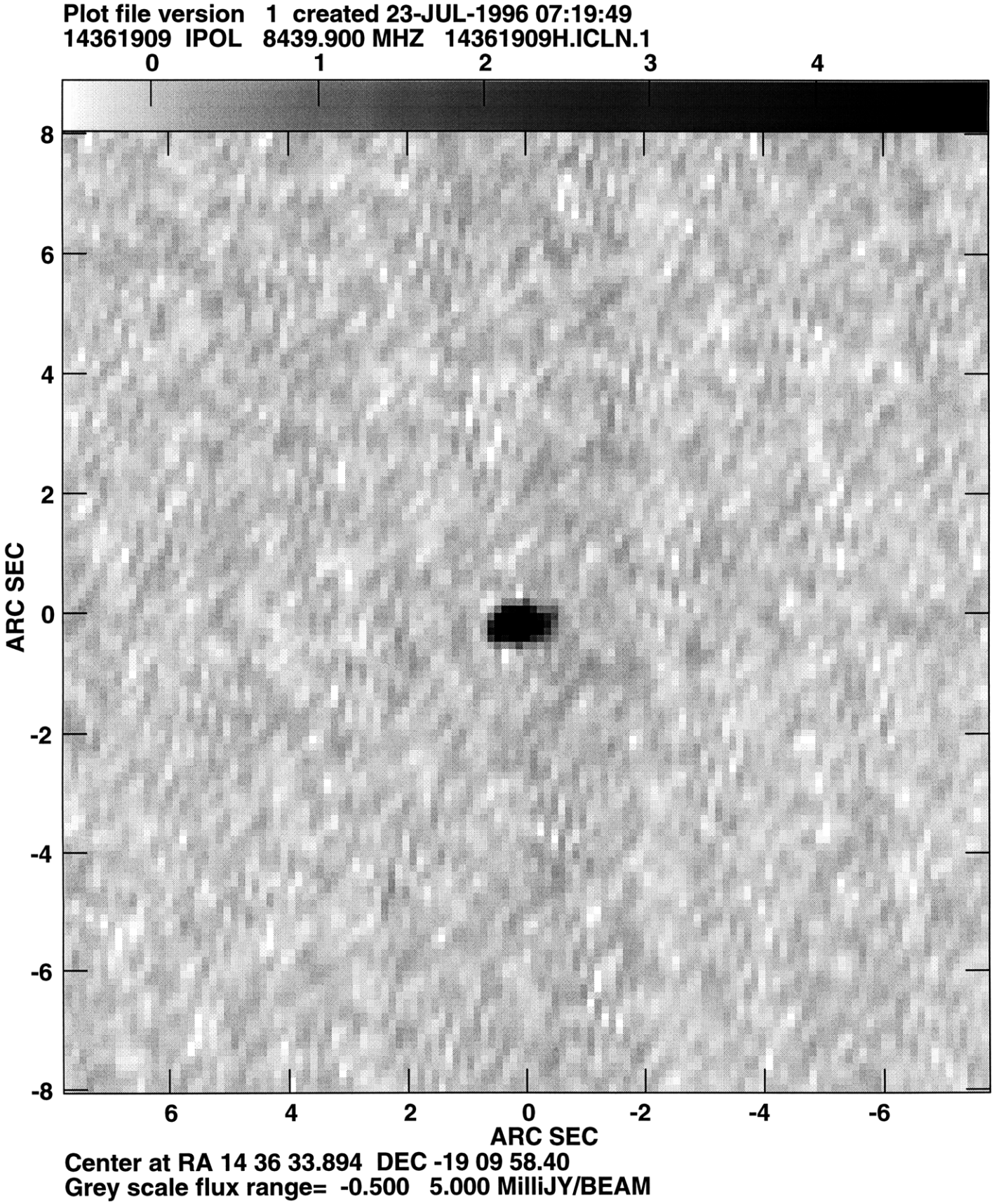
Plot file version 1 created 23-JUL-1996 07:19:49
14361909 IPOL 8439.900 MHZ 14361909H.ICLN.1
0
1
2
3
4
8
6
4
2
0
-2
-4
-6
-8
ARC SEC
6
4
2
0
-2
-4
-6
ARC SEC
Center at RA 14 36 33.894 DEC -19 09 58.40
Grey scale flux range= -0.500 5.000 MilliJY/BEAM

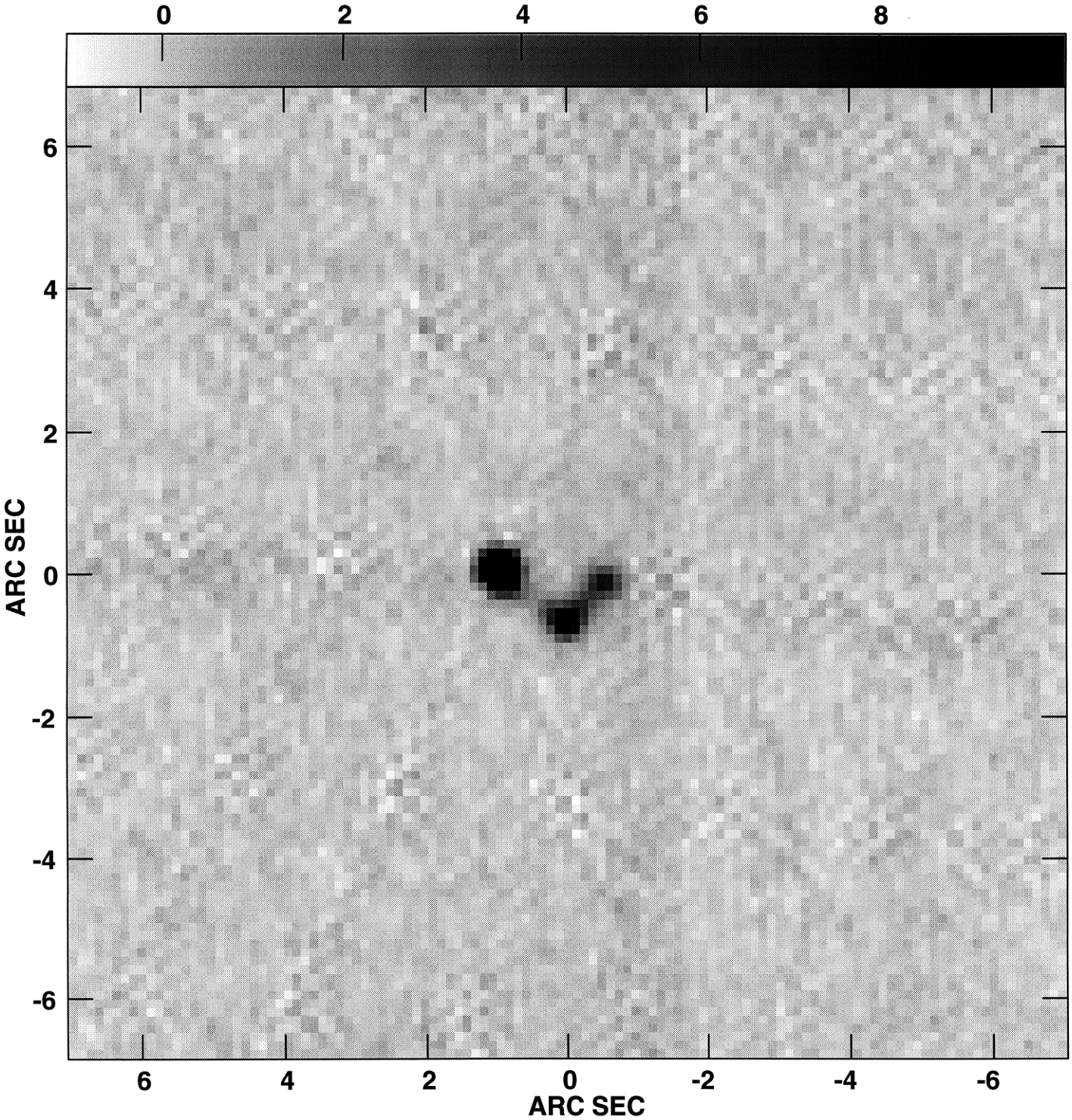
Plot file version 1 created 23-JUL-1996 07:22:46
14481122 IPOL 8439.900 MHZ 14481122H.ICLN.1
0
2
4
6
8
6
4
2
0
-2
-4
-6
ARC SEC
6
4
2
0
-2
-4
-6
ARC SEC
Center at RA 14 48 51.106 DEC -11 22 15.81
Grey scale flux range= -1.0 10.0 MilliJY/BEAM

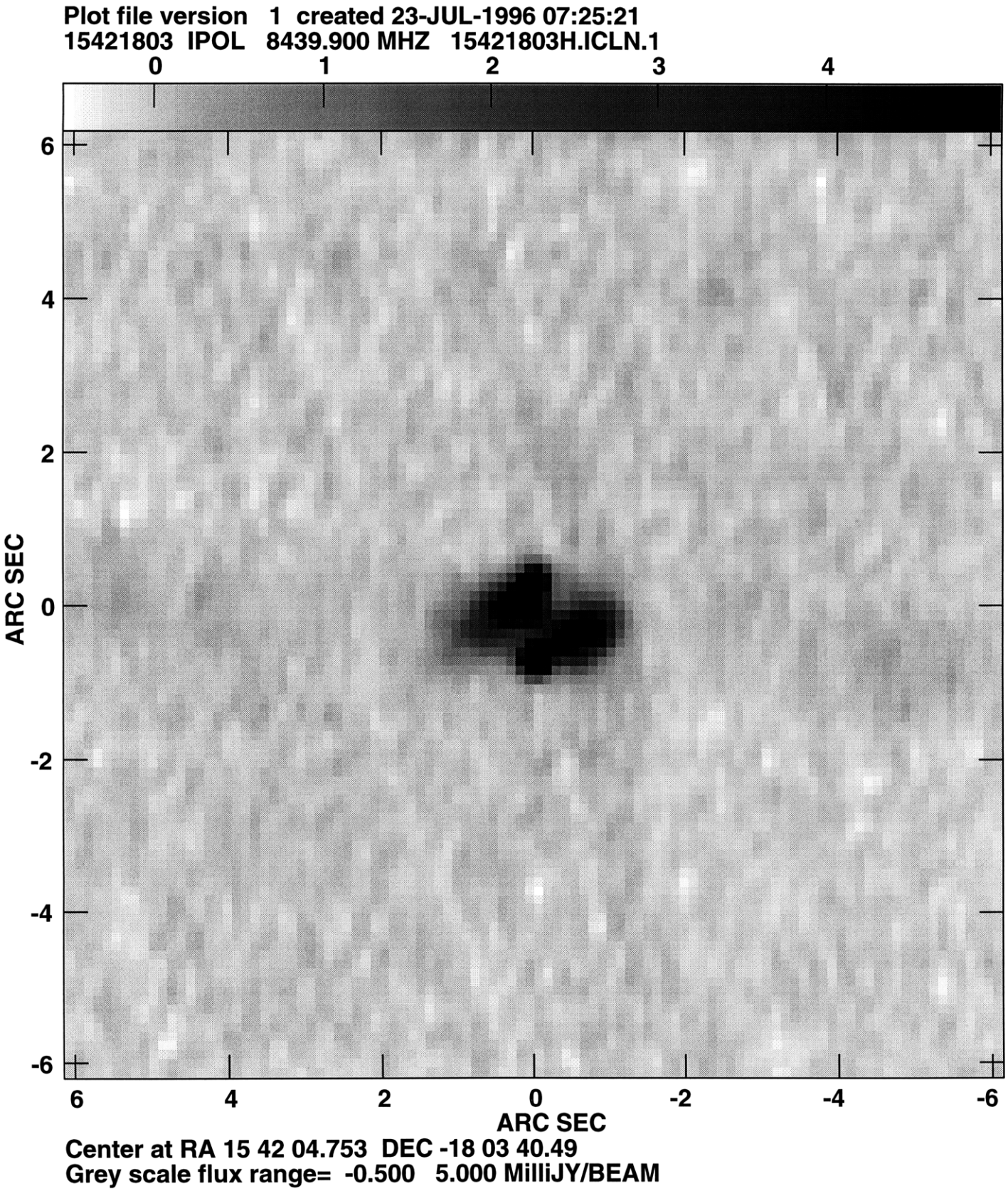
Plot file version 1 created 23-JUL-1996 07:25:21
15421803 IPOL 8439.900 MHZ 15421803H.ICLN.1
0
1
2
3
4
6
4
2
0
-2
-4
-6
ARC SEC
6
4
2
0
-2
-4
-6
ARC SEC
Center at RA 15 42 04.753 DEC -18 03 40.49
Grey scale flux range= -0.500 5.000 MilliJY/BEAM

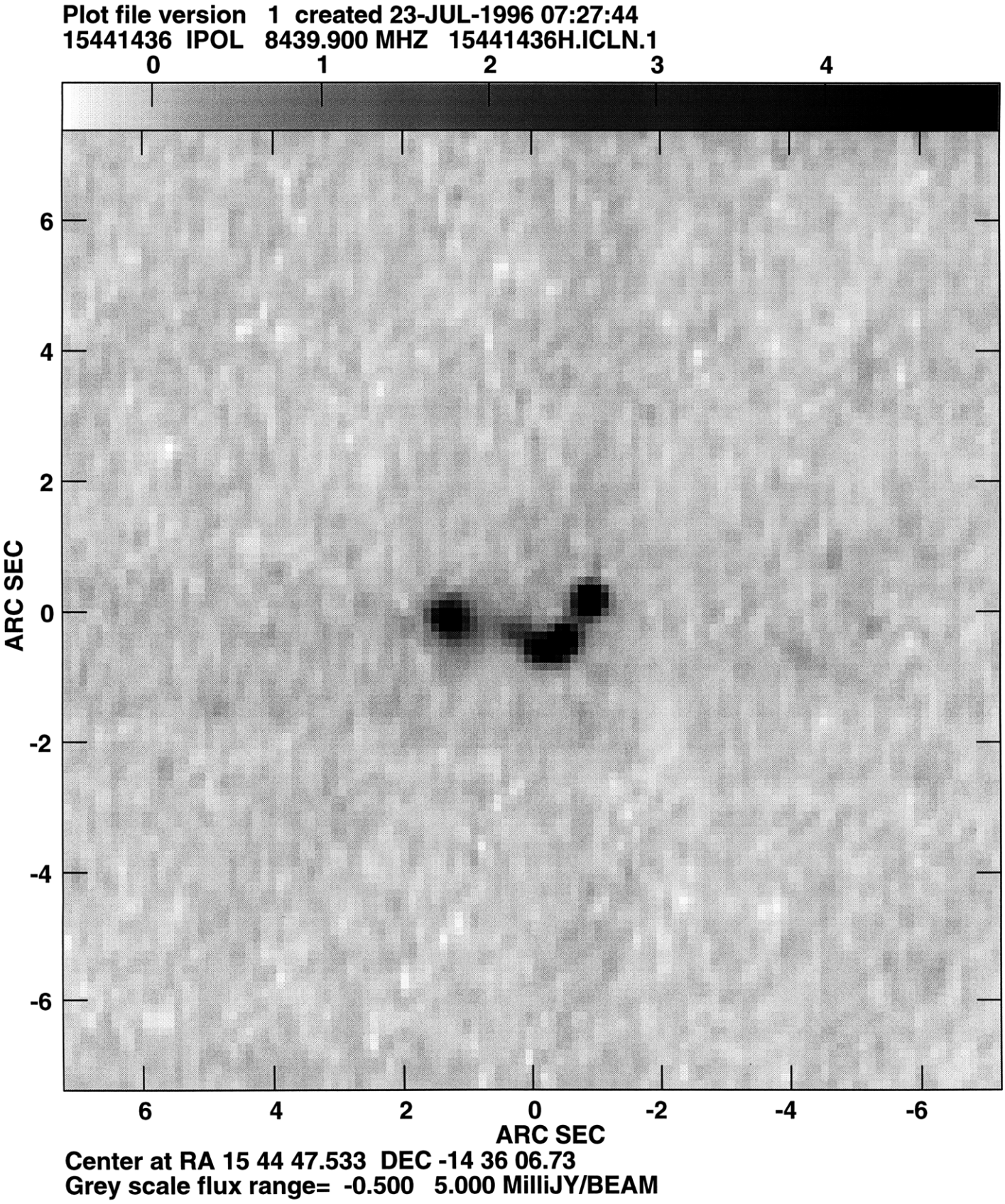
Plot file version 1 created 23-JUL-1996 07:27:44
15441436 IPOL 8439.900 MHZ 15441436H.ICLN.1
0
1
2
3
4
6
4
2
0
-2
-4
-6
ARC SEC
6
4
2
0
-2
-4
-6
ARC SEC
Center at RA 15 44 47.533 DEC -14 36 06.73
Grey scale flux range= -0.500 5.000 MilliJY/BEAM

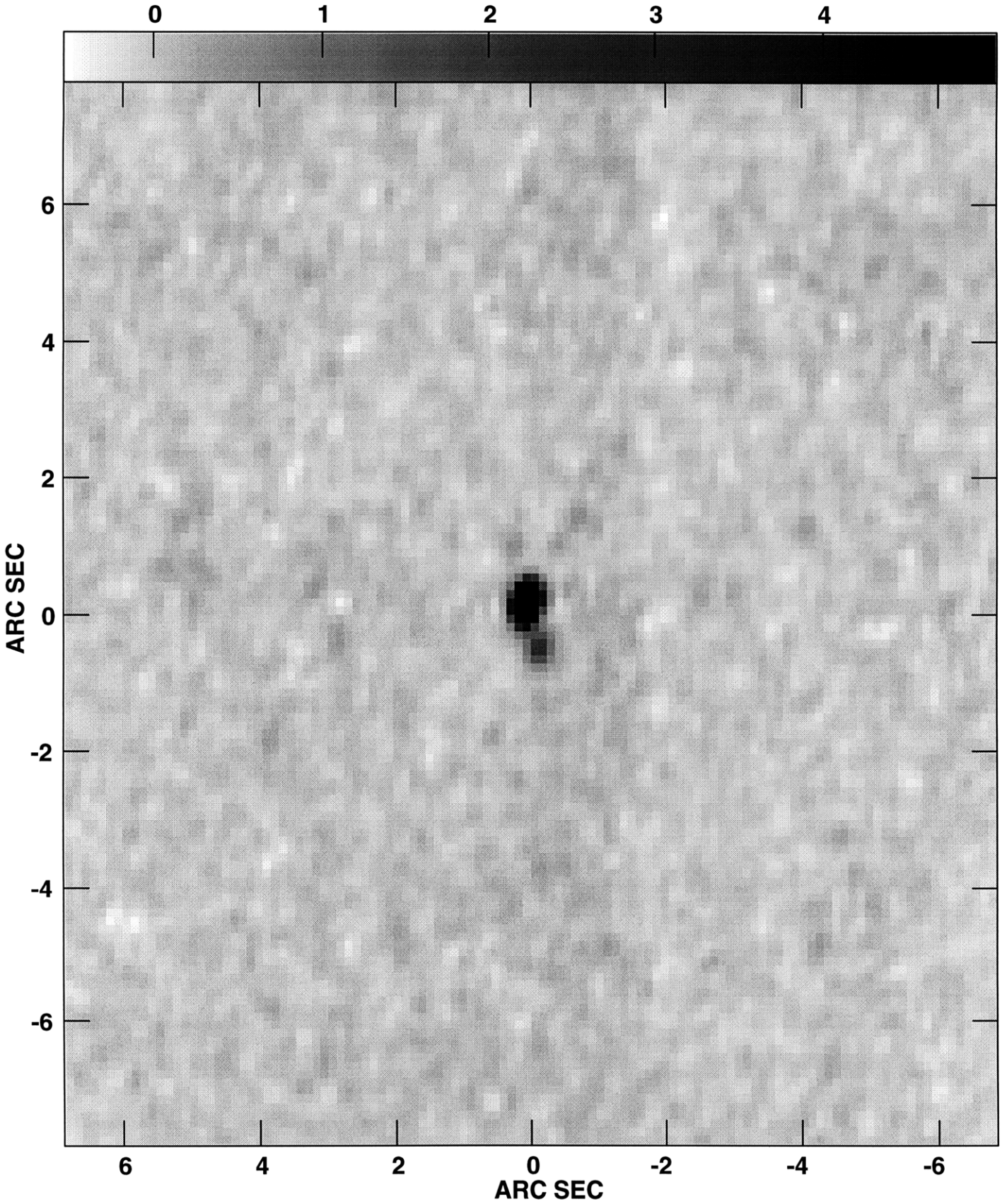
Plot file version 1 created 23-JUL-1996 07:31:04
15471416 IPOL 8439.900 MHZ 15471416H.ICLN.1
0
1
2
3
4
6
4
2
0
-2
-4
-6
ARC SEC
6
4
2
0
-2
-4
-6
ARC SEC
Center at RA 15 47 52.723 DEC -14 16 13.33
Grey scale flux range= -0.500 5.000 MilliJY/BEAM

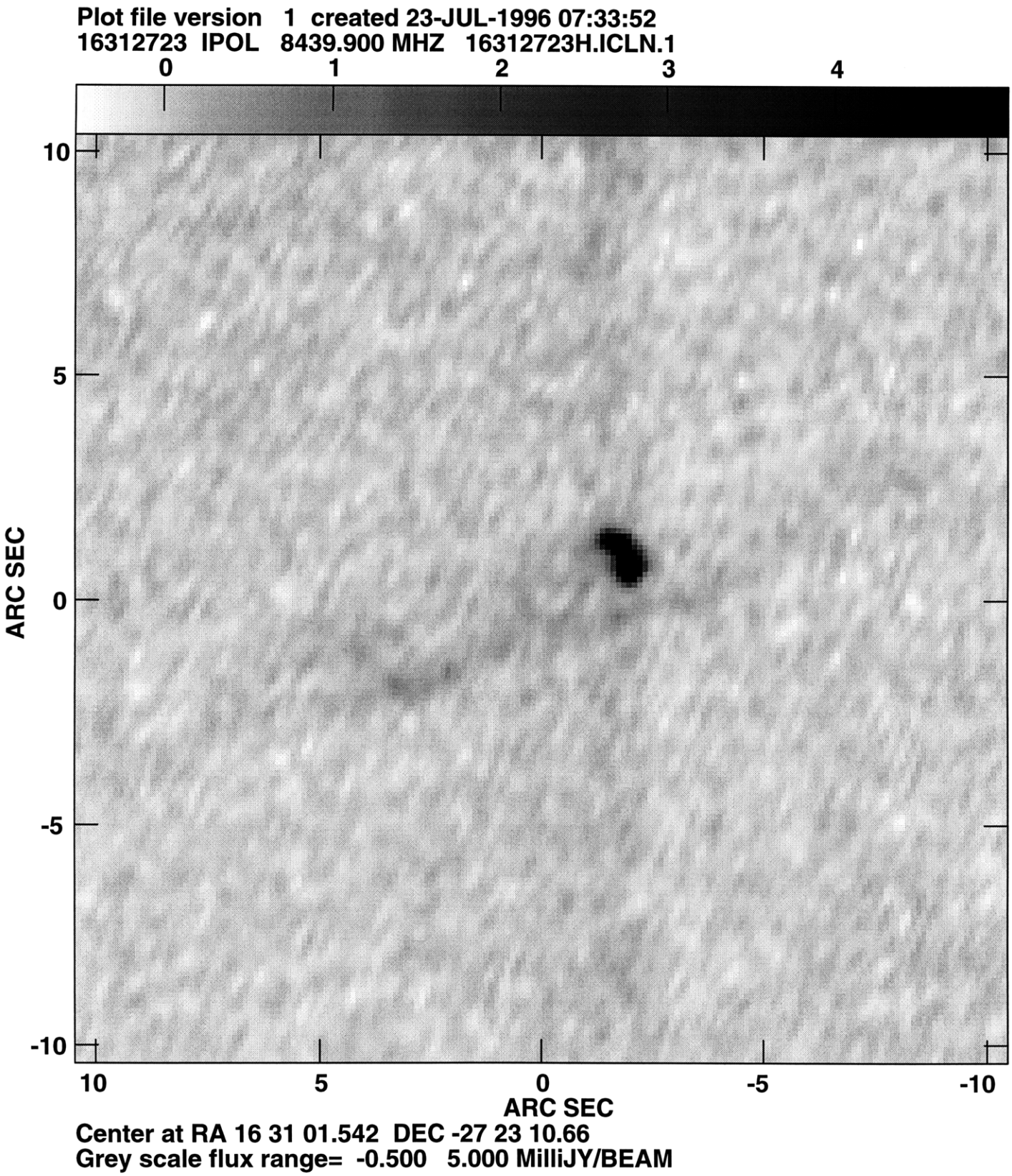
Plot file version 1 created 23-JUL-1996 07:33:52
16312723 IPOL 8439.900 MHZ 16312723H.ICLN.1
0
1
2
3
4
10
5
0
-5
-10
ARC SEC
10
5
0
-5
-10
ARC SEC
Center at RA 16 31 01.542 DEC -27 23 10.66
Grey scale flux range= -0.500 5.000 MilliJY/BEAM

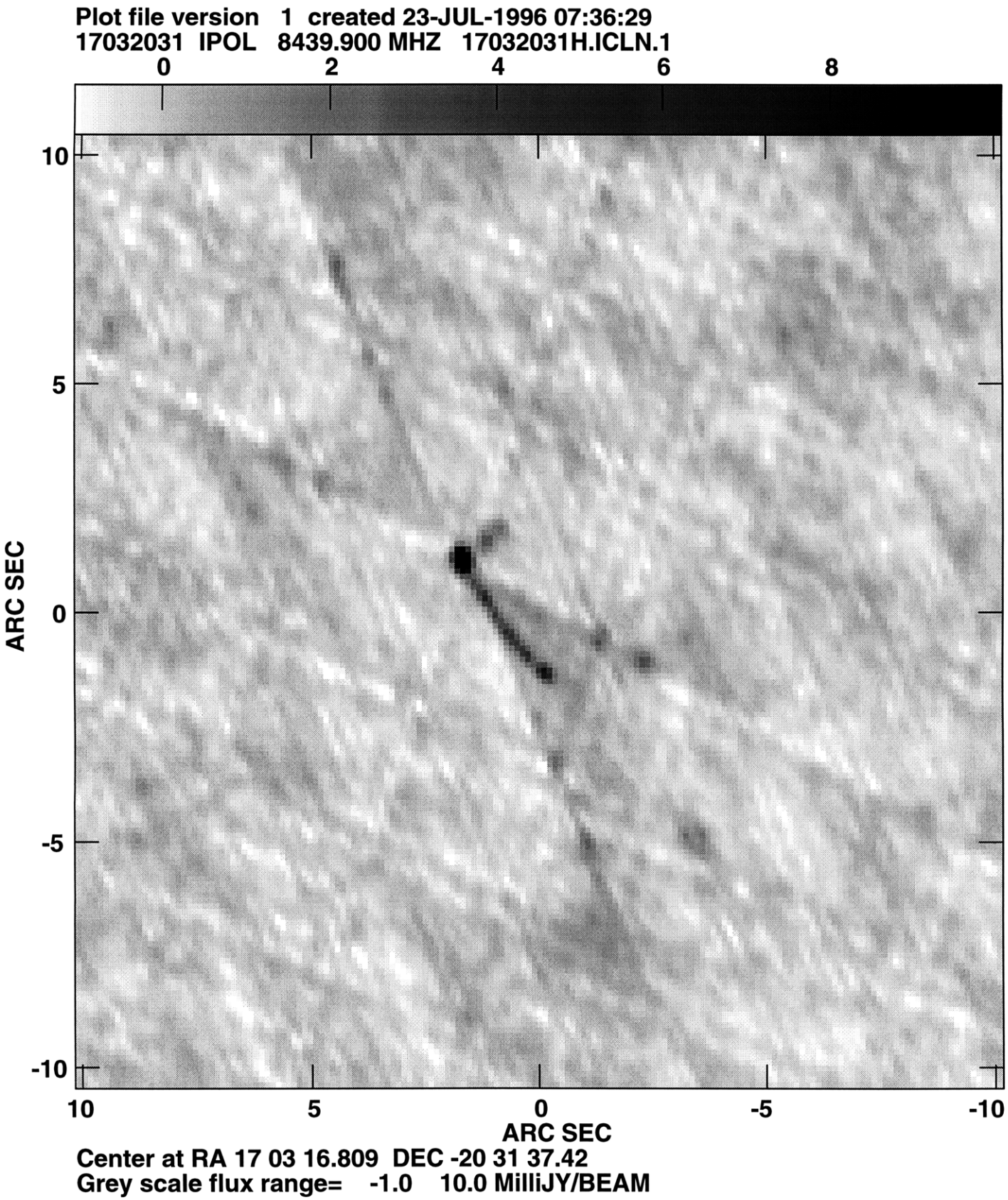
Plot file version 1 created 23-JUL-1996 07:36:29
17032031 IPOL 8439.900 MHZ 17032031H.ICLN.1
0
2
4
6
8
10
5
0
-5
-10
ARC SEC
10
5
0
-5
-10
ARC SEC
Center at RA 17 03 16.809 DEC -20 31 37.42
Grey scale flux range= -1.0 10.0 MilliJY/BEAM

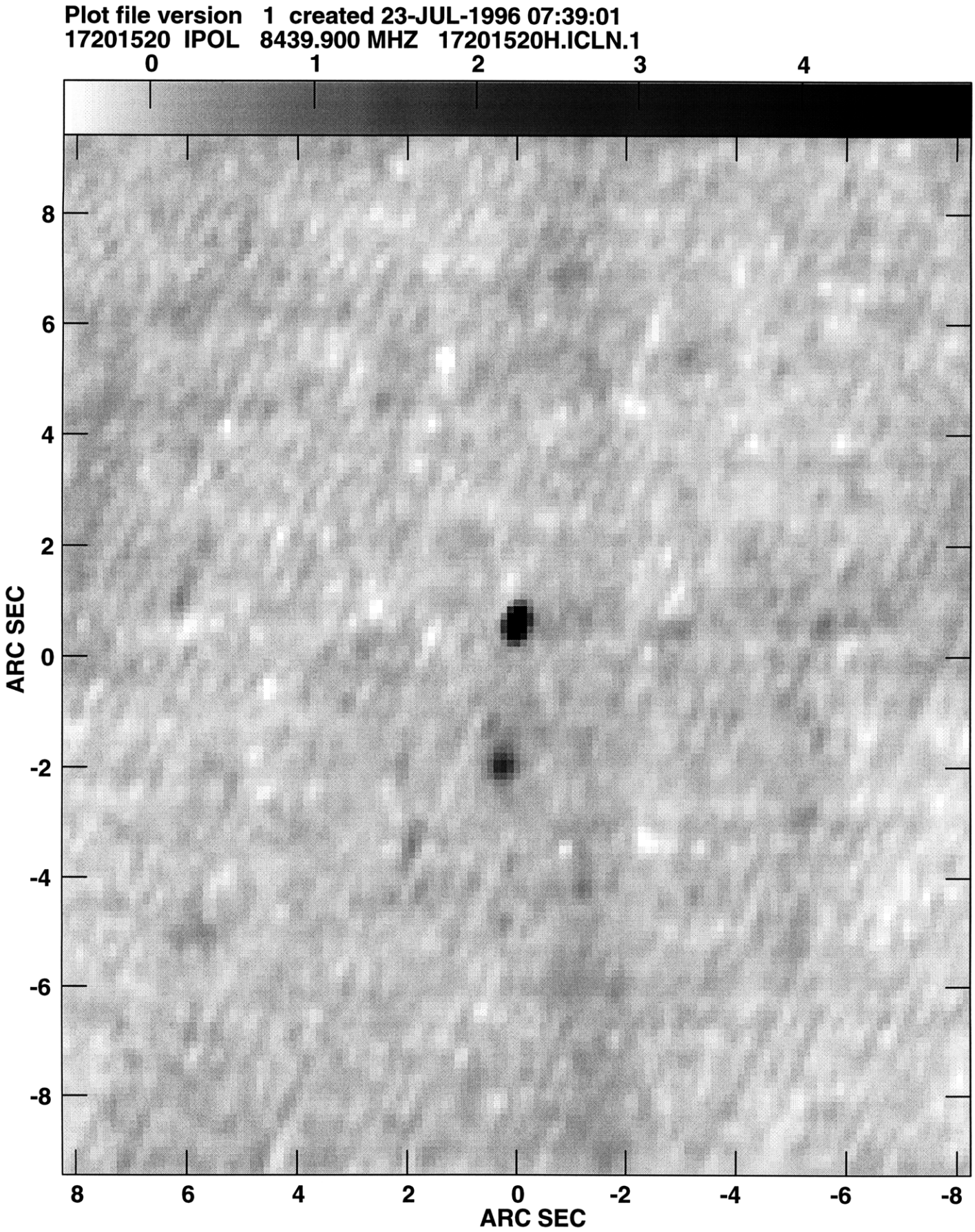
Plot file version 1 created 23-JUL-1996 07:39:01
17201520 IPOL 8439.900 MHZ 17201520H.ICLN.1
0
1
2
3
4
8
6
4
2
0
-2
-4
-6
-8
ARC SEC
8
6
4
2
0
-2
-4
-6
-8
ARC SEC
Center at RA 17 20 44.582 DEC -15 21 27.14
Grey scale flux range= -0.500 5.000 MilliJY/BEAM

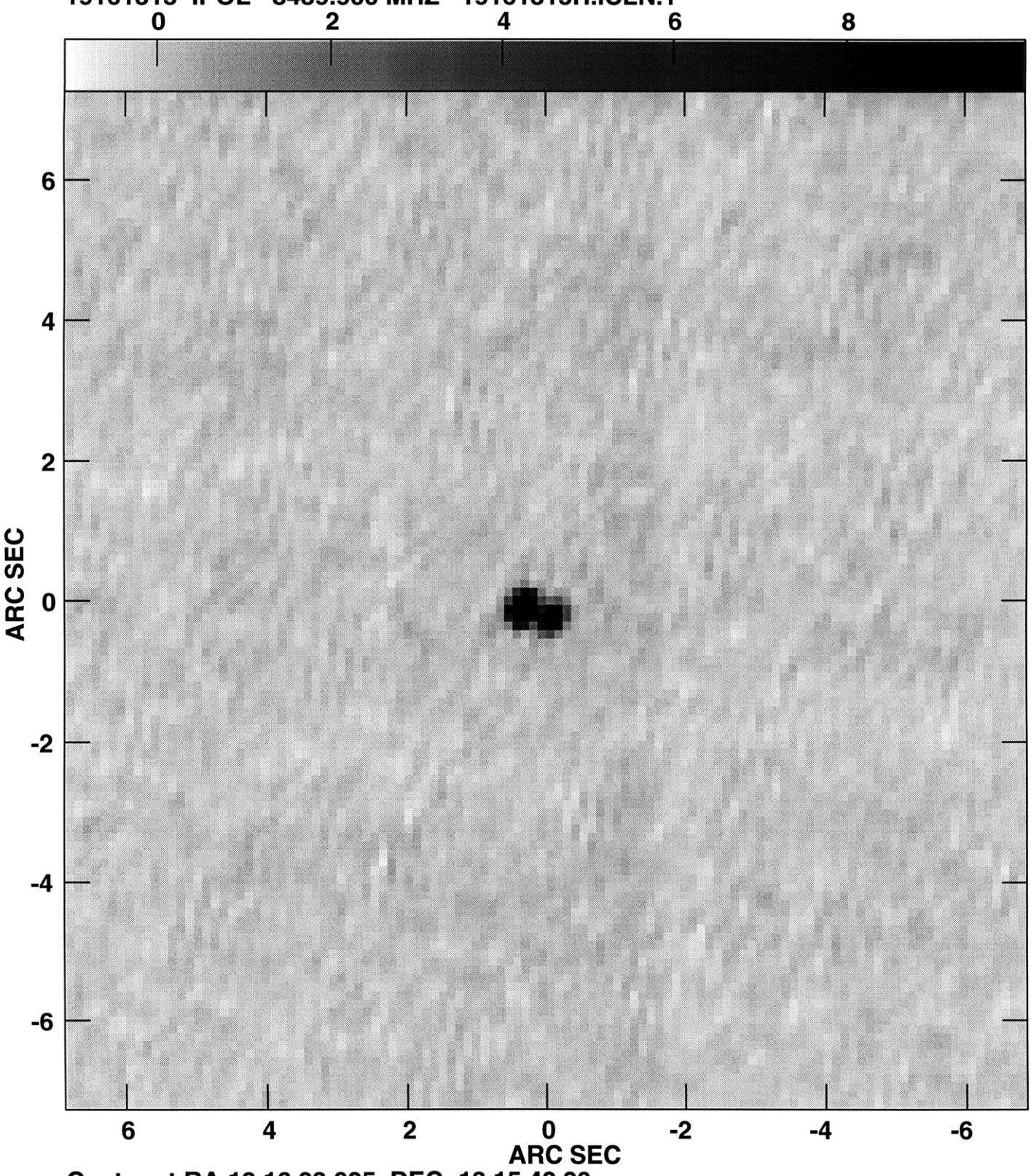
Plot file version 1 created 23-JUL-1996 07:41:46
19161315 IPOL 8439.900 MHZ 19161315H.ICLN.1
0
2
4
6
8
6
4
2
0
-2
-4
-6
ARC SEC
6
4
2
0
-2
-4
-6
ARC SEC
Center at RA 19 16 23.025 DEC -13 15 42.90
Grey scale flux range= -1.0 10.0 MilliJY/BEAM

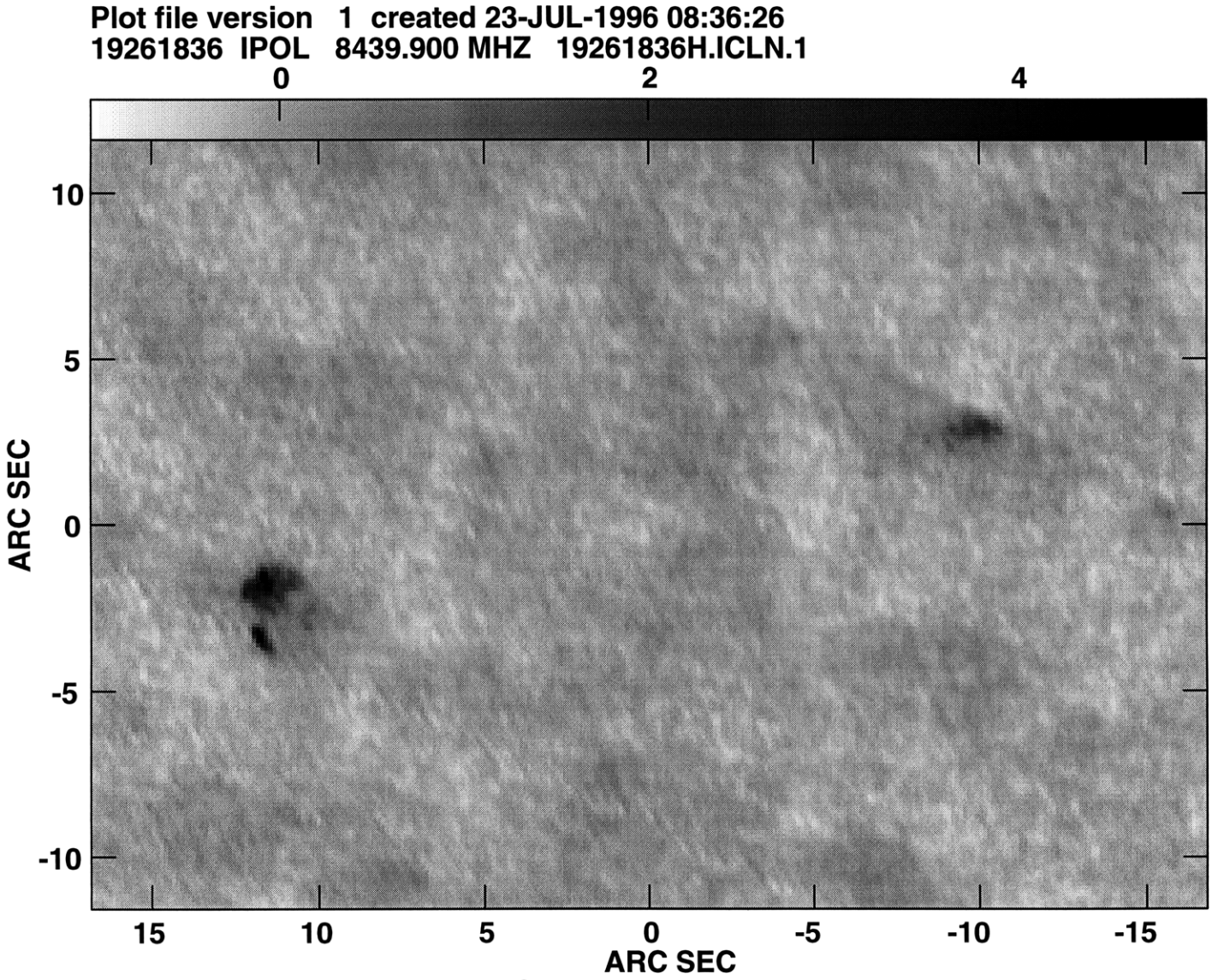
Plot file version 1 created 23-JUL-1996 08:36:26
19261836 IPOL 8439.900 MHZ 19261836H.ICLN.1
0
2
4
10
5
0
-5
-10
ARC SEC
15
10
5
0
-5
-10
-15
ARC SEC
Center at RA 19 26 00.504 DEC -18 36 37.17
Grey scale flux range= -1.000 5.000 MilliJY/BEAM

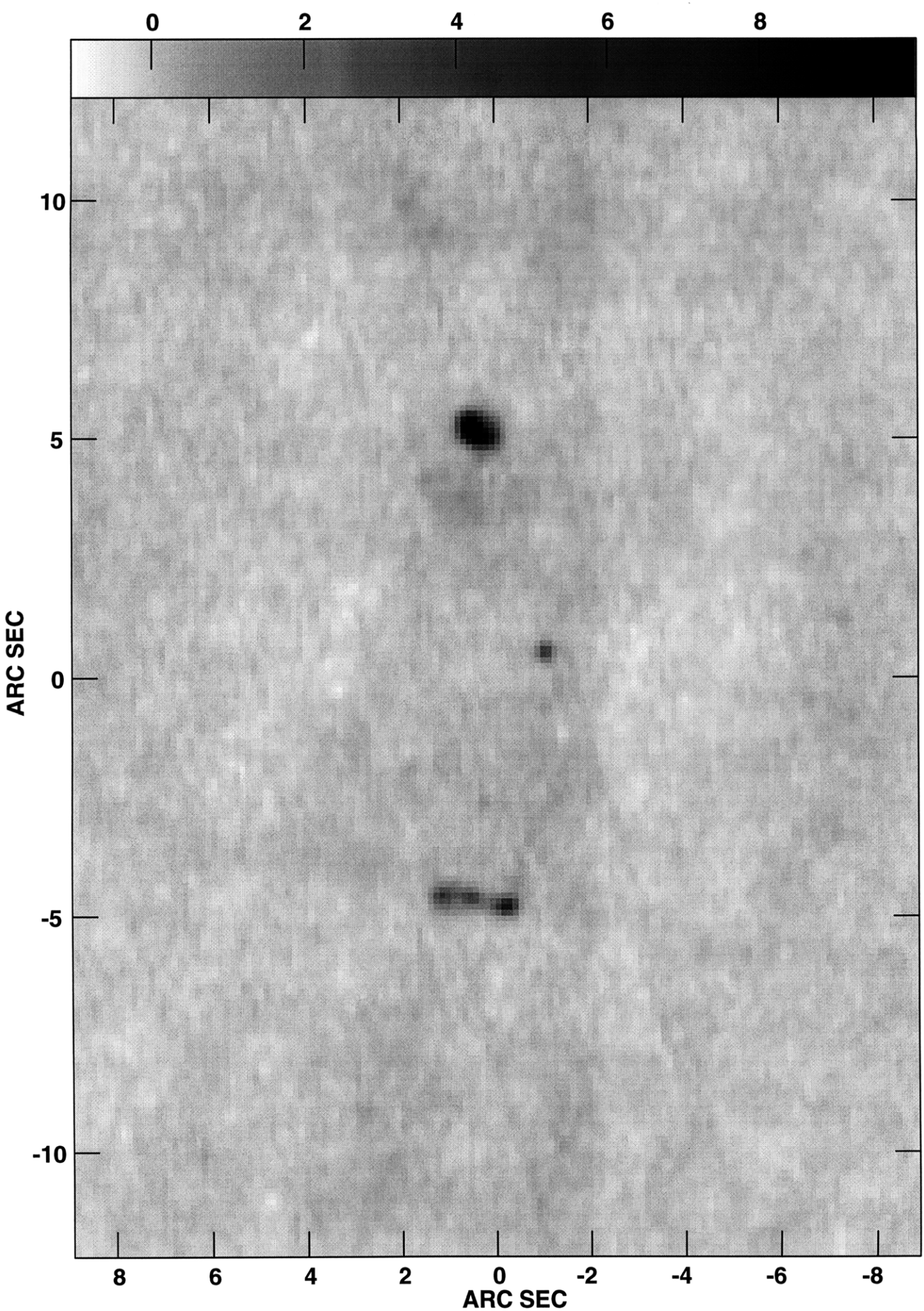

Center at RA 19 27 38.985 DEC -14 55 26.98
Grey scale flux range= -1.0 10.0 MilliJY/BEAM

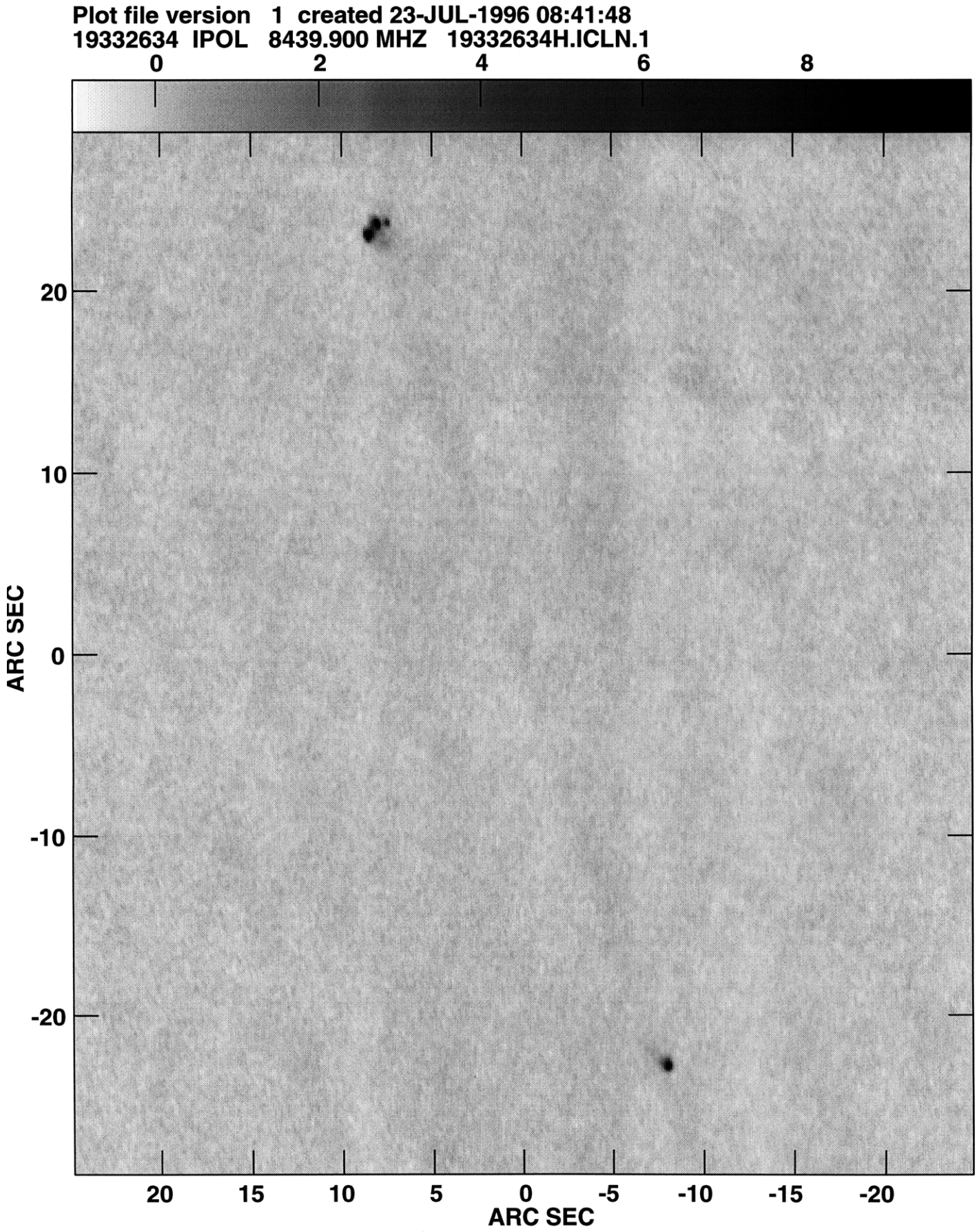
Plot file version 1 created 23-JUL-1996 08:41:48
19332634 IPOL 8439.900 MHZ 19332634H.ICLN.1
0
2
4
6
8
20
10
0
-10
-20
ARC SEC
20
15
10
5
0
-5
-10
-15
-20
ARC SEC
Center at RA 19 33 47.889 DEC -26 33 38.08
Grey scale flux range= -1.0 10.0 MilliJY/BEAM

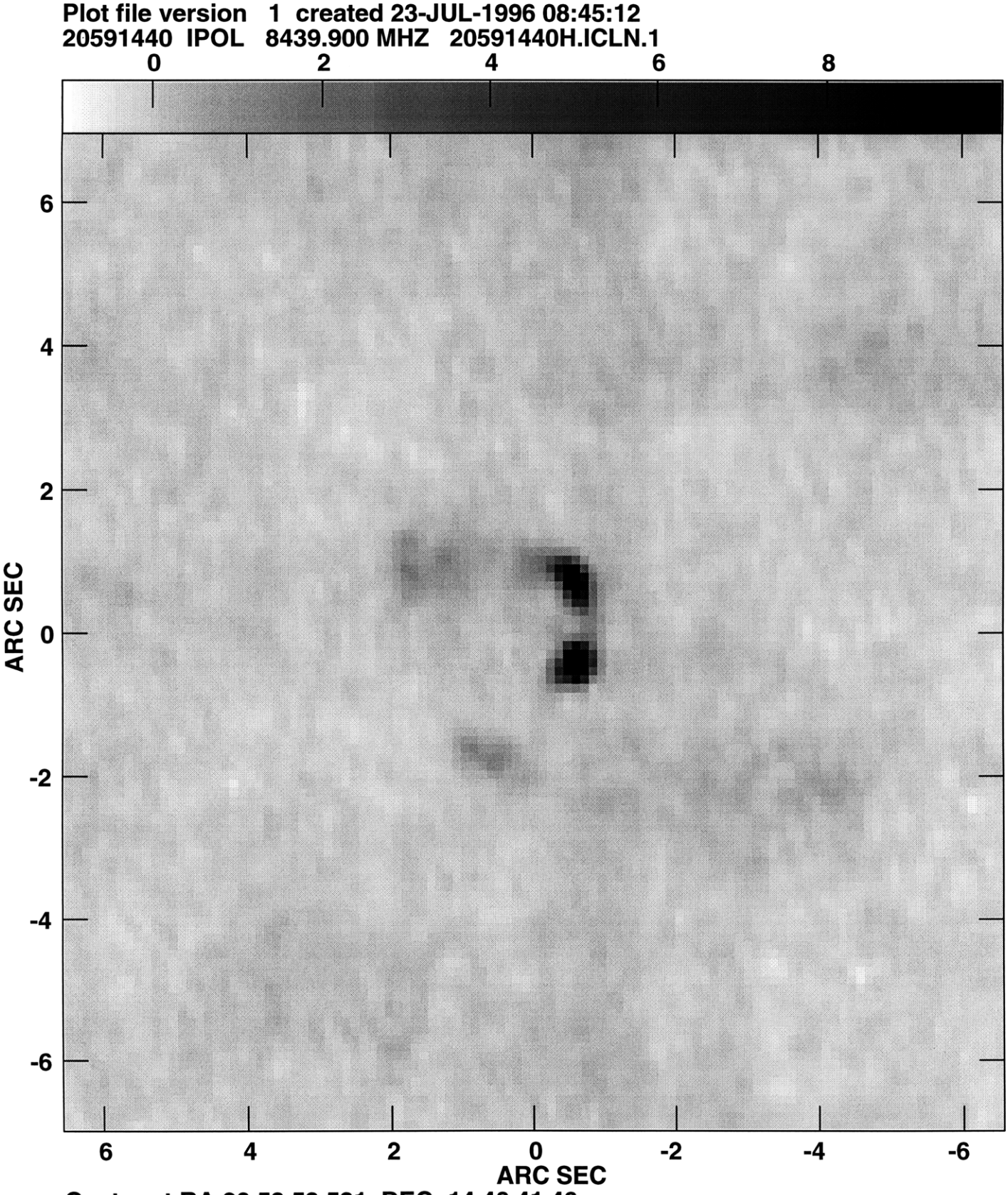
Plot file version 1 created 23-JUL-1996 08:45:12
20591440 IPOL 8439.900 MHZ 20591440H.ICLN.1
0
2
4
6
8
6
4
2
0
-2
-4
-6
ARC SEC
6
4
2
0
-2
-4
-6
ARC SEC
Center at RA 20 59 59.591 DEC -14 40 41.46
Grey scale flux range= -1.0 10.0 MilliJY/BEAM

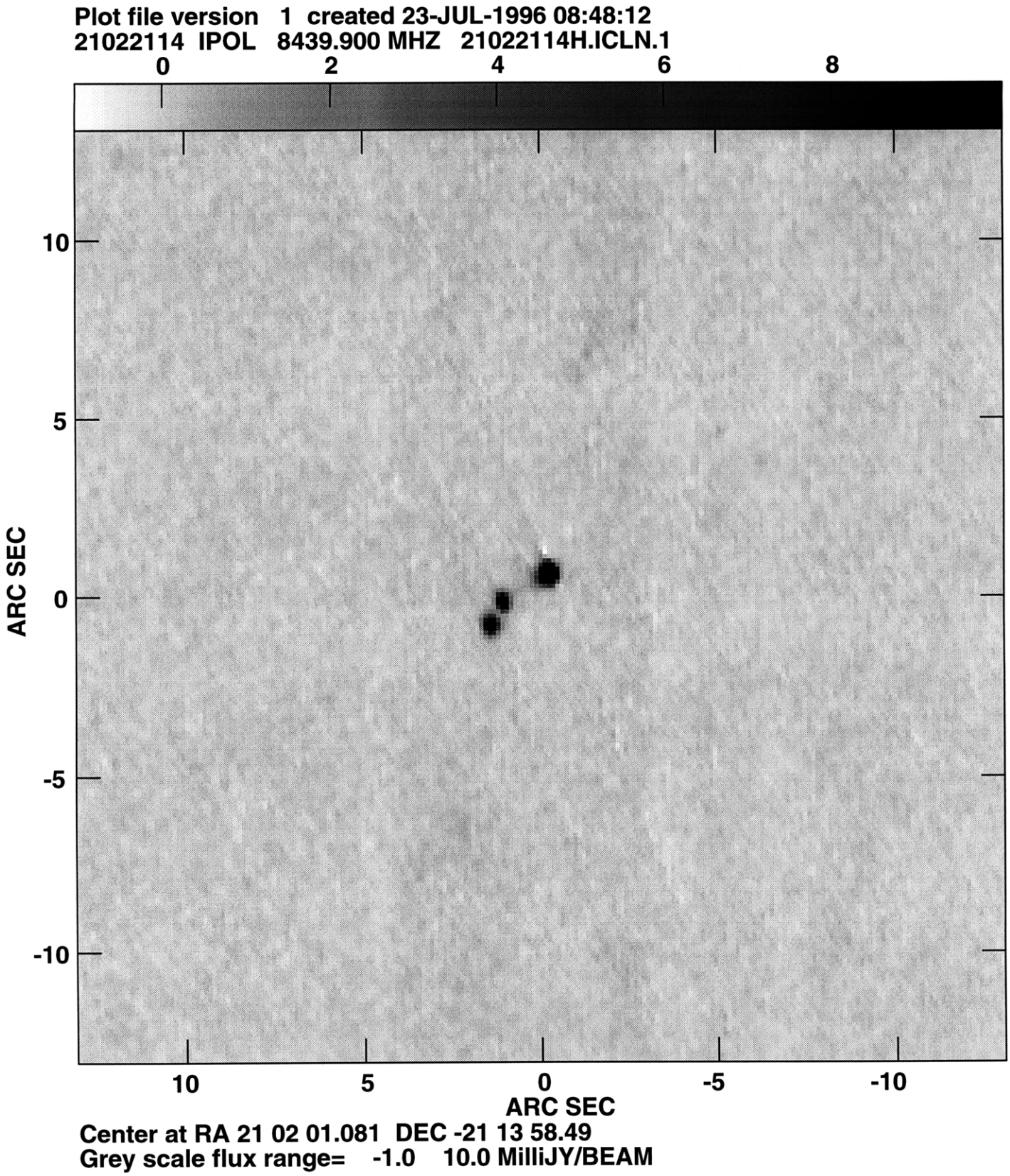
Plot file version 1 created 23-JUL-1996 08:48:12
21022114 IPOL 8439.900 MHZ 21022114H.ICLN.1
0
2
4
6
8
10
5
0
-5
-10
ARC SEC
10
5
0
-5
-10
ARC SEC
Center at RA 21 02 01.081 DEC -21 13 58.49
Grey scale flux range= -1.0 10.0 MilliJY/BEAM

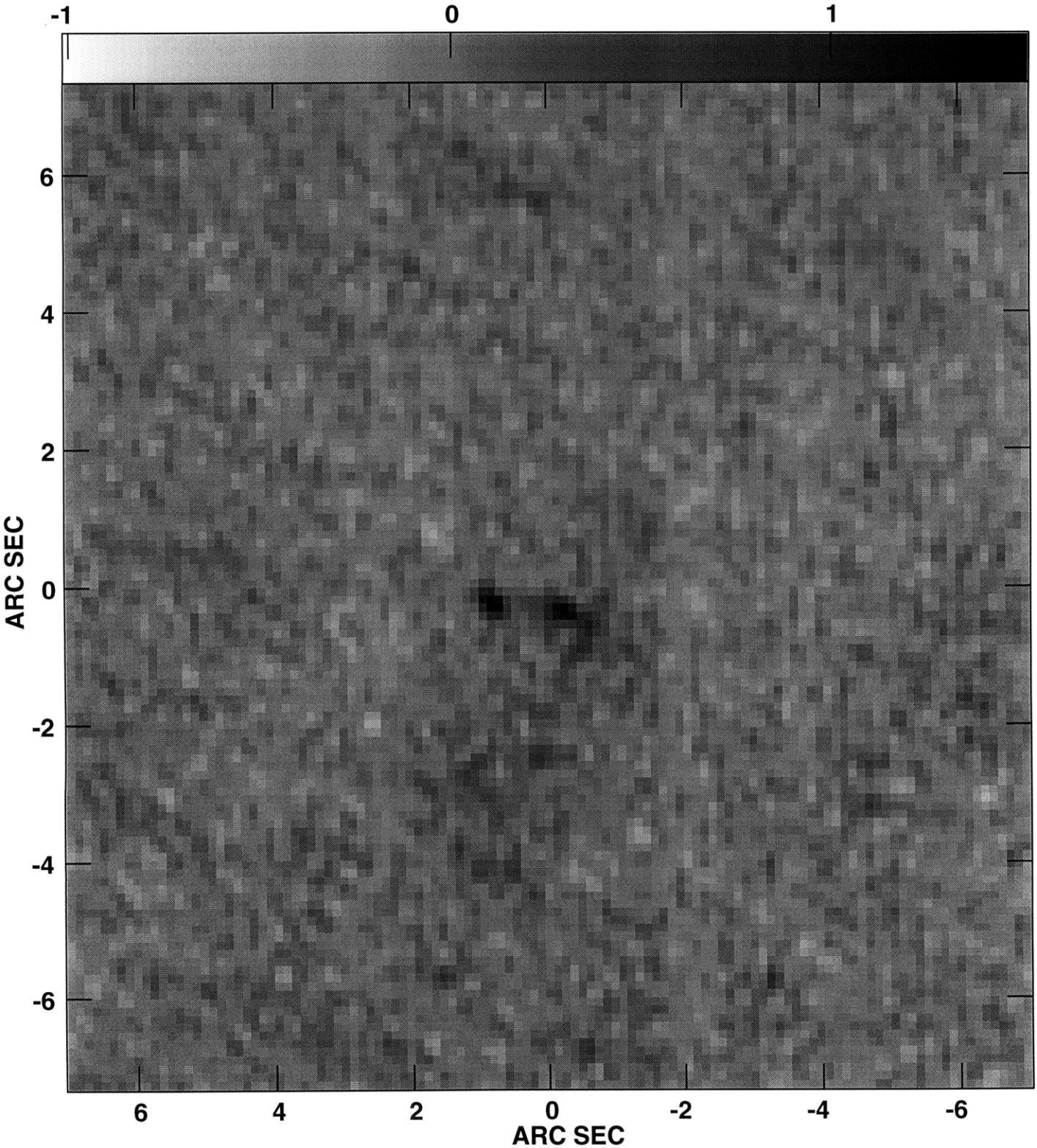
Plot file version 1 created 23-JUL-1996 08:53:20
21271211 IPOL 8439.900 MHZ 21271211H.ICLN.1
-1
0
1
6
4
2
0
-2
-4
-6
ARC SEC
6
4
2
0
-2
-4
-6
ARC SEC
Center at RA 21 26 57.169 DEC -12 12 49.20
Grey scale flux range= -1.000 1.500 MilliJY/BEAM

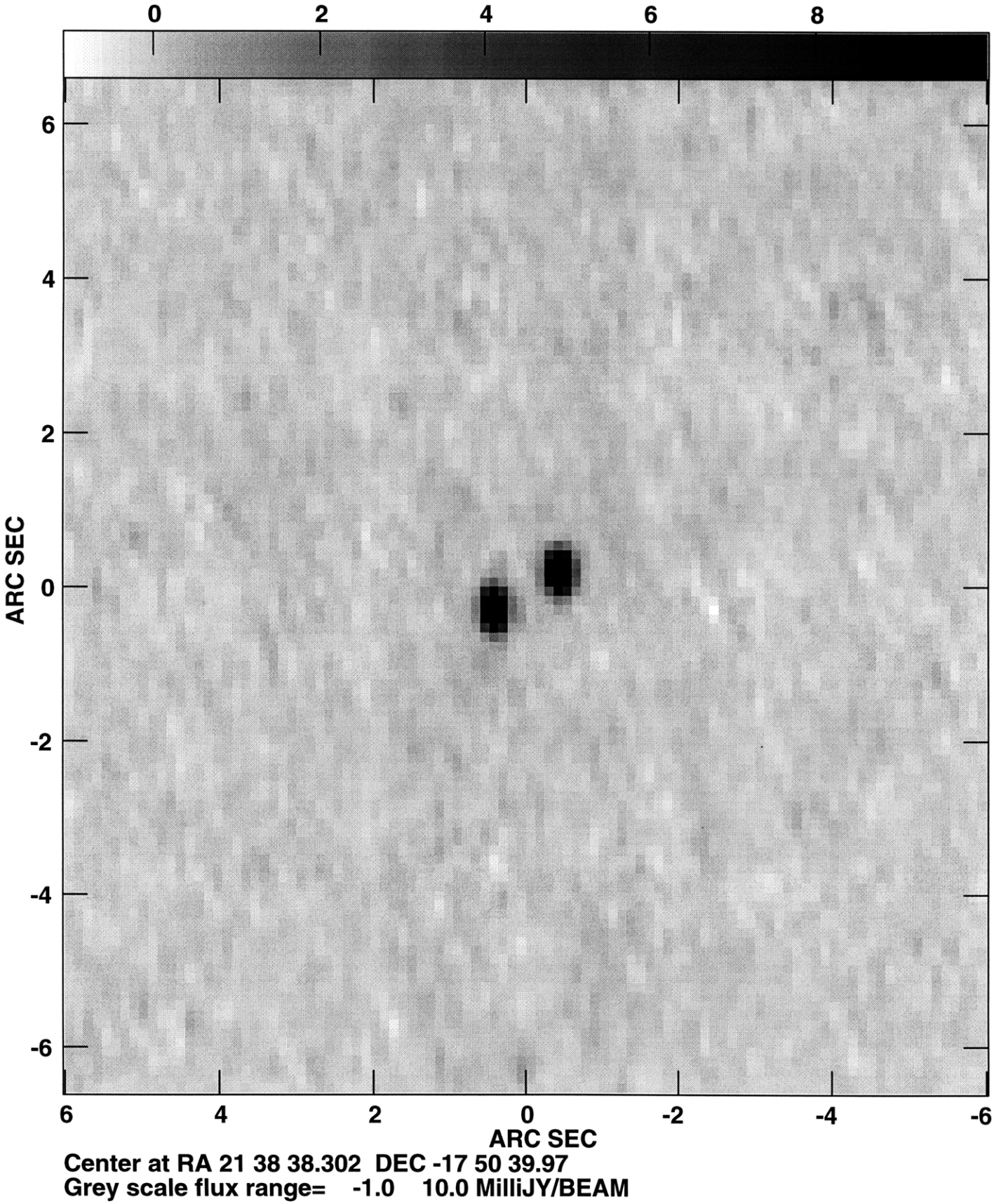
Plot file version 1 created 23-JUL-1996 08:56:09
21381750 IPOL 8439.900 MHZ 21381750H.ICLN.1
0
2
4
6
8
6
4
2
0
-2
-4
-6
ARC SEC
6
4
2
0
-2
-4
-6
ARC SEC
Center at RA 21 38 38.302 DEC -17 50 39.97
Grey scale flux range= -1.0 10.0 MilliJY/BEAM

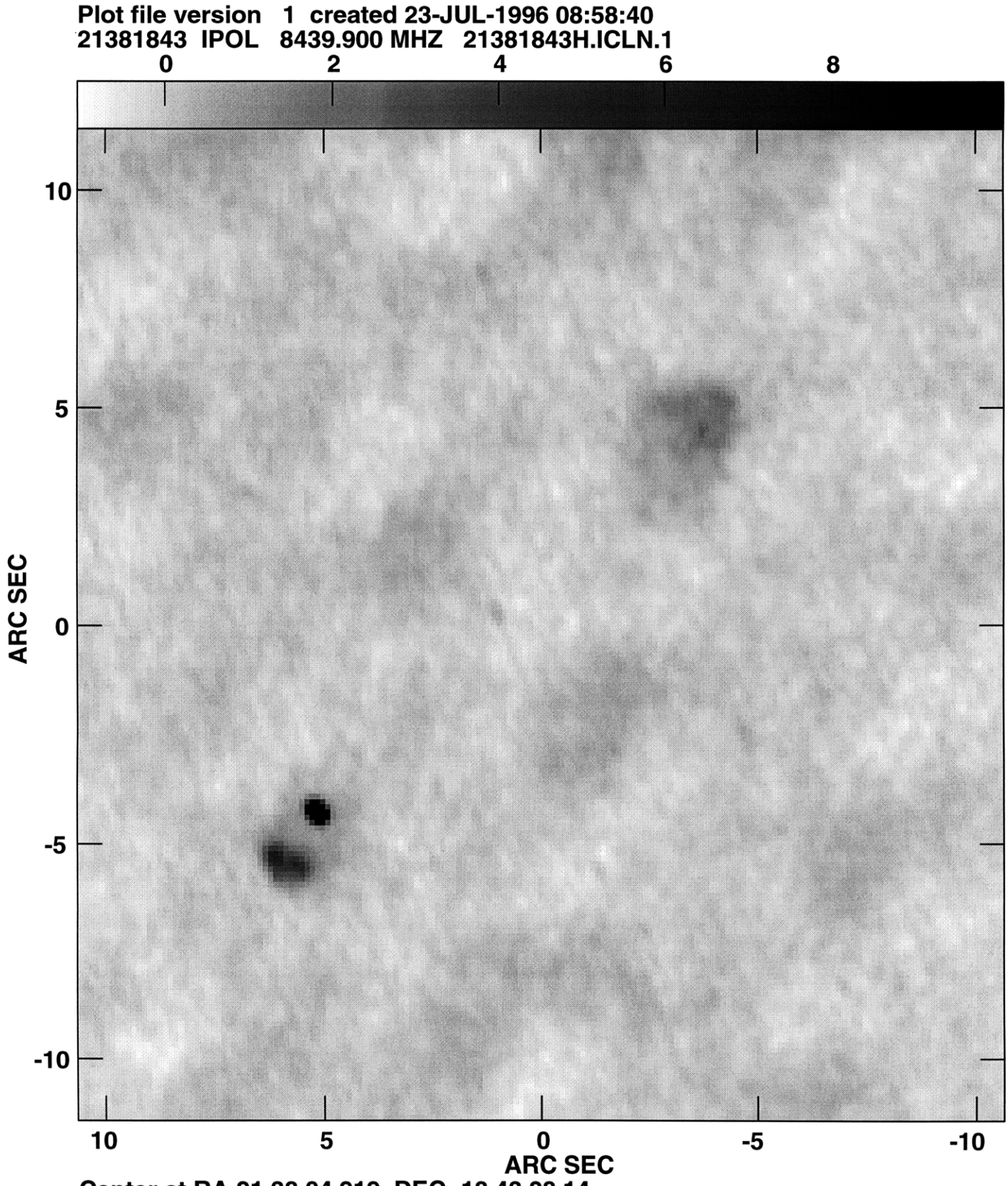
Plot file version 1 created 23-JUL-1996 08:58:40
21381843 IPOL 8439.900 MHZ 21381843H.ICLN.1
0
2
4
6
8
10
5
0
-5
-10
ARC SEC
10
5
0
-5
-10
ARC SEC
Center at RA 21 38 04.919 DEC -18 43 28.14
Grey scale flux range= -1.0 10.0 MilliJY/BEAM

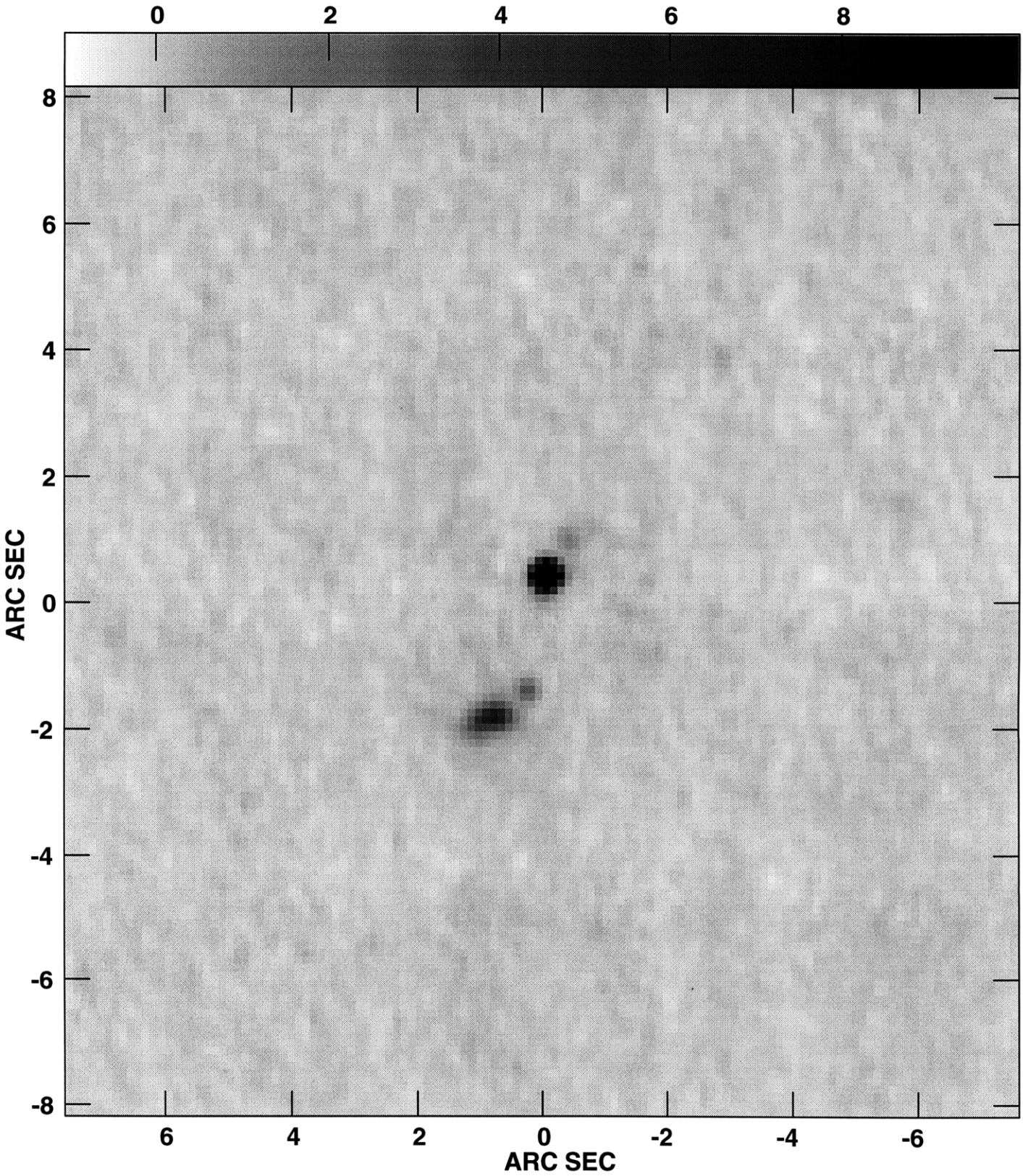
Plot file version 1 created 23-JUL-1996 09:01:28
21571120 IPOL 8439.900 MHZ 21571120H.ICLN.1
0
2
4
6
8
8
6
4
2
0
-2
-4
-6
-8
ARC SEC
6
4
2
0
-2
-4
-6
ARC SEC
Center at RA 21 57 10.329 DEC -11 20 38.18
Grey scale flux range= -1.0 10.0 MilliJY/BEAM

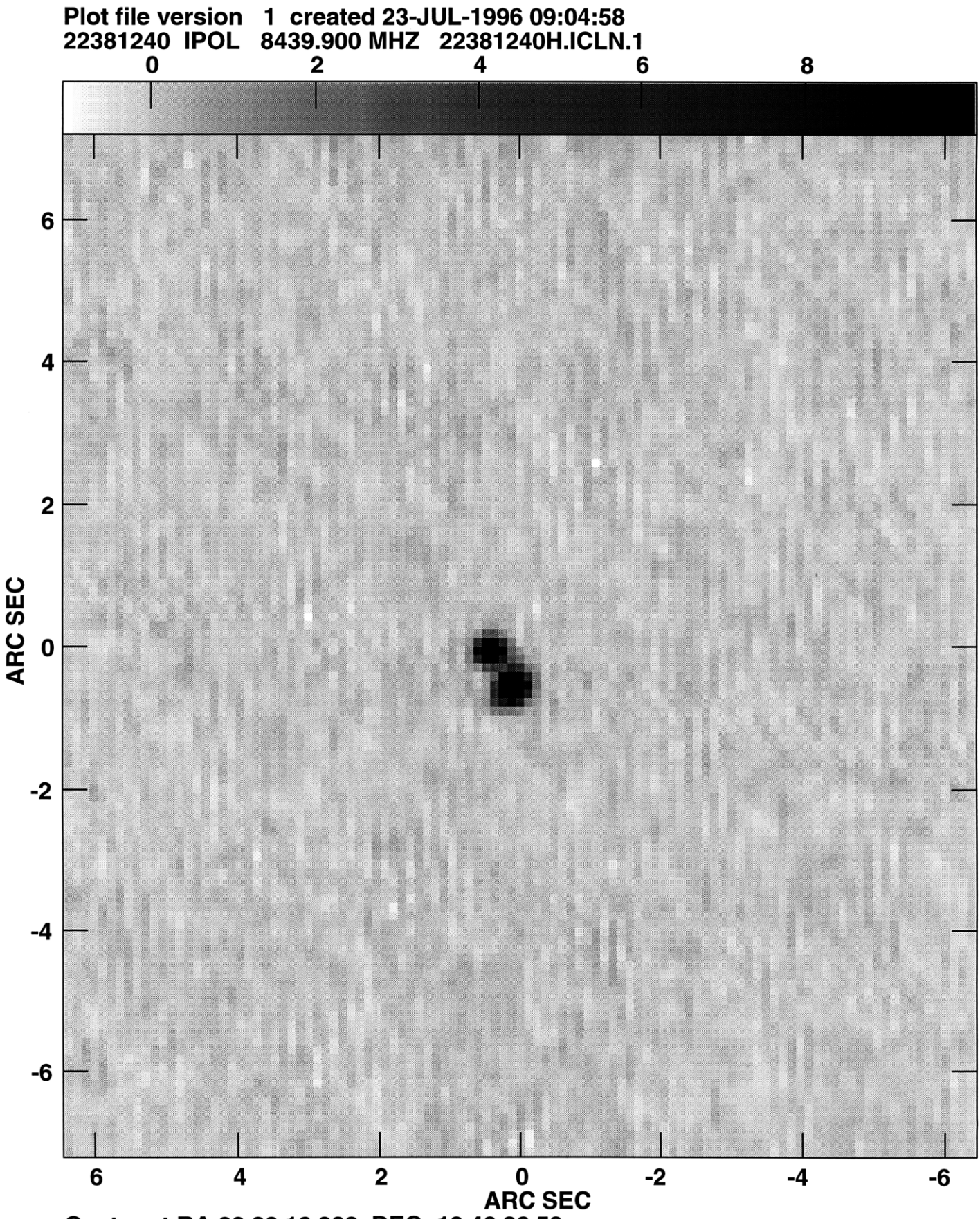
Plot file version 1 created 23-JUL-1996 09:04:58
22381240 IPOL 8439.900 MHZ 22381240H.ICLN.1
0
2
4
6
8
6
4
2
0
-2
-4
-6
ARC SEC
6
4
2
0
-2
-4
-6
ARC SEC
Center at RA 22 38 16.208 DEC -12 40 36.50
Grey scale flux range= -1.0 10.0 MilliJY/BEAM

Appendix C

Thesis Publications

C.1 Publication List

The following publications, presentations and documents are connected with my thesis research.

Refereed Publications

1. J.A. Muñoz, E.E. Falco, C.S. Kochanek, J. Lehár, L.K. Herold, **A.B. Fletcher**, & B.F. Burke, 1998, *"MGC 2214+3550: A New Binary Quasar"*, Astrophys. J. Lett. 492: L9–L12.

2. S.R. Conner, A.R. Cooray, **A.B. Fletcher**, B.F. Burke, J. Lehár, P.M. Garnavich, T.W.B. Muxlow, P. Thomasson, & J.P. Blakeslee, 1998, *"Ringlike Structure in the Radio Lobe of MG 0248+0641"*, Astron. J. 115: 37–48.

3. J. Lehár, B.F. Burke, S.R. Conner, E.E. Falco, **A.B. Fletcher**, M. Irwin, R.G. McMahon, T.W.B. Muxlow, & P.L. Schechter, 1997, *"The Gravitationally-Lensed Radio Source MG 0751+2716"*, Astron. J. 114 (1): 48–53.

4. **A. Fletcher**, S. Conner, F. Crawford, J. Cartwright, B. Burke, Y.N. Pariiskii, N.S. Soboleva, A.I. Kopylov, A.V. Temirova, O.V. Verkhodanov, & M.N. Naugol'Naya, 1996, *"Identification of objects from the RC catalog with accuracy exceeding 1" using the Palomar prints and VLA maps from the MIT Archive"*, Astronomy Reports 40: 759–767.

5. **A.B. Fletcher** & S.W. Stahler, 1994, *"The Luminosity Functions of Embedded Stellar Clusters. I. Method of Solution and Analytic Results"*, Astrophys. J. 435: 313–328.

6. **A.B. Fletcher** & S.W. Stahler, 1994, *"The Luminosity Functions of Embedded Stellar Clusters. II. Numerical Results"*, Astrophys. J. 435: 329–338.

7. M. Griffith, A.E. Wright, A.J. Hunt, E. Troup, R.D. Ekers, P. Buckett, D.J. Cooke, G. Freeman, J. Glowacki, D. Jennings, U. Knop, B. Lam, I. McGovern, D. McConnell, R.P. Norris, R. Otrupcek, R. Twardy, T. Williams, G. Behrens, C. Chestnut, B.F. Burke, **A. Fletcher**, K.S. Russell, A. Savage, J. Lim, A.E. Vaughan, S. Côté, M. Anderson, A. Hons, G.L. White, S. Amy, A. Burgess, S. Chan, L. Cram, A. Gray, W. Walsh, D. Campbell-Wilson, V. McIntyre, P. Randall, M. Suters, W.J. Zealey, 1991, *"The Parkes-MIT-NRAO Southern Sky Survey at 4850 MHz"*, Fifth Asian-Pacific Regional Astronomy Meeting, Sydney, Australia, Proc. Astronomical Society of Australia 9 (2): 243–245.

Conference Talks

1. **A.B. Fletcher**, B. Burke, S. Conner, J. Lehár, & L. Herold, 1997, *"The Angular Size Distribution of 4741 Radio Sources from the MIT-VLA Snapshot Archive"*, in conference on "Observational Cosmology with the New Radio Surveys", eds. M.N.

Bremer, N. Jackson, & I. Pérez-Fournon, Instituto de Astrofisica de Canarias, Puerto de la Cruz, Tenerife, Canary Islands, Spain, 11–13 January 1997, in press.

2. **A.B. Fletcher**, S. Conner, A. Cooray, B. Burke, & L. Herold, 1996, *"New Gravitational Lens Candidates from VLA Snapshots of MG and PMN radio sources"*, 187th American Astronomical Society Meeting, San Antonio, Texas, BAAS 117.05: 1449.

3. **A.B. Fletcher** & S.W. Stahler, 1995, *"The Luminosity Functions of Young Stellar Clusters"*, 186th American Astronomical Society Meeting, Pittsburgh, Pennsylvania, BAAS 12.01: 827.

4. S.W. Stahler & **A.B. Fletcher**, 1991, *"The Luminosity Functions of Embedded Clusters"*, in the Vulcano Workshop on Young Star Clusters and Early Stellar Evolution, Vulcano, Italy, 16–20 September 1991, Proc. Societa Astronomica Italiana, Memorie, 62, 4: 767–774.

Conference Posters

1. F. Crawford, I.M. Avruch, **A.B. Fletcher**, M.R. Griffith, & B. Burke, 1997, *"Calibration Issues in the Search for Large-Scale Anisotropies in the 87 Green Bank and Parkes-MIT-NRAO Surveys"*, in conference on "Observational Cosmology with the New Radio Surveys", eds. M.N. Bremer, N. Jackson, & I. Pérez-Fournon,

2. A.R. Cooray, **A.B. Fletcher**, S.R. Conner, B.F. Burke, & L. Herold, 1996, *"Radio and Optical Imaging of MG and PMN Sources: Close Doubles and Gravitational Lenses"*, 187th American Astronomical Society Meeting, San Antonio, Texas, BAAS 12.03: 1298.

3. A.R. Cooray, **A.B. Fletcher**, L. Herold, & B.F. Burke, 1996, *"New Infant Radio Galaxies: A Missing Link?"*, Press Release for San Antonio AAS Meeting, January 1996. Co-authored with A. Fletcher.

4. **A.B. Fletcher**, B. Burke, S. Conner, L. Herold, A. Cooray, D. Haarsma, F. Crawford, & J. Cartwright, 1996, *"Preliminary VLA Snapshots of Southern Radio Sources from the Parkes-MIT-NRAO Survey"*, 173rd International Astronomical Union Meeting, "Astrophysical Applications of Gravitational Lensing", 11–14 July 1995, Melbourne, Australia, eds. C.S. Kochanek & J.N. Hewitt, Kluwer Academic Publishers: Dordrecht, Holland, pp. 401–402.

5. A.R. Cooray, **A.B. Fletcher**, & B.F. Burke, 1995, *"Optical Identification of Radio Sources from the Parkes-MIT-NRAO Source Catalog"*, Acta Astronomica, 45(3): 679.

6. **A.B. Fletcher**, S.Conner, & B.Burke, 1995, *"First Results from 8.4 GHz VLA Imaging of 1800 Southern Sky Parkes-MIT-NRAO (PMN) Radio Sources"*, 185th American Astronomical Society Meeting, Tucson, Arizona, BAAS 109.03: 1503.

7. **A.B. Fletcher**, 1995, *"How Old is Rho Ophiuchus ?"*, poster in conference on "Astronomical Luminosity Functions"; a celebration of Maarten Schmidt's 60th birthday, 5–7 January 1995, California Institute of Technology.

8. S. Conner, **A. Fletcher**, L. Herold, & B.F. Burke, 1993, *"Undetected Lens Systems in the MIT-Green Bank-VLA 5 GHz Lens Search Sample"*, in conference on "Subarcsecond Radio Astronomy", Manchester, UK, 20–24 July 1992, eds. R.J. Davis & R.S. Booth, Cambridge University Press: UK, pp. 154–155.

Other Work

1. A.R. Cooray, 1997, *"Optical Identifications of Close Doubles and Gravitational Lenses from the MIT-Green Bank-VLA and Parkes-MIT-NRAO-VLA 8.43 GHz Surveys"*, BS Thesis, Massachusetts Institute of Techology; data collected and research supervised by **A. Fletcher**.

2. B.F. Burke, 1996, *"Forging a Radio and Optical Link"*, an article in the MDM report "Michigan-Dartmouth-MIT Observatory: An MIT Five-Year Report (1990-1995)", authored by **A. Fletcher** for Professor Burke.

Copies of most of the above publications and abstracts may be found in the following sections.

C.2 Publications for Part I

The following pages contain mostly pre-publication copies of papers, abstracts and articles associated with my thesis research into extragalactic radio sources, in the period 1990 through 1998. The documents are in time order, with the latest articles appearing first.

MGC 2214+3550: A New Binary Quasar [1]

José A. Muñoz, Emilio E. Falco, Christopher S. Kochanek & Joseph Lehár
Harvard-Smithsonian Center for Astrophysics
60 Garden Street
Cambridge, MA 02138, USA

Lori K. Herold, André B. Fletcher & Bernard F. Burke
Massachusetts Institute of Technology
77 Massachusetts Avenue
Cambridge, MA 02139, USA

ABSTRACT

We report the discovery of a binary quasar, MGC 2214+3550 A,B, whose components have similar optical spectra at a redshift $z = 0.88$. The quasars are separated on the sky by 3.″0, and have a magnitude difference of $\Delta m_I = 0.5$ mag. The VLA radio map at 3.6 cm shows a single 47 mJy radio source with a core-jet morphology that is coincident with the brighter optical quasar A. Gravitational lensing is ruled out by the lack of radio emission from quasar B, and the lack of any visible galaxies to act as the lens. We conclude that MGC 2214+3550 A and B are physically associated. With a projected separation of $12.7\,h^{-1}$ kpc ($\Omega_0 = 1$), MGC 2214+3550 A,B is one of the smallest $z > 0.5$ binary quasars.

Subject headings: Quasars: individual (MGC 2214+3550) — radio galaxies — gravitational lensing — binary quasars

1. Introduction

The first candidate gravitational lens to be discovered, Q 0957+561 (Walsh et al. 1979), had an image separation (6.″1) typical of a small cluster of galaxies. The cluster was rapidly discovered in optical images (Young et al. 1981) and Q 0957+561 is universally believed to be a gravitational lens. The third candidate gravitational lens to be discovered, Q 2345+007

[1] Observations reported here were made with the Multiple Mirror Telescope Observatory, which is operated jointly by the University of Arizona and the Smithsonian Institution.

(Weedman et al. 1982), also had an image separation (7.″3) typical of a small cluster of galaxies. No such cluster is seen in optical images, leaving Q 2345+007 as the prototypical "dark lens" candidate. There are now 9 high-redshift quasar pairs similar to Q 2345+007. They have separations from 3″ to 10″, identical redshifts ($\Delta v \lesssim 10^3$ km s^{-1}), similar spectra, and no detectable, normal object to serve as the lens. For the smaller separation lenses and the two wide separation radio lenses (see Keeton & Kochanek 1996)[2], a normal galaxy (or cluster) located in the correct position to serve as the lens is always seen in HST images of the system, unless the quasar to galaxy contrast is too severe to detect a normal galaxy (see Keeton, Kochanek & Falco 1997 for a summary of the optical properties), so explanations of the problematic pairs must invoke a class of group to cluster mass objects that have too few stars or too little hot X-ray emitting gas to be detected locally. However, the objects would be ~ 2 times more abundant than known massive objects, and would contradict most of the generally accepted models of structure formation (see Kochanek 1995; Wambsganss et al. 1995). Despite periodic theoretical attempts (e.g., Jimenez et al. 1997) and new observations (e.g.; Michalitsianos et al. 1997; Patnaik et al. 1996; Pello et al. 1996; Small, Sargent & Steidel 1997), little progress has been made in confirming or rejecting the wide-separation optical quasar pairs as gravitational lenses.

Most of the known lenses were not, in fact, found in surveys of optical quasars but in imaging surveys of radio sources (e.g.; Burke, Lehár & Conner 1992; Browne et al. 1997; King & Browne 1996). As we discuss in Kochanek, Falco & Muñoz (1997) a comparison of the optical and radio data yields a simple proof that most of the quasar pairs cannot be gravitational lenses. The 9 problematic doubles are all O^2 pairs, in which both quasars are radio-quiet. The other detectable permutations are O^2R^2 pairs in which both quasars are radio-loud, and O^2R pairs in which one quasar is radio-loud and the other is radio-quiet. The most important, disregarded facts about the wide-separation quasar pairs is the lack of a population of radio-loud O^2R^2 pairs and the existence of one O^2R pair.

The key observational discovery bearing on the "gravitational lens versus binary quasar" argument was the discovery by Djorgovski et al. (1987) of the first O^2R pair, PKS 1145–071. The system has an angular separation of $\Delta\theta = 4.''2$, a small magnitude difference of $\Delta m_B = 0.83$, and indistinguishable redshifts of $z = 1.345$. The lower limit on the radio flux ratio is 500:1, providing conclusive evidence that the system is not a gravitational lens. The spectral similarities of the two components are not particularly better or worse than the wide separation quasar pairs or many of the true gravitational lenses for that matter. Most quasars are radio-quiet, with only $P_R = 10\%$ (15%) showing 5 GHz radio fluxes exceeding

[2]A current summary of the lens data is available at `http://cfa-www.harvard.edu/glensdata`

50 (10) mJy (Hooper et al. 1997). Thus, for every O^2R pair we discovered, we would expect to find $(2P_R)^{-1} \sim 5\ O^2$ pairs similar to the claimed dark lenses. The very existence of PKS 1145–071 combined with the small fraction of radio-loud quasars essentially rules out the gravitational lens hypothesis for most of the O^2 quasar pairs. The only significant weakness in the chain of inference is the uniqueness of the system.

We report here on the discovery of a second O^2R binary quasar, MGC 2214+3550, with $z = 0.88$, $\Delta m_I = 0.5$ mag and $\Delta\theta = 3\farcs0$. We identified the object as a quasar in the course of our ongoing redshift survey of 177 flat-spectrum radio sources covering the 6 cm flux range 50–250 mJy (Falco, Kochanek & Muñoz 1997). The goal of our survey is to determine the radio luminosity function for faint radio sources, to set limits on cosmological models using the statistics of radio-selected gravitational lenses. A subsample of 108 flat-spectrum sources in the flux range 50–200 mJy was selected from the MIT-Green Bank (MG) II and III Surveys (Langston et al. 1990; Griffith et al. 1990). For each source in our sample, we obtained I band CCD images for optical identification and photometry. Finally, we procured low-resolution spectra of the candidate radio source counterparts with the MMT. Since the radio positions are accurate to better than $\sim 1''$, with the errors dominated by the small systematic offsets between the radio VLA and optical GSC coordinate reference frames, there was rarely any ambiguity in the identification of the optical counterparts. However, we oriented the spectrograph slit to obtain a spectrum of the next nearest optical source as a matter of routine. MGC 2214+3550 turned out to have a visible neighbor within $3''$; when we obtained the spectra of both objects, we discovered that both were quasars with indistinguishable redshifts. In §2 we describe the optical and radio data, and in §3 we discuss whether MGC 2214+3550 A,B is a binary quasar or a gravitational lens and its consequences.

2. Observations

MGC 2214+3550 was initially selected for our redshift survey from the single-dish 6 cm MG III catalog of Griffith et al. (1990). An accurate interferometric radio position was obtained from the MIT Archive of VLA snapshots of the MG survey radio sources (MG-VLA: Lawrence et al. 1986; Hewitt 1986; Lehár 1991; Herold-Jacobson 1996). MGC 2214+3550 was observed for 2 min using the A configuration at 3.6 cm. The interferometer data were calibrated and mapped using standard AIPS[3] procedures, and the flux densities were scaled

[3]AIPS (Astronomical Image Processing System) is distributed by the National Radio Astronomy Observatory, which is a facility of the National Science Foundation operated under cooperative agreement by Associated Universities, Inc.

to 3C 286 (Baars et al. 1977). Three iterations of mapping and self-calibration were performed to improve the map quality. The off-source map rms was 0.169 mJy beam^{-1}, only $\sim$ 20% higher than the expected thermal noise, and the FWHM beam size was approximately 0.″3. The source has a typical core-jet morphology (see Figure 1), with a compact core and an associated jet extending eastwards by $\sim$ 3″. The peak surface brightness of the core and the jet are 7.20 mJy beam^{-1} and 3.60 mJy beam^{-1}, respectively, and the total VLA interferometer flux density of the source is 47 ± 2 mJy. The VLA radio coordinates for the peak of the compact core are α=22:14:56.98, δ=35:51:25.8 (J2000.0), with an estimated astrometric uncertainty of $\sim$ 0.″2 (Lawrence et al. 1986).

After selecting MGC 2214+3550 for our redshift survey, we obtained an I band image of its optical counterpart with the Fred Lawrence Whipple Observatory (FLWO) 1.2m telescope; the detector was a Loral 2048^2 CCD, with a Kron-Cousins I filter. The pixel scale of the CCD was 0.″315, the nominal gain 2.30 electrons/ADU, and the nominal read-out noise 7.0 electrons per pixel. We bias-subtracted and flattened the image using standard procedures in IRAF[4]. We used the HST Guide Star Catalog (GSC) to perform the astrometric identifications. The instrumental magnitudes were calibrated using a GSC star in our field, with an assumed mean $V - I = 1.0$ color for GSC stars. As a result, our photometry is likely to have absolute uncertainties of $\sim$ 0.5 mag. The optical image revealed 2 compact objects, the brighter of which we named A, and the other B. The pair has a separation of $3.''02 \pm 0.''01$ in the direction with PA=13° east of north from A (see Figures 1 and 2). We used the IRAF task "daophot" to build an empirical model of the 1.″2 FWHM point spread function (PSF), and we found that A and B were unresolved. After subtracting the PSF, we could not see any significant residual. Table 1 lists the magnitudes and positions that we obtained for A and B.

We obtained spectra of A and B with the MMT and the Blue Channel spectrograph, with a slit of width 1″ and a 300 line mm^{-1} grating. The usable wavelength range is $\sim$3400–8100 Å, with a dispersion of 1.96 Å pixel^{-1}, and an effective resolution of 6.2 Å (FWHM). We took 4 exposures on 3 separate nights (the journal of observations is in Table 2). In exposures 1 and 4 we placed the slit on both components, while in exposures 2 and 3 it was placed on each component in turn, with the slit perpendicular to the line A–B, giving us a total of three spectra for each component. Because detailed spectra were not relevant to the goals of our redshift survey, and because of our relatively poor observing conditions, we did not obtain high quality spectra. Nonetheless, all 6 spectra of the two objects show

[4]IRAF (Image Reduction and Analysis Facility) is distributed by the National Optical Astronomy Observatories, which are operated by the Association of Universities for Research in Astronomy, Inc., under contract with the National Science Foundation.

the same two emission lines, corresponding to CIII] $\lambda 1909$ Å and MgII $\lambda 2798$ Å at the same redshift of $z = 0.88$. To improve the signal-to noise ratio (SNR), we combined the 3 spectra for each of the two QSO components, and we calibrated the fluxes using the spectrophotometric standard BD+40.4032, whose spectrum was acquired under photometric conditions. Unfortunately, we could not acquire standard spectra for all the nights; thus, our flux calibration is only approximate. The redshifts for the 2 components, based on the CIII] $\lambda 1909$ Å and MgII $\lambda 2798$ Å emission lines, are $z_A = 0.879 \pm 0.008$ and $z_B = 0.876 \pm 0.008$. In Table 3 we show the analysis of the redshifts obtained using each emission line. If the spectrum of component A is used as a template in a cross-correlation with the spectrum of B, a relative velocity of $v = -148 \pm 420$ km s^{-1} is obtained. The combined MMT spectra for the A and B components are shown in Figure 3. It is easy to notice the similarity in the shapes of these spectra, and especially in the detailed profiles of the CIII] and MgII emission lines. However, there is a difference between the continua of A and B, with the B continuum increasing slightly more rapidly than that of A, toward the blue. The measured equivalent widths are, for CIII]: $W_\lambda = 20 \pm 7$ Å ($W_\lambda = 52 \pm 30$ Å) in A (B); and for MgII: $W_\lambda = 85 \pm 20$ Å ($W_\lambda = 54 \pm 10$ Å) in A (B). The equivalent widths of lines in one component appear to differ from those in the other, but the low SNRs in the continua of our spectra imply that this dissimilarity is marginal. We also combined all 6 spectra; the emission lines then stand out more strongly above the continuum, but we could not identify any foreground absorption features.

We compared the optical and radio data by determining the relative astrometry of the optical and radio sources, and by determining an upper limit on the existence of other radio sources in the nearby field. We determined the position for optical component A with the program IMWCS[5] to set the world coordinate system in our CCD image. We matched 25 stars in the image with the reference catalog USNO-A (Monet 1996). The final absolute coordinates (see Table 1) have a standard error of $\sim 0\farcs8$. The coordinate difference between the optical A component and the radio source is $\Delta\alpha = -0\farcs1 \pm 0\farcs8$, $\Delta\delta = -0\farcs3 \pm 0\farcs8$. As an additional test, we determined the coordinates of the A component using 10 GSC stars falling within our CCD frame and the results were compatible with those given above. Thus, it appears that the optical counterpart to the radio source is the A component. There is no significant radio emission at the location of component B, with an upper limit of 0.17 mJy beam^{-1}, from the rms noise in the map. By comparing this to the peak surface brightness of the radio core, we obtain a lower limit of ≥ 42 on the A/B radio flux ratio.

Finally, we analyzed the morphologies of the other objects detected within a 70″ radius

[5]Originally written at the University of Iowa, and adapted and amplified by D. Mink at the Smithsonian Astrophysical Observatory.

region around each of the A and B optical quasars, and found that they are all point sources; therefore, we could not find any nearby galaxy or cluster of galaxies that was brighter than $m_I \approx 21.5$ mag.

3. Discussion

It is attractive, but difficult, to explain the MGC 2214+3550 A,B system as two gravitationally lensed images of a single quasar. The spectra for the two components are similar, with a redshift difference that is consistent with zero. The angular separation is only 3″, easily produced by a galaxy or galaxy-group-sized lens, and the 0.5 mag image brightness ratio is also typical of gravitational lensing. The differences in the equivalent widths of CIII] λ1909 Å and MgII λ2798 Å, and the differences between the continua of A and B, are weak evidence against lensing and are comparable to the differences in the optical properties of many of the O^2 pairs claimed as gravitational lenses. However, if the radio source is quasar A (or B, for that matter), then the difference between the radio flux ratio ($F_A/F_B \geq 42$) and the optical flux ratio ($F_A/F_B = 1.6$) cannot be readily explained by a lens model.

There are three possible explanations for the dissimilar radio and optical ratios, within the context of a gravitational lens scenario, but none is likely. First, extinction of A by $\sim$ 3.5 mag is ruled out by the minimal differences in the spectral continuum slopes of the two components. Second, a microlensing fluctuation making B brighter by at least 3.5 mag is unlikely. Even for true point sources we expect an rms magnitude fluctuation of only 1 mag (Witt, Mao & Schechter 1995), and the empirical evidence shows that the observed microlensing fluctuations are considerably smaller (see Corrigan et al. 1991; Houde & Racine 1994), implying that the quasar source sizes are insufficiently point-like for the images to exhibit the maximum fluctuation. With such a large microlensing effect we would also expect larger differences in the equivalent widths of the emission lines (e.g., Schneider & Wambsganss 1990). Third, strong differential variations in the optical and radio fluxes, combined with a suitable time delay between the two quasar images, may be able to produce the observed ratios. Our existing data cannot eliminate this hypothesis, since we lack optical and radio time series, but it is unlikely.

The flux ratio differences are not a problem if our astrometric identification is incorrect. In this case, it may be possible that the radio source is actually associated with the lens galaxy, so that it lies between the A and B images of a background radio-quiet quasar. Such a registration is improbable because there are only about 10^5 AGN over the entire sky with 6 cm total flux density above 30 mJy (Gregory et al. 1996; Griffith & Wright 1993). With $\sim 10^{11}$ galaxies in the observable universe, the probability of any lens galaxy being

sufficiently radio-bright is 1 in $\sim 10^6$.

The last serious problem with the lensing interpretation is that no lensing material can be seen optically. The mass to produce the 3″ image separation requires at least an L_* galaxy or a group of galaxies. An L_* galaxy member of a lensing group should be easily detected in our images, since even at the higher than optimal lens redshift of $z = 0.5$ an L_* galaxy would have $m_I \sim 18$. An anomalously faint lens is very unlikely, given the presence of lenses with the expected optical fluxes in all other convincing lens systems (see Keeton, Kochanek, & Falco 1997), and given that MGC 2214+3550 would have the lowest source redshift of any known lensed system.

We conclude that the MGC 2214+3550 A,B system is a binary quasar with a projected separation of $12.7\,h^{-1}$ kpc (for $\Omega = 1$), making it one of the smallest projected separation quasar binaries. The velocity differences, if interpreted as due to the Hubble flow, correspond to a line-of-sight separation of $\sim 0.5h^{-1}$ Mpc ($\Omega = 1$). However, the uncertainties in the velocity difference are so large that a far better estimate can be obtained from the density associated with the correlation function. If the quasar-quasar density is $n \propto r^{-1.8}$, 90% of the objects have line-of-sight separations smaller than approximately 10 times the projected separation, or about $130h^{-1}$ kpc. The existence of MGC 2214+3350 A,B proves that PKS 1145–071 was not a statistical fluke, and that we really are seeing the number of O^2R objects expected if most or all the large separation quasar pairs are binary quasars rather than gravitational lenses. Adding the absence of wide separation O^2R^2 radio pairs, we believe that the combination of the optical and radio data conclusively proves that a fraction $\sim 10^{-3}$ of bright, high redshift quasars are members of binary quasar systems. In Kochanek et al. (1997) we quantify the case against the lens interpretation in greater detail, and provide a simple physical argument for the excess of binary quasars over that predicted from the quasar-quasar correlation function (see Djorgovski 1991) based on the physics of galaxy mergers.

We are grateful to A. Milone for her help and perseverance during our MMT observations. We also thank A. Vikhlinin for a FLWO 1.2m image, L. Macri for an MMT spectrum, and C. Keeton for theoretical magnitude estimates. Our research was supported by the Smithsonian Institution. JAM is supported by a postdoctoral fellowship from the Ministerio de Educación y Cultura, Spain. CSK is supported by NSF grant AST-9401722 and NASA ATP grant NAG5-4062. JL acknowledges support of NSF grant AST93-03527.

REFERENCES

Baars, J. W. M., Genzel, R., Pauliny-Toth, I. I. K. & Witzel, A. 1977, A&A, 61, 99

Browne, I. W. A., et al. 1997, in "Observational cosmology with the new radio surveys", ed. M. Bremer, N. Jackson & I. Perez-Fournon (Dordrecht: Kluwer)

Burke, B. F., Lehár, J., & Conner, S. R. 1992, in Gravitational Lenses, ed. R. Kayser, T. Schramm, & L. Nieser (Springer: Berlin), 237

Corrigan, R. T., Arnaud, J., Fahlman, G. G., Fletcher, J. M., Hewett, P. C., Hewitt, J. N., Le Fevre, O., McClure, R., Pritchet, C. J., Schneider, D. P., Turner, E. L., Webster, R. L., Yee, H. K. C., 1991, AJ, 102, 34

Djorgovski, S., 1991 The Space Distribution of Quasars, ASP #21, D. Crampton, ed., (ASP) 349

Djorgovski, S., Perley, R., Meylan, G. & McCarthy, P. 1987, ApJ, 321, L17

Falco, E. E., Kochanek, C. S. & Muñoz, J.A. 1997, ApJ in press, astro-ph/9707032

Gregory, P. C., Scott, W. K., Douglas, K., Condon, J. J., 1996, ApJS, 103, 427

Griffith, M., Langston, G., Heflin, M., Conner, S., Lehár, J. & Burke, B. F. 1990, ApJS, 74, 129

Griffith, M. R., Wright, A. E., 1993, AJ, 105, 1666

Herold-Jacobson, L. K. 1996, Ph.D. Thesis, Massachusetts Institute of Technology

Hewitt, J. N., 1986, Ph. D. Thesis, Massachusetts Institute of Technology

Hooper, E. J., Impey, C. D., Foltz, C. B. & Hewett, P. C. 1996, ApJ, 473, 746

Houde, M., & Racine, R. 1994, AJ, 107, 466

Jimenez, R., Heavens, A. F., Hawkins, M. R. S. & Padoan, P. 1997, electronic preprint astro-ph/9709050

Kochanek, C. S. 1995, ApJ, 435, 545

Kochanek, C. S., Falco. E. E., & Muñoz, J. A. 1997, preprint

Keeton, C. R. & Kochanek, C. S. 1996, in "Astrophysical Applications of Gravitational Lensing", eds. C. S. Kochanek & J. N. Hewitt, Kluwer Academic Publishers: Dordrecht, Holland, 419

Keeton, C. R., Kochanek, C. S. & Falco, E. E. 1997, ApJ submitted, astro-ph/9708161

King, L. J., & Browne, I. W. A. 1996, MNRAS, 282, 67

Langston, G. I., Heflin, M. B., Conner, S. R., Lehár, J. L., Carilli, C. L. & Burke, B. F. 1990, ApJS, 72, 621

Lawrence, C. R., Bennett, C. L., Hewitt, J. N., Langston, G. I., Klotz, S. E., Burke, B. F., Turner, K. C., 1986, ApJS, 61, 105

Lehár, J. 1991, Ph.D. Thesis, Massachusetts Institute of Technology

Michalitsianos, A., Falco, E., Muñoz, J. A. & Kazanas, D. 1997, ApJ, 487, L117

Monet, D. 1996, BAAS, 188, 5404

Patnaik, A.R., Schneider, P., & Narayan, R. 1996 MNRAS, 281, 17

Pello, R., Miralles, J.M., Le Borgne, J.-F., Picat, J.-P., Soucail, G., & Bruzual, G. 1996, A&A, 314, 73

Schneider, P. & Wambsganss, J. 1990, A&A, 237, 42

Small, T. A., Sargent, W. L. W., Steidel, C. C. 1997, AJ in press, astro-ph/9709203

Walsh, D., Carswll, R. F., & Weymann, R. J. 1979, Nature, 279, 381

Wambsganss, J., Cen, R., Ostriker, J. P., & Turner, E. L. 1995, Science, 268, 274

Weedman, D. W., Weymann, R. J., Green, R. F. & Heckman, T. M. 1982, ApJ, 255, L5

Witt, H. J., Mao, S. & Schechter, P. L. 1995, ApJ, 443, 18

Young, P. J., Gunn, J., Oke, J. B., Westphal, J. A. & Kristian J. 1981, ApJ, 241, 507

This preprint was prepared with the AAS LaTeX macros v4.0.

Table 1. Optical astrometry and photometry for MGC 2214+3550 A,B

Object	α (J2000)	δ (J2000)	m_I
A	22:14:56.97 $\pm$0.″8	35:51:25.5 $\pm$0.″8	18.80 $\pm$ 0.08
B	$\Delta\alpha_{B-A} = 0.''82 \pm 0.''01$	$\Delta\delta_{B-A} = 2.''94 \pm 0.''01$	19.30 $\pm$ 0.08

Table 2. Journal of MMT observations for MGC 2214+3550 A,B

Exp. No	Object	Central λ (Å)	Exp. (s)	Date dd/mm/yy	Air Mass	P.A. ° E of N	Seeing (arcsec)
1	MGC 2214+3550	6000	2700	08/09/96	1.031	-176.9	0.9
2	MGC 2214+3550 A	6000	1769	05/07/97	1.002	-90.9	1.1
3	MGC 2214+3550 B	6000	2700	05/07/97	1.022	-83.9	1.3
4	MGC 2214+3550	6000	3600	09/07/97	1.055	11.9	2.1

Table 3. Redshift analysis for MGC 2214+3550 A,B

Object	CIII] λ1909 Å		MgII λ2798 Å		Redshift
	λ_{obs}(Å)	z	λ_{obs}(Å)	z	$< z >$
A	3576	0.873	5272	0.884	0.879$\pm$0.008
B	3570	0.870	5264	0.882	0.876$\pm$0.008

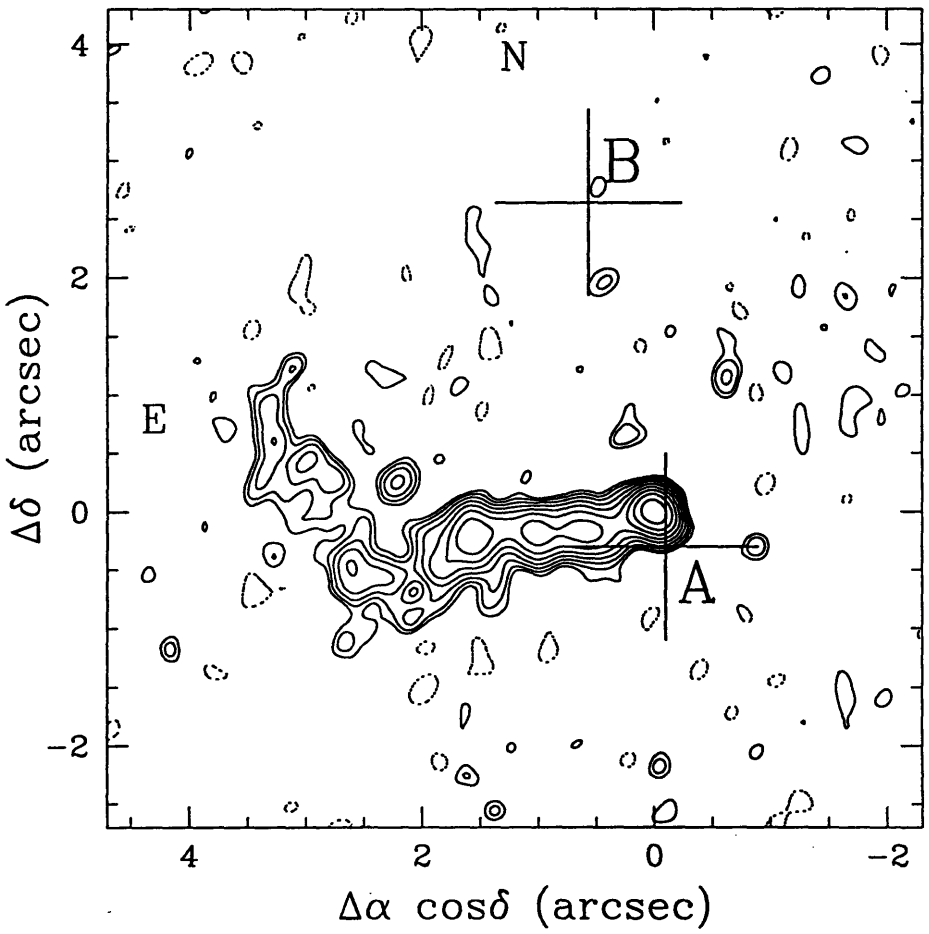

Fig. 1.— Radio total intensity 3.6 cm contour map of MGC 2214+3550. North is at the top, and east to the left. Coordinate offsets are given relative to the radio core component. The positions of the optical quasars A and B are marked with vertical crosses, the sizes of which indicate the 0.″8 uncertainty in our optical astrometry. The positive (negative) radio flux density is shown as solid (dotted) contours which increase by factors of $\sqrt{2}$ from twice the off-source map rms level of 0.169 mJy beam^{-1}; the FWHM beam is 0.″285 × 0.″267 with the major axis oriented at PA=−80°.

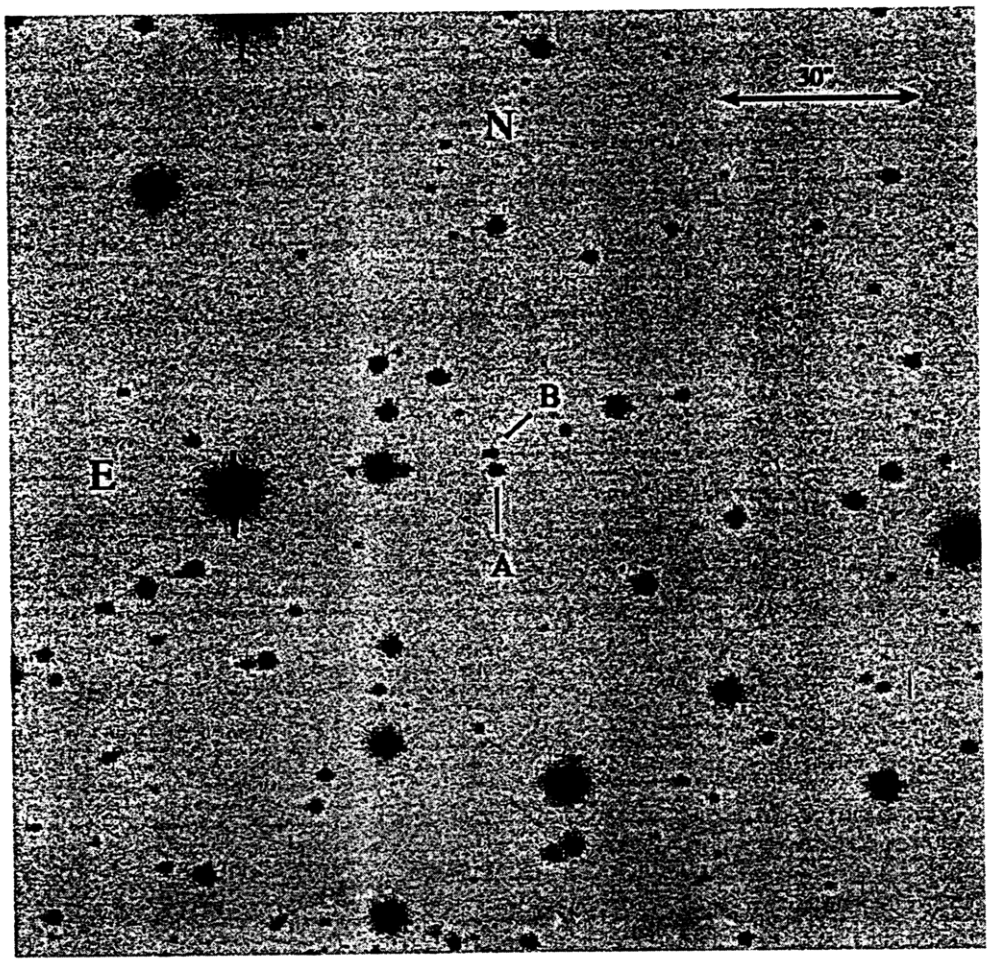

Fig. 2.— Optical I band 2.'5 × 2.'5 CCD image of the optical field in the direction of the radio source MGC 2214+3550, obtained with the FLWO 1.2m telescope. The two quasars are indicated by A and B, near the center of the frame. North is towards the top of the frame, East is to the left, and the angular scale is shown in the top right corner.

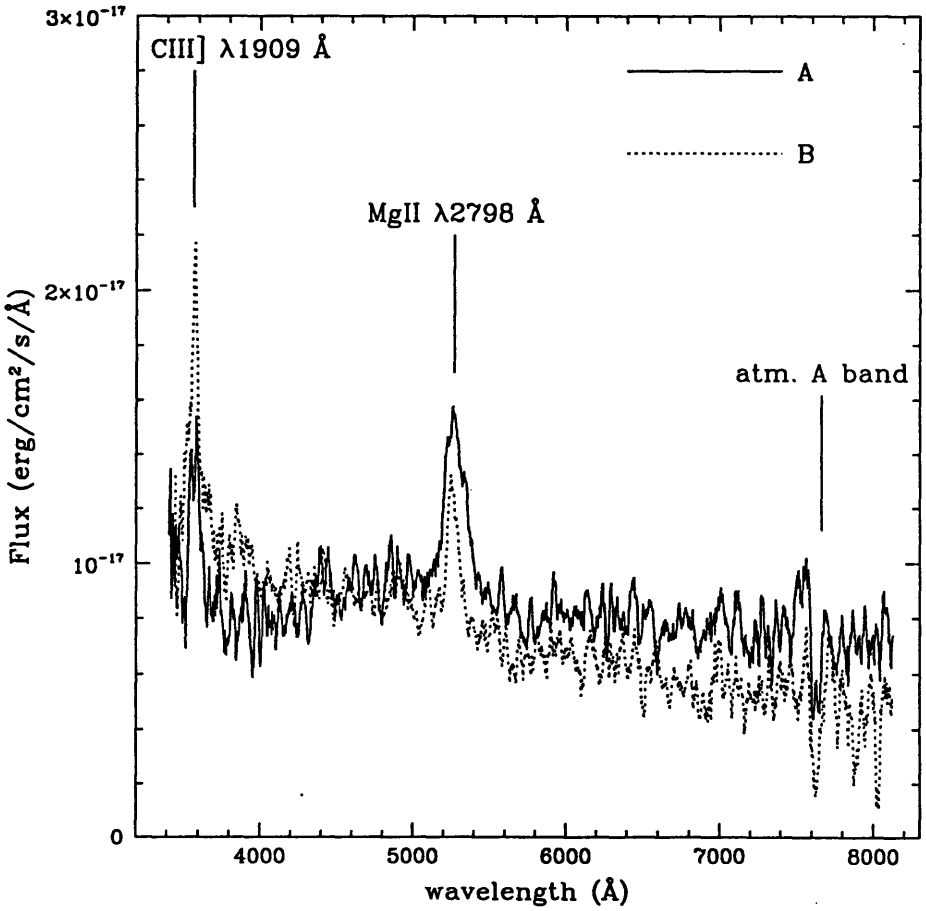

Fig. 3.— Calibrated spectra of the quasar pair in the direction of MGC 2214+3550, showing the spectrum of each of two QSO components A & B. The solid (dashed) line corresponds to the A (B) component. The abscissa shows observed wavelengths. Prominent emission lines, as well as the atmospheric absorption A band, are labeled.

Ring-Like Structure in the Radio Lobe of MG0248+0641

Samuel R. Conner[1], Asantha R. Cooray[1,2], André B. Fletcher[1], Bernard F. Burke[1], Joseph Lehár[3], Peter M. Garnavich[3,4], Tom W. B. Muxlow[5], Peter Thomasson[5], John P. Blakeslee[6]

Received _____; accepted _____

[1]Department of Physics, Massachusetts Institute of Technology, 77 Massachusetts Avenue, Cambridge MA 02139, USA.

[2]Now at Department of Astronomy and Astrophysics, University of Chicago, Chicago IL 60637, USA. E-mail: asante@hyde.uchicago.edu.

[3]Center for Astrophysics, 60 Garden Street, Cambridge MA 02138, USA.

[4]Visiting Astronomer, Kitt Peak National Observatory, National Optical Astronomical Observatories, which is operated by the Association of Universities for Research in Astronomy (AURA) under cooperative agreement with the National Science Foundation.

[5]Nuffield Radio Astronomy Laboratories, Jodrell Bank, Cheshire SK11 9DL, UK.

[6]Palomar Observatory, California Institute of Technology, MS 105-24, Pasadena CA 91125, USA.

ABSTRACT

We present radio and optical observations of MG0248+0641, which contains a kiloparsec-scale ring-like structure in one of its radio lobes. The radio observations show a typical core-double morphology: a central core between two lobes, each of which has a hotspot. The western radio lobe appears as a nearly continuous ring, with linear polarization electric field vectors which are oriented in a radial direction from the ring center. We consider several different interpretations for the nature of this ring, including gravitational lensing of a normal jet by a foreground galaxy. Even though simple lensing models can describe the ring morphology reasonably well, the high linear polarization seen around the ring cannot be easily explained, and no lensing object has yet been found in deep optical and infrared searches within the extent of the ring. If the radio ring is indeed caused by gravitational lensing, the implied mass-to-light ratio is typical of the very high values seen in other candidate "dark" gravitational lenses. The chance interposition of a galactic supernova remnant, nova, planetary nebula, or H II region, has been ruled out. The highly polarized ring of MG0248+0641 is much like the prominent ring seen in 3C219, and the multiple ones in 3C310 and Hercules A, suggesting that similar physical processes are producing shell structures in these radio galaxies. The ring in MG0248+0641 may be caused by the formation of "bubbles", as a result of instabilities in the energy flow down the western radio jet. It may also be possible that the required instabilities are triggered by the infall of gas, via tidal interaction of the central source with a nearby galaxy. This scenario may be indicated by our marginal detection of an optical source close to the western hotspot.

Subject headings: radio galaxies: individual (MG0248+0641) — active galactic

Ring-like structure in MG0248+0641, Conner et al.

nuclei - radio jets and lobes.

Ring-like structure in MG0248+0641, Conner et al.

1. Introduction

The MIT-Green Bank-VLA (MG-VLA) lens search surveys (Lawrence *et al.* 1986; Hewitt 1986; Lehár 1991; Herold-Jacobson 1996) have so far produced six confirmed lenses from snapshot maps of about 6000 sources: MG0414+0534 (Hewitt *et al.* 1992), MG0751+2716 (Lehár *et al.* 1997), MG1131+0456 (Hewitt *et al.* 1988), MG1549+3047 (Lehár *et al.* 1993), MG1654+1346 (Langston *et al.* 1989), and MG2016+112 (Lawrence *et al.* 1984). After an extensive improvement in mapping procedures the same data in the MG-VLA survey have been reanalyzed, the result being a promising subsample of radio sources with morphologies typical of gravitational lensing (Conner *et al.* 1993). Included in this was MG0248+0641, which, after recalibration and remapping of the original 6 cm data, showed an unusual ring-like structure in the total intensity map.

At 6 cm (4.85 GHz), the source has a measured single-dish flux density of 300 ± 38 mJy (Becker *et al.* 1991), and at 20 cm (1.4 GHz) 804 ± 60 mJy (White & Becker 1992), indicating an integrated spectral index $\alpha \sim -0.8$ ($S_\nu \sim \nu^\alpha$), which is moderately steep. The radio structure in MG0248+0641 (probably 4C+06.13) was first mapped by Lawrence *et al.* (1986) as part of a program to discover gravitational lenses in the MIT-Green Bank (MG) catalog. The observations were made with the NRAO [7] Very Large Array (VLA) A-array configuration for an on-source integration time of $\sim$ 2 minutes. Although the resolution was $\sim$ 0.″3, the original calibration and mapping of the data were not good enough to uncover the detailed structure of the extended emission.

As rings are a rare type of morphology within the MG-VLA sample, MG0248+0641 has now been observed with the VLA at 2 cm (14.9 GHz), 3.6 cm (8.4 GHz) and 6 cm (4.6

[7]The National Radio Astronomy Observatory (NRAO) is a facility of the National Science Foundation operated under cooperative agreement by Associated Universities, Inc.

GHz), and with MERLIN at 18 cm (1.6 GHz). Optical and infrared observations of the field containing the source have been made in R-band with the 2.4 m Hiltner telescope of the Michigan-Dartmouth-MIT (MDM) Observatory and in K-band with the KPNO 2.1 m telescope, respectively. The MDM 2.4 m and MMT have been used to obtain spectra of optical sources within one arcminute of MG0248+0641. These observations were carried out initially to determine the lensing nature of this radio source.

2. Observations

New VLA observations of MG0248+0641 have been made in the A-array at 3.6 and 6 cm in August 1995, and in B-array at 2 cm in October 1995. The on-source integration times of the 2, 3.6 and 6 cm observations were 40, 20, and 20 minutes respectively. Calibration and mapping of these data were performed using standard AIPS procedures. The maps were further self-calibrated, yielding final rms noise levels of typically twice the thermal limit.

The 1995 VLA maps are shown in Fig. 1. The overall structure of the source is a double-sided core-jet-hotspot system. The 3 bright peaks correspond to the central core and two hotspots, with the core being located at α=02:48:58.28, δ=06:41:43.6 (J2000), with an astrometric accuracy of $\sim$ 0.″2 (Lawrence *et al.* 1986). In the 3.6 cm map, the integrated flux densities of the core, western and eastern hotspots are 9, 23 and 3.2 mJy, respectively. The noise level in this map is $\sim$ 0.1 mJy beam^{-1}. The western lobe contains a prominent ring-like structure in between the core and western hotspot, and there appears to be a large extended area of diffuse emission north of this ring, which is most distinctively imaged in the 3.6 cm map. Diffuse low surface-brightness emission envelopes the ring and the eastern jet, though this is not well imaged by the CLEAN deconvolution algorithm. We do find several knots within this diffuse emission, on both sides of the core. At the sensitivity of our observations, there is no evidence for an undisturbed jet to the west of the core, but we

Ring-like structure in MG0248+0641, Conner et al.

detect a partial jet east of the core. In Fig. 2 we show the spectral index distribution of MG0248+0641, based on the VLA 2 and 6 cm observations, where the 6 cm A-array emission has been convolved to the 2 cm B-array resolution. The ring-like structure has a spectral index of $\sim$ -1.0, whereas the core component is found with a spectral index of $\sim$ -0.6. The two hotspots are found with a varying spectral index distribution, with an index value close to $\sim$ -0.5 at the ends closest to the core, and highly steep values $\sim$ -1.5 at the post-shock endpoints. All of these values are consistent with the integrated index $\alpha \sim -0.8$ from the single-dish measurements.

VLA linear polarization maps were made from all of the 1995 data, at each of the observed wavelengths, using observations of 3C48 as a polarization calibrator based on the polarization angle values given in Perley (1982). In Fig. 3, we show the total intensity contour plots of the radio emission, onto which we have overlaid the fractional linear polarization electric field E vectors. The ring exhibits high fractional linear polarization, from 20% to 70%, with vectors oriented radially outward from the ring center. The orientations of these vectors do not change by more than $\sim$ 10 degrees between 2 and 6 cm, indicating a small Faraday rotation in this wavelength range. Therefore, these vectors should be perpendicular to the magnetic flux density B field lines in the emitting plasma of the radio galaxy, assuming that the radiation is primarily due to the synchrotron process. The hotspots are 12% polarized. The diffuse emission north of the ring has a fractional polarization of only $\sim$ 5%, and it is noted that this falls to an unmeasurable value in the central and brightest part of this emission. The partial jet to the east of the core is 15% polarized. Thus, emission from non-ring portions of this source are weakly polarized ($\leq$ 15%), while the ring and its associated structures are highly polarized. In the brighter, outermost part of the eastern jet, the polarization vectors are oriented along the axis of the jet, but rotate towards the transverse direction as the jet arrives at the hotspot.

Ring-like structure in MG0248+0641, Conner et al.

We also observed MG0248+0641 with the MERLIN array in May 1997, using 7 antennae at 18 cm, with an on-source integration time of $\sim$ 8 hours. The observations of the source were phase referenced to the compact calibration source 0246+061 (Browne *et al.* 1997). 3C286, together with 0246+061, were used as polarization calibrators, assuming a polarization position angle of 33 degrees for 3C286 at 18 cm. The data were edited, calibrated and mapped using standard MERLIN-D programs and procedures within AIPS. The resulting map (Fig. 4) has a resolution of 0.″25. In Fig. 4, the core, western and eastern hotspot components are labeled A, B and C, with integrated flux densities of 14, 141, and 27 mJy, respectively. Several resolved knots of emission in and around the ring are seen. The partial eastern jet is also resolved into several knots, and the gap remains between the core and this jet, at this frequency. In Fig. 5, we show the MERLIN 18 cm fractional polarization map, with vectors overlaid onto the contour map of the total intensity. At this wavelength, it can be seen that the orientations of the vectors have changed by more than 70 degrees, especially along the arc-like feature adjacent to the western hotspot, suggesting a high Faraday rotation at this longer wavelength.

Based on astrometry using the Cambridge Automated Plate Measuring machine (APM) catalog, we found a faint optical counterpart at α=02:48:58.23, δ=06:41:43.3 (J2000). This source is 0.″6 southwest of the radio core, but does not lie inside the ring. Bearing in mind an estimated accuracy of 1 arcsecond in the APM position, we consider this source to be the optical counterpart of the radio core, and its position is marked with a cross in Fig. 4.

Optical observations of this field were carried out in visible wavelengths at the MDM 2.4 m Hiltner telescope in November 1995, and in the infrared K-band using the InSb 256 $\times$ 256 array on the KPNO 2.1 m telescope in January 1996, with total integration times of 50 and 54 minutes, respectively. The data were reduced using standard procedures in IRAF. In Fig. 6 we show a 4.5′ by 4.5′ field from the 2.4 m telescope, imaged to a limiting magnitude

Ring-like structure in MG0248+0641, Conner et al.

of R $\sim$ 25.5, with a seeing of 0.89″ (FWHM). The photometric observations of the object considered to be the optical counterpart of the radio core (marked by a square box in Fig. 6 and henceforth referred to as the counterpart) indicate an R magnitude of $\sim$ 18.6, and color R-K of $\sim$ 2.8. This counterpart is marginally resolved, with a circular isophote of $\sim$ 0.″92, and subtracting a stellar point-spread-function revealed a possible host galaxy underneath. There are two other nearby sources to the west of the core counterpart (see Fig. 7). The first is 3.″8 away at α = 02:48:57.98, δ = 06:41:42.9 (J2000) with R $\sim$ 24.7 (2.1 σ). The second is 9″ away at α = 02:48:57.62, δ = 06:41:44.3 (J2000), with R $\sim$ 22.6 (5.9 σ) and K $\sim$ 17.3 (9 σ), and which is slightly extended with $\sim$ 1.″06 (FWHM). The first source is probably detected in the infrared image with K $\sim$ 18.8 (3.2 σ). However, the positions of the peaks of this very faint optical and infrared source do not match precisely; this is understandable as being due to the low signal-to-noise level in both R and K detections, and also due to known problems with the KPNO 2.1 m tracking in the infrared image.

Amongst the several objects within 1 arcminute of the counterpart, there are two galaxies to the south, and two stars, one to the north and one to the east of it. The star to the east in obviously a foreground star in our own galaxy, and therefore has not been observed further. However, moderate resolution spectra have been obtained in November 1995 for the three other objects using the MODSPEC spectrograph on the MDM 2.4 m telescope. The star to the north is a late type star, with strong Fe I and Fe II lines, and a thermal spectrum of $T \sim$ 5000 K. Based on $H\beta$ and [O III] 4959 and 5007 $\AA$ emission lines, the two galaxies to the south, with R magnitudes of $\sim$ 15.7 and 16.1, have been shown to be at the same redshift of 0.1.

In December 1995, we used the Blue Channel spectrograph on the MMT to obtain a 45 minute spectrum of the core counterpart. Two 1200s exposures were combined to produce the final spectrum in Fig. 8. The 300 grooves mm^{-1} grating and 1″ slit provided a spectral

resolution of $\sim 5\AA$ (FWHM). The standard star BD28+4211 was used for flux calibration. The spectrum was extracted and calibrated using standard routines in IRAF. The spectrum has an unusually blue continuum ($F_\nu \sim \nu^\alpha, \alpha \sim 4.1$), which drops rapidly shortward of 6280 $\AA$, corresponding to 4000 $\AA$ in the rest-frame, and levels off sharply to a flat continuum at longer wavelengths. The spectrum shows a broad Mg II 2798 $\AA$ emission line at 4408 $\AA$, and two narrow [O III] 4959 $\AA$ and 5007 $\AA$ emission lines, at 7786 $\AA$ and 7881 $\AA$, respectively. These lines suggest a redshift of 0.57 for the radio core. The absorption features in the spectrum, other than prominent atmospheric lines, have equivalent widths no greater than ~ 6 $\AA$, and may result from stars in the host galaxy of the AGN core counterpart, rather than from intervening absorbers. We have also detected the 3000 $\AA$ bump, commonly known as the "weak blue bump" (Wills *et al.* 1985) in QSO spectra.

3. Discussion

Gravitational lensing could produce the ring morphology observed in MG0248+0641. As an illustration, we have constructed a simple lens model which accounts for the major features in the radio ring (Fig. 9). In this example, an elliptical singular isothermal potential (Blandford & Kochanek 1987) has been placed in front of a background source, which was built up to reproduce the observed structures. Probabilistic calculations based on simple lensing optical depth models (Turner, Ostriker & Gott 1984) suggest that there is 90% confidence for a lens to lie between redshifts 0.07 and 0.27. Assuming a point-mass potential at a redshift of 0.17, which is half the angular diameter distance to a background source at 772 h^{-1} Mpc (Ω_0 =1, Λ_0=0, H_0 = 70 km s^{-1} Mpc^{-1}), the observed ring size can be produced by a galaxy with a mass of $\sim 1 \times 10^{11}$ $M_\odot$ enclosed by the projection of the radio ring. Assuming a factor of five for the ratio of total to enclosed mass, this would imply a galaxy of mass $\sim 5 \times 10^{11}$ $M_\odot$. The angular size of the ring corresponds to a line-of-sight

Ring-like structure in MG0248+0641, Conner et al.

velocity dispersion of $\sim$ 235 km s^{-1}, which is typical for galaxies with mass $\sim 10^{11}$ $M_{\odot}$. The modeled lensing galaxy was given an isophotal ellipticity 0.3, and oriented to produce the observed gap at the southern edge of the ring. As shown in Fig. 9, the morphological structure of the western radio lobe can be easily produced with gravitational lensing.

Lens models cannot explain the observed radio polarization, however. Polarization is unaffected by lensing, so the radial orientation of the polarization vectors along the observed ring would have to correspond to a fortuitous variation along the proposed background jet. Higher resolution radio observations of Einstein ring gravitational lens MG1131+0456 have shown a complex polarization structure (Chen & Hewitt 1993), and such complex polarized intensity distributions are likely to occur in all lenses with ring morphology. The very high fractional polarization values observed are also hard to explain in the context of an ordinary background radio jet. Finally, a very strong objection to the lensing interpretation is the absence of any detectable lensing galaxy, inside the ring radius. An elliptical galaxy with one-dimensional velocity dispersion of 235 km s^{-1} would have a luminosity of $\sim 1 \times 10^{11}$ $L_{\odot}$ (Faber & Jackson 1976), corresponding to an absolute magnitude $M_R \sim$ -21 (Oegerle & Hoessel 1991). The *k*-corrected apparent R magnitude is then $\sim$ 18.6. According to Coleman *et al.* (1980), typical apparent R magnitudes at a redshift of 0.17 are $\sim$ 16.2 for an elliptical, and $\sim$ 17.5 for a spiral galaxy. No source has been found in our optical and infrared data inside the radio ring, where the galaxy is expected, down to a background 3 σ surface brightness of R $\sim$ 24.8 mag $arcsec^{-2}$ and K $\sim$ 19 mag $arcsec^{-2}$. If MG0248+0641 is indeed lensed, then the optical limiting magnitudes suggest an intervening galaxy with mass-to-light ratio at least $\sim$ 250 times higher than that of a typical galaxy (assumed here to have a mass-to-light ratio from 5 to 15 $M_{\odot}/L_{\odot}$), which is very large to be associated with a normal galaxy. If the MG0248+0641 ring is indeed caused by gravitational lensing, the implied mass-to-light ratio is estimated to lie in the range 1000–4000, in solar units. At least three candidate "dark" gravitational lenses with similar mass-to-light ratios are known:

Ring-like structure in MG0248+0641, Conner et al.

MG 0023+171 (Hewitt *et al.* 1987), MG 2016+112 (Hattori *et al.* 1997) and Q 2345+007 (Duncan 1991).

The marginally-detected optical source 3.8″ west of the radio core is not likely to be the lens. This faint optical source (Fig. 7) lies close to the western hotspot and may well represent optical emission from this hotspot, or from a satellite galaxy of the central quasar, assuming it is at the same redshift as the core. It is also likely that this source is located beyond a redshift of 0.57, given that its R-K color is $\sim$ 5.9, but exact determination of the photometric redshift is impossible due to the possible presence of dust.

Ring-like morphology in radio sources is also seen in supernova remnants, novae, planetary nebulae, and H II regions, but the radio and optical properties of MG0248+0641 appear to be inconsistent with these interpretations. Given the integrated spectral index, the ring's angular size, its radio luminosity, and the radial linear polarization vectors, these possibilities are unrealistic; the ring is too large to be an extragalactic supernova, nova, planetary nebula, or H II region, and the non-thermal and steep spectral index distribution of the ring is incompatible with the thermal sources, which have inverted or flat spectral indices. This rules out novae, planetary nebulae, and H II regions. Also, if this ring is due to the interposition of a galactic supernova remnant, the small size of the ring suggests that it is young; between the radio observations of 1980 and 1997, we would have expected to see an expansion in the ring. However, we have not found any evidence for a change in the ring's physical size. Also, the spectral index of the ring, $\alpha \sim$ -1, is too steep to be a shell-type supernova remnant, where typically a spectral index of about -0.5 is found. The location of MG0248+0641, far from the galactic equator at a latitude of $\sim -45°$, also suggests a negligible probability that a galactic supernova remnant is superimposed on the radio lobe. We searched the literature for prior radio polarization data on these types of sources, but found none with radial polarization vectors.

Ring-like structure in MG0248+0641, Conner et al.

The ring-like structure in MG0248+0641 cannot be easily explained within the context of standard radio morphologies. For the observed integrated spectral index of $\alpha \sim$ -0.8, the maximum degree of linear polarization expected for synchrotron emission is $\sim$ 72%, and we see values up to 70% in the circular structure of the western lobe. It is not unusual to see high degrees of fractional linear polarization, exceeding 50%, in the lobes of radio galaxies and quasars, a phenomenon commonly ascribed to shock compression accompanying the transverse expansion of radio lobes and jets (see the 1988 review by Saikia & Salter). Also, very high fractional polarizations, approaching the theoretical maximum, can only be observed if the angle between the plane of compression and the line-of-sight is small. These regions are most likely to be found in the outermost surfaces of the lobes, both where the lobe advances into the intergalactic medium (IGM), and also where the jet hits the hotspot. Terminal hotspots with low polarization suggest high inclination angles for radio galaxies (Laing 1981), i.e. the radio jet axis is pointed close to the line-of-sight. In the case of MG0248+0641, the fractional polarizations in the hotspots are indeed lower than that of the ring-like structure, suggesting that its jets are in fact inclined at a large angle to the plane of the sky. Given this suspected inclination in MG0248+0641, the light propagation delay time between photons from each of the lobes would be expected to cause an asymmetry in the jet lengths; the observed ratio of jet lengths would then suggest that it is the (longer) eastern jet which is approaching. Due to Doppler boosting, this approaching lobe is expected to have a more visible jet, to be brighter, and more polarized; we find instead that these particular features are associated with the (shorter) western jet. Furthermore, if the eastern jet is indeed approaching us, the expected flux ratio between the western and eastern lobes would be less than unity, which is again inconsistent with our observations. Since none of the standard explanations can be used to describe both the flux and length asymmetries in MG0248+0641, we are led to the conclusion that they are intrinsic; the western side of this radio galaxy experiences an environment different from the opposing side.

Ring-like structure in MG0248+0641, Conner et al.

If the observed ring is due to a disruption of a normal jet to the west of the core, a severe disturbance is required. Unusual structures in extragalactic radio sources have been commonly associated with cD galaxies in cluster centers, where internal dynamics may play a key role. The distribution of X-ray surface brightness in clusters suggests the existence of cooling flows (Fabian *et al.* 1991). Many of these cooling flow clusters have a central dominant galaxy which is associated with a radio source (Burns 1990). However, in our case we find no evidence for a cluster in the field of MG0248+0641. Recent ROSAT observations have not shown any significant X-ray emission, with an upper limit on the observed flux of $\sim 2 \times 10^{-16}$ W m^{-2} (Wolfgang Brinkmann, personal communication). Assuming a temperature of 5 kev, this corresponds to a X-ray luminosity of $\sim 10^{37}$ W, at a redshift of 0.57. The two galaxies we found to the south of the radio core, at a redshift of 0.1, may well belong to a galaxy group, rather than a foreground galaxy cluster.

Other sources with prominent circular lobes and rings have been observed, such as the southern lobe of 3C310 (van Breugel & Fomalont 1984), the northern lobe of 3C219 (Perley *et al.* 1980), and Pictor A (Perley *et al.* 1997), with more such sources listed in van Breugel & Fomalont (1984). At a redshift of 0.57, the projected overall size of MG0248+0641 (45 h^{-1} kpc) and the average diameter of the ring (7.5 h^{-1} kpc) are several times smaller than in these sources. However, the ratio of ring-to-overall size in MG0248+0641 is comparable to many of these sources. The rings in 3C219 and 3C310 are similarly polarized with high fractional values, and electric field intensity vectors oriented in the same configuration as in MG0248+0641. Given that we find no Faraday rotation between 2 and 6 cm, the polarization vectors in Fig. 3 are parallel to the electric field, indicating a circumferential magnetic field. The eastern side of MG0248+0641 is also compatible with the southern side of 3C219, which has been modeled by Clarke *et al.* 1992. These similarities have led us to the tentative conclusion that MG0248+0641 is a small-scale version of sources such as 3C310 and 3C219. However, MG0248+0641 is somewhat different from the known rings in these other sources,

Ring-like structure in MG0248+0641, Conner et al.

which have no terminal hotspots in their lobes (e.g. 3C310). This could likely be due to age differences between the respective lobes, with a smaller, and possibly younger, MG0248+0641 having been energized relatively recently.

The rings in 3C310 and 3C219 are in fact high-intensity spherical shells, with no actual hollow, but rather a decrease in brightness in their central regions. In MG0248+0641, we also find that the minimum brightness at the ring center is slightly higher than the rms noise (off-source), suggesting that the observed ring-like structure is a projected shell-like feature, or a "bubble". The confinement of such bubbles by a magnetic field and a hot ambient medium can easily produce the observed highly linearly polarized emission. Theoretical predictions of such bubbles, energized by plasma flows, exist in the literature. Smith *et al.* (1983) have predicted such shells of hot gas to be blown out by weak jets, through jet choking and other instabilities in the energy transportation. In 3C310, an optical source has been detected next to the optical counterpart of its core, which has led van Breugel & Fomalont (1984) to conclude that the release of energy in the form of bubbles can be triggered by infalling gas from tidal interaction with this companion. Also, Sadun & Hayes (1993) discovered an optical companion to the core counterpart of Hercules A, with a separation $\sim 4''$, and galaxy pairs are found in 3C219 separated by $\sim 8''$ (Crane, Tyson & Saslaw 1983). Recently, Morrison & Sadun (1996) have argued for a two-stage origin for the multiple rings seen within some extended radio lobes: in the first stage, a periodic outflow and weak shocks form the initial shell structure, with a drift that moves them around, and then the low-pressure portions of these bubbles are filled up with energized electrons in the second stage. The periodic tidal forces from the nearby perturbing companion determine the density modulations, which in turn produce the series of multiple shells.

The production of a shell in the western lobe may also be due to a jet instability. Theoretical predictions suggest that instabilities are likely to occur near the nuclear regions

of small and less energetic radio galaxies (Smith *et al.* 1983, and references therein), with more energetic radio galaxies requiring an external source, such as those arising in tidal interactions with other galaxies. The detection of an optical source 3.″8 away from the core counterpart, at the location near the western hotspot of MG0248+0641, is promising within the context of the model of van Breugel & Fomalont (1984). If this is indeed a companion to the central optical source, a tidal interaction may have produced the required instability, allowing a recent outflow of energetic plasma into the western radio jet. The circular structure may also have been due to a past, more active phase of the jet, causing a surge in the gas input to the lobes, and hence a more symmetrical subsequent expansion. Finally, it is also likely that the asymmetry in MG0248+0641 is due to the disruption of the western radio jet as it runs into its companion galaxy.

Since the current models cannot fully describe the energetics required to produce the observed high-intensity shell features, more investigative theoretical work is required in order to describe the above processes, and possibly others not suggested here. The MG0248+0641 field may also be a good candidate for deep observations with the Keck or HST; it would be interesting to search for more direct evidence of galaxy interactions. Also, direct redshift determination of the optical companion may help in accepting or rejecting the interaction hypothesis presented here; however, spectroscopic measurements will be challenging, given its faint magnitude.

We would like to acknowledge Rodney Davies for granting us Director's discretionary time to use MERLIN, Paul Schechter for useful discussions, Rick Perley for pointing out a problem with our initial polarization calibration, and Wolfgang Brinkmann for providing us with results from ROSAT observations of the MG0248+0641 field. The National Radio Astronomy Observatory is a facility of the National Science Foundation operated under co-operative agreement by Associated Universities, Inc. MERLIN is a national facility operated

Ring-like structure in MG0248+0641, Conner et al.

by the University of Manchester on behalf of the Particle Physics and Astronomy Research Council. IRAF is distributed by the National Optical Astronomical Observatories, which are operated by the Association of Universities for Research in Astronomy, Inc., under cooperative agreement with the National Science Foundation. The MDM Observatory is operated by a consortium of the University of Michigan, Dartmouth College and the Massachusetts Institute of Technology. The Multiple Mirror Telescope (MMT) is operated as a joint facility of the Smithsonian Institution and the University of Arizona by the Multiple Mirror Telescope Observatory, and is located on the grounds of the Fred Lawrence Whipple Observatory of the Smithsonian Astrophysical Observatory on Mount Hopkins. This research was supported by NSF grant AST92-24191 at MIT. JL gratefully acknowledges support from NSF grant AST93-03527.

Ring-like structure in MG0248+0641, Conner et al.

REFERENCES

Becker, R. H., White, R. L., Edwards, A. L. 1991, ApJS, 75, 1.

Blandford, R., Kochanek, C. 1987, ApJ, 321, 658.

Browne, I. W. A., Patnaik, A. R., Wilkinson, P. N., Wrobel, J. M. 1997, MNRAS, in press.

Burns, J. O. 1990, AJ, 99, 14.

Chen, G. H., Hewitt, J. N. 1993, AJ, 106, 1719.

Clarke, D. A., Bridle, A. H., Burns, J. O., Perley, R. A., Norman, M. L. 1992, ApJ, 385, 173.

Coleman, G. D., Wu, C., Weedman, D. W. 1980, ApJS, 43, 393.

Conner, S. R., Fletcher, A., Herold, L., Burke, B. F. 1993, *Sub-arcsecond Radio Astronomy*, eds. R. J. Davis and R. S. Booth, Great Britain: Cambridge University Press, 154.

Crane, P., Tyson, J. A., Saslaw, W. C. 1983, ApJ, 265, 681.

Duncan, R. C. 1991, ApJ, 375, L41.

Faber, S. M., Jackson, R. E. 1976, ApJ, 204, 668.

Fabian, A. C., Nulsen, P. E. J., Canizares, C. R. 1991, A&ARv, 2, 191.

Hattori, M., Ikebe, Y., Asaoka, I., Takeshima, T., Böhringer, H., Mihara, T., Neumann, D.M., Schindler, S., Tsuru, T., Tamura, T. 1997, Nature, 388, 146.

Herold-Jacobson, L. 1996, MIT Ph.D. Thesis.

Hewitt, J. N. 1986, MIT Ph.D. Thesis.

Ring-like structure in MG0248+0641, Conner et al.

Hewitt,J. N., Turner, E. L., Lawrence, C. R., Schneider, D. P., Gunn, J. E., Bennett, C. L., Burke, B. F., Mahoney, J. H., Langston, G. I., Schmidt, M., Oke, J. B., Hoessel, J. G. 1987, ApJ, 321, 706.

Hewitt, J. N., Turner, E. L., Schneider, D. P., Burke, B. F., Langston, G. I., Lawrence, C. R. 1988, Nature, 333, 537.

Hewitt, J. N., Turner, E. L., Lawrence, C. R., Schneider, D. P., Brody, J. P. 1992, AJ, 104, 968.

Laing. R. A. 1981, ApJ, 248, 87.

Langston, G. I., Schneider, D. P., Conner, S., Carilli, C. L., Lehár J., Burke, B. F., Turner. E. L., Gunn, J. E., Hewitt, J. N., Schmidt, M. 1989, AJ, 97, 1283.

Lawrence, C. R., Schneider, D. P., Schmidt, M., Bennett, C. L., Hewitt, J. N., Burke, B. F., Turner, E. L., Gunn, J. E. 1984, Science, 223, 46.

Lawrence, C. R., Bennett, C. L., Hewitt, J. N., Langston, G. I., Klotz, S. E., Burke, B. F., Turner, K. C. 1986, ApJS, 61, 105.

Lehár J. 1991, MIT Ph.D. Thesis.

Lehár J., Langston, G. I., Silber, A., Lawrence, C. R., Burke, B. F. 1993, AJ, 105, 847.

Lehár J., Burke, B. F., Conner, S. R., Fletcher, A. B., Irwin, M., McMahon, R. G., Muxlow, T. W. B., Schechter, P. L. 1997, AJ, 114, 48.

Morrison, P., Sadun, A. 1996, MNRAS, 278, 265.

Oegerle, W. R., Hoessel, J. G. 1991, ApJ, 375, 15.

Perley, R. A., Bridle, A. H., Willis, A. G., Fomalont, E. B. 1980, AJ, 85, 499.

Ring-like structure in MG0248+0641, Conner et al.

Perley, R. A. 1982, AJ, 87, 859.

Perley, R. A., Roser, H. -J., Meisenheimer, K. 1997, A&A, in print.

Sadun, A. C., Hayes, J. J. E. 1993, PASP, 105, 379.

Saikia, D. J., Salter, C. J. 1988, ARAA, 26, 93.

Smith, M. D., Smarr, L., Norman, M. L., Wilson, J. R. 1983, ApJ, 264, 432.

Strom, R. G., Willis, A. G., Wilson, A. S. 1978, A&A, 68, 367.

Strom, R. G., Willis, A. G. 1980, A&A, 85, 36.

Turner, E. L., Ostriker, J. P. Gott, J. R. III 1984, ApJ, 284, 1.

van Breugel, W. L., Fomalont, E. B. 1984, ApJ, 282, L55.

White, R. L., Becker, R. H. 1992, ApJS, 80, 211.

Wills, B. J., Wills, D., Netzer, H. 1985, ApJ, 288, 94.

This manuscript was prepared with the AAS LaTeX macros v4.0.

Ring-like structure in MG0248+0641, Conner et al.

Fig. 1.— VLA (a) A-array 6 cm, (b) A-array 3.6 cm, and (c) B-array 2 cm total intensity maps of MG0248+0641. The beam size in the 3.6 cm map is 0.″3, and the peak total intensity is 22 mJy beam^{-1}.

Fig. 2.— Spectral index distribution of MG0248+0641, based on VLA 2 and 6 cm observations (grey scale). The contours represent A-array 6 cm total intensity emission, but convolved down to the B-array 2 cm resolution. The ring-like structure has a spectral index of $\alpha \sim -1.0$, whereas the unresolved core and hotspot components have flat spectral indices $\sim$ -0.5.

Fig. 3.— VLA (a) A-array 6 cm, (b) A-array 3.6 cm, and (c) B-array 2 cm total intensity contour maps of MG0248+0641, onto which linear polarization vectors have been overlaid. The natural weighted beam size in the 6 cm map is 0.″48, and is shown in the bottom left corner. In all 3 wavelengths, the fractional polarization vectors are scaled such that 0.″33 corresponds to 100%, and they are oriented along the electric field.

Fig. 4.— MERLIN 18 cm total intensity contour map of MG0248+0641, with a restored beam size of 0.″25, which is shown in the bottom right corner. The optical counterpart position from the APM catalog is marked with a cross, scaled to the $\pm$ 1.″0 APM astrometric uncertainty.

Fig. 5.— MERLIN 18 cm total intensity contour map of MG0248+0641, onto which linear fractional polarization vectors have been overlaid. The vectors are scaled such that one arcsecond of vector length corresponds to 50%, and they are oriented along the electric field.

Fig. 6.— R band optical CCD image, with a total integration time 3000 seconds, of the MG0248+0641 field (4.5′ by 4.5′), observed with the MDM 2.4 m telescope. North is left; east is down. The counterpart is marked with a square box. The limiting magnitude is $\sim$

Ring-like structure in MG0248+0641, Conner et al.

25. The pixel scale is 0.″275.

Fig. 7.— MDM 2.4 m R band image overlaid on the 3.6 cm VLA map, with contours in steps of the 2 σ noise level in the optical data. We have positioned the optical core counterpart such that it lies on top of the radio core. A faint optical source is marginally detected close to the western hotspot, at a level of 2.1 σ.

Fig. 8.— The optical spectrum of the counterpart of core component (A), taken at the MMT with the Blue Channel Spectrograph. Wavelength is in angstroms, and the flux is normalized. The spectrum shows the "weak blue bump", and Mg II and [O III] emission lines, from which we calculate a redshift of 0.57. The prominent absorption near 7600 $\AA$ is a sky feature.

Fig. 9.— Lens model interpretation for MG0248+0641. The contours in the source plane show the background source as it would appear without lensing, and the diamond caustic is drawn in bold. The image plane shows the same source projected through the lens model, with the tangential critical line drawn in bold. The source was constructed to roughly produce the observed structures.

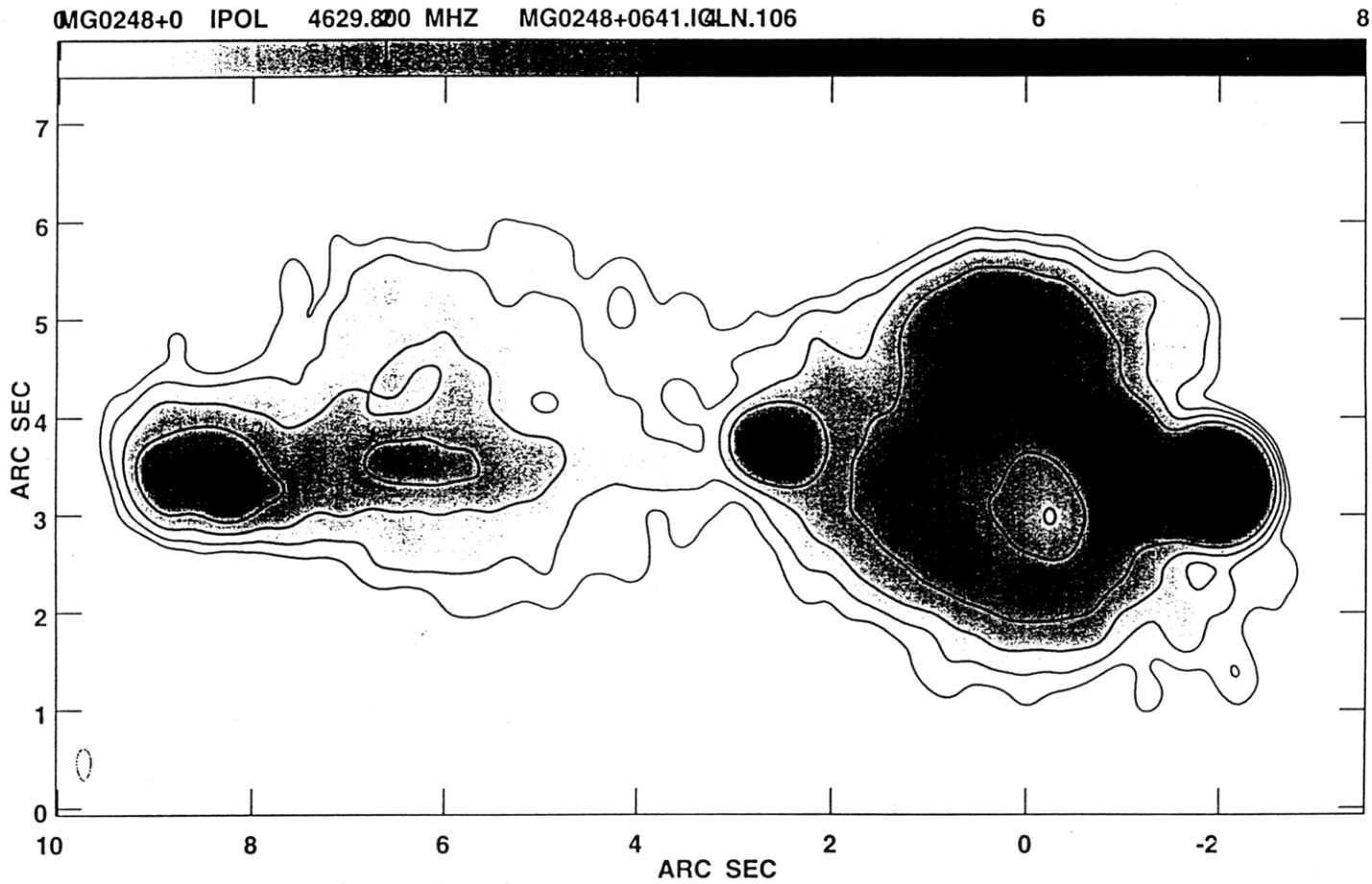

Center at RA 02 48 58.10000 DEC 06 41 40.0000
Grey scale flux range= 0.000 8.000 MilliJY/BEAM
Peak contour flux = 5.5934E-02 JY/BEAM
Levs = 5.5934E-04 * (-0.500, 0.500, 1.000,
2.000, 4.000, 8.000, 16.00, 32.00, 64.00,
95.00)

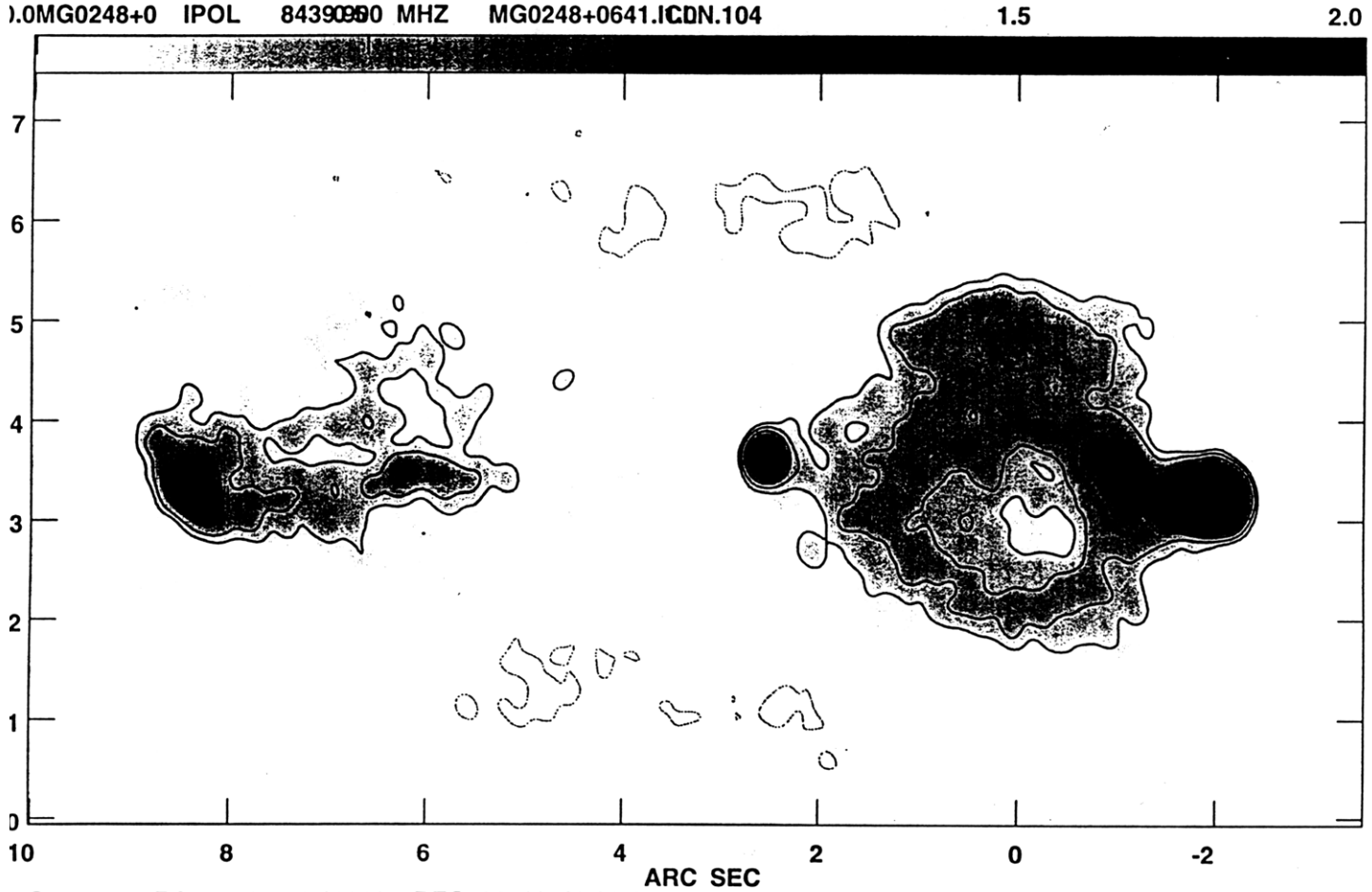

Center at RA 02 48 58.10000 DEC 06 41 40.0000
Grey scale flux range= 0.000 2.000 MilliJY/BEAM
Peak contour flux = 2.1973E-02 JY/BEAM
Levs = 2.1973E-04 * (-1.00, 1.000, 2.000,
4.000, 8.000, 16.00, 32.00, 64.00, 95.00)

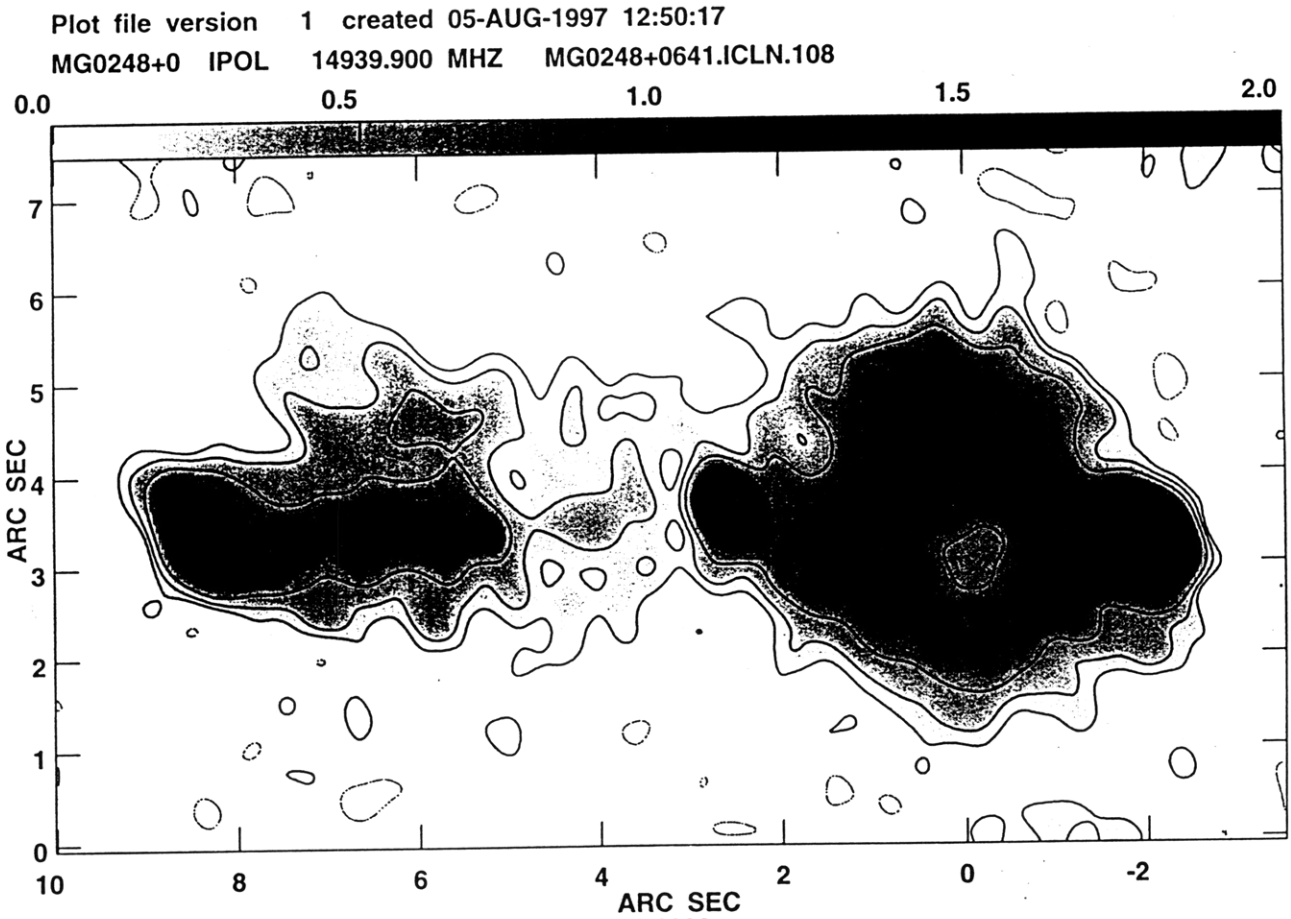

Center at RA 02 48 58.10000 DEC 06 41 40.0000
Grey scale flux range= 0.000 2.000 MilliJY/BEAM
Peak contour flux = 2.5814E-02 JY/BEAM
Levs = 2.5814E-04 * (-0.500, 0.500, 1.000,
2.000, 4.000, 8.000, 16.00, 32.00, 64.00,
95.00)

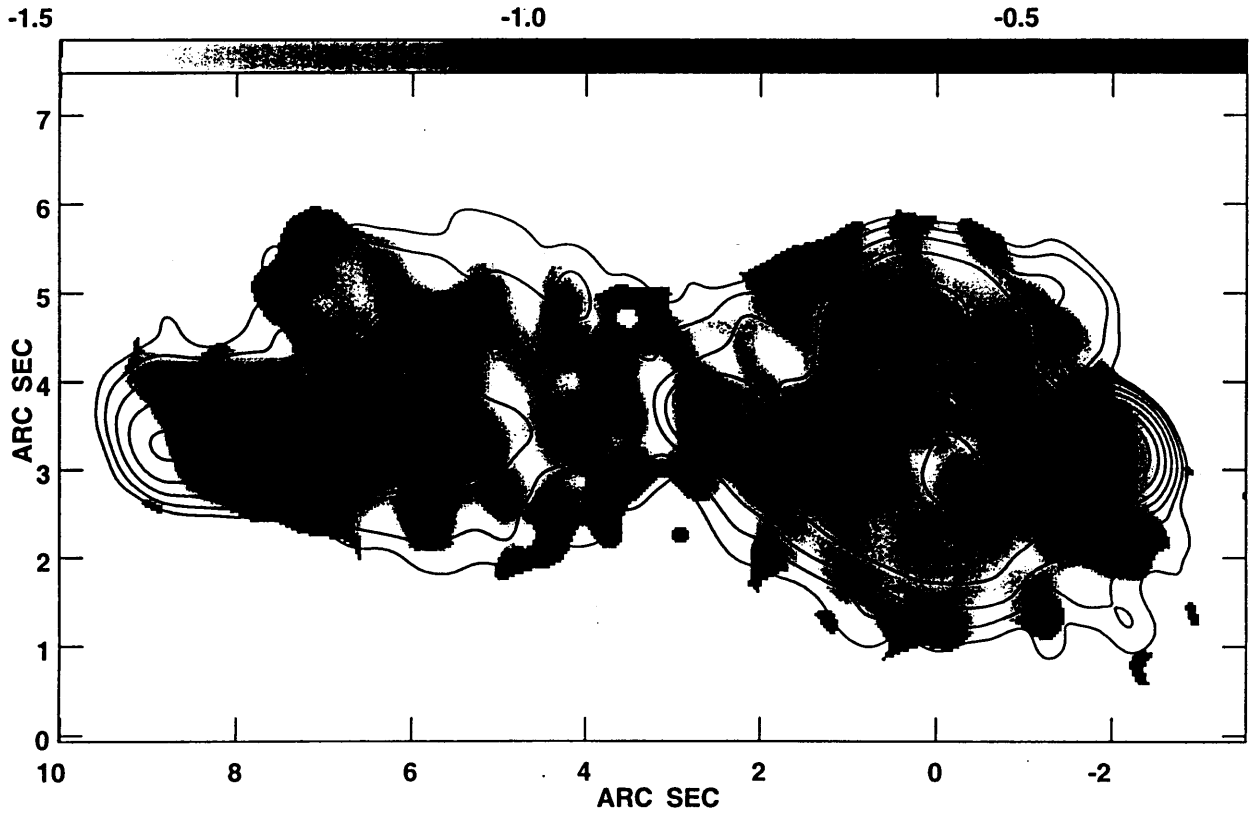

Center at RA 02 48 58.10000 DEC 06 41 40.0000
Grey scale flux range= -1.500 -0.300 SP INDEX
Peak contour flux = 6.0145E-02 JY/BEAM
Levs = 6.0145E-04 * (-0.500, 0.500, 1.000,
2.000, 4.000, 8.000, 16.00, 32.00, 64.00,
95.00)

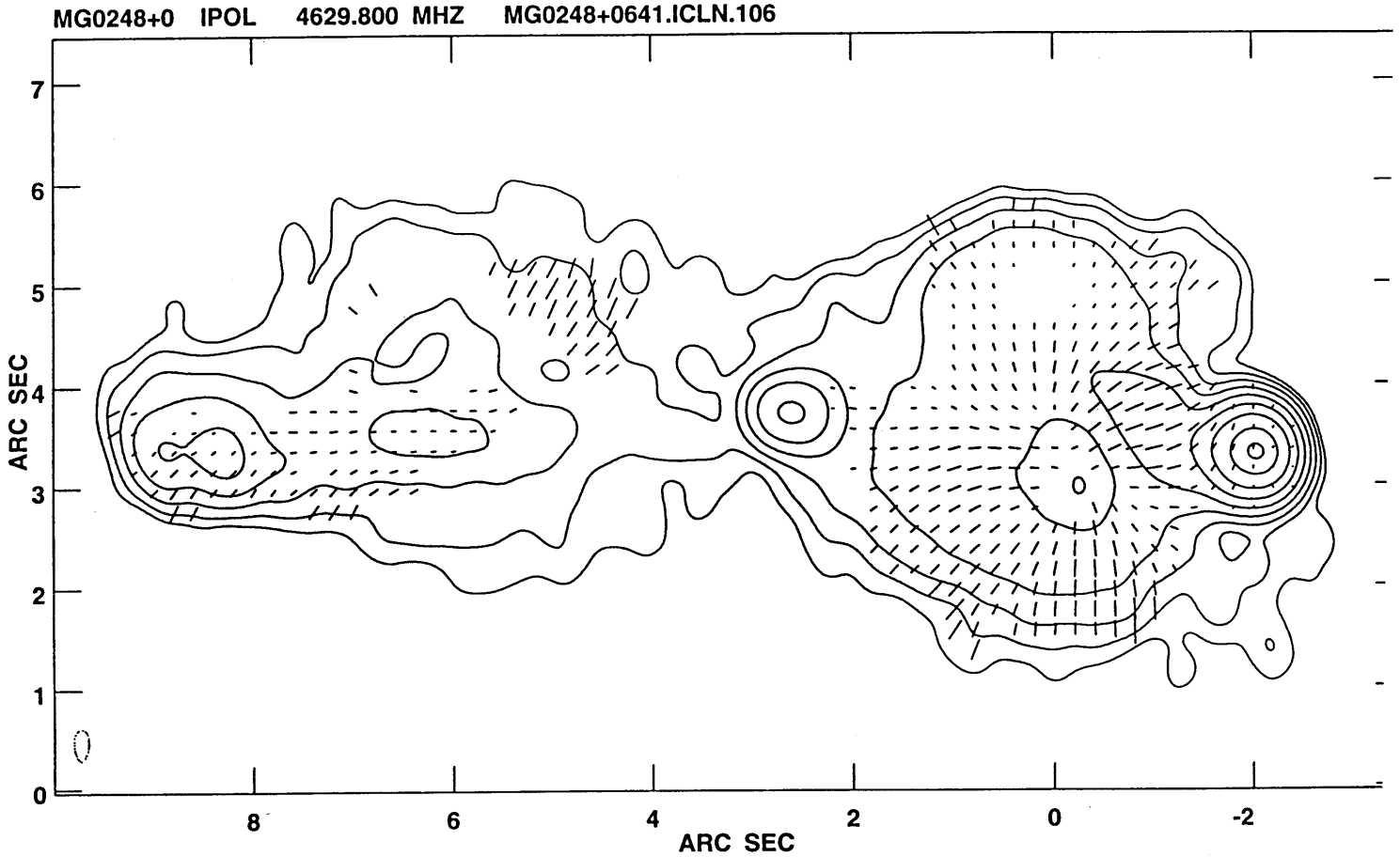

Center at RA 02 48 58.10000 DEC 06 41 40.0000
Pol line 1 arcsec = 3.0000E+00 RATIO
Peak flux = 5.5934E-02 JY/BEAM
Levs = 5.5934E-04 * (-0.500, 0.500, 1.000,
2.000, 4.000, 8.000, 16.00, 32.00, 64.00,
95.00)

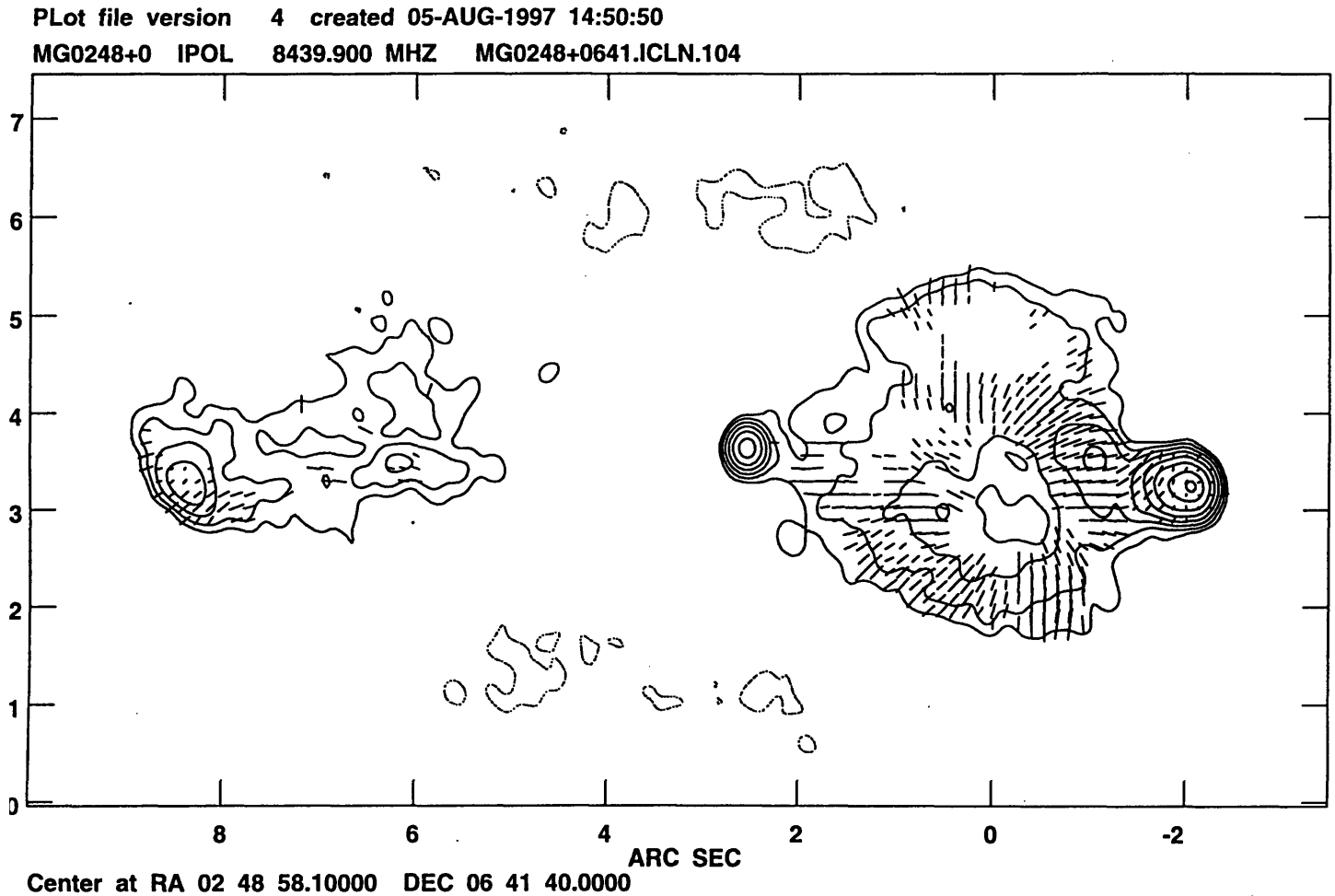

Center at RA 02 48 58.10000 DEC 06 41 40.0000
Pol line 1 arcsec = 3.0000E+00 RATIO
Peak flux = 2.1973E-02 JY/BEAM
Levs = 2.1973E-04 * (-1.00, 1.000, 2.000,
4.000, 8.000, 16.00, 32.00, 64.00, 95.00)

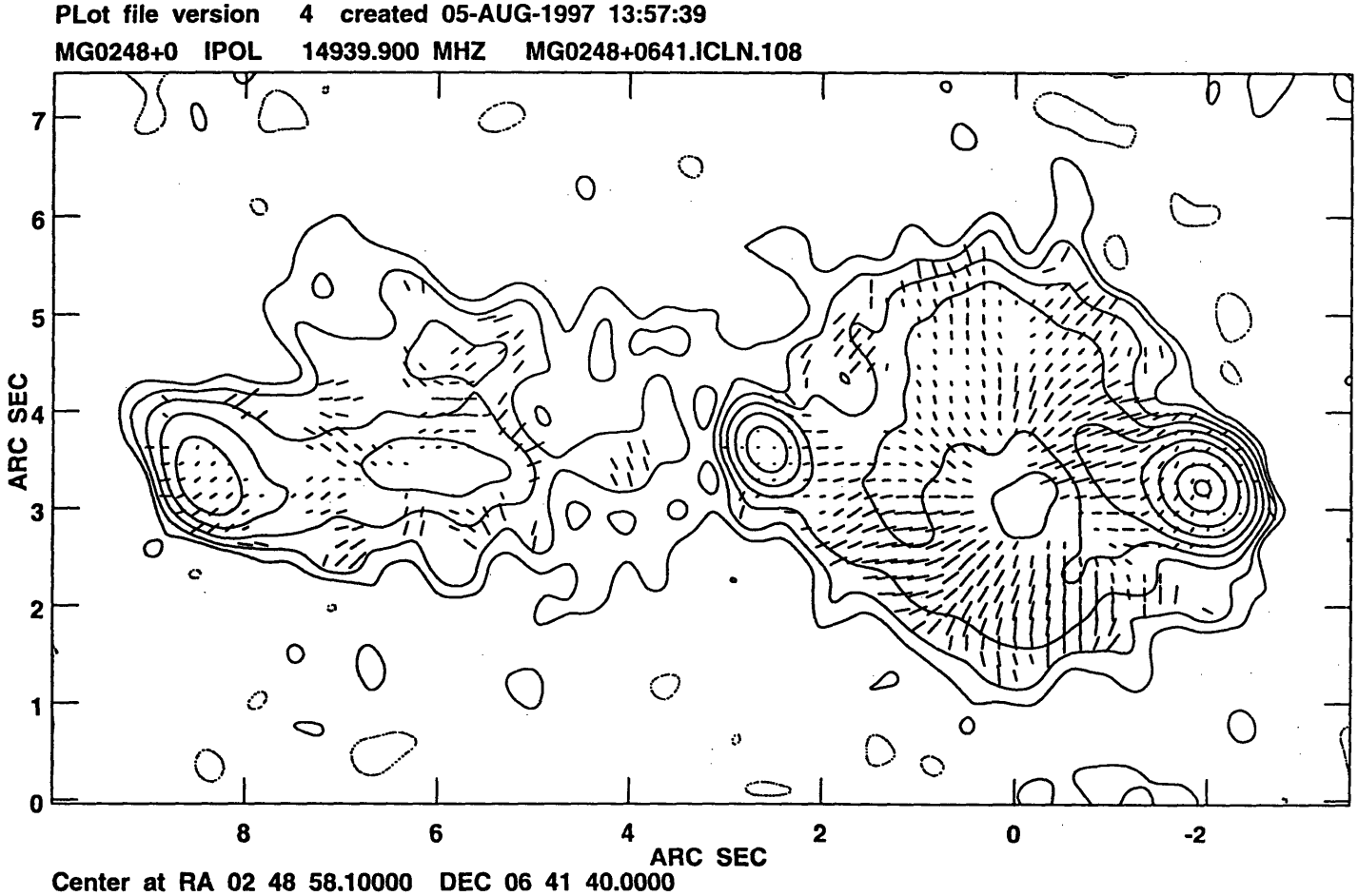

Center at RA 02 48 58.10000 DEC 06 41 40.0000
Pol line 1 arcsec = 3.0000E+00 RATIO
Peak flux = 2.5814E-02 JY/BEAM
Levs = 2.5814E-04 * (-0.500, 0.500, 1.000,
2.000, 4.000, 8.000, 16.00, 32.00, 64.00,
95.00)

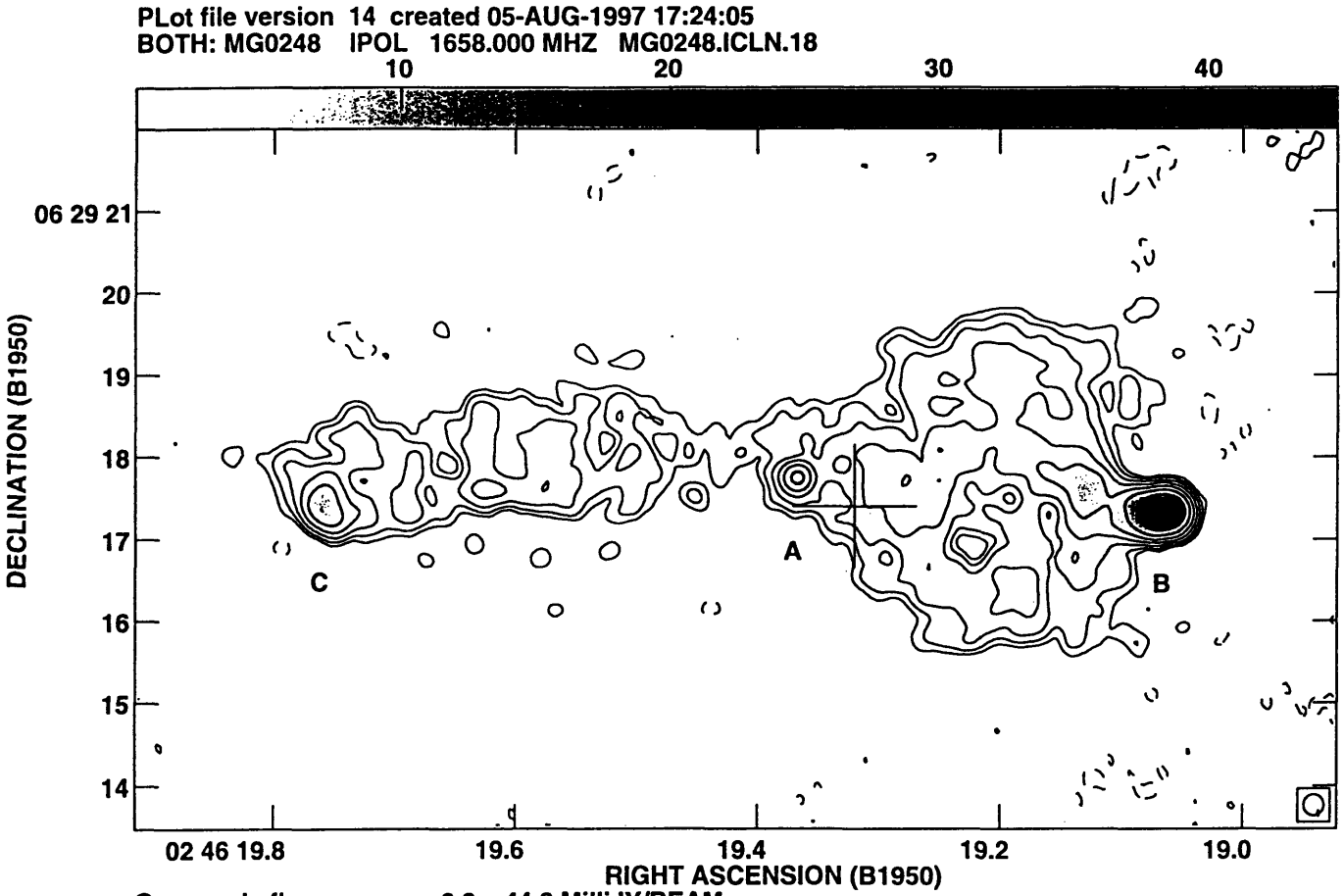

Grey scale flux range= 0.3 44.6 MilliJY/BEAM
Cont peak flux = 4.4579E-02 JY/BEAM
Levs = 3.0000E-04 * (-1.00, 1.000, 2.000,
4.000, 8.000, 16.00, 32.00, 64.00, 128.0,
256.0, 512.0, 1024.)

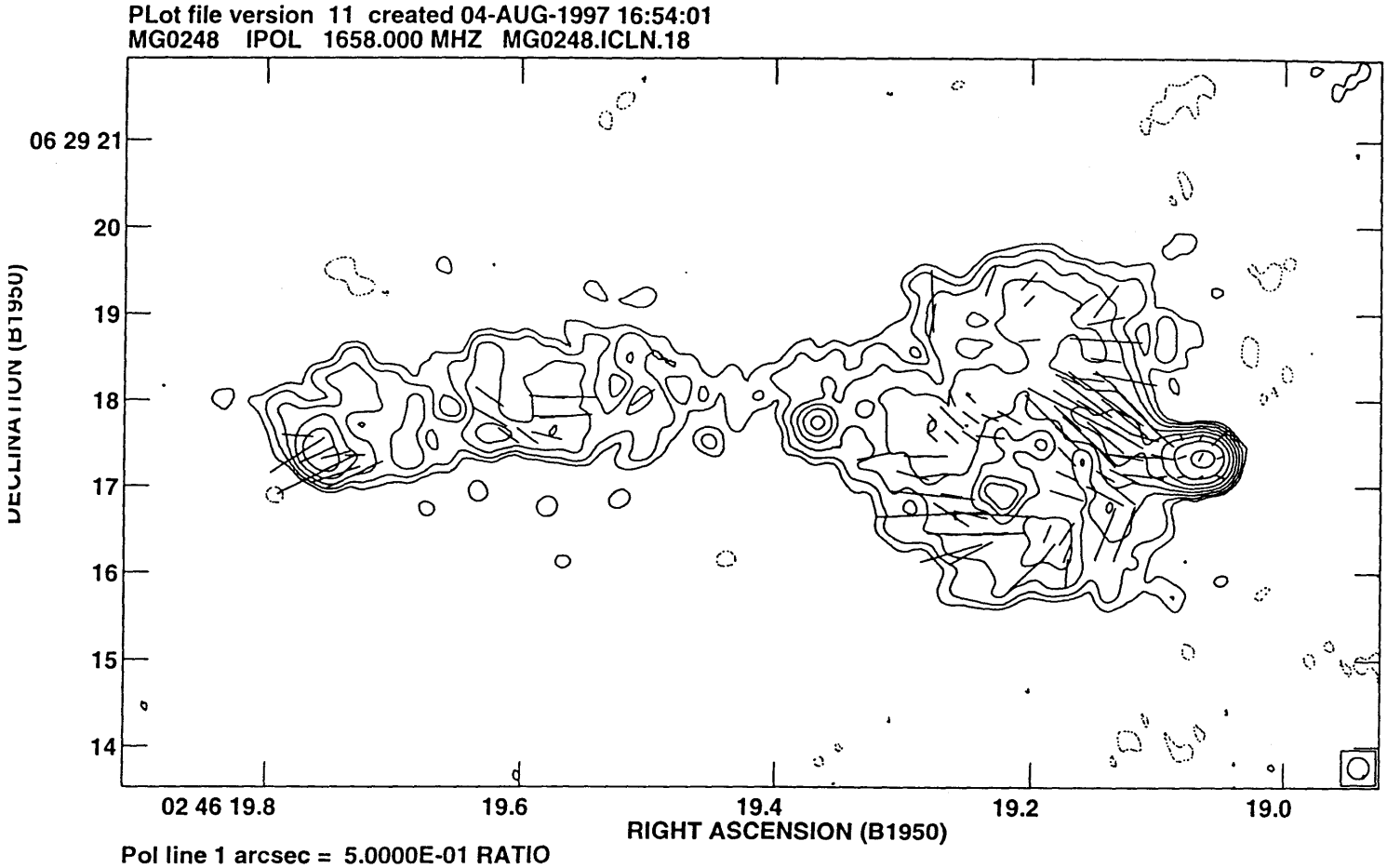
PLot file version 11 created 04-AUG-1997 16:54:01
MG0248 IPOL 1658.000 MHZ MG0248.ICLN.18
06 29 21
20
19
18
17
16
15
14
DECLINATION (B1950)
02 46 19.8
19.6
19.4
19.2
19.0
RIGHT ASCENSION (B1950)
Pol line 1 arcsec = 5.0000E-01 RATIO
Peak flux = 4.4579E-02 JY/BEAM
Levs = 3.0000E-04 * (-1.00, 1.000, 2.000,
4.000, 8.000, 16.00, 32.00, 64.00, 128.0,
256.0, 512.0, 1024.)

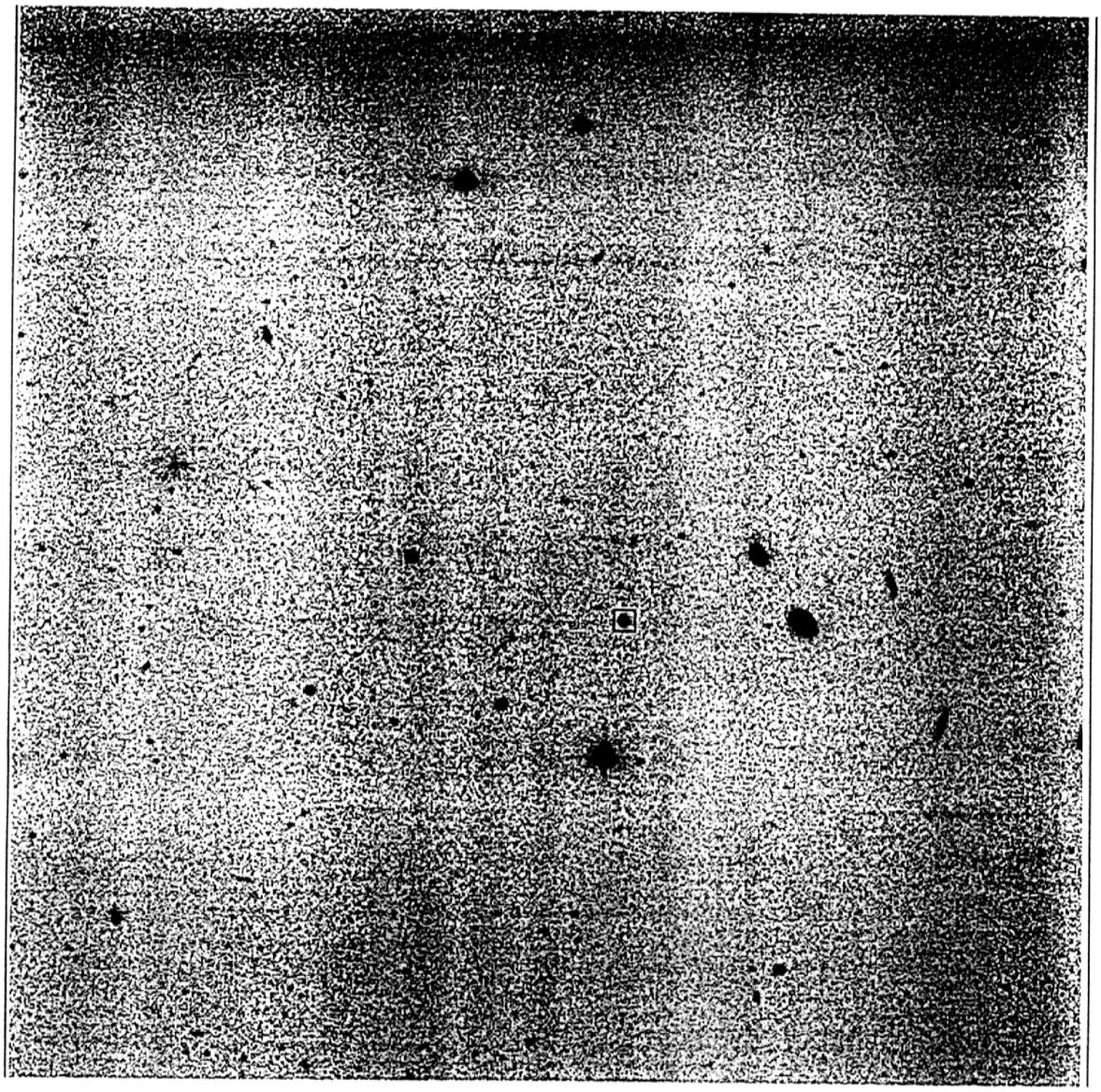

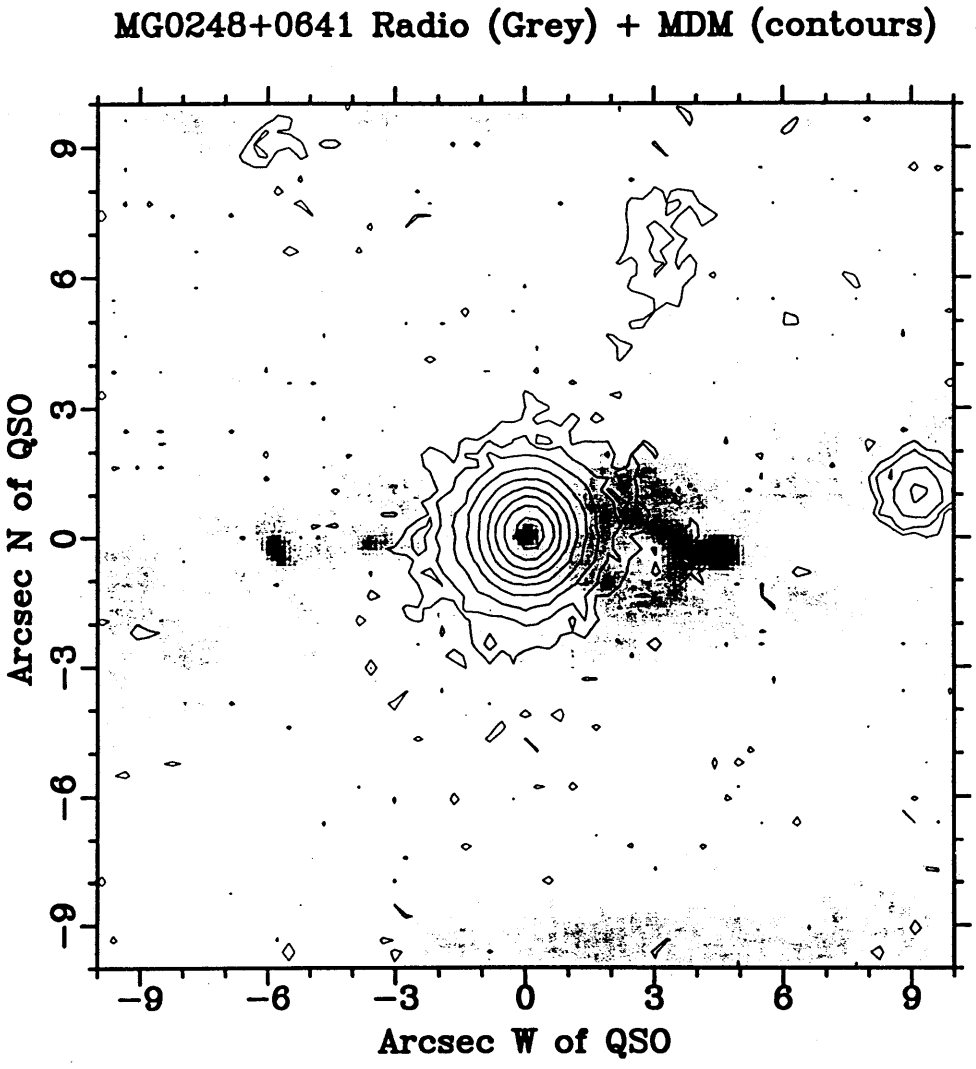
MG0248+0641 Radio (Grey) + MDM (contours)
Arcsec N of QSO
Arcsec W of QSO
9
6
3
0
-3
-6
-9
-9
-6
-3
0
3
6
9
mg0248comb2.ps, Wed Aug 6 13:17:09 1997

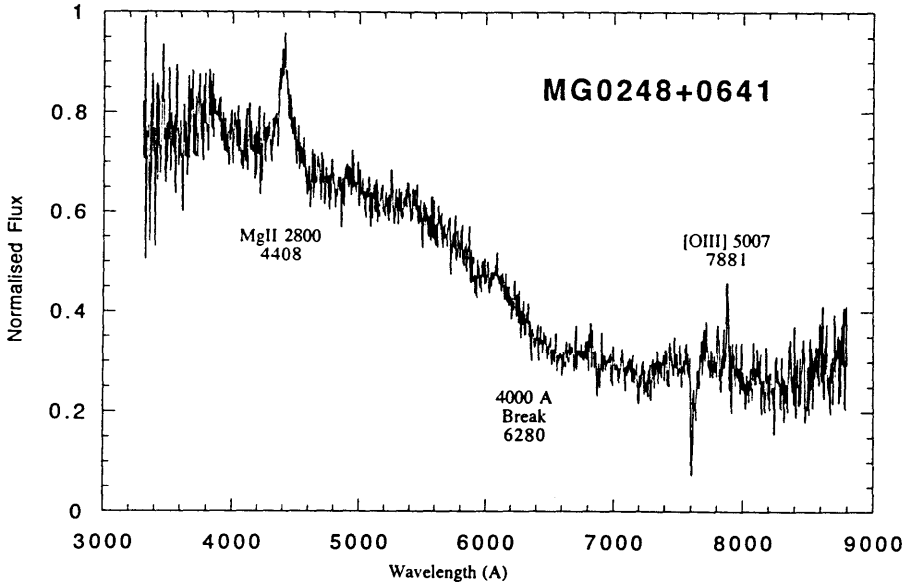
MG0248+0641
MgII 2800
4408
[OIII] 5007
7881
4000 A
Break
6280
Normalised Flux
Wavelength (A)
0
0.2
0.4
0.6
0.8
1
3000
4000
5000
6000
7000
8000
9000

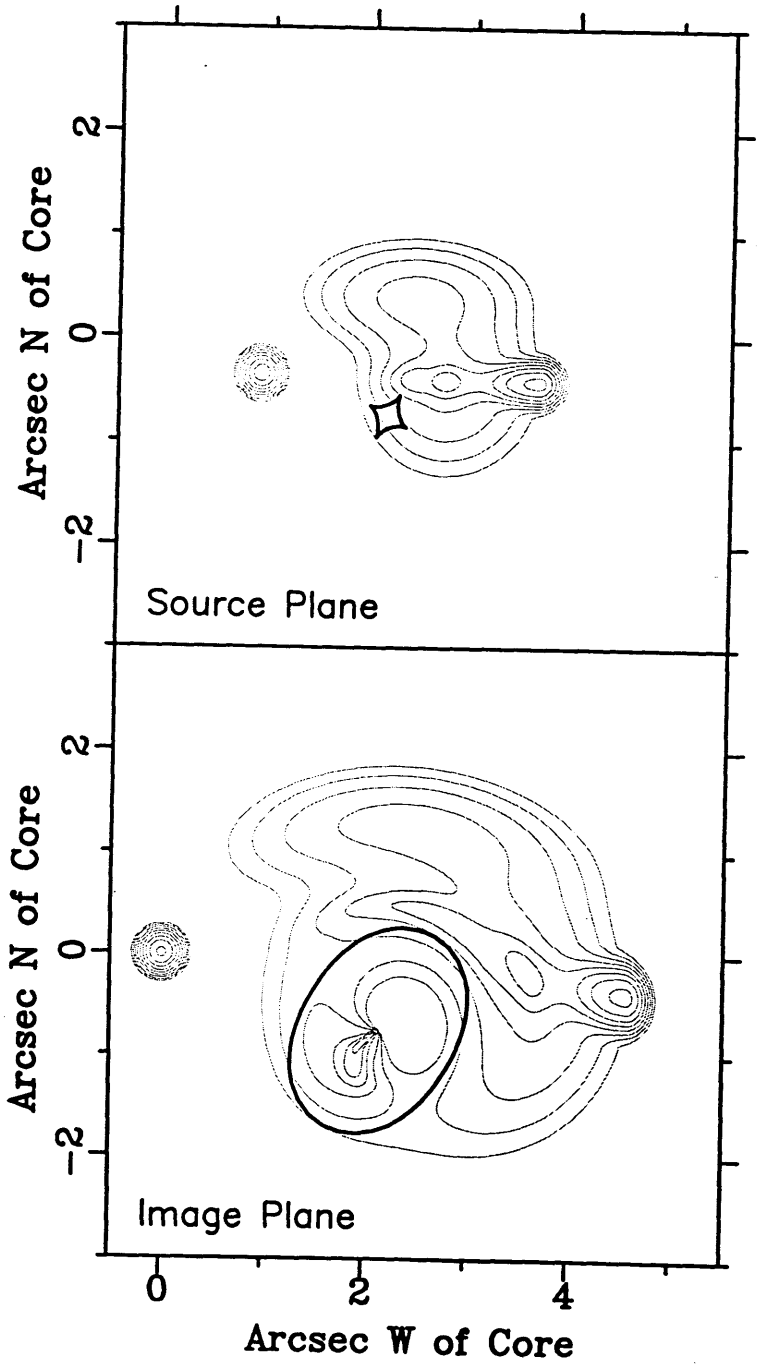
Arcsec N of Core
2
0
-2
Source Plane
Arcsec N of Core
2
0
-2
Image Plane
0
2
4
Arcsec W of Core

THE ANGULAR SIZE DISTRIBUTION OF 4741 RADIO SOURCES IN THE MIT-VLA SNAPSHOT ARCHIVE

A. FLETCHER, B. BURKE, S. CONNER AND J. LEHÁR
Massachusetts Institute of Technology
26-344 MIT, 77 Massachusetts Avenue
Cambridge, MA 02139-4307, USA.
EMAIL: bfburke@mit.edu

AND

L. HEROLD
Carnegie Institution of Washington, Dept. of Terrestrial Magnetism
5241 Broad Branch Road, NW, Washington DC 20015-1305, USA

Abstract. The MIT all-sky and VLA snapshot surveys are described, and the scientific results to date are summarized. The largest angular size distribution is given for 4741 MIT-VLA sources, and a Monte-Carlo algorithm is proposed for investigating the cosmological evolution of jets in radio-loud AGN. Further progress requires compiling redshifts for a complete sub-sample.

1. Introduction

Over the past 15 years, the MIT group has been searching for new examples of gravitational lensing, using the VLA. Lenses are useful for estimating H_0 from time delays in variable images, and Λ_0 from lens statistics; also for mapping both dark+visible mass. All-sky MIT surveys have reliably and completely sampled the extragalactic radio source population down to $S_{4.8GHz} \sim 40$ mJy. Flux-limited VLA snapshot surveys of MIT catalog sources have imaged 10 ksrc (1 ksrc = 1000 sources): 7 confirmed lenses have been discovered so far. Ongoing work reveals further lens candidates, and $N > 120$ compact steep-spectrum (CSS) doubles with $0.''2 < \theta < 2.''0$. The largest angular size (LAS) distribution for 4.7 ksrc is presented. With the advent of ultra-deep all-sky radio surveys, that will collect ~ 3 Msrc, the lack of redshift data frustrates the study of radio-loud AGN evolution. We propose an alternative attack on this problem: Monte-Carlo modeling of the evolving jet lengths, whose angular sizes can be measured from high-resolution maps of large ($N > 1$ ksrc) samples.

2. The MIT Surveys

Table 1 lists the MIT 4.8 GHz sky surveys: MIT-Greenbank (MG) in the northern sky, and Parkes-MIT-NRAO (PMN) in the south. $N \sim 71.2$ ksrc with $S_{4.8} > 5\sigma_{rms}$ have been published (Bennett et al. 1986; Langston et al. 1990; Griffith et al. 1990,1991,1993,1994,1995; Wright et al. 1994,1996). About 86% of the 4.8 GHz sky has been scanned to a surface density of $dN/d\Omega \sim 1.8 src/deg^2$ (Fig. 1a).

Survey	Ω(sr)	α_{min}	α_{max}	δ_{min}	δ_{max}	$N_{>5\sigma}$	S_{min}(mJy)
MG I	1.87	$0^h.0$	$24^h.0$	$-0°.5$	$+19°.5$	5974	53 – 106
MG II	1.51	$4^h.0$	$21^h.0$	$+17°.0$	$+39°.2$	6182	41
MG III	1.11	$16^h.0$	$5^h.0$	$+17°.0$	$+39°.2$	4761	40
MG IV	0.504	$15^h.5$	$2^h.5$	$+37°.0$	$+51°.0$	3427	41
PMN S	2.50	$0^h.0$	$24^h.0$	$-87°.5$	$-37°.0$	23277	20 – 50
PMN Z	0.667	$0^h.0$	$24^h.0$	$-37°.0$	$-29°.0$	2400	72
PMN T	2.01	$0^h.0$	$24^h.0$	$-29°.0$	$-9°.5$	13363	42 – 55
PMN E	1.90	$0^h.0$	$24^h.0$	$-9°.5$	$+10°.0$	11774	40

TABLE 1. The MIT 4.8 GHz Sky Surveys.

Survey	Observations	ν(GHz)	δ_{min}	δ_{max}	$N_{\rm VLA}$
MGVC	1981 – 1986	4.87	$+0°.0$	$+20°.0$	~ 4100
MGVX	1989 – 1993	8.44	$+20°.0$	$+40°.0$	~ 3700
PMNVX	1991 – 1995	8.44	$-30°.0$	$-0°.0$	~ 2100

TABLE 2. The MIT VLA 4.8 and 8.4 GHz Snapshot Surveys.

Table 2 lists the 3 MIT-VLA lens searches in $-30° < \delta < +40°$. The first 4 lenses were found in the MGVC survey at C-Band. The next campaigns to the north (MGVX) and south (PMNVX) used the more sensitive X-Band receivers. Raw data for 9.9 ksrc are stored at MIT. Resolution at 'A' array is $\theta \sim 0.''25$. With bandwidth $\Delta\nu \sim 50$ MHz in each of 2 IFs, and integrations of $\Delta t \sim 90s$, the map noise is typically $I_{rms} \sim 0.25$ mJy/bm, close to the theoretical limit.

3. Summary of Results

7 confirmed radio lenses are known in the MIT-VLA survey region; 1 was found in the JVAS/CLASS survey (MG2016 Lawrence et al. 1984; MG1131,MG0414 Hewitt et al. 1988,1992; MG1654 Langston et al. 1989; MG1549,MG0751 Lehár et al. 1993,1997; JVAS/MG1424 Patnaik et al. 1992). The current MIT-VLA lens rate is $\sim 1/1000$, which is half of the theoretical value (Turner, Ostriker & Gott

1984). If undetected lenses exist in our sample, then further promising candidates should be found (Conner et al. 1992; Fletcher et al. 1995; Herold 1996 & Fig. 2). Other statistics: with {S=steep-spectrum;F=flat;P=point;E=extended;O=POSS ID}, we find $f_S \sim 0.72, f_P \sim 0.47$ at 8.4 GHz. At 4.8 GHz, more sources appear unresolved: $f_P \sim 0.61$. At 8.4 GHz, we estimate: $f_{FP} \sim 0.17$, $f_{SP} \sim 0.30, f_{SE} \sim 0.42, f_{FE} \sim 0.11$. The overall optical ID rate $f_O \sim 0.40$, with f_O increasing with S & α; bright, flat-spectrum sources are the easiest to optically identify (Lawrence et al. 1984,1986; Herold 1996).

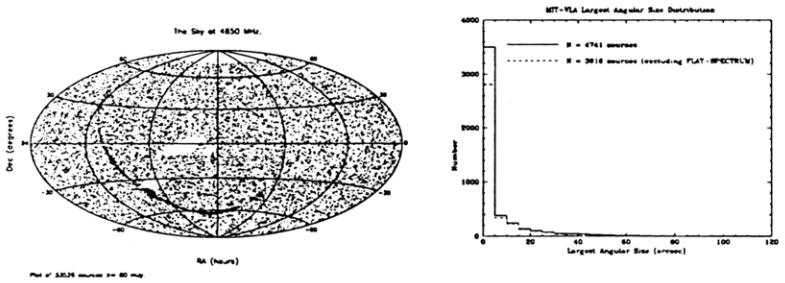

Figure 1. (a) Left: The radio sky at 4.8 GHz. The 87GB (Gregory & Condon 1991) and the PMN surveys (Griffith, Wright et al.) are plotted here. There are $N \sim 34$ ksrc with $S_{4.8} > 80$ mJy. (b) Right: The LAS between component peaks, for $N = 4741$ MIT-VLA sources (solid line). The dashed line is for the spectrally unbiased sample of $N = 3916$ sources (which excludes a sub-sample of purely flat-spectrum sources). The 5″ bin mainly contains unresolved 'point' sources with $\theta_{LAS} < 0.''3$; 'points' are $\sim 47\%$ of all radio sources, at 8.4 GHz.

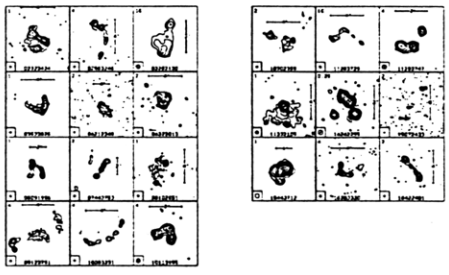

Figure 2. New MGVX gravitational lens candidates from Herold 1996. Included is the confirmed quadruple lens MG1424+2255, first discovered in the JVAS/CLASS flat-spectrum survey (Patnaik et al. 1992). Other MG & PMN candidates appear in Fletcher et al. 1995.

A representative sample of $N > 120$ compact double-lobed radio galaxies ($0.''2 < \theta < 2.''0$) has been extracted. These are mostly steep-spectrum, and thus belong to the CSS class (Fanti et al. 1995). Deep BVRI imaging, to $R_{lim} \geq 22$ at MDM 1.3m & CTIO 1.5m, shows that these 'close doubles' are red (Cooray et al. 1996,1997). Their narrow [OII]&[OIII] emission lines place them at low to intermediate redshift

($z < 1$). Why they appear so small is unknown. Other work on CSS sources rules out projection effects (Fanti et al. 1988), as there are too many observed cases. They may be young, just starting to propel jets into the IGM. Otherwise, they are mature, but with jets frustrated by a dense, dusty IGM. Finally, Fig. 1(b) shows the LAS histogram for 4.7 ksrc. Resolution bias limits analysis to $0.''2 < \theta_{LAS} < 120''$. As many as $\sim 47\%$ of all radio sources are unresolved by 'A' array. This compactness persists: 74% lie within 5", 82% within 10".

4. Simple Unified Models for Radio Jets in AGN

Equation 1 defines the jet angular size θ as the core-lobe separation in sources extended on kpc scales. The geometry is defined in Fig. 3(a).

$$\theta = \frac{\int_0^t v(\tau) \sin i \, d\tau}{d_A(z; H_0, \Omega_0, \Lambda_0)}. \quad (1)$$

The angular diameter distance d_A depends on the chosen Big Bang cosmology. We start with those extended sources that have a clear measure of core-lobe separation at the VLA, and seek unification of these in a single model. Supplementary modifications may, in future, be made by consulting data with different resolutions (e.g. VLBI surveys & NVSS); in this way, point sources and large, extended sources outside our resolution range could also be included within the unification hypothesis. The evolving radio luminosity function comes from other work (e.g. Condon 1984ab,1989; Dunlop & Peacock 1990). To estimate the typical jet head propagation velocity v, simple models for the speed as a function of jet length ($v = v(r)$) may initially be used (e.g. Daly 1994 & Fig. 3(b)). This is solved for $r(t)$, where t is the jet age. The inclinations i are isotropic, as relativistic beaming flux bias is negligible on kpc scales. Finer adjustments may include a dependence of v on the source power $P \sim f(L)$, and perhaps on the IGM density $\rho \sim g(z)$ (e.g. Kapahi 1989). The following Monte-Carlo algorithm is proposed (Fletcher 1997):

1. Choose a cosmology $(H_0, \Omega_0, \Lambda_0)$.
2. Choose a radio luminosity function evolving with redshift $\Phi(L, z)$.
3. Integrate $\Phi(L, z)$ to obtain the redshift distribution $N(z)$.
4. Choose a jet head propagation velocity model $v = v(r)$.
5. Start the loop through each source (index j): Pick a random z_j from $N(z)$.
6. Assign a random age t_j from a uniform distribution ($t_j < 10^8$ yr).
7. Assign a random inclination i_j from an isotropic distribution.
8. Assign a random luminosity L_j, from $\Phi(L, z)$, that survives Malmquist bias.
9. Integrate velocity v to estimate the jet length $r_{est,j}$ at age t_j.
10. Calculate the actual jet length r_j (if this depends on L_j and z_j) from $r_{est,j}$.
11. Calculate core-lobe separation θ_j from Eqn. 1; bin into histogram $N_{model}(\theta)$.
12. Repeat from step 5, looping through j for ~ 10 ksrc.
13. Find χ^2_ν of N_{model} fitted to N_{data}, in the resolution-unbiased region.
14. Repeat from step 1, until the best fits are found.

Without observed redshifts, the results will be model-dependent, and only suggestive at best. It is hoped that the typical jet advance speed may be 'measured' from

the MIT-VLA data. We propose that all unified radio source schemes be robustly tested against as many complementary data sets as possible. Models for the joint distribution $N(S,\theta)$ may be a useful discriminant (as redshifts are not required in the measurement of this function).

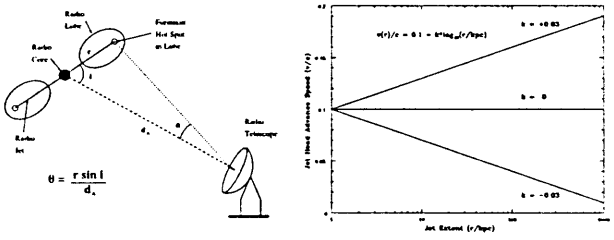

Figure 3. (a) Left: A simple geometric model for calculating the jet angular size θ. (b) Right: Simple models for jet speed v as a function of distance r from the core.

5. Future Prospects

As 90% of the MIT-VLA sample is spectrally unbiased, many interesting sub-samples may be defined: new VLA/ATCA calibrators; unresolved, flat-spectrum, compact steep-spectrum & ultra-steep-spectrum sources; high-redshift quasars & distorted radio galaxies, to name just a few possibilities. Multi-wavelength cross-correlation with other all-sky surveys (e.g. POSS, IRAS, ROSAT) holds great scientific potential for understanding radio-loud AGN physics. Optical identifications will be available from DSS/APM/COSMOS. Correlation with other radio surveys has begun (Fletcher et al. 1996). VLA data for a complete sample of the 400 brightest MG sources are available; redshifts may be estimated from K-Band imaging. Completion of the Archive will require a few person-years. The immediate tasks are to optically follow-up the lens candidates, and to reduce the photometric and spectroscopic data for the CSS 'close doubles'.

6. Conclusions

The MIT all-sky and VLA snapshot surveys have yielded 7 radio-loud gravitational lenses. The 10 ksrc MIT-VLA sample may be used to define many interesting sub-samples. With the precise VLA measurement of jet angular sizes, we propose an attack on the cosmological evolution of radio sources, by modeling the jet angular size distribution for large samples. However, real progress is only possible via systematic compilation of redshifts for complete sub-samples.

Acknowledgments: This work was supported in part by a National Science Foundation (NSF) Grant. The VLA is run by the National Radio Astronomy Observatory (NRAO), which is operated by Associated Universities, Inc., under cooperative agreement with the NSF. ABF and BFB acknowledge J. Condon (NRAO) and M. Bremer (IAP) for partial financial support of this presentation.

References

Bennett, C.L., Lawrence, C.R., Burke, B.F., Hewitt, J.N.,& Mahoney,J.,1986, ApJS 61:1 (MG I)

Condon, J.J., 1984a, ApJ, 284, 44; 1984b, ApJ, 287, 461

Condon, J.J., 1989, ApJ, 338, 13

Conner, S.R., Fletcher, A., Herold, L., & Burke, B.F., 1993, in "Sub-arcsecond Radio Astronomy", eds. R.J. Davis and R.S. Booth, 154

Cooray, A.R., Fletcher, A.B., Conner, S.R., Burke, B.F., Herold, L., 1996, 187th AAS Meeting, BAAS 12.03, 1298 (MIT-VLA CSS close doubles)

Cooray, A.R., 1997, MIT B.S. Thesis (MIT-VLA CSS close doubles)

Daly, R., 1984, ApJ, 426, 38

Dunlop, J.S., & Peacock, J.A., 1990, MNRAS, 247, 19

Fanti, C., Fanti, R., Parma, P., Nan Rendong, Schilizzi, R.T., 1988, IAU 129, "The impact of VLBI on astrophysics and geophysics", eds. M.J. Reid & J.M. Moran, 297 (CSS)

Fanti, C., Fanti, R., Dallacasa, D., Schilizzi, R.T., Spencer, R.E., & Stanghellini, C., 1995, A&A, 302, 317 (CSS)

Fletcher, A.B., Burke, B., Conner, S., Herold, L., Cooray, A., Haarsma, D., Crawford, F., & Cartwright, J., 1995, IAU 173, eds. C.S. Kochanek & J.N. Hewitt, 401

Fletcher, A., Conner, S., Crawford, F., Cartwright, J., Burke, B., Pariiskii, Y.N., Soboleva, N.S., Kopylov, A.I., Temirova, A.V., Verkhodanov, O.V., Naugol'Naya, M.N., 1996, Astronomy Reports 40, 759 (MGVC/RATAN-600m)

Fletcher, A.B., 1997, MIT Ph.D. Thesis, in preparation (PMNVX)

Gregory, P.C., & Condon, J.J., 1991, ApJS, 75: 1011 (87GB)

Griffith, M., Langston, G., Heflin, M., Conner, S., Lehár, J.L., & Burke, B., 1990, ApJS 74, 129 (MG III)

Griffith, M.R., Langston, G., Heflin, M., Conner, S., & Burke, B., 1991, ApJS, 75, 801 (MG IV)

Griffith, M.R., & Wright, A.E., 1993, AJ, 105, 1666 (PMN)

Griffith, M.R., Wright, A.E., Burke, B.F., & Ekers, R.D., 1994, ApJS, 90, 179 (PMN Tropical)

Griffith, M.R., Wright, A.E., Burke, B.F., & Ekers, R.D., 1995, ApJS, 97, 347 (PMN Equatorial)

Herold, L., 1996, MIT Ph.D. Thesis (MGVX)

Hewitt, J.N., Turner, E.L., Schneider, D.P., Burke, B.F., Langston, G.I., & Lawrence, C.R., 1988, Nature 333, 537 (MG1131)

Hewitt, J.N., Turner, E.L., Lawrence, C.R., Schneider, D.P., & Brody, J.P., 1992, AJ, 104, 968 (MG0414)

Kapahi, V.K., 1989, AJ 97, 1

Langston, G.I., Schneider, D.P., Conner, S.R., Carilli, C.L., Lehár, J.L., Burke, B.F., Turner, E.L., Gunn, J.E., Hewitt, J.N., & Schmidt, M., 1989, AJ 97, 1283 (MG1654)

Langston, G.I., Heflin, M.B., Conner, S.R., Lehár, J.L., Carilli, C.L., & Burke, B.F., 1990, ApJS 72: 621 (MG II)

Lawrence, C.R., Schneider, D.P., Schmidt, M., Bennett, C.L., Hewitt, J.N., Burke, B.F., Turner, E.L., Gunn, J.E., 1984, Science, 223, 46 (MG2016)

Lawrence, C.R., Bennett, C.L., Hewitt, J.N., & Burke, B.F., 1984, ApJL 278: L95 (MGVC)

Lawrence, C.R., Bennett, C.L., Hewitt, J.N., Langston, G.I., Klotz, S.E., Burke, B.F., & Turner, K.C., 1986, ApJS 61: 105 (MGVC)

Lehár, J.L., Langston, G.I., Silber, A., Lawrence, C.R., & Burke, B.F., 1993, AJ, 105, 847 (MG1549)

Lehár, J.L., Burke, B.F., Conner, S.R., Falco, E.E., Fletcher, A.B., Irwin, M., McMahon, R.G., Muxlow, T.W.B., Schechter, P.L., Feb. 1997, AJ, submitted (MG0751)

Patnaik, A.R., Browne, I.W.A., Walsh, D., Chaffee, F.H., & Foltz, C.B., 1992, MNRAS, 259, 1 (JVAS/MG1424)

Turner, E.L., Ostriker, J.P., & Gott, J.R. III, 1984, ApJ, 284, 1

Wright, A.E., Griffith, M.R., Burke, B.F., & Ekers, R.D., 1994, ApJS, 91, 111 (PMN Southern)

Wright, A.E., Griffith, M.R., Hunt, A.J., Troup, E., Burke, B.F., & Ekers, R.D., 1996, ApJS, 103, 145 (PMN Zenith)

CALIBRATION ISSUES IN THE SEARCH FOR LARGE-SCALE ANISOTROPIES IN THE 87 GREEN BANK AND PARKES-MIT-NRAO SURVEYS

F. CRAWFORD, I.M. AVRUCH, A.B. FLETCHER, M.R. GRIFFITH AND B.F. BURKE
Massachusetts Institute of Technology
MIT Room 37-624, 77 Mass. Ave., Cambridge, MA 02139, USA

1. Introduction

Until recently, there were no large scale radio surveys which were sensitive enough to have a sufficient number of sources to detect a dipole anisotropy. The 87 Green Bank (87GB) (Gregory and Condon, 1991) and Parkes-MIT-NRAO (PMN) (Griffith, 1993; Griffith *et al.*, 1994; Wright *et al.*, 1994) radio surveys are the first such efforts and are the most complete radio surveys to date. We would like to analyze the source counts in the 87GB and PMN surveys in order to test the isotropy of the sky distribution of extragalactic sources at cosmological redshifts. Of particular interest is a dipole anisotropy, which could arise from local motion with respect to the rest frame of extragalactic radio sources. Any detected anisotropy will give information about the source distribution at a redshift of z $\sim$ 1 (Condon, 1988), an epoch between the COBE observations at $z \sim 1000$ and the local universe.

2. Data Calibration Issues

Accurate flux calibration is extremely important when searching for the cosmic dipole effect. One must ensure that the surveys are calibrated both internally and with respect to each other before looking for a dipole. The 87GB and PMN surveys overlap in the region $0° < \delta < +10°$, and we can use the measured fluxes of common sources to compare the flux calibration between the two surveys. The left plot in Figure 1 shows PMN flux vs. 87GB flux with the line $S_{87GB} = S_{PMN}$ (error bars are not shown). At low fluxes ($S < 70$ mJy), there is a significant bias in the distribution. The right plot in Figure 1 shows the binned average of $(S_{PMN} - S_{87GB})$ as a function of S_{87GB} for sources with $50 < S_{87GB} < 100$ mJy. There is a significant offset below about 70 mJy. However, above 70 mJy there does not appear to be a clear convergence to zero offset. These results are problematic when considering the calibration of the surveys with respect to each other. The

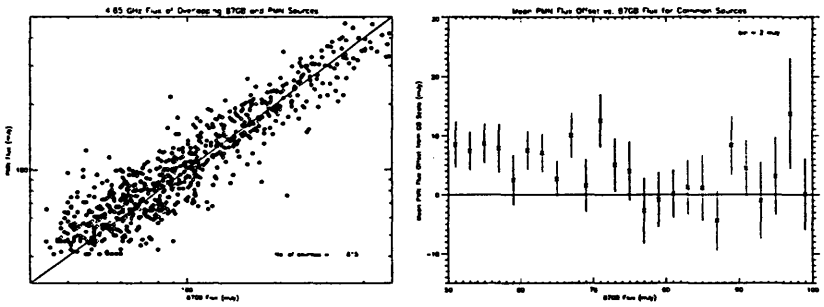

Figure 1. Left: Log plot of PMN flux vs. 87GB flux for sources common to both surveys. The diagonal line represents the expected relation $S_{GB} = S_{PMN}$. Right: Average flux offset (PMN minus 87GB) vs. 87GB flux for common sources between 50 and 100 mJy.

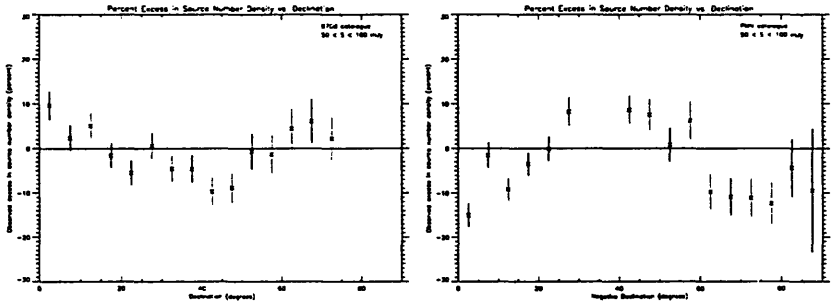

Figure 2. Observed excess surface density as a function of declination for sources with $50 < S < 100$ mJy in the 87GB (left) and PMN (right) catalogues.

87GB and PMN surveys also exhibit calibration variations internally as a function of declination. Figure 2 shows the observed excess surface density for sources with $50 < S < 100$ mJy in 5 degree rings of constant declination for both catalogues. One can see parabolic patterns in the data which may be related to the zenith angle gain curves for each telescope. Since the magnitude of the excess is of order 10%, the expected dipole effect (~500 km/s) will be overwhelmed by these effects. Thus the surveys must be both internally calibrated and calibrated with respect to each other before a complete search for large-scale anisotropies is undertaken.

References

Condon, J.J. 1988. in *Galactic and Extragalactic Astronomy*, eds. Verschuur, G.L., and Kellerman, K.I., Springer-Verlag

Gregory, P.C., and Condon, J.J. 1991. *Ap. J. Supp.*, **75**, 1011

Griffith, M.R. 1993. MIT Ph.D. Thesis

Griffith, M.R., Wright, A.E., Burke, B.F., and Ekers, R.D. 1994. *Ap. J. Supp.*, **90**, 179

Wright, A.E., Griffith, M.R., Burke, B.F., and Ekers, R.D. 1994. *Ap. J. Supp.*, **91**, 111

Optical Identification of Close Doubles and Gravitational Lenses from the MIT-Green Bank-VLA and the Parkes-MIT-NRAO-VLA 8.43 GHz Surveys.

by

Asantha Roshan Cooray

Submitted to the Department of Physics
on December 10, 1995, in partial fulfillment of the
requirements for the degree of
Bachelor of Science in Physics

Abstract

We present the results of the optical identifications and photometry from our survey of a sample of 61 objects selected from the MIT-Green Bank (MG) and Parkes-MIT-NRAO (PMN) radio source catalogs at 4.85 GHz. 60% of our sample consists of small angular size sources with double structure, similar to that found in double-lobed radio galaxies, with an angular size in the range $0.25'' \leq \theta \leq 2.0''$. The rest of the sample either consists of candidate gravitational lens systems or objects with multiple structure as seen in VLA X-Band (8.43 GHz) snapshots. All of these sources have moderate to steep radio spectral indices ($S_\nu \propto \nu^{-\alpha}$, $\alpha \geq 0.7$) with a minimum flux density of 90 mJy, at 4.85 GHz. Our selection was made primarily to identify and characterize the close double radio sources through optical CCD imaging, and to identify optical counterparts for the gravitational lens systems.

Our radio-selected sample was imaged mainly in the red (R) filter, using the Michigan-Dartmouth-MIT (MDM) 1.3m telescope at Kitt Peak, Arizona on September 12th to 27th, 1994. We also obtained I observations for 55% of our selected fields. Our identification rate for northern sky (MG) objects is 86%, whereas it is 65% for the southern sky (PMN) objects. The median R magnitude for 10 galaxies and 11 stellar-like objects identified as counterparts for MG sources is $\sim$ 19.8, whereas the median I magnitude for the same set of objects is $\sim$ 18.5. 3 more faint and presumably very distant galaxies and quasars in the MG catalog still lack optical source structure classifications, to a limiting magnitude of R $\sim$ 23.5. The median R and I magnitudes for the 8 galaxies and 3 stellar-like objects identified as PMN optical counterparts are 19.15 and 18.25 respectively. The completeness of our identifications is greater than 97%, whereas the reliability is 95% for both hemispheres. In this thesis, we discuss the optical structure of some of these objects, and compare them to the radio structure as seen with the VLA.

Thesis Supervisor: Bernard F. Burke

New Gravitational Lens Candidates from VLA snapshots of MG and PMN radio sources

A.Fletcher, S.Conner, A.Cooray, B.Burke (MIT), L.Herold (CIW & MIT)

The four 4.85 GHz MIT-Greenbank (MG) surveys together revealed 20,344 radio sources over 5.0 steradians ($-0.°5 < \delta < 51°; |b| > 10°$), down to a limiting flux density of $S_{4.85} \sim 41$ mJy. The 4.85 GHz Parkes-MIT-NRAO (PMN) Southern survey lists 23,277 sources over 2.5 steradians ($-87.°5 < \delta < -37°; |b| > 10°$), down to $S_{4.85} \sim 35$ mJy, while the Tropical and Equatorial surveys ($-29° < \delta < +10°; |b| > 10°$) together give 25,137 sources over 3.9 steradians, down to $S_{4.85} \sim 40$ mJy. The estimated completeness for each of these surveys is $> 93\%$, while their reliabilities are $> 90\%$. Over the past 15 years, the MIT group has been imaging flux-limited samples of these sources with the VLA, at 4.85 and 8.43 GHz. One of our goals is to find new instances of gravitational lensing, and another is to systematically study the radio and optical properties of radio-loud AGN. We now have VLA snapshots of ~ 6500 MG and ~ 2000 PMN sources. The initial 1980's 4.85 GHz imaging attempt on MG sources found 5 bona fide lenses: MG 2016 (triple), MG 1131 (ring), MG 0414 (quad), MG 1654 (ring), MG 1549 (ring). From the 1990's 8.43 GHz effort, we present 5 new examples of gravitational lens candidates: MG 0248 (ring?), MG 1011 (triple?), PMN 1254 (quad?), PMN 1542 (quad?) and PMN 0837 (ring?). We have also found ~ 120 "close" double-lobed radio galaxies ($0.''25 < \theta < 2''$), whose physical nature is not yet understood - perhaps some of these may be doubly-imaged lenses. Our deep CCD imaging campaign, using the Michigan-Dartmouth-MIT telescopes, has identified optical counterparts ($17 < R < 24$) for all of the lens candidates, and many of the close doubles. We intend to obtain spectroscopic data on the brighter counterparts, using larger telescopes, in the near future. Our most promising and intriguing source from the new crop is the candidate Einstein Ring MG 0248 ($\theta_{dia} \sim 2.''6$). While the background radio core is seen optically as an $R = 18.6$ object, the implied mass of $\sim 10^{12} M_{\odot}$, enclosed by the ring, is undetected down to $R \sim 24$. If this is an Einstein Ring, then the lensing mass has high M/L and is faint in optical, infrared and radio frequencies.
Abstract submitted for AAS [AAS] meeting

Date submitted: October 28, 1995 Electronic form version 1.6

RESEARCH LABORATORY *of* ELECTRONICS
MASSACHUSETTS INSTITUTE OF TECHNOLOGY
CAMBRIDGE, MASSACHUSETTS 02139-4307

FOR RELEASE: 10:00 am CST, January 15, 1996.

NEW "INFANT" RADIO GALAXIES: A MISSING LINK?

Astronomers are announcing today that they have found a large number of "infant" radio galaxies, which seem to have only recently started to pushing out their jets. The first results from a study of these sources is being presented by Asantha R. Cooray, André B. Fletcher, Samuel R. Conner, Lori K. Herold and Dr. Bernard F. Burke of the Massachusetts Institute of Technology, in Cambridge, Massachusetts to the American Astronomical Society Meeting in San Antonio, Texas. The investigators believe that these young radio galaxies will help answer one of the many key questions in modern extragalactic astronomy: what is the origin of the radio sources we see in the universe, and how do they evolve? Detailed investigations of these "infant" galaxies are turning up results that may link them with the very compact radio sources mapped with high-resolution Very Long Baseline Interferometry (VLBI), and also with the relatively huge arc-minute scale "classical doubles" easily observed by single dish radio telescopes.

The 36 km Very Large Array (VLA) near Socorro, New Mexico was used to make the findings during a systematic survey campaign to uncover new cases of gravitational lensing. Over 4000 VLA snapshot images revealed a large number of unusually small radio sources, now known as the "MIT Close Double" radio galaxies. These show two lobes of radio emission, of similar brightness, separated by an angle between 0.″25 and 2.″0 These tiny doubles occur at a rate of $\sim$ 4%. Five possibilities were considered for their physical nature and evolution: (1) normal-sized doubles but seen from a direction close to the jet axis, (2) cosmologically distant (high-redshift) radio galaxies, (3) a relatively young class of sources, having just started to push out jets beyond galactic scales, (4) a class of sources whose jets growth has been "frustrated" by a dense intergalactic medium (IGM), and (5) two images of a gravitationally lensed background source. Possibility (1) has been excluded by previous statistical studies on the angular size distribution of radio sources (there are too many Close Doubles to be explained only by simple projection effects), and (5) was thought to be highly unlikely, based on the relatively few confirmed cases of gravitational lensing known to date.

Which of the remaining possibilities apply to the Close Doubles? Over the past three years, the MIT Radio Astronomy Group has investigated these questions, in a project supported by National Science Foundation. These young galaxies were observed both in the radio with the VLA and the Multi-Element Radio-Linked Interferometer (MERLIN) in Manchester, England and in the optical with the Michigan-Dartmouth-MIT (MDM) Observatory on Kitt Peak, Arizona. The initial set of results of this sample is now released by A. Cooray, A. Fletcher and L. Herold, who studied the close doubles as part of their MIT thesis projects. Altogether, using 130 radio and optical maps, they were able to characterize and constrain the possibilities for the physical evolution of these sources. All of these objects were found to have steep radio spectral indices, and 85% of these galaxies were found with optical iden-

tifications to a limiting R magnitude of 23.5, and over 80% found in the range $19 < R < 23$. They also found these objects to be highly reddened, and most of them appeared as galaxies, rather than quasars. The other important results include the finding that steeper radio spectrum sources are hard to detect optically, and also that fainter optical counterparts are more infrared-bright, as judgged by their R-I colors. The first of these findings may be interpreted as the exhaustion of the core radio and optical emission, as a result of the driving of the jets into the IGM. The second finding seems to indicate a high dust content in the environment of these galaxies, possibly retarding the growth of their jets.

Spectroscopic observations of the Close Doubles at MDM, the Multiple Mirror Telescope (MMT) in Mt. Hopkins, Arizona, and the Canada-France-Hawaii Telescope (CFHT) on Mauna Kea, Hawaii with collaborators Peter Garnavich and Emilio Falco at the Center for Astrophysics, Cambridge, Massachusetts showed that a small sample of these objects have redshifts between 0.1 and 1.0. If these preliminary results are confirmed by future studies, possibility (2), in which these galaxies were considered to be at high redshifts, can be ruled out. This leaves possibilities (3) and (4) for further research.

The final scenario being presented by MIT researchers is the following (see figure 1). The MIT Close Double sample would be the third stage in the displayed evolutionary sequence, the next step beyond the milli-arcsecond scale ($\sim$ 100 LY) VLBI Compact Steep Spectrum (CSS) sources. Radio galaxies of this type, as studied by Roberto Fanti of the Dipartimento di Astronomia at dell'Universita, in Bologna, Italy and his collaborators, occur at a rate of 20% in typical radio surveys. As many as 90% of these CSS sources are succesfully identified in the optical regime, and these are found at redshifts of less than 2. At the top of the evolutionary chain, representing the birth of radio galaxies, are the VLBI Gigahertz Peaked Spectrum (GPS) sources, with high electron densities confined to a compact core. These sources have been extensively studied by Christopher O'Dea of the Space Telescope Science Institute (STScI), in Baltimore, Maryland and his collaborators. According to them, VLBI GPS sources are constrained by a dense and dusty IGM, at scales of $\sim$ 20 LY. VLBI CSS sources represent the stage where GPS sources are starting to grow their jets, and beam them outward. Current models of radio-loud AGN have not taken any of these steep-spectrum sources into account, and thus the exact mechanism of evolution is still unclear. In a recent paper by Megan Urry of the STScI and Paolo Padovani of the Universitia di Roma, Italy, they state that "unification schemes bear on the origin of GPS and CSS sources, and it is important to understand how they fit into the present paradigm." As these sources constitute a non-negligible part of radio samples, it is essential that they be considered in future models. The MIT Close Double sample is important because it is the stage where these sources start to grow their jets, possibly escaping the high IGM environment, to sizes as large as $\sim$ 100 000 LY. It is proposed that these Close Doubles then grow on to various forms of normal doubles, which are commonly found at redshifts of less than 0.1, with typical sizes of $\sim$ 500 000 LY. The "infant" radio galaxies discovered by the MIT Radio Astronomy Group has provided a necessary link in our current understanding regarding the growth of double-lobed radio galaxies.

Figure 1: A suggested evolutionary sequence for double-lobed radio galaxies. The VLBI sources in the top 2 stages come from the Caltech-Jodrell survey of GPS sources (Taylor et al. 1994). The MIT Close Double sample consists of double lobes with larger arcsecond separations. It is speculated that the MIT galactic-sacle sources may form a "missing link" in the chain of events leading to the production of arcminute "classical doubles" at later cosmic epochs, such as the powerful radio galaxy Cygnus A, shown in the bottom frame (from Hargrave and Ryle 1974). The projected lengths, corresponding to the indicated angular dimensions, are given in light years (LY), assuming the stated redshifts.

Figure 2: An example of radio and optical data for one of the ~ 120 MIT Close Doubles: PMN0312-1613. The VLA 8.4 GHz radio contours are overlaid on the optically identified emission found using the deep CCD imaging with the Michigan-Dartmouth-MIT (MDM) 1.3m telescope. Our astrometry shows some good agreement between the optical emission (in the R band) and the central region between the two radio lobes, which are separated by 0."6. Each CCD pixel subtends 0."64.

For more information:
Asantha R. Cooray (617-225-6350, asante@zenobia.mit.edu)
Andre B. Fletcher (617-253-3074, fletcher@zenobia.mit.edu)
Lori Herold (202-686-4399, lherold@dtm.ciw.edu)
Dr. Bernard F. Burke (617-253-2657, bfb@maggie.mit.edu)

Evolution of Double-Lobed Radio Sources.

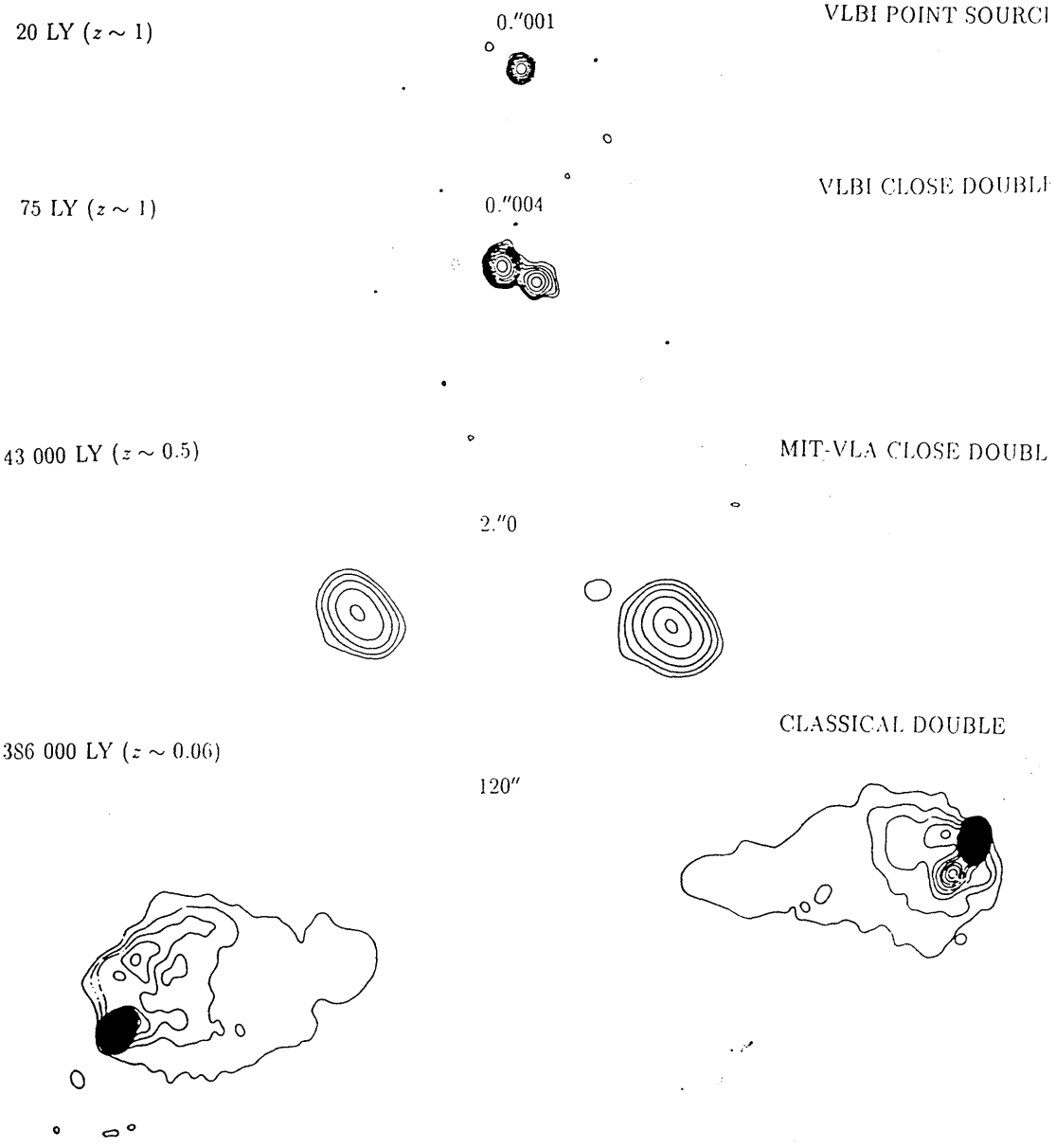

Radio and Optical Imaging of MG and PMN Sources: Close Doubles and Gravitational Lenses

Asantha R. Cooray, André B. Fletcher, Samuel R. Conner, Bernard F. Burke (MIT), Lori Herold (CIW & MIT)

We present VLA maps and optical identifications from our survey of a sample of 50 objects selected from the MIT-Green Bank (MG) and Parkes-MIT-NRAO (PMN) radio source catalogs, with $S_{4.85GHz} > 80mJy$. 85% of our subset belong to a class which is not yet well understood or characterized: the "close" double-lobed radio galaxies, taken here to have angular sizes in the range $0.25'' < \theta < 2.0''$. The rest of the objects either consists of candidate gravitational lens systems, or objects with multiple structure as seen in VLA 8.4 GHz snapshots. All of these objects have moderate to steep spectral indices ($\alpha \geq 0.5$). Over the last year, we have imaged this radio selected sample at the MDM Observatory. Our identification rate is atleast 70% for the optical counterparts of close doubles to a limiting magnitude R $\sim$ 23.5, with the median magnitude of R $\sim$ 19.2 ($17 < R < 23.5$). We also find these objects to be excess in red with all of them in the color range $0 < R - I < 2.5$.

Initial analysis of the close double sample suggest that the spectral index is correlated with the optical magnitude, and that the identification fraction decreases with increasing spectral index. We also find no evidence for alignment between the radio and optical axes, and have not found strong emission lines in a subsample for which we obtained spectroscopy. Physically close doubles may represent (a) cosmologically distant (high-redshift) radio galaxies, (b) normal doubles but seen from a direction close to the jet axis, (c) relatively young class of sources, having just started to push out their jets, (d) class of sources with growth of the jets been "frustrated" by a dense IGM, or (e) 2 images of a gravitationally lensed background source. Each of these possibilities and others will be discussed.

We also present optical identifications and maps for 2 MG and 3 PMN Gravitational Lens Candidates, including MG0248, which is very likely to be a new "Einestein Ring."

Abstract submitted for AAS meeting 183, January 11–14, 1994

Date submitted: February 1, 1998 Electronic form version 1.5

Forging a Radio and Optical Astronomy Link

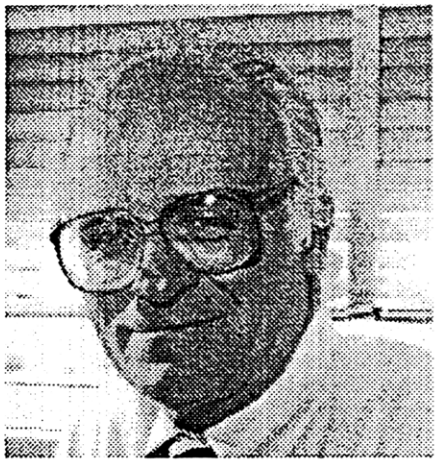

• **Bernard F. Burke**
William A. M. Burden Professor of Astrophysics

The Michigan-Dartmouth-MIT Observatory has been indispensable to the MIT Radio astronomy Group for a number of projects aimed at linking astronomical measurements between optical and radio wavelengths. One example of this has been the use of the McGraw-Hill 1.3-meter telescope over the last 2 years to search for optical counterparts of a sample of 135 radio galaxies which exhibit double lobes when mapped at radio frequencies. These galaxies were first discovered by the radio astronomy group in several systematic 5 GHz surveys of the radio sky: the MIT-Green

Michigan-Dartmouth-MIT Observatory

Bank (MG) surveys of the Northern sky, and the Parkes-MIT-NRAO (PMN) surveys of the Southern sky. Subsequent aperture-synthesis imaging using the Very Large Array (VLA) in New Mexico has revealed numerous examples of "close" double-lobed radio galaxies at 0.3 arc-second resolution. The radio lobes of these galaxies have unusually small separations (less than 2") when compared to the other double-lobed galaxies in a near-complete sample such as ours. While it is almost certain that these close doubles belong to the broad class of galaxies that possess an "active" galactic nucleus (AGN), which are universally observed to radiate over much of the accessible electromagnetic spectrum, not much more astrophysically important information can be gleaned from examining the VLA snapshot images alone. Ground-based observations of these radio-loud AGN at optical wavelengths are a natural way to piece together more clues about the physical nature of these objects. The broad-band power output characteristic of AGN makes it likely that they are detectable at shorter wavelengths, such as in optical light. However, detection of the optical counterpart of an individual radio galaxy depends directly on its radio-optical spectral index, which is a priori unknown within this newly discovered sample. Conversely, the success rate of finding optical counterparts for these radio galaxies can provide constraints on physical models, via the observed distribution of radio-optical spectral indices.

The widely-believed interpretation of the powerful radiation emitted by AGN is that we are witnessing the consequences of accretion of stellar-mass quantities of matter onto 1 million to 10 billion solar mass black holes (MBH) in the centers of the host galaxies. One striking manifestation of such activity is the formation of high-velocity jets that escape from the galaxy's nucleus and plow into the surrounding intergalactic medium (IGM). In this process, extended balloon-like "lobes" form at the ends of the two jets, and these are filled with relativistic electrons emitting primarily synchrotron radiation. The main physical question to be addressed is : why are the "close doubles" so much smaller than the arc-minute-scale lobe separations normally seen in most other double radio galaxies? At least five reasons spring to mind:

1. They are cosmologically distant (high-redshift) radio galaxies.
2. They are normal doubles seen from a direction close to the jet axis.
3. They are relatively young, having just started to push out their jets.
4. The growth of the jets has been "frustrated" by a dense IGM.
5. Some may be the 2 images of a gravitationally lensed background source.

An MIT Five-Year Report (1990-1995)

Whichever of these explanations is closest to the truth, it is clear that the close double sample warrants further investigation. This is also because similar double-lobed sources have been found at much higher radio resolution using Very Long Baseline Interferometry (VLBI) techniques, and the question arises as to whether our sample may form a "missing link" in a postulated angular size evolution of radio sources from milli-arcsecond to arc-minute scales. The optical imaging data from the MDM 1.3-m is a first step in the research direction, and will form part of the synthesis of new results within the Ph.D. theses of two graduate students: Andre Fletcher and Lori Herold-Jacobson, and the B.S. thesis of one undergraduate student: Asantha Cooray.

Preliminary astrometry and photometry by Asantha and Lori has shown that these close doubles have a fairly high detection rate (about 3 times out of 4) when optically imaged down to an apparent limiting magnitude of about R=22.0. This is possible within a half- hour integration using the MDM liquid-nitrogen-cooled charge-coupled devices (CCDs) as detectors. Without the high quantum efficiency of these CCDs, this survey work would not be possible. Figure 1 shows a marginal optical identification of a faint galaxy positionally coincident with a close radio double: PMN0029-1111. This particular counterpart is close to the detection threshold, and could not have appeared in either the Northern Palomar Observatory Sky Survey (POSS), nor in the European Southern Observatory (ESO) Survey. Both of these classic all-sky optical surveys relied on relatively inefficient photographic plates. Figure 2 shows a more convincing discovery of an optical counterpart to a close double: PMN0315-1613. These images are somewhat degraded by mediocre atmospheric seeing conditions at the MDM 1.3-m, but this problem can be alleviated by further imaging using the Hiltner 2.4-m, which enjoys better seeing. For the present, the seeing conditions are not crucial for establishing optical counterparts.

The photometry seems to indicate that these optical counterparts are highly reddened, presumably due to extinction from intergalactic gas and dust along cosmological lines of sight extending out into the high-redshift regions of our universe. The systematic MDM optical survey of the close double sample will provide necessary information for statistical studies of this cosmologically-distributed population, and also perhaps reveal clues about radio galaxy formation and evolution in the early universe. For this research program, and also for other radio-optical cross-identification survey work, the fundamental science made possible by routine access to the MDM 1.3-m telescope is essential for identifying

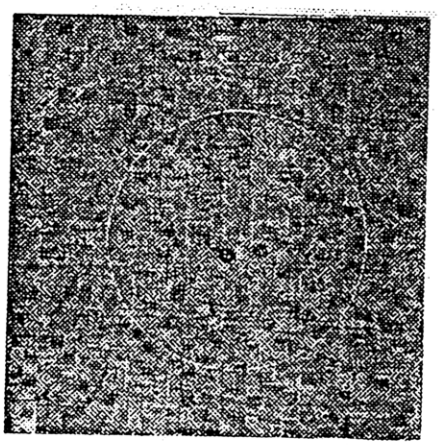

Figure 1: A greyscale image of a faint R=21.9 optical counterpart of a close double-lobed radio galaxy PMN0029-1111, detected in 30 minutes of integration with a cooled CCD detector, at the MDM McGraw-Hill 1.3-m telescope. The VLA 8.4 GHz contours are overlaid to show the positional coincidence of the optical counterpart with the close double radio source, of angular size 1.6". The pixel size is 0.63", the circle is 20 pixels = 12.6" in diameter, and the vertical scale has tick marks at 1" intervals. This marginal detection was not possible using the less efficient photographic plates of the well-known ESO all-sky optical survey. More sensitive observations using larger telescopes, in better seeing conditions, are required to detect and resolve this close radio double.

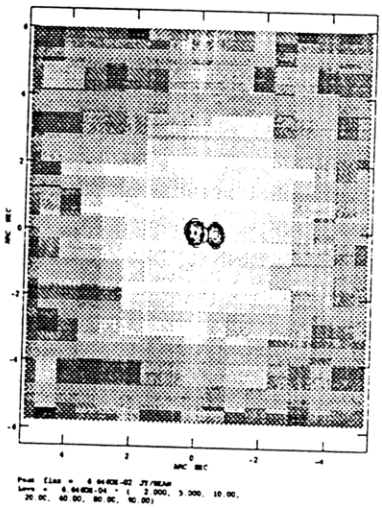

Figure 2: A greyscale image of a clearly identified R=18.3 optical counterpart of a close double-lobe radio galaxy PMN0312-1613, detected in 30 minutes of integration at the MDM 1.3-m. The VLA 8.4 GHz contours are overlaid to show the positional coincidence of the optical counterpart with the close double radio source, of angular size 0.6". The pixel size is 0.63", the circle is 20 pixels = 12.6" in diameter, and the vertical scale has tick marks at 2" intervals. Higher resolution HST observations, or ground-based observations in very good seeing conditions, are required to resolve this close radio double.

which objects are prime candidates for more extensive spectroscopic analysis using the MDM 2.4-m, or larger, telescopes. This spectroscopy is necessary to shed light on the physical and chemical conditions present in the optically-detected regions of the close doubles.

In addition to unusually small radio galaxies, the MDM 1.3-m and 2.4-m telescopes have both been used to achieve optical identifications of relatively rare gravitational lens candidates. In fact, it it possible that some of the many close doubles we have observed are actually instances of background radio sources doubly-imaged by modestly massive foreground lensing galaxies. Optical identifications of counterparts is again necessary as a first step towards pinning down these faint galaxies, in order to obtain spectra that would either confirm or disprove the lensing hypothesis. These MDM observations of lens candidates are parts of the Ph.D. thesis work of Joseph Lehar, Samuel Conner, Andre Fletcher and Lori Herold-Jacobson. Figure 3 shows a successful identification of an optical counterpart to a new gravitational Einstein ring lens candidate discovered from a careful remapping of the MG VLA data archive, by Samuel Conner. It appears in this case that the optical counterpart may well be the foreground lensing galaxy. Deeper imaging in very good seeing conditions is probably required in order to see if there is a faint optical Einstein ring coincident with the radio ring, and such work could be performed initially at the 2.4-m.

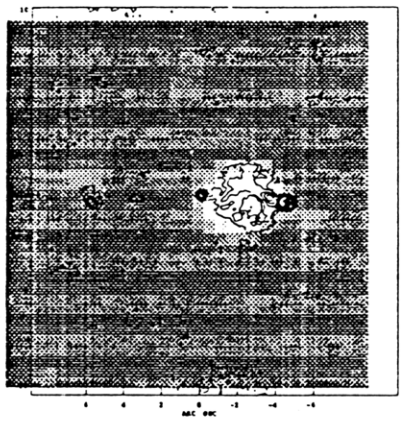

Figure 3: A greyscale image of a clearly identified R=18.1 optical counterpart of a radio Einstein ring gravitational lens candidate, detected in 30 minutes of integration at the MDM 1.3-m. The VLA 8.4 GHz contours are overlaid to show the approximate positional coincidence of the optical galaxy with the central hollow of the Einstein ring, of diameter 2.4". The pixel size is 0.63", the circle is 20 pixels = 12.6" in diameter, and the vertical scale has tick marks at 5" intervals. More sensitive and higher resolution observations are required to verify that there is an optical Einstein ring coincident with the radio ring.

We have also found that access to the 1.3-m telescope is a vital educational tool. Radio astronomy graduate students Deborah Haarsma, Fronefield Crawford and John Cartwright have accompanied the principal observers on intensive imaging sessions, and in thep process they have gained an understanding of the optical techniques in astronomy, and how these data

factor into their own observing at longer wavelengths. Undergraduate student Asantha Cooray has participated in these investigations through the MIT Undergraduate Research Opportunity Program (UROP), and has learned much about optical data reduction, the results of which are essential for future work with MDM and other observatories.

PRELIMINARY VLA SNAPSHOTS OF SOUTHERN RADIO SOURCES FROM THE PARKES-MIT-NRAO (PMN) SURVEY

A. FLETCHER, B. BURKE, S. CONNER, L. HEROLD-JACOBSON,
D. HAARSMA, F. CRAWFORD, J. CARTWRIGHT AND A. COORAY
Massachusetts Institute of Technology
Rm 26-344 M.I.T., 77 Mass.Ave., Cambridge, MA 02139, USA.
EMAIL: bfb@maggie.mit.edu

The Parkes-MIT-NRAO (PMN) Southern Hemisphere Sky Survey revealed 36,640 sources over $\Omega = 4.51$ sr, and is $> 95\%$ complete and $> 90\%$ reliable down to $S_{4.85GHz} \approx 35$ mJy [1],[2]. We have accumulated 1800 0.25″-resolution VLA snapshots of PMN sources ($S_{4.85} > 90$ mJy) in the $-30° < \delta < 0°$ strip. This sample is essentially complete down to 200 mJy, and is divided roughly equally into a flat-spectrum sample ($S_\nu \propto \nu^{-\alpha}; \alpha < 0.5$), and a purely flux-limited one. Our snapshot campaign for Northern sources in the $0° < \delta < 37°$ strip of our MIT-Greenbank (MG) Surveys [3] has already yielded 5 confirmed lenses from 4000 snapshots: MG2016,MG1131,MG0414,MG1654 & MG1549. Improvements in the MIT mapping pipeline [4] have uncovered several more good candidates, yielding a lensing frequency of $\approx 1/500$. Our initial candidate selection is by radio morphology. The 6 most promising cases from a new crop of 8.4 GHz MG & PMN snapshots are shown in Fig. 1. Optical R band imaging with the Michigan-Dartmouth-MIT (MDM) 1.3m telescope has secured identifications ($R > 22.5$) for all 6 candidates. MG0246 is almost certainly an Einstein Ring. MG1507 is just one of ≈ 130 'close doubles' ($0.25'' < \theta < 2.0''$) culled from the 8.4 GHz data. It is not yet well understood what these tiny radio galaxies are physically. While it is likely that most of them are the lobes of distant, young or 'frustrated' classical doubles, perhaps a few are doubly-imaged background radio sources. Theoretical predictions [5] that small angular size lenses should exist have been recently corroborated by several new discoveries, e.g. the 0.33″ ring B0218+35.7 [6]. Further optical imaging and spectroscopy is required to investigate the lensing hypothesis for these new MIT candidates. This work was supported in part by an NSF Grant. The VLA is run by the National Radio Astronomy Observa-

tory, which is operated by Associated Universities, Inc., under cooperative agreement with the National Science Foundation.

References

1. Griffith, M.R. (1993), M.I.T. Ph.D. Thesis.
2. Griffith, M.R., Wright, A.E., Burke, B.F. and Ekers, R.D. (1995), *Ap. J. Suppl.*, **97**: 347 - 453.
3. Griffith, M.R., Langston, G., Heflin, M., Conner, S., Burke, B. (1991), *Ap. J. Suppl.*, **75**: 801 - 833.
4. Conner, S.R., Fletcher, A., Herold, L. and Burke, B.F. (1992), in "Sub-arcsecond Radio Astronomy", Cambridge University Press, U.K., pp. 154 - 155.
5. Turner, E., Ostriker, J. and Gott, R. (1984), *Ap. J.*, **284**: 1-22.
6. Patnaik, A.R., Browne, I.W.A., King, L.J., Muxlow, T.W.B., Walsh, D. and Wilkinson, P.N. (1993), *MNRAS*, **261**: 435.

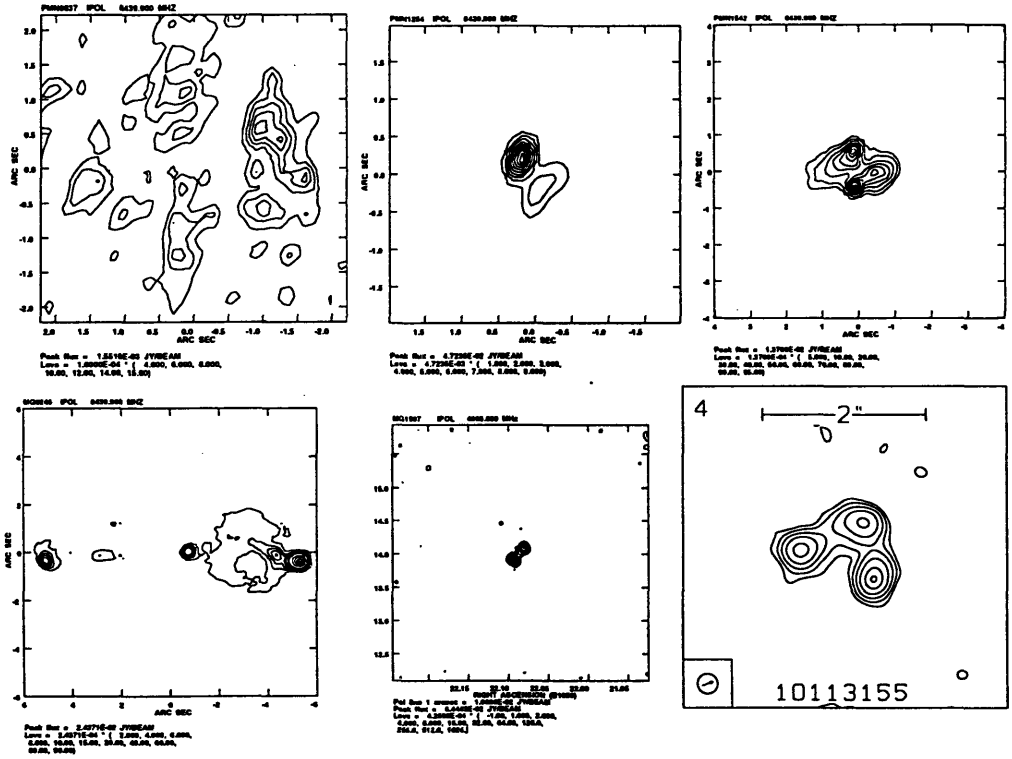

Figure 1. VLA 8.4 GHz contour plots of 3 new PMN & 3 new MG gravitational lens candidates.

First Results from 8.4 GHz VLA Imaging of 1800 Southern Sky Parkes-MIT-NRAO (PMN) Radio Sources

A.Fletcher, S.Conner, B.Burke (MIT)

The Parkes-MIT-NRAO (PMN) Sky Survey at 5 GHz radio frequency revealed 36,640 sources over an area of 4.51 steradians, down to a limiting flux density of typically 35 mJy. The estimated completeness is greater than 95%, and near the limiting flux the reliability is at least 90% (Griffith & Wright, A.J. 105 (5) May 1993). We have made VLA X-Band (3.6 cm) A-Array continuum emission snapshots of a bright, flux density-limited sample of 1800 sources from the PMN Survey list. These lie in the declination range $-30° < \delta < 0°$. Our sample selection was applied to yield two groups: the first consists of about 1000 flat-spectrum radio sources: $F_\nu \propto \nu^{-\alpha}, \alpha < 0.5$. The second group contains 800 sources whose radio spectral index was not selected. This large database of VLA snapshots of extragalactic radio sources provides a useful stepping stone towards any future statistical and individual astronomical work on such radio-emitting AGN. Here, we present some representative and interesting preliminary results from our data reduction pipeline: (a) incidence rates of sources with various radio morphologies; (b) a small but significant sample of the as-yet-uncharacterized class of close double lobe radio galaxies ($\theta < 2''$); (c) some gravitational lens candidates; (d) optical identification efforts targeting these lens candidates and close doubles. We suggest some future work that should be done in order to extract as much statistical information as possible from this sample, with an emphasis on estimating source sizes and morphologies in the context of radio-emitting AGN.

Abstract submitted for AAS [AAS] meeting

Date submitted: February 1, 1998 Electronic form version 1.6

The Luminosity Functions of Young Stellar Clusters

A.B. Fletcher (MIT), S.W. Stahler (UC Berkeley)

We describe a new theoretical framework for computing the evolution of both the mass function (MF) and luminosity function (LF) of a young stellar cluster that is forming within a molecular cloud core. Our method utilizes detailed results from stellar evolution theory, and assumes that young clusters arise from the continual collapse of dense cloud cores over an extended period of time. By further demanding that the stars reaching the main sequence conform to a prescribed Initial Mass Function (IMF), we are able to explicitly solve for the separate contributions, to the cluster MF & LF, from each of the evolving populations of protostars, pre-main-sequence (PMS) stars and main sequence (MS) stars. Among the many detailed results generally predicted by our calculations, we find that the protostellar LF is peaked at a characteristic luminosity throughout the time of cluster formation, and that the time-averaged number fraction in protostars is typically just a few percent. At most times, the vast majority of cluster members are PMS stars, but the cluster light is dominated in the first Myr by the intrinsically brighter protostars. After about $10\,Myr$, the higher mass MS stars provide most of the light. In the intervening period, a pronounced step in the cluster LF is seen at about $10\,L_{\odot}$. A preliminary application of our models to the ρ Ophiuchus embedded cluster indicates that it is reaching the end of its early evolution; we estimate its age to be about $1\,Myr$, to within a factor of two. This research was supported by NSF Grants AST-90-14479 & AST-90-22501.

Abstract submitted for AAS [AAS] meeting

Date submitted: February 1, 1998 Electronic form version 1.6

C.3 Publications for Part II

The following pages contain pre-publication copies of papers, abstracts and articles associated with my thesis research into young stellar clusters, in the period 1991 through 1995. The documents are in time order, with the latest articles appearing first.

The Luminosity Functions of Young Stellar Clusters

A.B. Fletcher (MIT), S.W. Stahler (UC Berkeley)

We describe a new theoretical framework for computing the evolution of both the mass function (MF) and luminosity function (LF) of a young stellar cluster that is forming within a molecular cloud core. Our method utilizes detailed results from stellar evolution theory, and assumes that young clusters arise from the continual collapse of dense cloud cores over an extended period of time. By further demanding that the stars reaching the main sequence conform to a prescribed Initial Mass Function (IMF), we are able to explicitly solve for the separate contributions, to the cluster MF & LF, from each of the evolving populations of protostars, pre-main-sequence (PMS) stars and main sequence (MS) stars. Among the many detailed results generally predicted by our calculations, we find that the protostellar LF is peaked at a characteristic luminosity throughout the time of cluster formation, and that the time-averaged number fraction in protostars is typically just a few percent. At most times, the vast majority of cluster members are PMS stars, but the cluster light is dominated in the first Myr by the intrinsically brighter protostars. After about $10\,Myr$, the higher mass MS stars provide most of the light. In the intervening period, a pronounced step in the cluster LF is seen at about $10\,L_{\odot}$. A preliminary application of our models to the ρ Ophiuchus embedded cluster indicates that it is reaching the end of its early evolution; we estimate its age to be about $1\,Myr$, to within a factor of two. This research was supported by NSF Grants AST-90-14479 & AST-90-22501.

Abstract submitted for AAS [AAS] meeting

Date submitted: February 1, 1998 Electronic form version 1.6

The Luminosity Functions of Embedded Stellar Clusters: I. Method of Solution and Analytic Results

André B. Fletcher

Dept. of Physics, M.I.T., Cambridge, MA 02139

and

Steven W. Stahler

Dept. of Astronomy, U. of California, Berkeley, CA 94720

Received: _____

ABSTRACT

We describe a method for computing the history of the luminosity function in a young cluster still forming within a molecular cloud complex. Our method, which utilizes detailed results from stellar evolution theory, assumes that clusters arise from the continuous collapse of dense cloud cores over a protracted period of time. It is also assumed that stars reaching the main sequence are distributed in mass according to a prescribed Initial Mass Function (IMF). We keep track separately of the contributions to the luminosity function from the populations of protostars, pre-main-sequence, and main-sequence stars.

We derive expressions for the fractional contribution of these populations to both the total number of stars produced and to the total cluster luminosity. In our model, the number of protostars rises quickly at first, but then levels off to a nearly constant value, which it maintains until the dispersal of the cloud complex. The number fraction of protostars always decreases with time. Averaged over the life of the parent complex, this fraction is typically a few percent. The protostar mass distribution can be expressed as an integral over the IMF.

1. Introduction

The observational study of very young clusters that are still cloaked in molecular gas and dust offers a unique opportunity to test theories of stellar formation and evolution on a statistically significant population. While such research is still in its infancy, the advent of infrared array cameras has provided a powerful impetus (Gatley, Depoy, & Fowler 1988). In the nearby ρ Ophiuchus complex, for example, Greene and Young (1992) have used array detectors in the J, H, and K bands (1.2, 1.6, and 2.2 μm, respectively) to identify about 300 cluster members, while Lada *et al.* (1991) have found over 400 stars in the Orion B cloud, using a K-band array camera. To sample adequately the spectral energy distributions of these deeply embedded sources, such surveys must be extended to longer wavelengths. The additional data will allow construction of bolometric luminosity functions, an enterprise already begun on a smaller scale (Wilking, Lada, & Young 1989; Kenyon *et al.* 1990; Prusti, Whittet, & Wesselius 1992; Wilking *et al.* 1992; Ladd, Lada, & Myers 1993). These luminosity functions are certain to play a central role in the confrontation between theory and observation.

The purpose of this paper, the first in a two-part series, is to provide a theoretical foundation for understanding the luminosity functions of embedded clusters. Until recently, the sole point of reference has been the so-called *Initial Luminosity Function (ILF)* (Mihalas & Binney 1981). The ILF gives the relative rates of appearance of main-sequence stars of specified luminosity. Similarly, the *Initial Mass Function (IMF)* gives the relative rates at different stellar masses. Although both functions, as originally derived by Salpeter (1955), refer to averages over all field stars in the Galactic neighborhood, there is ample evidence that they also describe, at least approximately, individual optically revealed clusters, provided the clusters contain sufficient numbers of stars (Scalo 1986; Straw, Hyland, & McGregor 1989; Garmany 1994). The intriguing fact that localized regions produce stars with a characteristic distribution of masses is still not understood, despite many years of theoretical speculation (*e.g.*, Larson 1973).

Though useful for many purposes, neither the ILF nor IMF is applicable to clusters still in the act of formation. In this case, many cluster members are pre-main-sequence objects, whose luminosity changes as a result of gravitational contraction. Furthermore, every star begins its life as a protostar accreting mass from its parent molecular cloud core. If, as is currently believed, an appreciable fraction of embedded sources are in this earliest phase, the IMF cannot describe their mass distribution. These considerations show that a more realistic theoretical luminosity function for a forming cluster must be *time-dependent*. This basic point has only recently come to be appreciated in a quantitative manner (Zinnecker, McCaughrean, & Wilking 1993; Lada 1991). The main product of our calculation, then, is a temporal sequence of luminosity functions.

We construct this sequence by employing a simple phenomenological model of cluster evolution, one that is consistent with current protostar and pre-main-sequence theory. Thus, we reject the earlier notion that clusters form by repeated fragmentation of an initially massive cloud. We assume instead that protostars are continually built

up throughout a cloud by the gravitational collapse of individual dense cores (Myers & Benson 1983). The luminosity function at any time is determined by summing over the contributions from these protostars and the other stellar populations in the cloud. We follow the current belief that an individual protostar ends its accretion by the action of a strong wind that disperses its parent dense core. The resulting star of fixed mass then evolves along its appropriate pre-main-sequence track, beginning at the "birthline" (Stahler 1983, Palla & Stahler 1990). Since the cause of the protostellar wind is not yet understood, we model its onset with a stochastic prescription. That is, we take a protostar of a given mass to have a certain probability per unit time of ending accretion. This probability function is determined by requiring that the mass distribution of stars arriving on the main sequence match the IMF.

Within the context of this model, we can calculate not only the history of the cluster luminosity function, but also of a number of other statistical properties of interest, such as the number fraction of protostars. We defer presentation of our numerical results until Paper II. Here we begin, in Section 2 below, with a more precise description of the phenomenological model. In Section 3, we formulate the problem of cluster evolution mathematically and solve the derived equations, ending with expressions for the luminosity function and related quantities. We obtain an explicit solution for the absolute and relative numbers of protostars. Our other expressions are evaluated in Paper II, using numerical data from existing stellar evolution calculations. Finally, Section 4 of this paper discusses possible modifications of the present model, and compares it with previous work.

2. Physical Model

2.1 Parent Cloud

It is well established observationally that molecular cloud complexes are the principal sites of active star formation in the Galaxy. Traditionally, it has been thought that high-mass stars form in different environments from their low-mass counterparts. However, recent sensitive infrared searches are challenging this view, through the discovery of many new low-luminosity sources in known OB associations (*e.g.*, Yang *et al.* 1990). Here, we assume that a single molecular cloud containing sufficient gas is capable of producing a broad range of stellar masses. Our calculations concern the star-formation history of such an idealized, isolated cloud. Clearly, comparison of our results with observations will require judicious selection of appropriate candidate regions.

Most stars apparently form within smaller dense cores embedded throughout the parent cloud. This substructure is most apparent in looser associations, such as the Taurus-Auriga complex. Molecular line studies reveal that the internal density of a core can peak at a value several orders of magnitude higher than that of the surrounding gas (Myers & Benson 1983). It is not yet understood how clouds evolve to the point of producing dense cores, nor why only certain locations within the cloud are susceptible to such condensation. Both magnetic and thermal pressure gradients support the parent cloud against gravity, and the core condensation process, once begun, can proceed

through the gradual loss of magnetic flux (Mestel & Spitzer 1956). Eventually, the rising central density in a core leads to gravitational instability (Nakano 1976). The subsequent collapse to a star proceeds in an inside-out fashion (Larson 1969).

The condensation of dense cores within the parent cloud must be a continuous process, since the observations of optically revealed young clusters show stellar age spreads of order 10^7 yr (Iben & Talbot 1966). For present purposes, we may ignore the history of each core prior to its collapse. We denote by $C(t)$, the *star formation rate*, the number of core collapses initiated per unit time throughout the parent cloud. The *cluster time* t is measured from the epoch at which star formation began in the cloud, *i.e.*, from the time the first dense core went into free-fall collapse. For now, we leave $C(t)$ as an arbitrary function.

The star-formation activity of the parent cloud is thought to continue until the cloud is destroyed by its own products. Disruption is mostly due to the highest-mass stars produced (Herbig 1962). Radiation pressure on gas and dust, and the acceleration of cloud material by powerful stellar winds are thought to be the most effective mechanisms (Elmegreen & Clemens 1985). For this study, which focuses on events *prior* to cloud disruption, a detailed accounting of the relevant physics is neither necessary nor appropriate. Since available evidence indicates that the disruption is relatively rapid (*e.g.,* Leisawitz 1990), we simply set the star formation rate to zero at a *cutoff time* t_c:

$$C(t) = 0 \qquad t \geq t_c. \tag{1}$$

Note that it is the initiation of dense core collapses which ceases at this time. As we will see, protostars continue to grow for a brief period thereafter. The time t_c is a free parameter in the model; it was set at 10^7 yr for most of the numerical runs (see Paper II).

2.2 Protostars

The collapse of a dense core leads to the buildup of a central hydrostatic protostar.[2] At early times, the protostar's envelope of gas and dust has a relatively low specific angular momentum, and thus can fall directly onto the stellar surface, after being processed through an accretion shock (Stahler, Shu, & Taam 1980). Gradually, however, the collapsing interior of the dense core spreads to regions with sufficiently high angular momentum that material begins to miss the star. An increasing fraction of the envelope falls instead onto a growing circumstellar disk (Cassen & Moosman 1981; Stahler *et al.* 1993). The manner in which disk material is transferred to the protostar is not known. However, the contribution to the luminosity of a protostar of mass M and radius R due to accretion is given by

$$L_{acc}(M) = GM\dot{M}/R, \tag{2}$$

[2] We assume here that the components of close binaries form individually through the same type of collapse process.

where $\dot{M}(t)$ is the mass accretion rate from the envelope. Equation (2) is valid regardless of the division of infalling material between the disk and the stellar surface, provided that the star does not gain a rotational energy comparable to that from self-gravity. The spectral appearance of the protostar, which is invisible optically, *does* depend on the amount of material passed through the disk, as well as on the detailed properties of the surrounding envelope. However, we do not address this issue in our calculations, which are concerned only with bolometric luminosities.

The mass accretion rate in equation (2) is taken from the physics of cloud collapse. A number of theoretical studies, both analytic and numerical, have established that $\dot{M}$ varies slowly throughout core collapse. For our purposes, we may consider this rate to be a strict constant. The magnitude of $\dot{M}$ is given approximately by a_T^3/G, where a_T is the core isothermal sound speed prior to collapse (Shu 1977, Boss & Black 1982). Since a_T is set by the core temperature, we assume here that all protostars within a cloud are built up at the same rate. For a temperature of 10 K, the formula yields an $\dot{M}$ of $2 \times 10^{-6}\, M_\odot$ yr^{-1}, which we adopt as our lower bound. We have constructed luminosity functions both with this value and with $1 \times 10^{-5}\, M_\odot$ yr^{-1}, a rate which corresponds to a temperature of 30 K. This latter value, when used in detailed stellar evolution calculations, yields a birthline, or upper envelope in the H-R diagram, that is in good agreement with observations of both low-mass T Tauri stars (Stahler 1983) and intermediate-mass Herbig Ae and Be stars (Palla & Stahler 1990). It may be that high-mass stars require a larger $\dot{M}$ for their formation, but we ignore this possibility here.

Evaluation of equation (2) also requires specifying a mass-radius relation for accreting protostars. Our adopted relation is shown in Figure 1. For higher masses ($1\, M_\odot < M < 8\, M_\odot$), we have used the result of Palla and Stahler (1991) for the case $\dot{M} = 1 \times 10^{-5}\, M_\odot$ yr^{-1}, while the relation for lower masses was taken from Stahler (1988), assuming the same $\dot{M}$. These studies show that the mass-radius relation for $M \gtrsim 0.1\, M_\odot$ is insensitive to the precise value of $\dot{M}$, but is largely set by the action of internal deuterium fusion. Palla and Stahler (1992) have also shown that the radii at intermediate masses are virtually unchanged if accretion occurs through a circumstellar disk rather than a spherical shock front. On the other hand, radii for $M \lesssim 0.1\, M_\odot$ are more dependent on accretion conditions. In addition, steady-state accretion is not yet established for too small a central mass (Winkler & Newman 1980). In view of these uncertainties, we arbitrarily allowed the radius, for masses lower than 0.1 $M_\odot$, to fall as a power law to $M = 0$. The power law index was chosen to be the same as that characterizing the surface temperatures of these very low masses, as we describe in Section 2.3 below.

In protostars of intermediate mass, the gravitational contraction of the star itself yields luminosities that rival the accretion contribution in equation (2). Moreover, if mass buildup continues, the star begins to burn ordinary hydrogen, and eventually settles onto the zero-age main sequence (ZAMS) while still undergoing accretion. According to the recent calculation of Palla and Stahler (1991), this transition occurs at a mass of 8 $M_\odot$. To take these effects into account, we evaluate the total protostellar

luminosity as the sum of the accretion component, which originates in the protostar's surface layers, and an interior contribution L_{int}:

$$L_{proto}(M) = L_{acc}(M) + L_{int}(M). \quad (3)$$

For $M < 8\,M_\odot$, L_{int} is taken to be the luminosity of a pre-main-sequence star of mass M and the appropriate protostellar radius $R(M)$. For $M \geq 8\,M_\odot$, L_{int} is simply the star's ZAMS luminosity. With this definition, L_{int} is continuous at 8 $M_\odot$, since the stellar birthline joins smoothly to the ZAMS at that mass (see Fig. 3 of Palla & Stahler 1990). Since the massive protostars which are on the ZAMS have $L_{int} \gg L_{acc}$, our possible underestimation of $\dot{M}$ for this population has little effect on the total luminosity. The function $L_{proto}(M)$, computed for the case $\dot{M} = 1 \times 10^{-5}\,M_\odot\ \mathrm{yr}^{-1}$, is shown in Figure 2. The luminosity first increases smoothly with mass, starts to level off at $M \simeq 0.3\,M_\odot$, then rises more steeply for $M \gtrsim 4\,M_\odot$. The leveling occurs in a regime where L_{acc} dominates, and stems from the swelling of the radius due to central deuterium burning (see Figure 1). The later steepening occurs after the dominance of L_{int} sets in, and reflects the sensitive dependence of luminosity on mass for stars in radiative equilibrium.

The phase of accretion is believed to end through the disruption of the dense core by a powerful protostellar wind. To date, there have been no confirmed direct observations of this wind, but there is ample indirect evidence for its existence, through the occurrence of narrow optical jets and broad molecular outflows near embedded young stars (Edwards, Ray, & Mundt 1993). Statistical analysis of nearby young associations indicates that the time for this wind to clear away the dense core is relatively brief, probably less than 10^5 yr (Myers *et al.* 1987). Here, we ignore the duration of this clearing process, and take $\dot{M}(t)$ to fall to zero instantaneously. Since the cause of the wind is not yet known, we model its onset with a stochastic prescription. We assume that each accreting protostar has a certain probability per unit time, $\nu(M)$, of disrupting its dense core via the wind. This probability, as indicated, is a function of the stellar mass.

A probabilistic treatment of the dense core dispersal is, of course, only a heuristic device. In a more complete theory of star formation than is yet available, the onset of the wind must be related to other factors, such as the rotation rate of the parent core. Until such a physical link is clarified, our use of a probability function is a reasonable first step, justified by the fact that stars do appear on the main sequence with a characteristic distribution of masses. Indeed, we use this fact to determine the mathematical form of $\nu(M)$, as we detail in Section 3.1 below.

2.3 Pre-Main-Sequence Stars

Once its parent core has been destroyed, a star of fixed mass begins its phase of quasi-static gravitational contraction toward the ZAMS. Although pre-main-sequence stars have traditionally been considered to be of fixed mass, observations of their excess infrared and ultraviolet radiation suggest that many of them continue to accrete matter

through circumstellar disks (Bertout, Basri, & Bouvier 1988). Quantitative estimates indicate that such residual accretion may augment the masses of T Tauri stars by as much as 10 percent (Hartmann & Kenyon 1990). The effect on the luminosity history has not yet been reliably assessed, but the net increase in system luminosity at any time must, on general grounds, be less than a factor of two (Palla & Stahler 1993). Additional corrections arising from source inclination and extinction tend to cancel out (Wilking, Lada, & Young 1989). In this study, accordingly, we have followed the pre-main-sequence luminosity contribution to the cluster by utilizing previously published evolutionary tracks for stars of fixed mass. From these tracks, we could tabulate numerically the luminosity as a function both of stellar mass and of the *track time* t_*, where t_* is measured from the birthline.

For masses in the range 0.01 to 0.3 $M_\odot$, we employed the tracks of Nelson (1991), while the interval from 0.3 to 1.3 $M_\odot$ was supplied by Vandenberg (1990). The tracks from 1.3 to 8.0 $M_\odot$ were adopted from Iben (1965). Stars of even higher mass exhibit no pre-main-sequence phase (Palla & Stahler 1991). For these, we needed only the ZAMS mass-luminosity relation, which we took from Ezer and Cameron (1967). Finally, to provide luminosity functions complete down to 0.01 $L_\odot$, we needed to follow the evolution of a set of masses even lower than 0.01 $M_\odot$. We assumed, following Nelson, Rappaport, and Joss (1986), that these objects contract as $n = 3/2$ polytropes. The luminosity at each track time was derived by assigning each mass a constant surface temperature. In reality, the onset of degeneracy causes the star to cool more slowly than this prescription would indicate, but the difference has a negligible effect on our luminosity functions. The assigned temperature was taken to fall to zero at zero mass in power-law fashion, where the power law was based on the Nelson, Rappaport, and Joss temperatures for $M = 0.02$ and 0.01 $M_\odot$. Using this prescription, the smallest mass we considered was $M_{min} = 3 \times 10^{-3}\, M_\odot$, which has a luminosity of 0.01 $L_\odot$ at the birthline.

In practice, some of the original tracks available to us had to be altered slightly to effect a smooth join between the results of various authors. Additionally, all tracks were truncated at large radius using the standard "birthline" prescription. That is, we took the initial radius of every pre-main-sequence star of mass M from the protostellar $R(M)$ described earlier. In the case of intermediate masses, Palla & Stahler (1993) have found that newly formed pre-main-sequence stars brighten steeply from a prior state of anomalously low luminosity (see also Stahler 1989). Here, we ignore this initial, transient phase, and assume for simplicity that all stars are thermally relaxed following the end of accretion.

Another complication concerns the fusion of interstellar deuterium. In pre-main-sequence stars of low mass, deuterium burning temporarily slows down or even halts gravitational contraction (Grossman & Graboske 1971), although stars with $M \gtrsim 1\, M_\odot$ exhaust their deuterium as protostars (Stahler, Shu, & Taam 1980). A standard interstellar concentration of deuterium ($[D/H] = 2.5 \times 10^{-5}$) was included in the original tracks of Nelson (1991), but neglected by Vandenberg (1990). For masses between 0.3 and 1.0 $M_\odot$, the initial abundance of deuterium declines smoothly from

its full interstellar value to zero, as found by Stahler (1988). In this mass range, we assumed that burning halts the contraction completely, and that the star retains a fixed luminosity until the deuterium is consumed. The duration of this pause, t_D, is thus given by

$$\begin{aligned} t_D &= f\,[D/H]\,X\,Q\,M/(m_H\,L) \\ &= 1.5 \times 10^6 \text{ yr } f\,(M/M_\odot)(L/L_\odot)^{-1}, \end{aligned} \tag{4}$$

where f is the initial deuterium concentration relative to the interstellar value, X the mass fraction of hydrogen, Q the energy released per fusion reaction, and m_H the hydrogen atom mass. After the interval t_D, each star was assumed to continue its normal pre-main-sequence contraction.

Table 1 is a compilation of important evolutionary properties for selected stellar masses. Listed are the birthline radius (R_b) and luminosity (L_b), the total contraction time from the birthline to the ZAMS (t_{pms}), the ZAMS luminosity (L_{ms}), and the main-sequence lifetime (t_{ms}). Figure 3 displays graphically the adopted pre-main-sequence evolutionary data. The horizontal axis measures, not the track time t_*, but a logarithmic *reduced time* τ_{red}, defined as

$$\tau_{red}(M, t_*) \equiv \log(1 + t_*/t_\circ)/\log(1 + t_{pms}/t_\circ), \tag{5}$$

where the fiducial time $t_\circ$ has been set equal to 10^5 yr. The quantity τ_{red} has the convenient property that it is zero on the birthline ($t_* = 0$) and reaches unity at the ZAMS ($t_* = t_{pms}$). In practice, we employed τ_{red} to interpolate values of $L(M, t_*)$ between the tabulated data. For masses too small to reach the ZAMS, we fixed t_{pms} at 8.45×10^9 yr, the value at $M = 0.085\,M_\odot$ (Nelson 1991). Notice that the highest mass displayed in Figure 3, 8 $M_\odot$, covers only the single luminosity corresponding to the ZAMS value. The figure also includes isochrones of constant track time.

Figure 3 shows how the character of pre-main-sequence contraction depends on both mass and time, and it gives an indication of the numerical complexities entailed when incorporating a complete and accurate set of tracks. The deuterium-burning phase is seen as the group of plateaus near the $\tau_{red} = 0$ axis. For masses below 0.5 $M_\odot$, deuterium does not burn until the star has contracted from the birthline; hence, the corresponding plateaus are detached from the axis. There is also a qualitative change in the tracks for $M \gtrsim 2\,M_\odot$. While lower-mass stars always begin their contraction along convective, vertical paths in the H-R diagram, heavier stars begin radiatively, and evolve with more nearly constant luminosity (see also Fig. 1 of Stahler 1989). This change has a qualitative effect on the luminosity functions, as we discuss in Paper II.

2.4 Brown Dwarfs and the IMF

Our model is based on the supposition that the mass distribution of cluster members, after all accretion has ceased, follows the field-star IMF. It was established by Salpeter (1955) that the IMF falls off steeply at high masses, and this conclusion has remained unchallenged. It is also generally accepted that, for masses below about 1 $M_\odot$, the slope of the IMF flattens, but the exact form at lower masses is still controversial

(Kroupa, Tout, & Gilmore 1990, Tinney, Mould, & Reid 1992). At present, the most widely used form is the "lognormal" prescription of Miller and Scalo (1979). Here, the relative number of stars per unit mass interval is given by

$$\sigma_{IMF} = A\,(M/M_\odot)^{-1} \exp\{-1.09\,[\log(M/M_\odot) + 1.02]^2\}, \qquad (6)$$

where A is a normalization constant of dimension $M_\odot^{-1}$. Equation (6) was chosen by Miller and Scalo as the best fit to available data under the assumption of a constant star formation rate in the Galactic disk over the past 1.2×10^{10} yr. We have adopted this form, for $M \geq 0.1\,M_\odot$, in all our numerical calculations.

Owing to the paucity of existing observations, the extension of equation (6) below $0.1\ M_\odot$ is highly uncertain. There seems to be no reason why substantial numbers of brown dwarfs - objects below the hydrogen-burning limit of $0.085\ M_\odot$ - should not exist, but there have been no confirmed sightings, despite extensive searches. Fortunately, our results do not depend sensitively on the IMF in this regime, since our luminosity functions are only complete down to $0.01\ L_\odot$. Nevertheless, to gauge the effect of the brown dwarf population, we have considered four IMF forms that span a reasonable range of possibilities. In order of increasing contribution from the brown dwarfs, these forms are:

1. *Zero Level* Here, we simply set σ_{IMF} to zero for $M < 0.1\,M_\odot$. Although such a sharp cutoff is not favored by current observations (Kroupa, Tout, & Gilmore 1990), it still serves as an instructive example.
2. *Flat* We take σ_{IMF} at small mass to be a constant, fixed at its value at $M = 0.1\,M_\odot$. This form has been advocated by Hubbard, Burrows, and Lunine (1990) from a comparison of theoretical brown dwarf cooling curves with Hyades data.
3. *Sloping* We assume that σ_{IMF} rises linearly as a function of mass below $0.1\ M_\odot$, with a slope that is continuous with that given by equation (6).
4. *Gaussian* This is the extension of equation (6) down to zero mass.

These four IMF forms, properly normalized, are displayed in Figure 4. The figure also gives the associated fraction of stars with masses below $0.1\ M_\odot$.

2.5 Main-Sequence and Post-Main-Sequence Stars

The eventual ignition of hydrogen in sufficiently massive pre-main-sequence stars halts their gravitational contraction, allowing them to maintain nearly constant luminosities for long periods of time. Here, we define the main sequence period to begin at the last time the gravitationally-generated fraction of the total luminosity falls below 0.01. The times to reach this state for various masses are the values of t_{pms} listed in Table 1.

Once a star has reached the track time t_{pms}, we consider its luminosity to be strictly constant during its hydrogen-burning phase. We do not model the subsequent,

more rapid phase of post-main-sequence evolution, but simply set the star's luminosity equal to zero. Our main-sequence lifetimes, as well as the radii and surface temperatures for $M > 8\,M_\odot$, were taken from Iben (1967) and Ezer & Cameron (1967). For stars less massive than about 2 $M_\odot$, the values of t_{ms} exceed 10^9 yr and are no longer of interest, since they are greater than the probable survival times of most Galactic clusters (Wielen 1985).

Within the stochastic picture of cluster formation adopted here, there is a finite probability that a protostar will gain such a large mass that it runs through its entire main-sequence evolution while still accreting cloud matter. In principle, this process adds to the supply of post-main-sequence objects. We show in the Appendix, however, that the relative number of stars that follow this route is negligibly small.

3. Mathematical Development

3.1 Evolution of Stellar Populations

In order to calculate the luminosity function, we first need to determine how the mass distribution of the cluster members evolves in time. We divide the stars into two basic groups - optically obscured *protostars*, which are accreting dense core material at the rate $\dot{M}$, and *post-accretion stars*, including both contracting pre-main-sequence objects and main-sequence stars.[3] We denote by $p(M,t)$ the number of protostars per unit of stellar mass at cluster time t. Similarly, $s(M,t)$ measures the number of post-accretion objects.

3.1.1 Protostar Mass Function

The evolution of both the protostar and post-accretion populations is depicted schematically in Figure 5. Focusing on the mass bin from $M - \Delta M/2$ to $M + \Delta M/2$, the number of protostars present at time t, $p(M,t)\,\Delta M$, will be completely depleted in the interval $\Delta t = \Delta M/\dot{M}$. A fraction $\nu(M)\Delta t$ of these will cease their accretion, while the remainder become higher-mass protostars. During the same interval, however, the bin is partially repopulated by protostars of lower mass. Specifically, a fraction $1 - \nu(M - \Delta M)\Delta t$ of the lower-mass protostars shift into the central bin. We can therefore write the temporal change in the protostar population as

$$[p(M,t+\Delta t) - p(M,t)]\,\Delta M = p(M-\Delta M,t)\,[1-\nu(M-\Delta M)\Delta t]\,\Delta M - p(M,t)\Delta M. \tag{7}$$

By taking the limit of (7) for small ΔM and Δt, and recalling that $\Delta M = \dot{M}\Delta t$, we obtain a partial differential equation for the evolution of the protostar mass function:

$$\left(\frac{\partial p}{\partial t}\right)_M + \dot{M}\left(\frac{\partial p}{\partial M}\right)_t + \nu(M)\,p(M,t) = 0. \tag{8}$$

[3] This terminology is consistent with our neglect of any residual disk accretion in pre-main-sequence stars. Note that post-accretion stars can also be optically invisible if they are still enshrouded in dust and gas.

This equation is subject to the condition that there be no protostars initially:

$$p(M,0) = 0. \tag{9}$$

Our derivation must be altered for a protostar mass near zero. In this special mass bin, the supply of new protostars comes from the initiation of new dense core collapses, rather than from other protostars. Recalling that $C(t)$ denotes the rate of core collapses per unit time, we have, in place of equation (7)

$$[p(0,t+\Delta t) - p(0,t)]\,\Delta M = C(t)\,\Delta t - p(0,t)\,\Delta M. \tag{10}$$

Taking the limit as before, we obtain the boundary condition

$$p(0,t) = C(t)/\dot{M}. \tag{11}$$

The solution of equation (8), subject to the boundary conditions (9) and (11), can be obtained readily through the use of Laplace transforms. That is, we define the transformed protostar mass function, $P(M,u)$, as

$$P(M,u) \equiv \int_0^\infty dt\, \exp(-ut)\, p(M,t)$$

and apply the same transform operation to equation (8), obtaining

$$uP(M,u) - p(M,0) + \dot{M}\left(\frac{\partial P}{\partial M}\right)_u + \nu(M)\,P(M,u) = 0. \tag{12}$$

The second left-hand term in this equation vanishes by virtue of equation (9). We integrate the remainder of (12) from $M = 0$ to an arbitrary mass M, and find, using (11), that

$$P(M,u) = \frac{C(u)}{\dot{M}} \exp(-Mu/\dot{M})\, \exp\left[\frac{-1}{\dot{M}}\int_0^M \nu(M')dM'\right], \tag{13}$$

where $C(u)$ is the transform of $C(t)$.

In order to invert (13), we use the fact that the inverse transform of any product of the form $F(u)\exp(-bu)$ is $H(t-b)\,F(t-b)$, where $H(t)$ is the Heaviside step function. Then equation (13) gives us the general solution for the protostar mass function:

$$p(M,t) = \frac{1}{\dot{M}}\, C(t - M/\dot{M})\; H(t - M/\dot{M}) \exp\left[\frac{-1}{\dot{M}}\int_0^M \nu(M')dM'\right]. \tag{14}$$

To make further progress, we must specify the functional form of $C(t)$. For simplicity, we choose a creation rate that is unchanging from $t = 0$ until the cutoff time:

$$C(t) = C_\circ \, H(t) \, H(t_c - t), \tag{15}$$

where $C_\circ$ is a constant. Substitution of (15) into (14) yields our final protostar mass function:

$$p(M,t) = \frac{C_\circ}{\dot{M}} \, H(t - M/\dot{M}) \; H(t_c + M/\dot{M} - t) \, \exp\left[\frac{-1}{\dot{M}} \int_0^M \nu(M') \, dM'\right]. \tag{16}$$

We see that, for any time t, $p(M,t)$ is a smooth function of mass, truncated by a "window" formed by the product of two step functions. Such sharp edges appear throughout our analysis, and are purely causal in nature. For $t < t_c$, the minimum protostar mass is zero, but it becomes $\dot{M}(t - t_c)$ at greater times, since no new protostars are made after t_c. Similarly, the upper mass limit at any time is $\dot{M}t$, since there can be no protostar more massive than that created at $t = 0$. Thus, the window, which selects the allowed range of protostar masses, moves in time. As expected, the smooth function in between the two mass limits depends on the probability function $\nu(M)$, which we have not yet specified. Note finally that the mass function scales inversely with the accretion rate.

3.1.2 Post-Accretion Mass Function

Referring again to Figure 5, we see that any addition to the post-accretion population at a given mass can come only from that fraction of protostars of the same mass which have actually ended their accretion. Thus, over a finite time interval Δt, we have

$$[s(M, t + \Delta t) - s(M,t)] \, \Delta M = p(M,t) \, \nu(M) \, \Delta M \, \Delta t. \tag{17}$$

Upon taking the limit of this equation for small ΔM and Δt, we obtain

$$\left(\frac{\partial s}{\partial t}\right)_M = \nu(M) \, p(M,t). \tag{18}$$

The initial condition for (18) is that there be no post-accretion stars at $t = 0$:

$$s(M, 0) = 0. \tag{19}$$

Equation (18) may be integrated with respect to time, yielding

$$s(M,t) = \nu(M) \int_0^t p(M,t) \, dt, \tag{20}$$

where we have employed equation (19) to eliminate the initial value of $s(M,t)$. To obtain the general solution for the post-accretion mass function, valid for arbitrary creation rate $C(t)$, we substitute (14) into (20) and obtain

$$s(M,t) = \frac{1}{\dot{M}}\,\nu(M)\,H(t - M/\dot{M})\,\exp\left[\frac{-1}{\dot{M}}\int_0^M \nu(M')\,dM'\right]\int_0^{t-M/\dot{M}} C(t')dt'. \quad (21)$$

In deriving this equation, we have used the identity

$$\int_0^t H(t'-a)\,C(t'-a)\,dt' = H(t-a)\int_0^{t-a} C(t')\,dt',$$

valid for any function $C(t)$ and positive constant a.

We now specialize to the case of constant creation rate. Substituting $C(t)$ from equation (15) into (21), we find

$$s(M,t) = \frac{C_o}{\dot{M}}\,\nu(M)\,H(t - M/\dot{M})\,\exp\left[\frac{-1}{\dot{M}}\int_0^M \nu(M')\,dM'\right] \times \int_0^{t-M/\dot{M}} H(t_c - t')dt'. \quad (22)$$

For $t - M/\dot{M} < t_c$, the final integral in equation (22) is $t - M/\dot{M}$, while for $t - M/\dot{M} > t_c$, the integral is simply t_c. Hence

$$s(M,t) = \frac{C_o}{\dot{M}}\,\nu(M)\,H(t - M/\dot{M})\,\exp\left[\frac{-1}{\dot{M}}\int_0^M \nu(M')\,dM'\right]\min\{t_c, t - M/\dot{M}\}, \quad (23)$$

where min{ } denotes the minimum of the indicated quantities.

As in the case of the protostars, the post-accretion mass function is truncated by a sharp edge arising from causality. The maximum mass is again $\dot{M}t$, but here there is no minimum, since low-mass post-accretion objects do not come directly from core collapse. Now for $t > t_c$, the minimum protostar mass was $\dot{M}(t - t_c)$. Thus, the mass function for post-accretion stars *below* this limit can no longer change as a result of protostars dispersing their dense core envelopes. In effect, the post-accretion population becomes frozen, at these late times, up to the mass $\dot{M}(t - t_c)$. Finally, we note that $s(M,t)$, like $p(M,t)$, scales inversely with $\dot{M}$; this fact is easily understood. Given a steady formation rate of stars, the number of protostars and pre-main-sequence stars in a given mass interval is proportional to the amount of time spent in that interval.

3.1.3 Probability of Core Dispersal

The mass functions derived so far cannot be evaluated without a prescription for the probability function $\nu(M)$. This function is derived by demanding that the post-accretion mass function approach the field-star IMF at late times:

$$\lim_{t\to\infty} s(M,t) = N\,\sigma_{IMF}(M). \tag{24}$$

Here $N \equiv C_o t_c$ is the final number of stars produced in the cluster. In writing equation (24), we have assumed that $\sigma_{IMF}(M)$ is normalized so that its integral is unity. Applying the time limit to equation (23) for $s(M,t)$, we obtain

$$\sigma_{IMF}(M) = \frac{\nu(M)}{\dot{M}} \exp\left[\frac{-1}{\dot{M}}\int_0^M \nu(M')\,dM'\right] \tag{25a}$$

$$= -\frac{d}{dM} \exp\left[\frac{-1}{\dot{M}}\int_0^M \nu(M')\,dM'\right]. \tag{25b}$$

To obtain $\nu(M)$ from equation (25b), we first integrate both sides from $M = 0$ to an arbitrary mass value:

$$\int_0^M \sigma_{IMF}(M')\,dM' = 1 - \exp\left[\frac{-1}{\dot{M}}\int_0^M \nu(M'')\,dM''\right].$$

We can use the normalization of $\sigma_{IMF}(M)$ to rewrite this last equation as

$$\int_M^\infty \sigma_{IMF}(M')\,dM' = \exp\left[\frac{-1}{\dot{M}}\int_0^M \nu(M'')\,dM''\right], \tag{26}$$

which can be recast as

$$\int_0^M \nu(M'')\,dM'' = -\dot{M}\,\ln\int_M^\infty \sigma_{IMF}(M')\,dM'. \tag{27}$$

If we differentiate (27) with respect to mass, we can solve for the probability function:

$$\nu(M) = \frac{\dot{M}\,\sigma_{IMF}(M)}{\int_M^\infty \sigma_{IMF}(M')\,dM'}. \tag{28}$$

For an IMF of power-law form, equation (28) implies that the probability of cloud dispersal is uniform for equal logarithmic intervals of protostar mass. In our analysis, of course, we do *not* assume a power-law form, but adopt instead the more realistic $\sigma_{IMF}(M)$ of equation (6). We will not discuss further the possible physical implications of equation (28), but only use it to determine the stellar mass functions.

We are now in a position to evaluate the exponential appearing in both equations (16) and (23). Using equation (26), the protostar mass function in (16) becomes

$$p(M,t) = \frac{C_\circ}{\dot{M}}\, H(t - M/\dot{M})\; H(t_c + M/\dot{M} - t) \int_M^\infty \sigma_{IMF}(M')\, dM', \tag{29}$$

while equation (23) for the post-accretion mass function becomes

$$s(M,t) = C_\circ\, \min\{t_c, t - M/\dot{M}\}\, H(t - M/\dot{M})\, \sigma_{IMF}(M). \tag{30}$$

Equation (30) shows that the mass distribution of post-accretion stars is modified from the IMF, at early times, by the factor $t - M/\dot{M}$, reflecting again the effect of causality. In addition, the post-accretion stars have a maximum mass of $\dot{M}t$. The mass distribution of protostars, according to equation (29), is *not* proportional to the IMF, but rather to its *mass integral*. This integral dependence reflects the fact that every post-accretion star of mass M or greater was previously a protostar of mass M. Thus, if one assigns a power-law index α to the high-mass end of the IMF, the appropriate index for the protostars is $\alpha + 1$.

3.1.4 Evolution of Post-Accretion Stars

Our description of the post-accretion population has thus far focused on the total number of stars of given mass that are present at a fixed cluster time t. This group is actually composed of stars with a range of evolutionary ages and, hence, luminosities. We therefore introduce another function, denoted $q(M, t_*, t)$, that describes in more detail the post-accretion population. We define $q(M, t_*, t)\Delta M \Delta t_*$ as the number of post-accretion stars at cluster time t with masses in the range $M - \Delta M/2$ to $M + \Delta M/2$, and with track times from $t_* - \Delta t_*/2$ to $t_* + \Delta t_*/2$. Recall that t_* measures the elapsed evolutionary time since the star's first appearance on the birthline. We now determine $q(M, t_*, t)$ in terms of previously derived quantities.

Figure 6 depicts schematically the evolution of a group of post-accretion stars (here taken to be pre-main-sequence objects) in the H-R diagram. All the stars share a common mass M, within the range ΔM, and therefore descend the birthline along a narrow strip centered on a single evolutionary track. At position A, the stars are next to the birthline, *i.e.*, they have recently completed their protostar phase. Track times here range from 0, for those stars just now ending accretion, to a small interval Δt_*. At position B, we see the same group after an elapsed *cluster* time t_1. As depicted, the range in luminosity spanned by the group has changed considerably, but the fact that the number of stars has remained fixed means that

$$q(M, t_*, t_1)\, \Delta M\, \Delta t_* = q(M, 0, t_1 - t_*)\, \Delta M\, \Delta t_*,$$

where we have ignored any mass change from stellar winds or disk accretion. After removing the subscript from the cluster time, this last relation becomes

$$q(M, t_*, t) = q(M, 0, t - t_*). \tag{31}$$

The function $s(M,t)$ represents a summation over groups of stars appearing at different epochs. At a fixed cluster time t, the minimum track time included is zero, while the longest is $t - M/\dot{M}$, which represents those stars that began as protostars at $t = 0$. Hence, the two functions $s(M,t)$ and $q(M,t_*,t)$ are connected through the relation

$$\int_0^{t-M/\dot{M}} q(M,t_*,t)\,dt_* = s(M,t). \tag{32}$$

In order to invert equation (32) and extract an expression for $q(M,t_*,t)$, we need to evaluate the derivative of q with respect to t. We accordingly differentiate both sides of (31), obtaining

$$\begin{aligned}\left[\frac{\partial q(M,t_*,t)}{\partial t}\right]_{M,t_*} &= \left[\frac{\partial q(M,0,t-t_*)}{\partial t}\right]_{M,t_*} \\ &= -\left[\frac{\partial q(M,0,t-t_*)}{\partial t_*}\right]_{M,t} \\ &= -\left[\frac{\partial q(M,t_*,t)}{\partial t_*}\right]_{M,t}.\end{aligned}$$

We now differentiate both sides of equation (32) with respect to t. In light of our last result, the left side of (32) becomes

$$\begin{aligned}&\int_0^{t-M/\dot{M}} \left[\frac{\partial q(M,t_*,t)}{\partial t}\right]_{M,t_*} dt_* \;+\; q(M,t-M/\dot{M},t) = \\ -&\int_0^{t-M/\dot{M}} \left[\frac{\partial q(M,t_*,t)}{\partial t_*}\right]_{M,t} dt_* \;+\; q(M,t-M/\dot{M},t) \\ &\qquad = q(M,0,t) \;-\; q(M,t-M/\dot{M},t) \;+\; q(M,t-M/\dot{M},t) \\ &\qquad = q(M,0,t)\end{aligned}$$

The derivative of the right side of (32) can be evaluated using equation (18). We find that

$$q(M,0,t) = \nu(M)\; p(M,t)$$

and, therefore

$$\begin{aligned}q(M,t_*,t) &= q(M,0,t-t_*) \\ &= \nu(M)\; p(M,t-t_*).\end{aligned}$$

Inserting the expressions for $\nu(M)$ and $p(M,t-t_*)$ from equations (28) and (29), respectively, we obtain our final result:

$$q(M,t_*,t) = C_0\, H(M-M_1)\; H(M_2-M)\,\sigma_{IMF}(M), \tag{33}$$

where the causality window edges, M_1 and M_2, are given by

$$M_1 = \dot{M}(t - t_* - t_c) \tag{34a}$$
$$M_2 = \dot{M}(t - t_*). \tag{34b}$$

For cluster times brief enough that M_1, as calculated in equation (34a), comes out negative, this mass should be set to zero.

We see again that the mass distribution of post-accretion objects is a relatively simple modification of the IMF. In this case, $q(M, t_*, t)$ can be viewed as arising from a time-dependent window sweeping across the IMF distribution. The window picks out that subset of stars which could have reached the designated track time. It will also prove convenient to write the step functions in terms of time rather than mass. Thus, we recast equation (33) as

$$q(M, t_*, t) = C_\circ\, H(t_* - t_1)\, H(t_2 - t_*)\, \sigma_{IMF}(M), \tag{35}$$

where

$$t_1 \equiv t - M/\dot{M} - t_c \tag{36a}$$
$$t_2 \equiv t - M/\dot{M}. \tag{36b}$$

3.2 Evolution of Luminosity Functions

3.2.1 Protostar Contribution

The luminosity function for protostars, $\Phi_{proto}(L, t)$, is defined as the number of protostars with a given value of $L = L_{proto}$ at the cluster time t. This number is measured per logarithmic unit of luminosity. We obtain Φ_{proto} by combining the protostellar mass function of equation (29) with the mass-luminosity relation of equation (3). We demand that the protostar population in a fixed luminosity interval equal that in the corresponding mass interval:

$$\Phi_{proto}(L, t)\ \Delta \log L = p(M, t)\, \Delta M,$$

from which we derive

$$\Phi_{proto}(L, t) = \frac{M(L)\, p(M, t)}{\log e} \left| \frac{d \log L}{d \log M} \right|^{-1},$$

where the absolute value of the derivative is used to ensure that $\Phi_{proto}(L, t)$ is positive. This last relation becomes, after using (29)

$$\Phi_{proto}(L, t) = \frac{C_\circ}{\dot{M} \log e} \left| \frac{d \log L}{d \log M} \right|^{-1} H(t - M/\dot{M})\ \dot{H}(t_c + M/\dot{M} - t)$$
$$\times\ M(L) \int_M^\infty \sigma_{IMF}(M')\, dM'. \tag{37}$$

Both the stellar mass $M(L)$ and the logarithmic derivative in equation (37) are to be evaluated using equation (3).

The basic form of Φ_{proto} is determined by the smooth function of mass, $M\int_M^\infty \sigma_{IMF}(M')\,dM'$, which appears in equation (37). This function, which we plot as Figure 7, falls to zero for both large and small values of M. Correspondingly, Φ_{proto} vanishes for large and small L, and reaches a maximum at some intermediate value. In addition, the luminosity function is modified by the causality window encountered previously. The presence of the window, viewed as a function of time, implies that the protostar population appears quite suddenly after $t = 0$ and disappears quickly after t_c, as we show in Section 3.3 below. Over a substantial period between $t = 0$ and $t = t_c$, the product of the step functions in equation (37) equals unity, and *the protostar luminosity function does not vary in time*, a result of key importance.

3.2.2 Post-Accretion Contribution

To evaluate $\Phi_{pa}(L,t)$, the luminosity function for post-accretion objects, we utilize the corresponding mass function $q(M,t_*,t)$, given in equation (33). The idea is to count up all contracting pre-main-sequence stars, over a range of track times, which have the luminosity L at cluster time t. Depending on the value of L, there may also be a unique mass which has this luminosity during the time deuterium burning is halting contraction, as well as a single mass on the main sequence. Thus, the final expression for $\Phi_{pa}(L,t)$ will consist of an integral over $q(M,t_*,t)$ together with several discrete terms. A convenient way to evaluate all terms is to first define a *cumulative luminosity function*, $\Sigma_{pa}(L,t)$, the total number of post-accretion stars at time t with luminosities from a minimum level, L_{min}, to L. The function $\Phi_{pa}(L,t)$ is then obtained by differentiating $\Sigma_{pa}(L,t)$ with respect to L.

Figure 8 shows the three regions of integration involved in the computation of Σ_{pa}. The figure is a schematic and highly simplified version of Figure 3, and again depicts the luminosity evolution for selected masses as a function of the reduced time τ_{red}. These schematic tracks are shown to be dimming with time; the general case includes tracks that brighten, as well as those that go through maxima and minima. Such eventualities have been taken into account in our calculations, but will only be discussed briefly. The lowest mass of interest, here labeled M_{min}, has a birthline luminosity equal to L_{min}, taken to be 0.01 $L_\odot$. A star with mass $M_D(L)$ starts with the luminosity L and maintains it, by virtue of deuterium burning, for an interval $t_D(M_D)$, given by equation (4). This interval shrinks to zero for masses below 0.3 $M_\odot$ and above 1 $M_\odot$, as described in Section 2.3. The dotted curve in the left portion of Figure 8 is obtained by setting $t_* = t_D$ for $M \le M_D$. The first region of integration, labeled A, is bounded on the right by this curve and on the left by the birthline ($\tau_{red} = 0$).

The luminosity of a star of mass M_D diminishes with time until $\tau_{red} = 1$, at which point the main sequence is reached, and the luminosity levels off. Higher-mass stars have correspondingly higher main-sequence luminosities, all reached at $\tau_{red} = 1$. The largest mass of interest, $M_{max}(L)$, has a main-sequence luminosity precisely equal to L. The vertical line corresponding to $\tau_{red} = 1$ forms the boundary between the

regions B and C. A track of arbitrary mass M only stays within any given region over a limited interval of track time, from a lower time t'_* to an upper one t''_*; the figure shows this interval for a track crossing region B. The maximum track time for any mass in region C, denoted $t_{max}(M)$, is taken to be the pre-main-sequence contraction time, $t_{pms}(M)$, plus $t_{ms}(M)$, the time to evolve off the main sequence.

With these definitions in hand, we write Σ_{pa} as a double integral over stellar masses and track times in all three regions:

$$\Sigma_{pa}(L,t) = \left(\int\int_A + \int\int_B + \int\int_C \right) dM\, dt_*\; q(M, t_*, t).$$

Substituting the expression for the mass function from equation (35), we have a sum of integrals of the form

$$I = C_\circ \int_{M'}^{M''} dM\, \sigma_{IMF}(M) \int_{t'_*}^{t''_*} dt_*\, H(t_* - t_1)\, H(t_2 - t_*), \tag{38}$$

where the integration limits in both mass and time depend on the specific region and on the luminosity L of interest.

Consider first the integration in region A. The temporal limits t'_* and t''_* are here zero and $t_D(M)$, respectively, and do not depend on the luminosity L. Similarly, both t_1 and t_2, as defined in equation (36), are independent of L, as is M', the lower bound in mass. Only the upper mass M'', here equal to $M_D(L)$, will vary when differentiating Σ_{pa} with respect to L. We have, therefore,

$$\left(\frac{\partial \Sigma_{pa}}{\partial L} \right)_t = N\, \sigma_{IMF}(M_D) \left(\frac{dL}{dM_D} \right)^{-1} J_A \qquad \textit{region } A, \tag{39}$$

where

$$J_A \equiv \frac{1}{t_c} \int_0^{t_D(M_D)} dt_*\, H(t_* - t_1)\, H(t_2 - t_*). \tag{40}$$

The term (dL/dM_D) in (39) is evaluated from the mass-luminosity relation for pre-main-sequence stars *on the birthline* that are actively burning deuterium. The dimensionless quantity J_A measures the degree of overlap between the window interval $[t_1, t_2]$, which is evaluated at the mass M_D using equation (36), and the deuterium-burning interval $[0, t_D(M_D)]$. In particular, if t_1 is greater than zero and if $t_2 < t_D(M_D)$, J_A has its maximum value of unity, since $t_2 - t_1 = t_c$.

Turning to region B, we note again the luminosity dependence of the upper mass limit, here equal to $M_{max}(L)$. However, Figure 8 shows that the two times t'_* and t''_* coincide for the track of mass M_{max}, so that the temporal integral in equation (38) vanishes. For tracks of lower mass, the time t'_* at which a star reaches the desired luminosity depends on the choice of L, while t''_*, the pre-main-sequence contraction

time, does not. We denote the former time by t_L. Using equation (33) for the step functions, and employing t_L as the track time in equations (34a) and (34b), we obtain

$$\left(\frac{\partial \Sigma_{pa}}{\partial L}\right)_t =$$
$$C_\circ \int_{M_{min}}^{M_{max}} \sigma_{IMF}(M) \left|\frac{\partial L}{\partial t_L}\right|_M^{-1} H(M-M_1)\, H(M_2-M)\, dM \qquad \textit{region } B. \tag{41}$$

In writing equation (41), we have again used the absolute value of the luminosity derivative to ensure a positive $\Phi_{pa}(L,t)$ when L diminishes with time. The lower mass limit will generally *not* be as low as M_{min}, as written, but the true value depends on the behavior of the tracks under consideration. For example, the limit is $M_D(L)$ in the situation depicted in Figure 8, since stars of lower mass never attain the luminosity L. Finally, we note that each mass only contributes to the integral if it lies within the causality window from M_1 to M_2. In evaluating these two masses from equation (34), the time t_L is used for t_*.

Consider finally the integration in region C. The lowest mass of interest, not depicted in Figure 8, is that which reaches the luminosity L_{min} at $\tau_{red} = 1$; its value is independent of L.[4] The largest mass is $M_{max}(L)$, while the temporal limits for any intermediate mass are, as in region A, independent of L. Thus, the contribution to the luminosity derivative of Σ_{pa} is

$$\left(\frac{\partial \Sigma_{pa}}{\partial L}\right)_t = N\, \sigma_{IMF}(M_{max}) \left(\frac{dL}{dM_{max}}\right)^{-1} J_C \qquad \textit{region } C, \tag{42}$$

where

$$J_C \equiv \frac{1}{t_c} \int_{t_L}^{t_{max}} dt_*\, H(t_*-t_1)\, H(t_2-t_*). \tag{43}$$

The derivative on the right side of equation (42) is to be evaluated for stars on the ZAMS. In addition, all the times in equation (43), including the integration limits, refer to the mass M_{max}. The integral J_C, whose value falls between 0 and 1, measures the degree of overlap between the window interval $[t_1, t_2]$ and the interval measured from the pre-main-sequence contraction time to t_{max}. Since the latter is set by the time required to leave the main sequence, equation (43) automatically deletes the luminosity of all those stars which have evolved past the point of hydrogen burning.

Adding together all of its contributions, and remembering that Φ_{pa} refers to the number of stars per unit *logarithmic* luminosity interval, we may write the post-accretion luminosity function in the form

$$\Phi_{pa}(L,t) = [\Phi_{pa}]_A + [\Phi_{pa}]_B + [\Phi_{pa}]_C\,, \tag{44a}$$

[4] As discussed in Section 2.3, very low masses never ignite hydrogen, so that τ_{red} is taken to be unity for them at an arbitrarily assigned track time.

where

$$[\Phi_{pa}]_A \equiv \frac{N}{\log e}\, M_D\, \sigma_{IMF}(M_D) \left(\frac{d\log L}{d\log M_D}\right)^{-1} J_A \tag{44b}$$

$$[\Phi_{pa}]_B \equiv \frac{N}{\log e} \int_{M_{min}}^{M_{max}} \sigma_{IMF}(M) \left|\frac{\partial \log L}{\partial \log t_L}\right|_M^{-1} J_B\, dM \tag{44c}$$

$$[\Phi_{pa}]_C \equiv \frac{N}{\log e}\, M_{max}\, \sigma_{IMF}(M_{max}) \left(\frac{d\log L}{d\log M_{max}}\right)^{-1} J_C\ , \tag{44d}$$

and where J_B in equation (44c) is defined as

$$J_B \equiv \frac{t_L}{t_c}\, H(M-M_1)\, H(M_2-M). \tag{45}$$

Note that J_B, unlike J_A and J_C, is no longer limited to a maximum value of unity, since the pre-main-sequence contraction time can be greater than t_c for sufficiently small masses. The term $[\Phi_{pa}]_C$ is itself of interest, since it represents the luminosity function of the main-sequence population of stars. The complete cluster luminosity function, $\Phi(L,t)$, is the sum of $\Phi_{proto}(L,t)$ from equation (37) and $\Phi_{pa}(L,t)$ from equation (44).

Figure 3 shows that, for many masses, the luminosity passes through temporary minima and maxima during pre-main-sequence contraction. In such cases, the terms in (44c) multiplying $\sigma_{IMF}(M)$ must be replaced by a discrete sum, each term corresponding to a track time when the luminosity L is reached for the mass in question. Since the luminosity can have local extrema, there are, for any fixed L, a finite number of masses for which $|\partial log L/\partial \log t_L|_M$ may vanish. The blowup of the integrand in (44c) is compensated by a shrinking of the interval of mass integration, so that the contribution to Φ_{pa} remains finite. Nevertheless, it is not feasible to continue a direct numerical integration of (44c) through such a point. The solution is to reconsider the evaluation of Σ_{pa} in the neighborhood of the extremum, reversing the order of integration in equation (38). If we then differentiate with respect to luminosity as before, and retain the temporal form of the step functions, we find a contribution to the luminosity function of $\Delta\Phi_{pa}$, where

$$\Delta\Phi_{pa} \equiv \frac{N}{\log e} \int_{t_<}^{t_>} \frac{dt_*}{t_c} M\, \sigma_{IMF}(M) \left|\frac{\partial \log L}{\partial \log M}\right|_{t_*}^{-1} H(t_*-t_1)\, H(t_2-t_*). \tag{46}$$

Here, $t_<$ and $t_>$ represent two track times bracketing the one at which $|\partial \log L/\partial \log t_*|_M$ vanishes. The mass M in equation (46) refers to that value which has luminosity L at track time t_*; the track times t_1 and t_2 are also evaluated at this mass. Since the new partial derivative in the integrand does not vanish, the integration can proceed smoothly. Equation (46) cannot, however, be used in place of equation (44c) everywhere. As suggested in Figure 3, two neighboring tracks occasionally intersect in the $L - t_*$

plane; hence, the term $(\partial \log L/\partial \log M)_{t_*}$ vanishes. Both forms of the integral, then, are needed to cover all eventualities.

Another practical difficulty appears at late epochs for stars of relatively low mass. As mentioned before, the contraction times t_L for such stars can greatly exceed t_c. The causality window in equation (44c) is then so narrow that few, if any, points from the tabulated tracks enter into the Riemann sum used to evaluate the integral numerically. In this regime, we adopt a "narrow-window approximation," in which we need only evaluate the integral in (44c) at a single point within the window of width ΔM:

$$[\Phi_{pa}]_B \longrightarrow \frac{N}{\log e}\,\frac{t_L(M_\circ)}{t_c}\,\Delta M\,\sigma_{IMF}(M_\circ)\left|\frac{\partial \log L}{\partial \log t_L}\right|^{-1}_{M_\circ}. \tag{47}$$

Here, $M_\circ$ is the mass obtained by solving the equation

$$t_L(M_\circ) = t - M_\circ/\dot{M}. \tag{48}$$

The width ΔM is, from equations (34a) and (34b):

$$\begin{aligned}\Delta M &= M_2 - M_1 \\ &= \dot{M}t_c - \dot{M}[t_L(M_2) - t_L(M_1)].\end{aligned}$$

In practice, equations (34a) and (34b) were solved iteratively to evaluate ΔM precisely. To see the approximate magnitude of ΔM in the present case, note that $t_L(M_2) - t_L(M_1) \approx (\partial t/\partial M)_L \Delta M \approx (t_L/M_\circ)\Delta M$. It follows that

$$\begin{aligned}\Delta M &\approx \frac{\dot{M}t_c}{1 + \dot{M}t_L/M_\circ} \\ &\approx \left(\frac{t_c}{t_L}\right) M_\circ \\ &\ll M_\circ.\end{aligned}$$

The narrow-window approximation consists essentially of viewing the entire cluster formation as a brief, impulsive event. The representative mass $M_\circ$ singled out by equation (48) is that which began to condense from its parent dense core at $t = 0$, and then stopped accreting early enough so that it could cool to luminosity L in time t.

3.3 Evolution of Number Fractions and Total Luminosities

Within the context of our model of cluster formation, it is a straightforward exercise to follow the fractional contribution of each of the stellar populations, both by number and by total luminosity. In this subsection, we derive the relevant formulae to be evaluated numerically in Paper II. Both the absolute and relative number of protostars, however, can be determined without recourse to the later numerical results, so we begin by finding these important quantities.

3.3.1 Protostar Fraction

At any cluster time t, the total number of protostars can be found by integration of the appropriate mass function:

$$N_{proto} = \int_0^\infty dM\, p(M,t). \tag{49}$$

The function $p(M,t)$ can be taken from equation (29), but with the window rewritten in terms of mass rather than time:

$$p(M,t) = \frac{C_o}{\dot{M}}\, H(M - M_{low})\; H(M_{high} - M) \int_M^\infty dM'\, \sigma_{IMF}(M'), \tag{50}$$

where $M_{low} \equiv \dot{M}\,(t - t_c)$ and $M_{high} \equiv \dot{M}\,t$. Substituting (50) into (49), we obtain

$$N_{proto} = \frac{C_o}{\dot{M}} \int_{M_{low}}^{M_{high}} dM \int_M^\infty dM'\, \sigma_{IMF}(M'). \tag{51}$$

In this equation, it is understood that M_{low} is zero if $t \le t_c$.

It is instructive to rewrite equation (51) in nondimensional form. To do so, we first need to define a fiducial mass $\bar{M}$. A convenient choice is the mass increment in which the Miller-Scalo function of equation (6) falls to e^{-1} of its value at the observational lower limit $M = 0.1\,M_\odot$. With this convention, $\bar{M} = 0.87\,M_\odot$. After defining a nondimensional mass $m \equiv M/\bar{M}$, we write a new function $\sigma(m)$ by requiring that

$$\sigma(m)\, dm = \sigma_{IMF}(M)\, dM.$$

Thus, $\sigma(m)$ is given by

$$\sigma(m) = \bar{M}\, \sigma_{IMF}(M),$$

and is also normalized to unity. Finally, we define a nondimensional time $\tau \equiv \dot{M}\, t/\bar{M}$. The variable τ measures the cluster's age relative to the time required to build up through accretion a protostar of characteristic mass $\bar{M}$.

With these definitions, equation (51) can be rewritten as

$$\frac{N_{proto}}{N} = \begin{cases} I(\tau)/\tau_c & \tau < \tau_c \qquad (52a) \\ [I(\tau) - I(\tau - \tau_c)]/\tau_c & \tau \ge \tau_c. \qquad (52b) \end{cases}$$

Here, $\tau_c \equiv \dot{M}\, t_c/\bar{M}$, and the nondimensional function $I(\tau)$ is given by

$$I(\tau) \equiv \int_0^\tau dm \int_m^\infty dm'\, \sigma(m'). \tag{53}$$

Notice that τ_c is expected to be a large number, at least under conditions resembling present-day galactic star formation. Thus, for a t_c of 10^7 yr and an $\dot{M}$ of $10^{-5}\,M_\odot\ \mathrm{yr}^{-1}$, τ_c equals 115.

The second integral in equation (53) has nearly its full value of unity for $m \ll 1$, and diminishes to zero as m increases. Thus, $I(\tau) \approx \tau$ for $\tau \ll 1$, begins to slow its rise for $\tau \sim 1$, and then levels off to a constant value I_∞, of order unity, as τ tends to infinity.

Since $I(\tau)$ monotonically increases with τ, it follows from equation (52) that N_{proto} reaches a maximum at τ_c. Moreover, equation (52b) shows that N_{proto} falls to zero at greater times. Neither result is surprising, since the cutoff time marks the end of new dense core collapses. More interesting is the nature of the rise of N_{proto}. From our discussion of the properties of $I(\tau)$, N_{proto} nearly reaches its peak value in a relatively brief time ($\tau \sim 1$), and then retains that value for a long period ($1 \lesssim \tau \lesssim \tau_c$), before dropping sharply to zero. This behavior is shown in Figure 9.

Our finding that N_{proto} maintains a nearly constant level for a substantial time emphasizes a basic difference between protostars and the other stellar populations. Protostars represent an intermediate, temporary phase for the diffuse interstellar material as it condenses into stars of fixed mass. Thus, the protostars need not increase in number along with other stars. Indeed, the peak value for N_{proto} of $(I_\infty/\tau_c)\,C_o t_c$ is a small fraction of the total number of stars produced in the cluster.

The fractional content of protostars is, in fact, another quantity which we can readily determine, and is more closely tied to observations than N_{proto}. We define f_{proto} as the number of protostars at any time relative to the total number of stars produced up to that time. Thus, f_{proto} is obtained by dividing N_{proto} by $C_o t$ for $t < t_c$, and by $C_o t_c$ for $t \geq t_c$. The result is

$$f_{proto} = \begin{cases} I(\tau)/\tau & \tau < \tau_c \qquad (54a) \\ [I(\tau) - I(\tau - \tau_c)]/\tau_c & \tau \geq \tau_c. \qquad (54b) \end{cases}$$

and is also displayed in Figure 9. The fraction of protostars begins at unity; this fact can be proved formally by taking the appropriate limit of equation (54a). After a brief transient period, f_{proto} declines approximately as τ^{-1} until $\tau = \tau_c$, after which it falls quickly to zero.

Since f_{proto} varies in time, it is convenient to determine a "typical" value. In a highly embedded cluster, we can assume that $t < t_c$, but we will not know, of course, the precise cluster age. Hence, a useful average is given by

$$< f_{proto} > \equiv \frac{1}{\tau_c} \int_0^{\tau_c} d\tau\, f_{proto}(\tau). \qquad (55)$$

Substituting $f_{proto}(\tau)$ from equation (54a), we find that

$$< f_{proto} > = \frac{1}{\tau_c} \int_0^{\tau_c} d\tau\, \frac{I(\tau)}{\tau}.$$

Taking our cue from the behavior of $I(\tau)$, we divide the integration interval at the point $\tau = 1$. We then extract the asymptotic value of $I(\tau)$ to find

$$< f_{proto} >= \frac{1}{\tau_c} \left(\int_0^1 d\tau \, \frac{I(\tau)}{\tau} - \int_1^{\tau_c} d\tau \, A(\tau) + \int_1^{\tau_c} d\tau \, \frac{I_\infty}{\tau} \right), \tag{56}$$

where

$$A(\tau) \equiv \frac{I_\infty - I(\tau)}{\tau} \, .$$

Since $I(\tau)$ is already close to I_∞ at $\tau = 1$, $A(\tau)$ rapidly falls to zero as τ increases above unity. Thus, in the second integral of equation (56), we can safely extend the upper limit to infinity. The first and second integrals can then be combined to give a constant, denoted B, which is of order unity. Carrying out the third integral, we arrive at the result

$$< f_{proto} >= \frac{I_\infty \ln(\tau_c) + B}{\tau_c} \, . \tag{57}$$

Numerical values for I_∞ and B are listed in Table 2 for the various brown dwarf contributions to the IMF.

Equation (57) shows that, for the values of $\dot{M}$ and τ_c quoted earlier, the average protostar fraction is only a few percent. If our parameter choice is indeed a reasonable one, it will be difficult to find protostars in clusters with less than several hundred member stars. In spite of their small numbers, however, protostars are expected to dominate the total cluster luminosity until the appearance of significant numbers of main-sequence stars, as we discuss in Paper II.

Our derivation of N_{proto} and f_{proto} has ignored the possibility, mentioned in Section 2.5, that stars gain enough mass through accretion to complete hydrogen burning while still in the protostar phase. Strictly speaking, then, M_{high} in equation (50) should be the lesser of $\dot{M}t$ and the critical mass at which this event occurs. As we demonstrate in the Appendix, this correction has no practical effect on the results thus far, since the critical mass is so much higher than the fiducial value $\bar{M}$. On the other hand, there *will* be an effect when we later determine the integrated luminosity of the protostar population.

3.3.2 Fractions of Other Populations

The total number of post-accretion stars, which is given by the integral over mass of $s(M,t)$ from equation (30), is found to be

$$N_{pa} = C_\circ \int_0^{\dot{M}t} dM \min\{t_c, t - M/\dot{M}\} \, \sigma_{IMF}(M).$$

For $t < t_c$, the integral becomes

$$N_{pa} = C_o \int_0^{\dot{M}t} dM\,(t - M/\dot{M})\,\sigma_{IMF}(M)$$
$$= C_o t \int_0^{\dot{M}t} dM\,\sigma_{IMF}(M) - \frac{C_o}{\dot{M}} \int_0^{\dot{M}t} dM\,M\,\sigma_{IMF}(M).$$

After doing the second integral by parts, this last equation becomes

$$N_{pa} = \frac{C_o}{\dot{M}} \int_0^{\dot{M}t} dM \int_0^{M} dM'\,\sigma_{IMF}(M') \qquad t < t_c. \tag{58}$$

Equation (58), together with equation (51), yields the expected result that, for $t < t_c$, $N_{proto} + N_{pa} = C_o t$. That is, all stars produced are either protostars or post-accretion objects. A similar exercise shows that, for $t \geq t_c$, $N_{proto} + N_{pa} = C_o t_c \equiv N$. In the nondimensional notation introduced earlier, the general result may be written

$$\frac{N_{pa}}{N} = \begin{cases} \tau/\tau_c - I(\tau)/\tau_c & \tau < \tau_c \qquad (59a) \\ 1 - [I(\tau) - I(\tau - \tau_c)]/\tau_c & \tau \geq \tau_c. \qquad (59b) \end{cases}$$

Let us now further subdivide the post-accretion population. The total number of main-sequence stars at any time, N_{ms}, is obtained by integrating $q(M, t_*, t)$ from equation (35) over all masses and over track times from the pre-main-sequence contraction time, $t_{pms}(M)$, to the end of the main-sequence phase at $t_{max}(M)$:

$$N_{ms} = C_o \int_0^{\infty} dM\,\sigma_{IMF}(M) \int_{t_{pms}}^{t_{max}} dt_*\,H(t_* - t_1)\,H(t_2 - t_*)$$
$$= C_o t_c \int_0^{\infty} dM\,\sigma_{IMF}(M)\,J_C(M, t),$$

where J_C is the nondimensional overlap integral defined in equation (43). The fraction of main-sequence stars is therefore given by

$$f_{ms} = \begin{cases} (\tau_c/\tau) \int_0^{\infty} dm\,\sigma(m)\,J_C(m, \tau) & \tau < \tau_c \qquad (60a) \\ \int_0^{\infty} dm\,\sigma(m)\,J_C(m, \tau) & \tau \geq \tau_c. \qquad (60b) \end{cases}$$

After a sufficiently long cluster t, the interval $[t_1, t_2]$ lies wholly inside the interval $[t_{pms}, t_{max}]$ for a large range of masses, so that $J_C = 1$ within this range and, from equation (60b), f_{ms} approaches $\int_0^{\infty} dm\,\sigma(m) = 1$.

If the cluster survives for even longer times, t_2 grows greater than t_{max} for some masses, which begin to leave the main sequence. Quantitatively, the fraction of post-main-sequence stars, f_{post}, is given by an expression identical to equation (60), but with a new overlap integral J_D:

$$J_D \equiv \frac{1}{t_c} \int_{t_{max}}^{t} dt_* \, H(t_* - t_1) \, H(t_2 - t_*). \tag{61}$$

Finally, the fraction of pre-main-sequence stars, f_{pms}, is found from

$$f_{pms} = 1 - f_{proto} - f_{ms} - f_{post}. \tag{62}$$

3.3.3 Luminosity Fractions

We can also follow the contribution of each stellar population to the total luminosity emitted by the cluster at any epoch. The cluster luminosity is found by integrating over the total luminosity function:

$$L_{tot}(t) = \int_{-\infty}^{+\infty} L \, \Phi(L,t) \, d\log L. \tag{63}$$

In practice, the lower integration limit in (63) is taken to be $L_{min} \equiv 0.01 \, L_{\odot}$. This truncation of the integral causes little error, since, for all cluster times of interest, $L\Phi(L,t)$ peaks at a luminosity well above L_{min}. The integration extends to the luminosity where $\Phi(L,t)$ falls to zero. At early times, this upper limit is that associated with the stellar mass Mt, i.e., the largest mass that can be accreted in time t. Later in the cluster evolution, $\Phi(L,t)$ is truncated at the luminosity corresponding to that stellar mass which is just leaving the main sequence.

The total luminosity of any stellar population, *e.g.*, protostars or main- sequence stars, is again given by equation (63), but with the corresponding luminosity function used in the integrand. The ratio of this integral to L_{tot} then gives the desired fractional contribution. Since the protostars dominate by number at very early times ($\tau \lesssim 1$), we expect them also to have the highest fraction of the total luminosity at this epoch. At later times, their number fraction falls steadily, as we have seen. However, we show in Paper II that their *luminosity* fraction continues to dominate for a substantial period of time.

4. Discussion

We have presented a method for calculating the history of the luminosity function in an idealized embedded cluster. Our basic assumption is that a typical cluster forms by the continuous collapse of individual dense cores located throughout a larger cloud complex. This picture, although rooted in the results of current observational and theoretical research, differs sharply from that traditionally found in the literature. Previous calculations, which have generally been directed toward explaining the IMF,

have posited schemes by which the parent cloud breaks apart into smaller subunits. These subunits either evolve independently, breaking into even smaller pieces, or perhaps coalesce or accrete gas from their surroundings (*e.g.*, Silk and Takahashi 1979, Smith 1985). Such schemes can be criticized for their *ad hoc* nature, since they have not been based on actual calculations of cloud dynamics.[5] In addition, they are designed to yield a final mass distribution of cloud fragments, rather than of stars. The connection between the two is not obvious. We now believe that dense cores forming embedded young stars are dispersed by powerful protostellar winds generated from within. Thus, the mass of a star is not simply that of its progenitor cloud, but is at least partially set by processes occurring in or near the star itself.

The route we have taken is to *assume* the final distribution of stellar masses, and then to link that distribution to the ending of accretion onto individual protostars. This link has changed the focus for any future explanation of the IMF, and, more importantly, has allowed us to follow the development in time of the luminosity function. Approaches similar to ours have been taken by several authors. In their discussion of the Taurus-Auriga association, Kenyon *et al.* (1990) attempted to construct the cumulative luminosity function for a forming cluster. They assumed that all embedded stars radiate at the accretion luminosity of equation (2) and are distributed by number according to the product of the IMF and the accretion time for the mass of interest. If one takes the IMF to be a single power law, then our own equation (29) actually reduces to this form, at least for the epoch in which the protostar luminosity function is constant in time. Motivated by the recent observations of ρ Ophiuchus, Zinnecker, McCaughrean, and Wilking (1993) calculated the changing luminosity function for a cluster of contracting pre-main-sequence stars; these stars were of fixed mass and were distributed according to a more realistic IMF than that used by Kenyon *et al.* However, the authors neglected the protostar phase entirely, and assumed for simplicity that all cluster members formed at the same instant. Finally, Lada (1991) has lucidly described, in a qualitative manner, the main features of luminosity functions for very young clusters.

Our derivation of the protostar fraction, f_{proto}, also departs from previous work. The traditional argument is to obtain f_{proto} by comparing a time scale for protostellar accretion to one for pre-main-sequence evolution (see, *e.g.*, eq. (1) of Kenyon *et al.* 1990). However, both times are strongly sensitive to stellar mass, so it is not at all clear how they should be evaluated. Furthermore, this argument ignores the essential time dependence of f_{proto}, a feature displayed in equation (54).

The underlying model of cluster formation used here is a simple one, and could be modified for future applications. For example, one could consider relaxing the abrupt nature of the beginning and ending of star formation, or the the strict constancy of $C(t)$ prior to cutoff. In a model with a slowly changing $C(t)$, N_{proto} would be expected to vary on the same time scale. The current state of cluster observations does not warrant such changes, but they could readily be incorporated into our mathematical framework.

[5] A notable exception is the hierarchical fragmentation picture of Bodenheimer (1978), which was inspired by numerical simulations of cloud collapse.

A second modification would be to introduce an increase of $\dot{M}$ with protostellar mass. A number of authors have advocated such a variation (*e.g.*, Cassen, Shu, & Terebey 1985), but the underlying evidence, both observational and theoretical, is still too weak to quantify the mass dependence. Furthermore, Palla and Stahler (1992) have shown that a fixed $\dot{M}$ of order $10^{-5}\ M_\odot\ \mathrm{yr}^{-1}$ yields a satisfactory birthline for stars up to about 10 $M_\odot$. An increase of $\dot{M}$ beyond this mass would alter only slightly the luminosity functions presented in Paper II. In any case, a new theoretical calculation of accretion onto massive stars should help to clarify the situation.

We thank F. Palla for extensive discussions that helped to define the direction and scope of this project. We are also grateful to L. Nelson and D. Vandenberg for generously supplying numerical evolutionary tracks prior to publication. Financial support for A. B. F. was provided by B. Burke through NSF grant AST-90-22501. S. W. S. was supported principally by NSF Grant AST-90-14479. In addition, he received funding from the NASA astrophysics theory program through its Center for Star Formation Studies, a consortium of U. C. Berkeley, U. C. Santa Cruz, and NASA-Ames Research Center.

this fraction declined to zero asymptotically at late times. Since, however, N_{proto}/N fell steeply once τ exceeded τ_c by an amount of order unity, the quantitative effect is again small. The reader may verify that similar modifications hold for the case $\tau_{crit} > \tau_c$.

Finally, consider the formation of post-main-sequence stars through hydrogen exhaustion in massive protostars. Using the schematic diagram of Figure 5, we find that the production rate is given by $\dot{M}p(M_{crit}, t)$. Now $p(M_{crit}, t)$ is zero until $t = M_{crit}/\dot{M}$. It is then a constant, which we denote as p_{crit}, until $t = t_c + M_{crit}/\dot{M}$, the time at which the entire protostar population vanishes. Thus, the total number of post-main-sequence stars created is

$$\begin{aligned} N'_{post} &= \dot{M}\, t_c\, p_{crit} \\ &= N \int_{\tau_{crit}}^{\infty} \sigma(m')\, dm' \,, \end{aligned} \tag{A4}$$

where equation (29) has been used for p_{crit}. Evaluating the integral in (A4), we find that $N'_{post}/N = 1.4 \times 10^{-4}$ for $\dot{M} = 1 \times 10^{-5} M_\odot$ yr^{-1}, and 4.8×10^{-4} for $\dot{M} = 2 \times 10^{-6}\, M_\odot$ yr^{-1}.

Appendix

Evolution of Massive Protostars

Our picture of cluster formation allows the possibility that protostars accrete so much mass that they evolve off the main sequence while still surrounded by their parent clouds. If we adopt the simplest assumption that $\dot{M}$ is still a constant through this epoch, then the critical mass can be estimated from the equation

$$\frac{M_{crit}}{\dot{M}} = t_{ms} \ , \tag{A1}$$

where t_{ms}, the main-sequence lifetime, is given in Table 1 as a function of stellar mass. Equation (A1) ignores the effect of mass loss, which could be substantial (Maeder 1987). For $\dot{M} = 1 \times 10^{-5} M_\odot$ yr^{-1}, we find that M_{crit} is 27 $M_\odot$, while it is 16 $M_\odot$ for $\dot{M} = 2 \times 10^{-6} M_\odot$ yr^{-1}. The corresponding main-sequence luminosities, L_{crit}, also taken from Table 1, are $8.9 \times 10^4 L_\odot$ and $2.8 \times 10^4 L_\odot$, respectively. The critical times, $t_{crit} \equiv t_{ms}(M_{crit})$, are 2.7×10^6 yr and 8.2×10^6 yr, respectively.

We suppose that the protostar smoothly builds up its mass to M_{crit}, after which it abruptly enters its post-main-sequence phase. In this case, the maximum stellar mass at any cluster time t would be the minimum of $\dot{M}t$ and M_{crit}. The protostar and post-accretion mass functions, given in equations (29) and (30), should therefore be truncated at this maximum mass, as should the luminosity functions derived in Section 3.2. Because of the rapid falloff of σ_{IMF} with mass, this truncation has no practical effect. We can demonstrate this fact more explicitly by re-examining N_{proto}, the protostar number derived in Section 3.3.1.

Consider first the double integral in equation (51). We define a critical dimensionless time, τ_{crit}, by

$$\tau_{crit} \equiv \frac{\dot{M} t_{crit}}{\bar{M}} = \frac{M_{crit}}{\bar{M}} \ . \tag{A2}$$

Suppose first that $\tau_{crit} \leq \tau_c$. If $\tau \leq \tau_{crit}$, the maximum protostellar mass, M_{high}, is still equal to $\dot{M}\,t$, and we may retain equation (52). If $\tau > \tau_{crit}$, however, M_{high} becomes M_{crit}. Provided $\tau \leq \tau_{crit} + \tau_c$, we also have $M_{low} \leq M_{crit}$, and equation (52) must be modified to

$$\frac{N_{proto}}{N} = \begin{cases} I(\tau_{crit})/\tau_c & \tau_{crit} < \tau < \tau_c \quad (A3a) \\ [I(\tau_{crit}) - I(\tau - \tau_c)]/\tau_c & \tau \geq \tau_c. \quad (A3b) \end{cases}$$

Now τ_{crit} is 32 for $\dot{M} = 1 \times 10^{-5} M_\odot$ yr^{-1} and 19 for $\dot{M} = 2 \times 10^{-6} M_\odot$ yr^{-1}. Since $I(\tau)$ levels off for τ greater than unity, the actual change in N_{proto}/N is minor.

Once a nondimensional time $\tau_{crit}+\tau_c$ has elapsed, even the protostars of minimum mass have evolved off the main sequence, so N_{proto}/N is identically zero. Previously,

Table 1

Adopted Stellar Properties

$M(M_\odot)$	$R_b(R_\odot)$	$\log_{10}(L_b/L_\odot)$	$t_{pms}(yr)$	$\log_{10}(L_{ms}/L_\odot)$	$t_{ms}(yr)$
0.010	2.16	-0.652			
0.020	2.25	-0.551			
0.040	2.35	-0.434			
0.060	2.41	-0.351			
0.085	2.47	-0.265	8.45×10^9	-3.94	
0.10	2.49	-0.219	1.15×10^9	-3.12	
0.20	2.52	+0.018	3.91×10^8	-2.34	
0.40	2.70	+0.213	2.97×10^8	-1.71	
0.60	3.53	+0.439	2.89×10^8	-1.20	
0.80	4.30	+0.691	1.26×10^8	-0.625	
1.00	4.88	+0.838	6.84×10^7	-0.163	
1.50	5.03	+0.968	1.80×10^7	+0.732	1.55×10^9
2.00	4.96	+1.01	7.54×10^6	+1.27	6.75×10^8
2.50	4.83	+1.30	3.59×10^6	+1.67	3.62×10^8
3.00	5.68	+1.78	1.84×10^6	+1.98	2.21×10^8
4.00	10.2	+2.30	7.85×10^5	+2.44	1.11×10^8
8.05	3.12			+3.49	2.65×10^7
10.0	3.61			+3.79	1.84×10^7
20.0	5.70			+4.67	5.39×10^6
30.0	7.30			+5.08	2.23×10^6

Note that there is no main sequence for $M < 0.085\,M_\odot$ and that the birthline and the ZAMS coincide for $M \geq 8.05\,M_\odot$. For these most massive stars, R_b in the table denotes the ZAMS radius.

Table 2

Terms in Protostar Fraction $< f_{proto} >$

Brown Dwarf Case	I_∞	B
Zero Level	0.713	0.405
Flat	0.488	0.338
Sloping	0.421	0.311
Gaussian	0.372	0.288

References

Bertout, C., Basri, G., & Bouvier, J 1988, ApJ, 330, 350

Bodenheimer, P. 1978, ApJ, 224, 488

Boss, A. P. & Black, D. C. 1982, ApJ, 258, 270

Cassen, P. M., Shu, F. H., & Terebey, S. 1985, in Protostars and Planets II, ed. D. C. Black & M. S. Matthews (Tucson: Univ. of Arizona Press), p. 448

Cassen, P. M. & Moosman, A. 1981, Icarus, 48, 353

Edwards, S., Ray, T., & Mundt, R. 1993 in Protostars and Planets III, eds. E. H. Levy & J. Lunine (Tucson: Univ. of Arizona Press), p. 567

Elmegreen, B. & Clemens, C. 1985, ApJ, 294, 523

Ezer, D. & Cameron, A. G. W. 1967, Can J Phys, 45, 3429

Garmany, C. 1994, PASP, 106, 25

Gatley, I., Depoy, D. L., & Fowler, A. M. 1988, Science, 242, 1264

Greene, T. & Young, E. T. 1992, ApJ, 395, 516

Grossman, A. S. & Graboske, H. C. 1971, ApJ, 164, 475

Hartmann, L. W. & Kenyon, S. J. 1990, ApJ, 349, 190

Herbig, G. E. 1962, Adv A & A, 1, 47

Hubbard, W. B., Burrows, A., & Lunine, J. I. 1990, ApJ, 358, L53

Iben, I. 1965, ApJ, 141, 993

Iben, I. 1967, ARAA, 5, 571

Iben, I. & Talbot, R. J. 1966, ApJ, 144, 968

Kenyon, S. J., Hartmann, L. W., Strom, K. M., & Strom, S. E. 1990, AJ, 99, 869

Kroupa, P., Tout, C. A., & Gilmore, G. 1990, MNRAS, 244, 76

Lada, C. J. 1991, in The Physics of Star Formation and Early Stellar Evolution, ed. C. J. Lada & N. D. Kylafis (Dordrecht: Reidel), p. 329

Lada. E. A., DePoy, D. L., Evans, N. J., & Gatley, I. 1991, ApJ, 371, 171

Ladd, E. F., Lada, E. A., & Myers, P. C. 1993, ApJ, 410, 168

Larson, R. B. 1969, MNRAS, 145, 271

Larson, R. B. 1973, MNRAS, 161, 133

Leisawitz, D. 1990, ApJ, 359, 319

Maeder, A. 1987, A & A, 173, 247

Mestel, L. & Spitzer, L. 1956, MNRAS, 116, 503

Mihalas, D. & Binney, J. 1981, Galactic Astronomy, Second Edition (New York: Freeman), pp. 229-232

Miller, G. E. & Scalo, J. M. 1979, ApJS, 41, 513

Myers, P. C. & Benson P. J. 1983, 266, 309

Myers, P. C., Fuller, G. A., Mathieu, R. D., Beichman, C. A., Benson, P. J., Schild, R. E., & Emerson, J. A. 1987, ApJ, 319, 340

Nakano, T. C. 1976, PASJ, 28, 355

Nelson, L. A. 1991, private communication

Nelson, L. A., Rappaport, S. A., & Joss, P. C. 1986, ApJ, 311, 226

Palla, F. & Stahler, S. W. 1990, ApJ, 360, L47

Palla, F. & Stahler, S. W. 1991, ApJ, 375, 288

Palla, F. & Stahler, S. W. 1992, ApJ, 392, 667

Palla, F. & Stahler, S. W. 1993, ApJ, 418, 414

Prusti, T., Whittet, D. C. B., & Wesselius, P. R. 1992, MNRAS, 254, 361

Salpeter, E. E. 1955, ApJ, 121, 161

Scalo, J. M. 1986, Fund Cosm Phys, 11, 1

Shu, F. H. 1977, ApJ, 214, 488

Silk, J. & Takahashi, Y. 1979, ApJ, 229, 242

Smith, G. H. 1985, ApJ, 293, 251

Stahler, S. W. 1983, ApJ, 274, 822

Stahler, S. W. 1988, ApJ, 332, 804

Stahler, S. W. 1989, ApJ, 347, 950

Stahler, S. W., Korycansky, D. G., Brothers, M. J., & Touma, J. 1993, ApJ, in press

Stahler, S. W., Shu, F. H., & Taam, R. E. 1980, ApJ, 241, 637

Straw, S. M., Hyland, A. R., & McGregor, P. J. 1989, ApJS, 69, 99

Tinney, C. G., Mould, J. R., & Reid, I. N. 1992, ApJ, 396, 173

Vandenberg, D. A. 1990, private communication

Wielen, R. 1985, in Dynamics of Star Clusters, IAU Symposium 113, ed. J. Goodman & P. Hut (Dordrecht: Reidel), p. 449

Wilking, B. A., Greene, T. P., Lada, C. J., Meyer, M. R., & Young, E. T. 1992, ApJ, 397, 520

Wilking, B. A., Lada, C. J., & Young, E. T. 1989, ApJ, 340, 823

Winkler, K.-H. & Newman, M. J. 1980, ApJ, 236, 201

Yang, J., Fukui, Y., Umemoto, T., Ogawa, H., & Chen, H. 1990, ApJ, 362, 538

Zinnecker, H., McCaughrean, M., & Wilking, B. A. 1993, in Protostars and Planets III, ed. E. H. Levy & J. Lunine (Tucson: Univ. of Arizona Press), p. 429

Figure Captions

Figure 1: Mass-radius relation for protostars. For $0.1\,M_\odot \leq M \leq 8\,M_\odot$, the radii are taken from Stahler (1988) and Palla and Stahler (1991), for the case $\dot{M} = 1 \times 10^{-5}\,M_\odot$ yr^{-1}. The radii for $M > 8\,M_\odot$ are the ZAMS values of Ezer and Cameron (1967). As explained in the text, a power-law mass-radius relation was adopted for masses below 0.1 $M_\odot$.

Figure 2: Mass-luminosity relation for protostars, in the case $\dot{M} = 1 \times 10^{-5}\,M_\odot$ yr^{-1}. The luminosity is shown as the sum of its accretion and internal contributions, as in equation (3).

Figure 3: Cooling curves for pre-main-sequence stars. The solid curves show, for a number of different masses, the luminosity, $\log(L/L_\odot)$, as a function of the reduced time, τ_{red}, defined in equation (5). The solid curves are labeled with the stellar mass, in solar units. The dashed curves are isochrones of constant track time, t_*; each isochrone is labeled by the time in years.

Figure 4: Four adopted forms for the IMF. Plotted as a function of stellar mass M, in solar units,is $\sigma_{IMF}(M)$, the number of stars per unit mass. Each of the four curves is normalized so that $\int_0^\infty \sigma_{IMF}(M)\,dM = 1$. The numbers in parentheses give, for each form, the fraction of stars with masses below 0.1 $M_\odot$.

Figure 5: Transfer of stars among the protostar and post-accretion populations. The expressions written near the arrows give the fraction of protostars of a given mass that take each of the two alternative paths.

Figure 6: Evolution of post-accretion stars. In this schematic H-R diagram, a group of stars, all with nearly the same mass M, descends from position A near the birthline (*dashed curve*) to position B, at cluster time t_1. The group spans a range Δt_* in track time.

Figure 7: Plot of $M \int_M^\infty \sigma_{IMF}(M')\,dM'$, the function which enters into $\Phi_{proto}(L,t)$ in equation (37). The mass M is in solar units, and $\sigma_{IMF}(M)$ is the Gaussian form given in equation (6) down to zero mass. Because of the presence of the mass factor preceding the integral, the plot does not differ substantially for other forms of the brown dwarf distribution.

Figure 8: Regions of integration for computing $\Sigma_{pa}(L,t)$. As in Figure 3, cooling curves are shown in the $L - \tau_{red}$ plane, but here they are only schematic. The lower dashed curve indicates L_{min}, the lowest luminosity considered, while the upper dashed curve marks L, the current luminosity of interest. The solid curves represent cooling curves for various masses, each described in the text. The dotted curve on the left is obtained by setting the track time equal to the deuterium-burning time at each mass, while the dotted curve on the right is the isochrone $\tau_{red} = 1$. Finally, t'_* and t''_* are the track times when mass M cools to luminosity L and to the ZAMS, respectively.

Figure 9: Absolute and relative numbers of protostars. Shown as a function of the nondimensional cluster time τ are N_{proto}, the number of protostars (*solid curve*) and f_{proto}, the ratio of the protostar number to the total number of stars produced (*dashed curve*). The quantity N_{proto} is displayed relative to N, the total number of stars produced by the cutoff time τ_c. The quantity τ_c has been set to a typical value of 100, and the Gaussian form of the IMF has been assumed.

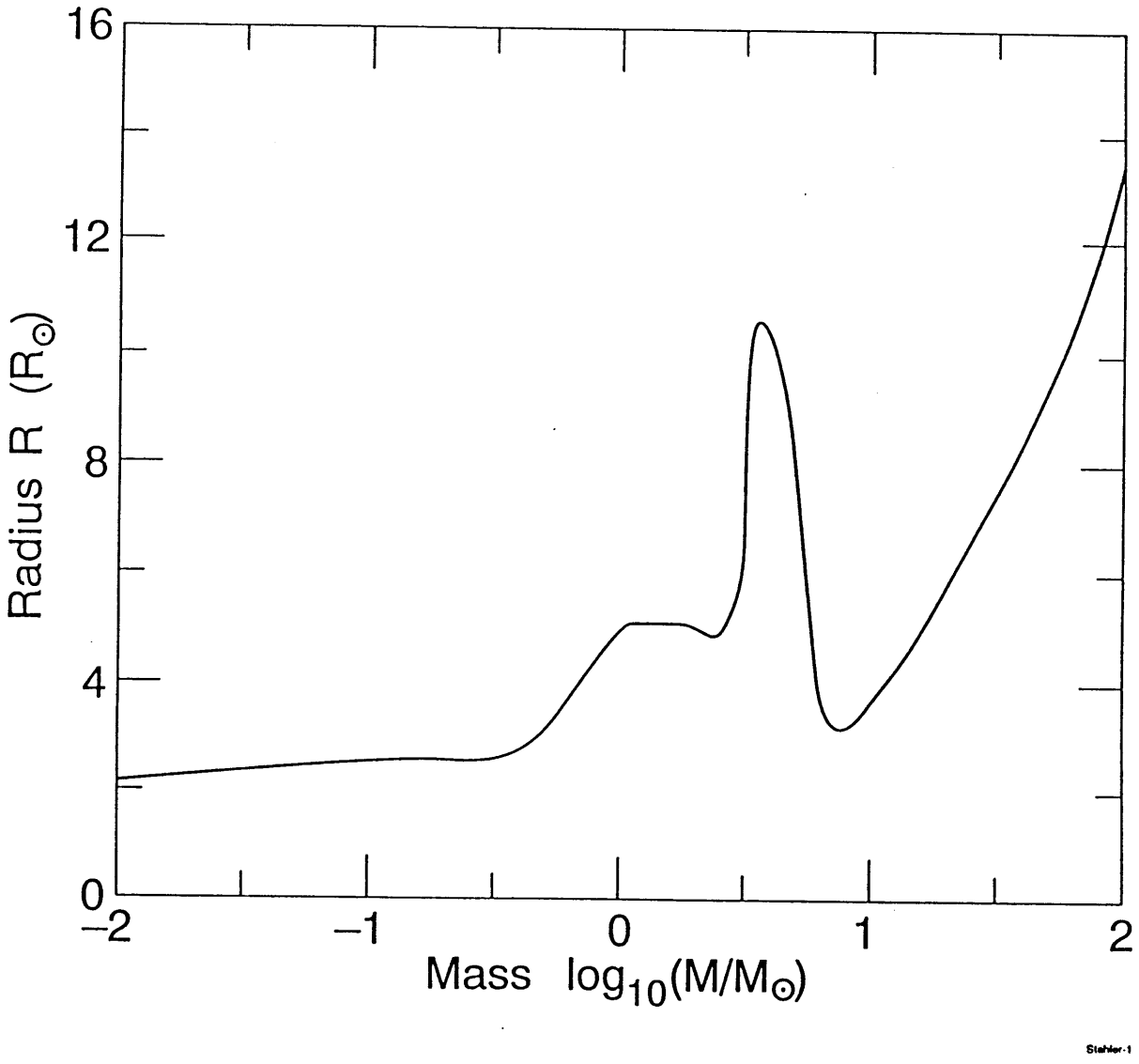
16
12
8
4
0
Radius R (R⊙)
−2
−1
0
1
2
Mass log10(M/M⊙)
Stahler-1

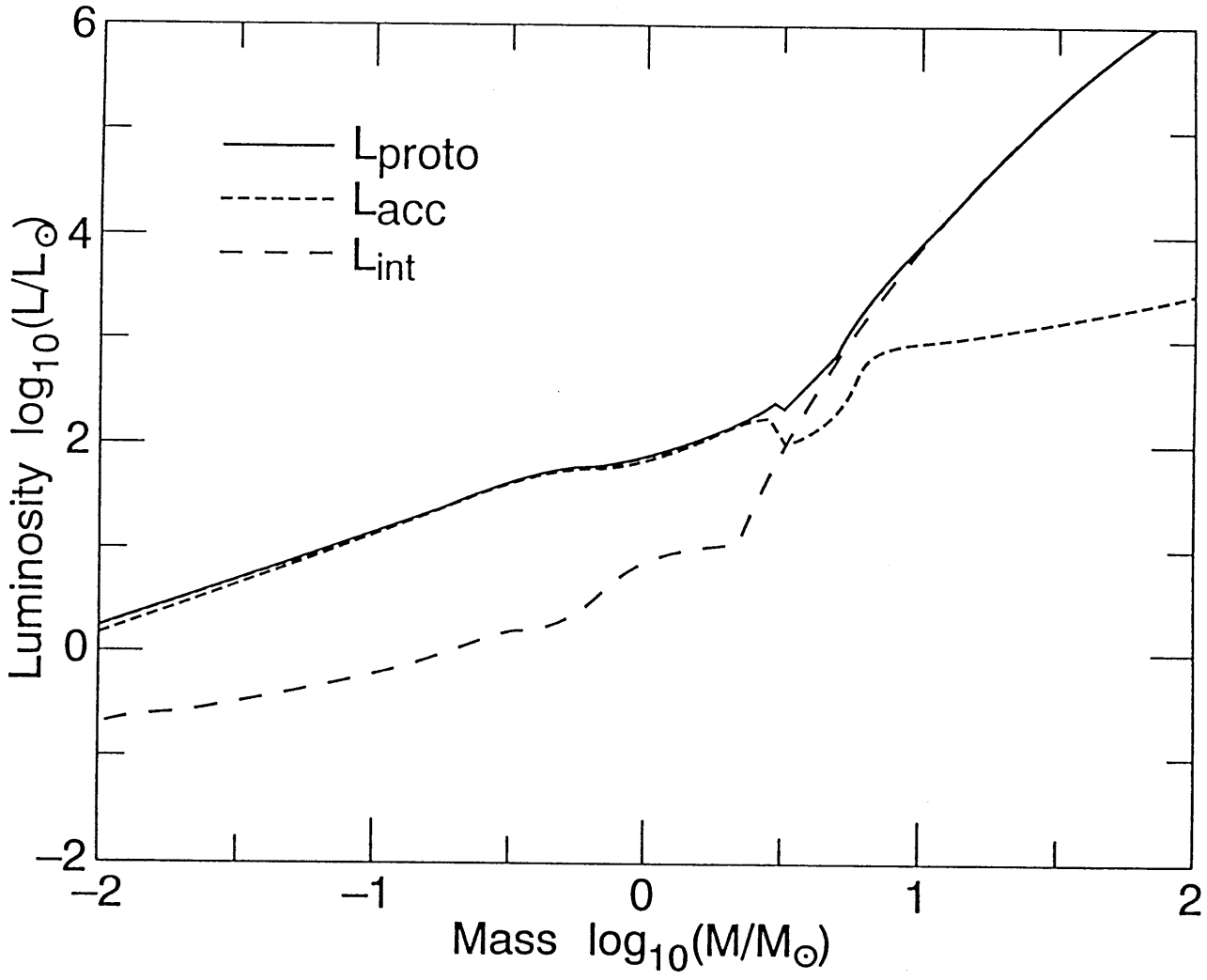
6
4
2
0
−2
−2
−1
0
1
2
Luminosity $\log_{10}(L/L_\odot)$
Mass $\log_{10}(M/M_\odot)$
L_{proto}
L_{acc}
L_{int}
Stahler-2

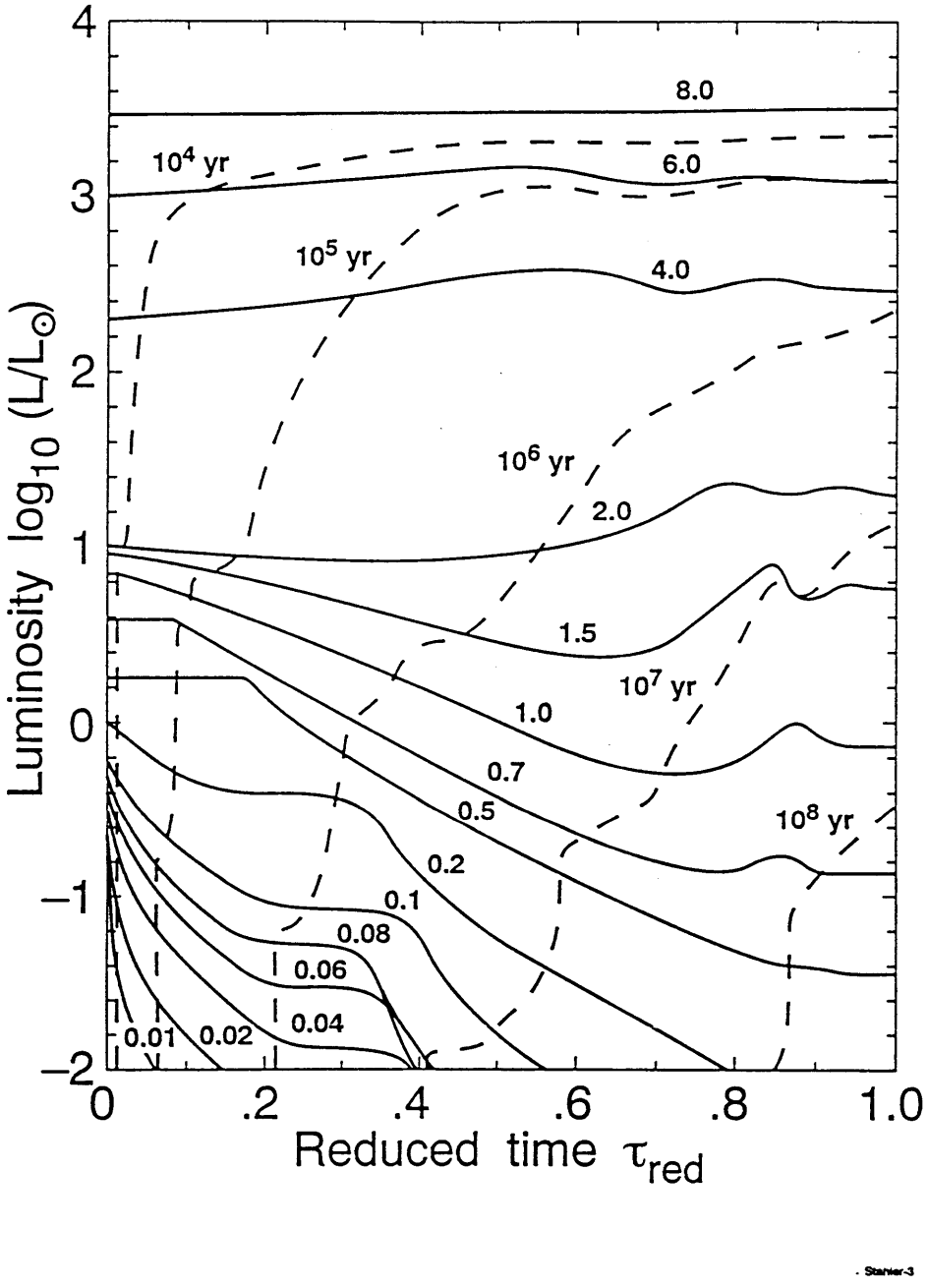
Luminosity $\log_{10}$ ($L/L_\odot$)
Reduced time τ_{red}
8.0
6.0
4.0
2.0
1.5
1.0
0.7
0.5
0.2
0.1
0.08
0.06
0.04
0.02
0.01
10^4 yr
10^5 yr
10^6 yr
10^7 yr
10^8 yr

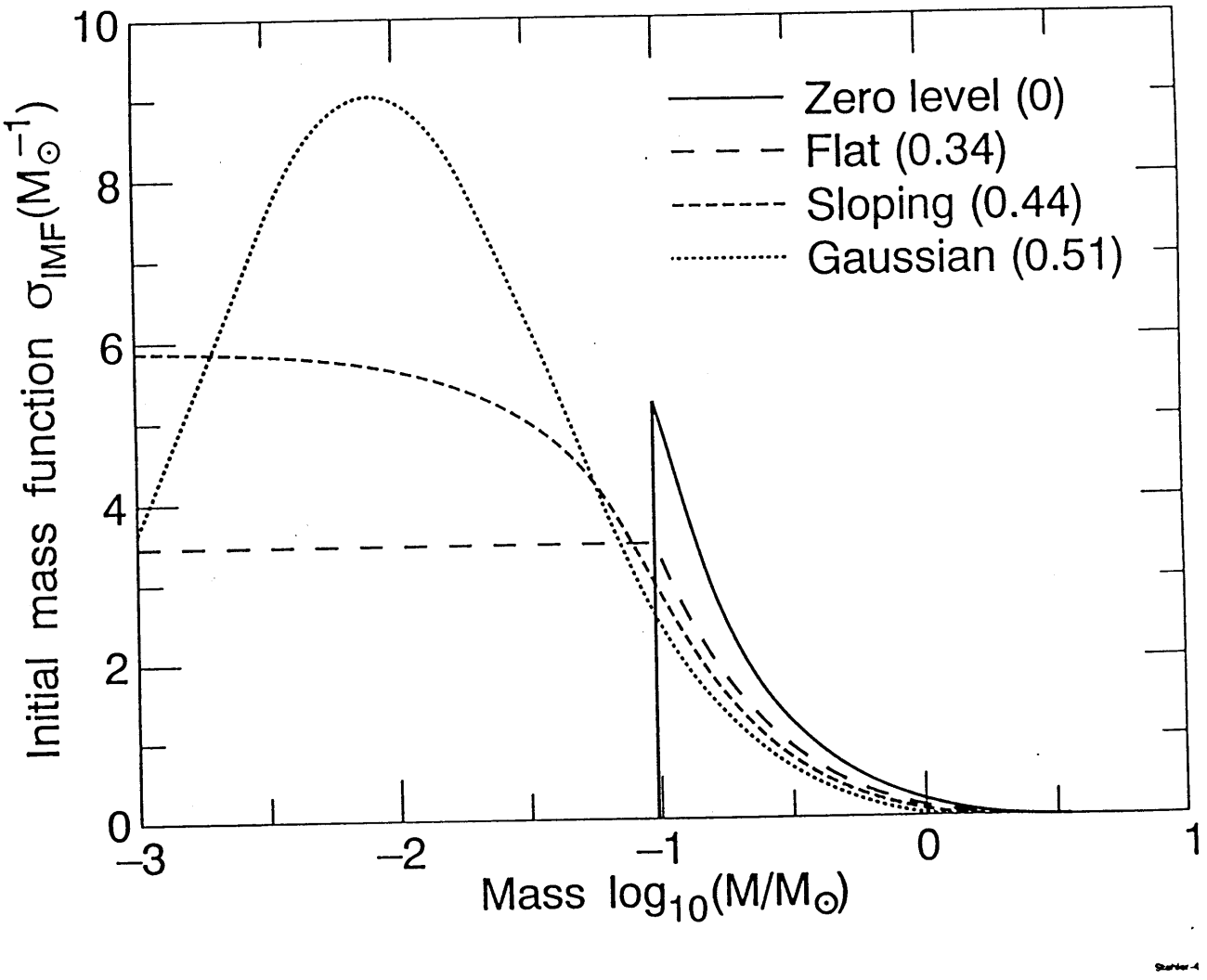
Zero level (0)
Flat (0.34)
Sloping (0.44)
Gaussian (0.51)
Initial mass function $\sigma_{IMF}(M_\odot^{-1})$
Mass $\log_{10}(M/M_\odot)$
10
8
6
4
2
0
−3
−2
−1
0
1

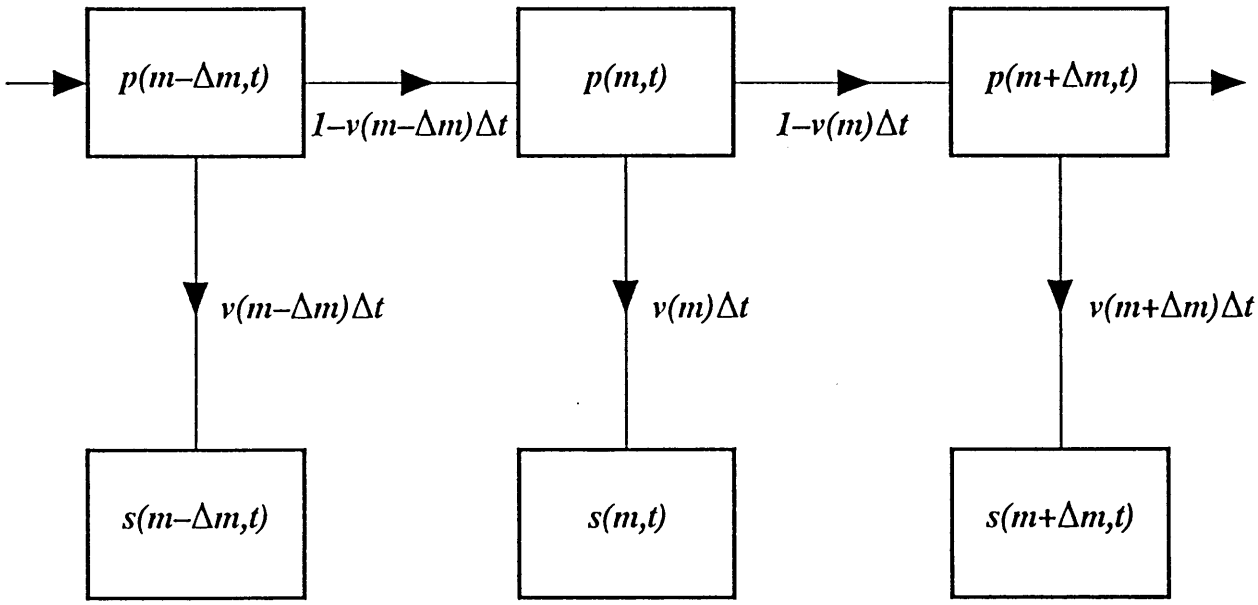
p(m–Δm,t)
p(m,t)
p(m+Δm,t)
1–v(m–Δm)Δt
1–v(m)Δt
v(m–Δm)Δt
v(m)Δt
v(m+Δm)Δt
s(m–Δm,t)
s(m,t)
s(m+Δm,t)

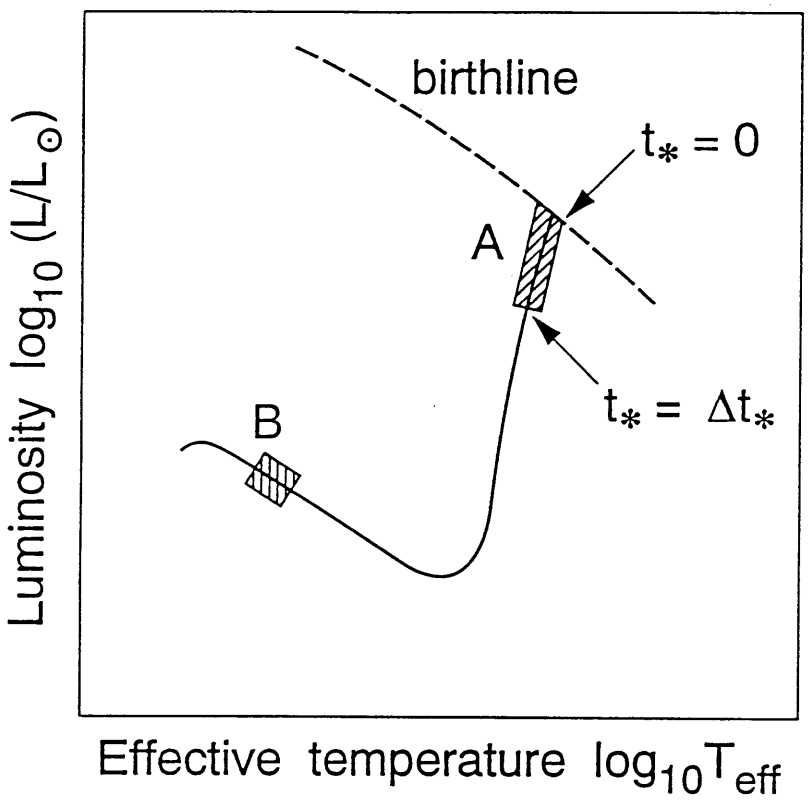
birthline
$t_* = 0$
A
$t_* = \Delta t_*$
B
Luminosity $\log_{10}(L/L_\odot)$
Effective temperature $\log_{10} T_{eff}$

Stahler-6

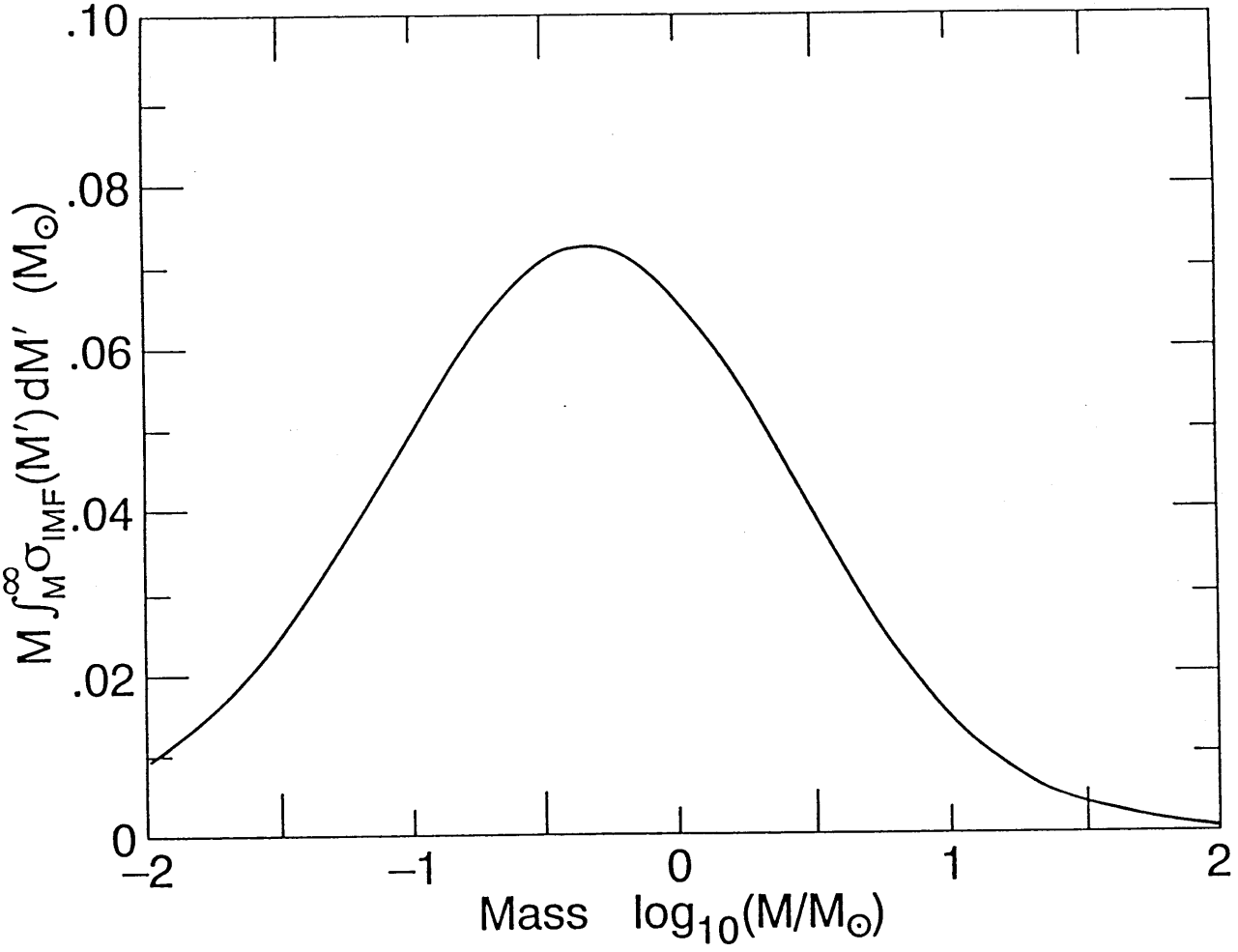
.10
.08
.06
.04
.02
0
$M\int_M^\infty \sigma_{IMF}(M')dM'$ $(M_\odot)$
−2
−1
0
1
2
Mass $\log_{10}(M/M_\odot)$
Stahler-7

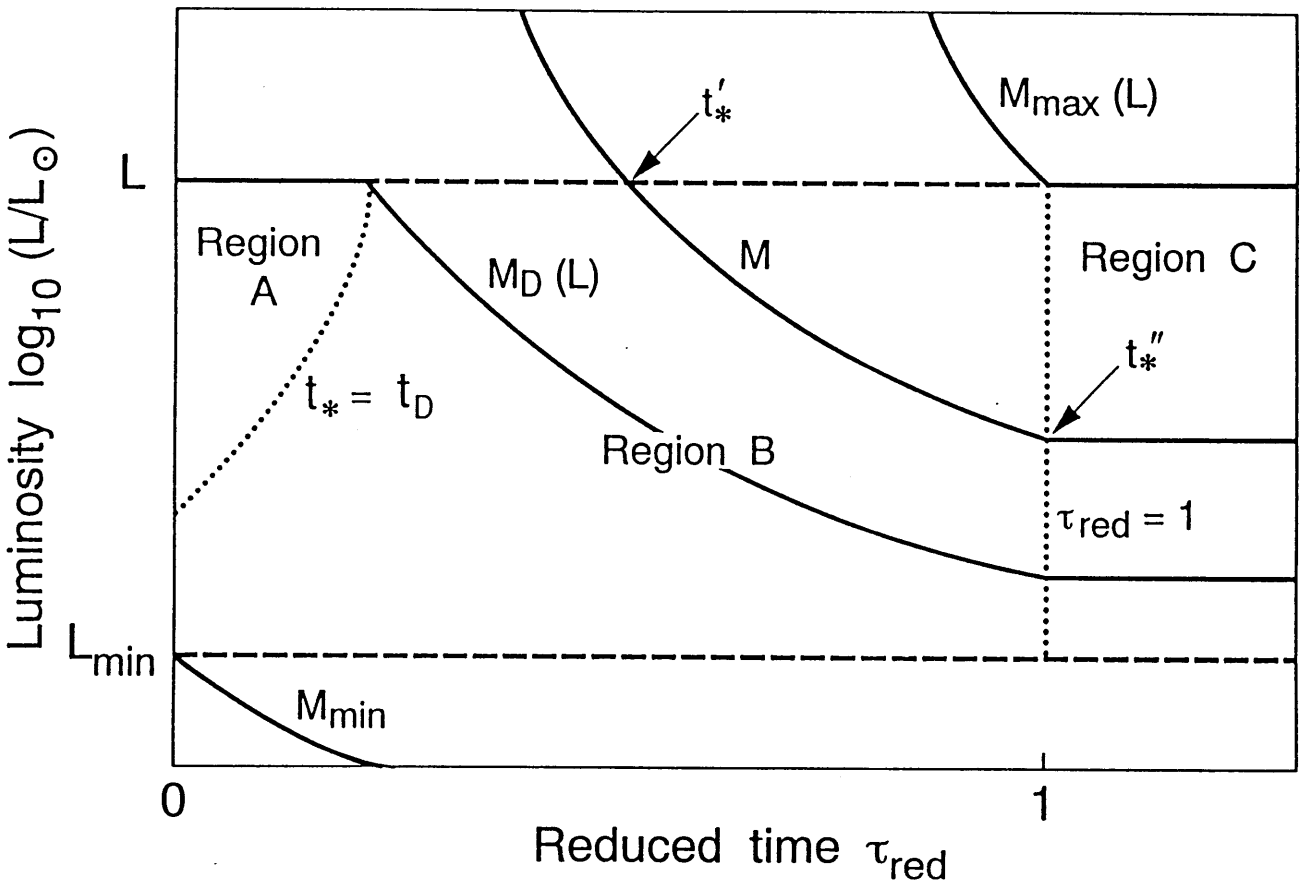
Luminosity $\log_{10}(L/L_\odot)$
L
L_{min}
t'_*
M_{max} (L)
Region A
M_D (L)
M
Region C
t''_*
$t_* = t_D$
Region B
$\tau_{red} = 1$
M_{min}
0
1
Reduced time τ_{red}
Stahler-8

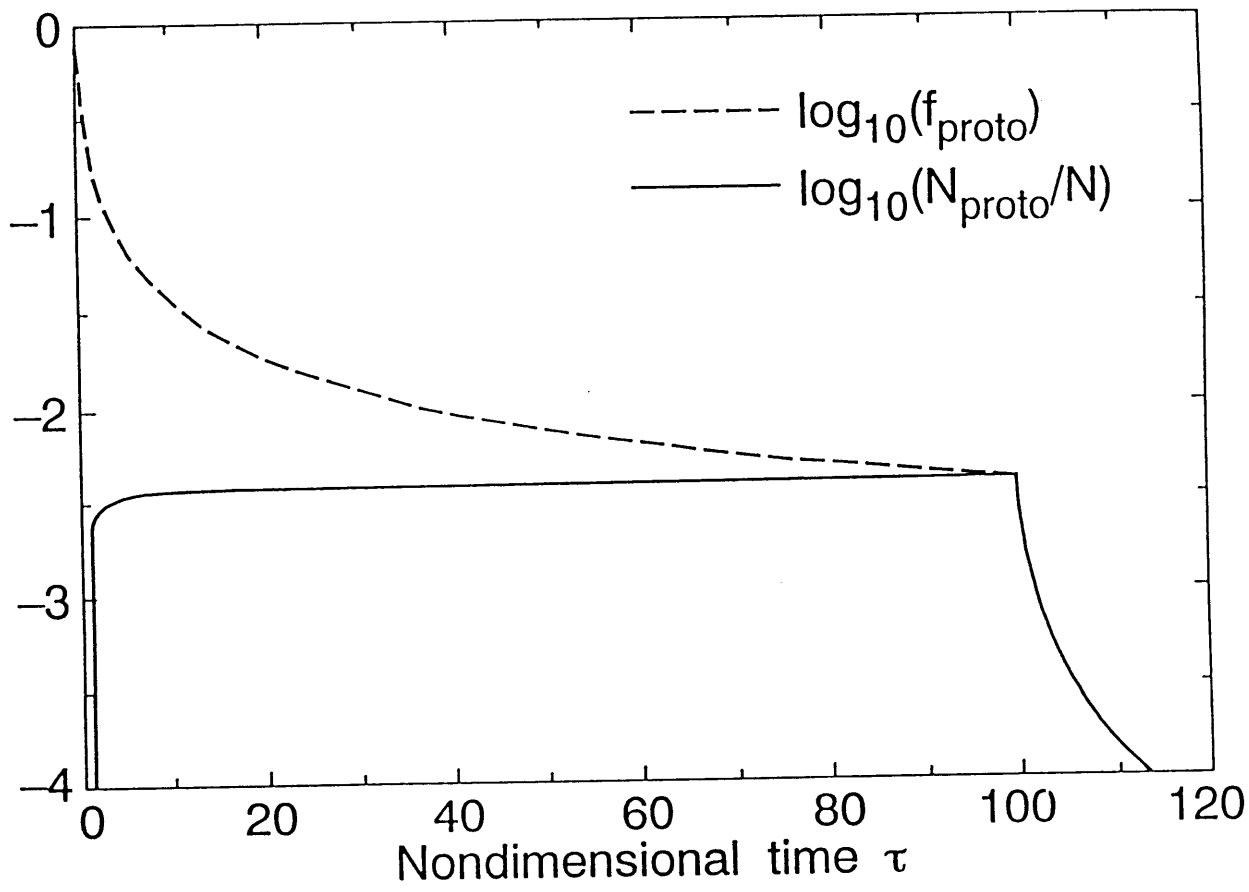
0
−1
−2
−3
−4
0
20
40
60
80
100
120
Nondimensional time τ
log10(fproto)
log10(Nproto/N)
Stahler-9

The Luminosity Functions of Embedded Stellar Clusters: II. Numerical Results

André B. Fletcher

Dept. of Physics, M.I.T., Cambridge, MA 02139

and

Steven W. Stahler

Dept. of Astronomy, U. of California, Berkeley, CA 94720

Received: _____

ABSTRACT

We use the theory developed previously to calculate the evolving luminosity functions of very young stellar clusters. The luminosity function of the protostars alone quickly attains a characteristic, sharply peaked shape, which it maintains throughout the time of cluster formation. For the pre-main-sequence stars, the function continually changes, but displays a pronounced "step" near a luminosity of $10\,L_{\odot}$ for a prolonged period. At most times, the vast majority of cluster members are pre-main-sequence stars. However the total cluster luminosity is dominated first by the protostellar and later by the main-sequence component. At these late times, it is the brightest stars which reach the main sequence first. Finally, a preliminary application of our model to the ρ Ophiuchus embedded cluster indicates that star formation has proceeded in that region for 1×10^6 yr.

1. Introduction

This is the second paper in a two-part series treating the luminosity functions of stellar clusters still forming within their parent molecular cloud complexes. In the previous article (Fletcher and Stahler 1993; Paper I), we presented our physical assumptions and computational approach. We also derived analytic expressions for the protostar population within such clusters. Here we focus on numerical results; we also make a first comparison of our findings with the limited observational data available at the present time.

Our basic approach has been to adopt a simple phenomenological model of cluster formation that is consistent with the current understanding of early stellar evolution. We envision clusters as arising from the continual gravitational collapse of dense cores scattered throughout an extended cloud complex. Each dense core forms at its center a protostar, which gathers in mass at an accretion rate, $\dot{M}$, that is both fixed in time and identical for all other protostars in the forming cluster. New cores go into collapse at a constant rate C_o, starting at $t = 0$ and ending at $t = t_c$. Here, t_c is an assigned "cutoff time" that represents the epoch at which the cloud complex is disrupted by the winds and radiation pressure from newly formed massive stars.

As an individual protostar grows by accretion, it has a certain probability per unit time of dispersing its infalling envelope of gas. Following this dispersal, which is presumed to arise from the action of an energetic wind, the star of fixed mass contracts to the main sequence according to standard pre-main-sequence theory. The probability of dense core dispersal, which is a function of protostar mass, is so tuned that the final distribution of masses, after all star formation has ceased, matches a field-star Initial Mass Function (IMF). Once this probability has been assigned, the entire history of the evolving cluster, and therefore its luminosity function, can be determined.

Within our model, the evolution of the luminosity function depends on the two free parameters $\dot{M}$ and t_c. The results also depend, of course, on the assumed form of the IMF. For the latter, we have adopted the Miller-Scalo "lognormal" function for $M \geq 0.1\,M_\odot$ (Miller & Scalo 1979; see also eq.(6) of Paper I, *i.e.*, eq.(I.6)). For $M < 0.1\,M_\odot$, the IMF is poorly constrained empirically, so we tested four simple functional forms, denoted *zero level*, *flat*, *sloping*, and *Gaussian* (see §2.4 of Paper I; *i.e.*, §I.2.4). With the exception of the rather extreme zero level case, our actual luminosity functions, which are complete down to $L = 0.01\,L_\odot$, turn out to be insensitive to the choice of the brown-dwarf IMF.

In the interest of economy, we have chosen to present the most complete results for a numerical model based on a particular, representative, choice of parameters. In this *canonical model*, $\dot{M}$ is fixed at $1 \times 10^{-5}\,M_\odot$ yr^{-1}, a value corresponding to the collapse of a centrally peaked dense core with an internal temperature of 30 K (Shu 1977). The canonical value of t_c is set at 1×10^7 yr. This time is typical of the stellar age spread seen in somewhat older clusters, *i.e.*, those composed of young, but visible, stars which can be placed in the H-R diagram (Iben & Talbot 1966, Stahler 1985). Finally,

the canonical model employs, for the brown-dwarf portion of the IMF, the Gaussian form, in which the Miller-Scalo function extends down to zero mass.

In Section 2 below, we give our results for the luminosity function of the protostars alone. Section 3 details the contribution from the pre-main-sequence and main-sequence stars. The complete cluster luminosity function is presented in Section 4, where we also describe the effect of varying parameters from their canonical values. Section 5 is devoted to the evolution of integral properties of the cluster, such as the total luminosity associated with each stellar population. Finally, Section 6 shows briefly how our results can profitably be tested against the data from infrared surveys.

2. Protostar Contribution

In Paper I, we calculated N_{proto}, the number of protostars produced in the cluster at any time. As seen in Figure I.9, N_{proto} at first rises rapidly, but soon levels off to a constant. The initial rise slows after the accretion time, equal to $\bar{M}/\dot{M}$. Here, $\bar{M}$, which has the value 0.87 $M_\odot$ in our model, is the typical mass scale of the IMF (see §I.3.3). The canonical accretion time is therefore 8.7×10^4 yr. At later times, the protostars near this representative mass are depleted by accretion to higher masses and production of pre-main-sequence stars as fast as they are being regenerated through dense core collapse. A steady state is reached, in which N_{proto} remains close to its peak value, here denoted N^*_{proto}. From equation (I.52), this maximum is given by

$$\begin{aligned} \frac{N^*_{proto}}{N} &= \frac{I(\tau_c)}{\tau_c} \\ &= \frac{\bar{M}\, I(\tau_c)}{\dot{M}\, t_c} \,. \end{aligned} \tag{1}$$

The quantity $N \equiv C_0 t_c$ is the total number of stars ever produced in the cluster, and the nondimensional time $\tau_c \equiv \dot{M} t_c / \bar{M}$ has the value 115 in the canonical model. Since Figure I.9 was constructed using the Gaussian form of the IMF and a τ_c of 100, it very closely depicts the behavior of N_{proto} in the canonical model. Finally, the dimensionless quantity $I(\tau_c)$ in equation (1) is close to I_∞, which equals 0.372 in this case, according to Table 2 of Paper I.

We can divide N^*_{proto} in equation (1) by $C_0 t$ to obtain a useful approximate expression for the protostar fraction, f_{proto}:

$$\begin{aligned} f_{proto} &\approx \frac{N^*_{proto}}{C_0 t} \\ &\approx \frac{\bar{M} I_\infty}{\dot{M} t} \\ &= \left(\frac{3.2 \times 10^4 \text{ yr}}{t} \right) \left(\frac{\dot{M}}{1 \times 10^{-5}\, M_\odot \text{ yr}^{-1}} \right)^{-1} . \end{aligned} \tag{2}$$

This approximation only holds for values of t in excess of the accretion time but less than the cutoff time.

Once the protostar population has leveled off in number, its mass spectrum, $p(M,t)$, also reaches an invariant form. From equation (I.29), $p(M,t)$ is determined by a mass integral over the IMF. Since the protostar luminosity function, $\Phi_{proto}(L,t)$, is obtained by combining $p(M,t)$ with the appropriate mass-luminosity relation, it, too, does not change for most of the cluster's lifetime prior to cutoff.

Figure 1 shows the canonical $\Phi_{proto}(L,t)$ at four representative times. The function was calculated using equation (I.37), after dividing through by the normalization factor N. The derivative $d\log L/d\log M$ was obtained numerically from the protostar mass-luminosity relation for the case $\dot{M} = 1\times10^{-5}\,M_\odot$ yr^{-1} (see Fig. I.2). At very early times of order $\bar{M}/\dot{M}$, the full luminosity spectrum is not present, since the larger protostellar masses have not yet built up inside their collapsing dense cores. Much later, for times somewhat greater than t_c, *smaller* masses are no longer being produced, but a diminishing remnant of massive protostars is still accreting from the last few collapsing cores. Our simplified picture of cluster formation assumes that both the onset and cessation of dense core collapse within the cloud complex are perfectly sharp transitions. Hence, Figure 1 shows the complete $\Phi_{proto}(L,t)$ appearing and vanishing within two knife-like edges that sweep across at the rate $\dot{M}$. The figure also shows that the *fraction* of protostars, $f_{proto}(t)$, is only close to unity during the very earliest epoch (see also Fig. I.9). After cutoff, $f_{proto}(t)$ drops to zero within a brief period of order $\bar{M}/\dot{M}$.

Throughout the long intermediate time interval $\bar{M}/\dot{M} \lesssim t \lesssim t_c$, $\Phi_{proto}(L,t)$ has the fixed form shown in Figure 1 at $t = 1\times10^6$ yr. The function is remarkable for the sharpness of its central peak. We already noted in Paper I that the falloff in Φ_{proto} at both large and small luminosities can be traced to the similar behavior with respect to mass of the function $M\int_M^\infty \sigma(M')dM'$ (see Fig. I.7). However, it is the protostar mass-luminosity relation which both sets the exact location of the peak and causes its sharpness. To see the latter point, note first that the maximum occurs at relatively low stellar mass, where the protostar luminosity, given in general by equation (I.3), is dominated by its accretion component, $L_{acc} \equiv GM\dot{M}/R$ (see eq. (I.2)). In this mass regime, internal fusion of deuterium is effective as a thermostat (Stahler 1988). The reaction keeps the central temperature of the accreting protostar close to 10^6 K by swelling the stellar radius until it is nearly proportional to the mass. Hence, at a fixed $\dot{M}$, L_{acc} is virtually unchanged over a significant range in mass, and Φ_{proto} correspondingly exhibits a narrow maximum.

The exact value of the luminosity at which Φ_{proto} peaks depends on $\dot{M}$. The increase of this luminosity, L^*_{proto}, with respect to $\dot{M}$ is very nearly linear, as would be expected. An alteration in $\dot{M}$ also changes the point during protostar evolution at which deuterium burning begins to swell the radius (Stahler 1988). Hence, the protostar *mass* corresponding to L^*_{proto}, which we denote M^*_{proto}, also depends on $\dot{M}$, though not sensitively. For $\dot{M} = 1\times10^{-5}\,M_\odot$ yr^{-1}, $L^*_{proto} = 45\,L_\odot$ and $M^*_{proto} = 0.44\,M_\odot$. At our

lowest adopted $\dot{M}$ of $2 \times 10^{-6}\,M_\odot$ yr^{-1}, these figures change to $9.5\,L_\odot$ and $0.30\,M_\odot$, respectively. The values of M^*_{proto} are close to those where deuterium burning turns the entire protostar convectively unstable (see Fig. 7a of Stahler 1988).

Now the values of M^*_{proto} are substantially greater than the brown-dwarf limit near $0.1\,M_\odot$. Hence, it is clear that any uncertainty regarding the lower end of the IMF has little effect on the steady-state form of Φ_{proto}. Figure 2a shows explicitly the minor changes in Φ_{proto} brought about by varying the choice of IMF. On the other hand, lowering $\dot{M}$ to $2 \times 10^{-6}\,M_\odot$ yr^{-1} *does* make a difference (Fig. 2b). Although the basic shape of Φ_{proto} is unaltered, the peak shifts downward in luminosity by a factor of five, as explained before. In addition, Figure 2b shows a global *increase* by the same factor in the actual values of the function. A lower $\dot{M}$ allows more protostars to build up before they can be depleted by the formation of pre-main-sequence stars. Notice, for example, that N^*_{proto}/N in equation (1) varies inversely with $\dot{M}$. The same equation indicates that a similar global rescaling, but without any shift in the peak, is effected by alteration of t_c.

3. Post-Accretion Contribution

3.1 Early Evolution

The luminosity function of the pre-main-sequence and main-sequence stars, which we denote collectively as "post-accretion" cluster members, does not have the simplicity of the protostar contribution. Once the steady-state population of protostars is established, pre-main-sequence stars begin to appear all along the birthline. These stars descend their evolutionary tracks over times which can be long or short compared to t_c. Eventually, the more massive main-sequence stars, whose luminosities remain constant for extended periods, begin to appear. The post-accretion luminosity function, $\Phi_{pa}(L,t)$, is therefore essentially time-dependent in a way that $\Phi_{proto}(L,t)$ is not.

Figure 3 shows $\Phi_{pa}(L,t)$, in the canonical model, at four times soon after the initiation of star formation. The function was computed from equation (I.44), and is again displayed normalized with respect to N. Each panel in the figure also gives $f_{pms}(t)$, the fraction of all stars which are in the pre-main-sequence phase, and $f_{ms}(t)$, the main-sequence fraction. The protostar fraction at this early epoch can be found from $f_{proto}(t) = 1 - f_{pms}(t) - f_{ms}(t)$. All fractions were calculated according to the prescription given in Section I.3.3.

The pre-main-sequence stars begin as a relatively small group of low-luminosity objects that descended from the first protostars to stop accreting from their parent dense cores. At $t = 1 \times 10^4$ yr, this population peaks in mass near $0.1\,M_\odot$, the mass singled out in the Miller-Scalo IMF. At this time, the pre-main-sequence members constitute less than one third of the total stars produced, but this fraction steadily rises with time. Thus, there is a global increase in $\Phi_{pa}(L,t)$, along with a spread toward higher luminosities. After several accretion times, the post-accretion luminosity function has assumed the characteristic form which it displays in all our models at this early epoch

– a broad plateau at low luminosities, and a sudden falloff, or "step," at $L \approx 10\,L_\odot$. There is still no appreciable main-sequence contribution at this time.

The step in Φ_{pa} can be understood from the thermal evolution of pre-main-sequence stars of various masses. This evolution, in turn, is conveniently summarized by comparison of two characteristic luminosities, L_{surf} and L_{rad} (Stahler 1989). Here, L_{surf} is the energy per unit time emitted from the stellar surface:

$$L_{surf} = 4\pi R^2 \sigma T_{eff}^4 \,. \tag{3}$$

The quantity L_{rad} is the interior luminosity transported by radiation, and is given, for pre-main-sequence stars of mass M, by

$$L_{rad} = L_o \left(\frac{M}{M_\odot}\right)^{11/2} \left(\frac{R}{R_\odot}\right)^{-1/2} \,, \tag{4}$$

where L_o is a luminosity of order $1\,L_\odot$ (Cox & Giuli 1968). Now L_{surf}, for stars appearing on the birthline, does not increase rapidly with respect to the stellar mass (Stahler 1983). On the other hand, L_{rad} *is* strongly mass-dependent as a result of the temperature sensitivity of the Kramers Law opacity dominating the stellar interiors. Hence, L_{rad} is smaller than L_{surf} for low-mass stars, while the inequality is reversed at higher masses. The dividing line is at a mass, M_{rc}, between 2 and $3\,M_\odot$, corresponding to a luminosity on the birthline of $L_{rc} \approx 10\,L_\odot$ (see Fig. 1 of Stahler 1989).

Stars for which $L_{rad} < L_{surf}$ are emitting higher luminosities than can be supplied internally by radiation. The difference is made up by convection, which transports the bulk of the energy at early times. In the H-R diagram, such stars follow the characteristic vertical tracks first described by Hayashi (1961). More massive stars, on the other hand, carry, at least temporarily, a greater luminosity than can be radiated into space. These stars first undergo a phase of "thermal relaxation," in which L_{surf} climbs quickly to match L_{rad} (Stahler 1989, Palla & Stahler 1993). Thereafter, they contract as fully radiative objects along more horizontal evolutionary tracks (Henyey, LeLevier, & Levee 1955). The qualitative change in the tracks above and below L_{rc} is evident in Figure I.3.[2]

Consider now a population of stars at the birthline which span, in a smooth fashion, the mass M_{rc}. The mass-sensitivity of L_{rad} implies that a given number of stars with $M > M_{rc}$ will be spread out over a much larger luminosity range than the same number with $M < M_{rc}$. Equivalently, $\Phi_{pa}(L,t)$, which measures the population per logarithmic unit of luminosity, must fall sharply at L_{rc}. Notice, in Figure 3, that

[2] Note that the pre-main-sequence tracks used in this study do not include the initial, transient phase of thermal relaxation. For simplicity, it has been assumed that every star promptly joins onto that portion of its classical evolutionary track corresponding to its birthline radius. Proper inclusion of the relaxation phase would have altered our results only slightly; see Palla & Stahler 1993.

the step first becomes well defined for $t \gtrsim M_{rc}/\dot{M}$, *i.e.*, after about 2×10^5 yr in the canonical model.

3.2 Later Developments

As star formation continues and the pre-main-sequence population grows, stars are eventually formed which have time to evolve from the birthline to the main sequence. The emergence of this new population can be followed in Figure 4, which is the continuation of Figure 3 up to the cutoff time of 1×10^7 yr. The luminosity function for the main-sequence stars is shown separately as the dashed curve; this function was computed from $[\Phi_{pa}]_C$ in equation (I.44d). We see that it is the most massive and luminous pre-main-sequence stars which first reach the main sequence. Indeed, stars with masses greater than about $8\,M_\odot$ skip the pre-main-sequence phase entirely (Palla & Stahler 1991). That is, all stars more luminous than $\log(L/L_\odot) \approx 3.5$ join the main-sequence as soon as they disperse their dense core envelopes. The less luminous part of the main sequence becomes populated later, as can be seen in Figure 4.

The figure also shows the gradual erosion of the step in Φ_{pa}. It is still true that fewer stars per unit luminosity appear on the birthline for $L \gtrsim L_{rc}$ than for slightly lower luminosities. However, such newly formed pre-main-sequence stars are a diminishing fraction of the total cluster membership. At $t = 1 \times 10^7$ yr (Fig. 4d), most stars of luminosity L_{rc} are close to the main sequence, and the original step is barely discernible. By this time, the main-sequence stars, though comprising only a few percent of the total population, outnumber the protostars by a factor of six. The function $\Phi_{pa}(L,t)$ is beginning to resemble, at higher luminosities, the smooth "Initial Luminosity Function" (ILF), formed by combining the IMF with main-sequence luminosities.

Figure 5 depicts the evolution of $\Phi_{pa}(L,t)$ for $t > t_c$. Also shown at each time is $f_{post}(t)$, the fraction of stars which have begun to evolve off the main sequence. Soon after the cutoff time, no more dense cores are going into collapse to form protostars or new pre-main-sequence stars, but most of the cluster members formed earlier have not yet had time to reach the main sequence. At $t = 5 \times 10^7$ yr (Fig. 5b), the main sequence is fully populated according to the IMF down to $\log(L/L_\odot) \approx 0.5$, corresponding to a stellar mass of $1.3\,M_\odot$. The luminosity function is nearly identical to the ILF except at the highest luminosities, where it is abruptly truncated at the main-sequence "turn-off" point. Stars with $\log(L/L_\odot) \gtrsim 3$ have had time to evolve off the main sequence, and are simply deleted from the luminosity function. By $t = 2 \times 10^8$ yr (Fig. 5d), the main-sequence "turn-on" point, where contracting young stars first ignite hydrogen, has decreased almost to $0.1\,L_\odot$, still a factor of ten higher than our lower limit of $0.01\,L_\odot$. Notice that even at this very late epoch, it is the slowly evolving pre-main-sequence stars of relatively low mass and luminosity which still comprise the majority of cluster members.

The smooth appearance of Φ_{pa} at all times is in contrast with the recent result of Zinnecker *et al.* (1993). Their theoretical luminosity function contains a sharp spike which migrates to lower luminosity in time. Zinnecker *et al.* attribute this feature to the onset of deuterium burning. As we previously noted in §I.2.3, deuterium ignition can

temporarily halt pre-main-sequence contraction, creating a transient pileup of stars in a time-dependent luminosity range. For Zinnecker *et al.* , this range was extremely narrow because of their basic assumption that all stars begin to contract at exactly the same instant. In our model, contraction is initiated over an extended period. Consequently, the pileup of stars is also spread out in luminosity, and no spike is evident in the integrated luminosity function.

4. Total Luminosity Function

4.1 Canonical Model

The history of the full luminosity function $\Phi(L,t)$, formed by adding together $\Phi_{proto}(L,t)$ and $\Phi_{pa}(L,t)$, is depicted in Figures 6-9. Also shown at each time are l_{proto}, l_{pms}, and l_{ms}, the fraction of the total cluster luminosity contributed by the protostars, pre-main-sequence stars, and main-sequence stars, respectively. These fractions were computed according to the method outlined in Section I.3.3. At early times (Fig. 6), the luminosity function is distinctly bimodal, with a sharp spike due to the protostar population, and a growing low-luminosity plateau from the pre-main-sequence members. By $t = 5 \times 10^5$ yr (Fig. 6d), the invariant profile of Φ_{proto} is nearly complete. The protostars have partially obscured the step in Φ_{pa}, which was much more pronounced when the pre-main-sequence stars alone were displayed (Fig. 3d). At this time, the number fraction of protostars is a mere 6 percent of the total cluster population. Nevertheless, from Figure 6d, they contribute 84 percent of the total luminosity. This striking discrepancy is due to the extraordinary brightness of the most massive protostars, as we will discuss in Section 5 below.

Later in the evolution (Fig. 7), the protostar spike is overwhelmed by the growing numbers of high-luminosity post-accretion stars. By $t = 2 \times 10^6$ yr (Fig. 7b), the main sequence is fully populated for $\log(L/L_\odot) \gtrsim 2$. The massive main-sequence stars outshine the protostars, so that the bulk of the cluster luminosity is henceforth from the main-sequence component. We thus find that *pre-main-sequence stars never dominate the total cluster luminosity*, although they clearly set the *form* of the luminosity function for much of the cluster's lifetime. By the cutoff time, for example, Figures 4d and 7d show that pre-main-sequence evolution is still changing $\Phi(L,t)$ for $\log(L/L_\odot) \lesssim 1$. The large population of contracting stars, 98 percent of the cluster by number, represents only 1 percent of its total luminosity.

Once t exceeds t_c by more than a few accretion times, the protostar contribution to $\Phi(L,t)$ has vanished. Thus, Figure 8, which shows the luminosity function at late epochs, essentially reproduces the earlier Figure 5. The contribution of the pre-main-sequence stars to the cluster luminosity continues to decline, as the remaining low-mass members of this group dim during their approach to the main sequence.

It is an important, general feature of our results that $\Phi(L,t)$ first becomes transformed to the ILF at the highest luminosities. To understand the transition more precisely, we show again, in Figure 9, the complete luminosity function at $t = 1 \times 10^7$ yr (*solid curve*), but now superimposed on the ILF (*dashed curve*). For consistency, the

latter was constructed using the Gaussian form of the IMF and the same main-sequence mass-luminosity relation employed in our evolutionary tracks. At high luminosities, $\Phi(L,t)$ is identical to the ILF except for the small protostar hump; the latter is centered at L^*_{proto}, as indicated. For lower luminosities, the presence of a substantial population of pre-main-sequence stars is evident in $\Phi(L,t)$. Now at any time t, there exists a unique stellar mass whose contraction time from the birthline to the main sequence is precisely t. We have denoted as L_{trans} the main-sequence luminosity of this mass, and have located it in Figure 9. Clearly, this luminosity marks the transition between the young, evolving $\Phi(L,t)$ and its endproduct, the ILF (see also Lada 1991). With the passage of time, stars of progressively lower mass can reach the main sequence, so that L_{trans} falls, as observed in all our numerical runs.

4.2 Variation of Parameters

Our derived sequence of luminosity functions is most strongly affected by the assumed protostellar mass accretion rate. The influence of $\dot{M}$ is naturally greatest at early times, when the protostars constitute a substantial fraction of the cluster. Consider, for example, a cluster which has all the properties of the canonical model, but with an $\dot{M}$ of $2\times10^{-6}\,M_\odot\,\mathrm{yr}^{-1}$, *i.e.*, smaller by a factor of five. According to current protostar theory (Shu 1977, Stahler, Shu, & Taam 1980), this value is appropriate for dense cores which have internal temperatures of about $10\,K$ and negligible magnetic and turbulent support prior to their collapse into protostars. Such an accretion rate may therefore represent a reasonable lower bound. Figures 10a and 10b display the full $\Phi(L,t)$ in this case, at two representative times.

Figure 10 illustrates that one obvious consequence of lowering $\dot{M}$ is to diminish $\dot{M}t$, the maximum protostar mass at any epoch. Thus, the truncation of $\Phi(L,t)$ at high luminosities for early times is much more severe in the low-$\dot{M}$ case. In addition, the luminosity of any individual protostar is correspondingly less. This latter effect, seen before in Figure 2b, is most apparent here in Figure 10b, which confirms that L^*_{proto} is indeed lower by a factor of five. For $L < L^*_{proto}$, where $\Phi(L,t)$ at early epochs is dominated by pre-main-sequence stars, Figure 10 shows that the change in accretion rate has little impact. Finally, the transition between $\Phi(L,t)$ and the ILF occurs just as before, at least for times long enough that the maximum mass $\dot{M}t$ exceeds the mass corresponding to the main-sequence turn-on luminosity L_{trans}.

The luminosity function also depends on the assumed form of the IMF. This function is fairly well constrained empirically for stars of several solar masses or greater, and is most poorly known in the brown dwarf regime, *i.e.*, for stars with mass less than about $0.1\,M_\odot$. As was the case with the accretion rate, the effect of varying the low-mass IMF is greatest at early times, when the brown dwarfs still have luminosities above our limit of $0.01\,L_\odot$. Figures 11a and 11b show the full luminosity function for models which have all the canonical parameters except for the brown-dwarf portion of $\sigma_{IMF}(M)$. The latter was selected from the four forms described in Section I.2.4 and shown graphically in Figure I.4.

Under the most extreme hypothesis, the "zero level" case, we simply set the IMF to zero for $M < 0.1\,M_\odot$. In the resulting luminosity function, there is a severe deficit of low-luminosity, contracting stars at $t = 1 \times 10^5$ yr (Fig. 11a). However, by $t = 1 \times 10^7$ yr (Fig. 11b), stars of higher mass have largely filled in this void as a result of the dimming of their own luminosities in the course of evolution. Adopting in turn the three other forms of the brown-dwarf IMF, we see that the effect on $\Phi(L,t)$ is minor, even at the earlier epoch. It should be recalled that the luminosity function depends on the *integral* of $\sigma_{IMF}(M)$ (see eq. (I.44)), and is therefore rather insensitive to variations in the low-mass regime. In any case, all brown dwarfs have dimmed below $0.01\,L_\odot$ by $t = 2 \times 10^7$ yr, and thereafter have no effect at all on $\Phi(L,t)$.

The last free parameter in our models is the cutoff time. Consider, then, a pair of clusters identical except for their values of t_c. At times early enough so that $t < t_c$ for both, the two clusters must be the same in all respects. For example, we can verify from equation (1) that the steady-state numbers of protostars are equal, since N^*_{proto} is independent of t_c. For times sufficiently long that $t \gg t_c$, the two clusters again converge in their properties, apart from a difference in the total number of stars produced. Thus, the transition luminosity $L_{trans}(t)$ does not depend on the value of the cutoff time. Furthermore, the contribution from pre-main-sequence stars of lower mass must also become independent of t_c. To see the latter point, we recall from Section I.3.2 that stars with relatively long contraction times are handled through the "narrow-window" approximation. From equation (I.47) and the ensuing estimate $\Delta M \approx (t_c/t_L)M_\bullet$, the factor t_c drops out of $\Phi(L,t)$, once it is normalized to N.

In the remaining situation, where star formation has recently ceased for one of the two clusters, the cutoff *does* matter. The point is illustrated in Figure 12, which displays the luminosity functions for two clusters that have values of t_c of 1×10^7 yr (*solid curve*) and 1×10^6 yr (*dashed curve*), respectively. At a time of 5×10^6 yr (Fig. 12a), the cluster with the larger t_c still displays a secondary peak due to the protostar population, while the other cluster is closer to the ILF over a broader luminosity range. In contrast, the two clusters are nearly identical by $t = 5 \times 10^7$ yr (Fig. 12b), a time which exceeds both values of t_c.

5. Evolution of Global Properties

5.1 Number Fractions

One of the striking results of our study is the contrast between the relative *numbers* of the various stellar populations and their relative *luminosities*. Beginning with the former, Figure 13 displays the evolution of the number fractions of protostars, pre-main-sequence, main-sequence, and post-main-sequence stars. The four panels show this history for both the canonical cluster model and for models with an altered accretion rate or cutoff time.

In all cases, the protostar population is largest only at the very earliest epoch. After about one accretion time, a duration which depends on $\dot{M}$, the pre-main-sequence stars overtake the protostars in number, and thereafter remain dominant. The protostar

fraction, meanwhile, steadily falls, dropping sharply, but not instantaneously, to zero after t_c. Even later in the evolution, the main-sequence fraction climbs to a significant level, and has begun to approach the pre-main-sequence contribution at the latest time shown, $t = 2 \times 10^8$ yr. By this point, the main sequence has been populated down to a turn-on luminosity, L_{trans}, approaching our lower limit of $0.01\,L_\odot$. The number of *post*-main-sequence stars, on the other hand, always remains an order of magnitude below the main-sequence population. In summary, then, the pre-main-sequence stars constitute a majority within the cluster during most of its lifetime.

Figure 13b demonstrates that a higher protostar population can be maintained by lowering $\dot{M}$ to $2 \times 10^{-6}\,M_\odot$ yr^{-1}. However, f_{proto} in this case still falls below 0.1 by $t = 2 \times 10^6$ yr, a time still brief by observational standards (see the discussion in §6 below). The final decline of the protostar fraction is affected by alteration of t_c, as can be seen by comparing Figures 13c and 13d. Such modification has a negligible impact on the dominant pre-main-sequence and main-sequence components.

5.2 Luminosity Fractions

Figure 14 displays the relative contributions of the protostars, pre-main-sequence, and main-sequence stars to the total cluster luminosity. Since our underlying model does not keep track of the stars' post-main-sequence evolution, the corresponding luminosity fraction was set to zero. The figure demonstrates that the pre-main-sequence stars, although they generally constitute a majority of the cluster members, contribute a minor fraction of the total luminosity. For all the cluster models shown, the quantity l_{pms} peaks at about 0.2 for $t \sim 10^6$ yr, and thereafter declines. At the time l_{pms} reaches its maximum, almost all the integrated luminosity comes instead from accreting protostars, although they account for less than ten percent of the cluster membership. At somewhat later times, it is the growing population of main-sequence stars that emits most of the luminosity. Figure 14b shows that lowering $\dot{M}$ lengthens the time during which the protostar luminosity dominates, while lowering t_c has the opposite effect, according to Figure 14c. On the other hand, Figure 14d demonstrates that *increasing* t_c from 1×10^7 yr to 1×10^8 yr has virtually no effect on the luminosity evolution.

Since it is the most massive, luminous portion of the main sequence which becomes populated first, it is understandable that the pre-main-sequence component, though numerically large, is underluminous by comparison. Figure 9, for example, shows that the typical luminosity function differs from the ILF principally by its excess of low-luminosity stars. More surprising is the dominance in luminosity of the numerically minor protostar population. This dominance stems from the disproportionate contribution from the most massive protostars.

According to equation (I.3), L_{proto}, the luminosity of an individual protostar, consists of both accretion and internal components. The energy for the latter is supplied by the star's bulk gravitational contraction for $M \lesssim 8\,M_\odot$, and by central hydrogen burning for greater masses. From Figure I.2, the two components are equal at a stellar mass of about $4\,M_\odot$, corresponding to a luminosity of about $100\,L_\odot$. For heavier protostars, the luminosity rises very steeply as a function of stellar mass.

Now the protostar mass at any time has an upper limit given by the minimum of $\dot{M}t$ and M_{crit}, where the latter can be estimated by equating the main-sequence and accretion time scales (Paper I; Appendix). The fraction of the population with masses near this limit is generally very low (see Fig. 1d). Nevertheless, the heaviest protostars are so bright that they collectively outshine their less massive counterparts. This latter point is illustrated in Figure 15, which plots $L_{proto}\Phi_{proto}$, a quantity proportional to the total luminosity contribution from protostars at each value of L_{proto}. The figure was constructed by using the steady-state, canonical form of Φ_{proto}, displayed in Figure 2a. Despite the fact that Φ_{proto} falls very steeply after reaching its peak, the product $L_{proto}\Phi_{proto}$ dips temporarily, but then continues to rise until the protostar luminosity reaches its maximum possible value of L_{crit} (Paper I; Appendix). At most times, therefore, the maximum contribution to the integrated protostar luminosity comes from those extraordinarily bright stars with masses near the upper limit.

Figure 15 also shows that the total protostar luminosity, obtained by integrating $L_{proto}\Phi_{proto}$, must rise steadily until the cluster time $t_{crit} \equiv M_{crit}/\dot{M}$, and then level off to a constant until t_c is reached. This behavior is shown in Figure 16, where the integrated luminosities from all the stellar populations are plotted, within the canonical model. These luminosities are normalized to the fiducial protostellar value L^*_{tot}, taken to be

$$L^*_{tot} \equiv N^*_{proto} L^*_{proto} ,$$

where the two righthand terms were defined earlier in Section 2. For $t \gtrsim 1 \times 10^6$ yr, the rising protostar contribution is overtaken by the more rapidly increasing main-sequence component. The main-sequence integrated luminosity, like the protostellar, is dominated at any time by the most massive member stars. However, it is these same stars which first begin to leave the main sequence, creating the drop in total cluster luninosity seen after 10^7 yr.

6. Comparison with Observations: ρ Ophiuchus

Having presented both the basic theory and our numerical results for luminosity functions, we turn finally to the observational data. As we stressed in Paper I, the empirical study of populous, embedded clusters is just now becoming feasible, with the introduction of infrared array detectors. Current detectors are sensitive only to near-infrared wavelengths, while the spectral energy distributions of many young stars peak in the mid- or far-infrared regime (see, *e.g.*, Lada 1987). To sample such distributions, ground-based observations must presently be supplemented with IRAS measurements at the longer wavelengths. Existing bolometric luminosity functions are thus limited to a few dozen member stars, and any comparisons with a stochastic model such as ours must be advanced with due caution.

Our model assumes that a cluster forms from a single parent cloud, so that its members share such properties as the protostellar accretion rate $\dot{M}$ and the cutoff time t_c. This assumption must be tested empirically, on a case by case basis. Thus, the innermost core of the ρ Ophiuchus molecular cloud, with its high density of embedded objects, indeed appears to be a unified site of star formation activity, as do each of the

four compact clusters identified by Lada *et al.* (1991) in the Orion B molecular cloud. [1] On the other hand, the well studied Taurus-Auriga complex is a looser association, in which stars are forming within a number of relatively isolated groups containing less than a dozen members each (see Fig. 1 of Kenyon *et al.* 1990). In this latter case, it is not clear that our model applies at all.

To date, bolometric luminosity functions have been obtained for only a handful of embedded clusters. To our knowledge, these include ρ Ophiuchus (Wilking, Lada, & Young 1989), Taurus-Auriga (Kenyon *et al.* 1990), Chameleon I (Prusti, Whittet, & Wesselius 1992), Corona Australis (Wilking *et al.* 1992), and Perseus (Ladd, Lada, & Myers 1993). The ρ Ophiuchus cluster remains the best studied, with bolometric luminosities estimated for 58 members. Since its morphology also seems appropriate, we focus on this region for the remainder of this discussion.

The histogram in Figure 17 reproduces the ρ Ophiuchus luminosity function from Wilking, Lada, & Young (1989), where we have omitted sources with only upper limits in bolometric luminosity (see their Fig. 5). As discussed by Wilking *et al.* , the drop in the stellar population at low luminosities reflects simply the sensitivity limit of their survey. We thus focus only on the 30 stars with $\log(L/L_\odot) \geq 0.25$.

Wilking *et al.* classified the broadband infrared spectra of their stars according to the scheme introduced by Lada (1987) and interpreted physically by Adams, Lada, & Shu (1987). Class I objects, which have rising spectral energy distributions from 2 to 25 μm, are thought to be accreting protostars. Class II sources have flat or gently falling spectra, and are identified as pre-main-sequence stars with circumstellar disks. Finally, Class III objects, with steeply falling spectra, are reddened stars on or near the main sequence. Within the restricted sample just defined, 17 stars are in Class I; these have $\log(L/L_\odot)$ ranging from 0.25 to 1.75, and are the dominant component within this interval. At the other extreme, the 4 Class III stars all have $\log(L/L_\odot)$ greater than 1.25.

Adams *et al.* reproduced the spectral energy distributions of the ρ Ophiuchus Class I stars WL 16 and Elias 29 by assuming a protostellar $\dot{M}$ of $1 \times 10^{-5}\, M_\odot$ yr^{-1}. We therefore search within our canonical model for a theoretical luminosity function to reproduce the observations. Our procedure was to vary the cluster time t and the star formation rate C_0 until the theoretical and empirical results were best matched according to a χ^2 test.

[1] In such crowded regions, the identity of the cloud fragments forming individual stars is not yet established (Lada, Strom, & Myers 1993). Nevertheless, we assume that protostellar collapse still proceeds in an inside-out manner, with a mass accretion rate that is roughly constant in time.

To compare with the histogram of observed results, we plot in Figure 17 not $\Phi(L)$ itself, but rather $\Delta N(L)$, defined as

$$\Delta N(L) \equiv \int_{\log(L/L_\odot)}^{\log(L/L_\odot)+\Delta} \Phi(L)\, d\log L \ ,$$

where Δ, the bin size in $\log(L/L_\odot)$, is set to 0.50, the value used by Wilking *et al.* . The figure shows the optimal $\Delta N(L)$, which corresponds to a cluster time of 1×10^6 yr. This time agrees well with the contraction age of 1.5×10^6 yr for the oldest detected pre-main-sequence star (Wilking *et al.* 1989). We estimate that any cluster time from 8×10^5 yr to 2×10^6 yr yields an acceptable fit to the data. At shorter times, the protostar peak is too pronounced, while the main-sequence population at later times is too large. Figure 17 also gives f°_{proto}, f°_{pms}, and f°_{ms}, the fractions of the various stellar populations, here measured relative to those stars with $\log(L/L_\odot) \geq 0.25$.

The figure graphically demonstrates the point that the vast majority of stars in this cluster, whose bolometric luminosities are still undetermined, are relatively dim pre-main-sequence objects. The Wilking *et al.* survey covered a 4.3 pc^2 area, encompassing the central cloud of the ρ Ophiuchus complex. Our reconstruction of the full luminosity function implicitly assumes that their survey was complete for $\log(L/L_\odot) \geq 0.25$. Figure 17 shows a maximum of 36 stars in a bin of width Δ, and a total cluster population of 160 stars with $\log(L/L_\odot) \geq -2$. However, Greene & Young (1992) estimated 340 cluster members embedded in just the innermost 1.4 pc^2 area of the same region. If their estimate proves accurate, the implication is that even the higher-luminosity sample detected by Wilking *et al.* is incomplete.

The theoretical luminosity function in Figure 17 exhibits a broad maximum at $\log(L/L_\odot) = -1.3$. Inspection of Figures 6 and 7 shows that this feature persists throughout the early evolution, gradually disappearing as stars of lower luminosity join the main sequence. The presence of such a peak stems from the fact that the IMF, when expressed as the number of stars per logarithmic mass interval, must itself have a maximum. In the Gaussian form used in our canonical model, this maximum is at $\log M = -1.02$ (see eq. (I.6)). Figure I.3 shows that stars of this mass are undergoing deuterium burning at a cluster time of 10^6 yr, when their luminosity is indeed near $0.1\, L_\odot$. As discussed in §3.2, the effect of deuterium burning in our model is to enhance temporarily the stellar population over a range in luminosity. In summary, the existence of a peak in the luminosity function is generic, but its precise location depends on the poorly known IMF for low-mass stars and brown dwarfs.

Our model correctly predicts that the *most* luminous stars are on the main sequence. However, Wilking *et al.* identified two Class III stars with luminosities below our theoretical lower bound of $\sim 500\, L_\odot$ (see Fig. 4a). Our protostar luminosities peak near $L^*_{proto} = 45\, L_\odot$, which is within the observed range for Class I sources. The theoretical f°_{proto} of 0.24 can be compared with the observational figure of 0.57. From equation (2), the fraction f_{proto}, measured relative to *all* stars, is much lower, about 3.2×10^{-2}.

Thus far, the sharply peaked protostar luminosity function we obtain is not evident in the data. The discrepancy can be seen by comparing the broad Class I distribution in Figure 5 of Wilking *et al.* with our own Figure 1c. A new extension of the Wilking *et al.* survey to lower luminosity shows a similar spread in the Class I population (Greene *et al.* 1994). Unfortunately, quantitative statements concerning the empirical protostar population are particularly suspect. One problem is that observations of Class I sources rely heavily on IRAS data. In a crowded field like ρ Ophiuchus, the relatively large IRAS beam might well have included flux from other sources unrelated to the star in question. This point is borne out by comparison with the sparser Taurus-Auriga association, in which Class I luminosities are generally lower (Kenyon *et al.* 1990). In addition, André & Montmerle (1993) have recently shown that the peak fluxes at 1.3 mm for the ρ Ophiuchus Class I and Class II objects are similar. Since their observations presumably measure the emission from slightly warmed dust located relatively close to the star, the implication is that Class I sources may *not* represent as early an evolutionary phase as is generally supposed. In any case, it will be interesting to see if future surveys both in this region and others reveal both the spike in relatively luminous, embedded objects and the much broader distribution of low-luminosity pre-main-sequence stars predicted by our model.

We thank P. André, T. Greene, T. Prusti, and H. Zinnecker for helpful discussions. The referee, C. Lada, offered numerous helpful comments on both papers and kindly supplied to us, in advance of publication, the luminosity function from the new Greene *et al.* survey. We are also grateful to B. Burke, who supported A. B. F. through NSF Grant AST-90-22501. S. W. S. was funded principally by NSF Grant AST-90-14479. In addition, he received funding from the NASA astrophysics theory program through its Center for Star Formation Studies, a consortium of U. C. Berkeley, U. C. Santa Cruz, and NASA-Ames Research Center.

References

Adams, F. C., Lada, C. J., & Shu, F. H. 1987, ApJ, 312, 788

André, P. & Montmerle, T. 1993, ApJ, preprint

Cox, J. P. & Giuli, R. T. 1968, Principles of Stellar Structure (New York: Gordon and Breach)

Fletcher, A. B. & Stahler, S. W. 1993 [Paper I], ApJ, in press

Greene, T. & Young, E. T. 1992, ApJ, 395, 516

Greene, T., Wilking, B. A., André, P., Young, E. T., & Lada, C. J. 1994, in preparation

Hayashi, C. 1961, PASJ, 13, 450

Hayashi, C., Hoshi, R., and Sugimoto, D. 1962, Progr Theor Phys Suppl, No. 22

Henyey, L. G., LeLevier, R. and Levee, R. D. 1955, PASP, 67, 154

Iben, I. & Talbot, R. J. 1966, ApJ, 144, 968

Kenyon, S. J., Hartmann, L. W., Strom, K. M., & Strom, S. E. 1990, AJ, 99, 869

Lada, C. J. 1991, in The Physics of Star Formation and Early Stellar Evolution, eds. C. J. Lada & N. D. Kylafis (Dordrecht: Reidel), p. 329

Lada, C. J. 1987, in Star Forming Regions, eds. M. Peimbert & J. Jugaku (Dordrecht: Reidel), p. 1

Lada, E. A., Depoy, D. L., Evans, N. J., & Gatley, I. 1991, ApJ, 371, 171

Lada, E. A., Strom, K. M., & Myers, P. C. 1993 in Protostars and Planets III, ed. E. H. Levy & J. I. Lunine (Tucson: U. of Arizona Press), p. 245

Ladd, E. F., Lada, E. A., & Myers, P. C. 1993, ApJ, 410, 168

Miller, G. E. & Scalo, J. M. 1979, ApJS, 41, 513

Palla, F. & Stahler, S. W. 1991, ApJ, 375, 288

Palla, F. & Stahler, S. W. 1993, ApJ, 418, 414

Prusti, T., Whittet, D. C. B., & Wesselius, P. R. 1992, MNRAS, 254, 361

Shu, F. H. 1977, ApJ, 214, 488

Stahler, S. W. 1983, ApJ, 274, 822

Stahler, S. W. 1985, ApJ, 293, 207

Stahler, S. W. 1988, ApJ, 332, 804

Stahler, S. W. 1989, ApJ, 347, 950

Stahler, S. W., Shu, F. H., & Taam, R. E. 1980, ApJ, 241, 637

Wilking, B. A., Greene, T. P., Lada, C. J., Meyer, M. R., & Young, E. T. 1992, ApJ, 397, 520

Wilking, B. A., Lada, C. J., & Young, E. T. 1989, ApJ, 340, 823

Zinnecker, H., McCaughrean, M., & Wilking, B. A. 1993, in Protostars and Planets III, ed. E. H. Levy & J. Lunine (Tucson: U. of Arizona Press), p. 429

Figure Captions

Figure 1: Evolution of the protostar luminosity function within the canonical model. The figure also gives the fraction of protostars in the total cluster population at the four times shown.

Figure 2: The effect on the protostar luminosity function of (a) the assumed brown-dwarf IMF, and (b) the assumed mass accretion rate $\dot{M}$. The function is shown in the invariant form it assumes after about one accretion time.

Figure 3: The post-accretion luminosity function at early times, within the canonical model. Also given, at the four times indicated, are the fractions of pre-main-sequence and main-sequence stars.

Figure 4: The post-accretion luminosity function at intermediate times. In panel (d), the fraction of post-main-sequence stars is also shown.

Figure 5: Evolution of the post-accretion luminosity function at late times.

Figure 6: Early evolution of the total luminosity function within the canonical model. The figure also gives the fractional contributions of the protostars, pre-main-sequence, and main-sequence stars to the total cluster luminosity, at each of the four times indicated.

Figure 7: The total luminosity function at intermediate times. All symbols have the same meaning as in Figure 6.

Figure 8: The total luminosity function at late times. Note the progressive truncation of the function at high luminosity due to post-main-sequence evolution.

Figure 9: Comparison of the total luminosity function at $t = 1 \times 10^7$ yr (*solid curve*) with the "Initial Luminosity Function" (*dashed curve*). For luminosities less than L_{trans}, there is a surplus of stars with respect to the ILF. For luminosities near L^*_{proto}, there is also a minor enhancement from the protostar population.

Figure 10: Effect of the mass accretion rate $\dot{M}$ on the total luminosity function (a) at an early epoch, and (b) at an intermediate cluster time.

Figure 11: Effect of the brown-dwarf portion of the IMF on the total luminosity function (a) at an early time, and (b) at the canonical cutoff time of 1×10^7 yr.

Figure 12: Effect of the value of the cutoff time t_c on the total luminosity function. (a) The specific cutoff time does matter when the cluster time is slightly less or greater than t_c. (b) Once the cluster age significantly exceeds the cutoff time, the value of t_c makes little difference.

Figure 13: The evolution, with respect to the cluster time t, of the fractional populations of protostars, pre-main-sequence, main-sequence, and post-main-sequence stars. In panel (a), the canonical parameters are assumed, while (b) shows the effect of lowering $\dot{M}$. The last two panels explore variations in the cutoff time t_c.

a

Figure 14: The evolution of the fractional contribution from each stellar population to the total cluster luminosity. All symbols have the same significance as in Figure 13, except that the contribution from post-main-sequence stars is not included.

Figure 15: Total luminosity within the cluster provided by the protostellar population. Shown is the product of the function Φ_{proto} with L_{proto}. This product is plotted against L_{proto} itself, *i.e.*, the luminosity of an individual protostar.

Figure 16: Evolution of the total luminosity within the cluster provided by protostars, pre-main-sequence, main-sequence, and post-main-sequence stars. The total luminosity is normalized to the quantity $L^{\bullet}_{tot}$, defined in the text.

Figure 17: Comparison of the empirical ρ Ophiuchus luminosity function (*histogram*) with the theoretical model (*solid curve*). The theoretical function shown is not Φ itself, but rather the bin-averaged ΔN, defined in the text. For the canonical parameters here assumed, the optimal fit is obtained at a cluster time of 1×10^6 yr. Also shown are the theoretical fractions of protostars, pre-main-sequence, and main-sequence stars, measured relative to those with $\log(L/L_{\odot}) \geq 0.25$.

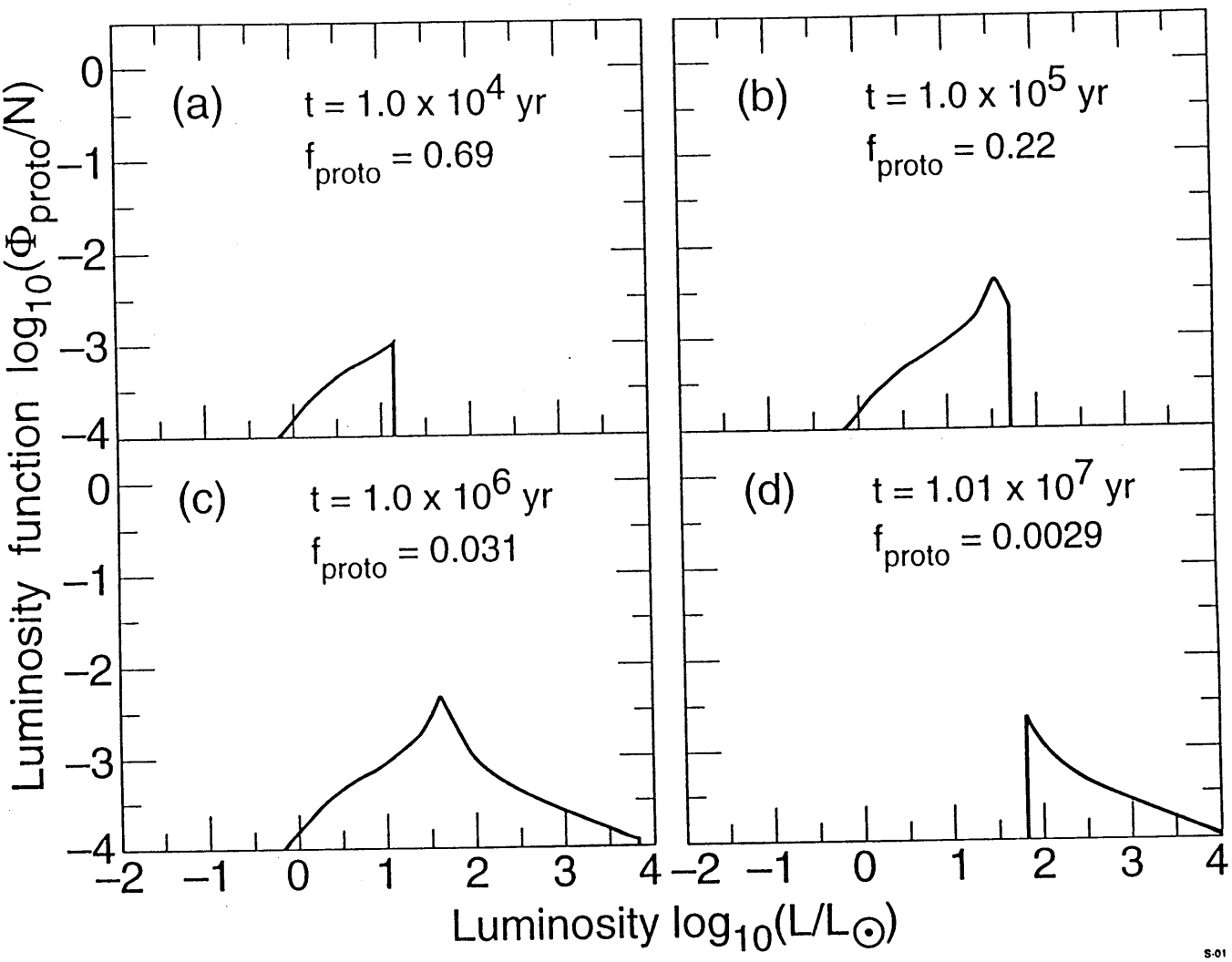
(a)
t = 1.0 x 10^4 yr
f_proto = 0.69
(b)
t = 1.0 x 10^5 yr
f_proto = 0.22
(c)
t = 1.0 x 10^6 yr
f_proto = 0.031
(d)
t = 1.01 x 10^7 yr
f_proto = 0.0029
Luminosity function log10(Φproto/N)
Luminosity log10(L/L⊙)
0
−1
−2
−3
−4
−2 −1 0 1 2 3 4
S-01

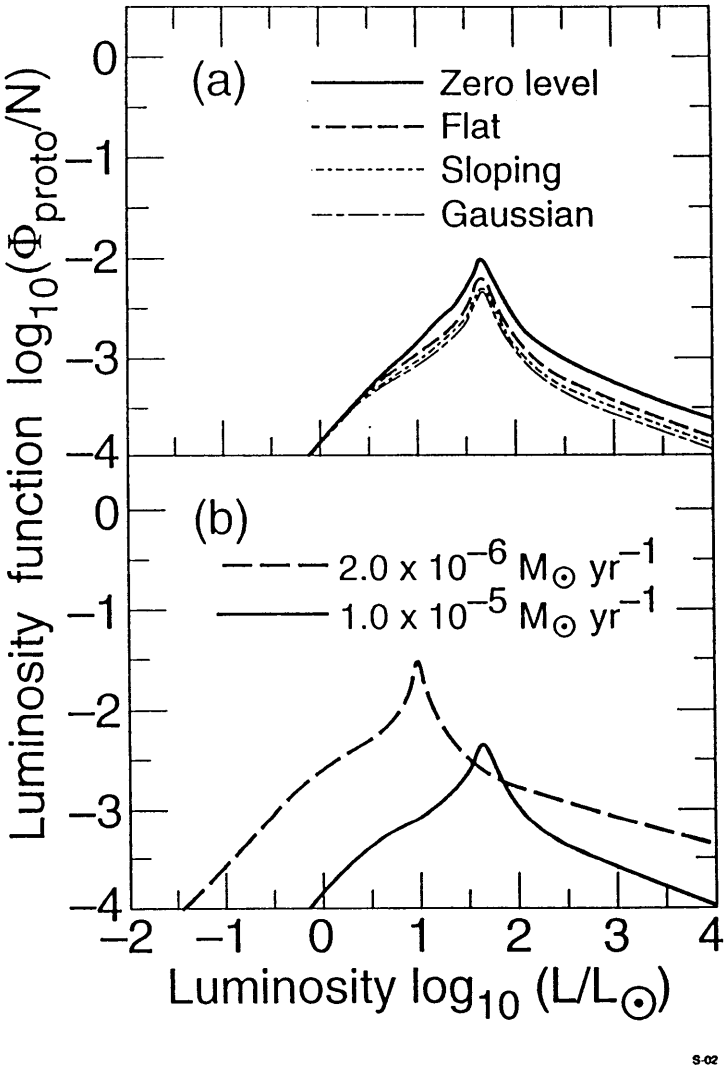
(a)
Zero level
Flat
Sloping
Gaussian
(b)
2.0 x 10^−6 M⊙ yr^−1
1.0 x 10^−5 M⊙ yr^−1
Luminosity function log10(Φproto/N)
Luminosity log10 (L/L⊙)
0
−1
−2
−3
−4
−2
−1
0
1
2
3
4
S-02

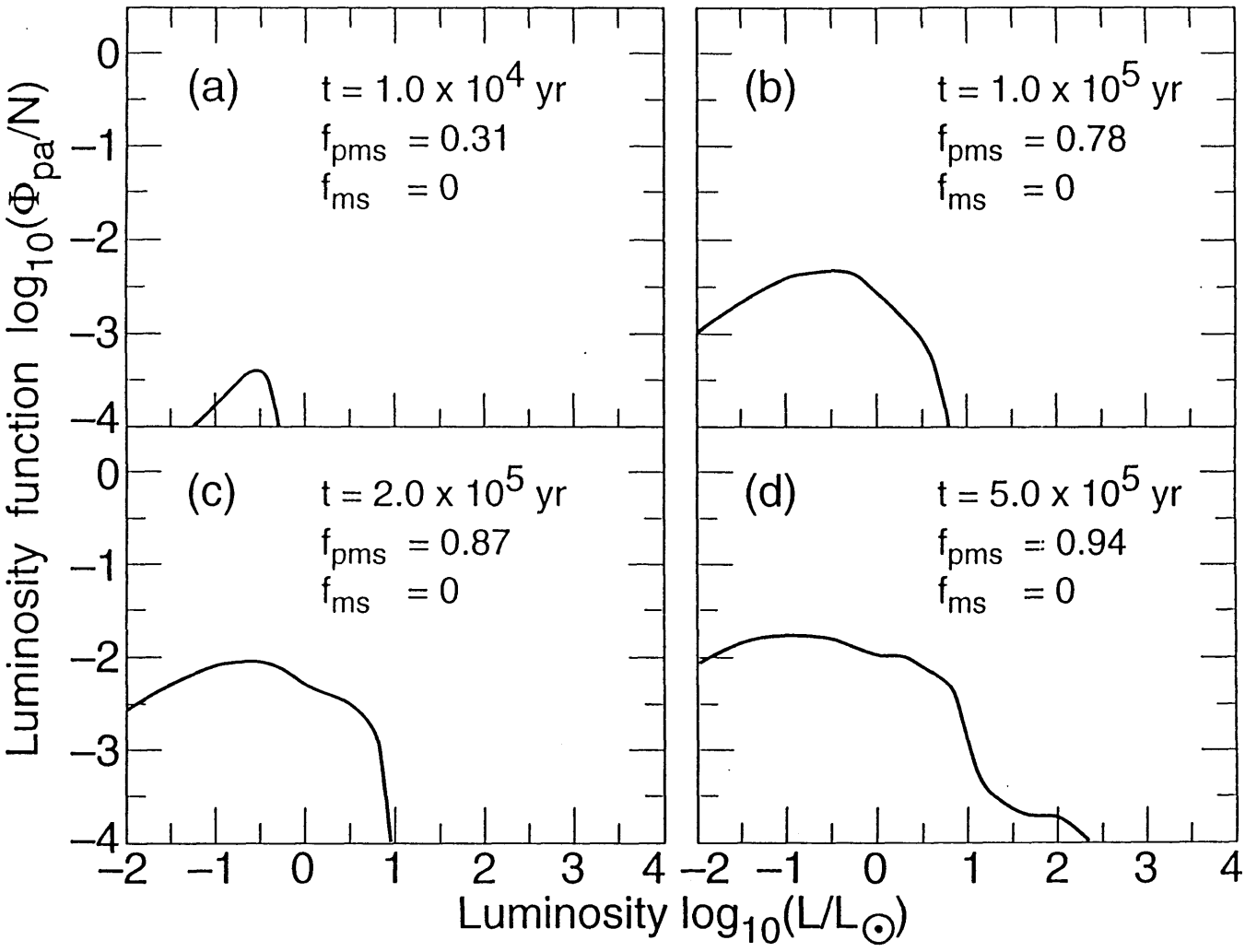
(a)
t = 1.0 x 10^4 yr
f_pms = 0.31
f_ms = 0
(b)
t = 1.0 x 10^5 yr
f_pms = 0.78
f_ms = 0
(c)
t = 2.0 x 10^5 yr
f_pms = 0.87
f_ms = 0
(d)
t = 5.0 x 10^5 yr
f_pms = 0.94
f_ms = 0
Luminosity function log10(Φpa/N)
Luminosity log10(L/L⊙)
0
−1
−2
−3
−4
−2 −1 0 1 2 3 4
S-03

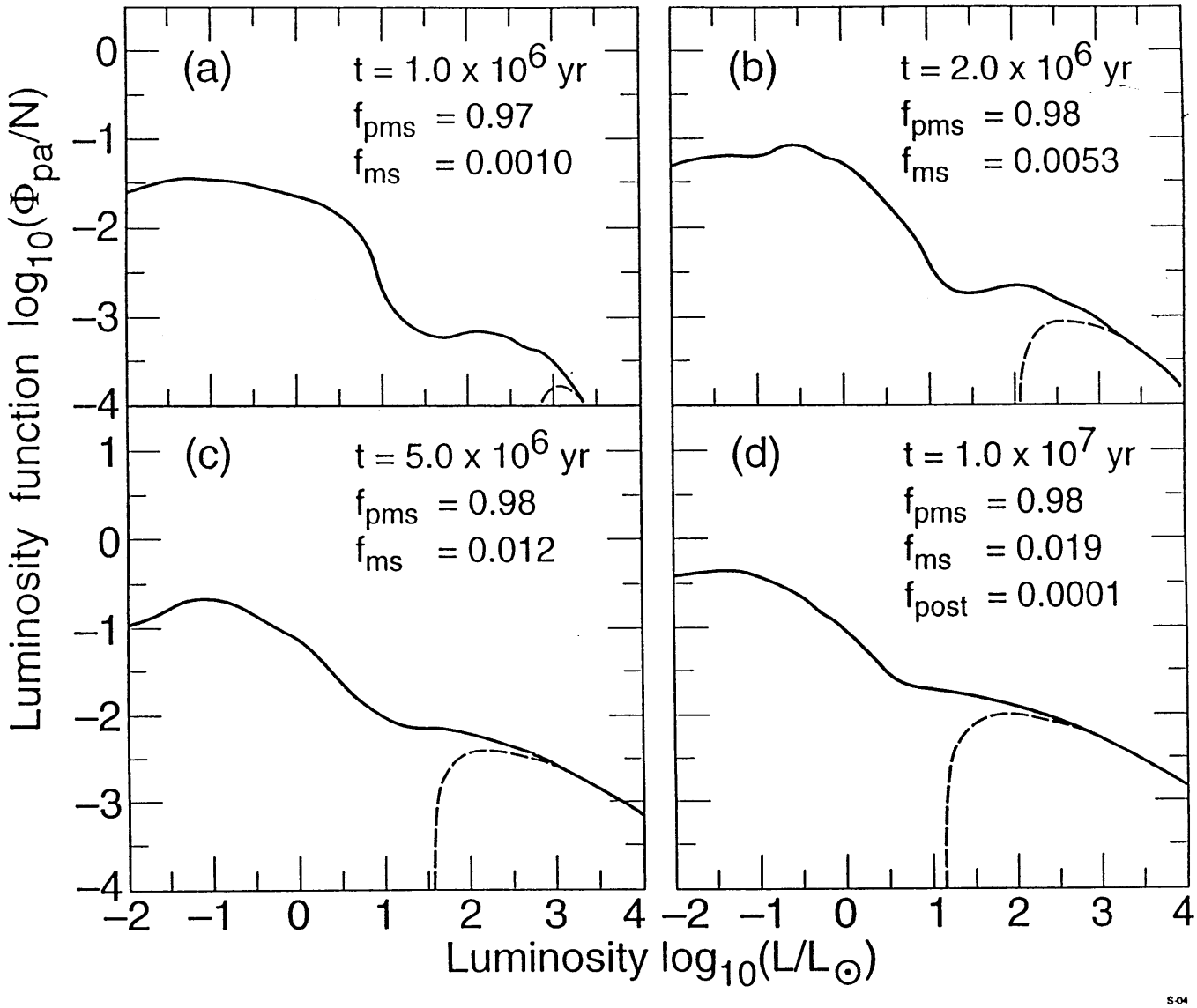
(a)
t = 1.0 x 10^6 yr
f_pms = 0.97
f_ms = 0.0010
(b)
t = 2.0 x 10^6 yr
f_pms = 0.98
f_ms = 0.0053
(c)
t = 5.0 x 10^6 yr
f_pms = 0.98
f_ms = 0.012
(d)
t = 1.0 x 10^7 yr
f_pms = 0.98
f_ms = 0.019
f_post = 0.0001
Luminosity function log10(Φpa/N)
Luminosity log10(L/L⊙)
0
−1
−2
−3
−4
1
−2 −1 0 1 2 3 4
S-04

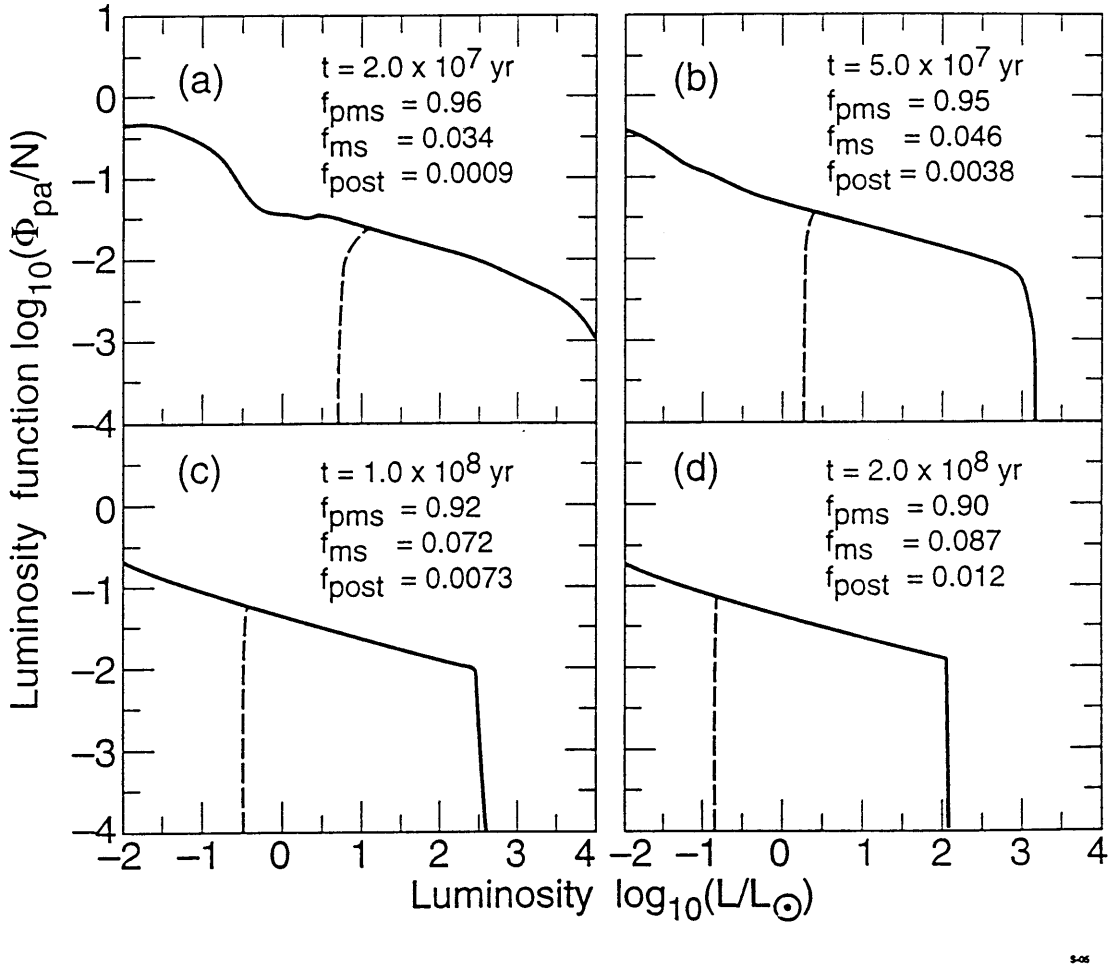
(a)
t = 2.0 x 10^7 yr
f_pms = 0.96
f_ms = 0.034
f_post = 0.0009
(b)
t = 5.0 x 10^7 yr
f_pms = 0.95
f_ms = 0.046
f_post = 0.0038
(c)
t = 1.0 x 10^8 yr
f_pms = 0.92
f_ms = 0.072
f_post = 0.0073
(d)
t = 2.0 x 10^8 yr
f_pms = 0.90
f_ms = 0.087
f_post = 0.012
Luminosity function log10(Φpa/N)
Luminosity log10(L/L⊙)

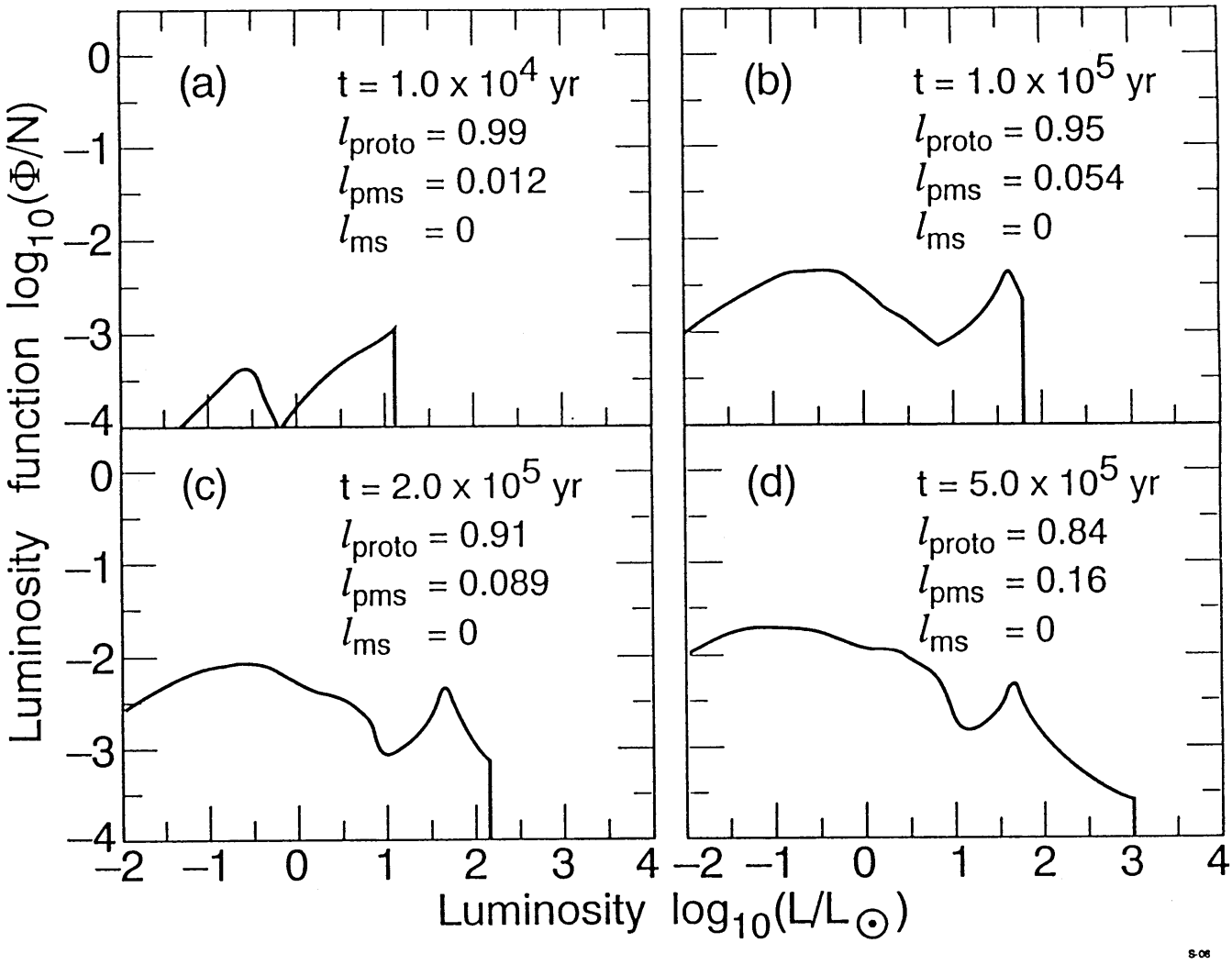
(a)
t = 1.0 x 10^4 yr
l_proto = 0.99
l_pms = 0.012
l_ms = 0
(b)
t = 1.0 x 10^5 yr
l_proto = 0.95
l_pms = 0.054
l_ms = 0
(c)
t = 2.0 x 10^5 yr
l_proto = 0.91
l_pms = 0.089
l_ms = 0
(d)
t = 5.0 x 10^5 yr
l_proto = 0.84
l_pms = 0.16
l_ms = 0
Luminosity function log10(Φ/N)
Luminosity log10(L/L⊙)
0
−1
−2
−3
−4
−2 −1 0 1 2 3 4

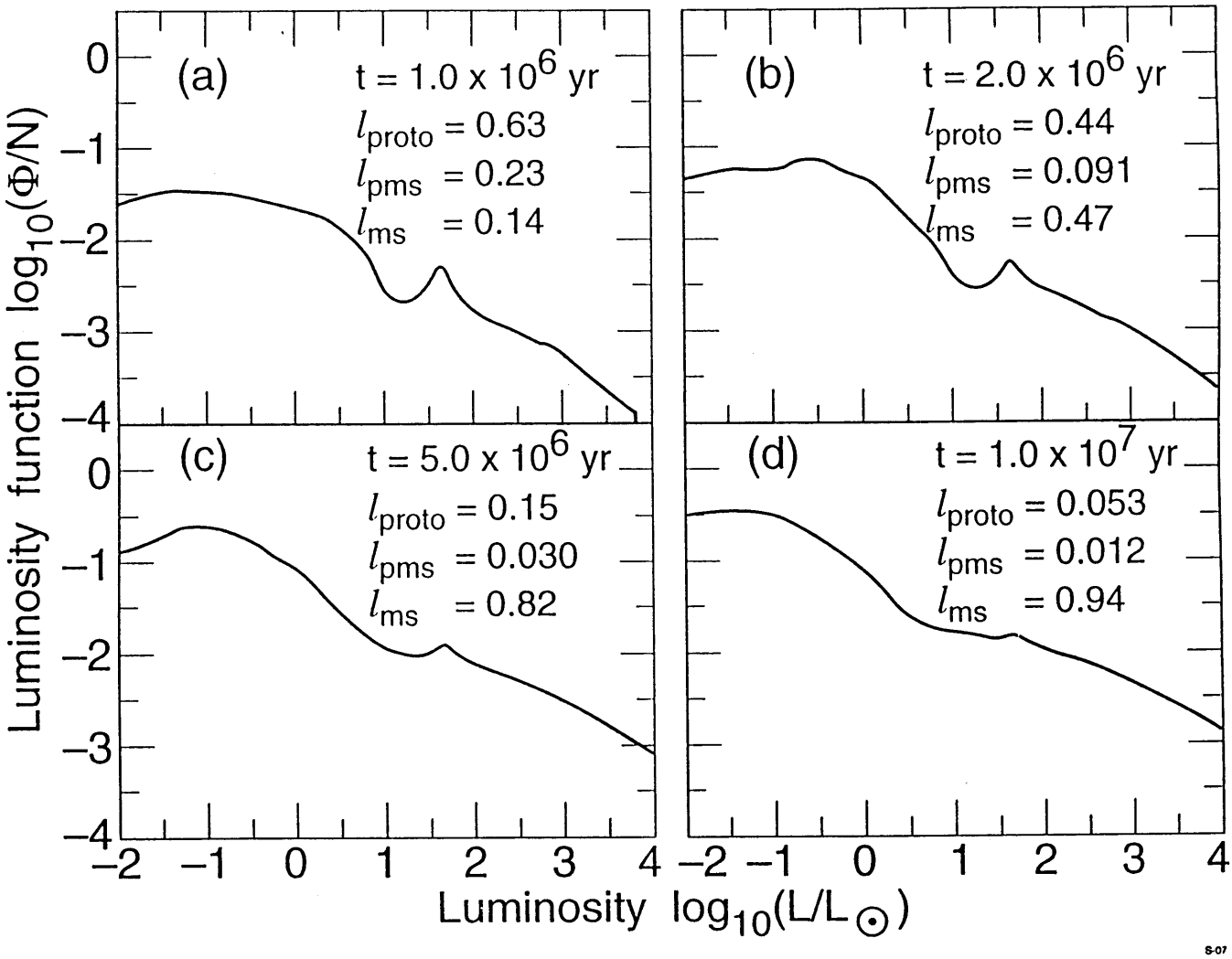
(a)
t = 1.0 x 10^6 yr
l_proto = 0.63
l_pms = 0.23
l_ms = 0.14
(b)
t = 2.0 x 10^6 yr
l_proto = 0.44
l_pms = 0.091
l_ms = 0.47
(c)
t = 5.0 x 10^6 yr
l_proto = 0.15
l_pms = 0.030
l_ms = 0.82
(d)
t = 1.0 x 10^7 yr
l_proto = 0.053
l_pms = 0.012
l_ms = 0.94
Luminosity function log10(Φ/N)
Luminosity log10(L/L⊙)
0
−1
−2
−3
−4
−2 −1 0 1 2 3 4
S-07

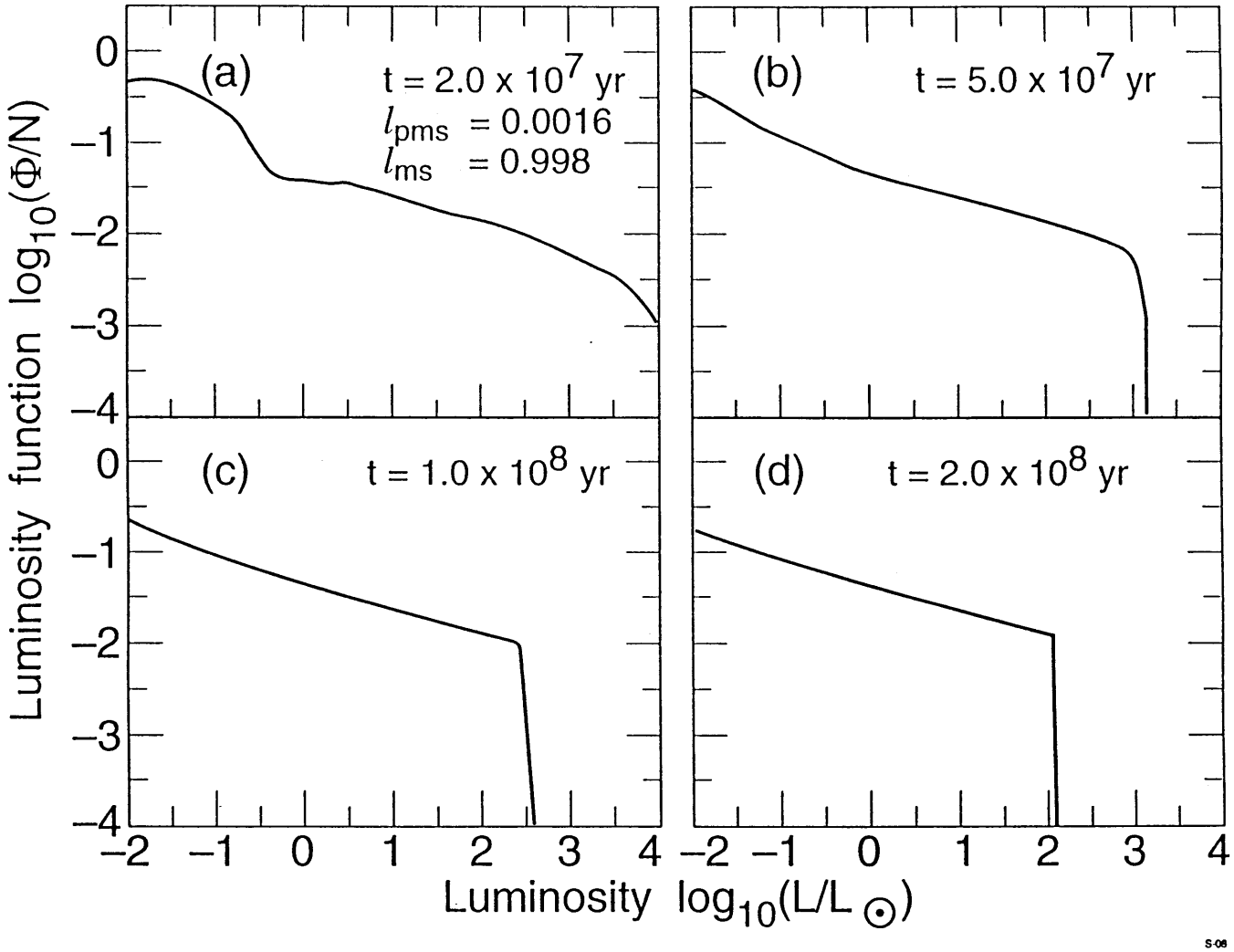
(a)
t = 2.0 x 10^7 yr
l_pms = 0.0016
l_ms = 0.998
(b)
t = 5.0 x 10^7 yr
(c)
t = 1.0 x 10^8 yr
(d)
t = 2.0 x 10^8 yr
Luminosity function log10(Φ/N)
Luminosity log10(L/L⊙)
0
−1
−2
−3
−4
−2 −1 0 1 2 3 4
S-08

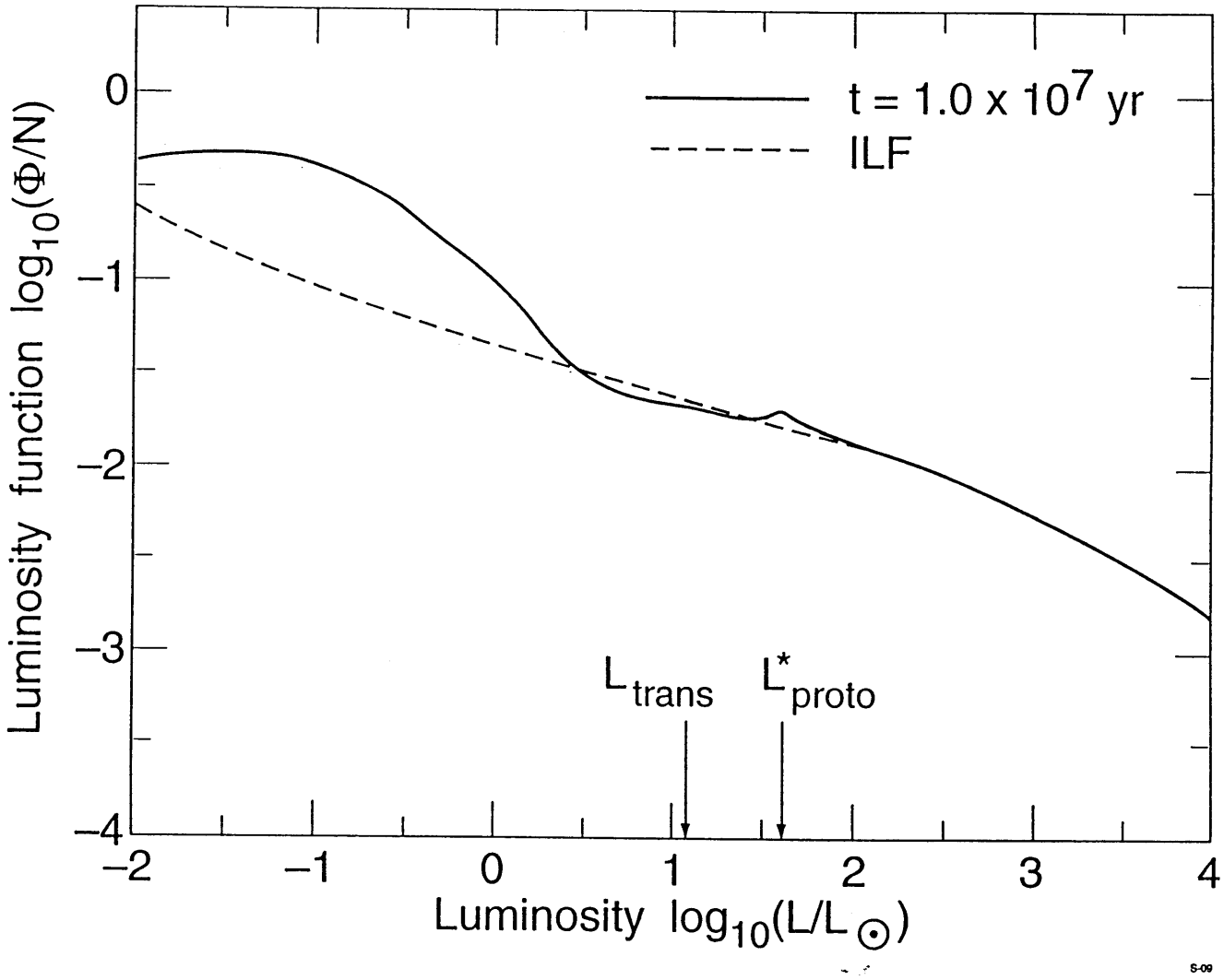
t = 1.0 x 10^7 yr
ILF
L trans
L* proto
Luminosity function log10(Φ/N)
Luminosity log10(L/L⊙)
0
−1
−2
−3
−4
−2
−1
0
1
2
3
4
S-09

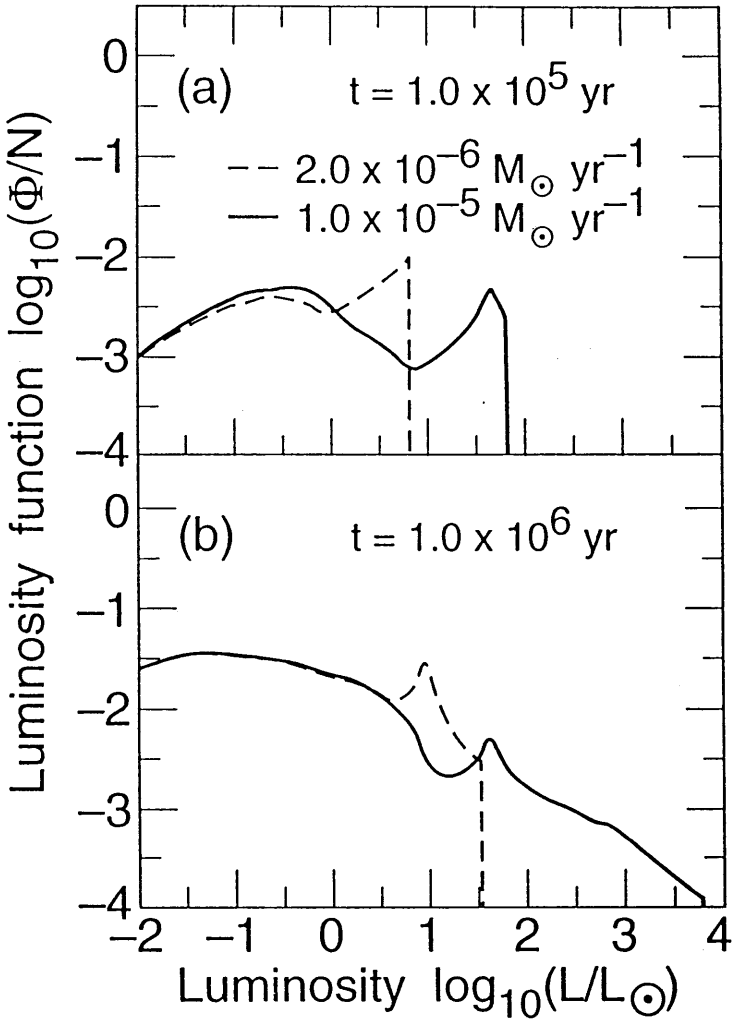
(a)
t = 1.0 x 10^5 yr
-- 2.0 x 10^-6 M⊙ yr^-1
— 1.0 x 10^-5 M⊙ yr^-1
(b)
t = 1.0 x 10^6 yr
Luminosity function log10(Φ/N)
Luminosity log10(L/L⊙)
0
−1
−2
−3
−4
−2
−1
0
1
2
3
4

S-10

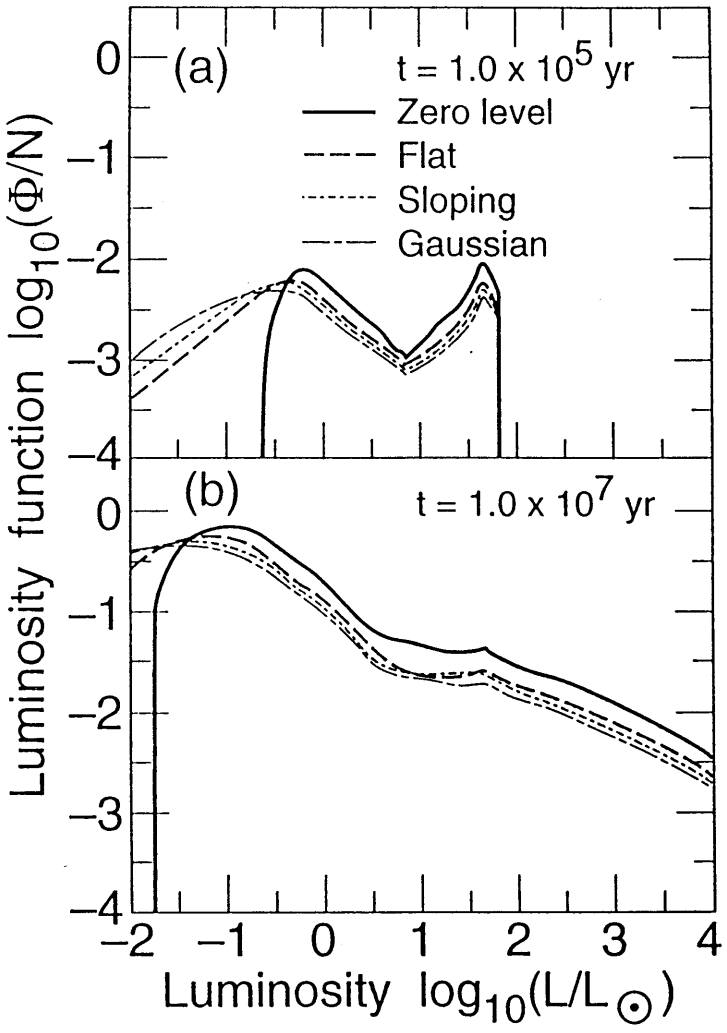
(a)
t = 1.0 x 10^5 yr
Zero level
Flat
Sloping
Gaussian
(b)
t = 1.0 x 10^7 yr
Luminosity function log10(Φ/N)
Luminosity log10(L/L⊙)
0
−1
−2
−3
−4
−2
−1
0
1
2
3
4

S-11

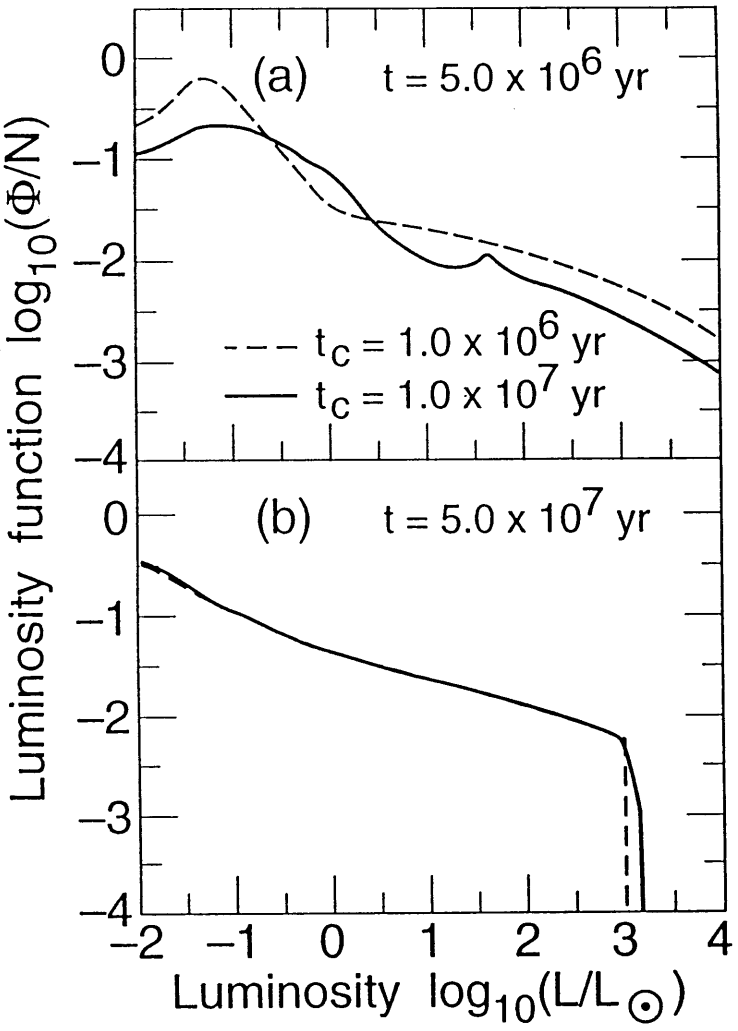
(a) t = 5.0 x 10^6 yr
--- t_c = 1.0 x 10^6 yr
— t_c = 1.0 x 10^7 yr
(b) t = 5.0 x 10^7 yr
Luminosity function log10(Φ/N)
Luminosity log10(L/L⊙)
0
−1
−2
−3
−4
−2 −1 0 1 2 3 4

S-12

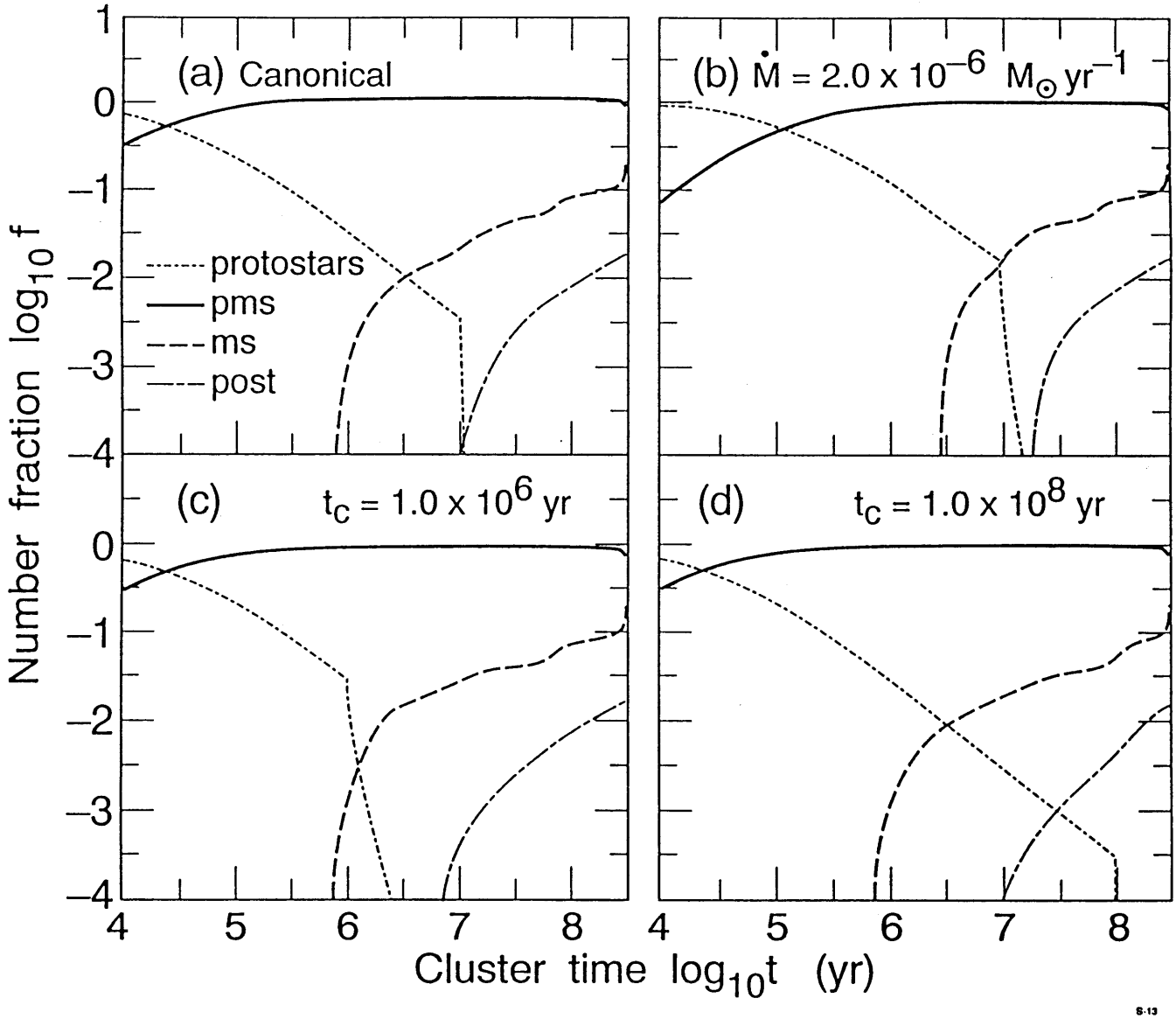
(a) Canonical
(b) $\dot{M}$ = 2.0 x 10^{-6} $M_\odot$ yr^{-1}
(c) t_c = 1.0 x 10^6 yr
(d) t_c = 1.0 x 10^8 yr
protostars
pms
ms
post
Number fraction $\log_{10} f$
Cluster time $\log_{10} t$ (yr)
1
0
−1
−2
−3
−4
4
5
6
7
8
S-13

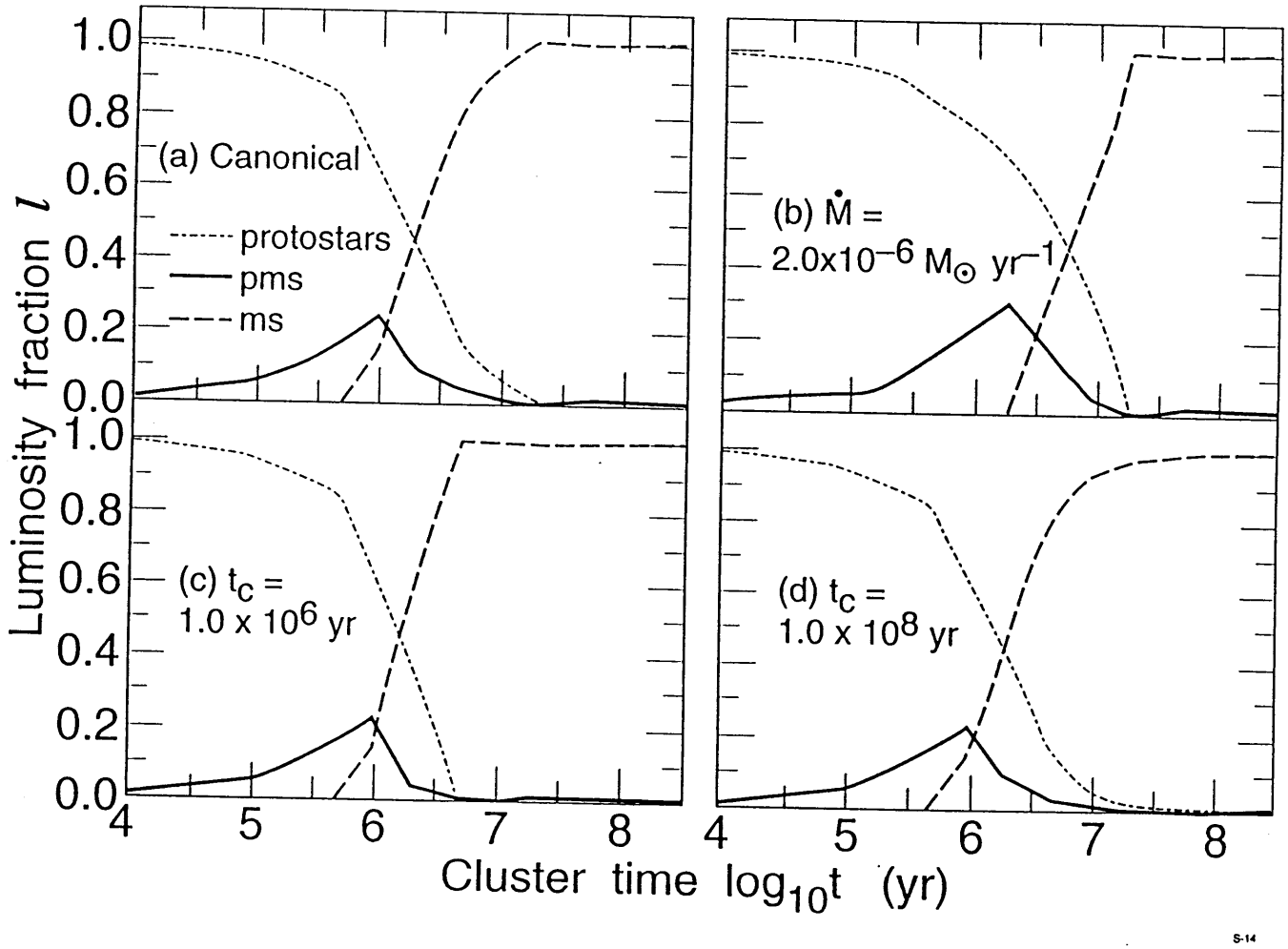
Luminosity fraction l
1.0
0.8
0.6
0.4
0.2
0.0
(a) Canonical
protostars
pms
ms
(b) $\dot{M}$ = 2.0×10^{-6} $M_\odot$ yr^{-1}
(c) t_c = 1.0×10^6 yr
(d) t_c = 1.0×10^8 yr
4
5
6
7
8
Cluster time $\log_{10} t$ (yr)
S-14

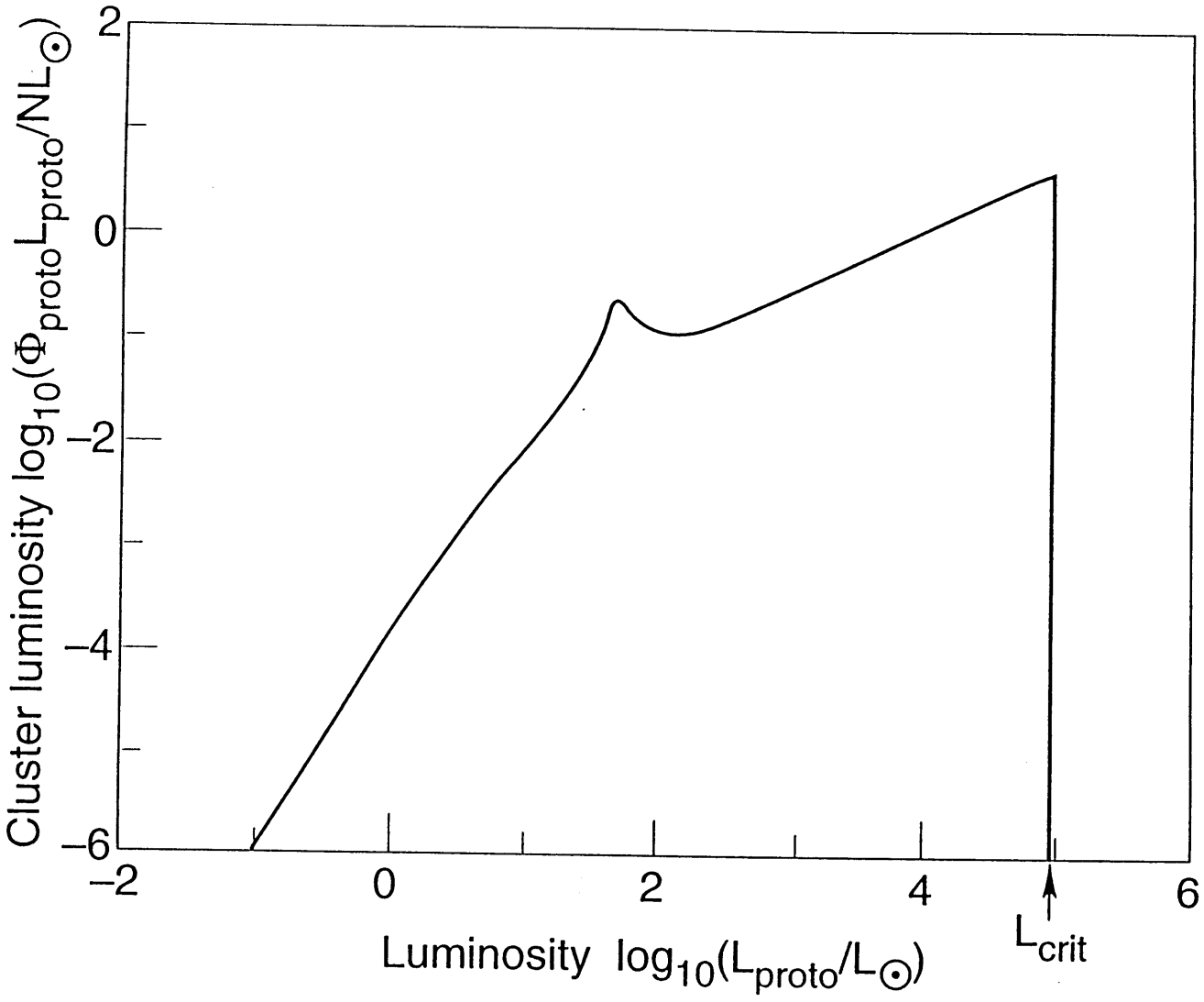
Cluster luminosity $\log_{10}(\Phi_{proto} L_{proto}/NL_\odot)$
2
0
−2
−4
−6
−2
0
2
4
6
Luminosity $\log_{10}(L_{proto}/L_\odot)$
L_{crit}
S-15

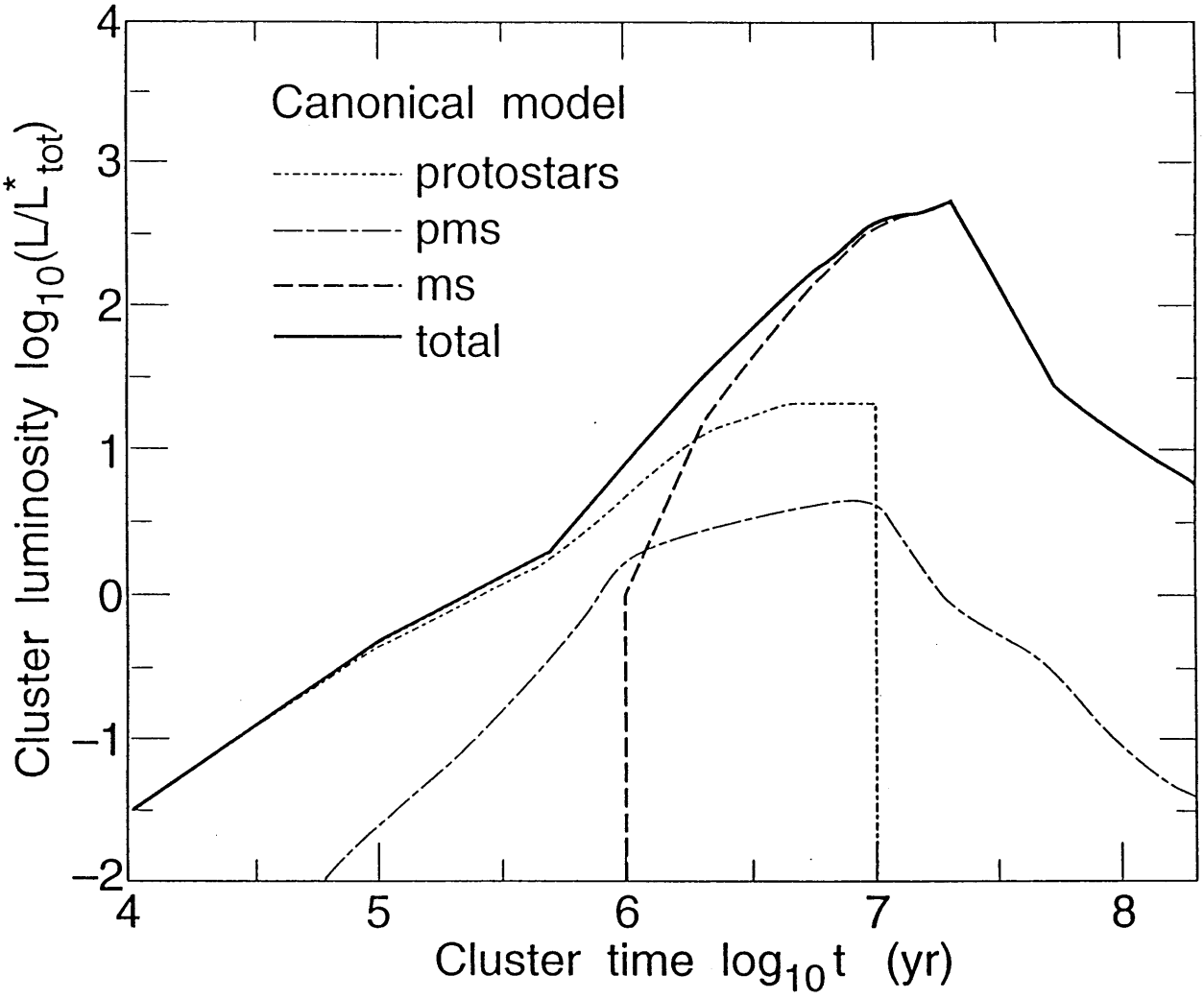
Canonical model
protostars
pms
ms
total
Cluster luminosity $\log_{10}(L/L^*_{tot})$
Cluster time $\log_{10} t$ (yr)
4
3
2
1
0
−1
−2
4
5
6
7
8

S-16

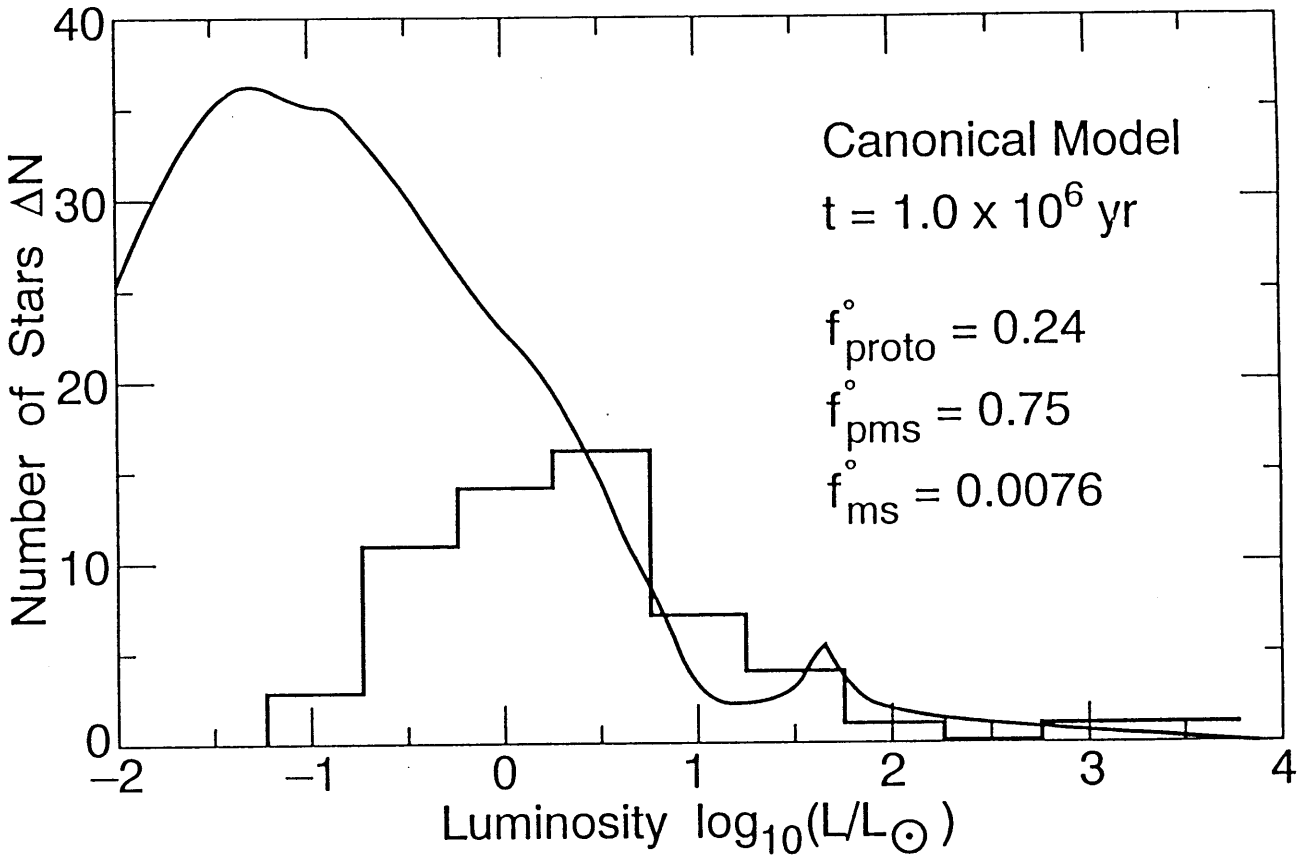
Canonical Model
t = 1.0 x 10^6 yr
f°proto = 0.24
f°pms = 0.75
f°ms = 0.0076
Number of Stars ΔN
Luminosity log10(L/L⊙)
40
30
20
10
0
−2
−1
0
1
2
3
4
Stahler-17

THE LUMINOSITY FUNCTIONS OF EMBEDDED CLUSTERS

Steven W. Stahler and André B. Fletcher
Department of Physics
Massachusetts Institute of Technology
Cambridge, MA 02139 U.S.A.

In the near future, bolometric luminosity functions will be available for large numbers of populous young clusters still heavily embedded in the gas and dust of their parent molecular cloud complexes. To understand these results, a theory is needed. We outline here a new approach for obtaining a temporal history of the luminosity function in a very young cluster. The method also yields other interesting statistical properties, such as the fraction of accreting protostars. We find that, for a cloud producing stars at a steady rate, the number of protostars is constant, after a brief transient period. Thus, the relative fraction of protostars declines inversely with time. We also find that the mass spectrum for protostars is distinct from that of pre-Main-Sequence stars. We display representative numerical results for a typical cluster.

Introduction

The observation of populous clusters still in the process of formation offers an exciting new route for corroborating and correcting our existing ideas of early stellar evolution. For this purpose, the compilation of *bolometric luminosity functions* will be particularly valuable. Significant progress has already been made in this direction, e.g., in the case of the ρ Ophiuchus complex (Wilking, Lada, and Young 1989). Once such luminosity functions become generally available, what can we expect to find?

Until now, the only theoretical result available for comparison has been the "Initial Luminosity Function." The ILF is formed by combining the mass-spectrum of newly-formed stars with a mass-luminosity relation. Symbolically, we have

$$\frac{dN}{dL} = \frac{dN}{dM} \Big/ \frac{dL}{dM} \quad , \tag{1}$$

where N is the number of stars of mass M and luminosity L. To obtain the ILF, the first factor on the right is taken from the Initial Mass Function (IMF) (Salpeter 1955, Miller and Scalo 1979), while the second factor is the standard Main-Sequence mass-luminosity relation. However, it is clear that *neither* choice for these factors is appropriate in the case of an actively forming cluster. At early times, many cluster members should still be protostars, i.e., objects whose luminosity is derived from their accretion of cloud material. There is no reason to expect that the mass distribution of accreting protostars should follow the IMF. Further, the Main-Sequence mass-luminosity relation cannot be used for either protostars or contracting pre-Main-Sequence stars.

These considerations show that a more realistic theoretical luminosity function for a forming cluster must be *time-dependent*. After star formation has ceased and cluster members have reached the Main Sequence, the ILF *does* provide an accurate model, provided that the mass spectrum can indeed be represented by the IMF. In fact, although the IMF was originally derived from the field star population, it appears to be suitable for individual clusters, as well, provided they contain sufficient numbers of stars (e.g., Straw, Hyland, and McGregor 1989).

Method of Solution

In order to make progress in this area, we have considered an idealized, phenomenological model of cluster formation. The model is consistent with current protostar and pre-Main-Sequence theory, and is simple enough to allow us to determine accurately a temporal history of the luminosity function. In addition, the model yields other useful statistical properties, such as the relative fraction of protostars and the age distribution of pre-Main-Sequence stars. A much more extended exposition of our calculation is available in our forthcoming article (Fletcher and Stahler 1992). Here, we will limit ouselves to outlining the method and presenting some representative results.

Imagine a massive cloud complex in which a large number of dense cores are continually collapsing to form protostars. Let $C(t)$ be the rate at which the cores undergo collapse, where $t = 0$ represents the time when star formation begins. We set $C(t) = 0$ for both $t < 0$ and for $t > t_c$, where t_c is the "cut-off time," after which no more cores collapse. For intermediate times, we set $C(t)$ to the constant value C. The physical cause of the cut-off, and, indeed, for the magnitude of C itself, need not concern us. Once a dense core collapses, the mass of the internal protostar is built up at the rate $\dot{M}$, while the protostar's luminosity is given by the accretion value $L_{acc} = GM\dot{M}/R$. Here, the protostellar mass-radius relation $R(M)$ is taken from the work of Stahler (1988) for low-mass stars, and Palla and Stahler (1991) for $M > 1\,M_\odot$. The mass accretion rate $\dot{M}$ is a free parameter.

As the protostar grows, it has a certain probability per unit time for ending accretion to become a pre-Main-Sequence object. It is currently believed that accretion is ended by the action of a powerful protostellar wind, probably associated with the observed bipolar outflows from infrared sources (Lada 1985). This probability per unit time, $v(M)$, is considered to be a function of protostellar mass. The function $v(M)$ is *not* freely specified, but is fixed by our requirement that the cluster mass distribution for $t \gg t_c$ approach the IMF. Once a protostar ceases to accrete, it descends conventional pre-Main-Sequence tracks, starting at the stellar birthline (Stahler 1983, Palla and Stahler 1990). Our pre-Main-Sequence tracks were taken from Iben (1965), Vandenberg (1990), and Nelson (1990), while the IMF was the "log-normal" prescription of Miller and Scalo (1979), extended to stellar masses below $0.1\,M_\odot$. The exact form of the IMF in the brown dwarf regime is unimportant for our luminosity functions, which cover the range $-2 < log(L/L_\odot) < +4$.

Overview of Results

By considering the change in the protostar population as a result of both continued mass accretion and the appearance of pre-Main-Sequence stars, we find that

$$p(M,t) = W_1(M,t,t_c) \int_M^\infty s(M')\,dM' \tag{2a}$$

$$s(M,t) = W_2(M,t,t_c)\,s(M) \ . \tag{2b}$$

Here, $p(M,t)$ and $s(M,t)$ are the numbers of protostars and pre-Main-Sequence stars, respectively, at time t in the mass interval $(M, M+dM)$. W_1 and W_2 are "window functions" (essentially combinations of Heaviside step functions) which enforce causality, e.g., by preventing the appearance of a pre-Main-Sequence star of mass M before a time $t = M/\dot{M}$. We also derive a similar expression for the number of pre-Main-Sequence stars of a given mass as a function of "track time," i.e., the star's age measured since its appearance on the birthline. The probability $v(M)$ does not appear in any of these equations, since it has been eliminated by the requirement that $s(M,t)$ approach $s(M)$ at long times.

Equation (2a) shows explicitly that the mass distribution of protostars is not the IMF, but rather the mass integral of the IMF. The underlying reason for this result is that a difference in the protostar population at neighboring masses is needed if a population of pre-Main-Sequence stars is to be created. Thus, if one assigns a power-law index α to the high-mass end of the IMF, the appropriate index for protostars is $\alpha + 1$. Moreover, the properties of the function W_1 show that the full protostar mass spectrum appears very quickly, within a time interval $\Delta t = \bar{M}/\dot{M}$, where $\bar{M}$ is an appropriate "width" of the IMF ($\bar{M} \approx 1\,M_\odot$ for the Miller-Scalo IMF). For $t > \Delta t$, *the entire protostar mass spectrum*

remains constant, as does the associated protostellar luminosity function. At the same time, the pre-Main-Sequence population continues to increase, until $t = t_c$. The constancy of the protostar population is evident once one realizes that the protostars represent a temporary, intermediate state for the stars being produced at the (assumed) constant rate C. After the initial transient period, the complex is exhibiting "contemporaneous star formation," in which stars of all mass form simultaneously, but with a relative probability governed by the IMF (Stahler 1985).

Since the protostar number becomes fixed, their relative fraction declines as t^{-1}. This fraction averaged over the interval $(0, t_c)$ is roughly given by $\bar{f}_p = \tau_c^{-1}$, where $\tau_c = t_c/\Delta t$. For the representative values $\dot{M} = 10^{-5} M_\odot\, yr^{-1}$ and $t_c = 10^7\, yr$, $\bar{f}_p$ is of order 10^{-2}. Yet another basic result is that *the luminosity function of protostars is strongly peaked.* This follows simply from the fact that the protostellar radius is approximately proportional to mass at low masses, as a result of the deuterium thermostat (Stahler 1988). Thus, L_{acc} is nearly a constant value at a given $\dot{M}$.

Numerical Luminosity Functions

In principle, there are a number of free parameters associated with our calculation: C, t_c, and $\dot{M}$. In practice, however, one finds that there is surprisingly little freedom in the final results, at least within the context of this simple model. Thus, the star formation rate C plays here the role of a normalization constant; its numerical value is irrelevant for the shapes of the luminosity functions. The value of t_c is also unimportant. The embedded clusters of interest are all presumed to still be undergoing active star-formation. The numerical results confirm our expectation that two time-sequences differing only in the value of t_c are identical for times $t < t_c$. The remaining parameter, $\dot{M}$, is constrained by the physical theory of cloud collapse to be of order $10^{-5} M_\odot\, yr^{-1}$, for both low and intermediate-mass stars (Stahler, Shu, and Taam 1980; Palla and Stahler 1992). For the following results, therefore, we limit ourselves to the values $t_c = 1 \times 10^7$ yr and $\dot{M} = 1 \times 10^{-5} M_\odot\, yr^{-1}$.

Figure 1 shows the luminosity function for accreting protostars. As noted before, there is a sharp maximum, here located at about $50\, L_\odot$. This luminosity represents L_{acc} at the peak IMF mass of $0.1\, M_\odot$. The protostar luminosity function does not appear at $t = 0$, but is gradually built up, over the time interval Δt. Similarly, it takes another interval of the same magnitude for the protostars to disappear after $t = t_c$. In between, the function remains strictly constant. The rather high value of the typical protostar luminosity is offset by the fact that so few members of the cluster are in this state at typical times. Figure 2 shows the evolution of the protostar number and relative fraction.

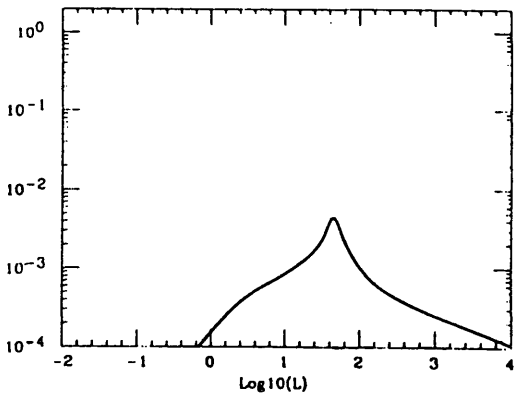

Figure 1. *Protostar luminosity function. Shown are the relative number of accreting protostars per unit luminosity, as a function of the luminosity.*

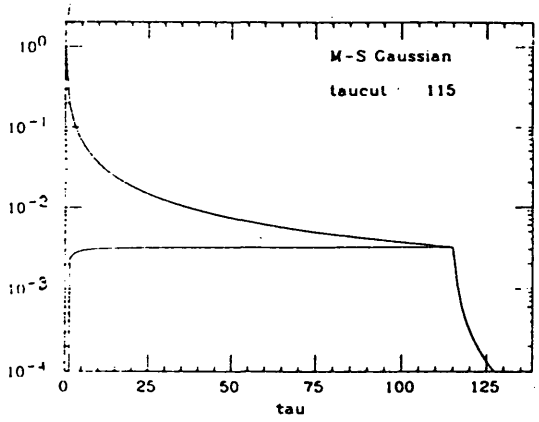

Figure 2. *Evolution of the protostar population. The upper curve shows the fraction of protostars, measured relative to N_{tot}, the total number of stars produced up to t_c. The bottom curve shows the total number of protostars in the cloud, also relative to N_{tot}. The abcissa represents the time measured relative to $t_c/\bar{M}$.*

Finally, we show a time sequence of the full luminosity function, including protostars, pre-Main-Sequence stars, and Main-Sequence stars. The precipitous dropoff at high luminosities for early times ($t \lesssim 10^5\ yr$) reflects the fact that sufficiently massive stars have not yet had time to form. During this phase, the peak due to the protostars is dominant, but the bulk of low-luminosity pre-Main-Sequence stars soon overwhelms it. By $t = 10^6\ yr$, the protostar peak is still visible, though greatly diminished. The sharp "step" near $log_{10}(L/L_\odot) = 1$ is not a numerical artifact, but is a result of the abrupt change in the mass-luminosity relation for newly visible pre-Main-Sequence stars near $M = 2\,M_\odot$ (Stahler 1989). Note also the plateau at lower luminosities. By $t = 10^7\ yr$, the luminosity function is beginning to resemble the smooth power-law behavior of the ILF. The protostar fraction is now less than 0.01. No abrupt change is seen for $t > t_c$, but rather a continual settling toward the ILF. For much longer times ($t \sim 10^8\ yr$), the high-luminosity end starts to be depleted, as massive stars evolve off the Main Sequence.

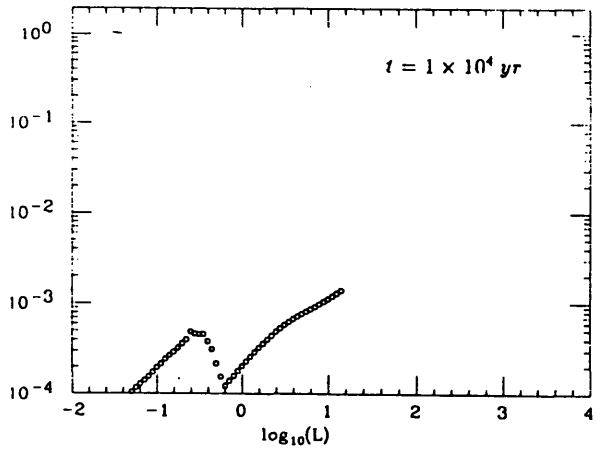

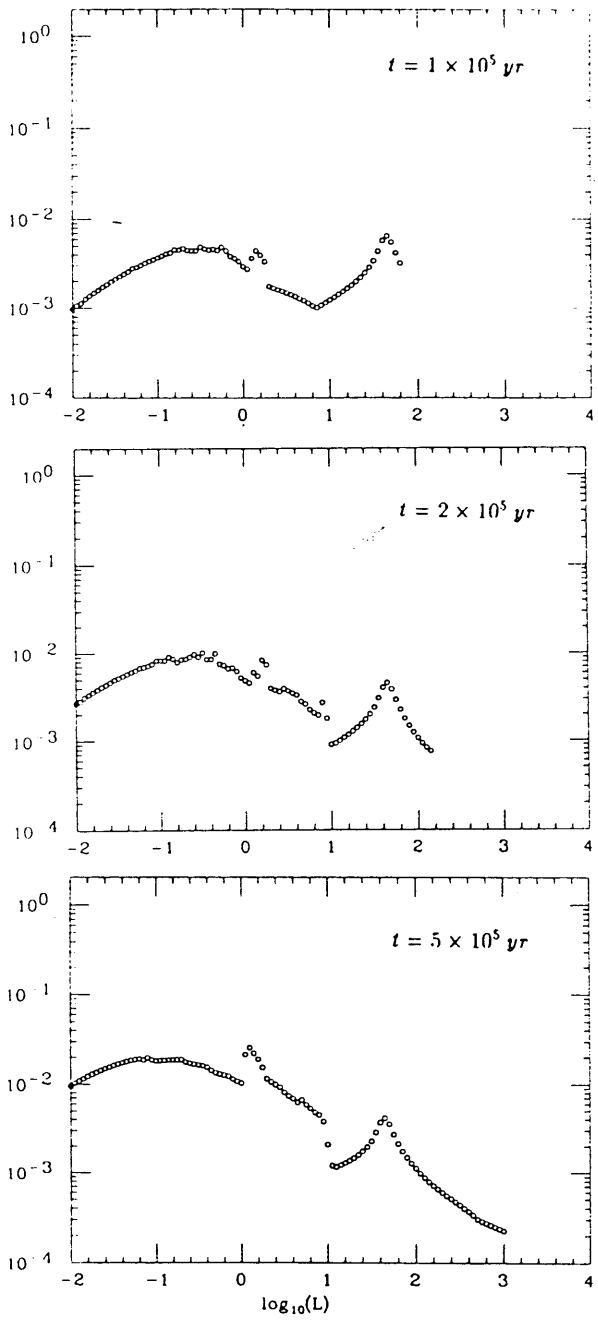
$t = 1 \times 10^5$ yr
$t = 2 \times 10^5$ yr
$t = 5 \times 10^5$ yr
$\log_{10}(L)$

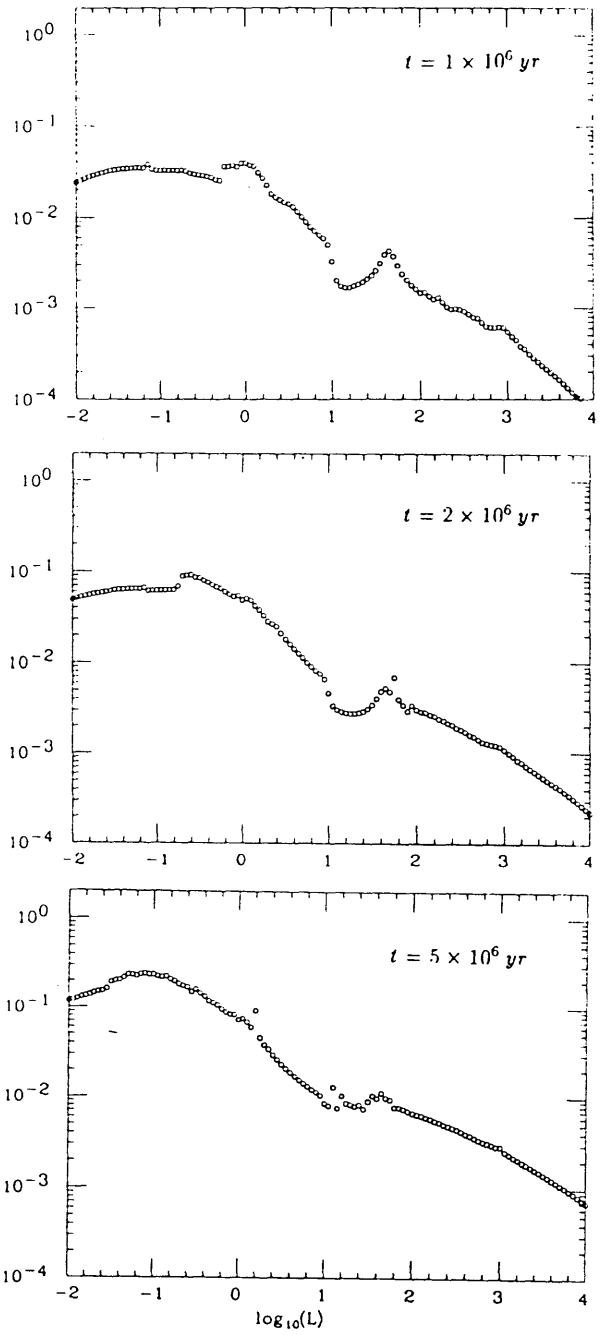
$t = 1 \times 10^6\ yr$
$t = 2 \times 10^6\ yr$
$t = 5 \times 10^6\ yr$
10^0
10^{-1}
10^{-2}
10^{-3}
10^{-4}
-2
-1
0
1
2
3
4
$\log_{10}(L)$

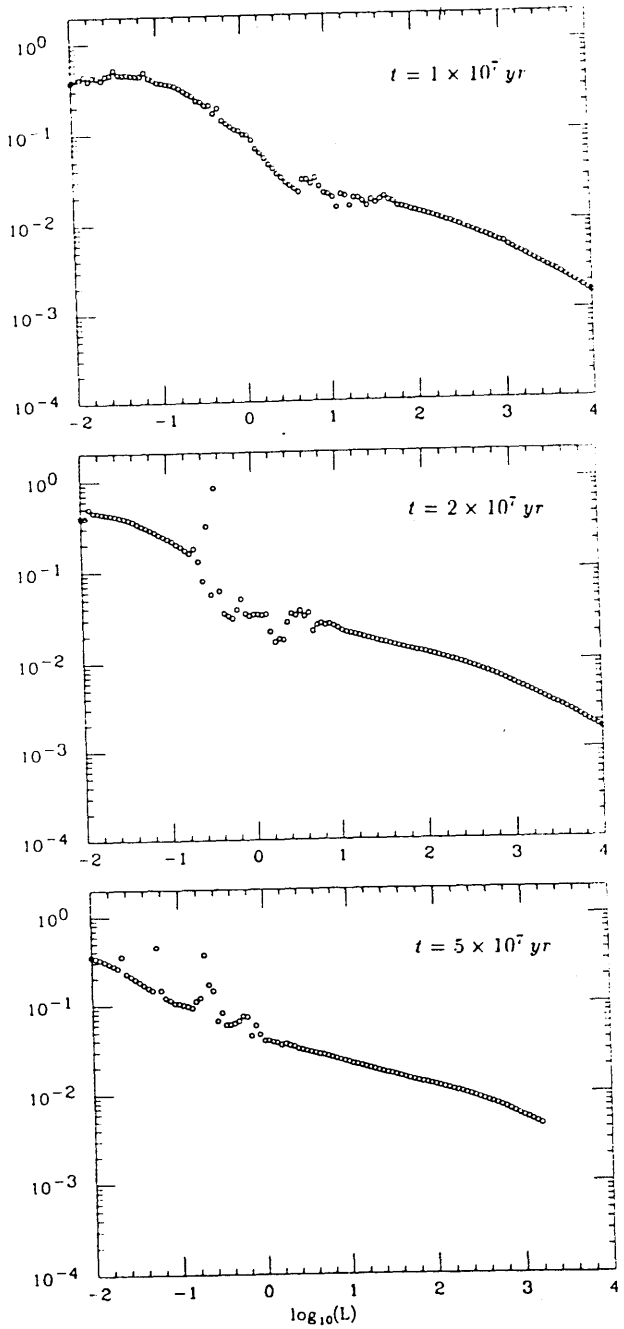
$t = 1 \times 10^7$ yr
$t = 2 \times 10^7$ yr
$t = 5 \times 10^7$ yr
10^0
10^{-1}
10^{-2}
10^{-3}
10^{-4}
-2
-1
0
1
2
3
4
$\log_{10}(L)$

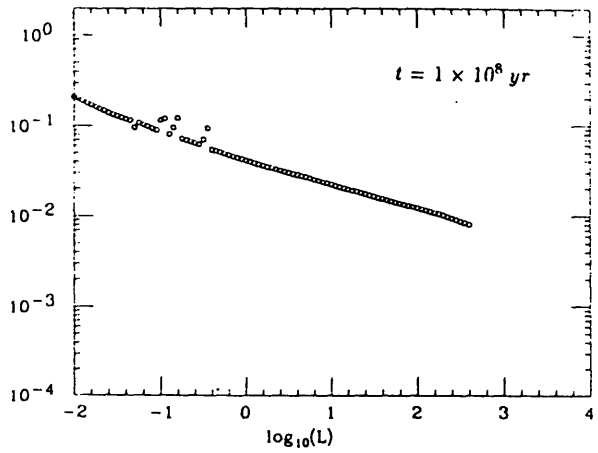

References

Fletcher, A. B. and Stahler, S. W. 1992, ApJ, in preparation.
Iben, I. 1965, ApJ, **141**, 993.
Lada, C. J. 1985, ARAA, **23**, 267.
Miller, G. E. and Scalo, J. M. 1979, ApJS, **41**, 513.
Nelson, L. A. 1990, private communication.
Palla, F. and Stahler, S. W. 1990, ApJ, **360**, L47.
Palla, F. and Stahler, S. W. 1991, ApJ, **375**, 288.
Palla, F. and Stahler, S. W. 1992, ApJ, in press.
Salpeter, E. E. 1955, ApJ, **121**, 161.
Stahler, S. W. 1983, ApJ, **274**, 822.
Stahler, S. W. 1985 ApJ, **293**, 207.
Stahler, S. W. 1988, ApJ, **332**, 804.
Stahler, S. W. 1989, ApJ, **347**, 950.
Stahler, S. W., Shu, F. H., and Taam, R. E. 1980, ApJ, **302**, 590.
Straw, S. M., Hyland, A. R., and McGregor, P. J. 1989, ApJS, **69**, 99.
Vandenberg, D. A. 1990, private communication.
Wilking, B. A., Lada, C. J., and Young, E. T. 1989, ApJ, **340**, 823.

The Luminosity Functions of Young Stellar Clusters

A.B. Fletcher (MIT), S.W. Stahler (UC Berkeley)

We describe a new theoretical framework for computing the evolution of both the mass function (MF) and luminosity function (LF) of a young stellar cluster that is forming within a molecular cloud core. Our method utilizes detailed results from stellar evolution theory, and assumes that young clusters arise from the continual collapse of dense cloud cores over an extended period of time. By further demanding that the stars reaching the main sequence conform to a prescribed Initial Mass Function (IMF), we are able to explicitly solve for the separate contributions, to the cluster MF & LF, from each of the evolving populations of protostars, pre-main-sequence (PMS) stars and main sequence (MS) stars. Among the many detailed results generally predicted by our calculations, we find that the protostellar LF is peaked at a characteristic luminosity throughout the time of cluster formation, and that the time-averaged number fraction in protostars is typically just a few percent. At most times, the vast majority of cluster members are PMS stars, but the cluster light is dominated in the first Myr by the intrinsically brighter protostars. After about $10\,Myr$, the higher mass MS stars provide most of the light. In the intervening period, a pronounced step in the cluster LF is seen at about $10\,L_{\odot}$. A preliminary application of our models to the ρ Ophiuchus embedded cluster indicates that it is reaching the end of its early evolution; we estimate its age to be about $1\,Myr$, to within a factor of two. This research was supported by NSF Grants AST-90-14479 & AST-90-22501.

Abstract submitted for AAS [AAS] meeting

Date submitted: February 1, 1998 Electronic form version 1.6

The Luminosity Functions of Young Stellar Clusters

A.B. Fletcher (MIT), S.W. Stahler (UC Berkeley)

We describe a new theoretical framework for computing the evolution of both the mass function (MF) and luminosity function (LF) of a young stellar cluster that is forming within a molecular cloud core. Our method utilizes detailed results from stellar evolution theory, and assumes that young clusters arise from the continual collapse of dense cloud cores over an extended period of time. By further demanding that the stars reaching the main sequence conform to a prescribed Initial Mass Function (IMF), we are able to explicitly solve for the separate contributions, to the cluster MF & LF, from each of the evolving populations of protostars, pre-main-sequence (PMS) stars and main sequence (MS) stars. Among the many detailed results generally predicted by our calculations, we find that the protostellar LF is peaked at a characteristic luminosity throughout the time of cluster formation, and that the time-averaged number fraction in protostars is typically just a few percent. At most times, the vast majority of cluster members are PMS stars, but the cluster light is dominated in the first Myr by the intrinsically brighter protostars. After about $10\,Myr$, the higher mass MS stars provide most of the light. In the intervening period, a pronounced step in the cluster LF is seen at about $10\,L_{\odot}$. A preliminary application of our models to the ρ Ophiuchus embedded cluster indicates that it is reaching the end of its early evolution; we estimate its age to be about $1\,Myr$, to within a factor of two. This research was supported by NSF Grants AST-90-14479 & AST-90-22501.

Abstract submitted for AAS [AAS] meeting

Date submitted: February 1, 1998 Electronic form version 1.6

The Luminosity Functions of Young Stellar Clusters

A.B. Fletcher (MIT), S.W. Stahler (UC Berkeley)

We describe a new theoretical framework for computing the evolution of both the mass function (MF) and luminosity function (LF) of a young stellar cluster that is forming within a molecular cloud core. Our method utilizes detailed results from stellar evolution theory, and assumes that young clusters arise from the continual collapse of dense cloud cores over an extended period of time. By further demanding that the stars reaching the main sequence conform to a prescribed Initial Mass Function (IMF), we are able to explicitly solve for the separate contributions, to the cluster MF & LF, from each of the evolving populations of protostars, pre-main-sequence (PMS) stars and main sequence (MS) stars. Among the many detailed results generally predicted by our calculations, we find that the protostellar LF is peaked at a characteristic luminosity throughout the time of cluster formation, and that the time-averaged number fraction in protostars is typically just a few percent. At most times, the vast majority of cluster members are PMS stars, but the cluster light is dominated in the first Myr by the intrinsically brighter protostars. After about $10\,Myr$, the higher mass MS stars provide most of the light. In the intervening period, a pronounced step in the cluster LF is seen at about $10\,L_{\odot}$. A preliminary application of our models to the ρ Ophiuchus embedded cluster indicates that it is reaching the end of its early evolution; we estimate its age to be about $1\,Myr$, to within a factor of two. This research was supported by NSF Grants AST-90-14479 & AST-90-22501.

Abstract submitted for AAS [AAS] meeting

Date submitted: February 1, 1998 Electronic form version 1.6

Bibliography

[1] Fred C. Adams and Gregory Laughlin. A Dying Universe: the Long-Term Fate and Evolution of Astrophysical Objects. *Rev. Mod. Phys.*, 69(2):337–372, 1997.

[2] R. R. J. Antonucci and J. S. Miller. Spectropolarimetry and the Nature of NGC 1068. *ApJ*, 297:621–632, October 1985.

[3] Robert Antonucci. Unified Models for Active Galactic Nuclei and Quasars. *ARA&A*, 31:473–521, 1993.

[4] W. Baade and R. Minkowski. Identification of Radio Sources in Cassiopeia, Cygnus A and Puppis a. *ApJ*, 119:206–214, 1954.

[5] J. W. M. Baars, R. Genzel, I. I. K. Pauliny-Toth, and A. Witzel. The Absolute Spectrum of Cas A - An Accurate Flux Density Scale and a Set of Secondary Calibrators. *A&A*, 61:99–106, October 1977.

[6] John N. Bahcall, Sofia Kirhakos, David H. Saxe, and Donald P. Schneider. Hubble space telescope images of a sample of 20 nearby luminous quasars. *ApJ*, 479:642+, April 1997.

[7] Joshua E. Barnes and Lars Hernquist. Dynamics of Interacting Galaxies. *ARA&A*, 30:705–742, 1992.

[8] Robert H. Becker, Michael D. Gregg, Isobel M. Hook, Richard G. McMahon, Richard L. White, and David J. Helfand. The First Radio-loud Broad Absorption Line QSO and Evidence for a Hidden Population of Quasars. *ApJ*, 479:L93–+, April 1997.

[9] Mitchell C. Begelman, Roger D. Blandford, and Martin J. Rees. Theory of Extragalactic Radio Sources. *Rev. Mod. Phys.*, 56(2(1)):255–351, April 1984.

[10] C. L. Bennett, C. R. Lawrence, and B. F. Burke. 5 GHz Source Variability and the Gain of the NRAO 300-foot Telescope. *ApJS*, 54:211–227, February 1984.

[11] C. L. Bennett, C. R. Lawrence, and B. F. Burke. Source Counts at 5 Gigahertz from the MG Survey. *ApJ*, 299:373–374, December 1985.

[12] C. L. Bennett, C. R. Lawrence, B. F. Burke, J. N. Hewitt, and J. Mahoney. The MIT-Green Bank (MG) 5 GHz Survey. *ApJS*, 61:1–7, May 1986.

[13] C. L. Bennett, C. R. Lawrence, J. A. Garcia-Barreto, J. N. Hewitt, and B. F. Burke. VLA Source Counts at 6-cm Wavelength. *Nature*, 301:686–688, February 1983.

[14] Charles Bennett. *The MIT-Green Bank 5 GHz Radio Survey.* PhD thesis, Massachusetts Institute of Technology, July 1984.

[15] B. Bertotti, R. Balbinot, S. Bergia, and A. Messina, editors. *Modern Cosmology in Retrospect.* Cambridge University Press, Cambridge, CB2 1RP, UK, 1990.

[16] R. D. Blandford and R. Narayan. Cosmological Applications of Gravitational Lensing. *ARA&A*, 30:311–358, 1992.

[17] R. D. Blandford, H. Netzer, and L. Woltjer. *Active Galactic Nuclei.* Springer-Verlag, Berlin, Heidelberg: Germany, 1990. 20th Advanced Course of the Swiss Society for Astrophysics and Astronomy (Saas-Fee), held at Les Diablerets, Switzerland, 1–6 April 1990.

[18] R. D. Blandford and K. S. Thorne. *Black Hole Astrophysics*, chapter 8, pages 454–503. In Hawking and Israel [66], 1979.

[19] R. D. Blandford and R. L. Znajek. Electromagnetic Extraction of Energy from Kerr Black Holes. *MNRAS*, 179:433–456, May 1977.

[20] J. G. Bolton, A. Savage, and A. E. Wright. The Parkes 2700-MHz Survey - Part Fourteen - Catalogue and New Optical Identifications. *Australian Journal of Physics Supplement*, 46:1+, 1979.

[21] J. G. Bolton, G. J. Stanley, and O. B. Slee. Positions of Three Discrete Sources of Galactic Radio Frequency Noise. *Nature*, 164:101–102, 1949.

[22] Richard L. Bowers and Terry Deeming. *Astrophysics I: Stars.* Jones and Bartlett Publishers, Inc., 1 Exeter Plaza, Boston, MA 02116, USA, 1984.

[23] Richard L. Bowers and Terry Deeming. *Astrophysics II: Interstellar Matter and Galaxies.* Jones and Bartlett Publishers, Inc., 1 Exeter Plaza, Boston, MA 02116, USA, 1984.

[24] Ronald N. Bracewell. *The Fourier Transform and Its Applications.* McGraw-Hill Publishing Company, USA, revised 2nd edition, 1986. 1st Edition 1965.

[25] Alan H. Bridle and Richard A. Perley. Extragalactic Radio Jets. *ARA&A*, 22:319–358, 1984.

[26] B. F. Burke, J. Lehár, and S. R. Conner. Einstein Rings and Related Phenomena. In Kayser et al. [83], pages 237–244. Proc. of Conference held in Hamburg, Germany, 9-13 September 1991.

[27] Bernard F. Burke. The MIT Search Program for Gravitational Lenses. In Mellier et al. [104], pages 127–135. Proceedings of a Workshop held in Toulouse, France, Sept. 13-15, 1989.

[28] Bernard F. Burke and Francis Graham-Smith. *An Introduction to Radio Astronomy.* Cambridge University Press, Cambridge, CB2 1RP, UK, 1997.

[29] Arati Chokshi and Edwin L. Turner. Remnants of the Quasars. *MNRAS*, 259:421–424, December 1992.

[30] Donald D. Clayton. *Principles of Stellar Evolution and Nucleosynthesis.* Chicago University Press, Chicago, IL 60637, USA, 1983 reprint edition, slightly modified from 1968 original edition, 1983.

[31] J. J. Condon. Cosmological Evolution of Radio Sources. *ApJ*, 287:461–474, December 1984.

[32] J. J. Condon. Cosmological Evolution of Radio Sources found at 1.4 GHz. *ApJ*, 284:44–53, September 1984.

[33] J. J. Condon. The 1.4 Gigahertz Luminosity Function and its Evolution. *ApJ*, 338:13–23, March 1989.

[34] J. J. Condon and J. J. Broderick. A 1400 MHz Sky Survey. I - Confusion-limited Maps covering 7h 30 m less than alpha less than 19h 30m, -5 deg less than delta less than 82 deg. *AJ*, 90:2540–2549, December 1985.

[35] J. J. Condon, J. J. Broderick, and G. A. Seielstad. A 4.85 ghz sky survey. ii - maps covering delta = -40 to +5 deg, alpha = 0-20 h. *AJ*, 102:2041–2046, December 1991.

[36] J. J. Condon, Mark R. Griffith, and Alan E. Wright. The Parkes-MIT-NRAO Surveys. IV - Maps for the Southern Survey covering delta in the range -88 to -37 deg. *AJ*, 106:1095–1100, September 1993.

[37] S. R. Conner, A. R. Cooray, A. B. Fletcher, B. F. Burke, J. Lehár, P. M. Garnavich, T. W. B. Muxlow, P. Thomasson, and J. P. Blakeslee. Ringlike Structure in the Radio Lobe of MG 0248+0641. *AJ*, 115:37–48, January 1998.

[38] Samuel Richard Conner. *The MIT-Green-Bank-VLA λ6cm Gravitational Lens Search.* PhD thesis, Massachusetts Institute of Technology, 1998. in progress.

[39] Asantha Roshan Cooray. Optical Identification of Close Doubles and Gravitational Lenses from the MIT-Green Bank-VLA and the Parkes-MIT-NRAO-VLA 8.43 GHz Surveys. BS thesis, Massachusetts Institute of Technology, May 1997.

[40] Paul Davies. *The New Physics.* Cambridge University Press, Cambridge, CB2 1RP, UK, 1989.

[41] Paul C. W. Davies. *The Accidental Universe.* Cambridge University Press, Cambridge, CB2 1RP, UK, 1986 reprinted edition, 1982.

[42] James N. Douglas, Frank Bash, and Geoffrey W. Torrence. Texas Survey: Preliminary +18 deg. Strip. Technical report, University of Texas Radio Astronomy Department, 1980. University of Texas, Austin, Radio Astronomy Observatory, Department of Astronomy, 1980, Publications in Astronomy No. 17.

[43] A. Dressler. Galaxy Morphology in Rich Clusters - Implications for the Formation and Evolution of Galaxies. *ApJ*, 236:351–365, March 1980.

[44] J. S. Dunlop. Cosmological Evolution of Radio Sources. In Jackson and Davis [78], pages 167–176. Proc. of meeting held at Jodrell Bank, University of Manchester, 22-26 Jan 1996.

[45] J. S. Dunlop and J. A. Peacock. The Redshift Cut-Off in the Luminosity Function of Radio Galaxies and Quasars. *MNRAS*, 247:19+, November 1990.

[46] R. Ekers, C. Fanti, and R. Padrielli, editors. *Extragalactic Radio Sources.* Kluwer Academic Publishers, Dordrecht, Holland, 1996. Proc. 175th IAU Meeting at Bologna, Italy, 10–14 October 1995.

[47] E. E. Falco, C. S. Kochanek, and J. Mu noz. Limits on Cosmological Models from Radio-Selected Gravitational Lenses. Preprint astro-ph/9707032, 2 July 1997.

[48] B. L. Fanaroff and J. M. Riley. The Morphology of Extragalactic Radio Sources of High and Low Luminosity. *MNRAS*, 167:31P–36P, May 1974.

[49] R. Fanti, C. Fanti, R. T. Schilizzi, R. E. Spencer, Nan Rendong, P. Parma, W. J. M. Van Breugel, and T. Venturi. On the Nature of Compact Steep Spectrum Radio Sources. *A&A*, 231:333–346, May 1990.

[50] A. B. Fletcher, B. Burke, S. Conner, J. Lehár, and L. Herold. The Angular Size Distribution of 4741 Radio Sources from the MIT-VLA Snapshot Archive. January 1997. In conference 'Observational Cosmology with the New Radio Surveys', eds. M.N. Bremer, N. Jackson, & I. Pérez-Fournon, Instituto de Astrofisica de Canarias, Puerto de la Cruz, Tenerife, Canary Islands, Spain, 11–13 January 1997, in press.

[51] Andre B. Fletcher and Steven W. Stahler. The luminosity functions of embedded stellar clusters. 1: Method of solution and analytic results. *ApJ*, 435:313–328, November 1994.

[52] Andre B. Fletcher and Steven W. Stahler. The luminosity functions of embedded stellar clusters. 2: Numerical results. *ApJ*, 435:329–338, November 1994.

[53] Dorothy E. Goddard and Raymond F. Haynes, editors. *Pioneering a New Astronomy: Papers in Memory of John G. Bolton*, volume 47(5). Australian Journal Physics, CSIRO, Australia, 1994. Papers presented at the John G. Bolton Memorial Symposium, Parkes Observatory, NSW, Australia, 9–10 December 1993.

[54] H. Bondi & T. Gold. The Steady State Theory of the Expanding Universe. *MNRAS*, 108:252–270, 1948.

[55] T. Gold. The Origin of Cosmic Radio Noise. In *The Dynamics of Ionized Media*, pages 101–102, 1951.

[56] P. C. Gregory and J. J. Condon. The 87GB Catalog of Radio Sources covering delta between 0 and + 75 deg at 4.85 GHz. *ApJS*, 75:1011–1291, April 1991.

[57] P. C. Gregory, J. D. Vavasour, W. K. Scott, and J. J. Condon. The Parkes-MIT-NRAO (PMN) Map Catalog of Radio Sources covering -88 deg less than delta less than -37 deg at 4.85 GHz. *ApJS*, 90:173–177, January 1994.

[58] M. Griffith, A. E. Wright, A. J. Hunt, E. Troup, R. D. Ekers, P. Buckett, D. J. Cooke, G. Freeman, J. Glowacki, D. Jennings, U. Knop, B. Lam, I. McGovern, D. McConnell, R. P. Norris, R. Otrupcek, R. Twardy, T. Williams, G. Behrens, C. Chestnut, B. F. Burke, A. Fletcher, K. S. Russell, A. Savage, J. Lim, A. E. Vaughan, S. Côté, M. Anderson, A. Hons, G. L. White, S. Amy, A. Burgess, S. Chan, L. Cram, A. Gray, W. Walsh, D. Campbell-Wilson, V. McIntyre, P. Randall, M. Suters, and W.J. Zealey. The Parkes-MIT-NRAO Southern Sky Survey at 4850 MHz. *Proc. Astron. Soc. Australia*, 9:243–245, 1991.

[59] Mark Griffith, Mike Heflin, Sam Conner, Bernard Burke, and Glen Langston. The Fourth MIT-Green Bank 5 GHz Survey. *ApJS*, 75:801–833, March 1991.

[60] Mark Griffith, Glen Langston, Mike Heflin, Sam Conner, Joseph Lehár, and Bernard Burke. The Third Mit-Green Bank 5 GHz Survey. *ApJS*, 74:129–180, September 1990.

[61] Mark R. Griffith and Alan E. Wright. The Parkes-MIT-NRAO (PMN) Surveys. I - The 4850 MHz Surveys and Data Reduction. *AJ*, 105:1666–1679, May 1993.

[62] Mark Robert Griffith. *The Parkes-MIT-NRAO (PMN) Survey of the Southern Sky.* PhD thesis, Massachusetts Institute of Technology, April 1993.

[63] A. Guth. Inflationary Universe: A Possible Solution to the Horizon and Flatness Problems. *Phys. Rev.*, D23:347, 1981.

[64] Lee W. Hartmann and Robert W. Noyes. Rotation and Magnetic Activity in Main-Sequence Stars. *ARA&A*, 25:271–301, 1987.

[65] S. W. Hawking. Particle Creation by Black Holes. *Comm. Math. Phys.*, 43:199, 1975.

[66] S. W. Hawking and W. Israel, editors. *General Relativity: An Einstein Centenary Srvey.* Cambridge University Press, Cambridge, CB2 1RP, UK, 1979.

[67] S. W. Hawking and R. Penrose. The Singularities of Gravitational Collapse and Cosmology. *Proc. Roy. Soc. Lond. A*, 314:529, 1970.

[68] K.-H. Hellwege, editor. *Landolt-Börnstein: Numerical Data and Functional Relationships in Science and Technology*, volume VI.2c. Springer-Verlag, Germany, 1982. Astronomy & Astrophysics: Interstellar Matter, Galaxy, Universe.

[69] Lori Herold-Jacobson. *Identification of Radio Sources from the MG-VLA Survey.* PhD thesis, Massachusetts Institute of Technology, May 1996.

[70] J. N. Hewitt, E. L. Turner, C. R. Lawrence, D. P. Schneider, and J. P. Brody. A Gravitational Lens Candidate with an Unusually Red Optical Counterpart. *AJ*, 104:968–979, September 1992.

[71] J. N. Hewitt, E. L. Turner, D. P. Schneider, B. F. Burke, and G. I. Langston. Unusual Radio Source MG 1131+0456 - A Possible Einstein Ring. *Nature*, 333:537–540, June 1988.

[72] Jacqueline Nina Hewitt. *A Search for Gravitational Lensing.* PhD thesis, Massachusetts Institute of Technology, August 1986.

[73] J. S. Hey, S. J. Parsons, and J. W. Phillips. Fluctuations in Cosmic Radiation at Radio Frequencies. *Nature*, 158:234, 1946.

[74] J. A. Hogbom. Aperture Synthesis with a Non-regular Distribution of Interferometer Baselines. *A&AS*, 15:417–426, 1974.

[75] Isobel Mary Hook. *Quasars at High Redshift.* PhD thesis, University of Cambridge, December 1994.

[76] F. Hoyle. A New Model for the Expanding Universe. *MNRAS*, 108:372–382, 1948.

[77] Philip A. Hughes. *Beams and Jets in Astrophysics*, volume 19 of *Cambridge Astrophysics Series.* Cambridge University Press, Cambridge, CB2 1RP, UK, 1991.

[78] N. Jackson and R. J. Davis, editors. *High-Sensitivity Radio Astronomy.* Cambridge University Press, Cambridge, CB2 1RP, UK, 1997. Proc. of meeting held at Jodrell Bank, University of Manchester, 22-26 Jan 1996.

[79] Walter Jaffe, Holland C. Ford, Laura Ferrarese, Frank Van Den Bosch, and Robert W. O'Connell. A Large Nuclear Accretion Disk in the Active Galaxy NGC 4261. *Nature*, 364:213–215, July 1993.

[80] R. C. Jennison and M. K. Das Gupta. Fine Structure of the Extraterrestrial Radio Source Cygnus 1. *Nature*, 172:996–997, 1953.

[81] D. M. Katz-Stone and L. Rudnick. An Analysis of the Synchrotron Spectrum in the Fanaroff-Riley Type I Galaxy 3C 449. *ApJ*, 488:146+, October 1997.

[82] D. M. Katz-Stone and L. Rudnick. A Spectral Analysis of Two Compact Steep-Spectrum Sources. *ApJ*, 479:258+, April 1997.

[83] R. Kayser, T. Schramm, and L. Nieser, editors. *Gravitational Lenses*, number 406 in Lecture Notes in Physics. Springer-Verlag, Germany, 1992. Conference in Hamburg, Germany, 9–13 September 1991.

[84] C. R. Keeton and C. S. Kochanek. Summary of Data on Secure Multiply Imaged Systems. pages 419–439. Kluwer Academic Publishers, Dordrecht, Holland, 1996. Proc. 173rd IAU Meeting at University of Melbourne, Australia, 9–14 July 1995.

[85] K. I. Kellermann and I. I. K. Pauliny-Toth. Compact Radio Sources. *ARA&A*, 19:373–410, 1981.

[86] John Kormendy and Douglas Richstone. Inward Bound – The Search for Supermassive Black Holes in Active Galactic Nuclei. *ARA&A*, 33:581–624, 1995.

[87] John D. Kraus. *Radio Astronomy.* Cygnus-Quasar Books, PO Box 85, Powell, Ohio 43065, USA, Cygnus-Quasar 2nd edition, 1986.

[88] H. Kühr, A. Witzel, I. I. K. Pauliny-Toth, and U. Nauber. A Catalogue of Extragalactic Radio sources having Flux Densities greater than 1 Jy at 5 GHz. *A&AS*, 45:367–430, September 1981.

[89] G. I. Langston, S. R. Conner, J. Lehár, J. N. Hewitt, B. F. Burke, and K. W. Weiler. Einstein ring mg 1654+1346. *BAAS*, 21:12.17+, 1989.

[90] Glen I. Langston. *Properties of Extragalactic Radio Sources detected in the MG 5 GHz Survey.* PhD thesis, Massachusetts Institute of Technology, September 1987.

[91] Glen I. Langston, Michael B. Heflin, Sam R. Conner, Joseph Lehár, Chris L. Carrilli, and Bernard F. Burke. The Second MIT-Green Bank 5 GHz Survey. *ApJS*, 72:621–631, March 1990.

[92] M. I. Large, B. Y. Mills, A. G. Little, D. F. Crawford, and J. M. Sutton. The Molonglo Reference Catalogue of Radio Sources. *MNRAS*, 194:693, January 1981.

[93] Tod R. Lauer and Marc Postman. The Motion of the Local Group with respect to the 15,000 kilometer per second Abell Cluster Inertial Frame. *ApJ*, 425:418–438, April 1994.

[94] C. R. Lawrence, C. L. Bennett, J. N. Hewitt, and B. F. Burke. 5 Gigahertz Structure and Optical Identifications of Weak Extragalactic Radio Sources. *ApJ*, 278:L95–L98, March 1984.

[95] C. R. Lawrence, C. L. Bennett, J. N. Hewitt, G. I. Langston, S. E. Klotz, B. F. Burke, and K. C. Turner. 5 GHz Radio Structure and Optical Identifications of Sources from the MG Survey. II - Maps and Finding Charts. *ApJS*, 61:105–157, May 1986.

[96] C. R. Lawrence, D. P. Schneider, M. Schmidt, C. L. Bennett, J. N. Hewitt, B. F. Burke, E. L. Turner, and J. E. Gunn. Discovery of a new gravitational lens system. *Science*, 223:46–49, 1984.

[97] Charles Ryan Lawrence. *Weak Extragalactic Radio Sources.* PhD thesis, Massachusetts Institute of Technology, July 1983.

[98] J. Lehár, B. F. Burke, S. R. Conner, E. E. Falco, A. B. Fletcher, M. Irwin, R. G. McMahon, T. W. B. Muxlow, and P. L. Schechter. The Gravitationally Lensed Radio Source MG 0751+2716. *AJ*, 114:48–53, July 1997.

[99] J. Lehar, A. J. Cooke, C. R. Lawrence, A. D. Silber, and G. I. Langston. The Lensing Galaxy in MG 1549+3047. *AJ*, 111:1812+, May 1996.

[100] J. Lehár, G. I. Langston, A. Silber, C. R. Lawrence, and B. F. Burke. A Gravitationally-Lensed Ring in MG 1549 + 3047. *AJ*, 105:847–852, March 1993.

[101] Joseph Lehár. *The Time Delay in the Double Quasar 0957+561 and a Search for Gravitational Lenses.* PhD thesis, Massachusetts Institute of Technology, August 1991.

[102] Malcolm S. Longair. *Our Evolving Universe.* Cambridge University Press, Cambridge, CB2 1RP, UK, 1996.

[103] Patrick J. McCarthy. High Redshift Radio Galaxies. *ARA&A*, 31:639–688, 1993.

[104] Y. Mellier, B. Fort, and G. Soucail, editors. *Gravitational Lensing*, number 360 in Lecture Notes in Physics. Springer-Verlag, Germany, 1990. Conference in Toulouse, France, 13–15 September 1989.

[105] George Miley. The Structure of Extended Extragalactic Radio Sources. *ARA&A*, 18:165–218, 1980.

[106] G. E. Miller and J. M. Scalo. The Initial Mass Function and the Stellar Birthrate in the Solar Neighborhood. *ApJS*, 41:513–547, November 1979.

[107] José A. Muñoz, Emilio E. Falco, Christopher S. Kochanek, Joseph Lehár, Lori K. Herold, André B. Fletcher, and Bernard F. Burke. MGC 2214+3550: A New Binary Quasar. *ApJ*, 492:L9–L12, January 1998.

[108] Hugh S. Murdoch, David F. Crawford, and David L. Jauncey. Maximum-likelihood Estimation of the Number-Flux-Density Distribution of Radio Sources in the Presence of Noise and Confusion. *ApJ*, 183:1–14, July 1973.

[109] Jayant V. Narlikar. *Introduction to Cosmology.* Cambridge University Press, Cambridge, CB2 1RP, UK, 1993.

[110] National Radio Astronomy Observatory. Aips cookbook. Technical report, National Radio Astronomy Observatory, Edgemont Road, Charlottesville, VA 22903-2475, USA, October 1990. AIPS stands for: Astronomical Image Processing System.

[111] National Radio Astronomy Observatory. The very large array calibrator manual. Technical report, National Radio Astronomy Observatory, Edgemont Road, Charlottesville, VA 22903-2475, USA, 1990. Up to date version aailable from Internet address http://www.nrao.edu.

[112] J. P. Ostriker. *Development of Large-Scale Structure in the Universe.* Cambridge University Press, Cambridge, CB2 1RP, UK, 1991. Notes prepared from the Lezioni Fermiane, Accademia Nazionale Dei Lincei, Pisa, Nov 1988.

[113] T. Padmanabhan. *Structure Formation in the Universe.* Cambridge University Press, Cambridge, CB2 1RP, UK, 1993.

[114] Francesco Palla and Steven W. Stahler. The Birthline for Intermediate-Mass Stars. *ApJ*, 360:L47–L50, September 1990.

[115] Richard A. Perley, Frederic R. Schwab, and Alan H. Bridle, editors. *Synthesis Imaging in Radio Astronomy: A Collection of Lectures from the Third NRAO Synthesis Imaging School*, volume 6 of *Astronomical Society of the Pacific Conference Series.* Astronomical Society of the Pacific, 390 Ashton Ave., San Francisco, CA 94112, USA, 1989. Proc. of a Summer School, NRAO Workshop No. 21, held at Socorro, New Mexico, USA, June 1988.

[116] Martin J. Rees. Black Hole Models for Active Galactic Nuclei. *ARA&A*, 22:471–506, 1984.

[117] Martin J. Rees. *Perspectives in Astrophysical Cosmology.* Cambridge University Press, Cambridge, CB2 1RP, UK, 1995. From the Lezioni Lincei lectures, given under the auspices of the Accademia Nazionale dei Lincei, Milan, Italy.

[118] Michael Rowan-Robinson. *Cosmology.* Oxford University Press, Walton St., Oxford, OX2 6DP, UK, 3rd edition, 1996.

[119] M. Ryle. The Counts of Radio Sources. *ARA&A*, 6:249–266, 1968.

[120] E. E. Salpeter. The Luminosity Function and Stellar Evolution. *ApJ*, 121:161–167, 1955.

[121] E. E. Salpeter. *ApJ*, 140:796, 1964.

[122] M. Schmidt. 3C 273: A Star-like Object with Large Red-Shift. *Nature*, 197:1040, 1963.

[123] P. Schneider, J. Ehlers, and E. E. Falco. *Gravitational Lenses.* Springer-Verlag New York Inc., New York NY, USA, 1992.

[124] Stuart L. Shapiro and Saul A. Teukolsky. *Black Holes, White Dwarfs and Neutron Stars: The Physics of Compact Objects.* A Wiley-Intersciece Publication. John Wiley & Sons, Inc., USA, 1983.

[125] P. A. Shaver, J. V. Wall, K. I. Kellermann, C. A. Jackson, and M. R. S. Hawkins. Decrease in the Space Density of Quasars at High Redshift. *Nature*, 384:439–441, 1996.

[126] Frank H. Shu, Fred C. Adams, and Susana Lizano. Star Formation in Molecular Clouds: Observations and Theory. *ARA&A*, 25:23–81, 1987.

[127] Joseph Silk. *Cosmic Enigmas.* American Institute of Physics, Woodbury NY, USA, 1994.

[128] Joseph Silk. *A Short History of the Universe.* Number 53 in Scientific American Library. Scientific American Library, HPHLP, W. H. Freeman and Company, 41 Madison Ave., New York, NY 10010, USA, 1994.

[129] Todd A. Small and Roger D. Blandford. Quasar evolution and the growth of black holes. *MNRAS*, 259:725–737, December 1992.

[130] S. W. Stahler. *Protostars: Their Structure and Evolution.* PhD thesis, University of Califronia at Berkeley., 1980.

[131] S. W. Stahler. The birthline for low-mass stars. *ApJ*, 274:822–829, November 1983.

[132] S. W. Stahler. The star-formation history of very young clusters. *ApJ*, 293:207–215, June 1985.

[133] S. W. Stahler, F. H. Shu, and R. E. Taam. The Evolution of Protostars. I - Global Formulation and Results. *ApJ*, 241:637–654, October 1980.

[134] S. W. Stahler, F. H. Shu, and R. E. Taam. The Evolution of Protostars. II - The Hydrostatic Core. *ApJ*, 242:226–241, November 1980.

[135] S. W. Stahler, F. H. Shu, and R. E. Taam. The Evolution of Protostars. III - The Accretion Envelope. *ApJ*, 248:727–737, September 1981.

[136] Steven W. Stahler. Deuterium and the Stellar Birthline. *ApJ*, 332:804–825, September 1988.

[137] Steven W. Stahler. Understanding Young Stars - A History. *PASP*, 100:1474–1485, December 1988.

[138] Steven W. Stahler. The Early Life of Stars. *Scientific American*, 265:48–55, July 1991.

[139] Steven W. Stahler. Early stellar evolution. *PASP*, 106:337–343, April 1994.

[140] Edward Sterl Phinney, III. *A Theory of Radio Sources.* PhD thesis, University of Cambridge, November 1983.

[141] A. Richard Thompson, James M. Moran, and George W. Swenson, Jr. *Interferometry and Synthesis in Radio Astronomy.* Krieger Publishing Company, Krieger Drive, Malabar, FL 32950, USA, 1994 re-issued, corrected, reprinted edition, 1986.

[142] E. L. Turner, J. P. Ostriker, and III Gott, J. R. The Statistics of Gravitational Lenses - the Distributions of Image Angular Separations and lens Redshifts. *ApJ*, 284:1–22, September 1984.

[143] Albrecht Unsöld and Bodo Baschek. *The New Cosmos.* Springer-Verlag, Germany, 4th completely revised english edition, 1991. Translated from the 4th German edition.

[144] C. Megan Urry and Paolo Padovani. Unified Schemes for Radio-loud Active Galactic Nuclei. *PASP*, 107(715):803–845, September 1995.

[145] Gerrit L. Verschuur and Kenneth I. Kellermann, editors. *Galactic and Extragalactic Radio Astronomy.* Springer-Verlag, New York, NY, USA, 1st edition, 1974.

[146] Gerrit L. Verschuur and Kenneth I. Kellermann, editors. *Galactic and Extragalactic Radio Astronomy.* Springer-Verlag, 175 5th Ave., New York, NY 10010, USA, 2nd edition, 1988.

[147] J. V. Wall. Populations of Extragalactic Radio Sources. In Goddard and Haynes [53], pages 625–655. Papers presented at the John G. Bolton Memorial Symposium, Parkes Observatory, NSW, Australia, 9–10 December 1993.

[148] J. V. Wall and C. A. Jackson. Dual-Population Radio Source Unification. *MNRAS*, 290:L17–L22, September 1997.

[149] D. Walsh, R. F. Carswell, and R. J. Weymann. 0957 + 561 A, B - Twin Quasistellar Objects or Gravitational Lens ? *Nature*, 279:381–384, May 1979.

[150] Bruce A. Wilking, Charles J. Lada, and Eric T. Young. Iras observations of the rho ophiuchi infrared cluster - spectral energy distributions and luminosity function. *ApJ*, 340:823–852, May 1989.

[151] A. E. Wright and R. Otrupcek. PKSCAT90 – The Southern Radio Database. Technical report, CSIRO: Australia Telescope National Facility, Parkes, NSW, Australia, 1990. Available via anonymous ftp from ftp.atnf.csiro.au:/pub/data/pkscat90.

[152] J. Anton Zensus. Parsec-Scale Jets in Extragalactic Radio Sources. *ARA&A*, 35:607–636, 1997.